Harmonics in transmission power systems

Wiechowski, Wojciech Tomasz

Publication date:
2006

Document Version
Publisher's PDF, also known as Version of record

AALBORG UNIVERSITY

Harmonics in transmission power systems

Wojciech Wiechowski

Institute of Energy Technology

Danish System Operator of the Electricity and Gas Transmission Grids

Harmonics in transmission power systems

by

Wojciech Wiechowski

Dissertation submitted to the Faculty of Engineering, Science and Medicine
at Aalborg University
in partial fulfillment of the requirements for the degree of
Doctor of Philosophy in Electrical Engineering

Institute Of Energy Technology
Aalborg University, Denmark
October, 2006

PhD Thesis
Harmonics in transmission power systems

Printed in Denmark by Uni-print, Aalborg
October, 2006

ISBN

AALBORG UNIVERSITY
Institute of Energy Technology
Pontoppidanstraede 101
DK-9220 Aalborg Øst, Denmark.
www.iet.aau.dk

For my Mother

Preface

This thesis is submitted to the Faculty of Engineering, Science and Medicine at Aalborg University in partial fulfillment of the requirements for the Ph.D. degree in Electrical Engineering. The research was conducted at the Institute of Energy Technology (IET), Aalborg University.

The project was initiated by Jens Peter Kjærgaard and Jan Lykkegaard from the Electricity Transmission Department of Danish Transmission System Operator Energinet.dk. Both Energinet.dk and Aalborg University sponsored this work and the purchase of measuring equipment.

This research was motivated by a desire of generating knowledge about harmonic distortion in high voltage transmission networks, harmonic modelling of components of such networks and high voltage harmonic measurements.

The aim of this work was to create a harmonic model of the transmission network in Jutland and Funen suited for harmonic analysis purposes and to verify it with harmonic measurements on the 400 kV level.

Three supervisors followed the project: Associate Professor Birgitte Bak-Jensen and Associate Professor Claus Leth Bak from Aalborg University and Jan Lykkegaard from Energinet.dk.

In autumn 2004 I spent three months at the consulting and software company DIgSILENT GmbH, Gomaringen in Germany, working under the guidance of Dr-ing. Markus Pöller, the Manager of Power System Applications & Consulting division, where I was developing the hybrid time/frequency model of HVDC converter and implementing the model of nonlinear transformer core in the simulation software PowerFactory.

Knowledge gained while working on this project resulted in organizing, together with Lucian Asiminoaei, Ph.D. student (IET), two sets of lectures, exercises and laboratory sessions for students: “Fundamentals of Power System Harmonics” and “Advanced Analysis and Mitigation Techniques of Power System Harmonics”. These courses have been given every semester since 2004. Also a 3-day version of the course was prepared, offered to industry engineers and PhD students: “Harmonics in Power Electronics and Power Systems”.

This thesis is structured in 9 chapters and appendices. An overall literature reference and a list of authored and co-authored publications written during this research project are presented at the end of the thesis. Literature references are shown as [X, 0000], where X is the surname of the main author of the reference and 0000 is the year of publication. Year of publication is given only if there is more than one publication of this author cited. References to figures and tables are shown as Figure C.F. or Table C.F and references to equations are shown as Equation (C.F.), where C is the chapter number and F indicates the figure, table or equation number in the actual chapter or appendix.

Acknowledgements

I owe gratitude to many people that helped me in various ways during the work on this research project. In particular, I would like to tank:

- My supervisors, Birgitte Bak-Jensen, Claus Leth Bak and Jan Lykkegaard, for their support and comments to my work during the entire project period. Additionally, I thank Jan Lykkegaard for the help with preparation and carrying out harmonic measurements in summer 2005 and for Energinet.dk's financial support to purchase the measuring equipment,

- Jesper Bak, Gunner Schmidt and Per Hertzum-Larsen from Electricity Transmission Dept, Energinet.dk, for the help with harmonic measurements,

- Martin Gunge from IET, for the help with harmonic measurements,

- Hans Abildgaard from Planning Dept, Energinet.dk, for the PowerFactory fundamental frequency load-flow models,

- All the people working at DIgSILENT GmbH for the cordial hospitality they showed. The months I spent in Gomaringen were very fruitful for my project. Especially I thank Dr.-ing. Markus Pöller, for his invaluable advice and guidance. I also want to thank Edgar Zimmermann and Flavio Fernandez, Analytical Engineers, for the help with implementation of the models in PowerFactory,

- Frans J. Sollerkvist formerly from STRI AB, now Carl Bro AB, for many pieces of advice concerning harmonic measurements and harmonic modelling issues,

- Lucian Asiminoaei, former Ph.D. student from IET and my colleague, who is now with Danfoss, for numerous professional discussions and for the great co-operation while preparing the courses on harmonics,

- Students Kim Søgaard, Jacek Wasilewski and Per Holst, for their contribution to the project.

Wojciech Wiechowski
October 2006, Aalborg

Abstract

Some time ago, Energinet.dk, the Transmission System Operator of the 150 kV and 400 kV transmission network in Denmark, had experienced operational malfunctions of some of the measuring and protection equipment. Also an overloading of a harmonic filter has been reported, and therefore, a need to perform more detailed harmonic studies emerged. Since the transmission network has a complex structure and its impedance varies with frequency in a nonlinear fashion, such harmonic study would require a detailed computer model of the network. Consequently, a PhD project proposal titled “Harmonics in transmission power systems” was formulated.

In this project, the entire 400 kV and 150 kV western transmission network of Energinet.dk is modelled using the simulation software DIgSILENT PowerFactory. A fundamental frequency load-flow model is used as a basis that is to be extended. The model is sought to be applicable for harmonic frequencies in the range from 50 Hz up to 2,5 kHz and should be verified by harmonic measurements.

The task is divided into modelling of the linear transmission network components and modelling of the nonlinear transmission network components that are installed directly on the transmission level, namely the transformer core nonlinearities and the HVDC converters.

While modelling the linear, frequency dependent components in the harmonic domain, priority is given to modelling the transmission lines, especially the effects of distributed parameters, the skin effect, the non-ideal ground return, the line unbalance and the sag of the conductors. The solution for the skin effect involves Bessel series and for the non-ideal ground it involves Carson series. Both aspects can be modelled in PowerFactory and are verified in the project by hand calculations. All other shunt and series linear elements are also considered and the aspects that have to be included in the models are pointed out.

The intention is to verify the created linear model of the network by harmonic measurements. Consequently, various verification techniques based on harmonic measurements are investigated. It is concluded that since some background harmonic distortion is practically always present in the network, a method based on variation of harmonic values must be used. The incremental values of harmonic distortion will allow to verify the harmonic model, despite the existence of background harmonic distortion, provided that background harmonic distortion, and the network configuration, are not changing during the measurement.

It is shown that switching of a shunt linear power system component can result in variation of the harmonic levels that can be measured and used to verify the harmonic model of the network. Three novel methods are also proposed, where switching of a series component can be used for the same purpose. Two of these methods are based on the determination of transfer harmonic impedance of the network and the third approach, which is actually used in the project, is based on injection of the incremental values of harmonic currents directly into the created computer model using current sources, and comparing the obtained harmonic voltage increments with the ones measured in reality.

The harmonic increments must be as high as possible, in order to ensure the highest signal-to-noise ratio. Therefore, in order to determine which power system component, when switched, results in the largest change in harmonic levels, some initial harmonic simulations, using the created harmonic model of Energinet.dk transmission network, are performed. The criterion is that the measuring equipment shall not be installed more than 100 km away from the city of

Aalborg. The simulations show that in such a case, the largest harmonic increments can be obtained by switching one of the 400 kV transmission lines.

Therefore, the following technique is applied. Harmonic currents and voltages are simultaneously measured using GPS-synchronized OMICRON CMC256 units. Two such units are installed at 400 kV substations at both ends of the disconnected line and a third unit is located at a substation in a distance of 80 km. Time domain "snap-shot" measurements of three-phase voltages and currents are synchronously taken for some period of time. The line is switched out and in, three times in row, and the harmonic currents and voltages are measured. In total, 24 channels are used for voltage and current measurement. 90 snapshot-measurements are performed, during 45 minutes. Harmonic frequencies up to the 50^{th} harmonic are monitored. All of the gathered data are later processed in Matlab.

The results show that the switching of the line affected mainly the levels of higher harmonics; lower order harmonics were not affected as much as the initial simulations indicated. The harmonic increments at higher frequencies are sufficiently large to be used for verification purposes.

The created network model is adjusted using the SCADA measurements of the actual conditions prevailing in the entire network, exactly at the time when the harmonic measurements were performed. These SCADA measurement results, obtained from Energinet.dk, are imported into the PowerFactory network model.

In the next step, the harmonic currents measured at both ends of the line are assigned to current sources and injected into the linear network model. The resultant voltage increments obtained in the simulation are compared with the voltage increments measured in reality. The results of this verification show that the incremental values of the harmonic voltages at three substations obtained in simulations and from the measurements agree for most of the harmonic frequencies. The differences are below 10% and are due to such factors like synchronization error of the measurements. The conclusion is that a key requirement of this technique is a good synchronization of the measurements.

Capacitive voltage transformers installed at the 400 kV substations are not suited to measure higher frequencies and the capacitive taps of the 400 kV/150 kV autotransformer bushings are used. Coaxial cables are lead for hundred of meters through the high voltage switchyard from the capacitive taps to the OMICRON units placed in the control rooms. The electromagnetic environment at a high voltage substation is very hostile, so various grounding techniques of the cables are inspected and measurements prior to the main measurement are performed. Configuration that reduces the level of noise induced in the cables to the possible minimum is found. It is confirmed that a way to reduce the magnetic coupling is to minimize the area of the loop; therefore the measuring circuit must be grounded at one end only so the ground is not used as a return path. A way to reduce the capacitive coupling is to provide shielding.

Harmonic currents are measured using the conventional inductive voltage transformers. Both protective and metering cores were compared if they could be used for harmonic measurements. The comparison shows that results obtained used both types of the cores are the same, so it is concluded that both cores can be used for harmonic measurements. Low-inductance resistors are introduced in the secondary circuits, in series with the metering and protective relaying. On those resistors, the harmonic voltage drop was measured.

The subsequent tasks of the project concern modelling of non-linear components present in the transmission network, HVDC converters and transformer core nonlinearities. Modelling of large frequency dependent linear networks in the time domain involves approximations by rational functions and it is time consuming. The frequency dependent impedances can be best modelled in the frequency domain where exact solution can be calculated. On another hand, modelling of nonlinear components is most precise in the time domain. In this project an iterative, three-phase,

hybrid time/frequency method is developed. The method enables to model linear networks in the harmonic domain, and the HVDC converters in the time domain. This developed model is implemented in the PowerFactory software. The results are verified with precise time domain simulations. The method converges after 4 - 6 iterations. It is presently used in the steady-state harmonic calculations, but it is concluded that after some future adjustments it can be used for inter-harmonic simulations and simulations of dynamically varying harmonics, as well.

Implementation of a nonlinear transformer core model [Neves] is shown. The core nonlinearities can be determined using $V_{rms} - I_{rms}$ curves and the no-load losses. Such data are present in the typical test reports of power transformers. The method is implemented using the DIgSILENT Programming Language (DPL) and verified with the original data from [Neves] and with measurements performed on a low voltage transformer. It is concluded that the method initially designated for single phase transformers, under certain circumstances can be used for modelling nonlinearities of three-phase autotransformers.

In general, it can be stated that the aim of the project is reached. The linear Western transmission network model is examined and models are extended so can be used for harmonic analysis studies. The model is verified by harmonic measurements. Additionally, both the hybrid time/frequency model and the implemented model of nonlinear transformer core are implemented in the PowerFactory software and verified with measurements or time domain simulations.

Dansk Resumé

Systemoperatøren for 150 kV og 400 kV transmissionsnettet i Danmark, Energinet.dk, har for nogen tid siden oplevet operationelle fejlfunktion på dele af deres måle- og beskyttelsesudstyr. Derudover har der også været reporteret om overbelastning af harmoniske filtre tilsluttet transmissionsnettet. Dette førte til et behov for et mere detaljeret studie af harmoniske frekvenser i transmissionsnettet. På grund af transmissionsnettets kompleks struktur og at impedanserne i nettet varierer ulineært med frekvensen, kræver et sådant harmonisk studie en detaljeret computermodel af transmissionsnettet. Konsekvensen af dette førte til et PhD-projektforslag med titlen ”Harmonics in transmission power systems”.

I dette projekt er der opstillet en model for hele Energinet.dk’s 400 kV og 150 kV transmissionsnet i Vestdanmark vha. simulationssoftwaren DIgSILENT PowerFactory. Der er anvendt en load flow model for grundtonen som basis, der er søgt udvidet til at være anvendelig i frekvensområdet fra 50 Hz til 2,5 kHz og verificeret vha. harmoniske målinger

Opgaven er delt op i modellering af lineære og ikke lineære komponenter i det harmoniske frekvensdomæne, der er installeret direkte på transmissionsniveau.

Under modellering af de lineære frekvensafhængige komponenter i frekvensdomænet, er der lagt vægt på modellering af transmissionslinier speciel med hensyn til effekten af fordelte parametre, skineffekt, den ikke ideelle returleder, ubalance for linien og nedhæng af lederne. Løsningen til skineffekt involverer Bessel-serier og for den ikke ideelle returleder involverer det Carson-serier. Begge aspekter kan modelleres i PowerFactory og er verificeret vha. egne beregninger. Alle øvrige lineære shunt- og seriekomponenter er også undersøgt og aspekter, der skal inkluderes i modellerne, er fremhævet.

Intentionen er at verificere den opstillede lineære model for transmissionsnettet vha. harmoniske målinger. Som en konsekvens af dette, er der undersøgt forskellige verifikationsteknikker baseret på harmoniske målinger. Det er konkluderet, at fordi der altid vil være en vis harmonisk baggrundsforstyrrelse i nettet, er det nødvendigt at anvende en metode baseret på variation af det harmoniske indhold i nettet. En forøgelse af det harmoniske frekvensindhold i nettet vil gøre det muligt at verificere de harmoniske modeller på trods af de harmoniske baggrundsforstyrrelser. Dette er forudsat, at de harmoniske baggrundsforstyrrelser og konfiguration af nettet ikke ændres under målingerne.

Det er vist, at ind og udkobling af en lineær højspændingskomponent i form af en shunt vil resultere i variation af det harmoniske indhold på nettet, der kan måles og anvendes til verifikation den harmoniske model for nettet. Tre nye metoder er også foreslået, hvor ind og udkobling af en seriekomponent kan anvendes til samme formål. To af disse metoder er baseret på bestemmelse af den harmoniske overføringsimpedans for nettet og den tredje fremgangsmåde, der er anvendt i dette projekt, er baseret på indfødning af harmoniske strømme direkte i den opstillede computermodel vha. strømkilder og sammenligne de opnåede harmoniske spændinger med de harmoniske spændinger fra målinger.

Forøgelsen af det harmoniske indhold på nette skal være så stor som muligt for at sikre et højt signal/støj-forhold. Med henblik på at bestemme hvilken komponent, der under ind og udkobling

vil resultere i den største ændring af det harmoniske frekvensindhold, er der foretaget indledende harmoniske simuleringer af den opstillede model for transmissionsnettet i Vestdanmark. Et kriterium for målingerne er, at måleudstyret ikke må være placeret mere end 100 km fra byen Aalborg. Simuleringerne viser, at der for denne situation opnås den største ændring i det harmoniske frekvensindhold ved ind og udkobling af en 400 kV transmissionslinierne.

I forbindelse med målingerne er der derfor anvendt følgende teknik, hvor harmoniske strømme og spændinger er målt samtidigt vha. GPS-synkronisering mellem flere OMICRON CMC256 måleapparater. To af disse måleapparater er placeret i hver sin ende af 400 kV transmissionslinien og en tredje er placeret i en afstand på 80 km. Der er løbende blevet taget øjebliksbilleder i tidsdomænet af trefasede strømme og spændinger over en periode, hvor transmissionslinien er blevet koblet ind og ud tre gange i træk. I alt er der anvendt 24 kanaler til strøm- og spændingsmålingerne og der er foretaget 90 øjebliksbilleder over en periode på 45 minutter. Vha. målingerne er der detekteret frekvenser op til den 50. harmoniske frekvens. Alle de indsamlede måledata er senere hen behandlet i MatLab. Resultaterne viser, at hovedsageligt højere harmoniske frekvenser blev påvirket af ind og udkoblingen af transmissionslinien., mens de lavere harmoniske frekvenser ikke blev påvirket i samme grad, som de indledende simuleringer forudsagde. Påvirkningen af de højere harmoniske frekvenser er dog tilstrækkeligt stor til at kunne anvendes til verifikationsformål.

Den opstillede model for transmissionsnettet er justeret vha. SCADA-målinger fra hele nettet for tidspunktet, hvor de harmoniske målinger blev udført. Resultaterne af SCADA-målingerne fra Energinet.dk er importeret til modellen for transmissionsnettet i PowerFactory.

I det næste skridt er de harmoniske strømme fra målinger i begge ender af transmissionslinien ført in i den lineære model for nette vha. strømkilder og de opnåede harmoniske spændinger vha. simuleringer er sammenlignet med de harmoniske spændingsmålinger. Resultatet af denne verifikation viser, at de simulerede harmoniske spændinger ved de tre målesteder passer overnes med de målte harmoniske spændinger for de fleste af de harmoniske frekvenser indenfor de grænser, der er bestemt af nøjagtigheden for synkroniseringen mellem måleapparaterne. Konklusionen på dette er, at en forudsætning for denne måleteknik er en god synkronisering mellem de anvendte måleapparater.

I forbindelse med målingerne på 400 kV ved transformerstationerne, er der foretaget målinger på de kapacitive udtag fra 400 kV/150 kV transformerne. Dette skyldes, at de kapacitive transformere ellers til rådighed ikke er egnede til måling af højere frekvenser. Der er derfor trukket flere hundrede meter koaksialkabel fra 400 kV/150 kV transformerne til OMICRON måleudstyret placeret i hvert kontrolrum ved de tre stationer.

Den elektromagnetiske udstråling er meget kraftig ved en transformerstation og der er derfor foretaget en undersøgelse af forskellige jordingsteknikker for kablerne og udført indledende målinger, før den endelige måling blev udført. Der er fundet en konfiguration, der reducerer den inducerede støj på kablerne til et minimum og det kan bekræftes, at en metode til minimering af den magnetiske kobling er ved at minimere de lukkede sløjfearealer for kablerne. Den valgte konfiguration er derfor en jording af målekredsløbene i kun den ene ende således, at jorden ikke anvendes som returleder. En metode til reducering af kapacitiv kobling er vha. afskærmning.

De harmoniske strømme er målt med konventionelle induktive strømtransformere. Både beskyttelses- og målekerne er undersøgt og en sammenligningen viser, at begge kernetyper kan anvendes til harmoniske målinger. På sekundærsiden af spændingstransformerne er der indsat modstande med en lav induktans i serie med målekredsløbene til måle- og beskyttelsesudstyret og de harmoniske strømme er målt i form af de harmoniske spændinger over modstandene.

Den efterfølgende opgave for dette projekt var at foretage en modeldannelse af de ulineære komponenter i transmissionsnettet, dvs. HVDC-konvertere og ulineariteten i transformerkerner. Modellering af store frekvensafhængige lineære netværk i tidsdomænet involvere approksimation af rationelle funktioner, hvilket er meget tidskrævende. Den frekvensafhængige impedans kan bedst modelleres i frekvensdomænet, hvor en eksakt løsning kan beregnes. På den anden side er modellering af ulineære komponenter mest præcis i tidsdomænet. I dette projekt er der udviklet en iterativ trefaset hybrid metode, der skifter mellem frekvens- og tidsdomænet og derved gør det muligt at modeldanne lineære netværk i frekvensdomænet og f.eks. HVDC-konvertere i tidsdomænet. Den udviklede model er implementeret i programmet PowerFactory.

Resultaterne er verificeret med præcise simuleringer i tidsdomænet. Simuleringerne viser, at den anvendte metode konvergere efter 4 – 6 iterationer. Metoden anvendes på nuværende tidspunkt til beregning af harmoniske frekvenser for stationære tilstande. Det er dog konkluderet, at den pågældende metode også kan anvendes til inter-harmoniske simuleringer og dynamisk varierende harmoniske simuleringer efter nogle fremtidige justeringer.

I dette projekt er der vist implementeringen af en ulineær model for en transformerkerne [Neves]. Kerneulineariteterne kan bestemmes ud fra $V_{rms} - I_{rms}$ kurverne og tabene ved ingen belastning. Disse data er til stede i en typisk testrapport for en effekttransformer. Metoden er implementeret i DIgSILENT programmeringssproget DPL og verificeret vha. originale data fra [Neves] og vha. målinger foretaget på en lavspændingstransformer. Det er konkluderet, at metoden oprindeligt anvendt til enfasede transformere under bestemte forhold kan anvendes til modellering af ulineariteterne for trefasede transformere.

Den overordnede konklusion for dette projekt er, at målet for dette projekt er opnået. Den lineære frekvensafhængige model for transmissionsnettet er implementeret og verificeret med harmoniske målinger. De ulineære modeller er implementeret i programmet PowerFactory og verificeret vha. målinger og simuleringer foretaget i tidsdomænet.

Table of contents

Chapter 1

Introduction

This dissertation presents a set of practical guidelines and focal points for modelling of an entire transmission network for harmonic analysis purposes. The 400 kV and 150 kV transmission network of Energinet.dk is modelled for that purpose using the computer simulation software DIgSILENT PowerFactory. State-of-the-art modelling of linear components is shown. The focus is put on verification of modelling overhead lines in PowerFactory, two nonlinearities present on the transmission level, namely HVDC converters and transformer core nonlinearities. Development of a Hybrid time/frequency HVDC converter model based on the HVDC benchmark model is presented and the implementation of a nonlinear transformer core model in the harmonic domain is discussed. Moreover, in the scope of this project are verification techniques and technical aspects of GPS-synchronized harmonic measurements in high voltage networks.

This chapter gives an overview of the factors that motivated this study. The aims of the project are underlined and the outline of this thesis is presented.

1.1 Background

The problem of non-sinusoidal waveforms in electrical power systems is not new - the first harmonic studies described in the literature are dated to 1890's. [Owen] reports that the first documented harmonic analysis was made in 1893, by Charles Proteus Steinmetz. Steinmetz had to solve a motor heating problem. He discovered that the reason was the current wave distortion and performed harmonic analysis using a special instrument called "wave meter". Later, power and telephone circuits were often placed on common right-of-way, and inductively coupled harmonics (originating from transformer magnetizing currents) were causing so large interference that the voice communication was some times impossible [Mack Grady]. Generally, at that time, nonlinear iron cores and rotating machinery was identified as the main source of waveform harmonic distortion [Acha].

In recent days harmonic problems become more complex, because of the introduction of harmonic-producing electronic equipment. Already in the 60s, traction applications had been using thyristors [Acha]. Today, besides the nonlinear iron cores of power transformers, there are lots of harmonic producing loads installed at all voltage levels. Typical non-linear loads at low voltage levels are TV-sets, computers, fluorescent lights with electronic ballasts, adjustable-speed drives, etc. Based on the research of German Association of Electric Utilities, in the beginning of 90s, 25% of the domestic loads were attributed to electronic loads [Schlabbach].

In addition, the increased use of shunt capacitors affect the harmonic levels in power networks, because of the alteration of system impedance. Together with the system inductance they may create resonance conditions and magnification of harmonics.

At the transmission system level nonlinear components also exist, for instance the HVDC converters, static VAR compensators, FACTS devices or power transformers. Transmission networks are particularly exposed to harmonic resonances because circuits have low resistance values and therefore the resonances have high quality factors [Fardanesh], [Dugan], [Arrillaga].

Since harmonic distortion of voltages and currents can have negative effects on system plant components, the need for performing harmonic studies and developing countermeasures to compensate for it is justified. The negative effects of harmonic distortion of voltages and currents usually pointed out in the literature [Wagner], [Smith], [Arrillaga], [Dugan], [Schlabbach], [Cividino], [Acha] are:

- reduction in the efficiency of the generation, transmission and utilization of electric energy because of harmonic power losses
- heating of system components caused by increased rms current value
- harmonic resonances resulting in excessive harmonic currents and voltages
- possibly increased crest factor
- ageing of the insulation of electrical plant components because of voltage or temperature stress
- stress on capacitor banks
- multiple zero crossings of voltage waveform that may affect synchronizing devices, accuracy of meters or converter controls
- effect on performance of electromechanical and electronic protective relays
- induced voltages and currents in the neighboring metallic structures and communication lines possibly degrading communication system performance
- vibration of some parts of power system components causing excessive audible noise (transformers with a laminated core)
- developed disturbing moments and noise in rotating machines
- harmonic currents can flow in adjustable speed drives through stray capacitance and motor bearings causing their failure
- triplen harmonics may overload neutral conductor in LV networks

A large number of papers concerning harmonic analysis in power systems has been already written. Only in IEEE/IEE database in the period 1988 – 2005, nearly 2000 papers dealing with various aspects of harmonics in power systems can be found, as shown in Figure 1.1, the majority of which written during the last decade.

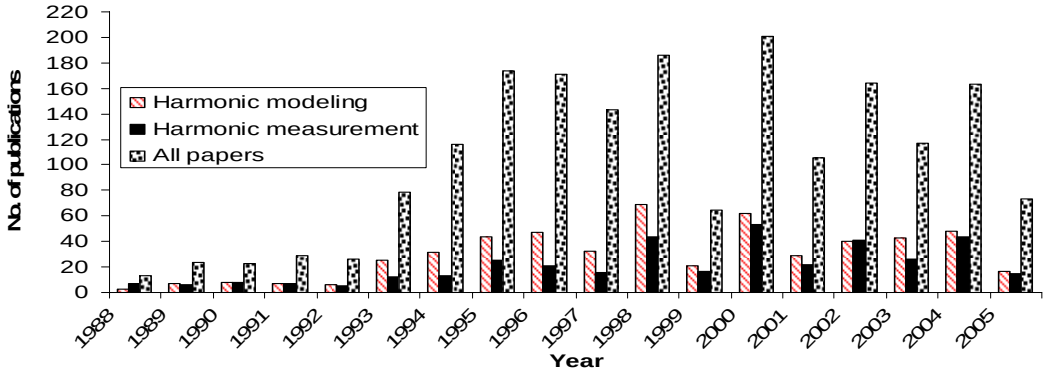

Figure 1.1 Number of IEEE/IEE papers per year in the period 1988 – 2005 dealing with power system harmonic analysis.

Among these 2000 papers, about 540 concern more specifically different harmonic modelling issues and 380 is related to miscellaneous aspects of harmonic measurements in power systems. Scientific papers on the subject were also written before year 1988 so the overall number of papers concerning harmonic analysis must be higher. A review of all the previous work described

in these publications would be very voluminous, and, therefore, only the main contributions related to the scope of this project are used and cited in this thesis.

1.2 Project motivation

Some time ago, Energinet.dk, the TSO of the 150 kV and 400 kV transmission network in Denmark, had experienced operational malfunctions of some of the measuring and protection equipment, as for instance protective relays and also an overloading of a harmonic filter has been reported [Andersen]. After a preliminary investigation it was concluded that the reason for that could be non-sinusoidal currents and voltages that propagate in the transmission grid. The causes of this increasing amount of harmonics were unraveled because the content of voltage and current distortion was constantly changing, somehow depending on the composition of the generation and the load, network configuration etc. For illustration, some results of monitoring of 5th and 7th voltage harmonic performed at one of the 400 kV substations during a one-week interval are shown in Figure 1.2.

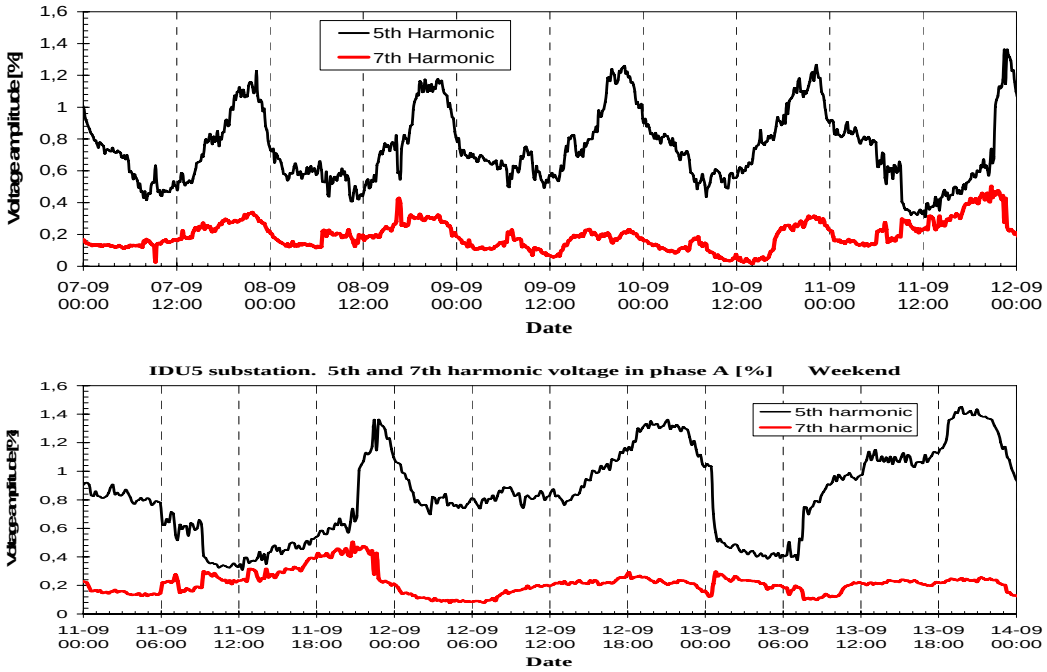

Figure 1.2 Weakly variation of 5th and 7th harmonic in the voltage of phase A, measured at substation IDU5 in Denmark (400 kV level). Upper plot shows weekdays and lower plot the weekend. These results were obtained from Energinet.dk.

Typical variation of the 5th harmonic can be recognized [Morrison], [Dugan], [Arrillaga]. These values were relatively low, and didn't explain the encountered problems. Therefore the need came forward to perform more detailed studies of harmonic propagation in the network.

Such harmonic propagation studies could be made for instance with the help of harmonic state estimation techniques (HSE) [Watson, 2005], [Du], [Kanao], [Meliopoulos, 1994]. If some of the harmonic voltages and currents are measured and the parameters of electrical power system are known, it is possible to estimate the unmeasured harmonic voltages and currents and the location and magnitude of harmonic sources. However, the system is usually partially observable, due to the usually small number of expensive instrumentation available.

An alternative approach to analyze harmonic flows in the network is by performing harmonic analysis (HA). This method requires detailed model of the electrical power system and knowledge about the harmonic sources. If harmonic distortion generated by nonlinear

components are independent on the voltage distortion level, they can be represented by current (or voltage) sources and a direct (nodal) analysis can be performed [Arrillaga], [Arrillaga, 1997], [Acha], [Herraiz], [Dugan], [Watson, 2005], [Schlabbach].

Both HSE and HA require the knowledge of the nodal admittance matrix of the studied system. A separate admittance matrix of the network is needed at each frequency of interest. The matrices are built up of the parameters of various system components, some of which are frequency dependent. Therefore, in both cases, to perform harmonic propagation studies, a linear, frequency dependent harmonic model of the examined network is needed.

1.3 Aim of the project

Taking into consideration the expectations of Energinet.dk, and after initial literature survey, the aim of the project has been defined as:

Harmonic domain modelling and verification of the entire 400 kV and 150 kV transmission system in Jutland and on the island of Funen, Denmark, model verification techniques based on harmonic measurements, hybrid modelling of HVDC power converters and modelling of transformer iron core nonlinearities.

The expected results of the project are:

i) State-of-the-art linear model of the 400 kV and 150 kV transmission network in Jutland and on the island of Funen, comprising of the models of the following main power system components:

   transmission lines, harmonic filters, shunt capacitors, linear impedances of power transformers, synchronous and asynchronous machines, shunt reactors, equivalent models of loads aggregated at the 60 kV busbars of 150/60 kV transformers

   The model must be verified with real-life harmonic measurements

ii) Hybrid, time/frequency model of an HVDC converter,

iii) Transformer core nonlinearities model implemented in the DIgSILENT PowerFactory software

The models shall be implemented in the DIgSILENT PowerFactory software and should reflect the behavior of the real components for harmonic frequencies up to the typical range 2,5 kHz [Arrillaga]. The DPL language will be used for modelling of ii) and iii). All the models have to be verified. Model i) will be verified with harmonic measurements on the high voltage network, model ii) will be verified with time domain simulations and model iii) will be verified with results of measurements on a power transformer.

1.3.1 Frequency dependent model of the linear transmission network

All important components with theirs frequency dependent parameters must be included in the transmission network model. This model must be verified with high voltage harmonic measurements.

Verification of the linear model by harmonic measurements

For monitoring the background levels of harmonic distortion it is necessary to carry the measurements for longer periods of time [Arrillaga], [Thunberg]. To verify simulation studies or fine-tune computer models it is sufficient to perform only snapshot measurements. In this case it is important to obtain results, which are independent from the variation of background harmonic distortion, therefore the measurements shall be made under several operation modes. Such measurements may be performed at single or multiple locations [Thunberg]. If measurements are

performed at more than one location and the phase angles of harmonics are required, then the measuring instruments must be precisely synchronized [Thunberg], [Arrillaga], [Meliopoulos], [Meliopoulos, 2000], [Fardanesh], [Kanao], [Ukai]. Thanks to synchronized measurements performed at several locations simultaneously, the largest amount of information is gathered so the verification of the harmonic model is enhanced [Thunberg].

The purpose of GPS-synchronized harmonic measurement performed during this project is the verification of the linear model of the 400 kV and 150 kV transmission network in Jutland and Funen. The measurements were performed at three substations on the 400 kV level.

1.3.2 Models of transmission network nonlinearities

At the transmission level of Energinet.dk network, principally two types of nonlinear network components can be found. These are: *i)* 12-pulse-configured, power electronic converters of HVDC links and *ii)* iron cores of power transformers and shunt reactors.

There are two possibilities of performing harmonic analysis, either in time or frequency domains. Frequency domain is intrinsically accurate for modelling frequency-dependent linear power system components. It provides great accuracy and speed of calculations [Acha], [Arrillaga], [Arrillaga, 1995], [Xia], [Xu, 1991]. Time domain is intrinsically accurate for modelling nonlinear or time dependent power system components. For that purpose it is very accurate, flexible and easy to perform [Dommel], [Mohan], [Arrillaga], [Watson], [Semlyen].

It is also possible to do the opposite, namely to model nonlinear system components in the frequency domain and linear, frequency-dependent components in the time domain. But:

While the simulations using nonlinear component models created in the harmonic domain are fast, the creation of the model itself is time-consuming and difficult because a set of non-linear equations describing the transfer of harmonics through the device must be derived. Moreover, different models must be created for each non-linear device [Bathurst], [Bathurst, 2000], [Bathurst, 2001], [Arrillaga], [Arrillaga, 1997], [Watson, 2005]. For example, in the case of deriving a HVDC converter model in the harmonic domain, the necessary variables are: the terminal voltage harmonic phasors, the dc current harmonics, the firing instants, the end of commutation instants, the average delay angle and the average dc current. For calculation of every harmonic up to the 50^{th}, there are 426 unknowns for a 6-pulse converter and 726 unknowns for a 12-pulse converter [Watson, 2005], [Arrillaga, 1997].

Modelling of the linear part of transmission network involves transmission line modelling. Frequency-dependent untransposed transmission lines have frequency-dependent modal transformation matrices T (calculated using eigenvalue analysis) [Dommel]. If the calculation is to be performed in the frequency domain, it is easy to evaluate theses transformation matrices T at each frequency of interest. Therefore frequency domain modelling using the modal circuits gives exact solution [EMTDC], [Marti]. If a transmission line is to be modelled in the time domain, these transformation matrices T are assumed constant or curve-fitted [EMTDC], [PowerFactory]. These simplifications introduce errors [EMTDC], [Wedepohl], [Marti], [Gustavsen], [Gustavsen, 1998], [Castellanos], [Abur]. An additional disadvantage of modelling large transmission networks in time domain is that it requires long simulation times.

Hybrid Time/Frequency harmonic modelling of HVDC converters

Therefore, some work has been done on hybrid methods that combine time and frequency domains and overcome the previously mentioned difficulties. In hybrid modelling, linear frequency-dependent networks are modelled in the frequency domain and nonlinear components are modelled in the time domain. Such algorithms are especially useful for modelling large transmission systems containing power converters, as concluded by [Medina]. So far, not much work has been done in this area. The initially presented hybrid algorithms, developed by [Semlyen] are used for solution of single-phase systems. [Medina] in 2004 stated that the

developments of hybrid model for practical three phase systems are currently in progress. However already in May 2003 [Moreno] presented a three-phase load-flow in frequency and time domains, where as the indication of the convergence he uses the differences in updated magnitudes of fundamental frequency bus voltages. In this project, a three-phase HVDC model will be developed in the hybrid time/frequency domain, where as the indication of convergence, the magnitudes and phase angles of the fundamental and low order characteristic harmonics are used, so it is possible to see when and how are the harmonic frequencies settling down. This model was implemented in the DIgSILENT PowerFactory software using the DLP language and verified with precise time domain simulations, in autumn, 2004.

Transformer core nonlinearities

It is possible to model transformer core nonlinearity in the time domain (EMT) simulation of DIgSILENT PowerFactory [PowerFactory]. In the frequency domain it is not possible to do it so far. Several ways of modelling the iron core nonlinearities exist, described for instance in [Dugui], [Santesmases] or [Chua]. These methods require that the dynamic hysteresis loops of the material are known. This is not always possible, especially if the nonlinearities of older transformers are of interest. In this project the only data available for the autotransformers are typical test reports. Therefore, a different method has been found, where the core nonlinearities can be determined using a simpler set of input data [Neves]. For computation, the method requires only $V_{rms} - I_{rms}$ curves and the no-load losses at fundamental frequency. These data are present in the test reports. In this project, the modelling of transformer core nonlinearity using the DIgSILENT Programming Language (DPL) is shown. This model is verified with harmonic measurements of the no-load current of a small, single phase power transformer.

1.4 Key features of the selected simulation software

The selected simulation software DIgSILENT PowerFactory is already in use by Energinet.dk for load-flow and stability studies. The software is flexible in the sense that it is possible to perform simulations both in time and in frequency domain. It also possesses its own simulation language, DIgSILENT Programming Language, (DPL), which is similar to C++ [PowerFactory]. With respect to the discussion from section 1.2, the crucial models for harmonic analysis are: transmission lines, power electronic converters and transformer core nonlinearities. These components are currently modelled in the PowerFactory software in the way shown in Table 1.1.

Model	Time domain simulation		Frequency domain simulation	
Unbalanced transmission line*	Modal domain. Transformation matrices T approximated	–	Modal domain. Transformation matrices T are frequency dependent	OK
Power electronic converters	State-of-the-art time domain modelling of power electronic converters	OK	Current source injecting idealized spectrum with the current harmonic Ih of amplitude 1/h, where h is the harmonic order	–
Transformer core nonlinear reactance	Modelled by polynomial function; defined: linear reactance, saturated reactance, knee-flux point and saturation exponent	OK	Linear impedance	–

Table 1.1 Comparison of the time and frequency domain modelling of three most important power system components in DIgSILENT PowerFactory software. (* - modelling of transmission lines is discussed in chapter 3).

The linear, frequency dependent transmission line model is well modelled in the frequency domain, whereas nonlinear components are modelled best in the time domain. The power converters are modelled in the frequency domain by first, determining the fundamental current component I_1 in the load-flow (unbalanced) studies, and then in the second step, the direct harmonic nodal analysis is started, where the harmonic currents I_h generated by HVDC converters are simply calculated as $I_h = I_1 \cdot \frac{1}{h}$, where h is the harmonic order, and injected by ideal current sources. No commutation or interaction with the bus voltage is taken into account. Such level of simplification has been considered not sufficient and ought to be improved. Similarly the transformer cores are modelled as constant linear impedance, therefore not injecting harmonic currents when transformer is saturated.

1.5 Methods

The solution method that will allow achieving the aim of the project is composed of the following items:

Literature survey

Literature survey has been made continuously at various stages of project realization. The following topics have been the main focus of this survey:

- Harmonic distortion in power systems – an overview
- Mathematical models of linear and nonlinear power system components for harmonic analysis studies
    - Identified linear components that *affect* harmonic levels to the largest extent are transmission lines, harmonic filters, shunt capacitors, series impedance of power transformers, synchronous and asynchronous machines, shunt reactors and the distribution network and the loads.
    - Identified nonlinear components present at the transmission network of Energinet.dk that *contribute* to harmonic distortion are power converters of HVDC links and saturating cores of power transformers
- Harmonic simulation techniques (methods and algorithms)
- techniques and methods of verification of harmonic models
- Technical aspects of harmonic measurements on high voltage transmission networks

Building a computer model of the transmission network in Jutland and Funen

This task is subdivided into two:

- Modelling of linear network components
- Modelling of nonlinear network components

The models used in the existing load-flow model are analyzed, and as a result, all oversimplifications are found. It is concluded what are the necessary improvements of the models to use them for harmonic analysis.

If the simplifications are resulting from the insufficient data used for modelling, then an adjustment is made, otherwise if the simplifications are resulting from software limitations, an attempt is made to develop and implement the missing models in the software.

Verification of created models

- Verification of the entire linear model of the transmission network
  - Analysis of various verification techniques based on harmonic measurements
  - Planning of the high voltage harmonic measurements
  - Carrying out GPS-synchronized harmonic measurements at three 400 kV substations synchronously
  - Verification of the linear model
- Verification of the nonlinear models implemented in the simulation software
  - Hybrid time/frequency model of the HVDC link verified against time domain simulation
  - Model of transformer core nonlinearity verified by comparison with original data and with measurements on a small power transformer

Conclusions from the project and recommendations for future work

1.6 Outline of the thesis

All the above-discussed topics that this research work contains will be described in the subsequent chapters. These chapters will be organized in the following way:

Chapter 1 Introduction

This chapter

Chapter 2 Key figures of the Western transmission network of Energinet.dk

This chapter contains a brief description of the Western transmission network that is to be analyzed. Also, the structure of the existing linear load-flow model of the network is described. Detailed description of modelling of particular components of this load-flow model is presented in chapter 3.

Chapter 3 Harmonic domain modelling of linear transmission network components

In this chapter, all of the linear components of the network model are analyzed with respect to their behavior at higher frequencies. Special focus is put to modelling transmission lines and their frequency dependent effects. Based on the conclusions from this chapter, the existing linear network model is extended. This extended network model is to be verified with real-life harmonic measurements.

Chapter 4 Analysis of validation techniques based on switching of network components

In order to verify the created linear network model by harmonic measurements, a proper verification technique must be selected. In this chapter, an analysis of such methods is presented. The focus has been put on methods where switching of a linear power system component results in a variation of the harmonic levels that can be measured and used to verify the harmonic model of the network. It is shown that both shunt and series elements can be used for that purpose. Two novel methods based on switching of a series element are proposed.

Chapter 5 Harmonic measurements on the 400 kV transmission network

As it was found in the previous chapter, both shunt and series elements can be used for verification. Therefore this chapter begins with initial harmonic domain simulations using the adapted linear network model, with the purpose of determining which component shall be switched to ensure the highest signal-to-noise ratio of the measurement. Also, best location for

measuring currents and voltages is determined. Next, practical aspects of GPS-synchronized harmonic measurements are considered. This includes harmonic voltage measurement and harmonic current measurement. The level of noise induced in coaxial cables led through high voltage switchyard is measured and optimal grounding technique is found. Harmonic measurements using protective and metering cores are compared. Then, the main measurement is described in detail, and example results of the measurement are shown. The obtained results will be used for verification of the linear model of the network. This verification process is addressed in the next chapter.

Chapter 6 Verification of the linear transmission network model

In this chapter the description of the verification of linear network model is described. Due to high level of unbalance of harmonic currents, an alternative verification method is proposed. The general idea of this verification method is explained. Next, the effect of synchronization error on the phase error of the measurement is discussed. Results of measurements are shown including the effects of synchronization errors. The effect of synchronization error on the modelling approach is presented and at the end, effects of measurements are compared with the effects of simulations using the created PowerFactory model.

Chapter 7 Hybrid time/frequency domain modelling of nonlinear components

In the previous chapters, the analysis, modification and final verification of the linear network model are described. In this chapter, the model and the simulation software is inspected whether it is possible to precisely model the HVDC converters in the frequency domain. It occurred that the modelling is simplified, i.e. idealized spectrum of power converter is used. Therefore, a hybrid time/frequency harmonic load-flow modelling technique is proposed. This technique and its development is described in this chapter in detail. The method is verified with precise time domain simulation.

Chapter 8 Modelling of transformer core nonlinearities

The last model that is inspected is the nonlinear core of power transformers. The software enables to model the transformer nonlinearities in time domain simulation. In the frequency domain it is not possible, and moreover, the time domain model requires knowledge about the magnetizing characteristic of the core. Therefore, an alternative algorithm has been found [Neves], where the rms curves and power losses only are needed to determine the transformer core nonlinearity. The results of implementation and verification of the algorithm are presented. The algorithm has been implemented using the DIgSILENT Programming Language (DPL) as an external script in the PowerFactory software. The algorithm is verified by harmonic measurements on a single-phase power transformer. A theoretical analysis of the core nonlinearities phenomena in single and three-phase transformers is also presented.

Chapter 9 Conclusion

This chapter summarizes the main conclusions of the project. The contributions that this project contains are highlighted and topics for future work are proposed.

Appendix A Paper: “Harmonic domain modeling of a distribution system using the DIgSILENT PowerFactory software”

Chapter 2

Key figures of the Western transmission network of Energinet.dk

The purpose of this chapter is to introduce the structure and list the main components of the Western Danish transmission network owned by transmission system operator Energinet.dk and to describe the existing fundamental frequency load-flow model of the network. The load-flow model is built in the DIgSILENT PowerFactory software and will be adapted for harmonic analysis studies.

2.1 Introduction

Danish transmission system consists of 400 kV and 150/132 kV facilities [Energinet.dk]. Energinet.dk owns the substations and the grid at the highest voltage level – 400 kV – as well as interconnections to Norway, Sweden and Germany. Energinet.dk also owns the cables between the mainland and the Horns Rev offshore wind farm and the submarine cable to Læsø [Energinet.dk]. The 150/132 kV installations are owned by the regional transmission companies that make the 150/132 kV grids accessible to Energinet.dk [Energinet.dk]. The transmission grid of Denmark is separated into two parts. One part covers Jutland peninsula and the island of Funen (the Western part) and the other part is covering Zealand and Bornholm islands (the eastern part), see Figure 2.1 on page 12. Presently there is no AC or DC interconnection between the two systems. They are not working synchronously. The Western grid is connected via two 220 kV AC lines to Germany and is a part of the European system UCTE (Union for the Co-ordination of Transmission of Electricity), whereas the eastern part works synchronously with the NORDEL interconnected Scandinavian system as it has AC connections to Sweden. A dc interconnection – Great Belt – is planned to be built and to be commissioned in 2010.

In this project only the Western part of the transmission system (Jutland and the island of Funen) is considered. In the Western network, the 400 kV and 150 kV grids constitute the "backbone". There are also the two 220kV AC interconnection lines to Germany and two HVDC connections to Sweden and Norway (two poles Konti-Scan link 1 and 2 and three poles Skagerrak link 1, 2 and 3). The distribution system in the area mainly based on 60 kV radial networks supplied from each 150 kV substation. The distribution networks are owned and operated by the distribution companies [Energinet.dk].

Chapter outline

This chapter is organized as follows:

First, general information about the Danish electrical power system is presented. Next, a brief description of the existing fundamental frequency load-flow model, created in the DIgSILENT PowerFactory software is given.

Figure 2.1 Map of Denmark with electrical power system of Energinet.dk shown. From the left, the Jutland peninsula and interconnected island of Funen (the Western part) and the other two islands are Zealand and Bornholm [www.energinet.dk]. Red 400 kV lines, blue – dc lines, orange, dotted – 60 kV cable.

2.2 Key figures of the Western electrical power system

The power system is relatively small. According to [Energinet.dk] the maximum winter-peak load forecast in the year 2006 is 3,9 GW. The key figures are presented in Table 2.1. The table shows the distinctive feature of Danish electric power system: large total capacity of installed wind turbines. The total generation in the Energinet.dk Western area is approx. 7,6 GW while as much as 33,4 % of it is the installed wind power.

	Unit	Forecast for year 2006
Maximum load:	MW	**3,901**
Wind turbines	MW	2,560
Local CHP	MW	1,596
Conventional generators	MW	3,502
Total installed capacity:	MW	**7,658**
Norway (HVDC)	MW	1,040
Sweden (HVDC)	MW	720
Germany (HVAC)	MW	1,200
Total capacity of interconnections	MW	**2,960**

Table 2.1 Peak demand and installed capacity forecast for the year 2006 [Energinet.dk].

A summary of all the main components in the Western power system is given in Table 2.2.

400 kV level:	Quantity	Total [MVA]
substations	18	
transmission power lines	19	
transformers	21	7259 MVA
switchable capacitive filter banks	7	390 MVar
switchable capacitor bank	1	55 MVar
switchable reactive shunt compensators	7	620 MVar
HVDC poles	2	860 MW
conventional power plants	4	1488MW
220 kV level:		
substations	2	
transmission power lines	2	
transformers	2	600 MVA
150 kV level:		
substations	77	
transmission power lines	105	
transformers	126	12463 MVA
switchable capacitive filter banks	5	231 MVar
switchable reactive shunts	9	761 MVar
HVDC poles	3	820 MW
conventional power plants	6	2014 MW
offshore wind park	1	80 x 2 MW

Table 2.2 Summary of all the main components in the Western transmission network [Energinet.dk]

These data shall be compared with Figure 2.3 on page 15, where a conceptual structure of the entire Western power network is shown. The figure shows all voltage levels present in the Western transmission network: 400 kV, 220 kV, 150 kV and distribution levels: 60 kV, 10 – 20 kV, 0.4 kV.

2.3 Existing 50 Hz load-flow model of the Western transmission network

A 50 Hz load-flow model of the transmission network is created in DIgSILENT PowerFactory software. A view of the network modelled in the software is shown in Figure 2.2 on page 14. In this network model, all essential elements of the 400, 220 and 150 kV network, including these shown in Table 2.2, are modelled in detail necessary for load flow calculations. All of the distribution network feeders supplied from the 150/60 kV transformers are modelled with equivalent lumped circuits.

This model is used as a basis that is to be modified and used for harmonic analysis.

The following assumptions were made with respect to this model:

- All the data of all the components present in the obtained model are correct,
- The structure of the obtained model reflects the actual network configuration,
- Vector group of all power transformers with high voltage side of 150 kV or higher is represented correctly,
- All of the 400 kV, 220 kV and 150 kV transmission lines are present in the load-flow model

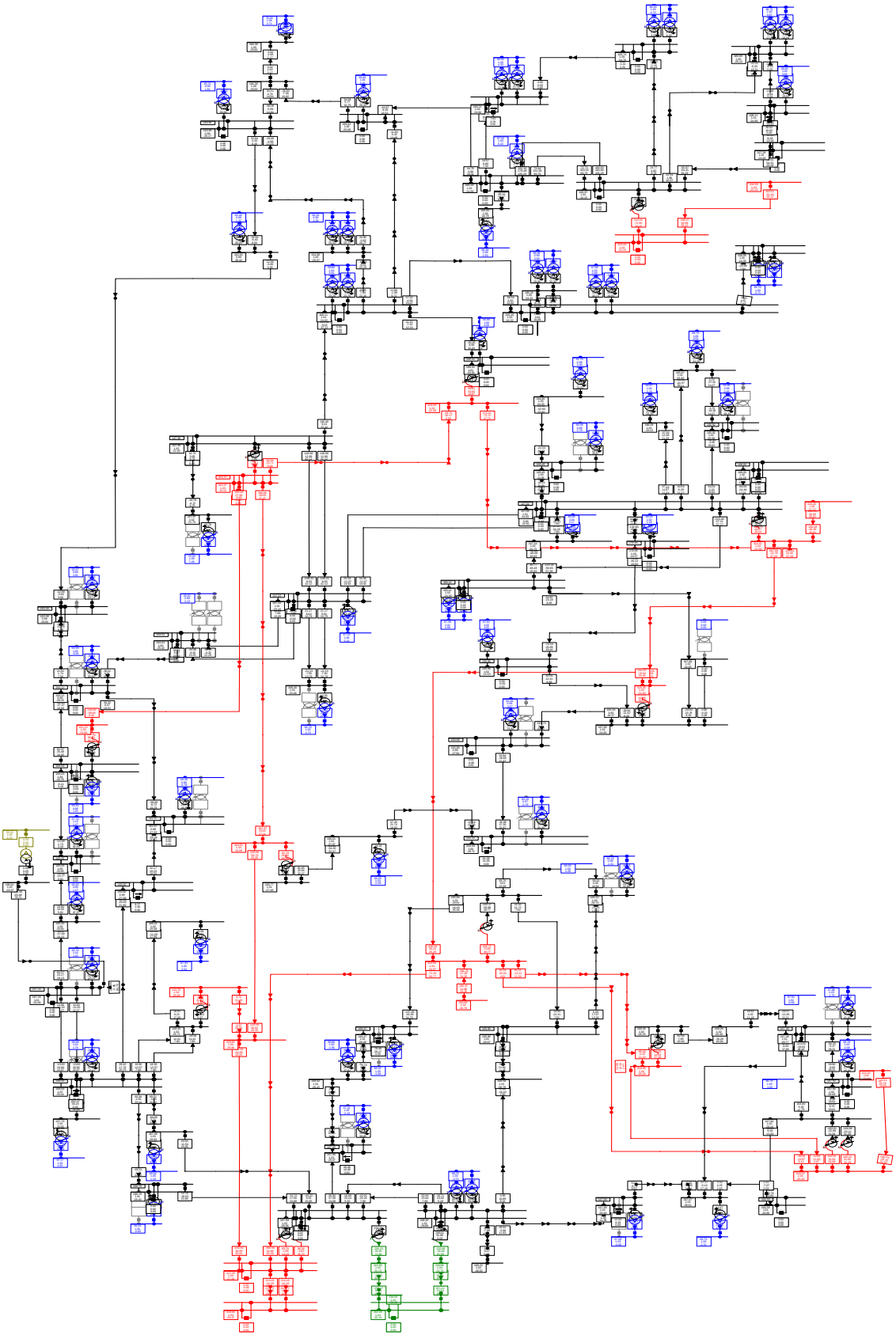

Figure 2.2 Load-flow model of Western transmission network of Energinet.dk made in DIgSILENT PowerFactory software. Red color – 400 kV lines and substations, black color –150 kV lines and substations, blue – 60 kV equivalent models of distribution network "islands".

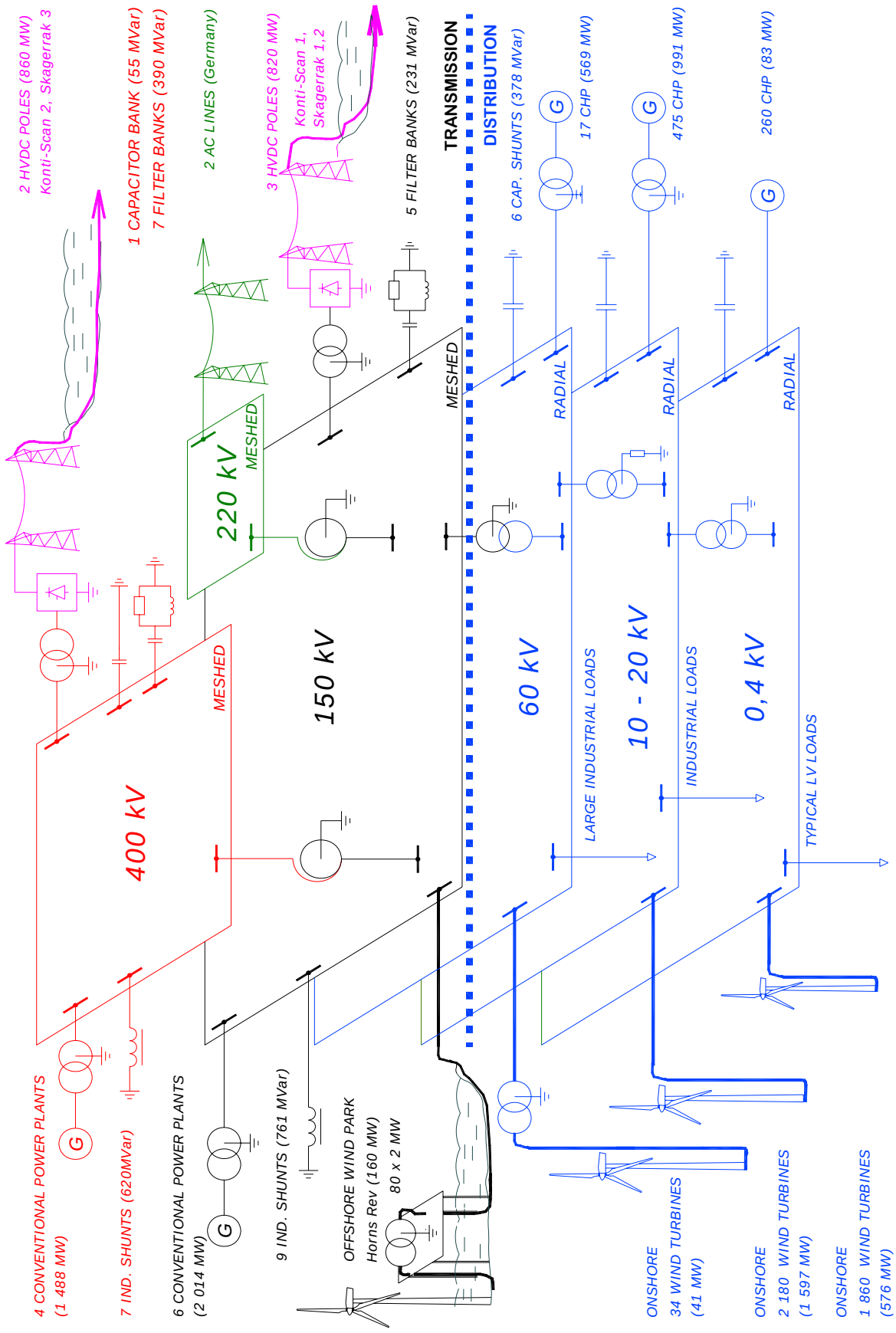

Figure 2.3 Structure of Western electrical transmission network of Energinet.dk

The models of power system elements used for 50 Hz load-flow are described below. The adjustments that have to be made to use them for harmonic analysis are discussed in detail in chapter 3.

Transmission lines

Transmission lines can be modelled in two ways:

a) By defining electrical parameters of the line (model *TypLne*):

Positive/negative and zero-sequence series inductance, resistance and shunt capacitance.

b) By defining geometrical dimensions of the towers and conductor data (model *TypTow*):

x,y co-ordinates of the phase conductors and earth wires, ground resistivity, conductor dc resistance, radius, internal inductance, bundle spacing - from which the software calculates the electrical parameters by itself.

Frequency dependence caused by the skin effect and non-ideal ground return of electrical parameters is calculated only for *TypTow*. However for *TypLne* is possible to define some frequency dependent characteristics manually.

In both cases *TypLne* and *TypTow* the nominal Pi circuit (lumped) or the equivalent Pi circuit (accounting for distributed parameters) can be used.

Line unbalance is taken into account only in case b). Unsymmetrical impedance matrices are calculated. However, the line may also be assumed perfectly balanced. In case a) the line can be only balanced.

Mutual coupling between two or more lines that are on the same right-of-way can be taken into account if lines are modelled using actual conductor geometry *TypTow* case b).

In the load-flow model, most of the lines are modelled as *TypTow,* which means that the exact geometrical dimensions of the towers and conductor data are present. The lines are divided into several sections, where each section is represented as a nominal Pi circuit. Moreover, ideal transposition is assumed and skin effect is ignored, but to include the distributed parameter model, skin effect, and "remove" ideal transposition, it is only a matter of selecting the proper options.

There are some sections of lines that are modelled by using the electrical parameters. These sections are modelled as lumped nominal Pi circuits, but can be converted to equivalent Pi circuits.

In some cases, the lines are divided into line routes *ElmLneroute*. This is done, because tower configurations often change along the line, and second, to include mutual couplings between some line sections. *ElmLneroute* elements can be both *TypLne* and *TypTow*. If an *ElmLneroute* is modelled as *TypLne,* so using the electrical parameters, it is modelled as lumped, nominal Pi circuit, and cannot be switched to equivalent Pi circuit. However, it can be divided easily into practically infinite number of nominal Pi circuits by introducing extra terminals along the line route.

Power transformers

For all power transformers where the high voltage side is 150 kV or higher, the following main data are present in the models:

Rated power, MVA; Short circuit voltage, %; copper losses, kW; zero-sequence short circuit voltage, %; resistive part of zero-sequence impedance, %, No-load current, %; no-load losses, kW; vector group.

Synchronous machines

Each of the synchronous generators of conventional power plants and also the two synchronous condensers are modeled using the standard synchronous machine model available in the program. The models have defined the following main reactance values: synchronous, transient and subtransient reactance, in both, p and q axes, p.u.; zero and negative sequence reactance, p.u. and are coupled to the network thought the unit transformers, as in reality.

However, the majority of the generators in the model are equivalent generators for representing the dispersed generation under each 150 kV substation [Energinet.dk]. All Combined Heat and Power units smaller than 10 MW are lumped and modeled as one equivalent synchronous machine under each 150 kV substation. Units with rated power higher than 10 MW are modeled individually [Energinet.dk] The main generator constants that are used for all of the Combined Heat and Power units are shown in Table 2.3. The network impedance between the machine and the 150 kV busbar is assumed to be 0.00 + j0.15 p.u. on machine MVA base [Energinet.dk].

Rs	Xl	Xd	Xq	X'd	X"d	X"q	X2	X0
p.u.	p.u.	p.u.	p.u.	p.u.	p.u.	p.u.	p.u.	p.u.
.0052	.0950	1.530	0.620	0.204	0.144	0.209	0.157	0.066

Table 2.3 Constants used for modelling synchronous machines representing CHP units [Energinet.dk], where Rs – stator resistance, Xl - stator leakage reactance, Xd, Xq, X'd, Xq, X"d, X"q synchronous, transient and subtransient reactances in d and q axes. X2, X0 – negative, zero sequence reactance.

Asynchronous machines

Generally, it can be assumed that all onshore wind turbines are modelled as standard induction machines [Energinet.dk]. Capacitive compensation is not present in the model.

There are 56 equivalent induction single-cage generators in the model. All of them have specified the following data:

Rs	Xs	Xm	RrA	XrA
p.u.	p.u.	p.u.	p.u.	p.u.
0.00744	0.0966	4.0252	0.00667	0.1168

Table 2.4 Constants used for modelling asynchronous machines representing wind turbines [Energinet.dk], where Rs – stator resistance, Xs - stator leakage reactance, Xm - magnetizing reactance, RrA - rotor resistance, XrA - Rotor reactance.

All of them are connected to the 60 kV network via two-winding transformers; the transformers are not necessarily present in reality; they are used as an assumption of the network impedance between wind turbines and the substation. The 56 transformers have only the following basic data defined: Yn/d 65/0,69 kV; short-circuit voltage $U_{sc}\% = 21{,}07$ %, losses in the windings ΔP_{cu} = different for each transformer. The offshore wind park of 80, 2MW doubly-fed induction generators is modeled as one lumped induction machine, in the same manner like the onshore wind turbines.

Load models

The loads are modelled with balanced, simplified purely resistive/inductive (in parallel) equivalent models of all loads and supplied from the 150 kV bus, based on the specified active and reactive power demand. They are connected in ABC-YN. More details concerning load equivalent models are described in chapter 3.

60 kV network representation in the load-flow model

Example 60 kV network equivalent operated as island under a 150 kV substation is shown in Figure 2.4.

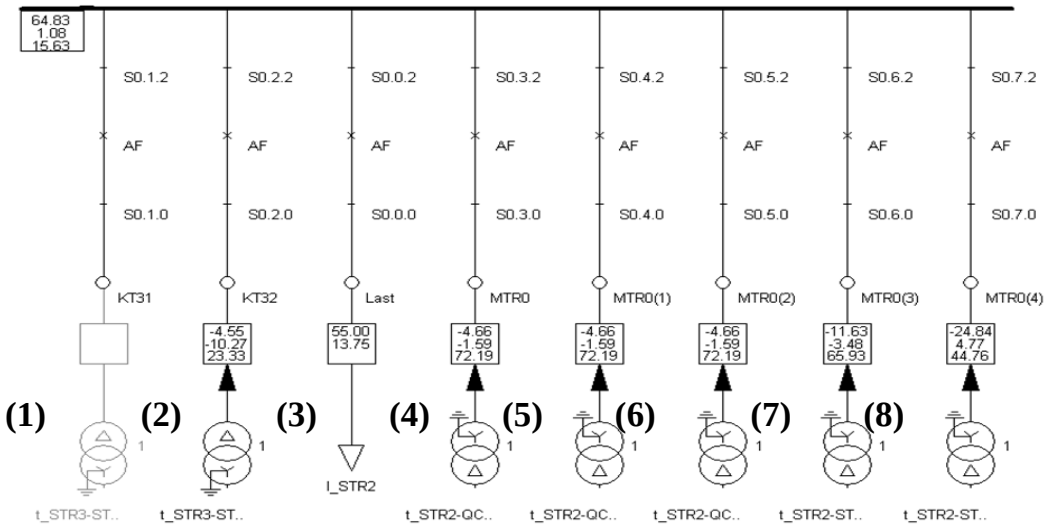

Figure 2.4 Typical 60 kV equivalent bus (here STR2) supplied from each 150 kV substation,. Where (1), (2) - 150/60 kV supplying transformers (1 - reserve), 3 – Balanced, simplified purely resistive/inductive equivalent model of all loads and networks supplied from the 150 kV bus, 55+j13,75 MVA, 4 - Equivalent CHP synchronous generator 5+j2 MVA, 5 - Equivalent CHP synchronous generator 5+j2 MVA, 6 - Equivalent CHP synchronous generator 5+j2 MVA, 7 - Equivalent CHP synchronous generator 13+j5 MVA, 8 - Equivalent asynchronous generator for onshore wind turbines, 49-j4,3 MVA. Diagram exported from PowerFactory software.

2.4 Conclusion

The existing network model is used for balanced load-flow calculations. It has to be inspected if it is possible to extend this model for unbalanced calculations. There are practically two dominating sources of unbalance in the network: loads and power lines [Jonas]. It is assumed that rotating machines and transforms are not introducing unbalance into the system. It can be assumed that other shunt elements like harmonic filters, shunt reactors are balanced as well.

Transmission lines are modelled as cascaded, balanced nominal Pi circuits. For most of the lines, the actual tower geometry is used, therefore simply by selecting the “distributed parameters model” and removing “ideal transposition” the lines become unbalanced distributed line models. For some line sections, for instance cable sections, the electrical parameters are defined. These sections are modelled either as nominal Pi sections or equivalent Pi circuits. It is assumed that they are balanced. For these sections no frequency dependent effects are included in the present model.

Skin effect is not included in none of the transmission line models, but the software is capable of calculating it, and can be included by selecting proper option. Ground return effect is always included in calculations.

Capacitive compensation at the distribution level is not included in the model.

All of the simplifications made while creating particular models of power system components will be inspected in the following chapter 3. The effect of these simplifications on the harmonic impedance of the models of particular components is analyzed. Based on the conclusions from chapter 3, the existing load-flow model will be adjusted to use for harmonic studies up to 2,5 kHz

Chapter 3

Harmonic domain modelling of linear transmission network components

This chapter is devoted to analyzing models of linear power system components for harmonic analysis studies for the frequency range above 50 Hz, up to 2500 Hz. The focus is put on the transmission line models, especially modelling of the frequency parameters in harmonic domain. Based on the observations described in this chapter, it will be concluded what modifications must be made to the existing 50 Hz load-flow model, to use it for correct harmonic calculations in the indicated frequency range.

3.1 Introduction

Modelling of linear power system components is a state-of-the-art task, well described in the literature, by such authors like: [Arrillaga], [Dommel], [Task Force], [Acha], [Medina], [Xu, 2004].

In this project, the existing PowerFactory 50 Hz load-flow model of the Western 400 kV and 150 kV transmission network of Energinet.dk will be used as a basis that is to be modified. After the modifications the model shall allow to accurately compute harmonic flows in the transmission network and to determine the harmonic impedance of the network using the harmonic domain calculations of the DIgSILENT PowerFactory software. The method of reaching this aim is as follows. For each of the components, a literature study is made. From this study it is found which aspects are necessary to include in the models. The models used in the existing load-flow network model are compared with the requirements found in the literature. In some cases, the effects of some of the existing simplifications are evaluated by additional computer simulations or hand calculations.

Power system components that mainly affect the propagation of harmonics in a transmission system are [Arrillaga], [Arrillaga, 1997], [Dugan], [Task Force], [Jonas]:

Transmission lines
Harmonic filters
Shunt capacitors
Series impedance of power transformers
Distribution network and loads
Synchronous and asynchronous machines
Shunt reactors

Table 3.1 Main linear components of high voltage transmission network that has to be modelled in harmonic analysis studies.

In the existing load-flow model all these models are present but the degree of detail, in which they are modelled differs. In the following sections, the most important aspects of these models are analyzed, the simplifications present in the load-flow models resulting from insufficient data are described, and also the modelling simplifications applied internally in the software are inspected. In case of a high voltage transmission network, transmission lines require perhaps most attention, because most of the phenomena that can be ignored in case of other elements, like phase unbalance, distributed parameters or non-ideal ground return, have to be modelled in case of transmission lines, due to their length. It may be also expected that very important are the harmonic filters and also shunt capacitors that alter the system impedance and resonate with system inductances [Arrillaga].

Chapter outline

This chapter is organized as follows:

The first part of this chapter is devoted to the analysis of harmonic domain modelling of transmission lines and their implementation in the PowerFactory software. Skin and non-ideal ground return frequency modelling implemented the PowerFactory software is verified. Next, a typical overhead line configuration is used for studies of the following issues: the importance of distributed parameters of transmission lines, the influence of shunt conductance, the skin effect, phase unbalance, assumption of ideal ground wires, the effect of average height of conductors due to sags. In the next sections, models of the shunt harmonic filters, shunt capacitors and shunt reactors are described, followed by description of the power transformer model and a description of modelling of synchronous and asynchronous machines. At the end, modelling of a distribution system is described.

3.2 Transmission lines

Modelling of transmission lines for harmonic analysis studies is quite a complex task and the number of literature positions where different aspects of modelling transmission lines are treated is large, just to mention a few: [EMTDC], [Dommel], [Abur], [Castellanos], [Gustavsen], [Marti], [Wedepohl]. Transmission lines combine several physical phenomena, which modelling may not be easy, such as the distributed nature of the line parameters, the skin effect in the conductors, the non-ideal earth return path impedance or coupling between phases of unbalanced lines, etc. All of them shall be taken into account for calculations of harmonic levels in the grid [Arrillaga], [Jonas].

In the existing load-flow model of the Western Energinet.dk network, overhead transmission lines are modelled with the simplifications according to Table 3.2.

	Effect	Load-flow model	Software capable?	Comments
1	Skin effect	NO	Yes	
2	Non-ideal earth return	Yes	Yes	*
3	Equivalent Pi circuit	NO	Yes	
4	NO ideal transposition	NO	Yes	
5	Reduction of earth wires	Yes	Yes	
6	Conductor sags	NO	Yes	**
7	Shunt conductance	NO	Yes	***
*	It is not clear how it is taken into account at higher frequencies			
**	Can be taken into account indirectly			
***	Not possible in the models based on line geometry			

Table 3.2 Modelling of overhead lines applied in the existing PowerFactory load-flow model.

Some of the effects not included in the existing model will result in errors when performing harmonic calculations. Therefore all of them shall be inspected and the resulting errors will be assessed.

3.2.1 Fundamentals

A theoretical basic of calculation of lumped line parameters is a common knowledge and therefore is omitted[1]. This section begins with an analysis of frequency dependent effects in transmission lines and how this is handled in the PowerFactory software.

Series impedance of transmission lines contains three components, whereas the shunt admittance contains one term (see Figure 3.1) [Arrillaga]:

$$[Z] = [Z_i] + [Z_G] + [Z_E], \tag{3.1}$$

$$[Y] = [Y_G], \tag{3.2}$$

Where Z_i is the internal impedance of the conductors, Z_G is the impedance due to the physical geometry of conductor arrangement, and Z_E is the non-ideal earth return path impedance, in (Ohm/km), and Y_G is the admittance due to the physical geometry of the conductor arrangement, in (Ohm^{-1}/km).

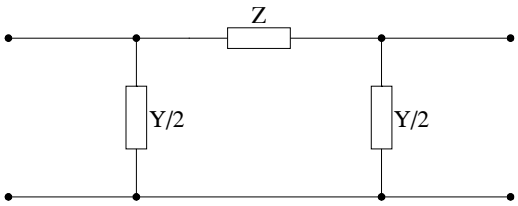

Figure 3.1 Simplified Pi circuit representation of a transmission line.

The geometrical impedance Z_G and admittance Y_G are practically linear functions of frequency [Arrillaga], and therefore only briefly described. The internal impedance of the conductors Z_C and the non-ideal earth return path impedance Z_E are nonlinear functions of frequency where both the resistive and the inductive terms are frequency dependent. Determination of both is more complicated, therefore more effort will be made to describe them in detail.

3.2.2 Geometrical impedance matrix [Z_G] and admittance matrix [Y_G]

The geometrical impedance matrix [Z_G] and admittance matrix [Y_G] (value of air conductance assumed zero) can be calculated using the following equations [Arrillaga], [PowerFactory]:

$$[Z_G] = j\omega K'[\Psi]\ \Omega/km, \tag{3.3}$$

$$[Y_G] = 1000\, j\omega 2\pi\varepsilon_a [\Psi]^{-1}\ \ \Omega^{-1}/km, \tag{3.4}$$

where K'=2 x 10^{-4}, ε_a is the permittivity of free space = 8.857 x 10^{-12} (F/m), $[\Psi]$ is a matrix of self and mutual potential coefficients [Arrillaga]:

$$\Psi_{ii} = \ln(2h_i/r_i), \tag{3.5}$$

$$\Psi_{ij} = \ln(D_{ij}/d_{ij}), \tag{3.6}$$

[1] A good description is given by [Grainger].

where r_i is the radius of the conductor i, (m), h_i and h_j are the heights of conductors i and j above ground,(m), d_{ij} is the distance between conductors i and j, (m), D_{ij} is the distance between conductor i and image of conductor j (m). Both $[Z_G]$ and $[Y_G]$ are linear functions of frequency that depend on the physical arrangement of the conductors (Below 100 kHz the effect of non-perfectly conducting earth on the shunt capacitance can be ignored [Dommel]). In that case, the capacitances are constant.

The shunt conductance is a result of the leakage currents at the insulators and the corona effect. Both conductances of the leakage at the insulators and corona effect are small and moreover they vary in a wide range depending on the atmospheric conditions and conducting properties of the dirt that collects at the insulators [Gross]. Therefore, they are usually omitted in steady state calculations. The power loss due to corona effect in normal whether conditions it is accounted to be approx. 1-2 kW/km for one phase consisting of three bundled conductors for a 500 kV overhead line, and in the worst case, with wet or covered with hoarfrost conductors it ca be as high as 30 kW/km per phase [Gross].

3.2.3 Conductor impedance matrix Z_C

Skin effect

When the frequency of alternating current increases, affected are, both the resistance and the inductance of the internal conductor impedance Z_C. Magnetic field created around a conductor that carries alternating current induces eddy currents I_S in the conductor, as shown in the Figure 3.2 [Jensen]. The result is a non-uniform current distribution throughout the conductor cross-section. The induced eddy current I_S will tend to oppose the main current I_m in the center of the conductor but enhance it near the surface [Jensen].

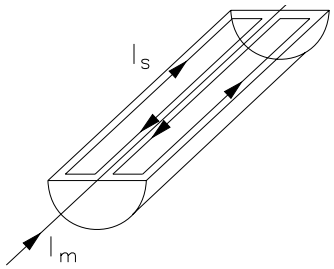

Figure 3.2 eddy currents induced by skin effect [Jensen].

Skin effect causes the resistance to increase because the effective cross-sectional area decreases and the conductor internal inductance lowers because there will be less internal flux linkages [Stevenson].

Analytic expressions that describe best the internal impedance of a solid circular conductor at any frequency are given by [Stevenson]:

$$Z_i = \frac{\rho m}{2\pi r}\frac{\mathrm{ber}\, mr + j\,\mathrm{bei}\, mr}{\mathrm{bei}'\, mr - j\,\mathrm{ber}'\, mr}\left[\Omega/m\right], \tag{3.7}$$

$$R_i = \frac{\rho m}{2\pi r}\frac{\mathrm{ber}\, mr\,\mathrm{bei}'\, mr - \mathrm{bei}\, mr\,\mathrm{ber}'\, mr}{(\mathrm{bei}'\, mr)^2 + (\mathrm{ber}'\, mr)^2}\left[\Omega/m\right], \tag{3.8}$$

$$\varpi L_i = \frac{\rho m}{2\pi r}\frac{\mathrm{bei}\, mr\,\mathrm{bei}'\, mr + \mathrm{ber}\, mr\,\mathrm{ber}'\, mr}{(\mathrm{bei}'\, mr)^2 + (\mathrm{ber}'\, mr)^2}\left[\Omega/m\right], \tag{3.9}$$

where Z_i, R_i, ϖL_i are the internal impedance, resistance and reactance expressed in [Ω], ρ is the resistivity of a conductor [Ω·m], r is the radius [m], $m = \sqrt{\varpi\mu/\rho}$, μ is the wire permeability

[Henry/m], terms "ber" and "bei" are the abbreviations for "Bessel real" and "Bessel imaginary" – Bessel series of the first kind and zero order [Stevenson]:

$$\text{ber}\, mr = 1 - \frac{(mr)^4}{2^2 \cdot 4^2} + \frac{(mr)^8}{2^2 \cdot 4^2 \cdot 6^2 \cdot 8^2} - \cdots \quad , \tag{3.10}$$

$$\text{bei}\, mr = \frac{(mr)^2}{2^2} - \frac{(mr)^6}{2^2 \cdot 4^2 \cdot 6^2} + \frac{(mr)^{10}}{2^2 \cdot 4^2 \cdot 6^2 \cdot 8^2 \cdot 10^2} - \cdots . \tag{3.11}$$

Terms $\text{ber}'\, mr$ and $\text{bei}'\, mr$ are Bessel series derivatives:

$$\text{ber}'\, mr = \frac{1}{m}\frac{d}{dr}(\text{ber}\, mr), \tag{3.12}$$

$$\text{bei}'\, mr = \frac{1}{m}\frac{d}{dr}(\text{bei}\, mr). \tag{3.13}$$

Bessel series is an infinite series, and the more terms of the series used in calculations, the higher the frequency at which equations (3.7)-(3.9) provide exact results. The infinite series is not convenient to use in calculations and therefore is often truncated. [Jensen] states that if the first three terms of the series are used, the resultant inductance and resistance values are correct up to approximately 2 kHz, and if six terms are used, this is extended up to 18 kHz.

The above statement has been verified. Equations (3.8) and (3.9) have been used and the resistance and internal inductance was calculated. The calculation was made for four cases, with three, four, five and with six terms of Bessel series included. The data used for calculation was for an aluminum conductor ($\mu = 4\pi \cdot 10^{-7}\, H/m$, $\rho = 2{,}83 \cdot 10^{-8}\, \Omega/m$). The radius of the conductor was set to a typical radius of a conductor of a 400 kV overhead line $r = 15\, mm$ (taken from the load-flow model). The results of calculations of the internal inductance L_i and resistance R_i, performed for all four cases, are shown in Figure 3.3.

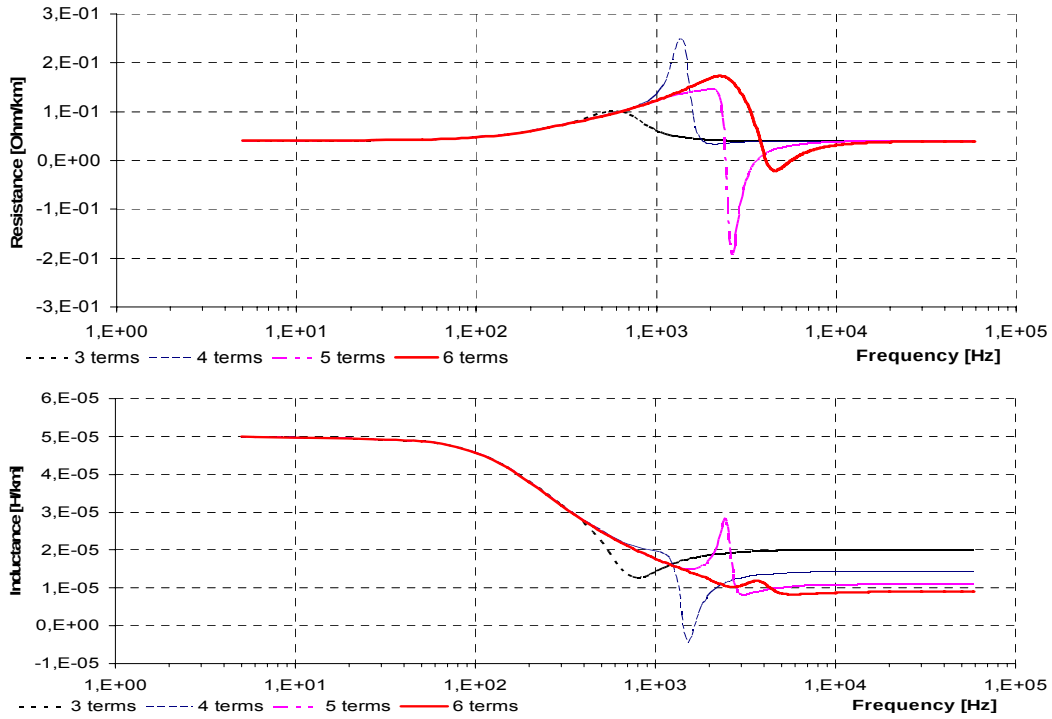

Figure 3.3 Internal resistance (upper plot) and inductance (lower plot) calculated from Equations (3.8) and (3.9) with the three, four, five and six first terms of Bessel series included, calculated for an aluminum conductor with radius 15 mm.

The increase in resistance value and the decrease of inductance value can be seen. Theoretically, the more terms of the Bessel series are used, the higher in frequency the plots show the actual resistance and inductance value.

The shape of the resistance and inductance plots based on three and six term expressions resemble the plots obtained in [Jensen], but the frequency is much lower and the value of resistance is also smaller. In this case, the three-term approximation gives good results for frequency up to 400 Hz (8^{th} harmonic) and the six-term approximation may be used up to 2,5 kHz (50^{th} harmonic). The reason of that lies in the radius of the conductor used for calculations. Jensen performed the calculations for a LV cable, and as it was tested, he must have made the calculations for a conductor of radius approximately r = 5 mm, see Figure 3.4. It can be seen that the limiting values of 2 kHz and 18 kHz for three and six-term based equations are correct, for a conductor with such a radius.

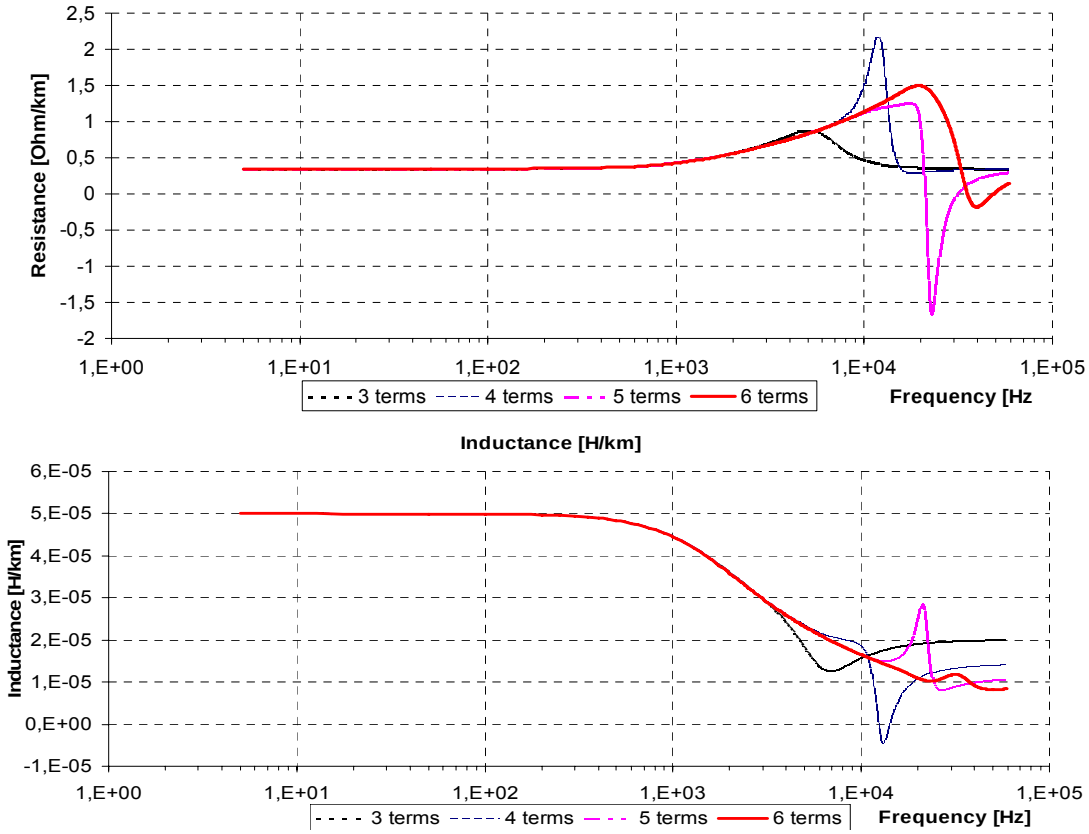

Figure 3.4 Internal resistance (upper plot) and inductance (lower plot) calculated from Equations (3.8) and (3.9) with the three, four, five and six first terms of Bessel series included, calculated for an aluminum conductor with radius 5 mm.

In general however, comparing Figure 3.3 with Figure 3.4 it can be concluded that the upper limit of the frequency, for which the approximation (with various number of terms of the Bessel series included) gives correct results at a given frequency, depends strongly on the radius of the conductor. The smaller is the radius, the higher is the conductor effective resistance and the higher the inductance at a given frequency. Also, the smaller the radius, the better the resistance and internal inductance is approximated with a lower number of terms of the Bessel series. In Table 3.3 the effect of the radius of a conductor on the validity of approximation of conductor resistance and internal inductance with three-term and six-term Bessel series is shown. The values are calculated for copper and aluminum solid circular conductors. As can be seen, for frequency range up to 2,5 kHz, 6-term expression is valid for any conductor cross-section almost up to 500 mm^2 and 700 mm^2 for copper and aluminum conductors respectively. The values of equivalent conductor radius for Energinet.dk overhead lines vary from 9,9 mm up to 26 mm (data

taken from the load-flow model obtained from Energinet.dk), therefore, to precisely take into account skin effect for harmonic analysis up to 2,5 kHz, more than 6 terms must be included in Equations (3.8) and (3.9).

cross-section	radius	copper		aluminium	
		3-terms	6-terms	3-terms	6-terms
mm2	mm	kHz	kHz	kHz	kHz
1,5	0,7	>50	>50	>50	>50
4	1,1	45	>50	>50	>50
16	2,3	10,00	>50	16,00	>50
25	2,8	7,40	40,00	10,00	>50
50	4,0	3,50	21,00	5,50	32,00
70	4,7	3,00	15,00	4,00	25,00
95	5,5	2,50	11,00	3,00	17,00
120	6,2	1,75	9,00	2,40	14,00
150	6,9	1,20	6,70	2,00	11,00
240	8,7	0,85	4,20	1,25	7,00
300	9,8	0,60	3,40	1,00	5,50
500	12,6	0,35	2,10	0,60	3,30
700	14,9	0,20	1,50	0,35	2,50
1000	17,8	0,15	1,10	0,25	1,70

Table 3.3 Effect of conductor cross-section (radius) on the maximum frequency, for which approximation of conductor resistance and internal inductance with three-term and six-term Bessel series is valid. Values calculated for copper and aluminum solid circular conductors.

If it is assumed that the ground is perfectly conducting, the entire conductor inductance L is a sum of internal conductor inductance L_i, and geometrical conductor inductance L_G [Arrillaga], with $L_E = 0$.

The expression for internal inductance of a conductor with skin effect ignored is [Grainger]:

$$L_i = \frac{\mu}{8\pi} = 0{,}5 \cdot 10^{-7} \left[H / m \right], \tag{3.14}$$

and expression for external average single phase inductance value of a three-phase overhead line is [Grainger]:

$$L_G = \frac{\mu}{2\pi} \ln\left(\frac{D_{eq}}{GMR} \right) = 2 \cdot 10^{-7} \cdot \ln\left(\frac{D_{eq}}{GMR} \right) \left[H / m \right], \tag{3.15}$$

where $D_{eq} = \sqrt[3]{D_1 + D_2 + D_3}$ is the geometric mean distance between three bundled conductors and GMR is the geometric mean radius of a bundled conductor. Assuming that the average distance between conductors is 8 meters and the GMR is 15mm, the external inductance of one conductor is: $L_E = 12{,}56 \cdot 10^{-7} \left[H / m \right]$. Comparing the results of (3.14) and (3.15) it can be seen that the internal inductance of the conductor L_i is a fraction of the entire inductance L. This implies that if the frequency dependence of L_i is ignored, it will not cause large errors in calculation results.

Skin effect will be also analyzed further in sections 3.2.6 and 3.3.3 of this chapter.

Proximity effect

Proximity effect is an effect inducing currents in a conductor placed in the proximity of another current carrying conductor. The magnetic field surrounding the current carrying conductor decreases rapidly with the distance from the conductor and the currents inside the second conductor are negligible once the distance is much larger than a few centimeters [Jensen]. For

overhead lines it can be disregarded completely, especially at the frequencies below 2,5 kHz [Jensen]. Consequently, the proximity effect will not be analyzed in this project.

Stranded steel-reinforced aluminum conductors

The presence of steel reinforcement in the aluminum conductors in the existing model is ignored. Alternating current flowing in the aluminum conductor steel reinforced (ACSR) causes magnetic induction in the steel. This induction causes hysteresis and eddy currents in the core [CIGRE SC22/WG12], [Morgan]. The result is an increased level of the ac/dc conductor resistance ratio. Several types of conductors were inspected in [CIGRE SC22/WG12] and [Morgan]. In general, the internal conductor resistance is a function of the current magnitude, and while increasing the fundamental frequency current magnitude the ratio Rac/Rdc increases up to maximally 1,1 [CIGRE SC22/WG12]. This effect is mostly present in conductors with odd number of layers of aluminum strands. In case of even number, the magnetization of the core caused by one layer is largely compensated by the other layer that is spiraled in the opposite direction [Dommel]. Assuming that the conductor is linear, the increase of the resistance due to increase of 50 Hz current component shall not have direct effect on the resistance at higher frequencies, therefore in this project it has been assumed that it does not affect the resistance seen by higher frequency components.

According to [Acha], [Dommel], stranding of conductors can be represented as tubular conductors with the same cross-section. This assumption has been also made in this project.

3.2.4 Earth return path impedance Z_E

The series impedance of a transmission line is a nonlinear function of frequency, due to the earth return path. Both the inductance and resistance are affected. For a homogenous earth, the commonly accepted solution to this problem has been developed by John R. Carson and published in 1926 [Carson]. Carson analysis was based on an electromagnetic field theory and allowed him to derive the expression for the earth impedance Z_E in the form:

$$Z_E = 4\omega J\,, \tag{3.16}$$

where ω is the frequency in radians per second and J is an infinite integral [Carson]. The solution to this integral has a form of a complex sum of two infinite series, P and Q [Carson]:

$$J = P + jQ\,, \tag{3.17}$$

where:

$$P = \frac{\pi}{8}(1 - s_4) + \frac{1}{2}\left(\ln\frac{2}{\gamma \cdot C_A}\right)s_2 + \frac{1}{2}\Theta \cdot s'_2 - \frac{1}{\sqrt{2}}\sigma_1 + \frac{1}{2}\sigma_2 + \frac{1}{\sqrt{2}}\sigma_3\,, \tag{3.18}$$

$$Q = \frac{1}{4} + \frac{1}{2}\left(\ln\frac{2}{\gamma \cdot C_A}\right)(1 - s_4) - \frac{1}{2}\Theta \cdot s'_4 + \frac{1}{\sqrt{2}}\sigma_1 - \frac{\pi}{8}\sigma_2 + \frac{1}{\sqrt{2}}\sigma_3 - \frac{1}{2}\sigma_4\,. \tag{3.19}$$

In these equations ln γ is Euler's constant: γ = 1,7811, and σ_1, σ_2, σ_3, σ_4, s_2, s'_2, s_4 and s'_4 are infinite series [Carson]:

$$s_2 = \frac{1}{1!2!}\left(\frac{C_A}{2}\right)^2 \cos 2\Theta - \frac{1}{3!4!}\left(\frac{C_A}{2}\right)^6 \cos 6\Theta + \ldots\,, \tag{3.20}$$

$$s'_2 = \frac{1}{1!2!}\left(\frac{C_A}{2}\right)^2 \sin 2\Theta - \frac{1}{3!4!}\left(\frac{C_A}{2}\right)^6 \sin 6\Theta + \ldots\,, \tag{3.21}$$

$$s_4 = \frac{1}{2!3!}\left(\frac{C_A}{2}\right)^4 \cos 4\Theta - \frac{1}{4!5!}\left(\frac{C_A}{2}\right)^8 \cos 8\Theta + \ldots, \tag{3.22}$$

$$s'_4 = \frac{1}{2!3!}\left(\frac{C_A}{2}\right)^4 \sin 4\Theta - \frac{1}{4!5!}\left(\frac{C_A}{2}\right)^8 \sin 8\Theta + \ldots, \tag{3.23}$$

$$\sigma_1 = \frac{C_A \cos\Theta}{3} - \frac{C_A^5 \cos 5\Theta}{3^2 \cdot 5^2 \cdot 7} + \frac{C_A^9 \cos 9\Theta}{3^2 \cdot 5^2 \cdot 7^2 \cdot 9^2 \cdot 11} - \ldots, \tag{3.24}$$

$$\sigma_3 = \frac{C_A^3 \cos 3\Theta}{3^2 \cdot 5} - \frac{C_A^7 \cos 7\Theta}{3^2 \cdot 5^2 \cdot 7^2 \cdot 9} + \frac{C_A^{11} \cos 11\Theta}{3^2 \cdot 5^2 \cdot 7^2 \cdot 9^2 \cdot 11^2 \cdot 13} - \ldots, \tag{3.25}$$

$$\begin{aligned}\sigma_2 = &\left(1 + \frac{1}{2} - \frac{1}{4}\right)\frac{1}{1!\cdot 2!}\left(\frac{C_A}{2}\right)^2 \cos 2\Theta \\ &- \left(1 + \frac{1}{2} + \frac{1}{3} + \frac{1}{4} - \frac{1}{8}\right)\frac{1}{3!\cdot 4!}\left(\frac{C_A}{2}\right)^6 \cos 6\Theta + \ldots\end{aligned}, \tag{3.26}$$

$$\begin{aligned}\sigma_4 = &\left(1 + \frac{1}{2} + \frac{1}{3} - \frac{1}{6}\right)\frac{1}{2!\cdot 3!}\left(\frac{C_A}{2}\right)^4 \cos 4\Theta \\ &- \left(1 + \frac{1}{2} + \frac{1}{3} + \frac{1}{4} + \frac{1}{5} - \frac{1}{10}\right)\frac{1}{4!\cdot 5!}\left(\frac{C_A}{2}\right)^8 \cos 8\Theta + \ldots\end{aligned}, \tag{3.27}$$

where Θ is can be expressed as = $\tan^{-1}$ $((x_1\text{-}x_2)/(y_1+y_2))$ [Jensen], as shown in Figure 3.5, and C_A is an article:

$$C_A = p\sqrt{4\pi\lambda\omega}\,, \tag{3.28}$$

where p = 2h if calculating the self impedance of a conductor, h is height above ground in centimeters, or p = $\sqrt{(y_1 + y_2)^2 + (x_1 - x_2)^2}$ if calculating the effect on mutual impedance between two conductors and λ is ground conductivity in cgs. units, and for typical value of ground resistivity ρ = 100 Ω/m, $\lambda = 10^{-13}$.

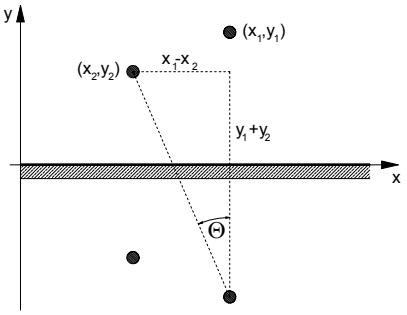

Figure 3.5 Two conductors at the height y_1 and y_2 above ground, and their images below the ground surface.

The equations for P and Q are extensive, but series (3.20) - (3.27) are very rapidly convergent, and therefore for small values of C_A only the leading terms need to be kept [Carson]. For $C_A \le 2$ only the first two terms must be included and for $C_A \le 1$ it is sufficient to use only the first terms of the series. For $C_A \le 1/4$ and calculation of self impedance terms (for self impedance terms Θ = 0) equations (3.18) and (3.19) simplify to [Carson]:

$$P = \frac{\pi}{8} - \frac{1}{3\sqrt{2}} C_A + \frac{C_A^2}{16}\left(0{,}6728 + \ln\left(\frac{2}{C_A}\right)\right), \tag{3.29}$$

$$Q = -0{,}0386 + \frac{1}{2}\ln\left(\frac{2}{C_A}\right) + \frac{1}{3\sqrt{2}} C_A . \tag{3.30}$$

After the values of P and Q are calculated, the resistance R and inductance L of the earth return path is calculated from:

$$\begin{aligned} R &= 4\omega P \cdot 10^{-4}\,\Omega / km \\ L &= 4Q \cdot 10^{-4}\,H / km \end{aligned}, \tag{3.31}$$

where the term 10^{-4} is necessary to convert the values from cgs. units to Ω/km and H/km.

Therefore, it can be seen that the decisive factor for selecting the number of terms of the series that are to be included in calculations is the article C_A. Variation of the maximal height of a conductor as a function of frequency, for the ground conductivity $\lambda = 10^{-13}$ is shown in Figure 3.6. The plot is made for three different values of the article $C_A = 2$, $C_A = 1$ and $C_A = ¼$, at which Carson equations calculated using (3.28) give correct results.

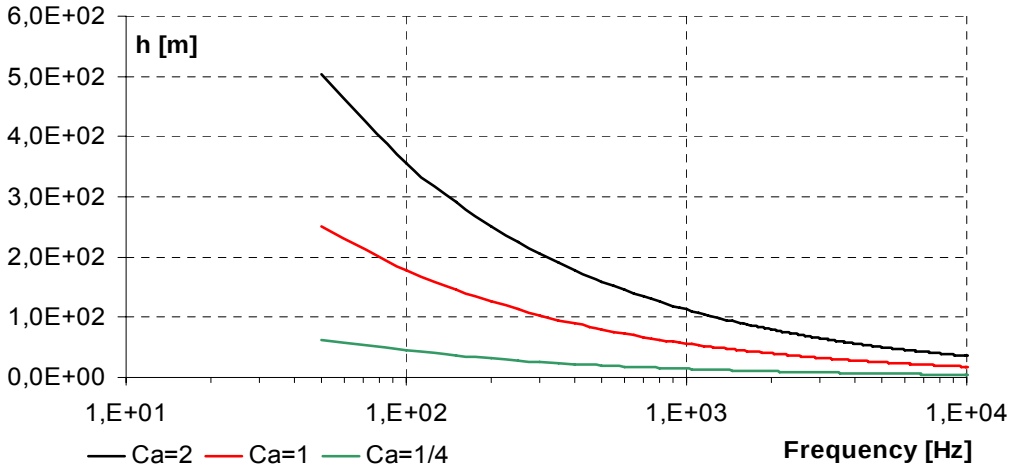

Figure 3.6 Variation of the maximal height of a conductor as a function of frequency, for three different values of the article $C_A = 2$, $C_A = 1$ and $C_A = ¼$.

The maximal values read out from Figure 3.6 are collected in Table 3.4.

	Frequency [Hz]		
C_A	50	2500	10000
0,25	63,00	8,90	4,45
1,00	252,00	35,60	18,00
2,00	503,00	71,00	35,60

Table 3.4 Maximal height of a conductor for frequency values 50 Hz, 2,5 kHz and 10 kHz, for three different values of the article $C_A = 2$, $C_A = 1$ and $C_A = ¼$.

As can be seen, if the Carson equations (3.29) and (3.30) for article value $C_A = ¼$ are used, the maximal height, for which they give exact results at 50 Hz is 63 meters. At 2,5 kHz, this height is reduced down to only 8,9 meters. For C_A=1, at 50 Hz it is 252 meters, and at 2,5 kHz it reduces to 35,6 meters. For C_A=2, at 2,5 kHz maximal height of a conductor is 71 meters.

As it was checked in the load-flow model obtained from Energinet.dk, the 150 kV lines are placed at the height from 13 m up to 33,5 meters above ground and 400 kV lines are placed at the height of 22 – 41 meters above the ground level. Comparing to Table 3.4 it can be seen that if

harmonic analysis is to be made for frequencies up to the 50th harmonic, it is not sufficient use equations (3.29) and (3.30), and it is also not sufficient to use full equations (3.18) and (3.19) with single terms of the series (3.20) - (3.27), but at least two terms of the series must be used in calculations.

The values of earth return path resistance R_E and inductance L_E have been calculated for three different values of C_A: C_A = ¼ (equations (3.29) and (3.30)), C_A = 1 and C_A = 2 ((3.18) and (3.19) with one and with two terms of the series included). The height of a conductor has been set to 40 meters above ground. Only the self impedance term is calculated, therefore Θ = 0 and all the terms in equations (3.18) - (3.27) that include Θ or sin Θ are also zero. Calculated values of series (3.20) - (3.27), with two first terms included are:

$$s_2 = \frac{C_A^2}{8} - \frac{C_A^6}{288};\ s'_2 = 0;\ s'_4 = 0;\ s_4 = \frac{C_A^4}{192} - \frac{C_A^8}{2880 \cdot 2^8};\ \sigma_1 = \frac{C_A}{3} - \frac{C_A^5}{1575};$$
$$\sigma_3 = \frac{C_A^3}{45} - \frac{C_A^7}{99225};\ \sigma_2 = \frac{5 \cdot C_A^2}{32} - \frac{47 \cdot C_A^6}{221184};\ \sigma_4 = \frac{5 \cdot C_A^4}{576} - \frac{262 \cdot C_A^8}{120 \cdot 2880 \cdot 2^8} \qquad (3.32)$$

The variation of the resistive and inductive terms of the ground return impedance for the above mentioned cases is shown in Figure 3.7 below. As can be seen, the resistive term R_E changes much more than the inductive term L_E. The resistance value of the ground return path at 50 Hz is 0,045 Ω/km, whereas at 2,5 kHz it is 1,55 Ω/km, which means an increase of 34 times. At the same time inductive term lowers from 5,05 x 10^{-4} H/m at 50 Hz down to 1,81 x 10^{-4} H/m at 2,5 kHz, which is only 2,8 times smaller. As can be also seen the curve corresponding to C_A < ¼ moves away from the other two curves at a frequency already below 1 kHz.

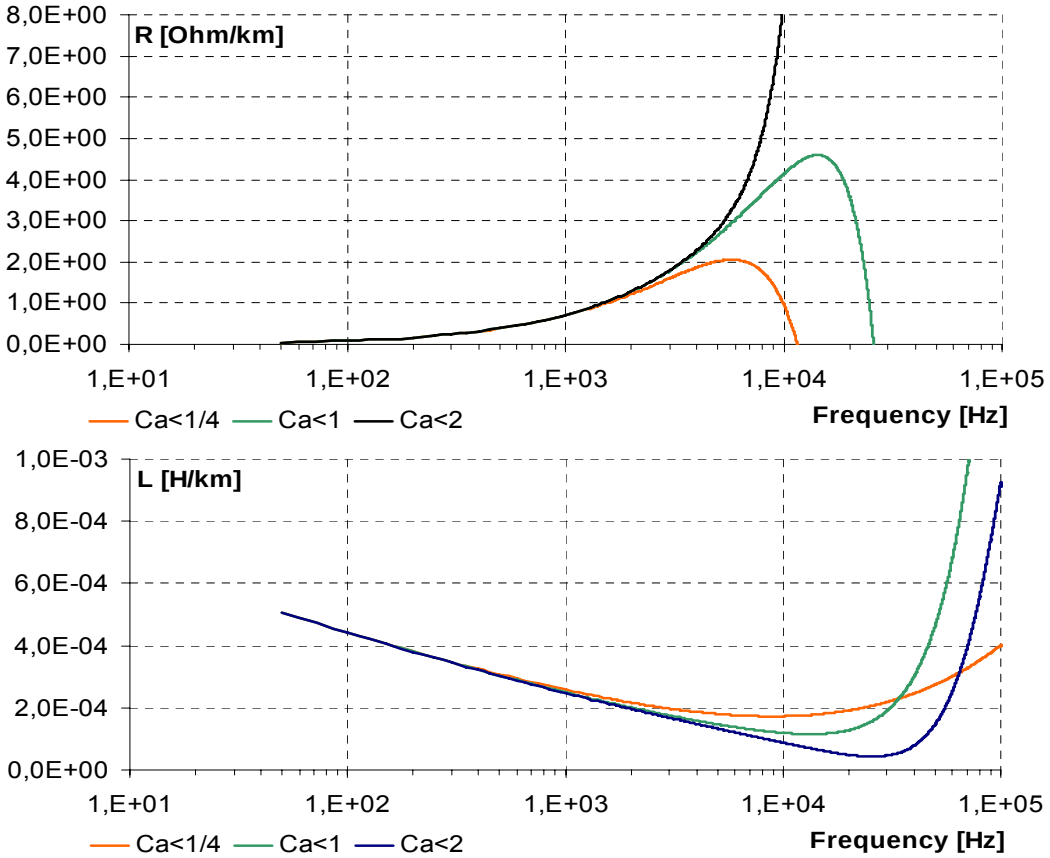

Figure 3.7 Variation of resistive (upper plot) and inductive (lower plot) terms of the ground return impedance as a function of frequency calculated using the Carson series, for three values of the Carson article C_A < ¼ - red curve, C_A < 1 – green curve and C_A < 2 – black curve. Calculations made for the height of a conductor h = 40 m above ground level.

In the PowerFactory manual it is stated that modelling of the earth return path is made using the Carson series, and for the fundamental frequency calculations, the first term of the series is included [PowerFactory]. This is sufficient but it was not clearly stated how many terms are included if the harmonic domain calculations are to be made in PowerFactory.

It is therefore necessary to inspect how the PowerFactory simulation software is dealing with frequency dependent parameters.

3.2.5 Hand verification of PowerFactory modelling of ground return impedance

In order to verify how PowerFactory takes into account the skin effect and the non-ideal earth return path impedance, a simple case has been set up. In this case, a single solid conductor with radius 15 mm has been placed at the height 40 m above the ground level. This solid conductor is made of aluminum ($\mu = 4\pi \cdot 10^{-7}\ H/m$, $\rho = 2{,}83 \cdot 10^{-8}\ \Omega/m$), see Figure 3.8. An identical simulation case has been set up in the PowerFactory software, see Figure 3.9.

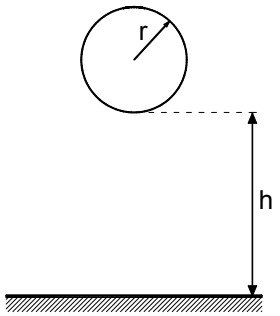

Figure 3.8 Single solid aluminum conductor of radius r = 0,015 m and height above ground h = 40 m used in hand-calculations. Ground resistivity 100 Ωm.

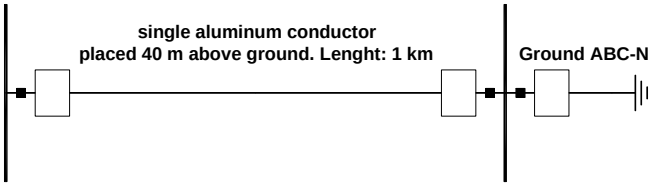

Figure 3.9 Single phase, l = 1000 m long line with parameters as described above, has been set up in PowerFactory software. Ground resistivity 100 Ωm.

Calculated conductor parameters

The series resistance R of this conductor is a sum of conductor resistance R_i and ground return resistance R_E:

$$R = R_i + R_E\,, \tag{3.33}$$

Both terms are frequency dependent, but at first the skin effect is ignored, so R_i is kept constant. Calculated internal dc resistance is: $R_i = \rho \cdot l / \pi \cdot r^2 = \mathbf{0{,}04}\,\Omega/km$

The series inductance L of this conductor is a sum of conductor internal inductance L_i, conductor geometrical inductance L_G and ground return path inductance L_E:

$$L = L_i + L_G + L_E\,, \tag{3.34}$$

The geometrical inductance L_G is constant, and since skin effect is ignored, L_i is also constant. The only variable term is L_E. Calculated internal conductor inductance L_i without skin effect

is: $L_i = 1000 \cdot \mu/8\pi = \mathbf{5 \cdot 10^{-5}}$ H/*km*, and the geometrical inductance L_G, assuming perfectly conducting ground is: $\mathbf{L_G} = 1000 \cdot \mu/2\pi \cdot \ln(2h/r) \cdot 10^{-7} = \mathbf{1{,}716346343 \cdot 10^{-3}}\, H/km$.

Verification of PowerFactory calculation of the resistive and inductive components of the earth impedance Z_E.

Using the Carson series equations for $C_A \leq 1/4$ (equations (3.29) and (3.30)), $C_A \leq 1$ and $C_A \leq 2$ (equations (3.18) and (3.19), with one and with two terms of the series included)) the value of total conductor resistance calculated at 50 Hz is:

$$R_{1/4} = 0{,}04 + 0{,}045275965 = 0{,}085275965\ \Omega/\text{km}; \quad \text{for } C_A \leq 1/4$$

$$R_1 = 0{,}04 + 0{,}045283725 = \mathbf{0{,}085283725}\ \Omega/\text{km}; \quad \text{for single term}$$

$$R_2 = 0{,}04 + 0{,}045283724 = 0{,}085283724\ \Omega/\text{km}; \quad \text{for two terms}$$

And the result obtained from simulation using the PowerFactory model is:

$$R_{PF} = \mathbf{0{,}08528373}\ \Omega/\text{km}.$$

After comparing the result from PowerFactory with the result of hand calculations, it can be seen that it is in agreement with the value obtained for Carson series wit only the first term included. PowerFactory truncates and rounds off the result after 8 digits after the decimal point.

In the same way the 50 Hz inductance L has been calculated:

$$L_{1/4} = (0{,}05 + 1{,}716346343 + 0{,}506004532) \cdot 10^{-3} = 2{,}272350875 \cdot 10^{-3}\ \text{H/km}; \quad \text{for } C_A \leq 1/4$$

$$L_1 = (0{,}05 + 1{,}716346343 + 0{,}505525036) \cdot 10^{-3} = \mathbf{2{,}271871379 \cdot 10^{-3}}\ \text{H/km}; \quad \text{for single term}$$

$$L_2 = (0{,}05 + 1{,}716346343 + 0{,}505400994) \cdot 10^{-3} = 2{,}271747336 \cdot 10^{-3}\ \text{H/km}; \quad \text{for two terms}$$

And the result obtained from simulation using the PowerFactory model is:

$$L_{PF} = \mathbf{0{,}00227187}\ \text{H/km}.$$

Again, the inductance calculation of PowerFactory shows a perfect agreement with the inductance value calculated from Carson series equations with only the first term of the series used in calculations.

In order to inspect more closely the exact behavior of the earth impedance term modelled in PowerFactory, the resistive and inductive terms of the earth return impedance have been calculated at frequencies in the range from 50 Hz up to 100 kHz. PowerFactory allows selecting whether the skin effect is to be used in the calculations, however non-ideal ground return path is always included in the model. Therefore, to extract only the ground return values from the obtained results, the calculated constant internal inductance and resistance and geometrical inductance were subtracted from the entire results, so only the earth impedance terms were obtained. The resultant curves, together with the curves calculated from Carson series are plotted in Figure 3.10. When looking at these plots it becomes clear that PowerFactory bases its calculation of both, the resistive and inductive components of the earth impedance Z_E on the truncated Carson series, with only the first terms of the series (3.20) - (3.27) included. However, as can be seen, the inductance and resistance curves do not follow the curves $C_A<1$ and at some point they are extrapolated with a line, that is closer to the actual value represented by the first segment of the curve $C_A<2$. This line is extended and its course is shown up to 1 MHz.

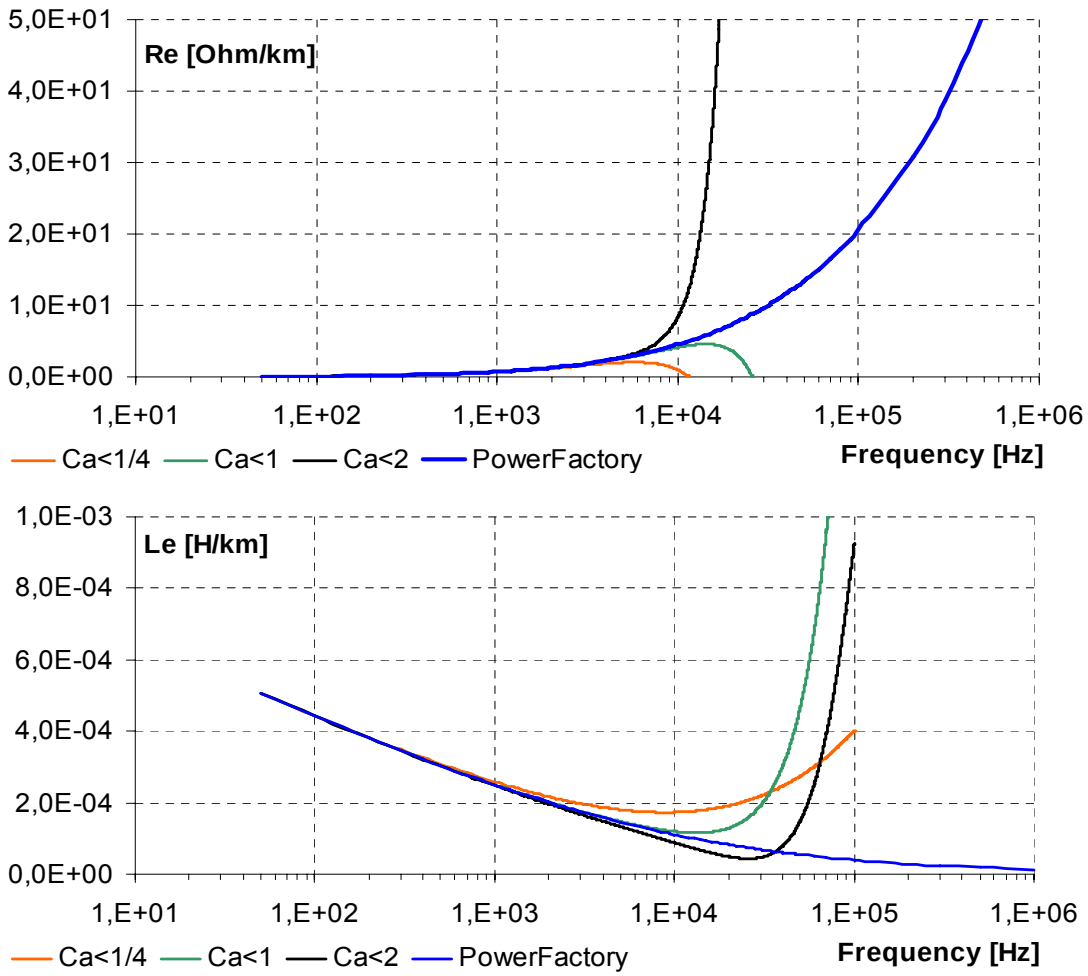

Figure 3.10 Variation of resistive (upper plot) and inductive (lower plot) terms of the ground return impedance as a function of frequency calculated using the Carson series, and obtained from PowerFactory simulations. $C_A \leq ¼$ - red curve, $C_A \leq 1$ – green curve, $C_A \leq 2$ – black curve and PowerFactory result – blue curve.

According to the findings presented earlier in this section, for modelling correctly the Western transmission network of Energinet.dk, 40 m high transmission lines shall be represented correctly for frequencies up to 2,5 kHz. According to [Carson] and Table 3.4, in order to achieve that, the two first terms of the Carson series shall be used in calculations. PowerFactory bases its calculations on the Carson equations but only the first terms are used in the computations. The curve is however extended in the way that it seems to give reasonably accurate results also at higher frequencies. If both plots from Figure 3.10 are inspected closer, it can be seen that at 2,5 kHz the difference between curve $C_A< 2$ and the PowerFactory result is still practically ignorable, see Table 3.5.

	R at 2,5 kHz Ohm/km	L at 2,5 kHz H/km
PF	1,5458070	0,000186844
$C_A<2$	1,5458209	0,000180668
Difference	0,0000139	0,0000062

Table 3.5 Differences in resistive and inductive terms of the earth impedance Z_E calculated using two terms of Carson series at 2,5 kHz, and obtained from PowerFactory simulations.

Although the differences are ignorable for the range of frequencies that are of interest in this project, it can be concluded that a more correct approach would be to include also the second

terms of all the series in the calculations. It would not require much additional effort to do so. Assumed in this study ground conductivity $\lambda = 10^{-13}$ is an average value, commonly used, that corresponds to resistivity $\rho = 100\ \Omega\cdot$m. For higher values of ground resistivity and also for conductors placed at larger distances from the ground, the differences present in Table 3.5 would be larger. Cases with larger values of ground resistivity or conductors installed at larger heights will not be analyzed in this project.

3.2.6 Hand verification of PowerFactory calculation of the skin effect

The above described case was used also to determine the variation of the internal conductor resistance R_i and inductance L_i, due to the skin effect. First, the entire value of circuit resistance R and inductance L was obtained from PowerFactory simulation at discrete values of frequency in the range from 50 Hz up to 60 kHz, with the skin effect included. Next, the following calculations were made:

$$R_i = R - R_E\,, \tag{3.35}$$

$$L_i = L - L_G - L_E\,, \tag{3.36}$$

where $R_{i,,}$ L_i are the internal resistance and inductance with the skin effect included, R_E, L_E are the resistive and inductive terms of earth return impedance obtained in previous section and L_G is the constant value of geometrical inductance.

The frequency dependence of R_i and L_i, together with the values calculated using three, four, five and six terms of Bessel series are compared in Figure 3.11.

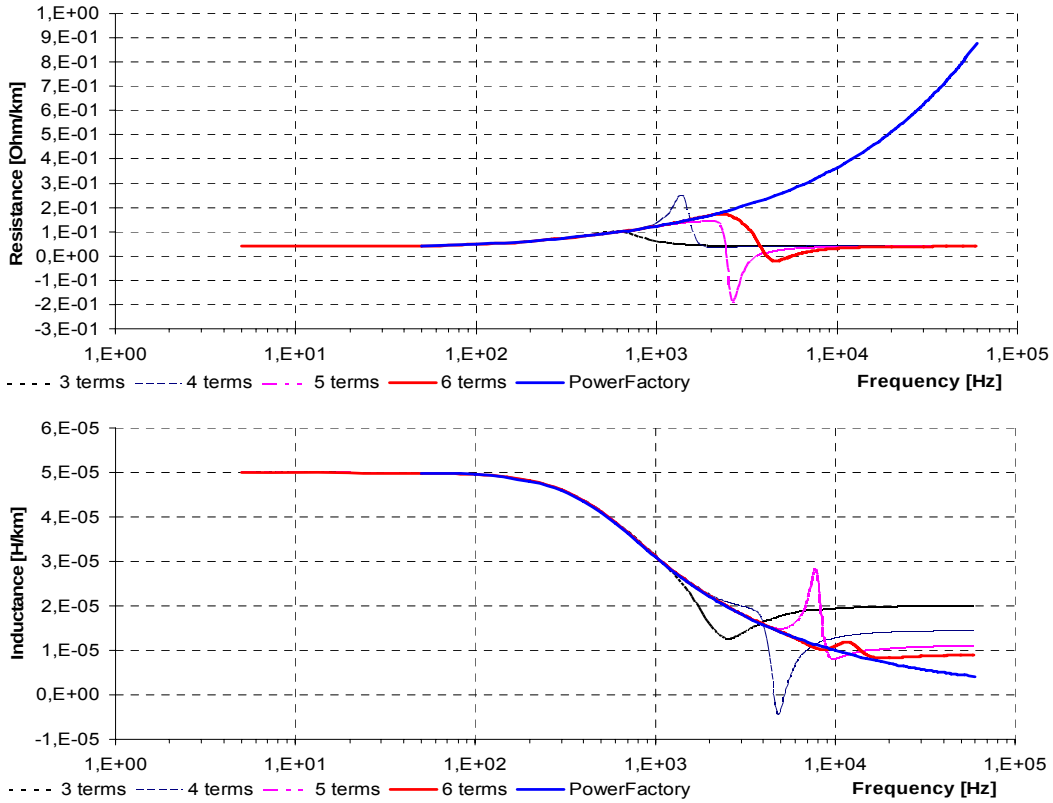

Figure 3.11 Internal resistance (upper plot) and inductance (lower plot) calculated from Equations (3.8) and (3.9) with the first three, four, five and six terms of Bessel series, calculated for an aluminum conductor with radius 15 mm, and comparison with the result obtained from PowerFactory.

As can be seen, PowerFactory approximates the Bessel functions calculations correctly. The approximation to the six-term curve is very good, but it seems that the approach used in PowerFactory is valid also at higher than 2,5 kHz frequencies. The behavior at such higher frequencies will not be inspected in this project further. Both the skin effect and non-ideal ground affects the series resistance and inductance of a line. However, in order to get some perspective on how much these frequency dependent effects influence the entire series impedance, see Figure 3.12.

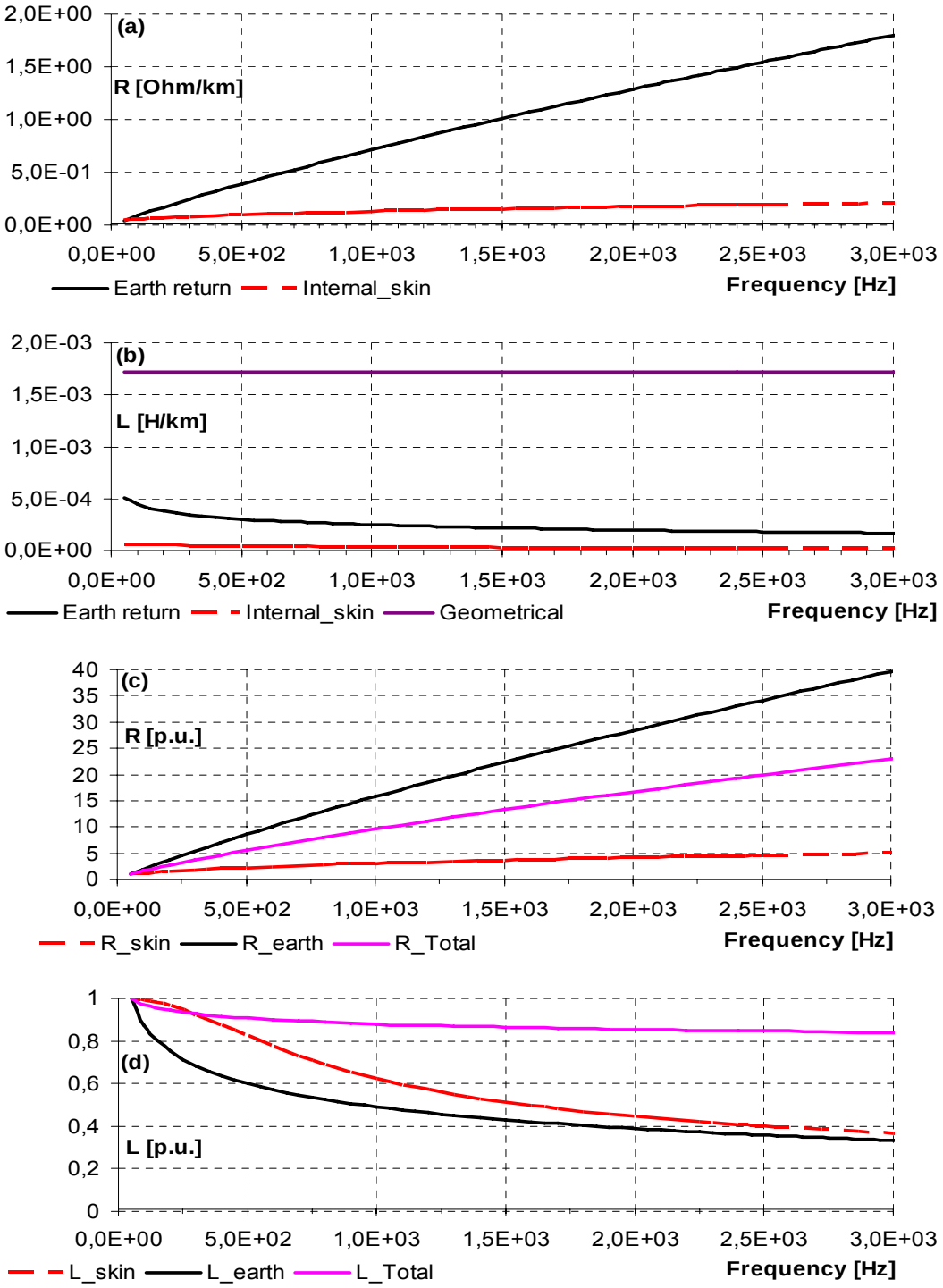

Figure 3.12 Comparison of varying resistive and inductive components of the internal conductor impedance with skin effect Z_i and the ground return impedance Z_E. Two upper plots (a) and (b): values in Ohm/km and H/km, two lower plots (c) and (d) show normalized values for 50 Hz.

In Figure 3.12 (a), the earth return resistive component and the internal conductor resistance are shown. It can be clearly seen how much higher the earth resistance is and that its frequency dependence affects the entire resistance much more than the internal conductor resistance. This is also confirmed in Figure 3.12 (c), where normalized for 50 Hz values are shown. The overall resistance value, for the analyzed case is increased 20 times at 2,5 kHz comparing to the 50 Hz value. In Figure 3.12 (b) the inductive terms are shown, at it can be seen that again the earth return inductance has higher value than the internal conductor inductance, however both of them are much lower than the geometrical inductance value, which is not frequency dependent. The geometrical inductance is dominating the overall inductance and therefore the change in the overall inductance from 50 Hz value to the 2,5 kHz value is approx. 18%, see Figure 3.12 (d). The term L_E decreases more rapidly at lower frequencies than the L_i term.

3.2.7 Nominal Pi versus equivalent Pi circuit line representation

There are two basic ways of representing transmission lines, namely by creating their nominal Pi circuit or equivalent Pi circuit [Grainger]. The first model is a simplified lumped equivalent circuit where the whole length line resistance and reactance are concentrated in the middle and shunt capacitance and conductance are concentrated at both ends [Grainger], see Figure 3.13.

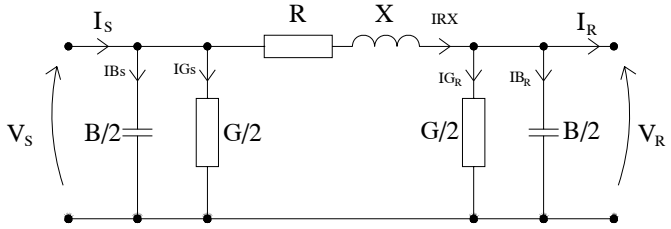

Figure 3.13 Nominal PI circuit of a transmission line [Grainger].

For the circuit presented in Figure 3.13, denoting G/2 +jB/2 = Y/2 and R + jX =Z, the following expressions describe the current and voltage at one end of a line if the voltage and current at the other end of the line are known [Grainger]:

$$\begin{aligned} V_S &= \left(\frac{ZY}{2}+1\right)V_R + ZI_R \\ I_S &= V_R Y\left(1+\frac{ZY}{4}\right)+\left(\frac{ZY}{2}+1\right)I_R \end{aligned} \quad . \tag{3.37}$$

Representing transmission lines as nominal PI circuits is convenient, but not precise and the errors introduced by lumped parameters will increase with the line length and the frequency [Arrillaga]. From Figure 3.13 can be seen that the current through the shunt capacitance B/2 is expressed as $IB_S = V_S$ x jB/2. In reality, the shunt capacitance is distributed along the line and therefore the voltage on the capacitance will not be always V_S but will change because of the increasing voltage drop on the distributed series impedance. Moreover the current that flows through the distributed series impedance and results in the voltage drop is also not constant like in Figure 3.13, $IRX = I_S - IB_S - IG_S$, but decreases as the distributed shunt capacitances and conductances increase. These relations are not reflected when using only single nominal PI circuit as a line representation.

Transmission line with distributed parameters

Figure 3.14 shows an actual transmission line representation with distributed impedance and admittance zdx and ydx.

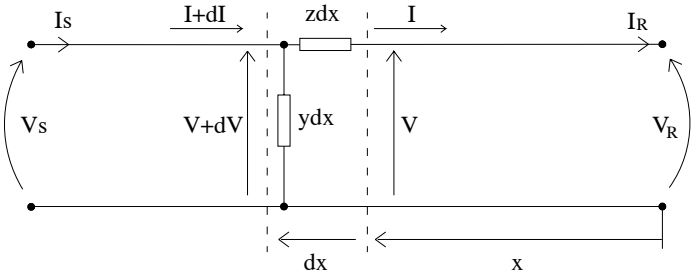

Figure 3.14 Distributed parameters transmission line [Grainger].

For this circuit the voltage and current change along the line can be written as [Grainger]:

$$\begin{aligned} \frac{dV}{dx} &= Iz \\ \frac{dI}{dx} &= Vy \end{aligned} \quad . \tag{3.38}$$

After differentiating, current and voltage can be separated [Grainger]:

$$\begin{aligned} \frac{d^2V}{dx^2} &= zyV \\ \frac{d^2I}{dx^2} &= yzI \end{aligned} \quad . \tag{3.39}$$

These two equations describe the wave propagation along a transmission line. After some transformations it is possible to express the rms values and phase angles of V and I at any point of the line [Grainger]:

$$\begin{aligned} V &= \frac{V_R + I_R Z_C}{2} e^{\gamma x} + \frac{V_R - I_R Z_C}{2} e^{-\gamma x} \\ I &= \frac{V_R / Z_C + I_R}{2} e^{\gamma x} - \frac{V_R / Z_C - I_R}{2} e^{-\gamma x} \end{aligned} \quad , \tag{3.40}$$

where $Z_C = \sqrt{z/y}$ and $\gamma = \sqrt{zy} = \alpha + j\beta$, are the characteristic impedance and propagation constant respectively. These expressions may be rewritten using the hyperbolic functions $\sinh \gamma x = \left(e^{\gamma x} - e^{-\gamma x}\right)/2$ and $\cosh \gamma x = \left(e^{\gamma x} + e^{-\gamma x}\right)/2$ [Grainger]:

$$\begin{aligned} V &= V_R \cosh \gamma x + I_R Z_C \sinh \gamma x \\ I &= I_R \cosh \gamma x + \frac{V_R}{Z_C} \sinh \gamma x \end{aligned} \quad . \tag{3.41}$$

And to calculate the sending end values x=l [Grainger]:

$$\begin{aligned} V_S &= V_R \cosh \gamma l + I_R Z_C \sinh \gamma l \\ I_S &= I_R \cosh \gamma l + \frac{V_R}{Z_C} \sinh \gamma l \end{aligned} \quad . \tag{3.42}$$

Representation of transmission lines – equivalent PI circuit

When looking at the ends of a transmission line, the distributed nature of line parameters can be accurately represented by the nominal Pi model, if the series impedance and shunt conductance are multiplied with proper factors $Z \cdot k_Z = Z'$ and $(Y/2) \cdot k_Y = Y'/2$. In this way the equivalent Pi circuit is created. The factors k_Z and k_Y can be derived by comparing both equations for V_S from (3.37) and (3.42) [Grainger]:

$$\begin{aligned} Z' &= Z_C \sinh \gamma l = \sqrt{Z/Y} \sinh \gamma l = zl\left(\sinh \gamma l \Big/ \sqrt{zy} \cdot l\right) \\ Z' &= Z \frac{\sinh \gamma l}{\gamma l} \end{aligned} \quad , \tag{3.43}$$

and

$$\begin{aligned} &\frac{Z'Y'}{2} + 1 = \cosh \gamma l = \frac{Y'Z_C \sinh \gamma l}{2} + 1 \qquad \Rightarrow \\ \Rightarrow \qquad &\frac{Y'}{2} = \frac{1}{Z_C} \frac{\cosh \gamma l - 1}{\sinh \gamma l} = \frac{1}{Z_C} \tanh \frac{\gamma l}{2} \qquad \Rightarrow . \\ \Rightarrow \qquad &\frac{Y'}{2} = \frac{Y}{2} \frac{\tanh\left(\gamma l/2\right)}{\gamma l/2} \end{aligned} \tag{3.44}$$

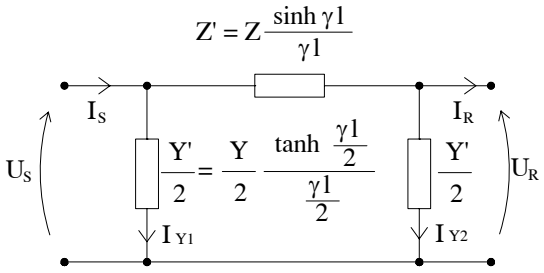

Figure 3.15 Equivalent PI circuit [Grainger].

It can be seen that that simple multiplication of the nominal PI impedance by the correction factor $\left(\sinh \gamma l\right)/\gamma l$ and admittance by the correction factor $\left(\tanh\left(\gamma l/2\right)\right)/\left(\gamma l/2\right)$ eliminate the errors coming from the lumped parameter circuit. For low γl terms (short lines and/or low frequencies) both *sinh (γl)* and *tanh (γl)* are almost equal to γl so the correction factors become close to unity – it means that in such cases applying the nominal PI circuits will not introduce significant errors [Grainger]. The computation burden of using equivalent Pi circuit does not increase in contradiction to using number of cascaded nominal Pi circuits [Arrillaga]. Therefore, it can be concluded that whenever it is not impossible, the equivalent PI circuit of transmission lines shall be preferred, especially when performing studies for long lines or higher frequencies.

As shown in Table 3.2, in the load-flow model the transmission lines are not modelled by equivalent Pi circuits but as single, lumped nominal Pi circuits. According to the theory presented above, this approach is not satisfactory. However, the software allows modelling the lines as equivalent Pi circuits. In section 3.3.1, the comparison of harmonic impedance from simulations of a line modelled as single nominal Pi circuit, 10 nominal Pi circuits and equivalent Pi circuits are shown.

3.3 Modelling of a 400 kV overhead line in harmonic domain

To verify the influence of the above described parameters, one of the existing power line models has been used for simulations.

***ASR5-REV5* transmission line model**

The line is located in Jutland, between two substations: Askær (ASR5) and Revising (REV5). The length of the modelled line used in calculations is 100 km.

The line is composed of bundled, duplex phase conductors and two ground wires. All the essential data are presented in Table 3.6 and Figure 3.16.

Conductors:	3 x 2 x AlFe; IN = 1,6 kA; Bundling distance 0,4 m; Rdc = 0,0514 Ω; A = 700 mm2; GMR = 14,889 mm.
Ground wires:	2 x 1 x Fe; IN = 0,1 kA; Rdc = 0,298 Ω; A = 185 mm2; GMR = 7,3 mm.
50 Hz data:	Z1= 0,333 Ω/km; φ1 = 85,56°; R1 = 0,026 Ω/km; X1 = 0,332 Ω/km; R0 = 18,06 Ω; X0 = 0,68 Ω/km, Ice = 1,64 A/km

Table 3.6 Data of a 400 kV transmission line ASR5-REV5 used in simulations.

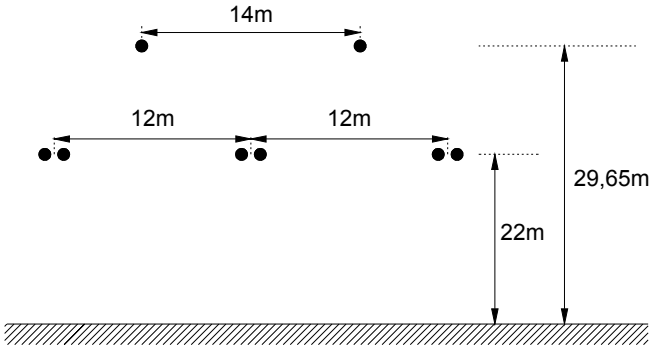

Figure 3.16 Configuration of the 400 kV transmission line ASR5-REV5 used in simulations.

This overhead line has been modelled in PowerFactory software, see Figure 3.17. The simulations have been made using the unbalanced frequency sweep option [PowerFactory].

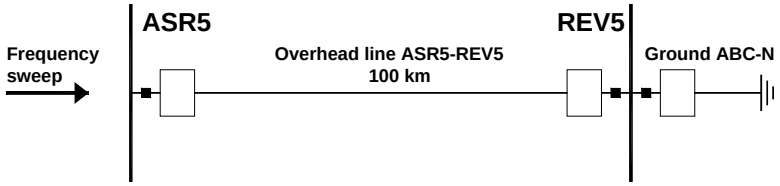

Figure 3.17 Transmission line ASR5-REV5 modelled in DIgSILENT PowerFactory.

ASR5-REV5 transmission line has been modelled in five different ways in order to investigate the effect of simplifications from Table 3.2. These models are listed in Table 3.7.

1	single nominal PI circuit
2	10 nominal PI circuits no shunt conductance
3	10 nominal PI circuits with shunt conductance
4	equivalent PI circuit, no skin effect
5	equivalent PI circuit with skin effect

Table 3.7 Five ways of modelling ASR5-REV5 overhead line.

Generally PowerFactory supports two ways of modelling transmission lines, by supplying ready electrical parameters or defining the geometrical and physical data of the towers, conductors and ground wires. In this project the geometrical data were used.

3.3.1 Nominal PI circuit vs. equivalent PI circuit

This simulation has been made for the frequency range from 10 Hz up to 4 kHz. The geometrical dimensions and conductor data have been entered and two separate models have been generated: the nominal (lumped) PI circuit of the line and the equivalent Pi circuit of the line. In this simulation the following simplifications have been assumed:

Effect	Nominal	Equivalent
Skin effect	NO	NO
Non-ideal earth return	Yes	Yes
Equivalent Pi circuit	NO	Yes
Ideal transposition	Yes	Yes
Reduction of earth wires	Yes	Yes
Conductor sags	NO	NO
Shunt conductance	NO	NO

Table 3.8 Assumed simplifications for the nominal Pi circuit and equivalent Pi circuit models.

The results of impedance calculation using the frequency sweep option are shown in Figure 3.18, where the black line represents the harmonic impedance of the nominal Pi circuit line model and the red line represents the harmonic impedance of the equivalent Pi circuit line model.

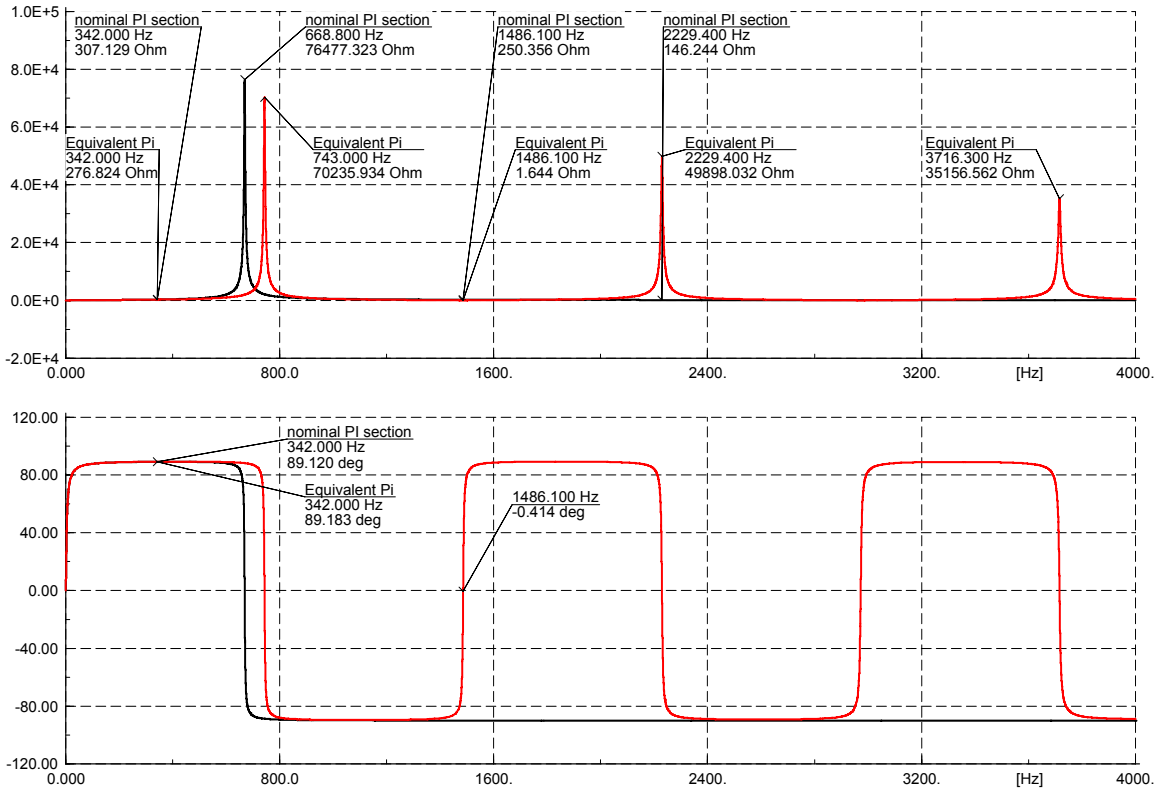

Figure 3.18 Harmonic impedance amplitude (upper plot) and phase (lower plot) of the (perfectly balanced) ASR5-REV5 transmission line. Black line – nominal PI circuit, red line – equivalent PI circuit.

Figure 3.18 shows that the single nominal PI model is an accurate representation of the line impedance at the fundamental frequency, but it is not a good model for higher frequency studies. It can be seen that it is not very accurate already at the first parallel resonance frequency. For the single nominal PI model there is only one parallel resonance at the frequency 668.8 Hz, resulting in the impedance amplitude of 76,48 kΩ. For the distributed line model, the first resonance is at 743 Hz with the impedance of 70,24 kΩ. The impedance amplitudes differ by almost 10% and the resonant frequency is shifted significantly. At higher frequencies it is much worse because no

resonances are reflected for the single nominal PI section model. The phase diagram shows that for low frequencies (up to the first resonance) the line has an inductive character; the impedance phase angle is 89,12°. At first resonant frequency the line impedance shifts and becomes capacitive, with the phase angle of –89,6°. The impedance of single PI model stays capacitive for the whole frequency range above first resonance. The full, distributed line model reflects the real line behavior; at frequency 1486,1 Hz the impedance shifts back and becomes inductive; at this frequency series resonance appears. During the series resonance, the capacitive reactance becomes again equal to inductive reactance with the opposite sign and the remaining impedance has the pure resistive nature and low value of 1,6Ω. Next two parallel resonances are at the frequencies 2223 Hz and 3716 Hz with the impedance amplitude of 49,9 kΩ and 35, 2 kΩ respectively.

It can be observed that if the first parallel resonance frequency of the distributed model is designated as ***F***, then the next parallel resonances are exactly at the odd multiples of F, i.e. 3F, 5F, 7F, etc. It can be checked that the parallel resonances occur at the half wavelength frequencies for the particular line length [Arrillaga]. Similarly the series resonances occur at even multiples of the first resonance frequency, i.e. 2F, 4F, 6F, etc [Arrillaga]; at the odd quarter of wavelength frequency [Arrillaga].

The correctness of amplitude plot from Figure 3.18 can be checked by hand calculation, knowing that the upper asymptote f the impedance plot at parallel resonance is described by [Arrillaga]:

$$|Z| = Z_0 \coth \alpha l \,, \tag{3.45}$$

where $Z_0 = \sqrt{Z/Y}$ Z and Y are per km, α is the attenuation constant calculated from $\gamma = \sqrt{ZY} = \alpha + j\beta$ and l is the length of the line in km.

Hand calculation of the parallel resonance impedance at 2229,4 Hz.

At 2229,4 Hz the total series positive-sequence impedance of the line is Z = 0,0394 + j14,7775 Ohm/km, and positive-sequence susceptance is B=150,26 μS/km, with shunt conductance ignored and l = 100 km. From these values the characteristic impedance is Z_0 = 313,57 Ohm and the propagation constant is $\gamma = \alpha + j\beta$ = 6,282 x 10^{-5} + j0,047. Calculated impedance at this parallel resonance is Z = **49916** Ohm. Comparing to the result from Figure 3.18, which is **49898** Ohm, it can be said that the agreement is very good (the difference is due to the rounding off error).

Hand calculation of the parallel resonance impedance at 743 Hz.

At 743 Hz, the total series positive-sequence impedance of the line is Z = 0,028008 + j4,9265 Ohm/km, and positive-sequence susceptance is B=50,0860 μS/km. From these values the characteristic impedance is Z_0 = 313,628 Ohm (larger than at 2229,4 Hz because of frequency dependent inductance), and the propagation constant is $\gamma = \alpha + j\beta$ = 4,46510 x 10^{-5} + j0,015708 and l = 100 km. Calculated impedance at this parallel resonance is Z = **70239** Ohm. Comparing to the result from Figure 3.18, which is **70236** Ohm, it can be said that the agreement is very good, better than at 2229,4 Hz, because more digits after decimal point were used in calculations.

Series resonance could be also verified by using the equation for lower asymptote [Arrillaga]:

$$|Z| = Z_0 \tanh \alpha l \,. \tag{3.46}$$

At very large frequencies, the two asymptotes shall approach the characteristic impedance Z_0 [Arrillaga].

Generally from Figure 3.18 can be concluded that a single PI lumped model can represent a transmission line for frequencies up to one half of the first resonant frequency. In the studied case the impedance magnitude difference at one half of the first resonant frequency was below 10%.

The length of the line has an effect on the line resonances. Figure 3.19 shows the frequency of the first parallel resonance, for the nominal PI section (black) and the equivalent PI circuit (red). It can be seen that for overhead lines below 30 km the first resonance frequency is above 2,5 kHz, and half of the first resonance frequency at 2,5 kHz is for a line that is approximately 15 km long.

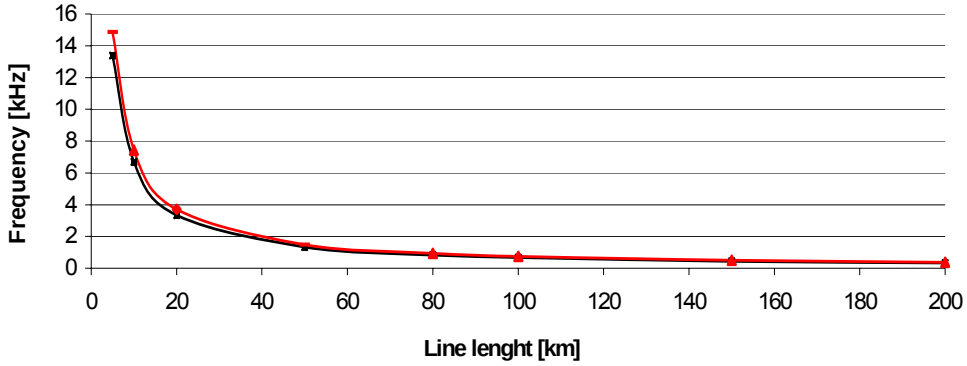

Figure 3.19 First resonance frequency vs. the length of the transmission line. Black line represents the single PI-section model and red line represents the distributed parameters line model.

10 nominal Pi sections vs. equivalent Pi circuit model

To reduce the error caused by the single lumped PI model, the line can be divided into several PI sections. The more PI sections used for calculations, the more accurate the model will be at higher frequencies. A comparison between harmonic impedance of the ASR5-REV5 transmission line modelled with 10 nominal Pi sections and an equivalent Pi circuit model is shown in Figure 3.20.

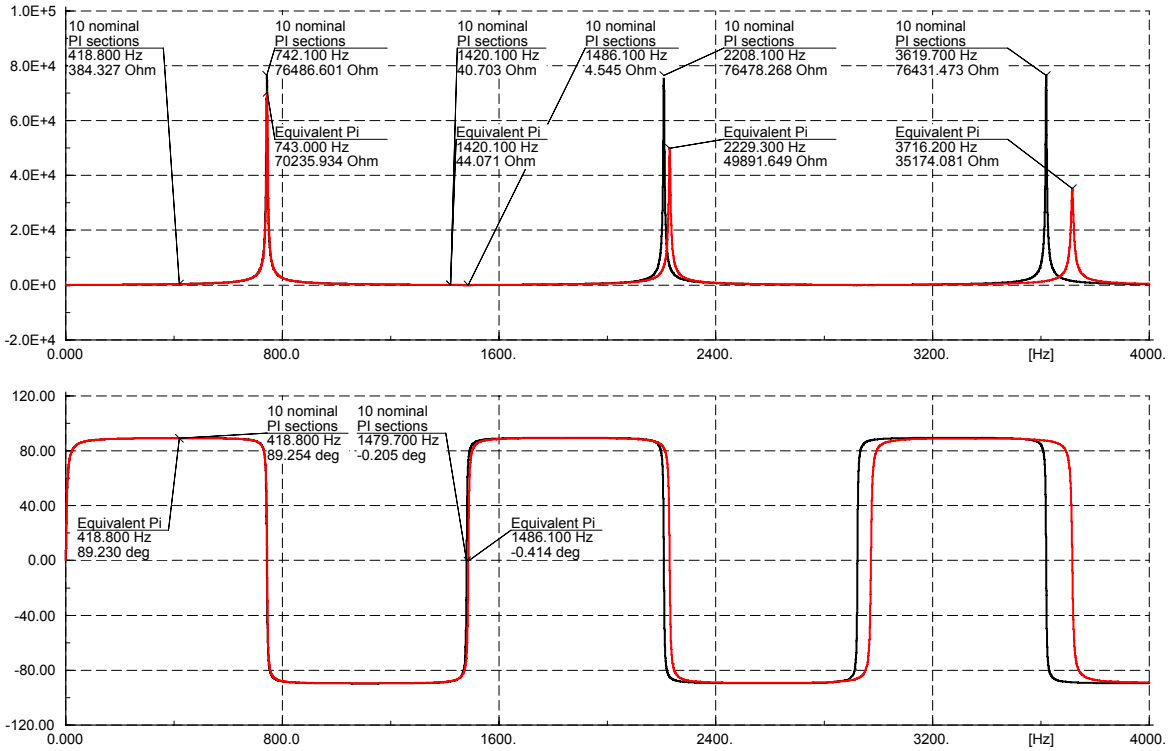

Figure 3.20 Harmonic impedance amplitude (upper plot) and phase (lower plot) of the of the ASR5-REV5 transmission line. Black line – 10 nominal PI circuits, red line – equivalent PI circuit.

It is can be seen that increasing the number of PI sections improves the accuracy of the modelled harmonic line impedance. The first resonance is almost ideally at the same frequency like in the distributed parameter model: 742.1 Hz and 743 Hz respectively. The resonance impedance differs; for the cascaded model it is higher by around 9%. The impedance amplitude accuracy is within 10% up to the first series resonance, around 1500 Hz. The second parallel resonance at 2229 Hz is already slightly shifted in the frequency (20 Hz) and differs in the amplitude by 50%. This means that the cascaded Pi model does not represent the damping effects present in reality.

The transmission line model composed of cascaded lumped PI sections will show as many parallel resonances as the number of PI-sections used to construct the model, see Figure 3.21. In the investigated case, for the 10 nominal Pi sections used to model the overhead line *Askær – Revising* there are 10 parallel resonances. Moreover the resonances do not occur at the actual resonant frequencies but are shifted, because of the effect of the lumped inductance and capacitance values.

Therefore, it can be concluded that though for low frequencies lumped PI models can be used, it is generally not advisable to use them for more accurate harmonic studies. Whenever possible, a model based on the equivalent Pi circuit shall be chosen.

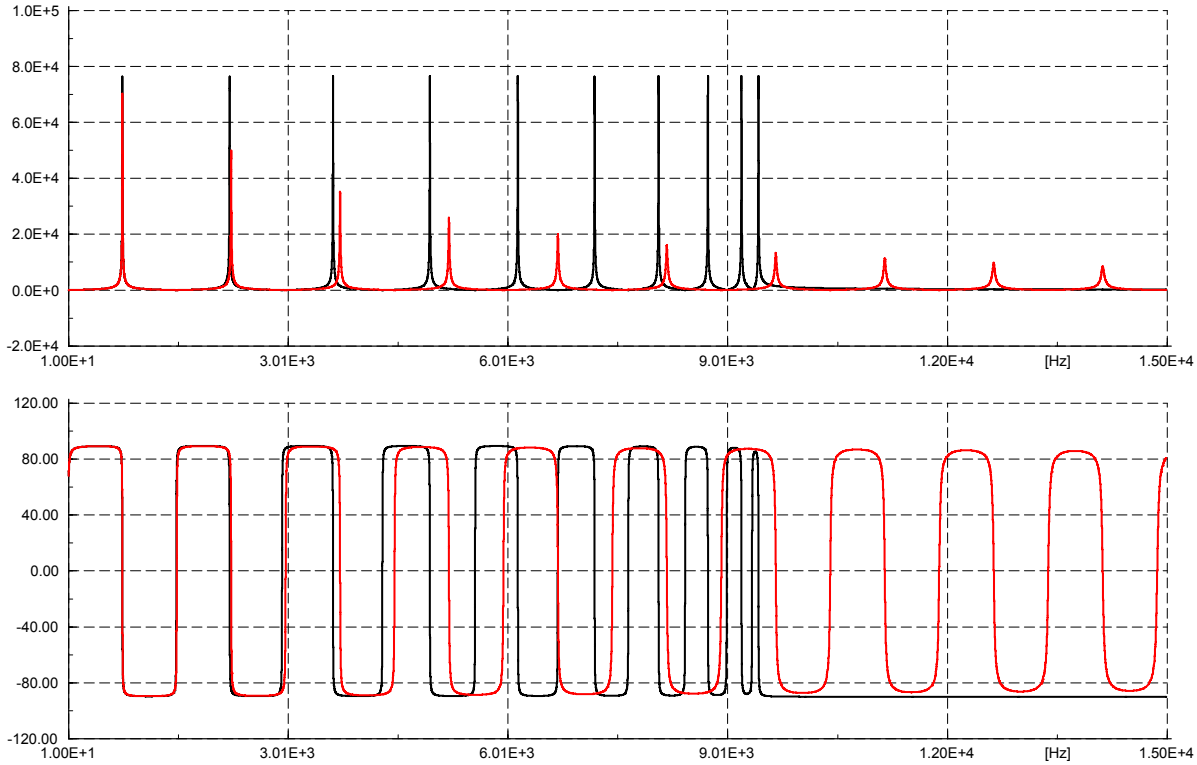

Figure 3.21 Harmonic impedance amplitude (upper plot) and phase (lower plot) of the of the ASR5-REV5 transmission line. Black line – 10 nominal PI circuits, red line – equivalent PI circuit. Frequency range: 15 kHz.

3.3.2 The influence of shunt conductance

It is not practically possible to calculate the exact current component caused by the leakage at the insulators and corona effect from pure information about the line geometry, because the corona effect is a result of many varying factors, like air pressure, presence of water vapor, conductor irregularities [Comber], [Gross]. The power loss caused by the corona effect is often described in kW/phase/km of the conductor. This power loss is small and in general varies in a vide range [Comber]. According to [Gross] this power loss can be as low as 2 kW/phase/km for a typical

high voltage overhead line at good weather conditions, and up to 30 kW/phase/km for bad weather conditions with hoarfrost covered conductors [Gross].

If the corona power loss has to be taken into account in load-flow studies, it is modelled as a linear, constant shunt conductance, incorporated into the Pi circuit line model. In the PowerFactory software it is also possible to incorporate it in the nominal Pi circuit model of a line. Such approximation is acceptable for load-flow studies, but is rather not correct at harmonic frequencies, because the corona current dependence on the voltage magnitude is nonlinear [Comber].

The purpose of this subsection is to deduct whether the corona losses shall be included in the line model when performing harmonic analysis studies, and what the consequence of modelling this power loss as linear shunt conductance is in the harmonic analysis studies. For that purpose, two line models were used in the simulation, each composed of 10 nominal Pi circuits (arbitrary chosen number). One of the models has the positive sequence conductance entered manually. Two cases are inspected. In the first one, "good weather conditions" are assumed with an active power loss of 2 kW per phase per kilometer, which corresponds to a shunt conductance of the three phase conductors 0,0375 μS/km, and second, a worst case, assuming 30 kW power loss per phase per kilometer (0,5625 μS/km) for "bad weather conditions". The resultant line impedances for the two cases are presented in Figure 3.22 and Figure 3.23

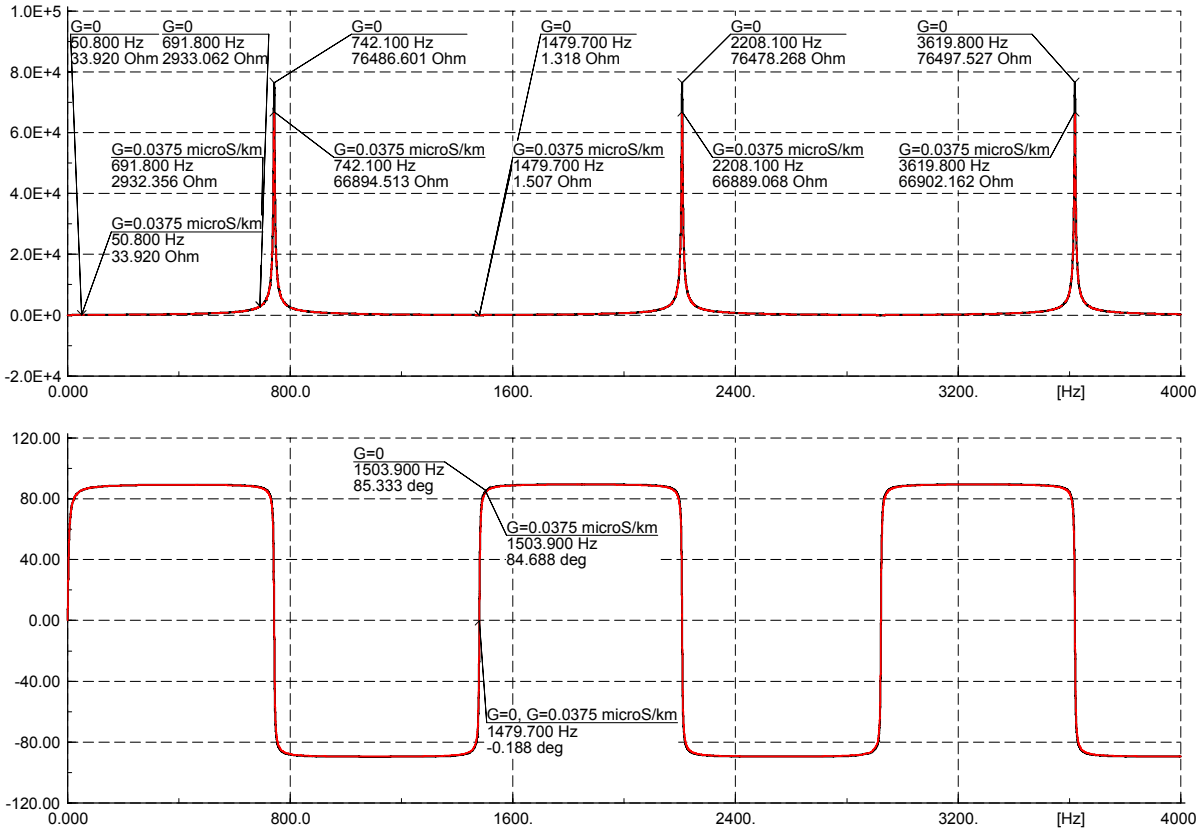

Figure 3.22 Influence of the shunt leakage conductance on the total line impedance for the *power loss of 6 kW/km*, 10 nominal Pi circuit line models: black – G=0, red – G=0.0375 μS/km

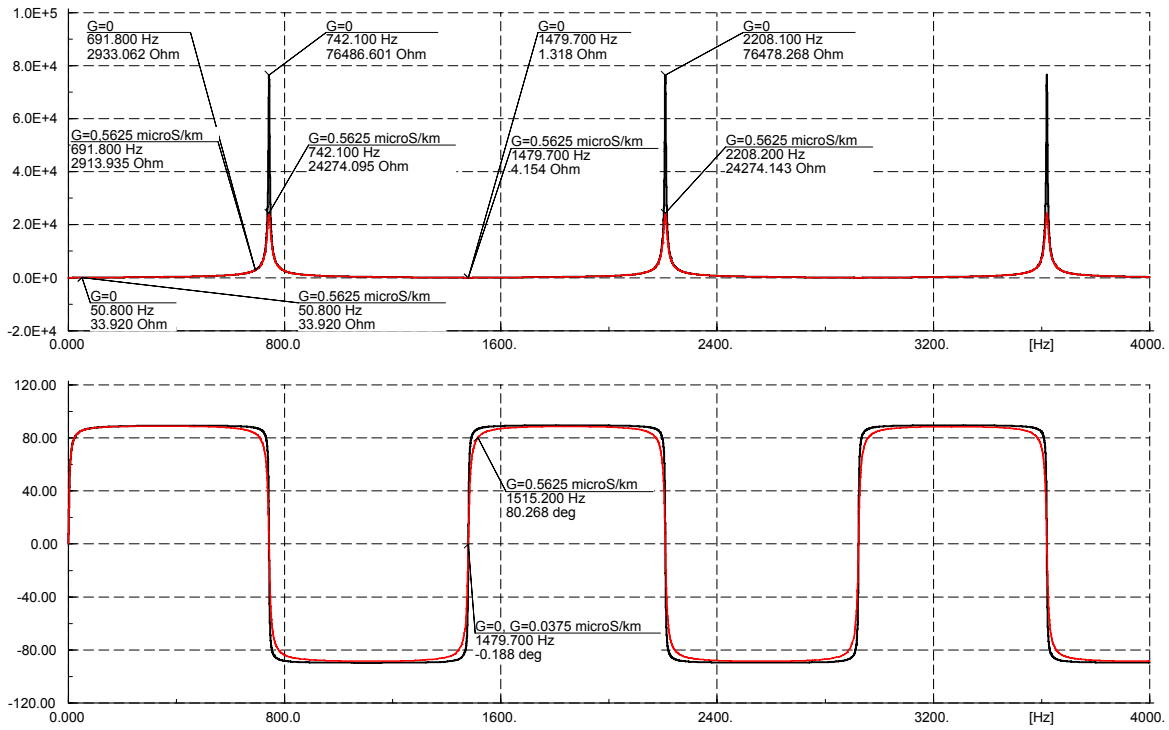

Figure 3.23 Influence of the linear shunt leakage conductance on the total line impedance for the power loss of 90 kW/km, 10 nominal Pi circuit line models: black – G=0, red – G=0.5625 μS/km.

When comparing Figure 3.22 with Figure 3.23 it can be seen that the resonant frequencies are not altered by the increased value of shunt conductance.

The magnitude of parallel resonance is lower when the shunt conductance is higher: the impedance of the first parallel resonance for G = 0 μS/km is Z = 76,486 kΩ, for G = 0,0375 μS/km it is Z = 66,89 kΩ and for G = 0,5625 μS/km it is Z = 24,27 kΩ. This is caused by the shunt conductance providing an alternate path for the current and bypassing the high impedance.

As can be seen, at fundamental frequency the effect of shunt conductance on the line impedance is practically unnoticeable and therefore negligible.

It can be also seen that also for other frequencies the shunt conductance does not really change the overall line impedance. The noticeable difference is at the resonant frequencies.

Therefore, it can be concluded that if the corona loss is modelled as a shunt conductance, it practically does not affect the propagation of higher harmonics on the transmission level at non-resonant frequencies. At the resonant frequencies the shunt conductance has a positive influence: it can lower harmonic overvoltages caused by the resonances by lowering the impedance of the resonant circuits.

Since the corona losses are varying in a vide range, and the corona current is nonlinear, the linear shunt conductance may cause excessive damping of harmonic resonances, higher than in reality and give optimistic levels (low) of harmonic distortion in the network. Therefore, the final conclusion of this section is that it is better to ignore the corona effect in harmonic studies than to include it in the form of a shunt linear conductance.

3.3.3 Skin Effect

As it was verified in section 3.2.5 for a single-phase conductor, PowerFactory takes into account skin effect correctly, the same as it was verified by hand calculations of the the equations based on Bessel functions (3.7)-(3.9).

The skin effect is also investigated using the 400 kV overhead line model ASR5-REV5 in order to assess its influence on the overall 3-phase transmission line impedance. Two equivalent Pi circuit line models were used. In one of them the skin effect was modelled. The frequency sweep simulations were performed for the frequency range up to 12 kHz.

The effects of the skin effect can be seen in Figure 3.24. The increase of the resistance of the conductors with frequency has damping effect and lowers the magnitudes of harmonic resonances. At the frequencies where no resonances appear, the increase in resistance does not have significant effect on the total line impedance since it is dominated by the series inductive reactance. At the resonant frequencies it has a considerable damping effect, and therefore it shall not be ignored for harmonic studies for frequencies that are close to or above the first parallel resonance.

The variation of the parallel resonance impedance amplitudes (upper asymptote described by equation (3.45)) for the line models with and without skin effect included is shown in Figure 3.25 whereas variation of impedance at series resonances (lower asymptote described by equation (3.46)) is shown in Figure 3.26. It can be seen that equations (3.45) and (3.46) are valid for a line model without the skin effect included. Skin effect reduces the impedance at the parallel resonance and raises the impedance at the series resonance (correct, since it raises series resistance). The lower asymptote is small and slowly increases whereas the upper asymptote is initially high but decreases fast with the frequency.

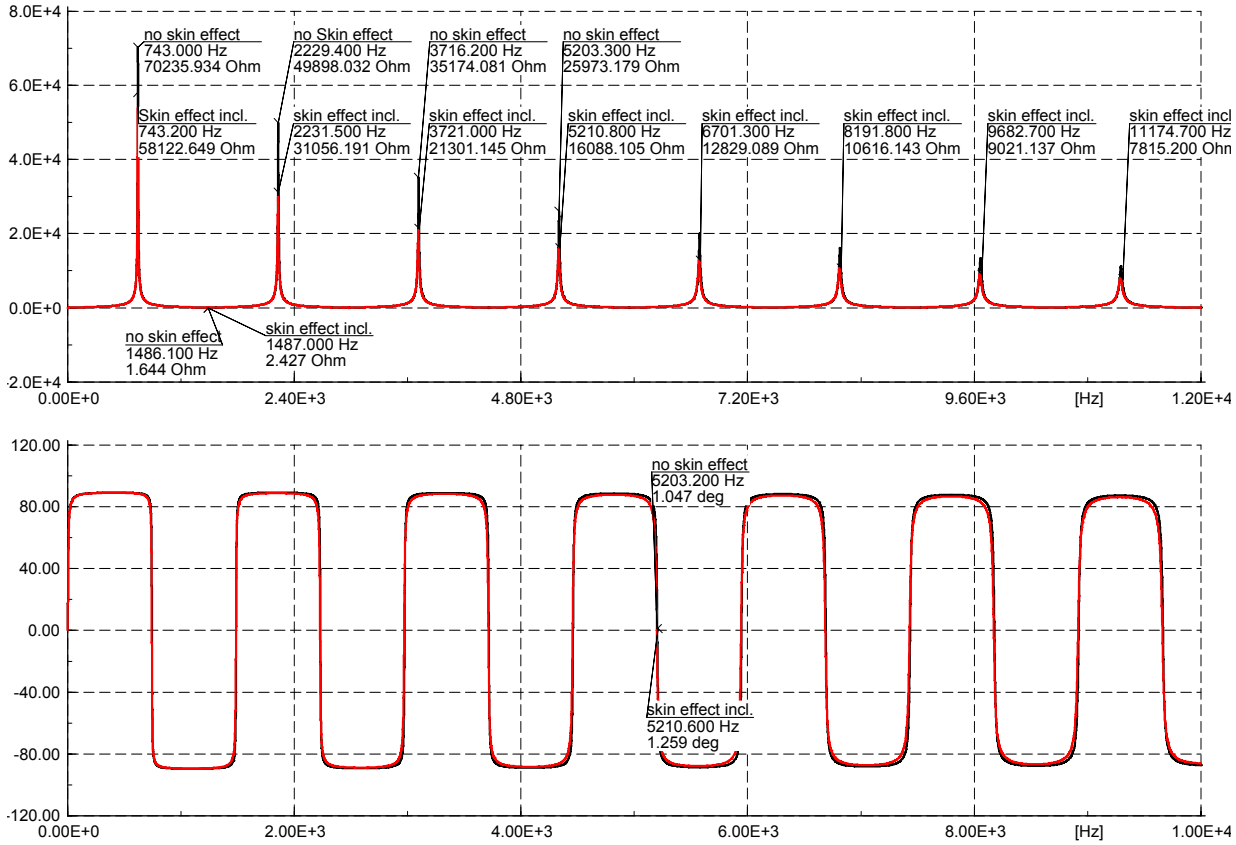

Figure 3.24 Skin effect influence on the total line impedance, up to 12 kHz. Black line – no skin effect, red line – skin effect included.

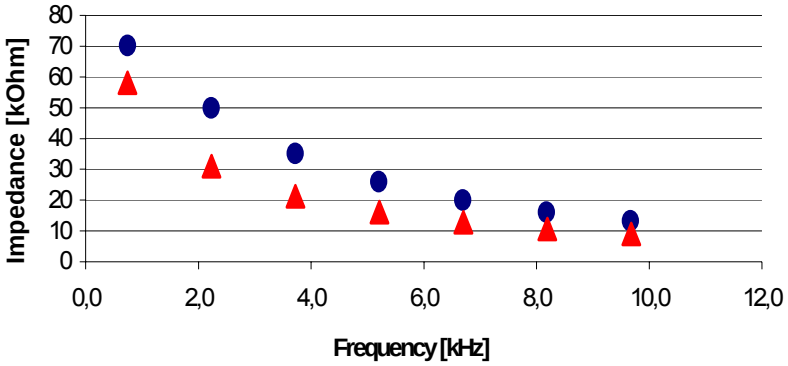

Figure 3.25 Impedance amplitude at the parallel resonance frequencies. Dots – no skin effect, triangles - model with the skin effect included.

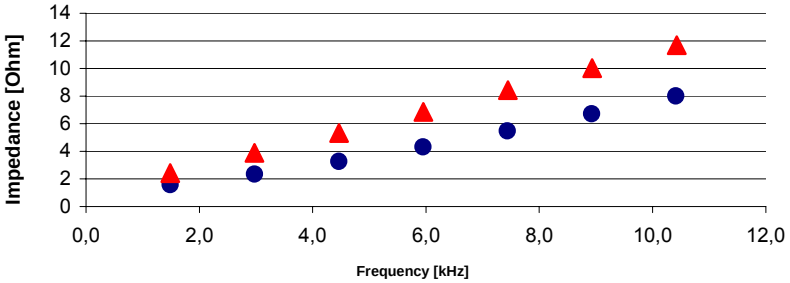

Figure 3.26 Impedance amplitude at the series resonance frequencies. Dots – no skin effect, triangles - model with skin effect included.

Te skin effect, in contradiction to the shunt conductance additionally has an influence on the frequency of the parallel and series resonances. The reason for this is that it lowers the internal conductor inductance, as discussed earlier. However this effect is not very much pronounced; at frequencies approaching 12 kHz the mismatch between parallel resonances with and without skin effect is 20 Hz, see Figure 3.27.

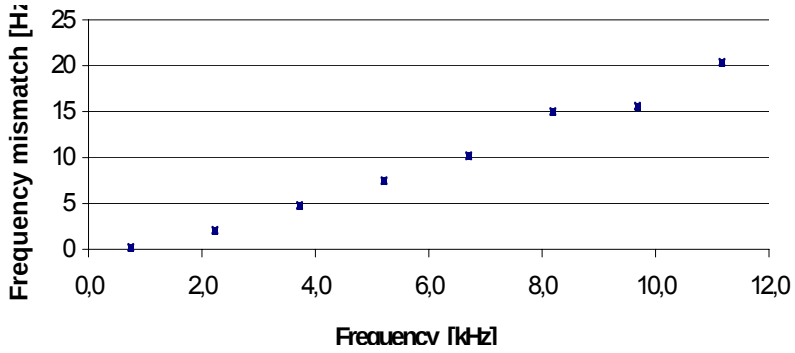

Figure 3.27 The frequency of parallel and series resonances of the line model with skin effect increases faster than the line model without the skin effect – caused by lowering of the internal conductor inductance due to the skin effect.

3.3.4 Ideal transposition versus phase unbalance

Transmission lines can be modelled:

- assuming an ideally transposed line where the average line parameters are calculated and single-phase instead of three-phase calculations are possible,
- modelling the actual line geometry i.e. taking into account the phase unbalance.

In the first case the theoretical physical conditions for each phase are the same, which means that a 1 p.u. current injected in each of the phases will result in a voltage drop, the same on each phase. The mutual impedances between phases Z_m are equal and self-impedances of all phases are Z. The resultant symmetrical impedance matrix Z_{ABC} after transformed to symmetrical components matrix has the form [Stevenson]:

$$Z_{012} = T^{-1} \cdot Z_{ABC} \cdot T =$$

$$= \frac{1}{3}\begin{bmatrix} 1 & 1 & 1 \\ 1 & a & a^2 \\ 1 & a^2 & a \end{bmatrix} \cdot \begin{bmatrix} Z & Z_m & Z_m \\ Z_m & Z & Z_m \\ Z_m & Z_m & Z \end{bmatrix} \cdot \begin{bmatrix} 1 & 1 & 1 \\ 1 & a^2 & a \\ 1 & a & a^2 \end{bmatrix} = \begin{bmatrix} \overbrace{Z + 2Z_m}^{Z_{00}} & 0 & 0 \\ 0 & \overbrace{Z - Z_m}^{Z_{11}} & 0 \\ 0 & 0 & \overbrace{Z - Z_m}^{Z_{22}} \end{bmatrix}, \qquad (3.47)$$

All the mutual terms in the symmetrical components matrix are zero; there is no coupling between the voltages and currents of different sequences of a perfectly balanced line. Therefore the analysis can be made for three single phase circuits separately. The sources can inject harmonic currents of all frequencies and the solution will be correct, as long as the assumption of perfectly balanced line can be made.

In reality however, the Z_{ABC} impedance matrix is not symmetrical due to the different distances between the phases and/or the phases and the ground wires and the ground itself. Therefore the full impedance matrix Z_{ABC} after transforming into sequence values will have the form:

$$Z_{012} = \frac{1}{3}\begin{bmatrix} 1 & 1 & 1 \\ 1 & a & a^2 \\ 1 & a^2 & a \end{bmatrix} \cdot \begin{bmatrix} Z_{AA} & Z_{AB} & Z_{AC} \\ Z_{BA} & Z_{BB} & Z_{BC} \\ Z_{CA} & Z_{CB} & Z_{CC} \end{bmatrix} \cdot \begin{bmatrix} 1 & 1 & 1 \\ 1 & a^2 & a \\ 1 & a & a^2 \end{bmatrix} = \begin{bmatrix} Z_{00} & Z_{01} & Z_{02} \\ Z_{10} & Z_{11} & Z_{12} \\ Z_{20} & Z_{21} & Z_{22} \end{bmatrix}, \qquad (3.48)$$

The resultant matrix is still full. This matrix usually is strongly diagonally dominant, but there are the off-diagonal terms that express the coupling between sequences [Acha]. It means that the injection of, say, 5th harmonic purely negative sequence current will give rise to 5th harmonic voltage of positive, negative and zero sequence. Neglecting the mutual coupling between sequence components will introduce errors that not always are acceptable. If the errors are not acceptable, the solution is no longer simpler in symmetrical components than in phase components. Calculations cannot be performed on full matrices because line impedances contain hyperbolic functions, logarithms, etc, and these cannot be directly calculated on matrices [Acha].

The state-of-the-art method of diagonalizing unbalanced impedance matrices is the modal analysis [EMTDC], [Arrillaga], [Dommel]. Modal analysis is based on the eigenvalue and eigenvector problem [Kreyszig]. The method will be briefly described here, as it is used In PowerFactory software. For a three-phase transmission line equations (3.39) contain the matrices [Dommel]:

$$\left[\frac{d^2V_{phase}}{dx^2}\right] = [Z_{phase}][Y_{phase}][V_{phase}]$$
$$\left[\frac{d^2I_{phase}}{dx^2}\right] = [Y_{phase}][Z_{phase}][I_{phase}] \quad (3.49)$$

Products $[Z_{phase}][Y_{phase}]$ and $[Y_{phase}][Z_{phase}]$ are full matrices. If these products can be diagonalized, the equations would become decoupled and could be separately calculated for each mode, like for single-phase circuits. When the solution is obtained in the modal domain, the results can be transformed back to the matrix form in phase domain. There will be the same number of modes in modal domain as number of conductors in the phase domain [Dommel]. The diagonalization of $[Z_{phase}][Y_{phase}]$ and $[Y_{phase}][Z_{phase}]$ is made using the diagonalizing matrices T_V and T_I, so that diagonal matrices [Dommel] are formed:

$$[\Lambda_V] = [T_V]^{-1}[Z_{phase}][Y_{phase}][T_V], \quad (3.50)$$

and

$$[\Lambda_I] = [T_I]^{-1}[Y_{phase}][Z_{phase}][T_I], \quad (3.51)$$

where $[T_I] = [T_V^t]^{-1}$. $[T_I] = [T_V^t]^{-1}$. Voltages and currents can be transformed from phase quantities to mode quantities by $V_{mode} = [T_V]^{-1}[V_{phase}]$ and $I_{mode} = [T_I]^{-1}[I_{phase}]$. The diagonal elements of $[\Lambda_V]$ and $[\Lambda_I]$ are the eigenvalues of the matrix products $[Z_{phase}][Y_{phase}]$ and $[Y_{phase}][Z_{phase}]$ [Dommel]. To calculate the eigenvalues of a square matrix, the characteristic equation has to be solved. For voltage it can be written that [Kreyszig]:

$$[Z_{phase}][Y_{phase}][T_V] = [T_V]\Lambda_V, \quad (3.52)$$

where Λ_V is a scalar value. Equation (3.52) can be written in the form [Kreyszig]:

$$([Z_{phase}][Y_{phase}] - \Lambda_V \cdot \mathbf{1})[T_V] = 0, \quad (3.53)$$

and the eigenvalues are the roots of characteristic equation [Kreyszig]:

$$\mathbf{det}([Z_{phase}][Y_{phase}] - \Lambda_V \cdot \mathbf{1}) = 0. \quad (3.54)$$

Analogous procedures are made for the currents. The diagonalizing transformation matrices T_V and T_I are the eigenvectors of the products $[Z_{phase}][Y_{phase}]$ and $[Y_{phase}][Z_{phase}]$. After the eigenvalues are calculated, the eigenvector for voltage T_V can be calculated from (3.52), since all other values are known now, and $[T_I] = [T_V^t]^{-1}$ [Kreyszig]. Having T_V and T_I calculated, the diagonal modal matrices from (3.50) and (3.51) can be calculated [Dommel]. Series impedance and shunt admittance matrices can be also expressed in the modal domain [Dommel]:

$$[Z_{mode}] = [T_V]^{-1}[Z_{phase}][T_V], \quad (3.55)$$

$$[Y_{mode}] = [T_I]^{-1}[Y_{phase}][T_I]. \quad (3.56)$$

The main idea of the modal domain method has been outlined above. There are various practical ways of obtaining the eigenvectors and eigenvalues, as mentioned by [Dommel] that however will not be investigated in this project.

If a power line is grounded at one end and a purely positive sequence voltage is applied to the other end, the resultant harmonic current will be also purely positive sequence if the off-diagonal terms of symmetrical components impedance matrix are ignored. The current will however contain all sequences if the line unbalance is represented. Such case has been setup in

PowerFactory. The ASR5-REV5 overhead line configuration of the phase conductors has been used. To one of the terminals, a purely positive sequence voltage is applied with the voltage amplitude 400 kV, see Figure 3.28. An unbalanced harmonic calculation was performed, for two cases, with and without ideal line transposition.

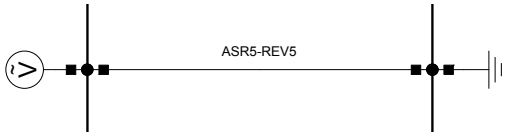

Figure 3.28 Overhead line ASR5-REV5 (equivalent Pi) with positive sequence voltage source

The line voltage is 400 kV, purely positive sequence, and the absolute phase angle of voltage in phase A is 0 deg. The resultant current in phase components and calculated by symmetrical components for ideally transposed line is:

$$I_{ABC} = \begin{bmatrix} 6{,}92\angle -85{,}5°kA \\ 6{,}92\angle 154{,}5°kA \\ 6{,}92\angle 34{,}5°kA \end{bmatrix} \rightarrow I_{012} = \begin{bmatrix} 0kA \\ 6{,}92\angle -85{,}5°kA \\ 0kA \end{bmatrix},$$

and when the unbalanced option was selected it is:

$$I_{ABC} = \begin{bmatrix} 6{,}69\angle -80{,}36°kA \\ 7{,}49\angle 154{,}78°kA \\ 6{,}80\angle 29{,}22°kA \end{bmatrix} \rightarrow I_{012} = \begin{bmatrix} 0{,}097\angle -16{,}59°kA \\ 6{,}975\angle -85{,}47°kA \\ 0{,}613\angle -39{,}00°kA \end{bmatrix},$$

which shows the effect of coupling between sequence components of the line.

Impedance matrices calculation and reduction of earth wires

PowerFactory calculates several different impedance matrices of a transmission line. First there is the so-called natural impedance matrix that is defined for the phase as well as earth wires [PowerFactory]:

$\begin{bmatrix} \Delta U_E \\ \Delta U_P \end{bmatrix} = \begin{bmatrix} Z_{EE} & Z_{EP} \\ Z_{PE} & Z_{PP} \end{bmatrix} \begin{bmatrix} I_E \\ I_P \end{bmatrix}$, where Z_{EE} and Z_{PP} are the self impedances of the earth and phase wires respectively and Z_{EP} and Z_{PE} contain all the mutual terms between the earth and phase wires. In standard calculations this matrix is reduced to a 3x3 matrix Z_{red} for three phases only by assuming that the earth wires are ideally grounded and therefore the voltage drop across them (ΔU_E) is zero. The reduced impedance matrix is calculated from [PowerFactory]:

$$\Delta U_P = \left[Z_{PP} - Z_{PE} Z_{EE}^{-1} Z_{EP} \right] I_P = Z_{red} I_P$$

As an example, impedance matrices calculated by PowerFactory for the line model ***ASR5-REV5*** (two earth wires and three phase conductors) are shown below. The values are calculated for **50 Hz**, unbalanced line (no ideal transposition) and take into consideration the ground and skin effects:

Natural Impedance Matrix $\begin{bmatrix} Z_{EE} & Z_{EP} \\ Z_{PE} & Z_{PP} \end{bmatrix}$ *(R+jX) [ohm/km]*

0.344	**0.742**	**0.046**	**0.266**	0.047	0.294	0.047	0.285	0.047	0.243
0.046	**0.266**	**0.344**	**0.742**	0.047	0.243	0.047	0.285	0.047	0.294
0.047	0.294	0.047	0.243	**0.073**	**0.593**	**0.047**	**0.276**	**0.047**	**0.232**
0.047	0.285	0.047	0.285	**0.047**	**0.276**	**0.073**	**0.593**	**0.047**	**0.276**
0.047	0.243	0.047	0.294	**0.047**	**0.232**	**0.047**	**0.276**	**0.073**	**0.593**

Reduced Impedance Matrix Z_{red} (R+jX) [ohm/km]

0.077	0.454	0.052	0.131	0.049	0.097
0.052	0.131	0.080	0.439	0.052	0.131
0.049	0.097	0.052	0.131	0.077	0.454

Symmetrical Impedance Matrix Z_{012} (R+jX) [ohm/km]

0.181	0.688	**0.004**	**-0.004**	**-0.006**	**-0.001**
-0.006	**-0.001**	0.027	0.329	**-0.023**	**0.015**
0.004	**-0.004**	**0.024**	**0.013**	0.027	0.329

Reduced Admittance Matrix Y_{red} (G+jB) [uS/km]

0.000	3.030	0.000	-0.453	0.000	-0.144
0.000	-0.453	0.000	3.143	0.000	-0.453
0.000	-0.144	0.000	-0.453	0.000	3.030

Symmetrical Admittance Matrix Y_{012} (G+jB) [uS/km]

0.000	2.368	-0.056	0.033	0.056	0.033
0.056	0.033	0.000	3.417	0.211	-0.122
-0.056	0.033	-0.211	-0.122	-0.000	3.417

The reduced impedance matrix Z_{red} has different coefficients than the Z_{pp} matrix because the influence of ideally grounded earth wires on the line impedance is included. Since the line is not balanced, the matrix of sequence components Z_{012} is not diagonal; the off-diagonal terms are not zero, which means that there are couplings between sequences. It can be seen that the couplings between impedances are small; the highest coupling observed is between the positive and negative sequences.

The same matrices generated for the same phase configuration, but with no earth wires are:

Natural Impedance Matrix [Z_{PP}] (R+jX) [ohm/km]

0.073	0.593	0.047	0.276	0.047	0.232
0.047	0.276	0.073	0.593	0.047	0.276
0.047	0.232	0.047	0.276	0.073	0.593

Reduced Impedance Matrix Z_{red} (R+jX) [ohm/km]

0.073	0.593	0.047	0.276	0.047	0.232
0.047	0.276	0.073	0.593	0.047	0.276
0.047	0.232	0.047	0.276	0.073	0.593

Symmetrical Impedance Matrix Z_{012} (R+jX)[ohm/km]

0.167	**1.116**	0.013	-0.007	-0.013	-0.007
-0.013	-0.007	**0.026**	**0.332**	-0.025	0.015
0.013	-0.007	0.025	0.014	**0.026**	**0.332**

Reduced Admittance Matrix Y_{red} (G+jB) [uS/km]

0.000	2.911	0.000	-0.569	0.000	-0.219
0.000	-0.569	0.000	3.005	0.000	-0.569
0.000	-0.219	0.000	-0.569	0.000	2.911

Symmetrical Admittance Matrix Y_{012} (G+jB) [uS/km]

0.000	2.038	-0.074	0.042	0.074	0.042
0.074	0.042	0.000	3.394	0.229	-0.132
-0.074	0.042	-0.229	-0.132	-0.000	3.394

When comparing the impedance matrices for lines with and without the ground wires it can be seen that:

- self impedance matrices Z_{PP} in both cases are the same,
- as could be expected, the reduced impedance matrix $Z_{red} = Z_{PP}$ for line without ground wires,
- the presence of earth wires reduces considerably the zero sequence line reactance. It is because in the case without earth wires the ground is the return path for the zero-sequence currents and if earth wires are present they become a part of the return circuit – so practically the overall distance to the return equivalent circuit is reduced,

In all calculations shunt conductance was ignored.

The matrices for a perfectly transposed line without the ground wires are:

Natural Impedance Matrix [Z_{PP}] (R+jX) [ohm/km]

0.073	0.593	0.047	0.276	0.047	0.232
0.047	0.276	0.073	0.593	0.047	0.276
0.047	0.232	0.047	0.276	0.073	0.593

Reduced Impedance Matrix Z_{red} (R+jX) [ohm/km]

0.073	0.593	0.047	0.261	0.047	0.261
0.047	0.261	0.073	0.593	0.047	0.261
0.047	0.261	0.047	0.261	0.073	0.593

Symmetrical Impedance Matrix Z_{012} (R+jX) [ohm/km]

0.167	1.116	-0.000	0.000	-0.000	0.000
0.000	0.000	0.026	0.332	-0.000	0.000
0.000	0.000	-0.000	0.000	0.026	0.332

Reduced Admittance Matrix Y_{red} (G+jB) [uS/km]

0.000	2.925	0.000	-0.445	0.000	-0.445
0.000	-0.445	0.000	2.925	0.000	-0.445
0.000	-0.445	0.000	-0.445	0.000	2.925

Symmetrical Admittance Matrix Y_{012} (G+jB) [uS/km]

0.000	2.034	0.000	0.000	0.000	0.000
-0.000	0.000	0.000	3.371	0.000	0.000
0.000	0.000	0.000	0.000	0.000	3.371

For the perfectly transposed line without the ground wires the natural impedance matrix is not symmetrical yet, it is the same matrix like for non-transposed line. The reduced matrix is already symmetrical, so the natural matrix for a "real", non-transposed line is given and then the line parameters averaging is performed so in all the later calculations symmetrical line is assumed. It is also seen that as a result of the line parameters averaging, the symmetrical Z_{012} matrix becomes diagonal - all mutual couplings between sequences are cancelled.

These matrix impedances were calculated for the fundamental frequency. In order to determine the behavior of the ***ASR5-REV5*** line impedance at higher frequencies, unbalanced frequency sweep simulations have been performed.

In Figure 3.29 the harmonic impedances are shown: (a) – impedance of an ideally transposed line, (b) - phase-to-ground impedances Z_A, Z_B, Z_C of an untransposed line, (c) - sequence impedances Z_0, Z_1, Z_2 of an untransposed line, (d) – magnified zero-sequence impedance of the untransposed line.

All transmission lines in the PowerFactory computer model of the Energinet.dk Western network are modelled as ideally transposed. Figure 3.29 shows the impedance of the line in the case when it is ideally transposed. This impedance shall be compared with the positive sequence impedance of the untransposed line, see Figure 3.29 (c). It can be seen that the 50 Hz impedance of the transposed line differs by about 1,6 % from the positive sequence value. It can be noticed here that the previously mentioned difference between impedances of the phases of 3,2 % is the maximal value, but taking into account that ideal transposition means averaging of the line parameters, it can be expected that the values will be somewhere in the middle and therefore the error shall be more or less one half of that 3,2 % value, which is actually 1,6 %. The error of 1,6 percent for line impedance is not significant but it is so only at the fundamental frequency. At higher frequencies the differences are larger. The first positive-sequence parallel resonance(s) have a magnitude of 33,16 kΩ and 31,38 kΩ at frequencies 739,8 Hz and 747,8 Hz respectively, whereas the same resonance but for an ideally transposed line has the magnitude almost twice higher, about 58,12 kΩ at 743,16 Hz. This shows clearly that ideal transposition of transmission lines can introduce large errors at the resonances and relatively small errors below the first resonance. At higher frequencies, but far from the resonances like for instance for the 23rd harmonic, the positive sequence impedance is 248,7 Ω whereas for the transposed line it is 270,3 Ω – difference of around 8%.

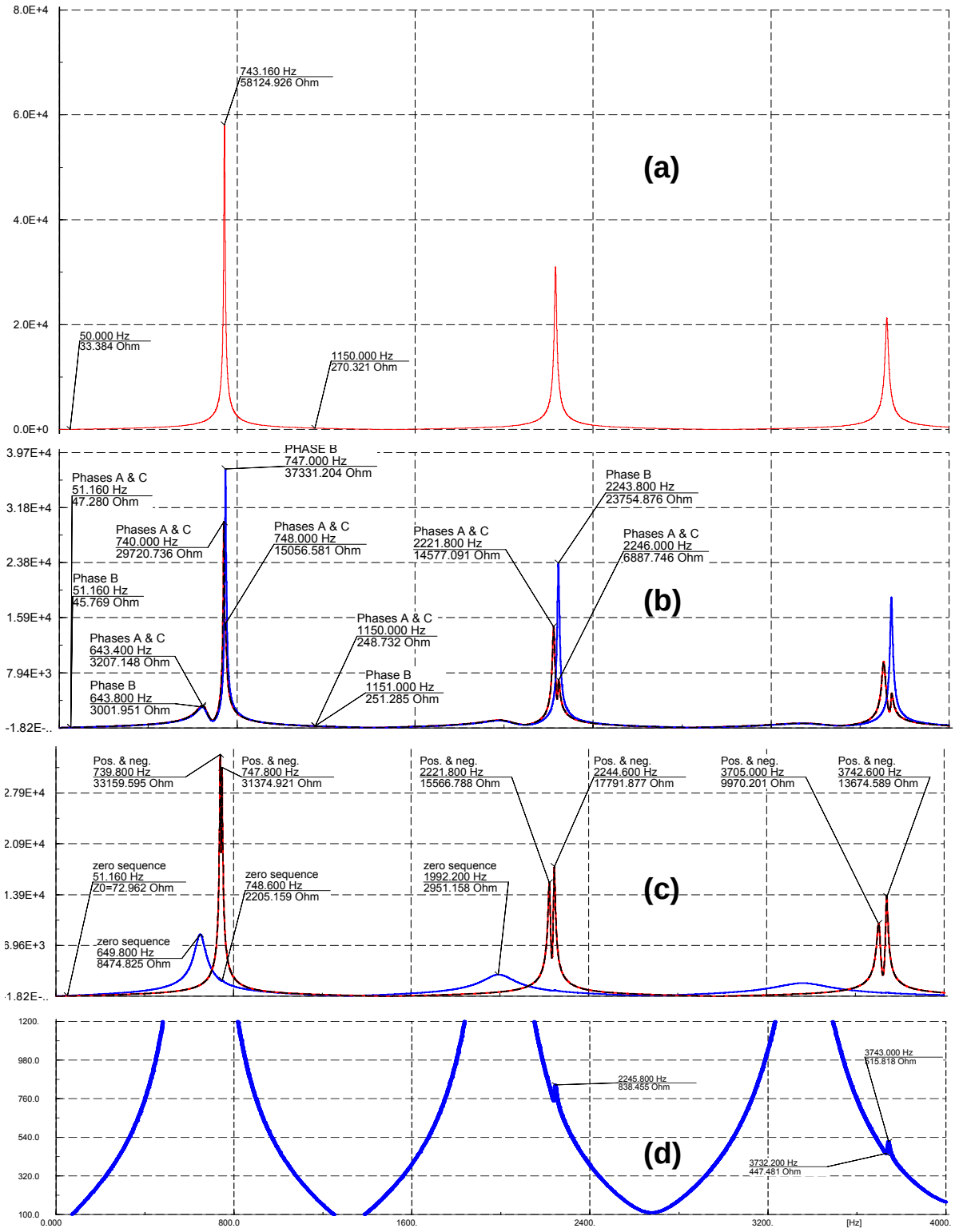

Figure 3.29 Impedance plots of the 400 kV overhead line ASR5-REV5. (a) – impedance of an ideally transposed line, (b) - phase-to-ground impedances of unbalanced line, (c) - positive, negative and zero sequence impedances of unbalanced line, (d) - magnified zero-sequence impedance of unbalanced line.

When considering the line impedance in phase components, as can be seen in Figure 3.29 (b), the impedances of phases A and C are exactly the same in the whole frequency range because of the vertical symmetry, but the impedance of phase B is different. At the fundamental frequency this

difference is not so significant; the impedance for phases A and C is $Z_A = Z_C = 47,.28\Omega$ whereas for phase B $Z_B = 45,77\Omega$. This difference of 3,2% again justifies the assumption of ideally transposed lines for fundamental frequency studies, but it can be seen that already at the 13th harmonic (650 Hz) the difference becomes more pronounced; Z_A impedance is approx. 3200 Ω whereas Z_B is 3000 Ω. The difference is almost 7%. When comparing Figure 3.29 (b) and Figure 3.29 (c) is can be seen that at this frequency, a parallel resonance related to the ground return mode becomes visible.

Figure 3.29 (b) shows that phase B has single parallel resonance, whereas phases A and C show double resonances. The first resonance can be the self impedance resonance of the phases A or C, but where does the second resonance come from? It can be noticed that it has always exactly the same frequency as the resonance of phase B. This suggests that it must be a result of the mutual coupling between the phases. The three phases of the line can be imagined as three separate circuits with the ground return. Harmonic current injected into phase A with the ground return will induce some back emf in the parallel circuit of phase B. This back emf will result in current to flow in phase B. The magnitude of this induced current will depend on the phase B impedance and therefore the magnetic field created by this current that links back phase A will reflect the impedance of phase B. This effect will be most distinct at the resonances. On another hand the impedance of phase B does not show the resonances of the other phases, only its own. This can be explained by the fact that it is symmetrically placed between phases A and C and the magnetic fields created by the induced currents of phases A and C will cancel out in the middle.

Figure 3.29 (c) shows the positive, negative and zero-sequence line impedances. As could be expected, the positive and negative impedances are the same, and they reflect the resonances of all the phases. The zero-sequence impedance shows resonances related to the ground return path. Figure 3.29 (d) shows magnified zero-sequence impedance. In this plot, the coupling between positive and zero sequence impedance is seen, i.e. the parallel resonance of phase B is reflected in the zero-sequence impedance. Thus it can be said that actually the conductor of phase B that is placed in the middle will introduce the impedance asymmetry. The coupling between positive/negative and zero-sequence impedances is quite small. It is present in the whole frequency range, is insignificant and cannot be seen, except at the resonances.

The general conclusion is that the higher the frequency, the difference between perfectly balanced and unbalanced line models becomes larger, especially at the resonant resonances. So if the harmonic studies are to be made for low frequencies and/or short lines, the perfectly balanced equivalent would suffice, but more detailed studies will require the full unbalanced line model.

3.3.5 The effect of ideal ground wires

In all standard applications PowerFactory simplifies calculations by reducing the transmission line impedance matrices to a 3x3 matrix Z_{red} for three phases. This reduced matrix takes into account the effect of earth wires on the phase impedances but with the assumption that the earth wires are ideally grounded and therefore, the voltage drop across them (ΔU_E) is zero. In order to precisely model the ground wires, PowerFactory requires constructing separate models for the 3-phase circuit and for the earth wires and defining an electromagnetic coupling between them. Then the earth wires are modelled as single-phase distributed line models with all the skin and non-ideal ground return effects included, and are coupled with the 3-phase circuit.

In reality, the earth wires are grounded at both ends of the transmission line, with a resistance value of usually 0,1 Ω [Machowski]. Grounding at each of the towers has higher resistance and vary around 10-15 Ω [Machowski]. The distance between the towers (the span) for a 400 kV overhead line could be around 300 m, which means that for a 100 km line there will be approx. 300 towers. It would be quite difficult to model all the wire groundings along the line as the PowerFactory software does not have such option predefined. Therefore, in the performed simulations the earth wires are grounded at both ends and at 10 locations along the line (every 10

km). It is far less than in reality but it shall show the main principles and allow judging whether reducing the impedance matrix is acceptable for harmonic analysis.

For the simulation purposes, the same 400 kV test line ***ASR5-REV5*** has been used (three duplex phase conductors + two steel simplex earth wires).

Four cases were inspected:

- Earth wires ignored (there phase conductors only),
- Earth wires present – reduced matrix Z_{red},
- Earth wires ideally grounded at both ends with zero resistance
- Earth wires grounded at both ends + grounded at 10 towers along the line.

In the last case, grounding resistance at both ends was R_g = 0,1Ω, at the towers wire-to-ground $R_{w\text{-}g}$=15 Ω.

The unbalanced frequency sweep was performed and resulting positive and zero-sequence impedances for all 4 cases are shown in Figure 3.30.

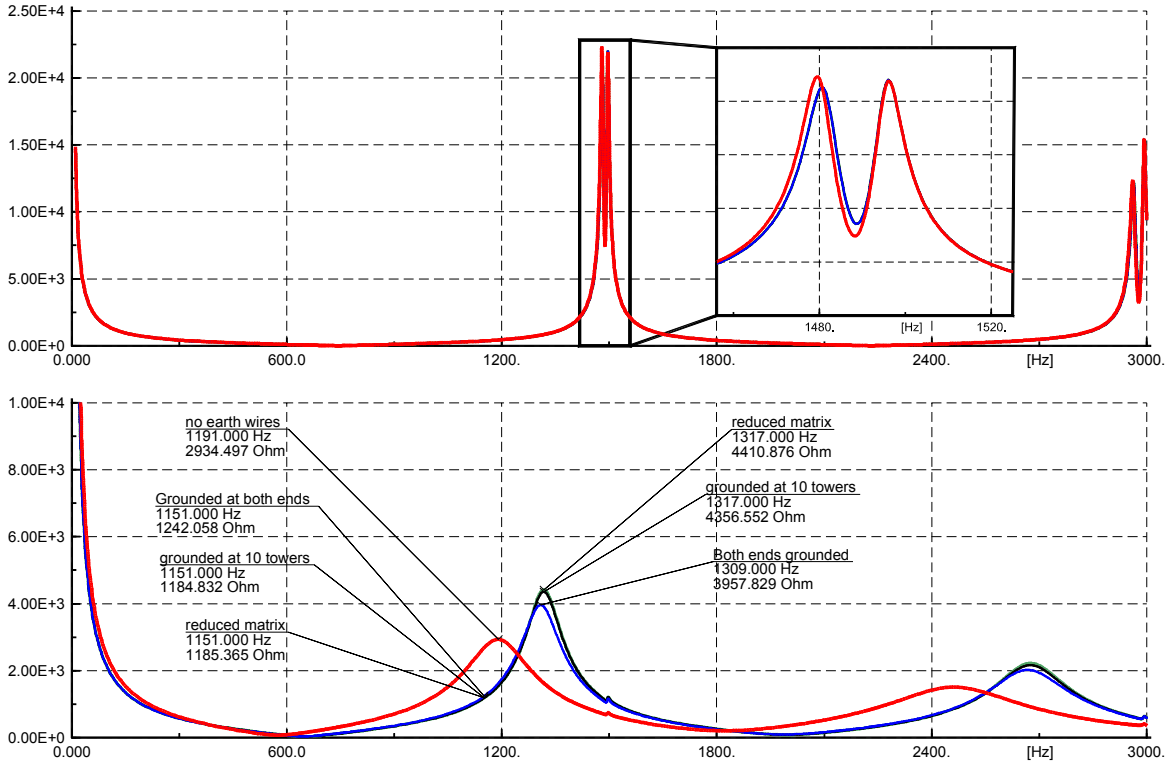

Figure 3.30 Positive-sequence impedance (upper plot) and zero-sequence impedance (lower plot) of the overhead line ASR5_REV5 for 4 cases. Red line – No earth wires, blue line – earth wires grounded at both ends, black line – earth wires grounded at 10 towers along the line, R = 15 Ω and at both ends, R = 0,1 Ω.

From the upper plot of Figure 3.30 it can be seen that the ground wires will generally very slightly affect the positive sequence line impedance. This influence can be actually visible only for the case without the ground wires and only at the resonance. This is in agreement with the previously calculated line impedances (50Hz) where the positive-sequence impedance was 0.027 + j0.329 ohm/km for line with the earth wires and 0.026 + j0.332 ohm/km without the earth wires.

It is different for the zero-sequence impedance. The lower diagram of Figure 3.30 shows the zero-sequence impedance for all cases. The zero-sequence impedance of the line without the

ground wires differs from the impedances for other cases at all frequencies; it can be especially seen for frequencies above 600 Hz. For the other three cases with the earth wires present the zero-sequence impedance is pretty much the same in the frequency range of interest. The highest deviations appear again at the resonances. When looking at the parallel resonance at the frequency 1317 Hz it is seen that the impedance of the line with earth wires grounded at both ends differs from the other two impedances, by approx. 10%. The plots reveal also that the curves for line with earth wires grounded at 10 locations and for the reduced matrix are in a surprisingly good agreement. The difference at the resonances is only 1,2%. At other non-resonant frequencies this difference is at the level of 0,1%. It can be recognized that grounding the earth wires only at 10 locations affects the zero-sequence line impedance so it becomes very close (even at the resonances) to the impedance of the reduced line matrix. From this simulation one can conclude that if the number of grounding points was increased to the real value of 300 along the line, the resultant zero-sequence impedance shall be in an even better agreement with the zero-sequence impedance of the typical PowerFactory line model with the reduced impedance matrix. if the earth wires were grounded in more and more locations along the line, finally we will end up with the theoretically ideally grounded earth wires and indeed, the voltage drop ΔU_E across them will be zero (with perfectly conducting ground), which is the assumption on which the matrix reduction is performed. Therefore, it can be stated here that in the frequency range of interests the reduced matrix line models used in PowerFactory do not introduce errors and transmission lines modelled this way can be used for harmonic analysis.

3.3.6 The effect of average height of a conductor due to sags

In the existing model of PowerFactory the sags are not considered, i.e. the existing model has been built in the PowerFactory ver. 13.0.223 and this version does not calculate the sags. The user shall calculate the effective (average) height of the conductor and enter it manually for each line. This has not been done in the existing model. In the new version 13.1.247 and upward there is a separate column where the sag distance shall be entered (when exporting the grid model from ver. 13.1.223 to the actual version 13.1.247 the sag column shows "0m") and the software calculates it automatically using a simplified equation [PowerFactory]:

$h_{average} = \frac{2}{3} \cdot h_{midspan} + \frac{1}{3} \cdot h_{connection}$, where $h_{midspan}$ is the connection height $h_{connection}$ minus the sag distance. This average height is used in all later calculations.

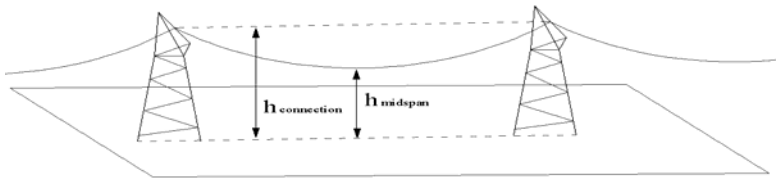

Figure 3.31 $h_{midspan}$ and $h_{connection}$ for equivalent height of conductors taking sag into consideration.

Besides the fact that the sag modelling is missing in the existing model, in reality the sag distances are not constant for a given line but strongly depend on the conductor temperature, which in turn depends on the line loading, ambient temperature wind speed, etc.

The test line model ***ASR5-REV5*** has been used and the harmonic impedances were investigated for 4, arbitrary chosen theoretical sag distances: 5m, 7m, 10m and 12m and the results are presented in Figure 3.32.

When looking at Figure 3.32, it becomes visible that different sag distances apparently do not affect the line positive and zero sequence impedances at 50 Hz. However at higher frequencies the differences start to be visible, especially for the zero-sequence impedance. For instance the positive sequence impedance for the 7th harmonic varies very little from 284.072 ohm for 5m sag, up to 284.904 ohm for 12m sag (0.35%). At the same frequency the zero-sequence impedance is more influenced, it varies from 601.442 ohm for 5m sag up to 618.041 ohm for 12m sag (2.7%).

As can be seen in Table 3.9, The different values of harmonic impedance as a function of the sag distance is a result primarily of altering the phase-to–ground capacitance, and alteration of the series inductance and resistance caused by the non-ideal ground return path, as was analyzed in section 3.2.4. The sag change from 5m to 12m resulted in zero-sequence capacitance change from 0.00783 μF/km to 0.00842 μF/km, which is about 7.6%, whereas the positive sequence capacitance was changed by 1.05%, from 0.1092 μF/km to 0.1103 μF/km. At 50 Hz, the zero-sequence inductance is changed by 0.08% (from 0.00218881 H/km to 0.00218703 H/km) and the change of the positive-sequence inductance was almost unnoticeable (value of 0.00104865 H/km for both sag distances). The resistance is mainly a function of frequency (due to ground and skin effects), where the zero sequence resistance increases almost 13 times when frequency changes from 50 Hz to 2,5 kHz, whereas positive sequence resistance increases by the factor of 2,6. Positive sequence inductance is almost not affected by the equivalent height; zero-sequence inductance is a little bit more affected, though still not very much.

Equiv. Height	Sag	Freq.	Resistance [Ohm/km]		Inductance [H/km]		Capacitance [μF/km]	
[m]	[m]	[Hz]	R1	R0	L1	L0	C1	C0
18,5	5	50	0,027064	0,180738	0,001049	0,002189	0,010920	0,007830
		1250	0,046072	1,129892	0,001044	0,001904		
		2500	0,071621	2,198908	0,001043	0,001845		
13,6	12	50	0,027066	0,180943	0,001049	0,002187	0,011035	0,008425
		1250	0,047226	1,186833	0,001044	0,001897		
		2500	0,075789	2,357921	0,001043	0,001835		

Table 3.9 Variation of line resistance, inductance and capacitance at different frequencies for two sag distances: 5m and 12m.

The conclusion is that reduction of equivalent height of a conductor does not affect the line parameters to such a large extent, except the shunt capacitance. Therefore, at 50 Hz it could be acceptable to ignore this change, but at higher frequencies it should not be ignored for frequencies that are close or above the first resonant frequency of the line.

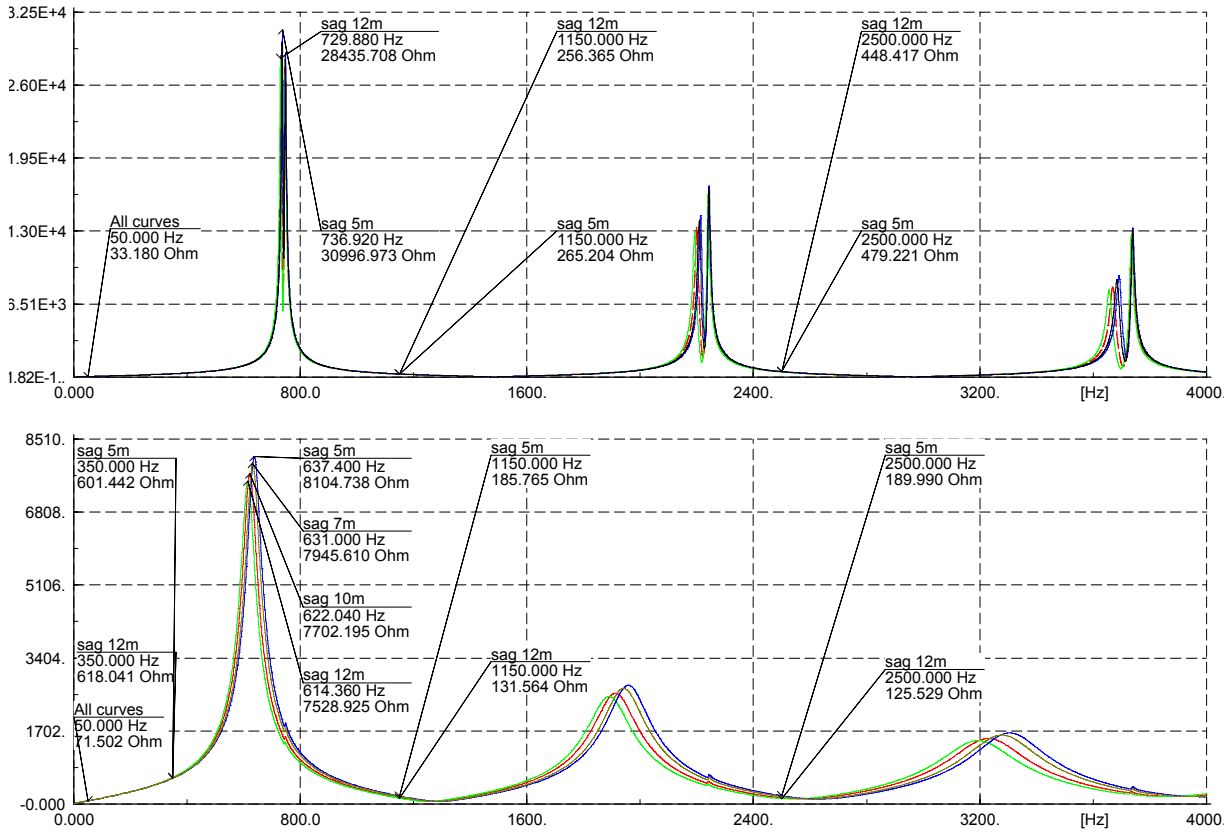

Figure 3.32 Positive-sequence impedance (upper plot) and zero-sequence impedance (lower plot) of the overhead line ASR5_REV5 for 4 different sag distances. Green line – sag 12m, red line – sag 10m, gray line – sag 7m and blue line – sag 5m.

In this section various aspects of harmonic domain modelling of transmission lines were investigated. All conclusions are summarized at the end of this chapter.

3.4 Shunt elements

The shunt elements described in this section are the shunt capacitors and reactors used for reactive power control [Kundur], and harmonic filters installed at substations where the HVDC links are connected. Harmonic filters are tuned to filter specific harmonic frequencies, but at fundamental frequency their impedance is capacitive. Since all of these shunt elements provide reactive power at fundamental frequency they are present in the PowerFactory load-flow model obtained from Energinet.dk, however the harmonic filters are modelled as pure capacitances. The inductive filter components are disregarded. Therefore, to all of them the resistive and inductive components have to be added, according to the proper datasheets obtained from Energinet.dk.

The load-flow model has been analyzed and the equipment installed at each of the 400 kV and 150 kV substations were verified with the station data catalogs and diagrams obtained from Energinet.dk [Stationsdata]. All of the shunt capacitors and reactors are present in the load-flow model. The entered parameter values of the reactive power were also verified with the catalogs [Stationsdata]. All of the shunt capacitors and reactors present in the load-flow model are shown in Chapter 2.

All the shunt elements are connected in YN. According to [Acha], [Arrillaga], the coupling between phases of the shunt components can be ignored, and therefore their admittance matrix is diagonal:

$$Y_{shunt} = \begin{bmatrix} Y_{AA} & & \\ & Y_{BB} & \\ & & Y_{CC} \end{bmatrix}, \tag{3.57}$$

and contributes only to the self-admittance of a node, to which it is connected.

3.4.1 Shunt capacitors

All of the capacitive compensation is installed at the HVDC substations to supply reactive power. Practically, all of the shunt capacitors present in the existing model are actually harmonic filters, with disregarded inductive components. There is only one pure capacitor ZC1, installed at the 400 kV HVDC substation VHA5, 55,3 MVar and capacitance of 1,1 μF. This capacitor is represented in the load-flow model.

3.4.2 Harmonic filters

Harmonic filters are installed at two 400 kV substations TJE5 and VHA5 and two 150 kV substations TJE3 and VHA3. In the load-flow model all of them are modelled as pure capacitances for the reactive power control. Therefore, these filter models had to be upgraded to reflect their high frequency characteristics. The existing capacitors have been set “out of service” and the exact harmonic filters have been installed instead. The upgraded harmonic filters have been installed at all four substations according to the following description:

TJE5 substation 400 kV

At the TJE5 substation there are four, harmonic filters of the same type installed, ZF1 – ZF4. The physical layout of the filter is shown in Figure 3.33 and values of the components are given in Table 3.10.

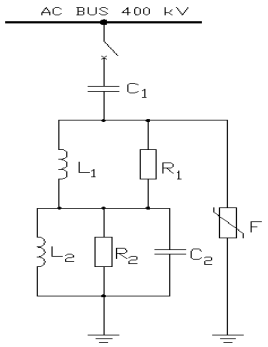

Figure 3.33 Physical layout of AC harmonic filter, double tuned, high pass filter installed at TJE5 substation.

Q = 65 Mvar, at 420 kV;
C_1 = 1.166 µF; L_1 = 32.26 mH; R_1 = 648 Ω;
C_2 = 2.013 µF; L_2 = 17.80 mH; R_2 = 383 Ω;
resonance frequency - F_1 = 589 Hz, F_2 = 1239 Hz

Table 3.10 Parameters of the double tuned, high pass filter installed at TJE5 substation.

The harmonic impedance of the filters has been determined using the PowerFactory software and is shown in Figure 3.34.

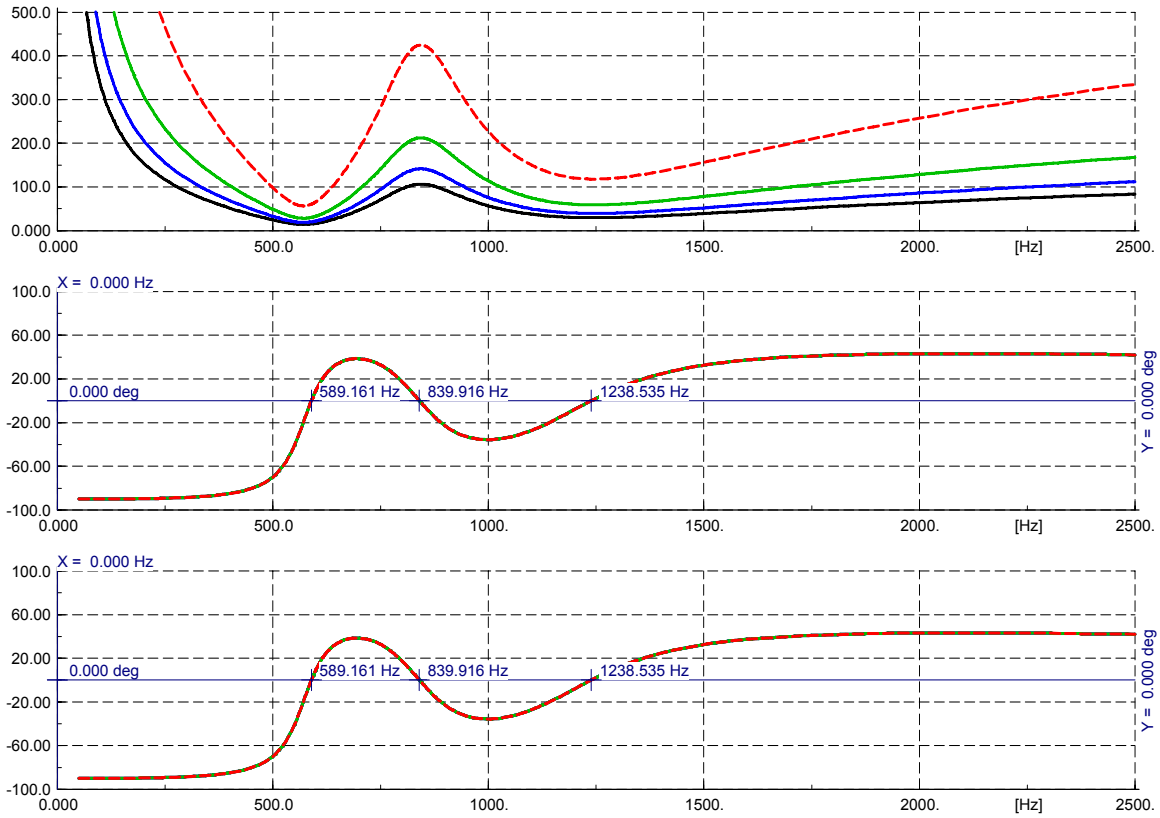

Figure 3.34 Harmonic impedance magnitude (upper plot) and phase angle (lower plot) of the harmonic filters installed at TJE5 substation. Black –four filters, blue – three filters, green – two filters and red – 1 filter.

PowerFactory does contain several, predefined filter topologies but the double-tuned, high-pass filter is not available, and therefore it had to be built from R, L and C components.

TJE3 substation 150 kV

The harmonic filters at TJE3 substation consist of two systems of filters tuned to 11th and 13th frequency, ZA1 and ZA3, and a high pass filter, see Figure 3.35. Data of the components are shown in the Table 3.11 and the harmonic impedance magnitude and phase angle of the filters determined in PowerFactory software is shown in Figure 3.36.

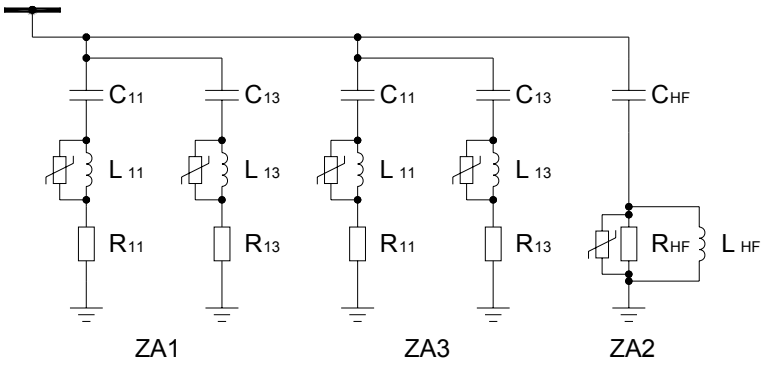

Figure 3.35 Physical layout of AC harmonic filters at TJE3 substation.

$Q_{ZA1} = Q_{ZA3} = 40$ MVar, $Q_{ZA2} = 80$ MVar
$C_{11} = 2{,}46$ µF; $L_{11} = 33.9$ mH; $R_{11} = 0{,}71$ Ω;
$C_{13} = 2{,}46$ µF; $L_{13} = 24{,}32$ mH; $R_{13} = 0{,}48$ Ω;
$C_{HF} = 8{,}79$ µF; $L_{HF} = 2$ mH; $R_{HF} = 1000$ Ω;
resonance frequency - $F_{11} = 551$ Hz, $F_{13} = 651$ Hz, $F_{HF} = 1200$ Hz

Table 3.11 Parameters of harmonic filters installed at TJE3 substation.

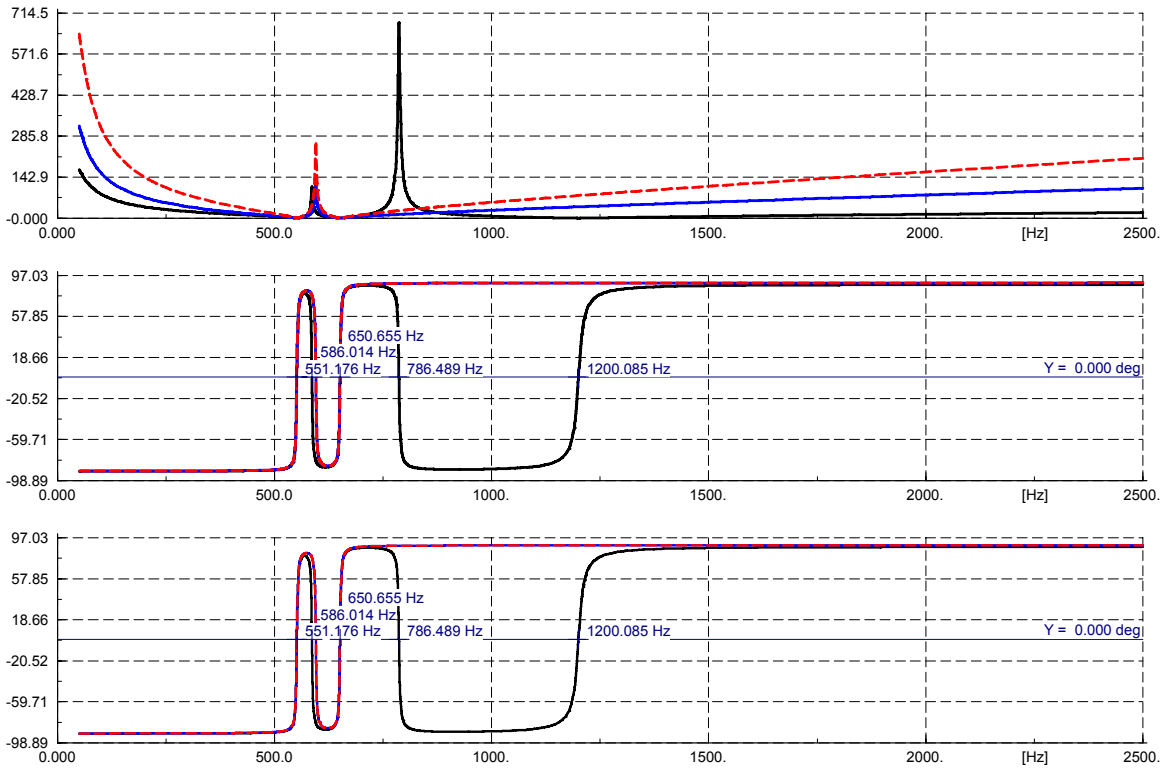

Figure 3.36 Harmonic impedance magnitude (upper plot) and phase angle (lower plot) of the harmonic filters installed at TJE3 substation. Black –all three filters, blue –filters ZA1 and ZA3 and red –only filter ZA1.

When inspecting the harmonic impedance of the filters it can be seen that the filters provide low impedance for harmonics of 11th and 13th order and the inclusion of the high-pass filter significantly lowers the resultant impedance of all the filters at higher frequencies.

VHA5 substation 400 kV

The harmonic filters at VHA5 substation consist of two harmonic filters tuned to 12th harmonic, ZF1 and ZF3, and a filter tuned to the 24th harmonic, see Figure 3.37. Data of the components are shown in the Table 3.12 and the harmonic impedance magnitude and phase angle of the filters determined in PowerFactory software is shown in Figure 3.38.

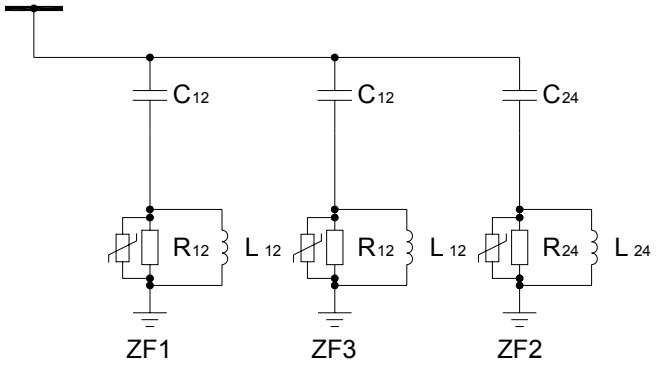

Figure 3.37 Physical layout of AC harmonic filters at VHA5 substation.

$Q_{ZF1} = Q_{ZF3}$ =55,3 MVar, Q_{ZF2} = 20,1 MVar,
C_{12} = 1,1 μF; L_{12} = 63,5 mH; R_{12} = 1250 Ω;
C_{24} = 0,4 μF; L_{24} = 43,5 mH; R_{24} = 1500 Ω;
resonance frequency - F_{12} = 600 Hz, F_{24} = 1200 Hz

Table 3.12 Parameters of harmonic filters installed at VHA5 substation.

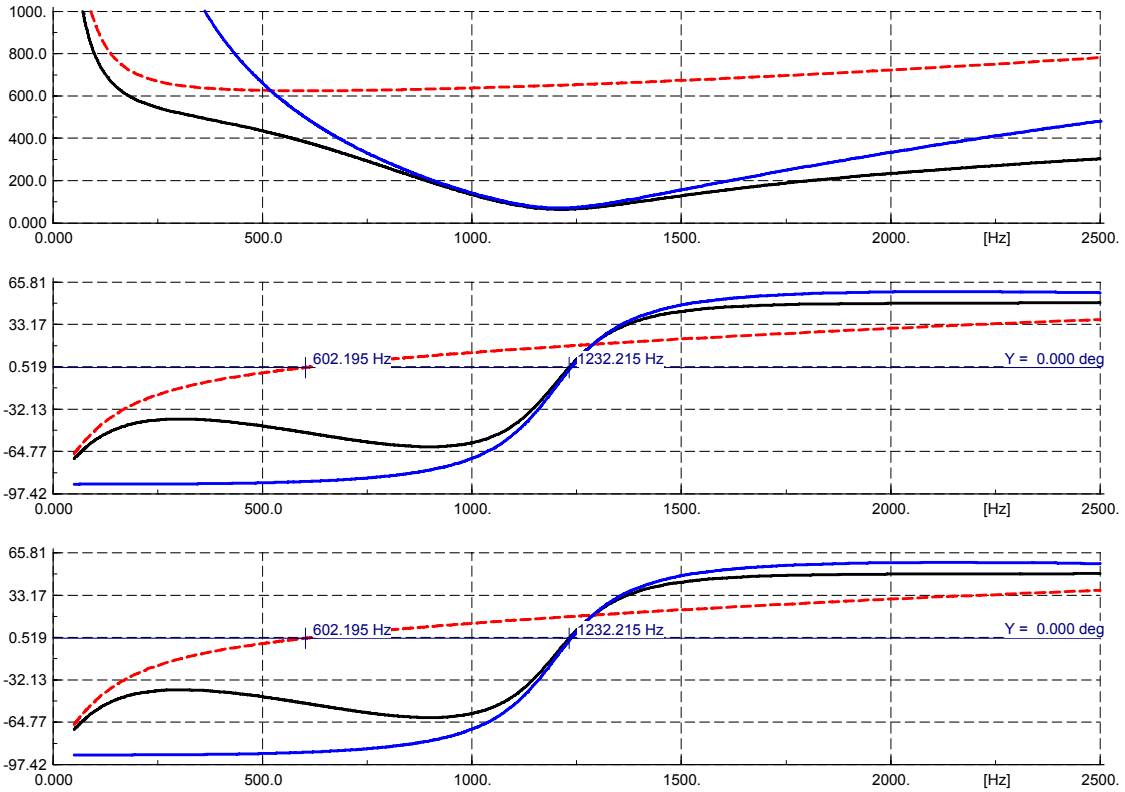

Figure 3.38 Harmonic impedance magnitude (upper plot) and phase angle (lower plot) of the harmonic filters installed at VHA5 substation. Black –all three filters, blue –filters ZF1 and ZF3 and red –only filter ZF2.

When inspecting the harmonic impedance of the filters it can be seen that the filters provide the lowest impedance for harmonics of 23rd and 25th order, due to the filter ZF2.

VHA3 substation 150 kV

The harmonic filters at TJE3 substation consist of two systems of filters, Z11 and Z12. Filter Z11 is composed of 3 filters, tuned to the 5th, 7th, and 11th harmonics respectively, and filter Z12 is composed of two filters, one tuned to 13th harmonic, and the other is high pass, see Figure 3.39. The values of the components are shown in the Table 3.1 and the harmonic impedance magnitude and phase angle of the filters determined in PowerFactory software is shown in Figure 3.40.

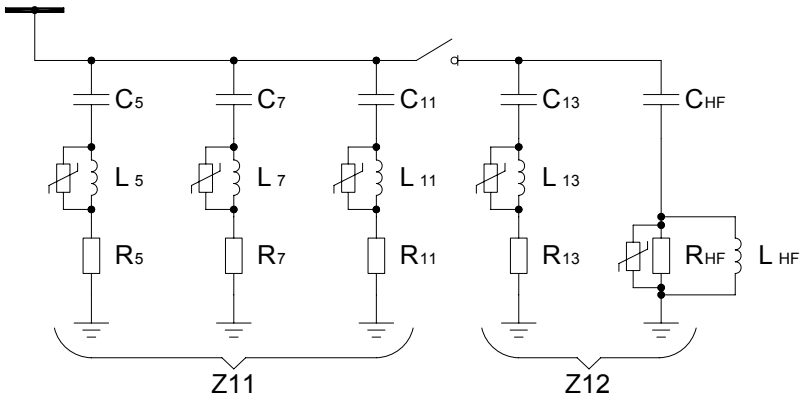

Figure 3.39 Physical layout of AC harmonic filters at VHA3 substation.

Q_{Z11} = 44,6 MVar, Q_{Z12} = 25,4 MVar
C_5 = 2,08 μF; L_5 = 195 mH; R_5 = 6,12 Ω;
C_7 = 1,06 μF; L_7 = 195 mH; R_7 = 8,57 Ω;
C_{11} = 1,97 μF; L_{11} = 42,5 mH; R_{11} = 2,94 Ω;
C_{13} = 1,41 μF; L_{13} = 42,5 mH; R_{13} = 3,48 Ω;
C_{HF}= 1,57 μF; L_{HF} = 12,2 mH; R_{13} = 96 Ω;
resonance frequency F_5= 250Hz, F_7= 350Hz, F_{11}= 550Hz, F_{13}= 650Hz, F_{HF}= 1150Hz

Table 3.13 Parameters of harmonic filters installed at VHA3 substation.

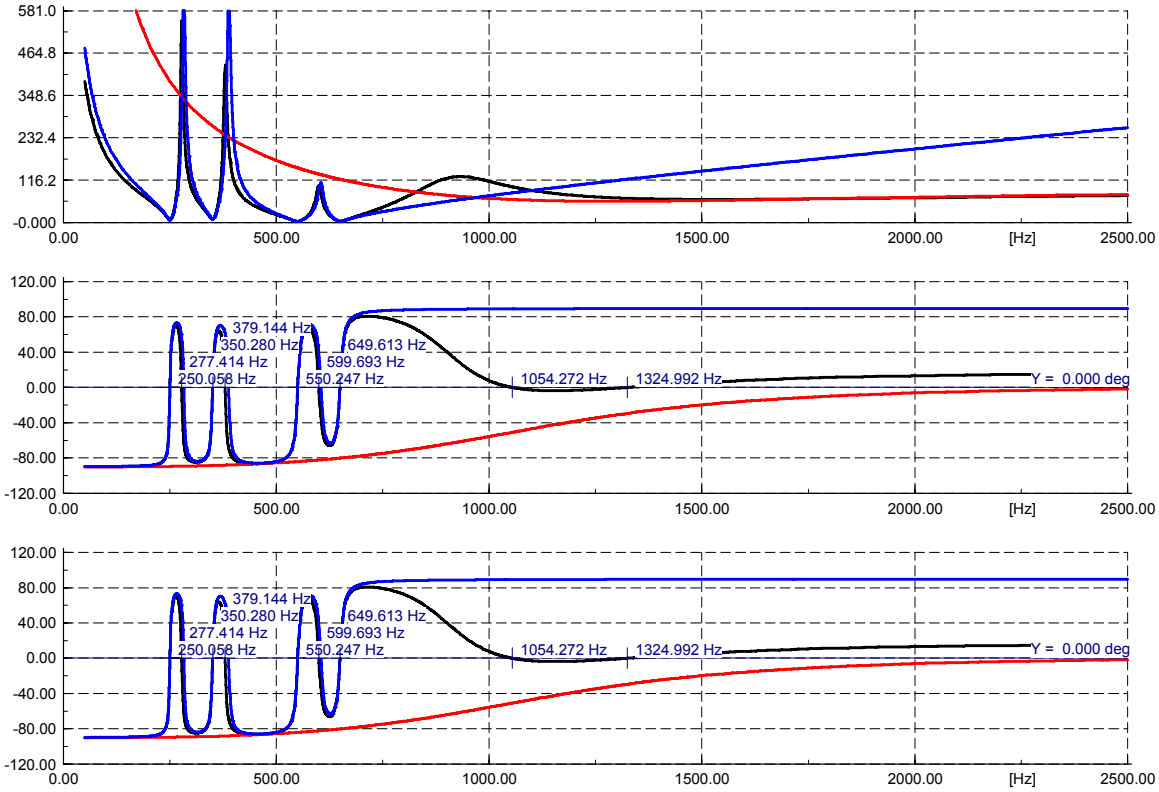

Figure 3.40 Harmonic impedance magnitude (upper plot) and phase angle (lower plot) of the harmonic filters installed at VHA3 substation. Black –all filters, blue – all filters ZF11 and 13th harmonic section of Z12 and red – only high pass section of the filter Z12.

From the impedance plots, it an be concluded that the filters are correctly implemented, since are tuned to the proper frequencies. All the filters modelled in the model are gathered on one graphic and shown in Figure 3.41.

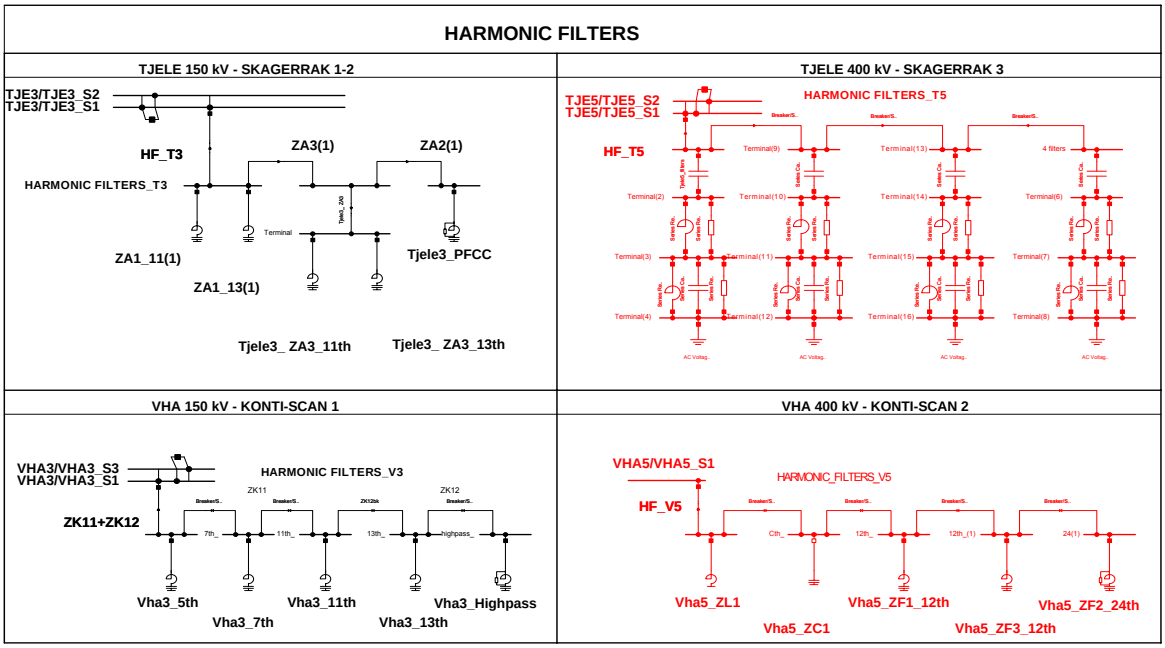

Figure 3.41 Harmonic filters modelled in the PowerFactory harmonic model of the transmission network. Red color indicates 400 kV voltage level, and black color indicates 150 kV voltage level. The filters are grouped on a common graphic board.

3.4.3 Shunt reactors

The data for each of the shunt reactors entered into the load-flow model are given in the form of design parameters, i.e. the rated reactive power and the quality factors are given. Form these parameters, the software calculates the value of inductance and resistance at fundamental frequency. An example dialog box of a shunt reactor installed at the substation KIN3 (150 kV) is shown in Figure 3.42, where for the reactive power of 80 MVar and quality factor of 551,72 the resultant value of the inductance and resistance (the layout parameters) is L = 1149.895 mH and R = 0.6547706 Ω. The grounding impedance of the starpoint is assumed zero, as no data were available for that.

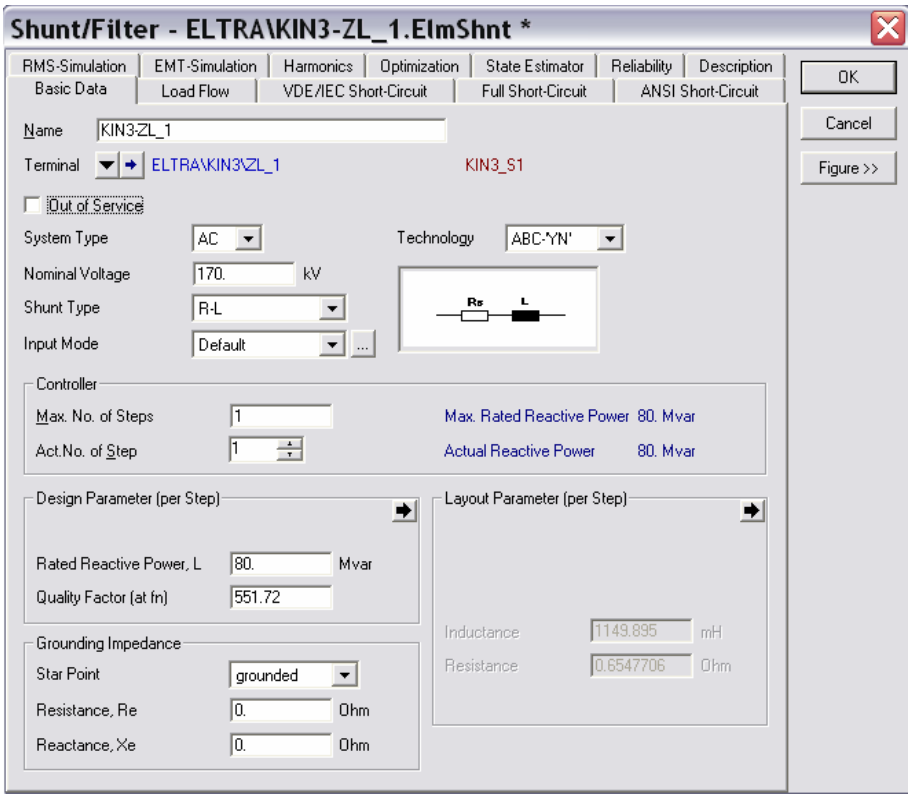

Figure 3.42 PowerFactory dialog box of a shunt reactor installed at the 150 kV substation KIN3.

Frequency dependence of layout parameters

The inductance and resistance of the iron-core shunt reactors is in general frequency dependent. The resistance increases with frequency due to the winding eddy current losses and losses in the core, tank walls, etc [Elmoudi]. The resistance changes much more than the inductance, therefore the inductance can be assumed constant for typical harmonic analysis of power systems [Dugui], [Task Force].

It is possible to take into account the frequency dependence of the lumped resistive components of shunt reactors in the PowerFactory software by defining for each of them a frequency characteristic [PowerFactory], see Figure 3.43.

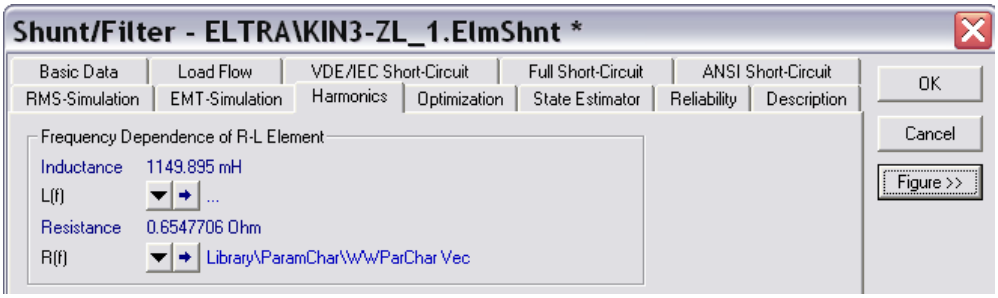

Figure 3.43 Frequency dependence of shunt inductance and resistance can be defined by assigning either the continuous polynomial characteristic (ChaPol) or by a frequency table (ChaVec).

The frequency dependence of the parameters can be characterized in two ways, either by defining the continuous polynomial characteristic (ChaPol) or by the user defined frequency table (ChaVec) [PowerFactory].

Continuous polynomial characteristic (ChaPol)

For example, to take into account the frequency dependence of a resistance $R(f_h)$ of an object, the polynomial characteristic can be used in the way that:

$$R(f_h) = R \cdot Y(f_h), \tag{3.58}$$

where $R(f_h)$ is the frequency dependent resistance, R is the constant resistance specified as the input parameter, and $Y(f_h)$ is described by the following formula [PowerFactory]:

$$Y(f_h) = (1-a) + a \cdot \left(\frac{f_h}{f_1} \right)^b, \tag{3.59}$$

where f_h is the frequency of interest, f_1 is the fundamental frequency, and a and b are the parameters that can be freely specified. The PowerFactory dialog box of polynomial characteristic where the frequency dependent resistance is defined as $R(f_h) = R \cdot \sqrt{f_h / f_1}$ and the resultant resistance variation versus frequency is shown in Figure 3.44.

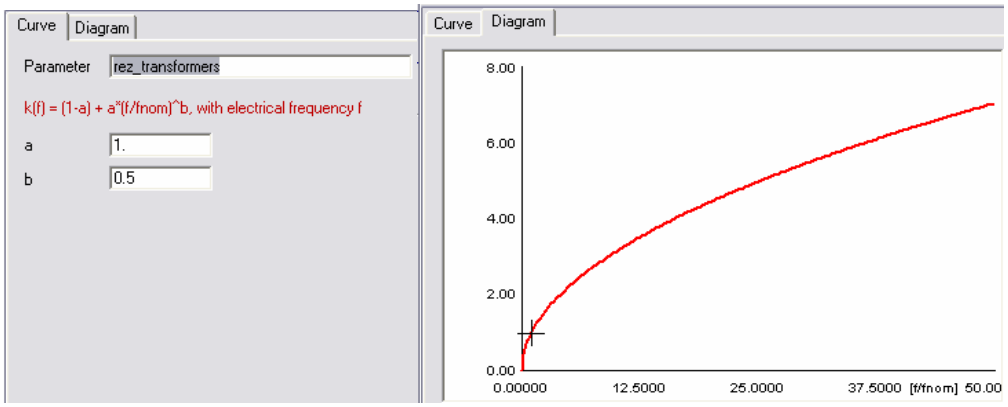

Figure 3.44 PowerFactory dialog box of polynomial characteristic where the frequency dependent resistance is defined as $R(f_h) = R \cdot \sqrt{f_h / f_1}$ (left) and the resultant resistance diagram (right).

The above mentioned way of assigning the frequency dependence is convenient, especially if analytical equations are to be used to describe the frequency dependence.

Frequency table (ChaVec)

The second way of defining the frequency dependence is to define a frequency table (ChaVec**).** This table is a vector of either relative of absolute values defined at discrete values of frequency, see Figure 3.45. This is a convenient way of defining the frequency dependence of a parameter if it has been physically measured at discrete frequencies and no analytical expressions describing its frequency dependence are available.

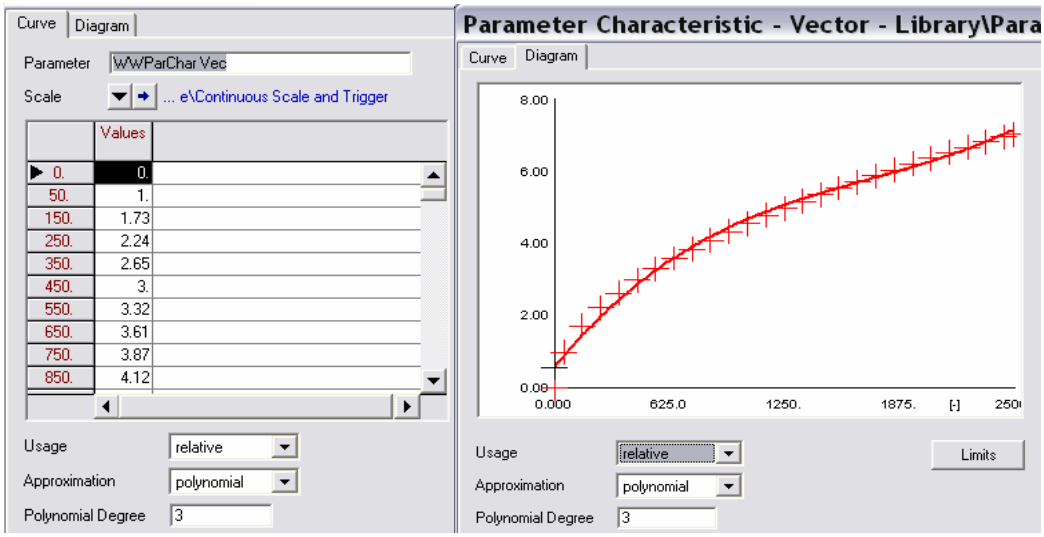

Figure 3.45 Example of using the frequency table ChaVec with the resistance values measured at harmonic frequencies and entered as relative values in the dialog box (left) and the resultant resistance, approximated by a polynomial of 3rd degree (right).

The values at the non-specified frequencies can be interpolated by the functions [PowerFactory] shown in Table 3.14.

Constant	resistance changes in steps and is constant in between the defined points
Linear	uses a linear interpolation
Polynomial	uses a polynomial function with freely defined degree
Spline	uses spline function
Hermite	uses a Hermite interpolation

Table 3.14 Interpolation functions available in PowerFactory for the frequency table ChaVec.

Both the inductance and resistance of iron-core transformers and shunt reactors are frequency dependent. This effect is due to the skin effect, proximity effect and the eddy currents induced in the core.

There are in total 16 shunt reactors present in the existing model of transmission network. All of them have been modelled with the constant value of inductance and frequency dependent resistance according to the equation (3.59), using the ChaPol characteristic.

3.5 Linear models of power transformers

Series impedance

The most simplified model of a power transformer is shown in Figure 3.46, where the constant series resistance of the windings R_T and leakage inductance L_T are derived from the short-circuit test using the basic equations (3.60) and (3.61) [Kujszczyk].

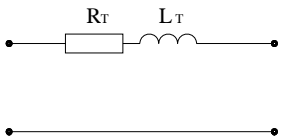

Figure 3.46 The simplest model of a power transformer

$$R_T = \frac{\Delta P_{cu} U_N^2}{1000 S_N^2} [\Omega], \tag{3.60}$$

$$Z_T = \frac{\Delta U_Z U_N^2}{100 S_N} [\Omega], \tag{3.61}$$

where ΔP_{cu} are the copper losses, U_N is the nominal voltage, kV; S_N is the rated power, MVA, $Z_T = \sqrt{R_T^2 + X_T^2}$, ΔU_Z is the short-circuit voltage, %.

This model is often used for simple fundamental frequency studies but is not preferred for harmonic analysis because it ignores the frequency dependence of winding parameters. Both winding resistance and inductance are frequency dependent. The resistance increases with frequency above the dc value due to the winding eddy current losses and losses in structures other than windings such as core clamps, magnetic shields, tank walls, etc [Elmoudi]. The resistance changes much more than the inductance, (inductance change is due to skin and proximity effects in the windings), therefore the inductance can be assumed constant for typical harmonic analysis of power systems [Dugui], [Task Force], [Arrillaga], [Acha], [schlabbach]. The frequency dependence of the series resistance $R_T(f)$ can be taken into account in different ways [Dugui], [Task Force], [STRI], however the most commonly met way is to use the formula:

$$R_T(f) = R_{50Hz} \cdot \sqrt{\frac{f}{f_1}}, \tag{3.62}$$

where R_{50Hz} is the resistance at 50 Hz derived from the transformer losses, f_1 is the fundamental frequency and f is the frequency at which the resistance is calculated. Alternatively, if the dc winding resistance R_{DC} is known, the following formula is used in practice [STRI]:

$$R_T(f) = R_{DC} + (R_{50Hz} - R_{DC}) \cdot \left(\frac{f}{f_1} \right)^{1.8}. \tag{3.63}$$

In this project only the typical resistance value R_{50Hz} derived from the short-circuit test is known; therefore the most common equation (3.62) is used.

There are in total 363 power transformers present in the load-flow model. Sixteen of these transformers are autotransformers. 149 of these transformers have the nominal voltage of the high voltage side of 150 kV or higher, which means that they belong the transmission network directly. Practically all the other transformers are distribution transformers with the high voltage of 60kV and various values of the low voltage.

Exciting current

The effect of a non-ideal transformer iron-core with losses and finite core permeability is the exciting current, which is composed of the core loss current and the magnetizing current [Matsch]. The core losses are due to the hysteresis losses and eddy current losses. The magnetizing current is related to the mmf needed to overcome the reluctance of the core and is shifted with respect to the resistive core loss current by 90 degrees [Matsch]. This exciting current is represented in the equivalent circuit of the transformer by a shunt branch of magnetizing inductance L_m and a resistance R_m, see Figure 3.47. Such linear model of a power transformer for harmonic studies in power networks is used in practice [STRI].

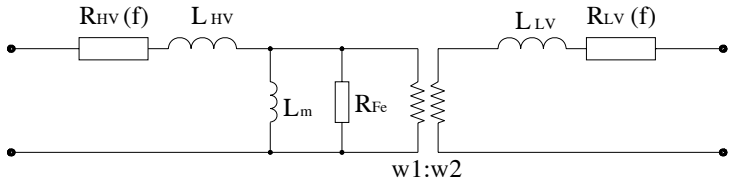

Figure 3.47 Equivalent circuit of a power transformer with the frequency dependent winding resistance R(f) and with linear exciting current taken into account by the shunt connection L_m and R_m.

The amplitude of the exciting current of a power transformer is small, and varies in the range from 0,03%I_N for large 400/150 kV autotransformers (load-flow model obtained from Energinet.dk) up to 5 %I_N for small single-phase LV units (own measurement).

As it is known, the transformer magnetizing current is nonsinusoidal, due to the saturation of the core [Dugui], [STRI], [Neves], [Matsch]. The resistive core loss current is also voltage dependent (the area of the hysteresis loop is a nonlinear function of voltage magnitude) and frequency dependent (due to eddy currents in laminations) [Dugui], [Matsch], [Watson]. A practical approach to modelling of the nonlinear core of power transformers is discussed in detail in chapter 8. In general, since the entire exciting current has such a small magnitude, it is sufficient to model the nonlinear magnetizing current of the transformer. As shown in chapter 8, the nonlinear resistive core loss current is so small that its nonlinearity and frequency dependence may be ignored for harmonic studies and it is sufficient to model it as linear constant conductance.

In the existing model, the exciting current is defined as the no-load current in %I_N and no-load losses in kW. These parameters are not defined for all of the transformers but only for the 116 largest ones.

Transformer capacitances

Power transformers are characterized by some value of stray capacitance [Schlabbach], [Watson], [Liew], [Task Force]. The capacitance exists between turns of the same winding or two different windings, the layer-to-layer capacitance between two layers in the same winding or two different windings, the capacitances between the windings and the magnetic core, and the capacitances between the windings and the ground, etc [Hai]. Usually for harmonic studies at frequencies below 4 – 5 kHz their effect is ignored [Schlabbach], [Watson], [Task Force], as the transformer first resonant frequency is higher in the frequency. In this project it has been ignored.

3.6 Synchronous and asynchronous machines

For modelling synchronous and asynchronous machines as linear loads for harmonic analysis purposes state-of-the-art models have been used. The models are well described in the literature [Arrillaga], [Acha], [Task Force], [Wasilewski]. The principal assumption in modelling the rotating machines is that the harmonic fluxes produced by the stator windings are rotating faster

than the rotor that is rotating with synchronous or close to synchronous speed. Therefore, the reaction to the harmonics is related not to the synchronous parameters but to the leakage path [Arrillaga].

3.6.1 Synchronous machines

Synchronous machines are characterized by its synchronous, transient and subtransient reactance. During synchronous operation, the flux produced by the stator is rotating with the same speed as the rotor. This flux is penetrating the rotor core and the resultant reluctance, this flux runs through, is a sum of the stator reluctance and rotor reluctance, see Figure 3.48 (taken from [Machowski]), and the relation between the reactance and reluctance is given by the formula [Matsch]:

$$X = \omega \cdot L = \omega \cdot \frac{N^2}{\Re}, \tag{3.64}$$

Where X is the reactance, Ω, N is number of turns, $\Re$ is the reluctance, H^{-1}, ω is the frequency in radians per second, L is the inductance, H.

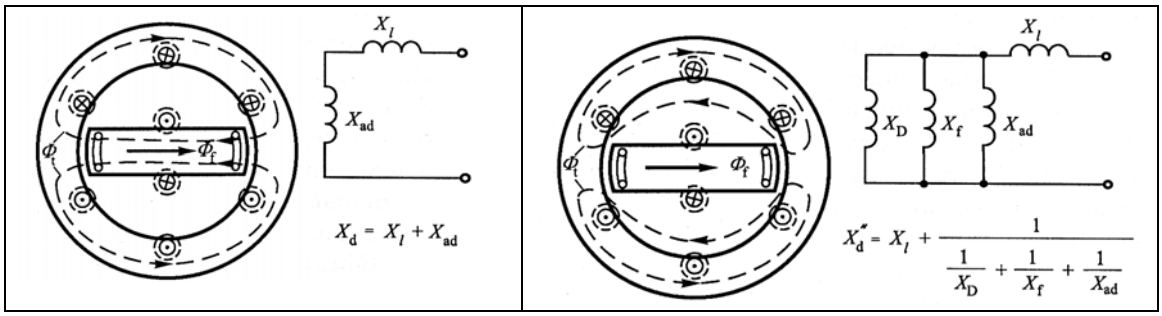

Figure 3.48 Difference between synchronous (left) and subtransient (right) reactance of a synchronous machine *(Source: [Machowski]),* where X_d is the synchronous reactance, X_{ad} is the reactance corresponding to the air gap reluctance, X_l is the leakage stator reactance, X''_d is the subtransient reactance, X_D is the reactance corresponding to the reluctance of the flux that is pushed out by the damped windings and runs through the air gap, and X_f is the reactance corresponding to the reluctance of the flux that is pushed out by the field winding and runs through the air gap.

In the subtransient state, which occurs directly after faults [Machowski], the rotation of the flux is varying with respect to the rotating rotor. This varying flux induces currents in the field winding and the damper winding on the rotor. These currents in turn produce opposing fluxes that push the original flux out of the rotor, and the resultant flux in the subtransient condition runs therefore through the high reluctance of the air gap, and the corresponding subtransient reactance is small, as can be seen from equation (3.64).

The fluxes produced by positive or negative sequence harmonic currents in the stator are also rotating with respect to the rotor, and are therefore also pushed out of the rotor by the damper windings and the field winding. Therefore, the assumption is made that the reactance of a synchronous machine for harmonic analysis shall be the subtransient reactance X''_d, or more often the average value of the direct and quadrature axis subtransient reactances is used [task Force], [Acha], [Arrillaga]:

$$X''=(X''_d+ X''_q)/2. \tag{3.65}$$

PowerFactory uses equation (3.65) for modelling synchronous machines.

The resistive component of synchronous machines used for harmonic analysis studies, similarly to the winding resistances of a transformer, increases with frequency due to the winding eddy

current losses and losses in stator core. Therefore, the most common approach found in the literature is to use the equation [task Force], [Acha], [Arrillaga]:

$$R_S(f) = R_{50Hz} \cdot \sqrt{\frac{f}{f_1}}\,. \tag{3.66}$$

The equivalent diagram of a synchronous machine used for fundamental frequency load-flow studies and higher frequency harmonic studies is shown in Figure 3.49.

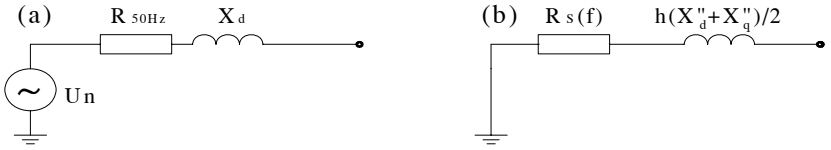

Figure 3.49 Equivalent diagram of a synchronous generator. (a) – for fundamental frequency load-flow studies, (b) – for harmonic analysis. Assumption: the generator supplies perfectly sinusoidal voltage.

The frequency dependence described by (3.66) is implemented in PowerFactory using the (ChaPol) characteristic.

There are in total of 140 synchronous machines present in the model, the largest of 626 MW and the smallest being installed on the distribution level with the size of 30 kVA.

3.6.2 Asynchronous machines

The equivalent circuit of an asynchronous machine is shown Figure 3.50 [Matsch], [Arrillaga].

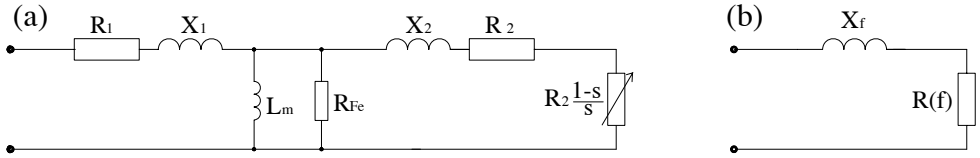

Figure 3.50 (a) – equivalent circuit of an asynchronous machine, (b) – its approximate representation [Arrillaga], where R_1, X_1 are the stator winding resistance and leakage reactance, R_2, X_2 are the rotor resistance and leakage reactance, and $R_2[(1-s)/s]$ is the dynamic resistance that represents the mechanic load, and s is the slip.

The slip is:

$$s = \frac{\omega_s - \omega_r}{\omega_s}\,. \tag{3.67}$$

where ω_s is the synchronous frequency and ω_r is the frequency related to rotor speed. Also a harmonic apparent slip can be defined for harmonic h:

$$s_h = \frac{\pm h\omega_s - \omega_r}{\pm h\omega_s}, \tag{3.68}$$

where '+' is for positive sequence harmonics and '-' is for negative sequence harmonics.

For harmonic analysis it can be assumed that the slip is approximately 1, so the locked rotor resistance shall be used. For example, assuming that the rotor rotates with 49 rps, the fundamental frequency slip is (50-49)/50 = 0,02. The apparent slip at, say, 25th harmonic is (1250-49)/1250=0.96, and at 23rd harmonic is (1150+49)/1150 =1.04. for the slip equal to 1, the dynamic resistance that represents the mechanic load equals zero.

Therefore, asynchronous machines have to be represented by their locked-rotor impedance. The impedance of an induction machine can be approximated as shown in Figure 3.50 (b), where

$$R(f) = (R_1 + R_2) \cdot \sqrt{\frac{f}{f_1}} \tag{3.69}$$

and

$$X_f = \frac{f}{f_1}(X_1 + X_2) \tag{3.70}$$

There are in total 56 induction machines (some of them are aggregated models of many machines) present in the load-flow model. The rated voltage of all of them is 0,7 kV and they are coupled to the rest of the transmission network via power transformers. The largest asynchronous machine in the model has rated apparent power of 178 MVA and the smallest has the rated apparent power of 34 kVA.

3.7 Distribution system equivalent models

The principles used for creating the distribution system equivalents present in the existing load-flow model were described in chapter 2.

These existing equivalent models are evaluated to see if they need to be improved and if it is possible to improve them in a simple way in terms of the harmonic impedance seen from the high voltage transmission network.

This task has been performed by a guest student from Warsaw University of Technology, Mr J. Wasilewski, as a part of his Master's Thesis. The author of this dissertation has formulated this project proposal and was a supervisor for Mr Wasilewski. The efforts of Mr Wasilewski have been published in the form of a research report, and a scientific paper [Wasilewski]. This paper is attached in the appendix C. The main findings of this work are summarized below.

The idea of the verification was as follows:

A distribution feeder supplied from the 150/60 kV busbar was selected. The feeder had a typical load composition, was not very extensive, and it was possible to obtain detailed data of it, including the 60 kV lines, the PFC capacitors, the distributed generators, the large rotating loads, the loading of MV/LV transformers, together with the PFC installed at lower voltage levels.

From the obtained data, a precise, linear impedance model of the network was build. The software used for that purpose was PowerFactory.

The corresponding, simplified model of this distribution feeder was copied from the existing load-flow model.

The harmonic impedance seen from the higher voltage side of both of the models was determined and the results compared.

Based on this comparison it had to be deducted whether the existing, simplified aggregated models of the distribution network in terms of the harmonic impedance is acceptable and similar to the impedance of the detailed model. If not, some methods of improving the network equivalents had to be studied.

The conclusions of the work were among others, that:

The PFC capacitors had a significant effect on the harmonic impedance of the distribution network in the frequency range of interest.

An attempt to modify the existing load-flow model by attaching the entire capacitance of the PFC capacitors and the shunt capacitance of the lines as single lumped component to the 60 kV busbar gave resultant harmonic impedance values that differed from the impedance of the exact model in the frequency range of interest more than the linear impedance of the unmodified model. Only the main resonance has been reproduced this way. The main resonance was however at frequencies above the frequency range of interest in this project. Therefore, it has been shown that it is better to leave the linear inductive/resistive models of the distribution network without the attempts of entering aggregated values of capacitance. Further details of this study can be found in appendix B.

In general, since the load models are separated and the synchronous and asynchronous machines are separated from the rest of the loads, it could be assumed that the remaining loads defined by the active and reactive demand, are predominantly domestic.

If such assumption can be made, the PowerFactory load model fulfills the requirements of the Model 2, described by the task force on harmonic modelling and simulation [Burch]. This task force in 2003 was investigating different aggregated linear models for harmonic analysis purposes. For relatively small motor load participation, a parallel connection of a resistance and an inductance was suggested, see Figure 3.51. For this load the resistive an inductive parts are given by the formula:

$$R = \frac{V^2}{P}, \tag{3.71}$$

$$L = \frac{V^2}{\omega Q}, \tag{3.72}$$

where V is voltage in kV, P is active power demand in MW, Q is reactive power demand in MVar, and ω is the frequency in radians per second.

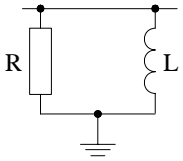

Figure 3.51 Load model 2, suggested by the task force on harmonic modelling and simulation for small motor load participation [Burch]

There are 63 aggregated loads present in the model, all of them together representing the actual demand in the network. The largest equivalent model has the size of 600 MW and the smallest of 6 MW. All of the models are balanced.

3.8 Conclusions

The first part of this chapter was devoted to the analysis of harmonic domain modelling of transmission lines and their implementation in the PowerFactory software.

It was shown that:

If an infinite number of terms of Bessel series are used in calculation of the conductor resistance and inductance, taking into account the skin effect, equations (3.7)-(3.9) provide exact results regardless of the conductor radius and the frequency.

If the Bessel series are truncated, then the smaller the conductor radius is, the smaller the number of terms of the Bessel series needed to calculate proper values of resistance and inductance at a given frequency.

The larger the conductor radius is, the higher is the effect of the skin effect on the conductor impedance.

A simple case has been setup in the PowerFactory software and both the skin effect and the non-ideal earth return path impedance has been verified by hand calculations.

It was shown that the PowerFactory calculation of the skin effect is precise, at least in the frequency range of interest (2,5 kHz).

The frequency dependent impedance of the ground return path has been plotted. It was noticed that the resistive term of the ground return path impedance changes much more than the inductive term (if the frequency changes from 50 Hz and 2,5 kHz , resistive term rises 34 times and inductive term lowers 2.8 times).

It was also found that PowerFactory bases its calculation of the impedance of the non-ideal earth return path on the truncated Carson series, with only the first term used in the calculations.

At higher frequencies, the values are extrapolated in a manner that allows obtaining reasonably accurate results.

At 2,5 kHz, and for ground resistivity value of 100 Ωm, the maximal height, at which the Carson equation with only the first terms of the series included, gives exact result, is 35,6 meters above ground.

Assuming that the maximal height, at which the conductors of the 400 kV and the 150 kV overhead lines are placed is 40 meters, with the ground resistivity equal to 100 Ωm and the frequencies of interest lower than 2,5 kHz, then the approach used in PowerFactory theoretically does not satisfy the requirements described by [Carson].

If two terms of the Carson series are used, then the maximal height allowable for 2,5 kHz is 71 meters above ground and then the lines present in the Western Energinet.dk area have their conductors placed below that limit.

In practical terms, at the frequency of 2,5 kHz and the height of the conductor 40 meters above ground, the difference between the PowerFactory approximation and the values calculated using two terms of Carson series are still insignificant.

However, a more correct approach would be to base the calculations also on the second terms of the Carson series, since it shall not be difficult to implement it in the frequency domain calculations of the simulation software.

In the analyzed case, the frequency dependent resistive term of the non-ideal ground return is more pronounced than the frequency dependent resistive term of the conductor

In the analyzed case, the inductance of the conductor was dominated by the constant geometrical inductance. The inductive term of the earth return path that is a nonlinear function of frequency had much smaller value. The smallest contribution to the entire conductor inductance had the internal conductor inductance.

The above dependencies are a function of many factors, like conductor radius, height of the conductor above ground, ground resistivity, etc. For other values of these factors the dependences could differ.

In the PowerFactory software, the non-ideal ground return is always included in calculations if the tower geometry is used.

Skin effect of the conductors can be taken into account by simply selecting a flag “consider skin effect”.

In the next part of the chapter, a typical overhead line configuration was used for studies of the following issues: the importance of distributed parameters of transmission lines, the influence of

shunt conductance, the skin effect, phase unbalance, assumption of ideal ground wires, the effect of average height of conductors due to sags.

It was shown that:

The single nominal PI model is an accurate representation of the line impedance at fundamental frequency but it is not a good model for frequencies higher than one half of the first parallel resonance. For higher frequencies large errors will occur, especially at the resonances.

Only the first parallel resonance is reflected if the single nominal PI section is used.

Cascading several PI sections will improve the accuracy; more resonances will be present (as many parallel resonances as the number of PI-sections used to construct the model). However, the resonances will be shifted in frequency comparing to these obtained if using the exact equivalent PI model. Additionally, cascading a number of PI circuits will increase the computation time.

Therefore, whenever harmonic studies are to be performed, the equivalent PI model shall be preferred, because it exactly reflects the harmonic impedance of a line and does not increase the simulation task.

If the corona losses are modelled as a linear shunt conductance, they practically don't affect the propagation of higher harmonics on the transmission level at non-resonant frequencies. Shunt conductance lowers harmonic overvoltages caused by the resonances by lowering the impedance of the resonant circuits.

The shunt conductance does not shift the resonance frequencies

Corona losses are varying in a vide range, and the corona current is nonlinear.

The linear shunt conductance may cause excessive damping of harmonic distortion in the network.

It is better to ignore the corona effect in harmonic studies than to include it in the form of a shunt linear conductance.

The skin effect plays an important role at resonant frequencies because it alleviates the effects of resonances.

In the performed simulations it has lowered the parallel resonance impedances by 30 – 40 % (such as from 49.9 kΩ down to 31.1 kΩ) and raised the series resonant impedances by approx. 40 % (such as from 1,644 Ω up to 2, 434 Ω).

The skin effect has also an influence on the conductor internal inductance and consequently it alters the resonant frequencies. This effect is not very significant; in the frequency range up to 2,5 kHz a shift of about 2 Hz has been observed.

At the resonances around 12 kHz this shift rises to about 20 Hz.

At the frequencies lower than the first parallel resonance the skin effect changes the line impedance below 1% and therefore it is an acceptable assumption to ignore it for power-flow simulations.

Also at higher but "non-resonant" frequencies it alters the impedance only a few percent (at 25^{th} harmonic by 2,3 % and at 50^{th} harmonic by 2,7 %).

Assumed ideal line transposition will influence the harmonic impedance of a line. In a real life scenario each phase has different harmonic impedance. The simulation revealed that at the fundamental frequency the impedance of different phases differs by 3,2 %. This is considered acceptable. At higher frequencies the differences grow; at the 13^{th} harmonic it is already 7%. In PowerFactory the line transposition is realized by averaging the line parameters for different phases. For such ideally transposed line no mutual coupling between positive, negative and zero-sequence exist. In reality an injected positive sequence current will always cause voltage drop

that will be not purely positive sequence. For the investigated unbalanced line, the coupling between positive and zero-sequence impedances was most pronounced at the resonances.

PowerFactory allows to take into consideration the line unbalance. A transmission line supplied with a purely positive sequence voltage gives rise to currents that contain all sequence components.

In the PowerFactory software the earth wires of an overhead transmission line are included in the model. However, the calculations are simplified, i.e. the full impedance matrix of phase and earth conductors is reduced to a 3x3 matrix for the phase conductors only by assuming that the earth wires are ideally grounded and the voltage drop across them is zero.

It has been shown that when the number of groundings along the line increases then the line impedance gets closer to the impedance of a line modelled with the reduced matrix. As a result it was shown that the standard models available in PowerFactory are appropriate for harmonic analysis.

In the existing model the sag of the overhead line conductors are not modelled. A simulation was performed where 4 theoretical sag distances were modelled: 5m, 7, 10, and 12 m. The simulation revealed that ignoring the sags does not have a noticeable effect on the line impedance at the fundamental frequency. At higher frequencies this influence starts to be visible, especially for the zero-sequence impedance. At the 7^{th} harmonic the impedance difference between line with 5m sag and line with 12m is 0.35% for the positive sequence and 7.6% for the zero-sequence impedance.

In the last part of the chapter, modelling of the following elements was described:

Shunt harmonic filters, shunt capacitors, shunt reactors, power transformers, synchronous and asynchronous machines and at the end, distribution system equivalent models.

The conclusions are that:

The harmonic filters were modelled in the existing load-flow model as pure capacitors. That is obviously insufficient for harmonic studies and the elements have been upgraded by including the inductive and resistive components. The harmonic impedance of the created filters has been determined and it was shown that as a result of the modification the filters have harmonic impedances tuned to the correct frequencies.

There is only a single pure capacitor installed in the entire Western network and it is included in the load.-flow model

There are 16 shunt reactors installed in the network, and all of them are present in the load-flow model. Their inductance and resistance data are present in the models. The only modification that was made for the harmonic analysis was to include the frequency dependence of the reactor resistance by using the equation (3.62) and the ChaPol characteristic.

For modelling of power transformers, the first thing is to model the series impedance. The second most important element is to model the frequency dependence of the series resistance. The frequency dependence of the leakage inductance can be ignored. The exciting current has to be modelled by a parallel connection of a magnetizing reactance and a conductance that corresponds to the power losses in the core. This is a linear model. If the nonlinear properties of a transformer have to be included, the magnetizing inductance shall be exchanged with a current source that injects distorted current. The power losses are both voltage dependent and frequency dependent. The resistive current corresponding to the power losses has small magnitude, therefore its contribution to the harmonic distortion of the entire exciting current is small and as discussed later I chapter 8, can be ignored. The frequency dependence of the resistive current can therefore also be omitted, and consequently, it can be concluded that it is sufficient to model the transformer core losses as a constant linear conductance.

The principal assumption in modelling the rotating machines is that the harmonic fluxes produced by stator the windings are rotating faster than the rotor.

This indicates that in case of synchronous machines the flux is pushed out of the rotor and runs through the air gap. The overall reactance of the machine is therefore similar like the negative sequence reactance or the subtransient reactance. PowerFactory models synchronous machines at harmonic frequencies by an average value of the direct and quadrature values of the subtransient reactance. The resistance of the machine is related to the losses in the windings and stray losses in the laminates.

In case of asynchronous machines, the locked rotor resistance shall be used, because the apparent slip is very close to 1. The locked rotor resistance is the sum of the stator and rotor winding resistance. The stray losses in the laminates shall not be ignored.

In the existing distribution network equivalents, the large synchronous and asynchronous machines are separated from the overall load value and modelled as aggregated. Thanks to this, an assumption can be made that the remaining loading at each 60 kV busbar is predominantly domestic. For loads with relatively small motor load participation, a parallel connection of a resistance and an inductance can be used. The existing models of PowerFactory loads are modelled this way.

The PFC capacitors have a significant effect on the harmonic impedance of the distribution network in the frequency range of interest.

Chapter 4

Analysis of validation techniques based on switching of network components

The created linear model of the transmission network needs to be verified. The verification is to be made by real-life harmonic measurements. The basic requirement that must be ensured is that the background harmonic distortion present in the network is not introducing errors in the verification result. Various methods are described in the literature, for instance methods based on transient measurements or on injection of inter-harmonic currents. In this chapter, various verification techniques based on switching of linear and nonlinear network elements and measurements of incremental values are analyzed. The contribution described in this chapter is the development of two verification techniques based on switching series components and computation of transfer harmonic impedance of a linear network.

4.1 Introduction

The verification of a linear transmission network is based on measurement of its harmonic impedance. The methods of measurement of harmonic impedance described in the literature are usually made by injection of transients or steady state harmonics onto a node of a network from a shunt source, measuring the voltage or current response and calculating the harmonic impedance [De Oliveira], [Robert], [Arrillaga], [Watson], [Moreau]. If it is possible to assume that there is no background harmonic distortion, the methods can be used in a strait-forward manner. However, such assumption would lead to errors. Therefore, incremental methods need to be applied [De Lorenzi], [Robert], [Watson], [Xu]. Another way of determining the harmonic impedance is to vary the impedance of a shunt linear load [Robert], [Bridgeman], [De Oliveira], [Xu]. All these methods concern measurements of the driving-point impedance by using a shunt element. None of them describes measurement of the transfer harmonic impedance between two nodes of a network. Such method would be desirable because under certain conditions (for instance if large harmonic currents propagate through a series element in a meshed network) switching a series impedance may give better results (higher signal-to-noise ratio) than using a shunt element. For general validation a linear harmonic model of a network it does not matter if the driving-point or transfer impedance is measured and used for that purpose.

Therefore, two methods are derived in this chapter, both adequate for measuring transfer harmonic impedance between two nodes of a network. In the first method, a purely series linear element is used, and the second method allows to use for that purpose a series element that contains also a shunt impedance. Such an element may be a transmission line. Both methods are verified by calculation examples and using computer simulation.

In this chapter an overview of various existing verification techniques is presented. Each of the methods is analyzed with respect to its advantages, drawbacks, requirements and necessary assumptions. Also, two developed in this chapter methods are described and their advantages and

drawbacks are discussed. The technical details of how to physically perform harmonic measurements, requirements for the measuring instruments, signal transducers, wiring connections, analysis of the results etc are the theme of chapter 5 and therefore, are not discussed here.

Chapter outline

The organization of this chapter is as follows:

First, a classification of basic methods of harmonic measurements is given, then basic circuit theories are refreshed and factors that should affect the selection of verification technique are listed. In the subsequent sections, a description of verification methods found in the scientific literature is presented. A derivation of two verification techniques based measuring transfer harmonic impedance is given. A summary concludes this chapter.

4.2 Main factors affecting selection of the verification method

The factors that will certainly affect the selection of verification method are:

Costs of the equipment and the labor work, features of available measuring instruments, difficulty of the methods, possession of know-how, extent of the network that is to be verified, magnitude and variation of background harmonic distortion, existence of large source of harmonics in the network, possession of external sufficiently large (inter)harmonic source that is possible to connect at the desired voltage level, possibility of disconnecting a series or shunt power system element.

It can be stated that in general, selection of the measuring technique should be aiming at ensuring the highest signal-to-noise ratio (SNR) of the measurement.

The overall SNR of a measurement is composed of:

i) The SNR of the physical measuring system (SNR_{ph}), which is affected by the noise introduced while the signals are being transformed, transmitted, conditioned and measured. To ensure high SNR_{ph}, the physical measuring equipment shall have proper physical features, especially with respect to the transfer function (current and voltage transducers), electromagnetic immunity to radiated and conducted noise (wiring) and sufficient vertical and horizontal resolution (measuring instruments). High SNR_{ph} has to be ensured in any case, regardless of the selected measuring approach. Methods to ensure high SNR_{ph} will be discussed in chapter 5, where technical aspects of harmonic measurements are described.

ii) The SNR of the measured signal itself (SNR_{sig}), which is a ratio of the harmonic distortion that carries the information to the part of the distortion that does not carry useful information (so is perceived as noise).

It may be recognized that the main factors affecting the SNR_{sig} and the selected measuring technique are:

The magnitude and variation of background harmonic distortion, features of available measuring instruments, existence of large source of harmonics, possession of external large (inter)harmonic source, possibility of disconnecting a power system element.

The main goal of the work shown in this chapter is to describe various verification methods that allow to eliminate the effects of the background harmonic distortion using one of the methods from group iii)- Techniques that use existing harmonic sources.

Existence and variation of background harmonic distortion

One of the aspects that affect the measuring approach is the presence and the variation of background harmonic distortion. The background distortion is a superposition of all the responses from all the harmonic loads installed in the system. Theoretically, three states could be distinguished with this respect:

a) There is no background distortion

b) Background distortion is present but is stable, not varying

c) Background distortion is present and varies

Depending which conditions prevail in the system (a, b or c), a proper verification technique has to be chosen. Case c) is the most common, because some level of harmonic distortion is practically always present and moreover this level varies in a random manner. It can be recognized that the randomness of this variation is principally an effect of:

- Constantly changing number of nonlinear loads that are in operation. This group includes also the practically constant loads with constant harmonic spectra (TV sets, computers, etc.)
- Variation of the loading of large nonlinear loads (HVDC converters, TCR's)
- Variable switching techniques of power electronic converters (PWM schemes)
- Randomly and rapidly varying currents of arcing devices (arc furnaces, discharge-type lighting)
- Distorted magnetizing current of saturable magnetic cores depends on the magnitude of supplying voltage (power transformers)
- Variation of the harmonic impedance of the power system due to switching of various series and shunt linear components and varying number of linear loads supplied (power lines, large consumers)

4.3 Driving-point and transfer harmonic impedance

4.3.1 Driving-point harmonic impedance of a node

The relation between harmonic currents injected into the nodes of a power network and the harmonic voltages at the nodes can be expressed in the form of a symmetrical harmonic impedance matrix of complex components

$$V = Z^{h}_{bus} I^{h} . \tag{4.1}$$

Such matrix shall be created at each frequency of interest. The terms on the diagonal of this matrix are called driving-point impedances of a node Z^{h}_{kk}. The off-diagonal terms of the matrix are the transfer impedances between two nodes $Z^{h}_{kj} = Z^{h}_{jk}$. The driving-point harmonic impedance of a node is an equivalent harmonic impedance Z^{h}_{eq} of a network between the node k and a reference node. This impedance can be simplified and represented as a single component, as shown in Figure 4.1.

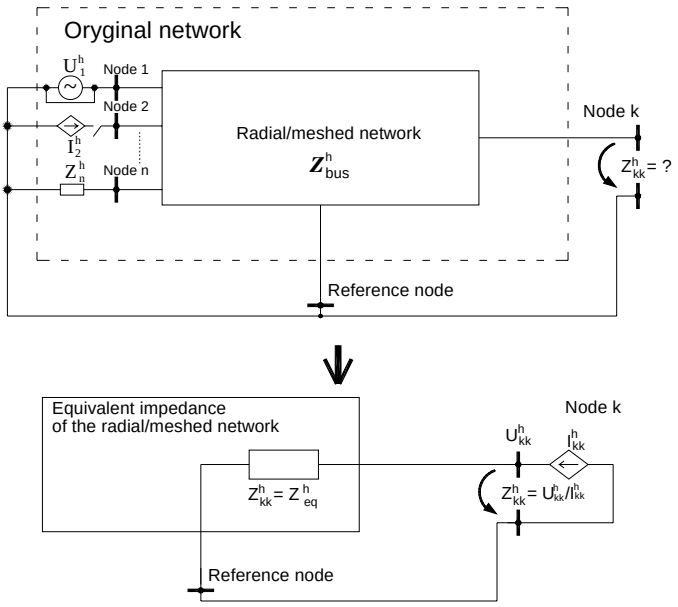

Figure 4.1 Determination of driving-point harmonic impedance $Z^h_{kk} = Z^h_{eq}$ of a node of a radial/meshed network [Grainger]

To determine the driving-point harmonic impedance $Z^h_{kk} = Z^h_{eq}$ of a node of a radial/meshed network, all voltage sources existing at a given frequency shall be shorted, and all current sources existing at a given frequency shall be open-circuited.

4.3.2 Transfer harmonic impedance between two nodes

Transfer harmonic impedance of a network is an equivalent harmonic impedance Z^h_{kj} seen between any two nodes of the network, and is represented by a single component. This impedance includes the impedance of all the series components that are linking both nodes and the impedance of all the shunt components that also provide a path through the reference node as shown in Figure 4.2.

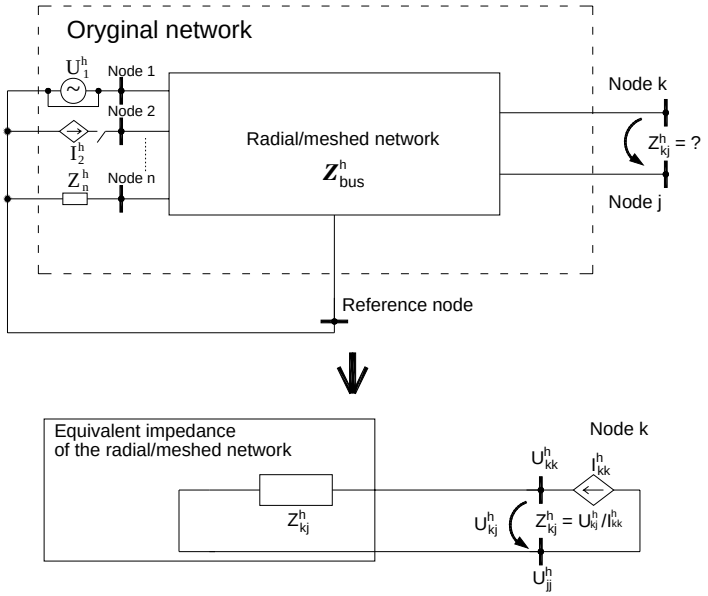

Figure 4.2 Determination of the transfer harmonic impedance $Z_{kj}^{h} = Z_{eq}^{h}$ between nodes k and j of a radial/meshed network [Grainger]

To determine the transfer harmonic impedance between nodes k and j, all voltage sources existing at a given frequency shall be shorted, and all current sources existing at a given frequency shall be open-circuited.

Transmission power networks may have a very complicated topology consisting of meshes and radial segments. Fortunately, if nonlinear elements in such grid can be represented by ideal current or voltage sources, according to Thévenin and Norton theories, the harmonic impedance of such network can be approximated by a single current or voltage source at each frequency, together with single, equivalent harmonic impedance.

4.4 Basic methods of harmonic impedance measurements.

Whatever is the way of measuring the harmonic impedance, the main principle is always the same: at the end, it is about measuring the ratio between the voltage and the current. From this point of view it doesn't matter if voltage is the excitation and current is the response or vice versa. However, because of the real-world difficulties and constraints, some times one or the other method is more convenient.

From another point of view, harmonic impedance measurement methods can be divided depending on the physical origin of the harmonic distortion used as the excitation.

In this respect, the harmonic impedance measuring techniques may be divided into three groups [Watson]:

i) techniques that use external instruments to inject harmonic currents into the network,

ii) analysis of transient waveforms

iii) Techniques that use existing harmonic sources.

This chapter is entirely devoted to methods that use existing harmonic sources, because such measuring technique will be used in this project. However, the two other groups are also briefly described and few references are given.

Techniques that use external instruments to inject harmonic currents into the network

To determine the driving-point harmonic impedance of a bus, an external source of harmonics can be used. The injected current harmonics will result in a frequency response in the bus voltage allowing the determination of the harmonic driving-point impedance at the bus. This technique is analogous to the techniques described later in sections 4.5.1 and 4.5.2, with the difference that here the source of harmonic distortion is external. Such methods were described for instance by [Robert], where for determination of harmonic impedance of high voltage network, a traction rectifier of a single phase locomotive was used. [Moreau] used a single-phase, 25 kW IGBT power electronic converter coupled to the network by a MV/LV distribution transformer.

The difficultly associated with using harmonic frequencies is that the source needs to be of considerable power since there is already some background distortion present in the network. Therefore, to obtain sufficiently large signal-to-noise ratio, harmonic current of significant amplitude must be injected. The variation of this current magnitude should result in variation of the voltage distortion, and the relative differences can be used to describe the harmonic impedance. If the source of harmonics produces distortion that is sufficiently higher than the background distortion, then the background distortion may be ignored. Also a very good possibility for measuring the harmonic impedance would be to adjust/change the control of an active harmonic filter, so it will produce additional harmonic distortion. Such a filter is for instance installed at the HV network of the Energinet.dk grid, at the substation Tjele [Soeder].

Another way of reducing the effects of background harmonic distortion can be obtained by injecting non-integer multiples of the fundamental frequency. Since the level of inter-harmonic frequency in the background distortion is usually low, the impedance at inter-harmonic frequencies can be calculated directly and the impedance at harmonic frequencies can be interpolated. Such a method is described for instance by [Tsukamoto], where a PWM converter is connected in shunt with a distribution feeder and by injection of inter-harmonic frequencies it measures harmonic impedance of the power system, both upstream and downstream from the connection point.

The advantage of using external source of harmonics is that usually it is possible to control the injected harmonic currents with respect to their amplitude, phase, phase sequence, etc.

Analysis of transient waveforms

Transient waveforms can be also used to determine the frequency characteristic of a network. The transient currents and voltages can be produced by switching operations of for instance capacitor banks (PFC), and the measured voltages and resultant currents can be correlated and the harmonic impedance estimated. Switching a PFC can be perceived as an instantaneous short-circuit, so the charging current that it will produce will be rich in harmonics [Nagpal], [Robert]. Another kind of transient is produced by transformer energization. The magnitude of transformer energizing current can reach 5-10 p.u. of the rating and is also rich in harmonics and of high amplitude. This current can be present in the network for several seconds, and its decay is a function of the primary winding resistance. Such technique is reported by [Xie], [Robert] and also briefly in [Watson]. Other sources of transients may be external, where for instance voltage transients injected by a power converter are used [Sumner].

The techniques that use existing harmonic sources

- Stationary harmonics originating from an existing nonlinear load
- Varying harmonics originating from an existing nonlinear load
- Background harmonic distortion present in the network

All of them will be described in the following sections of this chapter.

4.5 Methods based on existing non-linear components or existing background harmonic distortion

Methods using existing harmonic distortion can be divided into two groups. First group, where the level of injected harmonic current (or applied harmonic voltage) is constant and the second group, where a change in the level of injected harmonic current (or applied voltage) is forced.

4.5.1 Constant amplitude harmonics from a nonlinear load

This method takes advantage of an existing nonlinear component. Such method was applied by [De Lorenzi]. He has measured the driving-point harmonic impedance of a 400 kV network by a 340 MVA converter (supplying large device for the production of hot plasmas for Thermonuclear Fusion research) through a 400/21.6 kV transformer. It is assumed that the level of background harmonic distortion is so small that cen be ignored.

In general, it is assumed that the level of injected harmonic current (or applied harmonic voltage) does not change in time. The value of equivalent harmonic impedance Z_{eq}^{h} seen from terminals of the nonlinear component accounts for all harmonic impedances of all series and shunt elements, as shown in Figure 4.3.

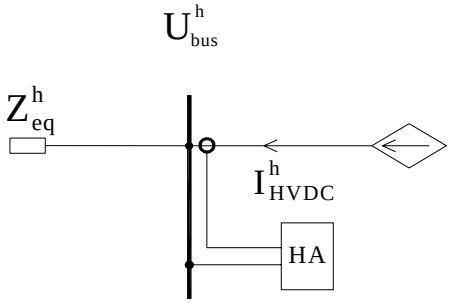

Figure 4.3 Derivation of the equivalent harmonic impedance Z_{eq}^{h} from the ratio of current harmonics injected from a harmonic source I_{HVDC}^{h} and the bus voltage response U_{bus}^{h}. HA – harmonic measuring unit

The harmonic impedance Z_{eq}^{h} can be determined from by measuring the injected harmonic current I_{HVDC}^{harm} and the resultant harmonic voltage at the bus U_{bus}^{harm}:

$$\frac{U_{bus}^{h}}{I_{HVDC}^{h}} = Z_{eq}^{h} \cdot \tag{4.2}$$

Voltages and currents in equation (4.2) are vectors of complex quantities and the impedance is a matrix of complex numbers.

Assumptions

The main assumption of the method is at the same time its main limitation, namely that no background harmonic distortion can be present during the measurement. If any background distortion is present then it will superimpose with the voltage produced by the harmonic injection resulting in erroneous calculation of the harmonic impedance. Such assumption can be made if the injected harmonic current causes very large voltage distortion with comparison to the background distortion (large SNR_{sig}). In theory, it could be possible to account for the distortion coming from other nonlinear components, if the harmonic currents of at least the significant ones are also measured, and the measurements are precisely synchronized, so the information about

the absolute phase angle is present. In such a case, the background distortion (the noise of the SNR_{sig}) is a result of the unknown harmonic sources only.

Special requirements

for three-phase measurements, a harmonic analyzer must have 6 channels synchronously sampled. Length of the measurement is not important since there is no background distortion and the level of injected harmonic distortion is constant. Stored values can have the form of Fourier coefficients - rectangular components of each harmonic or their magnitudes and phase angles. Recording time domain waveforms is not obligatory.

Advantages of the method

i) The method is non-invasive and relatively easy to perform. No switching of power system component is required.

ii) Calculation of the equivalent harmonic impedance directly from the ratios of measured converter current and bus voltage is strait-forward.

iii) It is possible to calculate the harmonic impedance also in cases when the nonlinear load used for verification is the only nonlinear load in the network[1].

Drawbacks of the method

i) No background harmonic distortion can be present during the measurement. Practically it is difficult to reach high SNR_{sig} due to the randomly varying background distortion and limited magnitude of injected harmonic current or applied harmonic voltage.

ii) Measurements can be made only at the sites where large nonlinear loads are installed.

iii) Harmonic impedance is calculated only at the frequencies generated by nonlinear load. Impedance at other frequencies has to be interpolated.

A method, where a converter of an HVDC station was treated as harmonic source has been presented by [Brewer]. Similar methods are also mentioned by [Arrillaga] and [Robert].

4.5.2 Variable amplitude harmonics from a nonlinear load

Usually, the amount of randomly varying background distortion exceeds the levels that allow for precise harmonic impedance calculation using the method described in section 4.5.1. In such a case it is still possible to perform correct measurements of harmonic impedance and eliminate the effect of background distortion. To achieve that, incremental values have to be used in equation (4.2). In order to obtain these values, a nonlinear load has to be run at two operating points. In this way, two values of harmonic currents are injected into the network, which will effect in two values of harmonic voltages. Assuming that the equivalent harmonic impedance is constant during the measurement, the increase in injected current will be proportional to the increase in harmonic voltage, i.e.

$$\frac{U^{\mathrm{h}}_{\mathrm{bus}}(\mathrm{t}_1)-U^{\mathrm{h}}_{\mathrm{bus}}(\mathrm{t}_2)}{I^{\mathrm{h}}_{\mathrm{HVDC}}(\mathrm{t}_1)-I^{\mathrm{h}}_{\mathrm{HVDC}}(\mathrm{t}_2)}=\frac{\Delta U^{\mathrm{h}}_{\mathrm{bus}}}{\Delta I^{\mathrm{h}}_{\mathrm{HVDC}}}=Z^{\mathrm{h}}_{\mathrm{eq}}\,. \tag{4.3}$$

In the extreme case, as illustrated in Figure 4.4, the nonlinear load can be simply connected at (t_2) so $I^{\mathrm{h}}_{\mathrm{HVDC}}(\mathrm{t}_1)$ in (4.3) will become zero:

[1] In contradiction to methods, where passive components are used and pre-existing harmonic distortion is obligatory. Such methods are described in the following sections.

$$\frac{U^{h}_{bus}(t_1)-U^{h}_{bus}(t_2)}{0-I^{h}_{HVDC}(t_2)}=\frac{\Delta U^{h}_{bus}}{I^{h}_{HVDC}}=Z^{h}_{eq}. \tag{4.4}$$

Voltage $U^{h}_{bus}(t_1)$ in this case will be entirely a background distortion $U^{h}_{BGD}(t_1)$ caused by other harmonic sources in the network:

$$\left.\begin{aligned} U^{h}_{bus}(t_1) &= U^{h}_{BGD}(t_1) \\ U^{h}_{bus}(t_2) &= U^{h}_{BGD}(t_2)+\overbrace{Z^{h}_{eq}\cdot I^{h}_{HVDC}}^{U^{h}_{HVDC}} \end{aligned}\right\}. \tag{4.5}$$

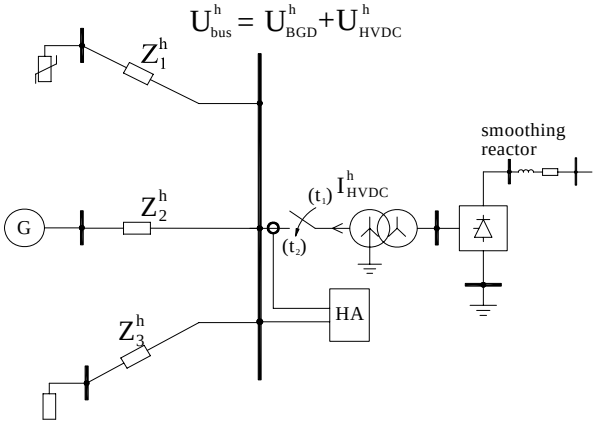

Figure 4.4 Derivation of the equivalent harmonic impedance Z^{h}_{eq} from ratio of incremental values of harmonic currents injected by non-linear load and the resultant increments of bus voltages.

The main assumption of the method is that the background harmonic distortion coming from other nonlinear components is stable:

$$U^{h}_{BGD}(t_1)=U^{h}_{BGD}(t_2)=U^{h}_{bus}(t_1) \tag{4.6}$$

This assumption is true as long as the time span t_{span} between both measurements is as short as possible

$$(t_{span})=\min((t_2)-(t_1)), \tag{4.7}$$

but at the same time both measurements must be made during steady state operation, which means that t_{span} must be longer than the complete transition period between two operating points:

$$(t_{span})>(t_{tr}). \tag{4.8}$$

If the assumption (4.6) is justified, background harmonic distortion is eliminated from further calculations:

$$Z^{h}_{eq}=\frac{U^{h}_{bus}(t_1)-U^{h}_{bus}(t_2)}{I^{h}_{HVDC}}=\frac{U^{h}_{bus}(t_1)-U^{h}_{bus}(t_1)-U^{h}_{HVDC}}{I^{h}_{HVDC}}=\frac{U^{h}_{HVDC}}{I^{h}_{HVDC}}. \tag{4.9}$$

Assumptions

i) Background harmonic distortion is not varying throughout the measurement

ii) Network configuration is not varying throughout the measurement

iii) Measurements are made during steady state operation

Special requirements

i) Basic requirements are analogous to those described in section 4.5.1.

ii) To ensure that assumptions i) and ii) are correct, the time gap between both measurements must be short. Before the actual measurement is done, it is advisable to monitor the background distortion for some time and prove that it is stable, i.e. if magnitudes and phase angles of harmonics that are of interest vary within the required, predefined limits, during periods comparable with t_{span} of the actual measurement.

iii) To ensure that assumption iii) is correct, the period of the transition from one operating point to another, together with associated transients shall be shorter and entirely within the time span separating the two measurements $t_{tr} < t_{span}$.

iv) Precise method must be developed to measure complex quantities at different moments (synchronization, time stamp)

Advantages of the method

i) The method takes advantage of harmonic distortion created by existing nonlinear load. No external source of harmonics is needed.

ii) It enables to eliminate effects of background harmonic distortion and perform correct measurements of harmonic impedance. Strictly speaking, the background distortion is allowable, but it is not necessary and it decreases the SNR_{sig}.

iii) Non-linear loads are relatively common in power networks.

Drawbacks of the method

i) Measurements can be made only at the sites where a large nonlinear load is installed.

ii) Harmonic impedance is calculated only at the frequencies generated by nonlinear load. Impedance at other frequencies has to by interpolated.

iii) All measured values are complex quantities of which both the amplitude and the phase angle must be measured and evaluated at different moments.

4.5.3 Calculation of harmonic driving-point impedance by varying shunt impedance

It may be apprehended that harmonic impedance of a network can be determined by switching a shunt linear load instead of a nonlinear one, as shown in Figure 4.5. The difference between current injected by a non-linear load I^h_{NLL} in the method illustrated in section 4.5.2 and the current I^h_{LL} injected into a linear load in the present method is principally a matter of sign.

A fundamental requirement of this technique is that voltage harmonic distortion U^h_{BGD} *must* be present at this node. This harmonic voltage will cause harmonic currents flowing into the load.

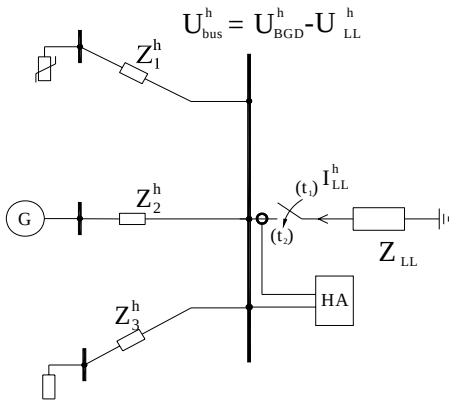

Figure 4.5 Derivation of the equivalent harmonic impedance Z^h_{eq} from ratio of incremental values of harmonic currents flowing into linear load and the resultant increments in harmonic bus voltages.

The effect of a negative harmonic current injection can be seen as a negative harmonic voltage at the bus:

$$U^h_{LL} = \frac{-I^h_{LL}}{Z_{LL}}, \tag{4.10}$$

that means that the resultant harmonic distortion at the bus is lower:

$$U^h_{bus} = U^h_{BGD} - U^h_{LL}. \tag{4.11}$$

The higher the background harmonic distortion U^h_{BGD} is, the higher amplitude of the harmonic current I^h_{LL} flowing into the load and the more precise the overall measurement is (both SNR_{sig} SNR_{ph} are higher). The second requirement of ensuring high SNR_{sig} is that the linear load must have low value of harmonic impedance at one operating point and a high value of impedance at the other operating point (best if it can be switched out completely, like shown in Figure 4.5). For this verification method, the number, location and character (whether approximated by current or voltage source) of nonlinear loads is not important. The same results would be obtained if there is one or more harmonic sources present in the grid. This independence will be proved by referring to Thévenin or Norton theories, which can be applied if nonlinear loads can be represented by ideal harmonic current or voltage sources. Any configuration of a power network with multiple harmonic sources can be represented this way, see Figure 4.6.

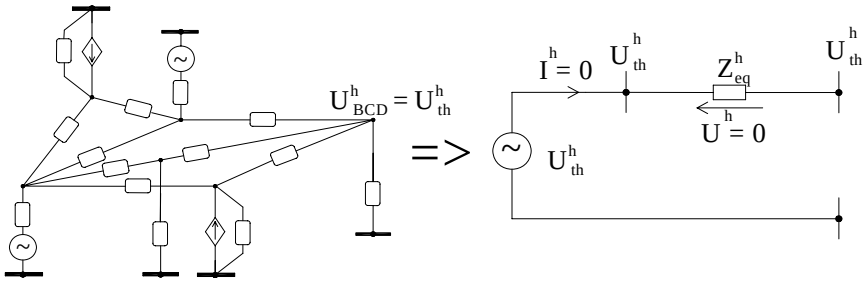

Figure 4.6 Representation of a power network by equivalent harmonic impedance and equivalent Thévenin voltage source.

Initially, at time $t=t_1$, there is no voltage drop on the equivalent impedance Z^h_{eq} because the circuit is not loaded, as shown in Figure 4.7 (a). Connection of a linear load of some unknown value of impedance Z^h_{LL} between terminals A and the reference node closes the loop and causes a current

I^h_{LL} to flow, Figure 4.7 (b). Since the Thévenin voltage source is ideal, the voltage at its terminals U^h_{BGD} does not depend on the load. If a harmonic analyzer (HA) is setup at node A to measure both bus voltage U^h_{bus} at instants (t_1) and (t_2), and the current I^h_{LL} flowing into the linear load at instants (t_1) and (t_2), then it can be shown that the equivalent, driving-point harmonic impedance can be calculated at each frequency present in the background distortion, in a simple manner.

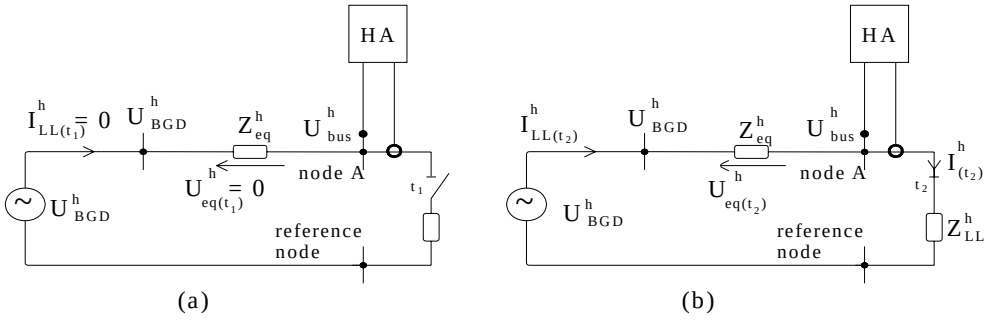

Figure 4.7 Method of determining driving-point impedance by switching linear load. (a) – Circuit in no-load state, (b) – Circuit loaded with linear load. HA – harmonic measuring unit.

The calculated value of impedance does not depend on the magnitude of background harmonic distortion or on the size of the impedance of the linear load, because the higher the voltage distortion, the higher the current – the ratio will stay the same. From the following equations (4.12) and (4.13), incremental quantities are determined that allow to calculate explicitly the impedance Z^h_{eq} :

$$\left.\begin{aligned} U^h_{bus}(t_1) &= U^h_{BGD}(t_1) + \overbrace{Z^h_{eq}\cdot\left(-I^h_{LL}(t_1)\right)}^{(-U^h_{eq}(t_1))} \\ U^h_{bus}(t_2) &= U^h_{BGD}(t_2) + \overbrace{Z^h_{eq}\cdot\left(-I^h_{LL}(t_2)\right)}^{(-U^h_{eq}(t_2))} \end{aligned}\right\}, \tag{4.12}$$

$$\frac{U^h_{bus}(t_1) - U^h_{bus}(t_2)}{I^h_{LL}(t_1) - I^h_{LL}(t_2)} = \frac{\Delta U^h_{bus}}{\Delta I^h_{LL}} = Z^h_{eq}. \tag{4.13}$$

The main assumption is the same like in the case of other methods based on measurements performed at different instants, namely that the background harmonic distortion is stable:

$$U^h_{BGD}(t_1) = U^h_{BGD}(t_2) = U^h_{bus}(t_1). \tag{4.14}$$

This assumption has a chance to be correct as long as the time span t_{span} between both measurements fulfils the two conditions,

$$(t_{span}) = \min\left((t_2) - (t_1)\right) > (t_{tr}), \tag{4.15}$$

where t_{tr} is the transition period between two operating points. For the linear load, a capacitor bank is particularly well suited for the reason that it's impedance decrease with increasing frequency.

Background distortion is necessary, because the injected current that is being switched out is a result of the harmonic voltage applied to the switched impedance.

Assumptions

i) Background harmonic distortion is not varying throughout the measurement

ii) Network configuration is not varying throughout the measurement

iii) Measurements are made during steady state operation

Special requirements

i) All the requirements which are described in section 4.5.2

ii) Presence of background distortion is necessary

Advantages of the method

i) Linear components like capacitor banks are common in power systems and their switching is an ordinary operation

ii) High level of background harmonic distortion is supportive – it increases the SNR instead of decreasing it. It is because the magnitude of injected current increases, instead of being constant like in the method described in section 4.5.2.

iii) Any distribution of harmonic sources gives the same results

Drawbacks of the method

i) $U^{h}_{bus}(t_1), U^{h}_{bus}(t_2), I^{h}_{LL}(t_1), I^{h}_{LL}(t_2)$ are complex quantities of which both the amplitude and the phase angle must be measured and evaluated at different moments.

ii) The presence of proper linear load is necessary.

iii) Background harmonic distortion must be present in sufficient amplitude at each frequency of interest to ensure large SNR.

4.5.4 Calculation of harmonic transfer impedance by varying series linear impedance

Another possibility of verifying a harmonic model of transmission network is to determine, instead of the driving-impedance of a node -the transfer impedance between two nodes. This can be achieved in analogous way as described in section 4.5.3, by switching or changing the impedance value, but of a series power system component. The author hasn't found such a method of verifying harmonic models in the literature. The reason of that may be the need for specialized equipment that allows for synchronized measurements at both sides of the disconnection point, or another reason could be that switching a series element is rarely possible because to continuously supply the consumers some alternative path for the power flow must be provided. Yet, it may be possible and some times desired, in cases when switching a series element affects the harmonic levels in the most distinct way, thereby increasing the SNR_{sig}.

Let's take one of the series elements, connected between nodes **A** and **B** in Figure 4.8 (a). This element can be represented by some unknown series harmonic impedance Z^{h}_{AB}. Let's assume that this impedance can be in general terms varied, from one value of impedance at the instant (t_2) to another at (t_1). The next thing what should be done is to represent this network by a Thévenin equivalent. For that purpose the network from Figure 4.8 (a) can be rearranged to the form shown in Figure 4.8 (b). By representing the network as on Figure 4.8 (b) it becomes clear that it can be represented as a sum of two equivalent Thévenin circuits, as shown in Figure 4.8 (c).

From the Thévenin circuits of Figure 4.8 (c) it can be realized that at state (t_1) the node voltages are:

$$\begin{aligned} U_{\mathrm{A}}^{\mathrm{h}}(\mathrm{t}_1) &= U_{\mathrm{A}}^{\mathrm{h-th}} - U_{\mathrm{A-eq}}^{\mathrm{h}}(\mathrm{t}_1) = U_{\mathrm{A}}^{\mathrm{h-th}} - I_{\mathrm{AB}}^{\mathrm{h}}(\mathrm{t}_1)\cdot Z_{\mathrm{eq}}^{\mathrm{h-A}} \\ U_{\mathrm{B}}^{\mathrm{h}}(\mathrm{t}_1) &= U_{\mathrm{B}}^{\mathrm{h-th}} - U_{\mathrm{B-eq}}^{\mathrm{h}}(\mathrm{t}_1) = U_{\mathrm{B}}^{\mathrm{h-th}} - I_{\mathrm{AB}}^{\mathrm{h}}(\mathrm{t}_1)\cdot Z_{\mathrm{eq}}^{\mathrm{h-B}} \end{aligned}, \tag{4.16}$$

and at state (t_2) the node voltages are:

$$\begin{aligned} U_{\mathrm{A}}^{\mathrm{h}}(\mathrm{t}_2) &= U_{\mathrm{A}}^{\mathrm{h-th}} - U_{\mathrm{A-eq}}^{\mathrm{h}}(\mathrm{t}_2) = U_{\mathrm{A}}^{\mathrm{h-th}} - I_{\mathrm{AB}}^{\mathrm{h}}(\mathrm{t}_2)\cdot Z_{\mathrm{eq}}^{\mathrm{h-A}} \\ U_{\mathrm{B}}^{\mathrm{h}}(\mathrm{t}_2) &= U_{\mathrm{B}}^{\mathrm{h-th}} - U_{\mathrm{B-eq}}^{\mathrm{h}}(\mathrm{t}_2) = U_{\mathrm{B}}^{\mathrm{h-th}} - I_{\mathrm{AB}}^{\mathrm{h}}(\mathrm{t}_2)\cdot Z_{\mathrm{eq}}^{\mathrm{h-B}} \end{aligned}. \tag{4.17}$$

Both harmonic sources $U_{\mathrm{A}}^{\mathrm{h-th}}$ and $U_{\mathrm{B}}^{\mathrm{h-th}}$ are the Thévenin voltage sources. Both impedances $Z_{\mathrm{eq}}^{\mathrm{h-A}}$ and $Z_{\mathrm{eq}}^{\mathrm{h-B}}$ shouldn't be mixed up with driving-point impedances of the nodes, but their sum gives the equivalent Thévenin impedance $Z_{\mathrm{eq}}^{\mathrm{h}}$ of the entire network seen between points A and B (with the varied impedance branch $Z_{\mathrm{AB}}^{\mathrm{h}}$ open-circuited):

$$Z_{\mathrm{eq}}^{\mathrm{h}} = Z_{\mathrm{eq}}^{\mathrm{h-A}} + Z_{\mathrm{eq}}^{\mathrm{h-B}}. \tag{4.18}$$

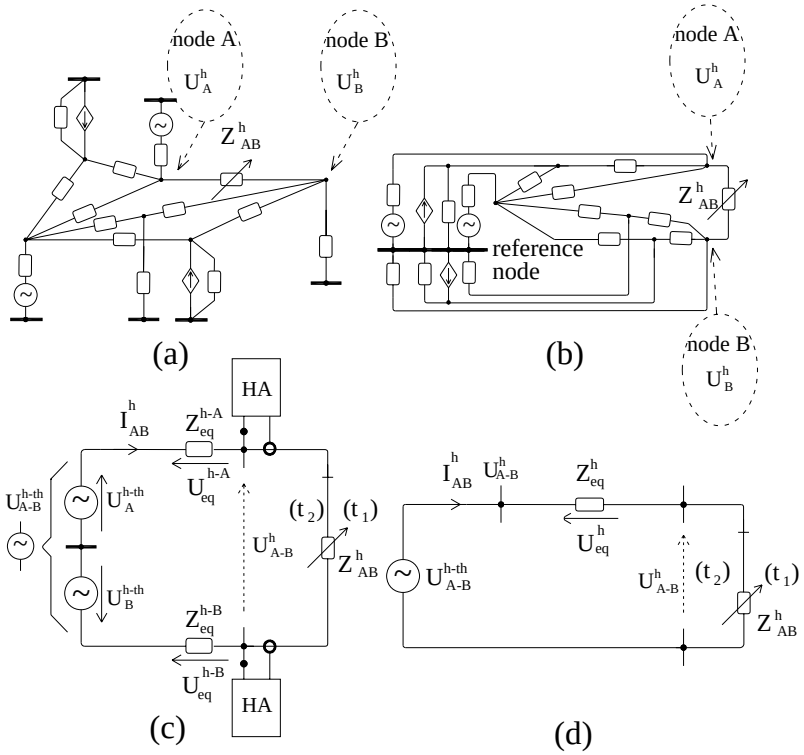

Figure 4.8 Method of determining harmonic transfer impedance by switching linear series element. (a) – original circuit, (b) – circuit redrawn to emphasize the idea, (c) – circuit in "no-load" state, (d) the resultant circuit analogous to circuit from Figure 4.6 (b).

Harmonic current flowing through series impedance $Z_{\mathrm{AB}}^{\mathrm{h}}$ is proportional to the voltage difference between both nodes:

$$\begin{aligned} I_{\mathrm{AB}}^{\mathrm{h}}(\mathrm{t}_1) &= \frac{U_{\mathrm{A}}^{\mathrm{h}}(\mathrm{t}_1) - U_{\mathrm{B}}^{\mathrm{h}}(\mathrm{t}_1)}{Z_{\mathrm{AB}}^{\mathrm{h}}(\mathrm{t}_1)} = \frac{U_{\mathrm{A-B}}^{\mathrm{h}}(\mathrm{t}_1)}{Z_{\mathrm{AB}}^{\mathrm{h}}(\mathrm{t}_1)} \\ I_{\mathrm{AB}}^{\mathrm{h}}(\mathrm{t}_2) &= \frac{U_{\mathrm{A}}^{\mathrm{h}}(\mathrm{t}_2) - U_{\mathrm{B}}^{\mathrm{h}}(\mathrm{t}_2)}{Z_{\mathrm{AB}}^{\mathrm{h}}(\mathrm{t}_2)} = \frac{U_{\mathrm{A-B}}^{\mathrm{h}}(\mathrm{t}_2)}{Z_{\mathrm{AB}}^{\mathrm{h}}(\mathrm{t}_2)}. \end{aligned} \tag{4.19}$$

Both Thévenin circuits can be combined into one, shown in Figure 4.8(d), with the equivalent Thévenin harmonic voltage source defined as the difference between both Thévenin sources:

$$U_{\mathrm{A-B}}^{\mathrm{h-th}} = U_{\mathrm{A}}^{\mathrm{h-th}} - U_{\mathrm{B}}^{\mathrm{h-th}} \tag{4.20}$$

The main assumption of the method is that the equivalent voltage source is constant, so the voltage at its terminals is the same at both states t_1 and t_2. This fact reduces the number of variables because it allows writing:

$$U_{\mathrm{A-B}}^{\mathrm{h-th}} = U_{\mathrm{A-B}}^{\mathrm{h}}(\mathrm{t}_1) + I_{\mathrm{AB}}^{\mathrm{h}}(\mathrm{t}_1)\cdot Z_{\mathrm{eq}}^{\mathrm{h}} = U_{\mathrm{A-B}}^{\mathrm{h}}(\mathrm{t}_2) + I_{\mathrm{AB}}^{\mathrm{h}}(\mathrm{t}_2)\cdot Z_{\mathrm{eq}}^{\mathrm{h}}. \tag{4.21}$$

The voltage drops on the equivalent impedances can be summed up:

$$\begin{aligned} U_{\mathrm{eq}}^{\mathrm{h}}(\mathrm{t}_1) &= U_{\mathrm{A}}^{\mathrm{h-eq}}(\mathrm{t}_1) + U_{\mathrm{B}}^{\mathrm{h-eq}}(\mathrm{t}_1) = I_{\mathrm{AB}}^{\mathrm{h}}(\mathrm{t}_1)\cdot Z_{\mathrm{eq}}^{\mathrm{h}} \\ U_{\mathrm{eq}}^{\mathrm{h}}(\mathrm{t}_2) &= U_{\mathrm{A}}^{\mathrm{h-eq}}(\mathrm{t}_2) + U_{\mathrm{B}}^{\mathrm{h-eq}}(\mathrm{t}_2) = I_{\mathrm{AB}}^{\mathrm{h}}(\mathrm{t}_2)\cdot Z_{\mathrm{eq}}^{\mathrm{h}}. \end{aligned} \tag{4.22}$$

So finally it can be written that:

$$\begin{aligned} U_{\mathrm{A-B}}^{\mathrm{h-th}} &= U_{\mathrm{A-B}}^{\mathrm{h}}(\mathrm{t}_1) + U_{\mathrm{eq}}^{\mathrm{h}}(\mathrm{t}_1) \\ U_{\mathrm{A-B}}^{\mathrm{h-th}} &= U_{\mathrm{A-B}}^{\mathrm{h}}(\mathrm{t}_2) + U_{\mathrm{eq}}^{\mathrm{h}}(\mathrm{t}_2). \end{aligned} \tag{4.23}$$

Equations (4.23) combined give:

$$U_{\mathrm{A-B}}^{\mathrm{h}}(\mathrm{t}_1) + U_{\mathrm{eq}}^{\mathrm{h}}(\mathrm{t}_1) = U_{\mathrm{A-B}}^{\mathrm{h}}(\mathrm{t}_2) + U_{\mathrm{eq}}^{\mathrm{h}}(\mathrm{t}_2). \tag{4.24}$$

And after the substitution, the equation for describing the transfer impedance can be derived:

$$U_{\mathrm{A}}^{\mathrm{h}}(\mathrm{t}_1) - U_{\mathrm{B}}^{\mathrm{h}}(\mathrm{t}_1) + I_{\mathrm{AB}}^{\mathrm{h}}(\mathrm{t}_1)\cdot Z_{\mathrm{eq}}^{\mathrm{h}} = U_{\mathrm{A}}^{\mathrm{h}}(\mathrm{t}_2) - U_{\mathrm{B}}^{\mathrm{h}}(\mathrm{t}_2) + I_{\mathrm{AB}}^{\mathrm{h}}(\mathrm{t}_2)\cdot Z_{\mathrm{eq}}^{\mathrm{h}} \tag{4.25}$$

$$\left[I_{\mathrm{AB}}^{\mathrm{h}}(\mathrm{t}_1) - I_{\mathrm{AB}}^{\mathrm{h}}(\mathrm{t}_2)\right]\cdot Z_{\mathrm{eq}}^{\mathrm{h}} = U_{\mathrm{A}}^{\mathrm{h}}(\mathrm{t}_2) - U_{\mathrm{B}}^{\mathrm{h}}(\mathrm{t}_2) - U_{\mathrm{A}}^{\mathrm{h}}(\mathrm{t}_1) + U_{\mathrm{B}}^{\mathrm{h}}(\mathrm{t}_1)$$

$$Z_{\mathrm{eq}}^{\mathrm{h}} = \frac{U_{\mathrm{A}}^{\mathrm{h}}(\mathrm{t}_2) - U_{\mathrm{B}}^{\mathrm{h}}(\mathrm{t}_2) - U_{\mathrm{A}}^{\mathrm{h}}(\mathrm{t}_1) + U_{\mathrm{B}}^{\mathrm{h}}(\mathrm{t}_1)}{I_{\mathrm{AB}}^{\mathrm{h}}(\mathrm{t}_1) - I_{\mathrm{AB}}^{\mathrm{h}}(\mathrm{t}_2)}$$

$$Z_{\mathrm{eq}}^{\mathrm{h}} = \frac{U_{\mathrm{B}}^{\mathrm{h}}(\mathrm{t}_1) - U_{\mathrm{B}}^{\mathrm{h}}(\mathrm{t}_2) - \left[U_{\mathrm{A}}^{\mathrm{h}}(\mathrm{t}_1) - U_{\mathrm{A}}^{\mathrm{h}}(\mathrm{t}_2)\right]}{I_{\mathrm{AB}}^{\mathrm{h}}(\mathrm{t}_1) - I_{\mathrm{AB}}^{\mathrm{h}}(\mathrm{t}_2)}, \tag{4.26}$$

which can be written in the incremental form:

$$Z_{\mathrm{eq}}^{\mathrm{h}} = \frac{\Delta U_{\mathrm{B}}^{\mathrm{h}} - \Delta U_{\mathrm{A}}^{\mathrm{h}}}{\Delta I_{\mathrm{AB}}^{\mathrm{h}}}. \tag{4.27}$$

From the above equations it becomes apparent that if simultaneous measurements at two instances are performed and voltages $U_{\mathrm{A}}^{\mathrm{h}}(\mathrm{t}_1), U_{\mathrm{B}}^{\mathrm{h}}(\mathrm{t}_1), U_{\mathrm{A}}^{\mathrm{h}}(\mathrm{t}_2), U_{\mathrm{B}}^{\mathrm{h}}(\mathrm{t}_2)$ at nodes A and B are measured, together with harmonic currents flowing into the series impedance $I_{\mathrm{AB}}^{\mathrm{h}}(\mathrm{t}_1)$ and $I_{\mathrm{AB}}^{\mathrm{h}}(\mathrm{t}_2)$, then the equivalent Thévenin harmonic impedance from Figure 4.8(d) can be determined, by using the incremental equation (4.27).

It is enough to verify the harmonic model of the grid, but equation (4.27) does not include the value of the impedance $Z_{\mathrm{AB}}^{\mathrm{h}}$, therefore, it is not the actual transfer harmonic impedance $Z_{\mathrm{ABtr}}^{\mathrm{h}}$. It can be noticed that the impedance $Z_{\mathrm{AB}}^{\mathrm{h}}$ is in parallel with the equivalent Thévenin impedance $Z_{\mathrm{eq}}^{\mathrm{h}}$:

$$Z^{h}_{ABtr}(t_1) = \frac{Z^{h}_{eq} \cdot Z^{h}_{AB}(t_1)}{Z^{h}_{eq} + Z^{h}_{AB}(t_1)} \tag{4.28}$$

$$Z^{h}_{ABtr}(t_2) = \frac{Z^{h}_{eq} \cdot Z^{h}_{AB}(t_2)}{Z^{h}_{eq} + Z^{h}_{AB}(t_2)} \tag{4.29}$$

To express the transfer impedance between nodes A and B at two instances (t_1) and (t_2) purely by means of the measured values, equations (4.19),(4.27) and (4.28) has to be combined in the form:

$$Z^{h}_{ABtr}(t_1) = \frac{\frac{\Delta U^{h}_{B} - \Delta U^{h}_{A}}{\Delta I^{h}_{AB}} \cdot \frac{U^{h}_{A}(t_1) - U^{h}_{B}(t_1)}{I^{h}_{AB}(t_1)}}{\frac{\Delta U^{h}_{B} - \Delta U^{h}_{A}}{\Delta I^{h}_{AB}} + \frac{U^{h}_{A}(t_1) - U^{h}_{B}(t_1)}{I^{h}_{AB}(t_1)}} \cdot \tag{4.30}$$

$$Z^{h}_{ABtr}(t_2) = \frac{\frac{\Delta U^{h}_{B} - \Delta U^{h}_{A}}{\Delta I^{h}_{AB}} \cdot \frac{U^{h}_{A}(t_2) - U^{h}_{B}(t_2)}{I^{h}_{AB}(t_2)}}{\frac{\Delta U^{h}_{B} - \Delta U^{h}_{A}}{\Delta I^{h}_{AB}} + \frac{U^{h}_{A}(t_2) - U^{h}_{B}(t_2)}{I^{h}_{AB}(t_2)}} \tag{4.31}$$

Any components which can be represented as lumped series impedances, for instance power transformers, series capacitors, etc, can be used in this verification technique. Moreover, any element which has zero impedance can be also used, because for instance separating two busbar systems by switching a circuit-breaker and measuring current flowing through it before the separation and the voltage at both busbars before and after the separation, the same information is obtained. In such case, the variation of series impedance is from zero to infinity. Referring to Figure 4.8, the values of particular components will be: $Z^{h}_{AB}(t_1) = 0$, $Z^{h}_{AB}(t_2) = \infty$, $U^{h}_{A}(t_1) = U^{h}_{B}(t_1) \Rightarrow U^{h}_{A-B}(t_1) = 0$, $U^{h}_{A}(t_2) \neq U^{h}_{B}(t_2)$, and the same equations can be used.

Switching a component of zero impedance is a very good approach, because the impedance is varied in the highest possible range.

Verification of the method.

This method has been verified with simple calculation and computer simulation. A simple model of meshed circuit has been used for that purpose (Figure 4.9). The impedance that is being varied is Z_{11}.

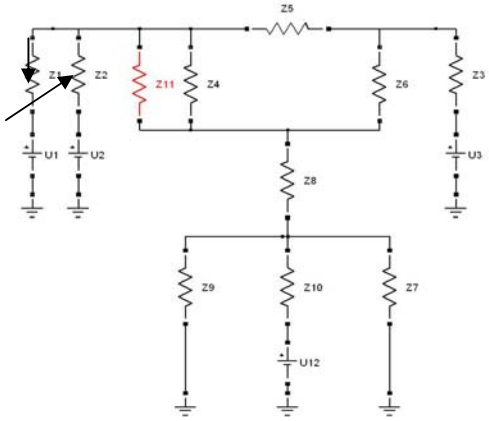

Figure 4.9 Circuit used for verification of the measuring technique.

The data of all the components are:

$$\begin{aligned}
&Z_1 = 1\Omega; Z_2 = 2\Omega; Z_3 = 3\Omega; Z_4 = 4\Omega; Z_5 = 5\Omega;\\
&Z_6 = 6\Omega; Z_7 = 7\Omega; Z_8 = 8\Omega; Z_9 = 9\Omega; Z_{10} = 10\Omega;\\
&Z_{11}(t_1) = 5\Omega; Z_{11}(t_2) = \infty;\\
&U_1 = 1\text{kV}; U_2 = 2\text{kV}; U_3 = 3\text{kV}; U_{12} = 4\text{kV};
\end{aligned} \tag{4.32}$$

In the first step, the equivalent Thévenin impedance has been calculated by hand, and from these calculations, the Thévenin impedance between nodes A and B was obtained:

$$Z_{eq} = 2{,}2091184\Omega, \tag{4.33}$$

and the calculated value of equivalent Thévenin source is:

$$U_{th} = 192{,}274178\,\text{V}. \tag{4.34}$$

These values are shown on the equivalent Thévenin circuit in Figure 4.10.

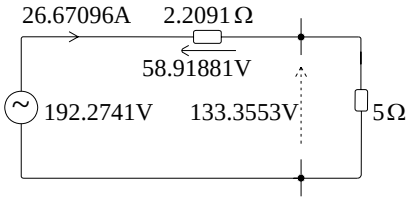

Figure 4.10 calculated Thévenin equivalent of the circuit shown in Figure 4.9.

The "measured" values were also calculated:

$$\begin{aligned}
&U_A(t_1) = 1474{,}434572\text{V};\ U_A(t_2) = 1468{,}707868\text{V};\\
&U_B(t_1) = 1607{,}789419\text{V};\ U_B(t_2) = 1660{,}982046\text{V};\\
&I_{AB}(t_1) = 26{,}67096948\text{A};\ I_{AB}(t_2) = 0\text{A};
\end{aligned} \tag{4.35}$$

The calculated entire transfer impedance between nodes A and B, as the parallel connection of Z_{11} and Z_{eq} is: $Z_{ABtr}(t_1) = 1{,}532169\Omega$ before the disconnection, and $Z_{ABtr}(t_2) = 2{,}2091184\Omega$ after the disconnection.

Now the question is whether the same values of equivalent and transfer impedances can be obtained by using the "measured" values (4.35) and the incremental equation (4.27). Thévenin impedance calculated directly from equation these equations is:

$$Z_{eq} = \frac{\Delta U_B - \Delta U_A}{\Delta I_{AB}} = \frac{U_B(t_1) - U_B(t_2) - \left[U_A(t_1) - U_A(t_2)\right]}{I_{AB}(t_1) - I_{AB}(t_2)}$$

$$Z_{eq} = \frac{1607{,}789419 - 1660{,}982046 - 1474{,}434572 + 1468{,}707868}{26{,}67096948}$$

$$Z_{eq} = \left|\frac{-58{,}919331}{26{,}67096948}\right| = \left|-2{,}2091184\right|\Omega = 2{,}2091184\Omega \tag{4.36}$$

It can be seen that the agreement between equivalent impedance calculated directly (4.33) and the result obtained from the incremental equation (4.36) is very good.

The entire transfer impedance between nodes A and B at instants (t_1) and (t_2) can be also determined from equations (4.28) and (4.29):

$$Z_{\mathrm{ABtr}}(\mathrm{t}_1)=\frac{Z_{\mathrm{eq}}\cdot Z_{11}(\mathrm{t}_1)}{Z_{\mathrm{eq}}+Z_{11}(\mathrm{t}_1)}=\frac{Z_{\mathrm{eq}}\cdot\dfrac{U_{\mathrm{A}}(\mathrm{t}_1)-U_{\mathrm{B}}(\mathrm{t}_1)}{I_{\mathrm{AB}}(\mathrm{t}_1)}}{Z_{\mathrm{eq}}+\dfrac{U^{\mathrm{h}}_{\mathrm{A}}(\mathrm{t}_1)-U_{\mathrm{B}}(\mathrm{t}_1)}{I_{\mathrm{AB}}(\mathrm{t}_1)}}=$$

$$=\frac{2{,}2091184\cdot\dfrac{U_{\mathrm{A}}(\mathrm{t}_1)-U_{\mathrm{B}}(\mathrm{t}_1)}{I_{\mathrm{AB}}(\mathrm{t}_1)}}{2{,}2091184+\dfrac{U_{\mathrm{A}}(\mathrm{t}_1)-U_{\mathrm{B}}(\mathrm{t}_1)}{I_{\mathrm{AB}}(\mathrm{t}_1)}}=$$

$$=\frac{2{,}2091184\cdot\dfrac{1474{,}434572-1607{,}789419}{26{,}67096948}}{2{,}2091184+\dfrac{1474{,}434572-1607{,}789419}{26{,}67096948}}=$$

$$Z_{\mathrm{ABtr}}(\mathrm{t}_1)=\frac{2{,}2091184\cdot 5}{2{,}2091184+5}=1{,}53216959\Omega \tag{4.37}$$

$$\mathbf{Z}_{ABtr}(t_2)=\frac{\mathbf{Z}_{eq}\cdot\mathbf{Z}_{11}(t_2)}{\mathbf{Z}_{eq}+\mathbf{Z}_{11}(t_2)}=\mathbf{Z}_{eq}=2{,}2091184\Omega \tag{4.38}$$

In the next step, the circuit from Figure 4.9 has been also modelled using Matlab and the same results were obtained. Transfer impedances between nodes A and B have been determined using the impedance measurement module, and in second step, the values of obtained in simulations currents and voltages at both instants (t_1) and (t_2) have been used to calculate the transfer impedances. Both simulation approaches gave the same result:

$$\begin{aligned} Z_{\mathrm{ABtr}}(\mathrm{t}_1)&=1{,}5321696\Omega\\ Z_{\mathrm{ABtr}}(\mathrm{t}_2)&=2{,}2091184\Omega \end{aligned} \tag{4.39}$$

It can be seen that the agreement between equivalent impedance calculated directly (4.33), result obtained from the incremental equation (4.36), and obtained from simulations (4.39) is perfect.

Assumptions

i) All the assumptions that were described in section 4.5.3.

ii) Branch of which the impedance is varied does not have any shunt path for the current.

Special requirements

i) All the requirements which are described in section 4.5.3.

ii) Measurements at both nodes A and B need to be precisely synchronized in order to preserve the phase angle information of particular harmonics. If the distance is long, then a GPS clock for synchronization should be used.

Advantages of the method

i) All the advantages of the method described in section 4.5.3.

ii) It allows to calculate transfer impedance between two nodes

iii) Often it can assure higher SNR_{sig} than by using a shunt component due to the higher value of disconnected current

Drawbacks of the method

i) $U^{\mathrm{h}}_{\mathrm{A}}(\mathrm{t}_1), U^{\mathrm{h}}_{\mathrm{A}}(\mathrm{t}_2), U^{\mathrm{h}}_{\mathrm{A}}(\mathrm{t}_1), U^{\mathrm{h}}_{\mathrm{A}}(\mathrm{t}_2), I^{\mathrm{h}}_{\mathrm{AB}}(\mathrm{t}_1), I^{\mathrm{h}}_{\mathrm{AB}}(\mathrm{t}_2)$ are complex quantities of which both the amplitude and the phase angle must be measured and evaluated at different moments.

ii) May be difficult to find a series component that can be freely disconnected

iii) Background harmonic distortion must be present in sufficient amplitude at each frequency of interest to ensure large SNR.

4.6 Determination of transfer harmonic impedance by switching a series component composed of shunt and series elements.

The technique described in section 4.5.4 allows determining harmonic transfer impedance between two nodes of a power network by varying impedance of a series component. This is true for all elements that have shunt admittance so small that it can be neglected. In the case when shunt admittance is larger, a method is needed to compensate for the potential errors it can introduce.

The technique and principles revealed in this section allows determining harmonic transfer impedance a network by switching a series component, which is composed of a combination of series and shunt linear impedances or harmonic sources. This component may be also a transmission line, impedance of which can be represented by a nominal or equivalent Pi circuits.

The discussion will be based on the example network from previous section, which was shown on the Figure 4.8 (b), with the difference that now the impedance which will be switched out is a distributed parameter transmission line with shunt admittance. The example network with the line approximated by an equivalent PI circuit is shown in Figure 4.11.

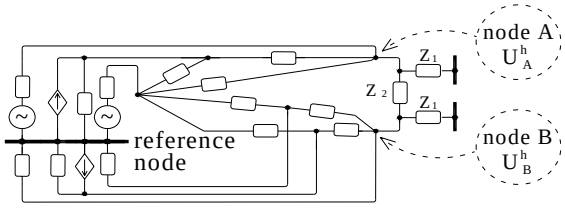

Figure 4.11 Example network with a transmission line connected between nodes A and B.

For convenience of further calculations the equivalent pi circuit of a transmission line is reconfigured to a T circuit (using delta/star transformation), as demonstrated in Figure 4.12.

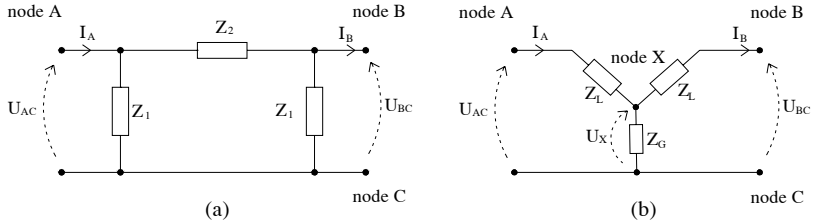

Figure 4.12 Impedance Z_{ABN} represented as an equivalent Pi circuit (a) and its equivalent T representation (b).

The following symbols are introduced in Figure 4.12:

$Z_1 = \frac{2}{Y'} = \frac{2}{Y}\frac{\gamma l/2}{\tanh \gamma l/2}$, $Z_2 = Z' = Z\frac{\sinh \gamma l}{\gamma l}$, $Z_L = \frac{Z_1 Z_2}{2Z_1 + Z_2}$, $Z_G = \frac{Z_1^2}{2Z_1 + Z_2}$, where ***Y*** is the lumped value of shunt admittance of the line in Ω; ***Z*** is the lumped value of series impedance of the line in Ω; l is the length of the line in km, $\gamma = \sqrt{ZY}$ is the propagation constant at the frequency of interest.

Equivalent Pi circuit accounts for the distributed nature of line parameters. It will be shown that switching of such transmission line represented as a T circuit (Figure 4.13) will allow determining the transfer impedance between both nodes A and B.

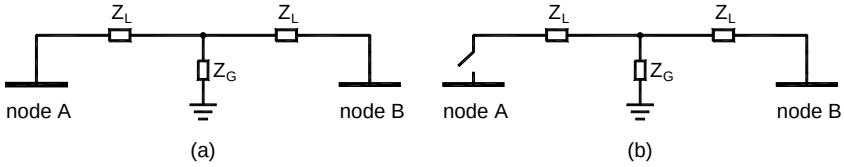

Figure 4.13 Determination of transfer impedance between nodes A and B by switching a transmission line represented by a T circuit. (a) before and (b) after the switching.

Equivalent diagram of the network from Figure 4.11 composed of Thévenin circuits with the line represented by T equivalent circuit is shown in Figure 4.14.

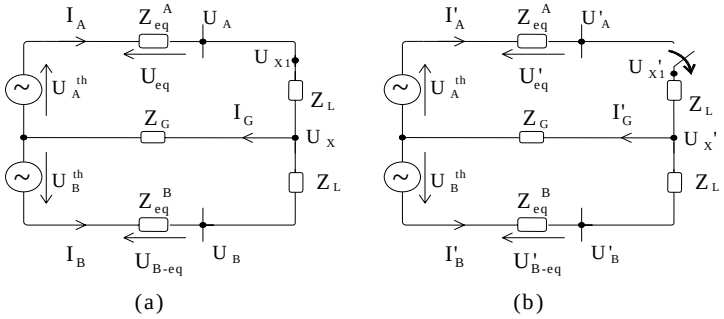

Figure 4.14 Equivalent Thévenin circuit of the network shown in Figure 4.11. (a) Initial state at instant t_1, (b) at instant t_2 one end of the line is disconnected.

As can be seen from Figure 4.14, the smaller the shunt impedance Z_G, the larger the difference between currents flowing in and flowing out of the disconnected line. If equation (4.27) from section 4.5.4 is used directly and the voltage and current values measured at nodes A and B are used, the resultant impedance will differ from the actual value. It can be concluded that in order to use equation (4.27) for determination of the transfer impedance, both voltage and current need to be measured directly at both sides of the disconnection point, i.e. the entire current that flows out of one node through the series variable impedance shall flow into the other node at which measurements are performed.

Therefore, in order to use such component containing shunt impedance, the errors it introduces has to be compensated, for instance by calculating the desired values of voltages directly at both sides of the disconnection point from the quantities measured at other locations.

Calculation of voltages U_X and U_{X1}.

When looking at Figure 4.14 it can be seen that the two nodes that are near the disconnection point and that the whole disconnected current flows in and out directly from them, are the points with voltage amplitudes U_A and U_X (eventually U_{X1}).

At the beginning, the transmission line is connected to both nodes A and B. From Figure 4.14 (a) the value of harmonic impedances of the line, $\boldsymbol{Z}_L$ and $\boldsymbol{Z}_G$ can be estimated:

$$Z_L = \frac{U_A - U_B}{I_A - I_B}, \tag{4.40}$$

$$Z_G = \frac{U_A - I_A \dfrac{U_A - U_B}{I_A - I_B}}{I_A + I_B}. \tag{4.41}$$

It can be deducted that the voltage U_X at the artificially introduced star-point can be expressed by means of the measured quantities:

$$U_X = U_A - I_A \frac{U_A - U_B}{I_A - I_B}, \tag{4.42}$$

$$U_X' = I_B' \cdot Z_G = I_B' \cdot \frac{U_A - I_A \frac{U_A - U_B}{I_A - I_B}}{I_A + I_B}. \tag{4.43}$$

Voltages $\boldsymbol{U}_A$' and $\boldsymbol{U}_X$' are the Thévenin equivalent voltages at both nodes. At the very end of the line, near node A, the voltage $\boldsymbol{U}_{X1}$ is equal to $\boldsymbol{U}_A$ before the line disconnection, and, since the T equivalent circuit provides correct response at its terminals also in no-load state, after the line disconnection voltage $\boldsymbol{U'}_{X1}$ becomes equal to $\boldsymbol{U}_X$':

$$\begin{aligned} U_{X1} &= U_A \\ U'_{X1} &= U'_X \end{aligned}. \tag{4.44}$$

Both voltages $\boldsymbol{U}_X$ or $\boldsymbol{U}_{X1}$ can be used in calculations. If the voltage at the artificial star point is used, the resulting transfer impedance will not include the impedance $\boldsymbol{Z}_L$ of the disconnected arm of the T circuit. If $\boldsymbol{U}_{X1}$ is used instead, the transfer impedance will be the entire transfer impedance at node A, in the sense that it is an impedance of an entire loop seen be a current injected in series, for instance between two busbar sections of the node A. Having the values U_A and U'_A, $\boldsymbol{U}_X$ and $\boldsymbol{U'}_X$ or $\boldsymbol{U}_{X1}$ and $\boldsymbol{U'}_{X1}$ calculated, and also knowing the value of current I_A, it is possible to use directly the equations:

$$Z_{eq} = \frac{\Delta U_X - \Delta U_A}{\Delta I_A} + Z_L = \frac{U_X - U'_X - \left[U_A - U'_A\right]}{I_A - I'_A} + \frac{U_A - U_B}{I_A - I_B}, \text{ or} \tag{4.45}$$

$$Z_{eq} = \frac{\Delta U_{X1} - \Delta U_A}{\Delta I_A} = \frac{U_A - U'_X - \left[U_A - U'_A\right]}{I_A - I'_A}. \tag{4.46}$$

Verification of the method.

The method has been verified using the modified circuit from previous section, and is illustrated in Figure 4.15.

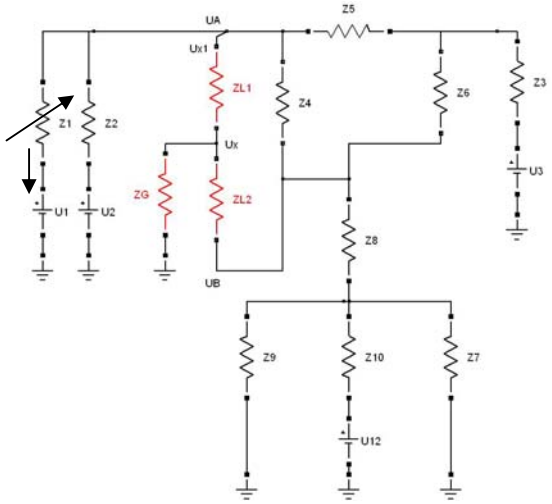

Figure 4.15 Circuit used for verification of the measuring technique.

The data of all the components are:

$$\begin{aligned}
&Z_1 = 1\Omega; Z_2 = 2\Omega; Z_3 = 3\Omega; Z_4 = 4\Omega; Z_5 = 5\Omega;\\
&Z_6 = 6\Omega; Z_7 = 7\Omega; Z_8 = 8\Omega; Z_9 = 9\Omega; Z_{10} = 10\Omega;\\
&Z_{L1} = Z_{L2} = 2\Omega; Z'_{L1} = \infty; Z_G = 1\Omega;\\
&U_1 = 1\text{kV}; U_2 = 2\text{kV}; U_3 = 3\text{kV}; U_{12} = 4\text{kV};
\end{aligned} \tag{4.47}$$

The series component that is switched out is connected between nodes A and B. It is modelled with the two impedances Z_{L1} and Z_{L2}, and the shunt impedance Z_G.

Impedance calculations

Transfer impedance between node A and the star-point X is:

a) with the assumption that $Z'_{L1} = \infty$:

$$Z'_{AX} = 1{,}23601\ \Omega, \tag{4.48}$$

b) with the assumption that $Z'_{L1} = 2\Omega$:

$$Z_{AX} = 0{,}76391\ \Omega, \tag{4.49}$$

Transfer impedance between node A and point X1 with the assumption that $Z'_{L1} = 2\Omega$, disconnected from node A:

$$Z_{eq} = 3{,}23601\ \Omega, \tag{4.50}$$

Additionally transfer impedance between node A and node B with the line disconnected at both ends ($Z'_{L1} = Z'_{L2} = \infty$) is calculated:

$$Z_{AB} = 2{,}20912\ \Omega, \tag{4.51}$$

Calculation of voltages and currents:

$$\begin{aligned}
&U_A = 1194{,}91380\text{V}; && U'_A = 1353{,}54239\text{V};\\
&U_B = 1003{,}69237\text{V}; && U'_B = 928{,}52958\text{V};\\
&U_X = 549{,}65080\text{V}; && U'_X = 309{,}50986\text{V};\\
&I_A = 322{,}63013\text{A}; && I'_A = 0\text{A};\\
&I_B = 227{,}02067\text{A}; && I'_B = 309{,}50986\text{A};
\end{aligned} \tag{4.52}$$

The derived equations (4.40) - (4.48) will be verified using the calculated values (4.52):

$$Z_L = \frac{U_A - U_B}{I_A - I_B} = 2{,}00003\Omega,$$

$$Z_G = \frac{U_A - I_A \dfrac{U_A - U_B}{I_A - I_B}}{I_A + I_B} = 0{,}99999\Omega.$$

$$U_X = U_A - I_A \frac{U_A - U_B}{I_A - I_B} = 549{,}64507\text{V},$$

$$U_X' = I_B' \cdot Z_G = I_B' \cdot \frac{U_A - I_A \dfrac{U_A - U_B}{I_A - I_B}}{I_A + I_B} = 309{,}50663\text{V},$$

$$Z_{eq} = \frac{\Delta U_X - \Delta U_A}{\Delta I_A} + Z_L = 3{,}23602\Omega, \tag{4.53}$$

$$Z_{\text{eq}} = \frac{\Delta U_{\text{X1}} - \Delta U_{\text{A}}}{\Delta I_{\text{A}}} = 3{,}23601\Omega \cdot \tag{4.54}$$

It can be seen that the value of transfer impedance calculated using purely the measured values and the equations (4.53) and (4.54) are in agreement with the value calculated directly (4.50).

Assumptions

i) All the assumptions that were described in section 4.5.3.

Special requirements

ii) All the requirements which are described in section 4.5.4.

Advantages of the method

i) All the advantages of the method described in section 4.5.4.

Drawbacks of the method

i) All the drawbacks of the method described in section 4.5.4.

4.7 Summary

In this chapter various existing verification techniques based on the measurement of driving-point harmonic impedance were presented and analyzed. Their advantages, drawbacks, and necessary assumptions were examined. On that basis two new methods were developed, in which the verification is based on the measurement of the transfer harmonic impedance between two nodes of a meshed network. The work on this chapter has resulted in the following main conclusions:

- For the general validation of a linear harmonic model of power network it does not matter if the driving-point or transfer impedance is used for that purpose.
- Injection of harmonic currents or voltages can be used to calculate harmonic impedance of a network directly assuming that that there is no background harmonic distortion or that its level is sufficiently low to ensure high SNR_{sig}.
- In cases if the level of background harmonic distortion cannot be ignored, the injected harmonic signal need to be varied and the varying response need to be measured. The ratio of the increment of excitation to the increment of response will be the driving-point harmonic impedance of the node and the effect of the background harmonic distortion is eliminated, under the assumption that it is not changing during the measurement, and the topology (impedance) of the network doesn't change either.
- If sufficient level of background distortion is present in the voltage at a node, it will cause harmonic current to flow into a linear shunt element (for instance capacitor bank). Switching or varying the impedance of this shunt element will cause the background harmonic distortion to vary at the node, and therefore, an incremental equation will allow calculating the driving-point impedance of this node. No nonlinear element is needed. The level of background distortion and topology of the network needs to stay unchanged.
- In some cases the highest variation (highest SNR_{sig}) will be ensured by switching a series power system component. Therefore, a method was developed in this chapter that allows determining the transfer harmonic impedance between two nodes by varying impedance of a series linear element linking them. The difference between switching a shunt element and a series element is that in the first case potential of the reference node is constant, and in the later case the potential of both nodes is affected.

- This series element may be simply a connection between two sections of a busbar at a substation. In such case the impedance is changed from zero to infinity.
- In practical terms, driving point impedance is usually more desired, because the nonlinear loads that are connected to a power network are mostly shunt loads that inject harmonic currents into the driving-point impedance. However, such transfer harmonic impedance is needed if a Thyristor Controlled Series Capacitor (TCSC) or a Thyristor Controlled Series Reactor (TCSR) are to be installed. Both compensators inject harmonic currents in series with the power system (not in shunt) and the harmonic impedance that the harmonic currents will see is the transfer impedance at the spot where it is installed.
- A modification of the method is presented where the transfer harmonic impedance can be determined by switching series linear impedance with a shunt branch. The method allows eliminating the errors resulting from the additional shunt path. A more general case was also presented and analyzed where the series element is a distributed parameter transmission line with shunt admittance. The line is disconnected only at one end, and it is impossible to calculate transfer impedance directly because part of the current flows to the ground at both instances and the overall voltage response at both nodes is a combination of the effects series current and shunt admittance currents of the line. However, it is shown that by representing the transmission line as an equivalent T circuit, voltage at the artificially created star point can be calculated and used in further calculations and the effects of the shunt admittance are compensated for.
- Simple hand calculations and computer simulations validated the developed methods.

Chapter 5

Harmonic measurements on the 400 kV transmission network

The principal purpose of this chapter is to present the results of GPS-synchronized harmonic measurements performed on the 400 kV Western network of Energinet.dk. Before the main measurement, the initial simulations were performed and the component that when switched out - causes the largest difference in harmonic levels is found. The chapter also contains description of main technical details of the measurements and presents the results of preliminary measurements of the noise induced in coaxial cables laid in the 400 kV switchyard and shows the comparison between using protective and metering cores of current transformers for harmonic measurements.

5.1 Introduction

Classical measurements in power networks assume that measured currents and voltages have perfectly sinusoidal shapes. Their actual distortion from ideal sinusoids was in the past commonly ignored and therefore not measured [Acha]. Consequently, existing measuring circuits, transducers and equipment in reality allows for precise measurements of fundamental frequency signals only.
While measuring harmonic distortion, both currents and voltages have to be transformed down to proper levels, which especially in high voltage transmission networks indicate large transformation ratios. These transformed signals are then lead to a control room in a hostile EM environment. Then the signals are signal-conditioned, filtered and sampled by measuring instruments characterized with sufficient sampling rate and vertical resolution. Finally, signal processing techniques can be applied to obtain a frequency spectrum and the obtained results have to be stored and analyzed.

The following reasons make harmonic measurements more difficult than the measurement of pure sinusoidal signal:

- Higher sampling rate is required
- High frequency signals are transformed by voltage and current transformers that are not suited for harmonic measurement and their transformation ratio may largely depend on the frequency
- harmonics with small amplitudes have to be transmitted through hostile EM environment
- Measurement of small amplitude harmonics together with large amplitude of fundamental frequency implies large vertical resolution of measuring instruments

- Amplitude and phase angle of harmonics can vary rapidly. In some cases to assess the levels – long term measurements are necessary

- Time domain measurements have to be processed to extract necessary information

Chapter outline

This chapter is organized as follows:
At the beginning, results of initial simulations are given. These initial simulations indicated which power system component has to be switched to obtain the largest difference in harmonic levels. Next, all practical aspects considered in this project are given. This includes harmonic voltage measurement and harmonic current measurement, noise induced in coaxial cables led through high voltage switchyard and technical data of available measuring equipment. Then, the main measurement and the obtained results are described, and at the end the results of measurements are compared with the results of initial simulations.

5.2 Selecting the location for the measurements

5.2.1 Initial analysis

It has been decided that the measurements should be performed on the 400 kV transmission network. At this voltage level there are 18 substations distributed all over Jutland and Funen. The two principal criteria for selection of the substations where harmonic measurements can be performed, are that they should be located:

- In the area where potentially high harmonic distortion may occur
- Not far away from the city of Aalborg

To fulfil the first criterion, it can be assumed that the measurements shall be performed in the area where large nonlinear loads are present. Such large nonlinear elements in the Western network of Energinet.dk are the two HVDC interconnections with Norway and Sweden.
Therefore, only the substations located in the vicinity of these HVDC converters will be considered. Actually, by selecting this area near the HVDC interconnections, also the second criterion is fulfilled, because the HVDC interconnection to Sweden is located near Aalborg.
The HVDC interconnection to Sweden (the Konti-Scan link) consists of two poles. Pole 1 (250 MW) is connected to the 150 kV level and is equipped with the mercury-arc valves. Pole 2 (300 MW) is connected to the 400 kV level. Both poles of Konti-Scan link are located at the substation VESTER HASSING (VHA3 and VHA5).
The HVDC interconnection with Norway (the Skagerrak Link) consists of three poles, Skagerrak 1 and 2 (2 x 250 MW) connected to the 150 kV voltage level and Skagerrak 3 (500 MW) on the 400 kV level. All three poles are equipped with thyristor converters and geographically located at the same substation TJELE **(**TJE3 and TJE5).
These two substations are located approximately 100 km away from each other. Between them, two other 400 kV power substations are located, FERSLEV (FER5) and VENDSYSSELVÆRKET (NVV5). Substation VHA5 is connected to the rest of 400 kV network through a single overhead line ended at substation NVV5. At substation NVV5 also a power plant (Nordjyllandsværket B3; 372 MW) is connected. Substation FER5 is located close to substation TJE5.
Substations TJE and VHA are in reality composed of two substations, one 400 kV (TJE5 and VHA5) and one 150 kV (TJE3 and VHA3). The poles of HVDC links are connected to both voltage levels, together with harmonic filters. The harmonic filters are tuned to the characteristic

harmonic frequencies generated by the converters. Between substations NVV5 and FER5 two transmission lines are installed: FER5-NVV5-0 (In = 1,2 kA, Z1 = 4,38 Ω) and FER5-NVV5-X(IN = 1,2 kA, Z1 = 6,83 Ω). This is a temporary solution, due to the grid modifications. The length of the lines is 20 km and 22 km respectively [data from the load-flow model]. As can be seen, one of the lines has significantly lower impedance than the other. The reason for this is that this line with lower impedance contains a 7 km underground cable section. The cable section has much lower positive sequence impedance than the overhead line section; the overhead section of the line FER5-NVV5-0 has the impedance Z1 = 253,795 mΩ/km, while the positive sequence impedance of the cable section is Z1 = 99,567 mΩ/km. This means that the lines are not loaded equally, but larger currents flow through the line FER5-NVV5-0.

The finally selected substations are

- TJE5, where the HVDC converter and harmonic filters are installed,
- NVV5, where the power line from the substation VHA5 (Konti-scan link) is conneted,
- FER5, which is located in between TJE5 and NVV5 substations.

Figure 5.1 shows a map of Jutland, with three substations marked (TJE, FER and NVV) with the two HVDC connections to Norway and Sweden shown. The detailed diagram of the surrounding part of the power system is shown in Figure 5.2.

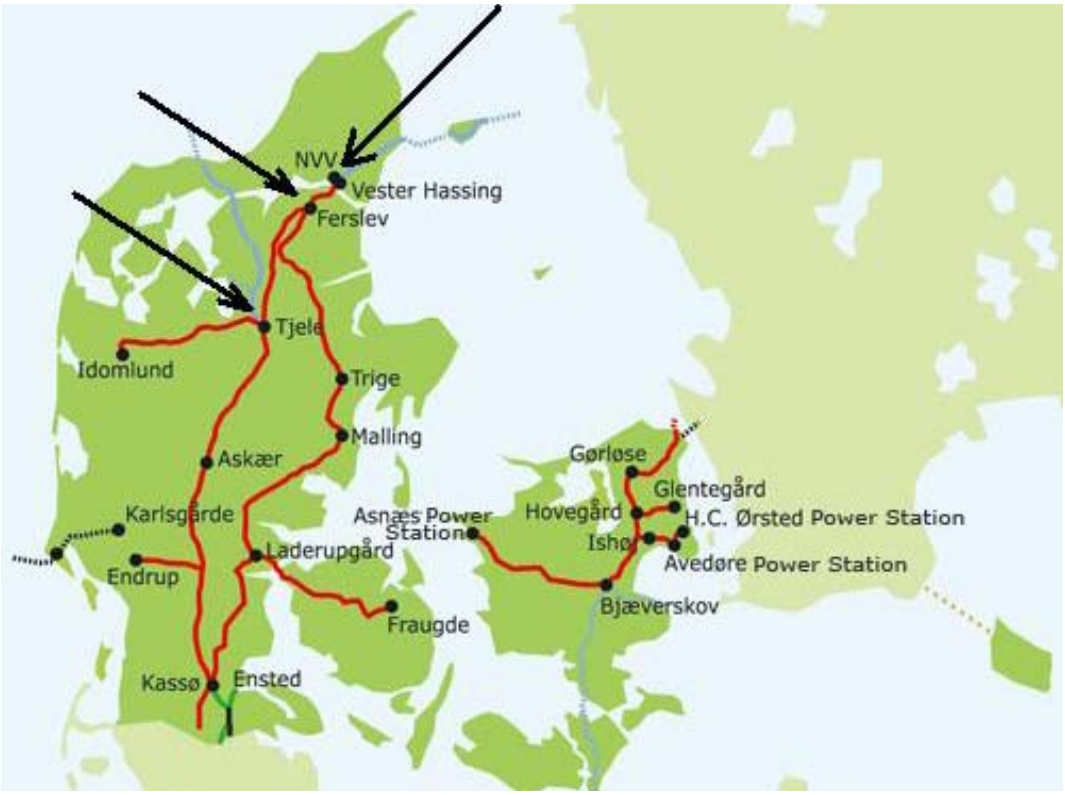

Figure 5.1 Three selected substations are TJELE (TJE5), FERSLEV (FER5) and VENDSYSSELVÆRKET (NVV5), shown in the picture with arrows.

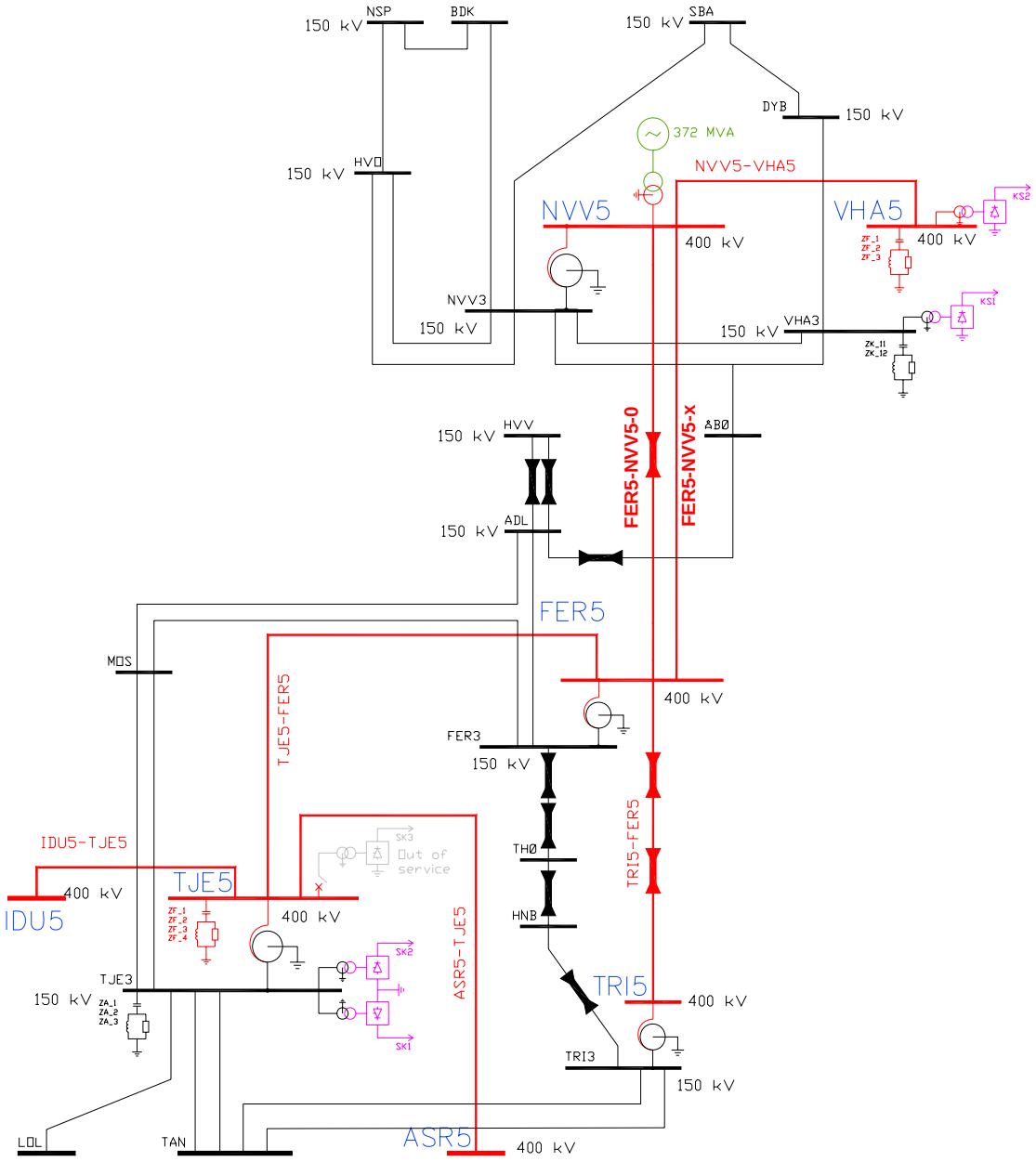

Figure 5.2 Diagram of the transmission network near the selected for measurement substations: NVV5, FER5 and TJE5. Red – 400 kV level, Black – 150 kV level, Magenta – HVDC links.

Detailed diagrams of the three substations with current transformers (CT), capacitive voltage transformers (CVT) and capacitive taps in transformer bushings (CTB) are shown in Figure 5.3 (NVV5), Figure 5.4 (FER5) and Figure 5.5 (TJE5).

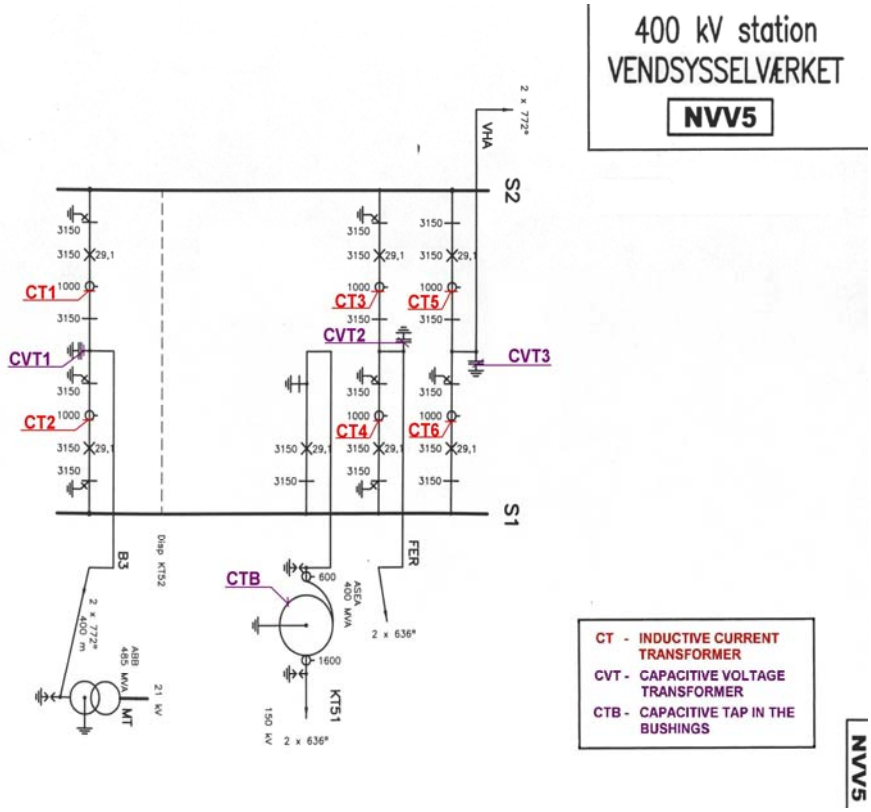

Figure 5.3 Schematic diagram of substation NVV5 [Stationsdata].

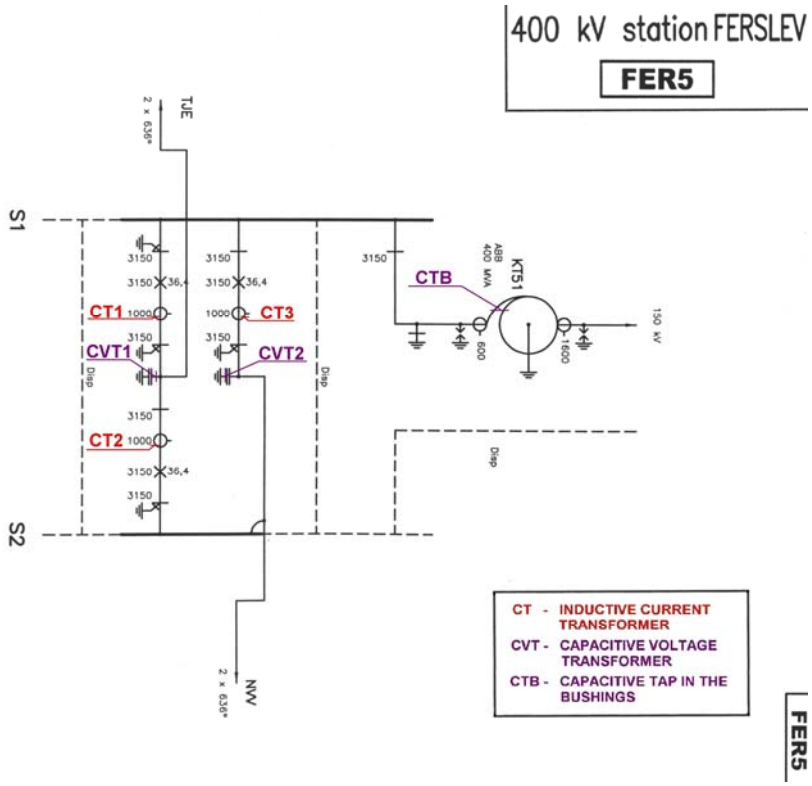

Figure 5.4 Schematic diagram of substation FER5 [Stationsdata].

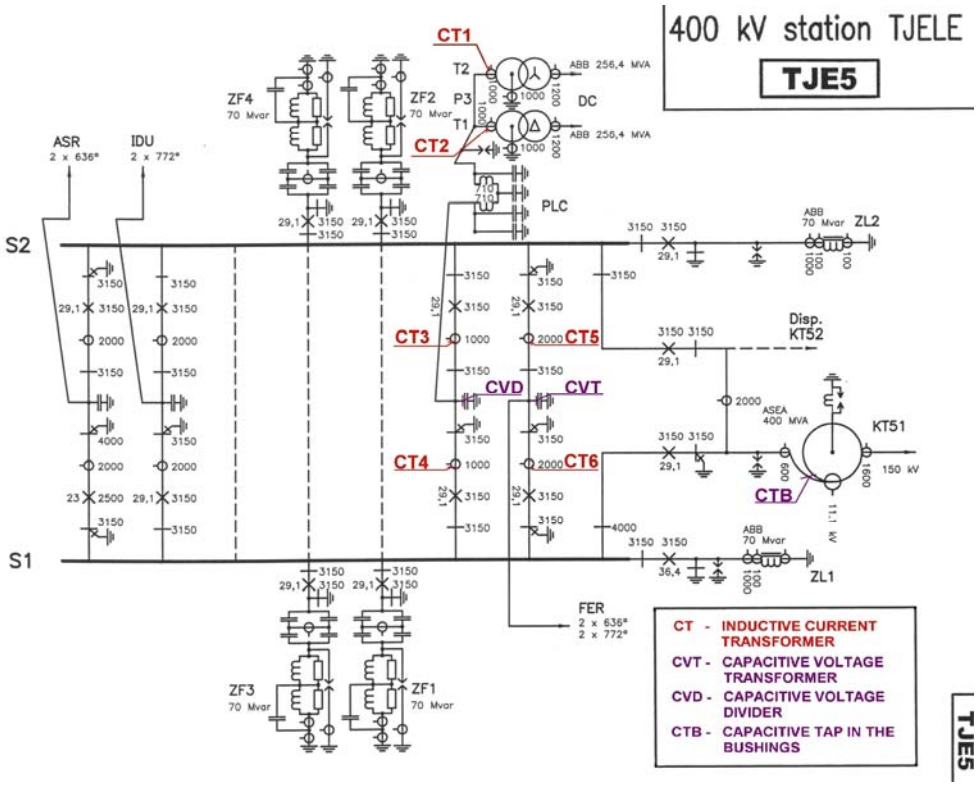

Figure 5.5 Schematic diagram of substation TJE5 [Stationsdata].

5.3 Initial simulations

Next step was to decide which component must be switched to obtain the incremental voltage values, according to the finding from chapter 4. As it was written there, the component and location of the measurements shall be chosen to ensure the best accuracy of verification by ensuring high signal-to-noise ratio with respect to the background harmonic distortion.

A number of PowerFactory computer simulations has been performed where various network components were switched out and in, and the differences in harmonic levels were inspected. The element must be chosen that affects mostly the harmonic voltage levels at the previously selected substations: TJELE (TJE5), FERSLEV (FER5) and VENDSYSSELVÆRKET (NVV5),

For the simulations, the entire linear network model of the Western network is used. The model contains all necessary modifications, according to the findings from chapter 3.

The level of harmonic distortion in a power network can be principally affected in two ways:

- by switching a source of harmonic distortion,
- by changing the harmonic impedance of the system.

The harmonic impedance of a power system can be affected most effectively by:

- switching a passive harmonic filter,
- switching a PFC capacitor bank,
- switching a power line.

The only large source of harmonic distortion at the 400 kV level are the HVDC links but it is not practically possible to “switch” them off. Also the natural variations of the loading of an HVDC link cannot be used, because it is slow and background harmonic distortion during this time can change.

The only way therefore, is to switch on/off a passive power system component.

Grid configurations

In the initial simulations, the effects of switching of passive power system components have been investigated. 10 cases have been analyzed. The selected for switching components are harmonic filters, a power line and a shunt capacitor. These elements are switched out and switched in, in different configurations, and the harmonic incremental values are investigated.
The summary of the simulated cases is presented in Table 5.1.

Case 1	base case
Case 2	1 harmonic filter switched off - TJELE 5 substation
Case 3	2 harmonic filters switched off - TJELE 5 substation
Case 4	base case + line FER5-NVV5-0 switched off
Case 5	1 filter (TJELE 5)+ line FER5-NVV5-0 switched off
Case 6	2 filters (TJELE 5)+ line FER5-NVV5-0 switched off
Case 7	Harmonic filter ZA1 at TJELE 3 substation switched off
Case 8	PFCC (capacitor) at TJELE 3 substation switched off
Case 8a	TJE3_PFCC + Line FER5-NVV5-0 switched off
Case 9	Filter TJE3_ZA1 + Line FER5-NVV5 switched off

Table 5.1 Initial simulations performed in DIgSILENT PowerFactory software.

All the results of these initial simulations are extensive, and therefore are not present in this report. The complete set of tables can be found on the compact disc attached to the project. More detailed tables are shown only as an example, for two cases 1 and 4 (Table 5.2, Table 5.3).

Case 1 - basic configuration												
Station	VHA5		TJE5		FER5		NVV5		VHA3		TJE3	
	Name	ON	Name	ON	Name	ON	Name	ON	Name	ON	Name	ON
Name of the Filter	ZF1**	x	ZF1**	x	ZL1				ZK11**	x	ZA1**	x
	ZF2**	x	ZF2**	x	ZL2				ZK12**	x	ZA2**	x
	ZF3**	x	ZF3**	x	ZL**	x					ZA3**	x
	ZF4	_	ZF4**	x							ZL1	
	ZF5	_	ZL1									
	ZF6	_	ZL2									
	ZL1											
	ZC1											
** - these filters are switched on in the original file (Case 1). Other are ***out of service***												

Table 5.2 Case 1 - basic configuration. The table shows the configuration of harmonic filters and shunt reactors connected at 6 substations. Compare with Figure 5.5-Figure 5.3.

CASE 4 -- base case + line FER5-NVV5-0 switched off												
Station	VHA5		TJE5		FER5		NVV5		VHA3		TJE3	
	Name	ON	Name	ON	Name	ON	Name	ON	Name	ON	Name	ON
Name of the Filter	ZF1**	x	ZF1**	x	ZL1				ZK11**	x	ZA1**	x
	ZF2**	x	ZF2**	x	ZL2				ZK12**	x	ZA2**	x
	ZF3**	x	ZF3**	x	ZL**	x					ZA3**	x
	ZF4	_	ZF4**	x							ZL1	
	ZF5	_	ZL1									
	ZF6	_	ZL2									
	ZL1											
	ZC1											
** - these filters are switched on in the original file (Case 1). Other are ***out of service***												

Table 5.3 Case 4 -- base case + line FER5-NVV5-0 switched off. The table shows the configuration of harmonic filters and shunt reactors connected at 6 substations. Compare with Figure 5.5-Figure 5.3.

The whole model used for simulations is practically composed of linear models of power lines, transformers, etc. The only sources of harmonic distortion in the model are the 12-pulse HVDC converters. Of the Skaggerak and Konti-scan links. In the performed harmonic domain simulations they are modelled as ideal 12-pulse converters, with idealized spectra.
Harmonic content of these converters is therefore excessive, but in order to determine the component that causes the largest differences in harmonic levels, the values of actual amplitudes of the harmonic currents are not important.
10 cases were simulated, and the changes in the following values were monitored:

- Voltage distortion at substations VHA5, TJE5, FER5, NVV5, VHA3, TJE3,
- Currents flowing into harmonic filters installed at substations TJE5 and TJE3,
- Currents flowing into harmonic filters installed at substations VHA5 and VHA3,
- Currents injected by the HVDC links,
- Currents flowing in power lines connecting substation TJE5 with substations ASR5, FER5, IDU5 and in the autotransformer TJE5-TJE3,
- Currents flowing in power lines connecting substation TJE3 with substations LOL3, MOS3, TAN3 (lines 1 and 2) and in the autotransformer TJE5-TJE3,
- Currents flowing in power lines connecting substation VHA5 with substation NVV5 and substation VHA3 with substations DYB3, NVV3, NVT3,
- Currents flowing in power lines connecting substation FER5 with substations NVV5 (two lines 0 and X), TJE5 and TRI5,
- Currents flowing in power lines connecting substation NVV5 with substations FER5 (two lines 0 and X), and VHA5.

All the results of simulations are gathered in 90 tables and are present on the compact disc attached to the report. However the most voltage harmonic distortion at six neighbouring 400 kV and 150 kV substations for the two important cases is given here (Table 5.4 and Table 5.5).

CASE 1 --- BASE CASE						
Station	VHA5	TJE5	FER5	NVV5	VHA3	TJE3
Harmonic	% fund	% fund	% fund	% fund	% fund	% fund
11	1,3150	0,1566	0,2390	0,7577	0,1817	0,0738
13	0,3418	0,3224	0,8791	0,7439	0,1783	0,0388
23	0,6320	0,2900	0,6593	0,1393	1,4015	3,2103
25	0,4971	0,2836	0,7943	0,1333	0,4431	2,3609
35	0,0733	0,2449	1,7478	1,4691	0,1858	0,9551
37	0,1834	0,3220	0,2028	0,1649	0,3602	0,7805
47	0,3312	0,3288	0,1660	0,1718	0,4236	0,3592
49	0,2966	0,0269	0,1302	0,5289	0,4620	0,3828
THD % >>	**1,6520**	**0,8622**	**2,2441**	**1,9129**	**1,6681**	**4,2051**
Urms [kV]	**414,9655**	**413,4205**	**414,1606**	**415,0716**	**167,3923**	**168,1309**

Table 5.4 Case 1 - basic configuration.

CASE 4 --- base case + line FER5-NVV5-0 switched off						
Station	VHA5	TJE5	FER5	NVV5	VHA3	TJE3
Harmonic	% fund	% fund	% fund	% fund	% fund	% fund
11	2,9000	0,1915	0,3629	0,7900	0,2861	0,0764
13	1,1786	0,3680	1,0939	0,5930	0,2131	0,0367
23	0,8362	0,5871	0,5365	1,0243	1,4336	2,9795
25	0,6137	0,6596	0,4424	1,1440	0,4468	2,1924
35	1,0777	0,2788	2,6867	2,8174	0,6896	0,8725
37	1,3172	0,4348	0,8813	1,3152	0,3795	0,7302
47	0,6959	0,7255	0,7593	0,6667	0,3613	0,3734
49	0,8642	0,0837	2,2640	1,0121	0,4002	0,3138
THD % >>	**3,8733**	**1,3236**	**3,9381**	**3,8039**	**1,8145**	**3,9017**
Urms [kV]	**415,2122**	**413,3124**	**413,9720**	**415,2829**	**166,7740**	**168,1259**

Table 5.5 Case 4 - base case + line FER5-NVV5-0 switched off.

SUMMARY OF THE RESULTS.

This is a summary based on the whole set of results that can be found on the compact disc.

Voltage distortion

When comparing the tables containing voltage distortion (compact disc) it can be seen that highest change in total harmonic voltage distortion occurs between Case 1 and Case 4 (basic configuration vs. disconnection of power line FER5-NVV5), for substations VHA5 (THD_U change from 1,65% to 3,87%). FER5 (THD_U change from 2,24% to 3,94%), NVV5 (THD change from 1,91% to 3,7%) and The highest THD_U occurred in the TJE3 substation in case 8 THD_U =6,8 %. THD_U at TJE3 station in the base case is quite high, around 4 % with a high contribution of 23rd and 25th harmonic. It is probably caused by the fact that the high pass filter (PFCC or ZA2) is presently modelled as pure capacitance.

Currents flowing into harmonic filters installed at substations TJE5 and TJE3.

At the TJE5 substation, 4 identical double-tuned + highpass filters are installed. When one or two of these filters are switched off (Case 2 and 3), the rms current in the remaining filters does not rise significantly: from 89,1 A, THD_I=16% up to 89,7A, THD_I =21% and 91,6A, THD_I =31% respectively. The highest current will flow in Case 6 where two filters and the power line is disconnected. The rms current in the remaining filters rises to 98,8 A and the THD_I is 52,6 %.

At TJE3 substation, two, double tuned filters ZA1 and ZA3 (11^{th} and 13^{th} harmonic) and one highpass filter are installed. The highpass filter (PFCC or ZA2) is presently modelled as pure capacitance however, due to the lack of data (in the received datasheet it is stated that the inductive part is insignificant and the filter is almost a pure capacitance). In the final model the inductive part shall also be included. In all cases, except cases 7 and 9, rms currents of the filters ZA1 and ZA3 are approx constant and equal to 191 A. The THD_I is practically also constant and is 82%. In cases 7 and 9 filter ZA1 is disconnected. The rms current in the filter that remains connected rises to 264 A with the THD_I value of 144 %. The rms value of the current in PFCC in the base case is 385 A, and THD_I is approx. 100%. The current values in PFCC will most likely be different if the inductance is also modelled.

Currents flowing into harmonic filters installed at substations VHA5 and VHA3.

At substation VHA5 two identical filters are installed, tuned to 12^{th} harmonic (ZF1 and ZF3). Additionally, highpass filter tuned to 24^{th} harmonic ZF3 is also present. The rms current in filters ZF1 and ZF3 is 76,5 A with THD_I of 4% in the cases 1, 2, 3, 7, and 8. In all the other cases the line FER5-NVV5 is disconnected and the THD_I rises to approx. 9% - all harmonics rise. It does not affect the rms current significantly. The rms current in the highpass filter ZF2 is approx 40A with THD_I of 80% basically in all the cases 1, 2, 3, 7, and 8. In all the other cases the line FER5-NVV5 is disconnected and the rms rises to 48 A and THD_I rises to approx. 120% - all harmonics rise. At substation VHA3 two filters are installed, ZK11 tuned to 5^{th}, 7^{th} and 11^{th} harmonic and ZK12 tuned to 13^{th} harmonic and above. The rms current in the filter ZK11 is 260 A, THD_I = 30% in the cases 1, 2, 3, 7, and 8. In all the other cases the line FER5-NVV5 is disconnected and the rms value rises to approx. 272 A and THD_I rises to approx. 40%.

Harmonics of HVDC converters.

Harmonics generated by the HVDC converters and their loading does not change when the network topology is changed. It is due to the fact that the converters are modelled as ideal current sources. Depending on the voltage value at a bus, the fundamental and harmonic currents slightly vary, proportionally to the applied rms voltage. However the ratio between the fundamental and different harmonics remains constant. There is no interaction modelled between bus voltage harmonics and the harmonic currents generated by the converters.

Currents flowing in power lines supplied from TJE5 substation.

The highest effect on the harmonic currents in the power lines connected to TJE5 station has the disconnection of the line FER5-NVV5. The difference is especially pronounced for line FER5-TJE5; in case 1, Irms = 111 A, THD_i = 31%, loading 7%, and in Case 4 the values are: Irms = 136 A, THD_i = 45%, loading 8,5%.

Currents flowing in power lines supplied from TJE3 substation.

Harmonic distortion in all the lines is low, approx. 2-5%. The highest effect on the harmonic currents in the lines connected to TJE3 station has the disconnection of the harmonic filters installed at the TJE3 substation. The THD changes no more than 1-2%.

Currents flowing in power lines supplied from VHA5 and VHA3 substations.

Harmonic distortion in all the lines is approx. 9-12%. The THD_I changes are insignificant, max 2% in all the lines. The highest effect on the harmonic currents flowing in the lines has the disconnection of the power line FER5-NVV5.

Currents flowing in power lines supplied from FER5 substation.

The two lines FER5-NVV5-0 and FER5-NVV5-X, which are connected in parallel, are not loaded equally. Line FER5-NVV5-0 is 50% loaded while line FER5-NVV5-X is only 10% loaded. The rms current flowing in the lines are 582A and 121A respectively. The THD_i in line FER5-NVV5-0 is lower and is 6,27% while for the line FER5-NVV5-X it is 10,5%. This is in relation to the fundamental component. The particular harmonics expressed in amperes are higher in the line where the rms current is higher, for example 23^{rd} harmonic in line FER5-NVV5-0 is 19,5 A whereas in line FER5-NVV5-X it is 4,6A. The impedances of the two lines are different and vary with the frequency in a different manner. For instance at 50 Hz the impedance of line FER5-NVV5-X is 4.8 times higher than the line FER5-NVV5-0, whereas at 13^{th} harmonic the ratio lowers to 1,9. At 35^{th} harmonic the ratio rises to 35, etc. The results are exact for line FER5-NVV5-X since it is a pure overhead line and line FER5-NVV5-0 contains a 7 km cable section.

Large difference in the current flowing in the power line FER5-TJE5 is between simulation of case 2 and case 3, due disconnection of the harmonic filter at TJE5 substation. The rms currents are 98A and 134A and their THD_i is 28% and 19%. The difference is mainly due to change in the fundamental component, and also 11^{th} and 13^{th} harmonic currents.

The biggest and most noticeable difference is however caused by disconnection of the highly loaded line with the cable section FER5-NVV5-0. The line is disconnected at both ends. The remaining line FER5-NVV5-X takes over the loading of line FER5-NVV5-0. The amplitudes of different harmonics are higher. The disconnection of line FER5-NVV5-0 affects also to a less extent harmonics in the line FER5-TJE5.

Currents flowing in power lines supplied from NVV5 substation

Three power lines are connected to the NVV5 substation. The two described previously parallel lines FER5-NVV5-0 and FER5-NVV5-X and the third line, which is linking NVV5 substation with the substation VHA5. To the VHA5 substation the HVDC link Konti-Scan and harmonic filters are connected. All the phenomena related to the two lines FER5-NVV5-0 and FER5-NVV5-X described in the section concerning FER5 substation are the same on the other end at the NVV5 substation. It can be also seen that the loading and harmonic currents that flow in line VHA5-NVV5 are practically constant in all of the cases. This is related to the fact that at VHA5 station the HVDC link with harmonic filters are connected and no switching on this station has been made. All the switching of harmonic filters has been performed at the TJE5 and TJE3 substations. These harmonics are simply injected by the HVDC link Konti-Scan. Part of the currents flow into the harmonic filters and the rest is injected thorough the VHA5-NVV5 power line into the system. That is the reason that the harmonic currents in the line VHA5-NVV5 are not changing. The impedance of the rest of the network, as seen from this line at NVV5 substation shall rise, due to the disconnection of the FER5-NVV5-0 power line. This should result in higher levels of harmonic distortion at the NVV5 substation. The voltage harmonic distortion rises from 1,86 % up to 3,69%.

Conclusion

Performed simulations show that the biggest effect on the levels of harmonic distortion in the area of interest has the disconnection of one of the parallel power lines between substations NVV5 and FER5 - line FER5-NVV5-0. This line is more loaded then line FER5-NVV5-X so the effect of disconnecting it will be more pronounced. The disconnected line contains the 7km long underground cable section. It has been shown that this switching operation has the highest effect on the voltage harmonic distortion at substations NVV5, FER5 and VHA5. Values that have to be

measured are voltages at substations NVV5, FER5 and TJE5. Additionally currents in the disconnected line at both ends have to be measured; these measured values will be assigned to current sources that will be connected instead of the disconnected line.

5.4 Technical aspects of measurements

There are special requirements with respect to voltage and current transducers due to the fact that they are usually not suited for measuring higher frequencies. These aspects are described in sections 5.4.1 and 5.4.2. Special attention must be also given to the cables led from current and voltage transducers. These cables are the longest parts of such a harmonic measuring system, and so they act as antennas, picking up noise and lowering the signal-to-noise ratio SNR_{ph}. These issues are treated in section 5.4.3. Proper measuring equipment must be also chosen in terms of signal-conditioning, filtering, sampling rate and vertical resolution. The equipment that was used in the measurements is described in section 5.4.4.

5.4.1 Voltage measurement

There are several types of voltage transducers. They can be classified into three main groups, depending on their principle of operation. These are the Conventional Voltage Transformers [Xiao], which include Magnetic Voltage transformers with a ferromagnetic core (called also Potential Transformers, PT) and Capacitive Voltage Transformers (CVT) in which a capacitive potential divider is combined with a magnetic voltage transformer. Second subgroup contains Voltage Dividers, where the most common are RC dividers [Minkner]. The third group are the Unconventional Voltage Transformers [Watson]. This group includes the Optic Voltage Transformers based on the Pockels effect [Santos], or Kerr effect [Hidaka]. All of them have various advantages and drawbacks with respect to measurement of higher frequencies. Both RC dividers and Optic transformers perform well for harmonic measurements [Ghassemi], [Minkner], [Santos], [Hidaka]. Potential transformers are also usable for harmonic measurements, especially if transfer function correction algorithms are used [Meliopoulos], [Meliopoulos 1993]. The main source of errors in potential transformers is the parasitic capacitance between primary and secondary windings. The resonant frequency of the resonance it creates, together with the winding leakage inductances of the windings is approximately inversely proportional to the transformation ratio, and for high voltage transformers is above 1 kHz [Meliopoulos 1993].

The most commonly used capacitive voltage transformers are a combination of capacitive divider and an inductive potential transformer, see Figure 5.6. In this way, the insulation requirements for the potential transformer are much lower, and the overall cost of the voltage transformer can be reduced [Ghassemi]. Unfortunately, due to the fact that they contain both capacitances and inductances, they are tuned to measure fundamental frequency component precisely. At higher frequencies resonance effects affect the actual ratio of the transformer to such degree that they are not suitable for higher frequency measurements [Ghassemi], [Meliopoulos], [Meliopoulos 1993]. They experience severe response fluctuation in the frequency range of interests, as low as several hundred Hertz, as can be seen in Figure 5.6. [Xiao].

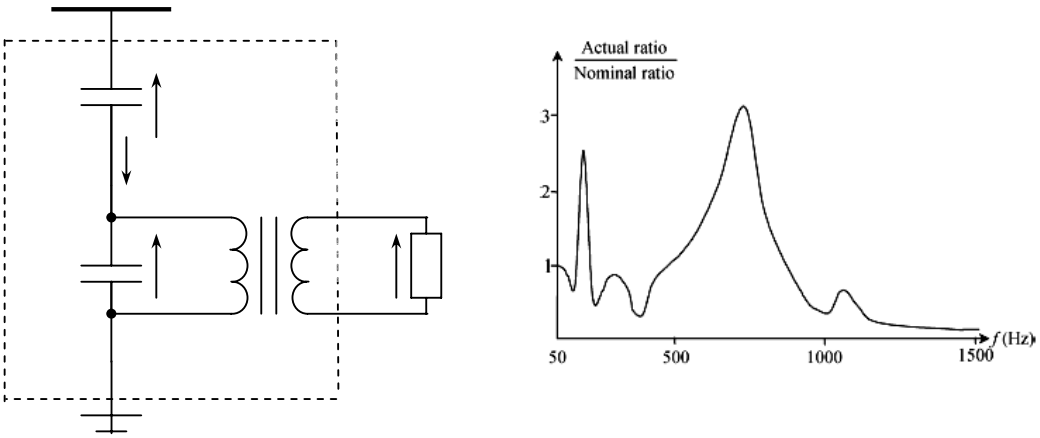

Figure 5.6. Capacitive voltage transformer and example variation of the actual ratio over frequency range [Xiao], where C_1/C_2 is the capacitive divider, PT is the inductive potential transformer.

Moreover, the value of frequency response of a CVT near resonances can vary significantly during repeated test. Thus, measurements of harmonics using CVT's are unreliable, even when processed by error correction algorithms, as discussed by many authors [Germain], [Ghassemi], [Meliopoulos], [Seljeseth], [Minkner] and another measuring technique has to be used.

With the need to accurately measure harmonic distortion of the power system voltage, voltage transformers should have a well-defined (preferably flat) frequency response over the frequency range of interest. In general, there are two conventional approaches to achieve that. One possibility is that the frequency response of a voltage transducer is known in the frequency range of interest (because it was for instance precisely measured). In such a case, principally any static component connected in shunt with the power system can be used as a voltage divider or voltage transducer. Because the transfer function is known, actual values of harmonic voltages can be determined. Frequency response of such component does not have to be linear. An example of such component can be a capacitive voltage transformer or a harmonic filter. Another option would be that a voltage transducer has such physical construction that it is allowed to assume that its frequency response is linear in the frequency range of interest. In order to make such assumption the transducer has to be a purely resistive R, capacitive C, or inductive L divider. It can be also a combination or resistive and capacitive components RC, or resistive and inductive components RL. Since the impedance of resistors is constant, impedance of capacitors decrease proportionally to harmonic order and impedance of inductors rise proportionally to harmonic order, the ratio at each harmonic is known because it is the same as at fundamental frequency or it rises/declines proportionally to harmonic order. The ratio at the fundamental frequency can be determined by measuring the fundamental frequency voltage and comparing it with the fundamental frequency voltage measured by conventional voltage transformers. An example of such component that has a linear frequency response is a capacitor bank or capacitive tap in electrical bushings of power or current transformers, as described in the following section.

Capacitive tap in the transformer bushings (CTB)

Capacitive layers in the HV transformer bushings form C1 (main) and C2 (tap) capacitances, see Figure 5.7 and Figure 5.8 a) and b). Capacitance C_1 is formed by the main oil/paper insulation between the central conductor and the C_1 layer/foil [Pritpal]. The C_2 capacitance is formed by the tap insulation between the C_1 and the C_2 layers. Layer C_1 is internally connected to the voltage tap whereas the C_2 layer is permanently connected to the tank wall. Under normal operating condition, layer C_1 is grounded to the tank wall by a voltage tap cover that makes a connection

between the tap and the mounting flange. The C_2 insulation under normal operating condition is therefore shorted.

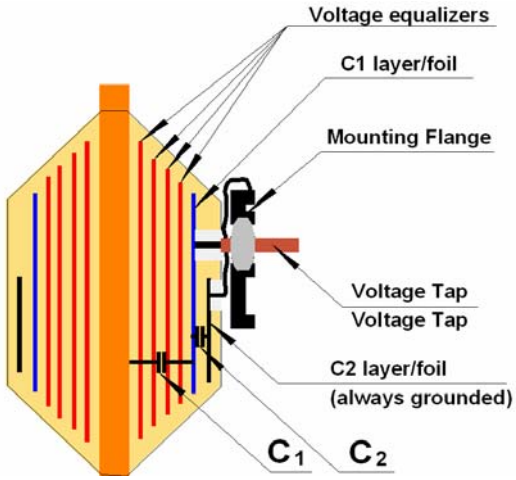

Figure 5.7. Construction details of a typical HV transformer bushings with a capacitive tap [Pritpal].

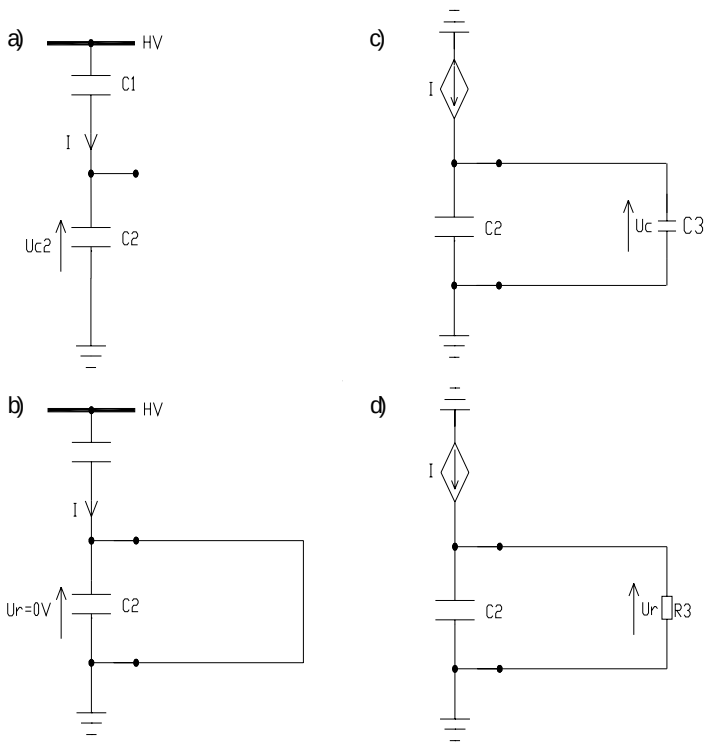

Figure 5.8. a) C1 and C2 capacitances of transformer bushing, b) capacitance C2 bypassed, c) capacitance C2 with additional capacitance C3 in parallel d) capacitance C2 with additional 2 Ohm resistor R2 in parallel.

When such a bushing is used for harmonic measurements, the voltage tap is not grounded, and under this condition, the C_1 and C_2 capacitances are in series and perform like a voltage divider. The voltage developed across capacitance C_2 is modified because a measuring circuit forms a parallel circuit with the capacitance C_2 as shown in Figure 5.8 c) and d). This capacitive voltage divider is linear over the frequency range thus it can be used for measurement of the higher harmonic components of the distorted voltage [Pritpal]. Exact values of the capacitances C_1 and C_2 are not known, however, value of C_1 can be expected to be in the range 300 – 1000 pF

[Pritpal], [Xiao]. Value of C_2 usually varies in the range from 40% to 90% of C1 [Pritpal]. These values of capacitance correspond to impedance values in the range of mega Ohms.

Normally the voltage at a capacitive tap would be very high, and cannot be used directly for measurement. Therefore, an additional capacitor C_3 or a resistor R_3 must be introduced, as shown in Figure 5.8 c) and d). The impedance of this component Z_3 is in the range of several Ohms, and should be chosen so the voltage drop on it will be suited to the input range of a measuring device. Of course proper overvoltage protection has to be installed. High voltage behind the very high impedance of capacitance C_1 will behave as a current source in case of small changes of additional impedance Z_3. Therefore, the equivalent diagram can be drawn like on Figures 8 c) and 8 d). If an impedance is connected in parallel with C_2, as shown in figures 8 c) and 8 d), the capacitive current that flows thorough capacitance C_1 will split. For instance, if the impedance of C_2 is 1 MOhm, then the current flowing through the connected 2-Ohm resistor would have the magnitude of 99, 9998% of the total current, so practically the entire capacitive current $\boldsymbol{I}$ flows through additional impedance Z_3. The exact values of capacitances of CTB are not known, and as a result also the voltage ratio is not known in advance. Therefore, before the actual measurement is done, this ratio must be determined. This can be achieved by a simultaneous measurement of the secondary voltage of CTB and secondary voltage of a conventional capacitive voltage transformer CVT. CVT's are not suited for harmonic measurements, but they are designed to measure the fundamental frequency component very accurately. Therefore, their voltage ratio at the fundamental frequency is very accurate and it can be used as a reference for determining the ratio of CTB's. Ignoring the high impedance of C2, The capacitive current $\boldsymbol{I}$ is expressed as

$$I = \frac{U_{HV}}{Z - j\dfrac{1}{\omega C_1}}, \tag{5.1}$$

where Z is the introduced capacitance or resistance. The amplitude of this current will increase linearly with the frequency, thus if a resistance is used instead of the capacitance, the resultant voltage drop $\boldsymbol{U_2}$ would increase with the frequency effecting in the necessity of using different ratio for each harmonic. However, if a capacitance is used, its impedance will decrease with the frequency so the same ratio as was determined for the fundamental component can be used. Example results of a measurement where both, a capacitor and a resistor were used are shown in Figure 5.9.

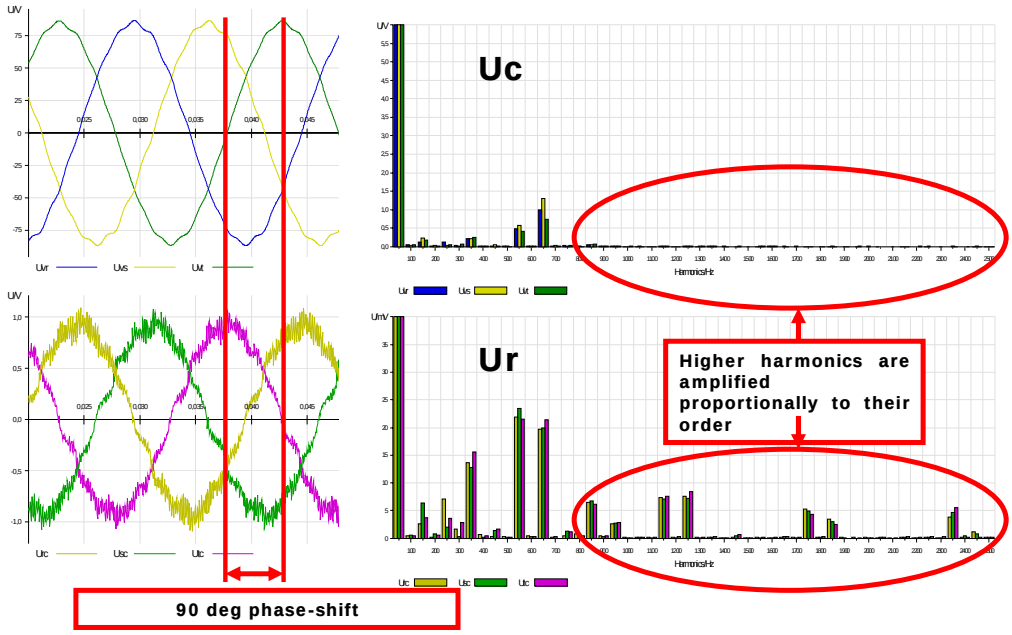

Figure 5.9. Amplification of higher order harmonics. Uc – voltage drop measured on a capacitor, Ur – voltage drop measured on a resistor.

It can be seen that the harmonic components of the voltage drop on a resistor are magnified, proportionally to their order. The disadvantage is that the analysis of results is more difficult, because each harmonic component must be divided by its ratio and there is a 90 deg phase shift between the measured and actual voltage signals. However, there is also a large advantage of such measurement, since higher harmonic components tend to have low amplitudes, and therefore this amplification effect increases the signal-to-noise ratio of the physical circuits SNR_{ph}. To be specific, this means that the magnitude of harmonic components is effectively increased with comparison to:

- The level of noise induced along the cables, lead through the switchyard
- The level of quantization noise introduced by quantization in the analogue to digital conversion process

For example, a measuring instrument with 12-bit A/D converter has an input range of 100 V. The fundamental frequency component of the measured signal has the amplitude U_{fund} = 100V, but it also contains 13^{th} harmonic in the level of 1% of the fundamental frequency component. This value will be also 1% if transformed using a capacitor, but will have the magnitude of 13% if transformed using a resistor. Therefore, if a capacitor is used, then the measuring instrument would measure the 13^{th} harmonic as 1% ± 0,0244% of the range, so 1V ± 2,44% of the magnitude of 13^{th} harmonic, but if a resistor is used then the measuring instrument would measure the 13^{th} harmonic as 13% ± 0,0244% of the range, so 1V ± 0,19% of the magnitude of 13^{th} harmonic.

At all three substations TJE, FER and NVV the capacitive taps of autotransformer bushings are used for fundamental frequency voltage measurement. The existing setup had to be disconcerted, in order to avoid errors that may come from its unknown harmonic impedance, as shown in Figure 5.10. The signal is taken out from the capacitive tap and voltage drop on an additional capacitor C_{CTB} was measured in the existing setup. This capacitor C_{CTB} had to be bypassed, in order to have the whole current flowing to the harmonic measuring setup.

If the cables are accidentally disconnected from the capacitive tap, a dangerous high voltage will appear on the capacitive tap. In order to protect against the results of such unintended disconnection, an overvoltage protection must be installed there. Since this overvoltage protection will be placed outdoors in the switchyard, close to the capacitive tap, it must be

furnished with a resistant, metal waterproof housing. The housing is equipped with a grounding tap, which must be grounded always when the equipment is connected to the capacitive tap (see Figure 5.11).

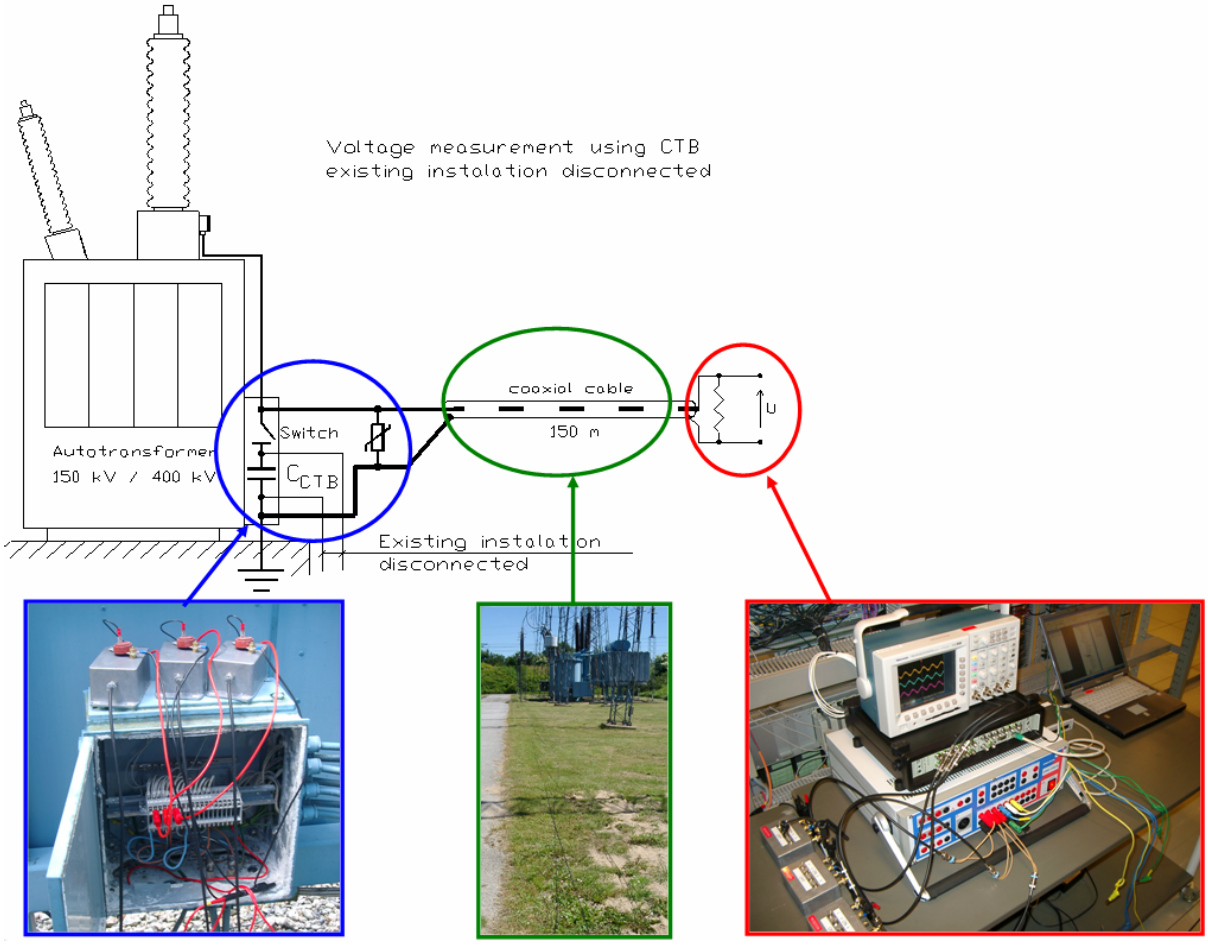

Figure 5.10 Voltage measurement using the capacitive tap in the transformer bushings.

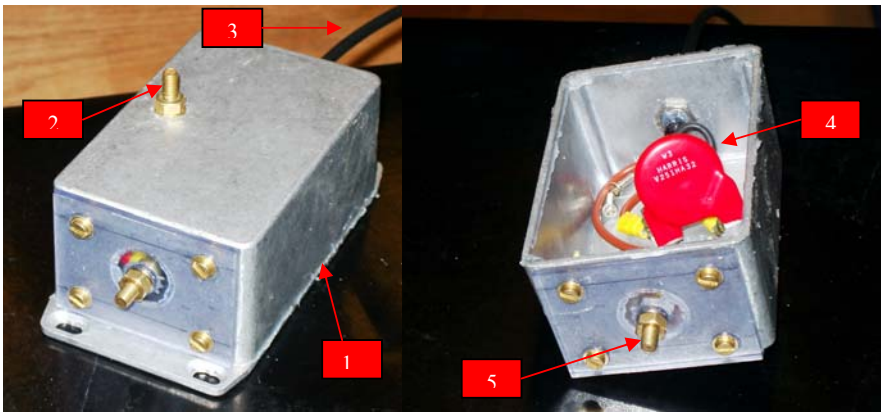

Figure 5.11 Overvoltage protection - varistor Harris V251HA32 in a waterproof housing, where: 1 - Waterproof housing, 2 - Grounding tap, 3 - 60 cm-long coaxial output cable RG58 ended with a BNC plug, 4 - Varistor Harris V251HA32; U_{Nrms} = 250V; Energy (10/1000 μs) = 300J; I_{Peak} (8/20μs) = 25 kA; I_N = 200A, 5 - Capacitive current input (signal from the capacitive tap insulated from the housing)

At the end of the coaxial cables in the control room, the voltage drop on resistances or capacitances is measured. The value of capacitance/resistance can be varied in order to adjust the voltage drop to the input range of measuring instrument. Also here, an overvoltage protection is installed. The capacitor boxes contain one capacitor permanently connected of 1μF and 4 switchable capacitors of 2,2μF, see Figure 5.12. The variable capacitance enables to match the voltage drop U_2 to the max range of the measuring inputs of Omicron CMC256. The following values of capacitance are possible: 1μF; 3,2μF; 5,4μF; 7,6μF and 9,8 μF. the resistor boxes contain one resistor permanently connected of 50Ω and 9 switchable resistors of 50Ω, see Figure 5.13. The following values of resistance are possible: 50Ω; 25Ω; 16,7Ω; 12,5Ω; 5Ω. Each box an overvoltage protection; varistor S20K150; U_{Nrms} = 150V; max energy (2ms) = 85J; I_{Peak} (8/20 μs) = 8 kA; P_{max} = 1W. The housing has a grounding tap, but the main circuit is insulated from it.. Figure 5.14 shows constructed capacitor boxes, resistor boxes and the overvoltage boxes.

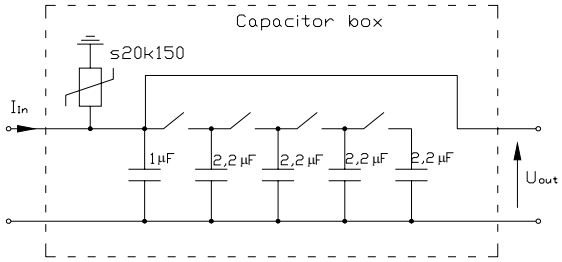

Figure 5.12 Schematic diagram of the capacitor box installed in the control room.

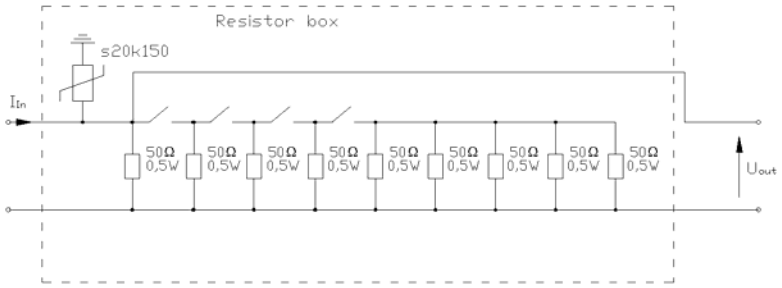

Figure 5.13 Schematic diagram of the resistor box installed in the control room.

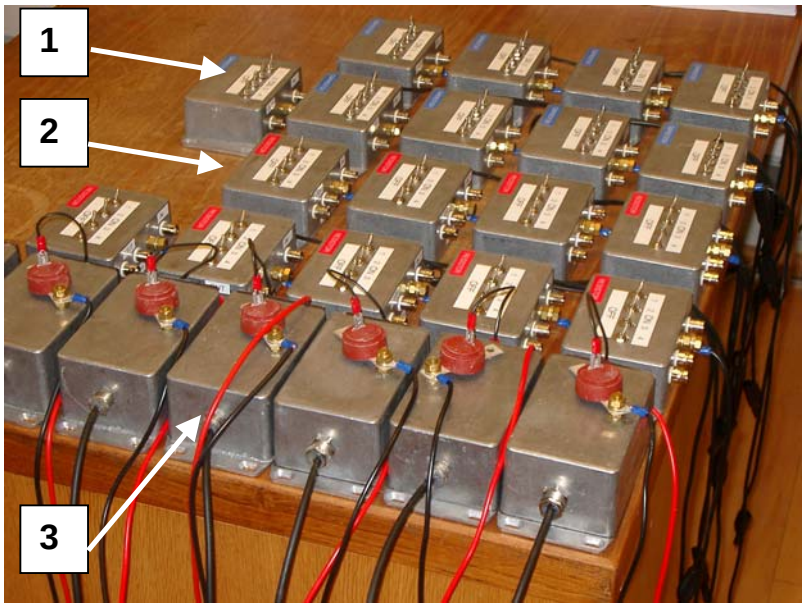

Figure 5.14 (1) - Capacitor boxes; (2) - Resistor boxes and (3) - overvoltage protection.

Comparison of results of harmonic measurement using the Capacitive Voltage Transformer (CVT) and the Capacitive tap in the Bushings (CTB).

The ratio CTB at fundamental frequency was determined by comparing the magnitude of the fundamental frequency component measured by CVT and CTB, at each of the substations TJE, FER and NVV. Harmonics up to 49th were measured using both CTB and CVT, and the results are shown in Figure 5.15, Figure 5.16 and Figure 5.17.

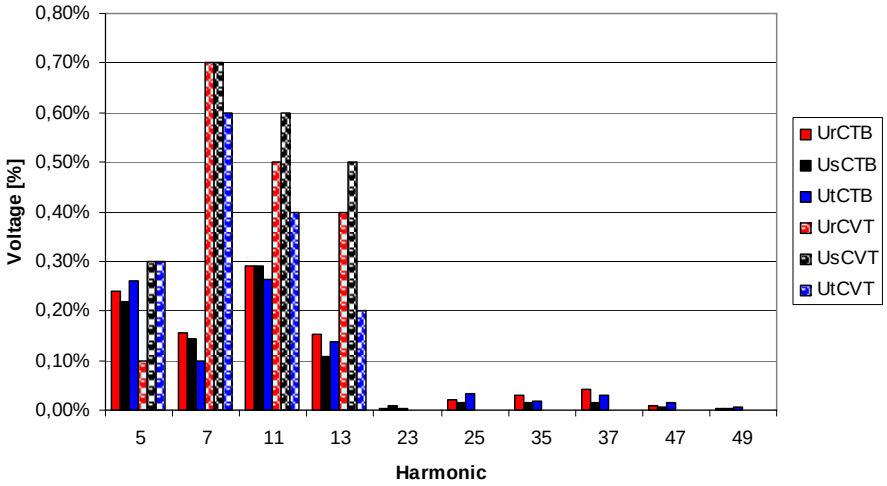

Figure 5.15 Voltage measured at substation **TJE** using the voltage drop on a resistor connected to the CTB and to the regular CVT. Higher harmonics measured at CTB are scaled down proportionally to their order.

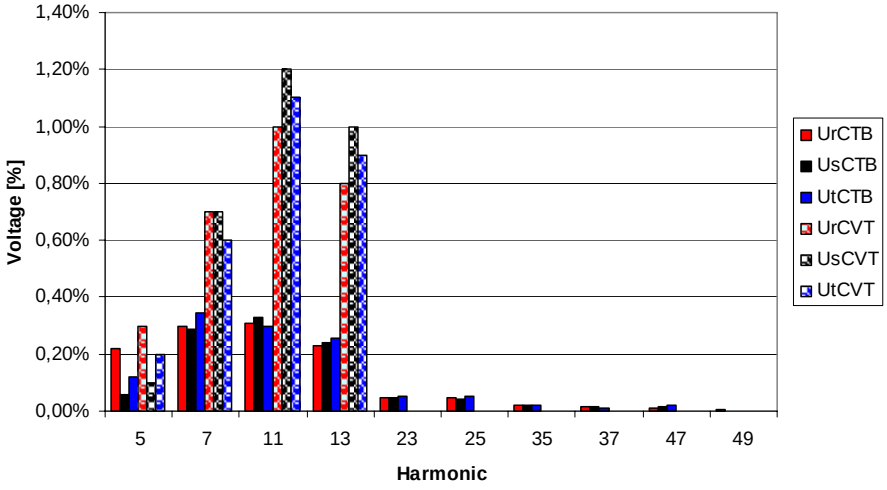

Figure 5.16 Voltage measured at substation **FER** using the voltage drop on a resistor connected to the CTB and to the regular CVT. Higher harmonics measured at CTB are scaled down proportionally to their order.

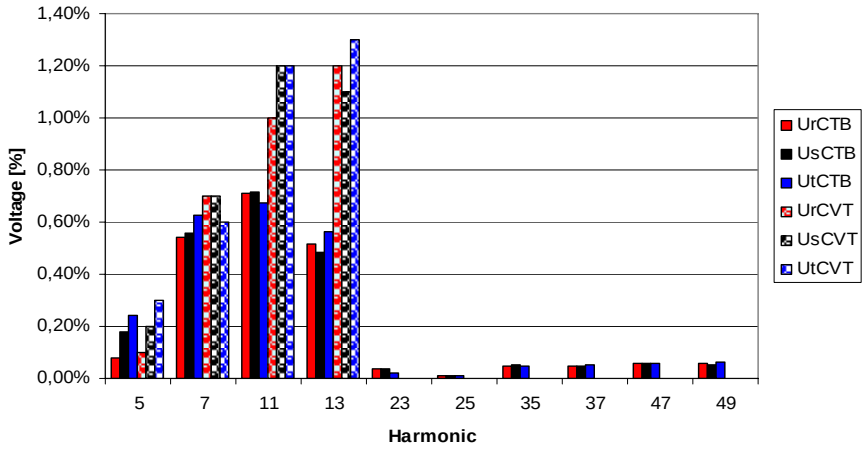

Figure 5.17 Voltage measured at substation **NVV** using the voltage drop on a resistor connected to the CTB and to the regular CVT. Higher harmonics measured at CTB are scaled down proportionally to their order.

It can be seen that harmonic components of orders 5, 7, 11, and 13 have much larger amplitudes if measured using CVT's than CTB's. The reason for that are the resonances between capacitances and inductances of the CVT. The differences are large and reach 800% at 13th harmonic, and are lower at lower order harmonics. At the same time, harmonics of order 23rd and higher, were not measured picked up by the measurement made by CVT, but were measured using the CTB. The reason for that is that first of all, the levels of these harmonics are in general low. The other factor is that the frequency response of CVT is unknown, and may be much lower at higher frequency. The third reason is that when harmonics were measured using CTB as a voltage drop on a resistor then they were amplified proportionally to their order. Values in the figures are already scaled down. It is a clear advantage of using a CTB with a resistor for the measurement, because it increases the effective resolution of the measurement and the signal-to-noise ratio SNR_{ph}.

The ratios of CTB's at fundamental frequency were determined and the results are shown in Table 5.6, Table 5.7 and Table 5.8. Different number of resistors was used in substation TJE phase B than in other phases due to an equipment failure.

Ratio **TJE** Phase A, B, C CVT -->	400kV/0,1kV
Ratio Phase A CVT/CTB (50Hz) -->	59,71V/0,503V = 118,708
Ratio Phase B CVT/CTB (50Hz) -->	59,72V/2,03V = 29,419
Ratio Phase C CVT/CTB (50Hz) -->	59,60V/0,0,502V = 118,725
Ratio Phase A total CTB (50Hz) -->	4000 * 118,708 = **474832**
Ratio Phase B total CTB (50Hz) -->	4000 * 29,419 = **117676**
Ratio Phase C total CTB (50Hz) -->	4000 * 118,725 = **474900**

Table 5.6 Determination of ratio of CTB at fundamental frequency, substation **TJE**.

Ratio **FER** Phase A, B, C CVT -->	400kV/0,1kV
Ratio Phase A CVT/CTB (50Hz) -->	60,14V/0,652V = 92,239
Ratio Phase B CVT/CTB (50Hz) -->	60,02V/0,650V = 92,338
Ratio Phase C CVT/CTB (50Hz) -->	60,04V/0,651V = 92,227
Ratio Phase A total CTB (50Hz) -->	4000 * 92,239 = **368956**
Ratio Phase B total CTB (50Hz) -->	4000 * 92,338 = **369352**
Ratio Phase C total CTB (50Hz) -->	4000 * 92,239 = **368908**

Table 5.7 Determination of ratio of CTB at fundamental frequency, substation **FER**.

Ratio **NVV** Phase A, B, C CVT -->	400kV/0,1kV
Ratio Phase A CVT/CTB (50Hz) -->	59,62V/0,620V = 96,161
Ratio Phase B CVT/CTB (50Hz) -->	59,79V/0,611V = 97,856
Ratio Phase C CVT/CTB (50Hz) -->	59,80V/0,622V = 96,141
Ratio Phase A total CTB (50Hz) -->	4000 * 96,161 = **384644**
Ratio Phase B total CTB (50Hz) -->	4000 * 97,856 = **391424**
Ratio Phase C total CTB (50Hz) -->	4000 * 96,141 = **384564**

Table 5.8 Determination of ratio of CTB at fundamental frequency, substation **NVV**.

5.4.2 Current measurement

At the high voltage substations of Energinet.dk, current is measured through toroidally-wound current transformers with ferromagnetic core (CT). The frequency response of these transformers may be affected by the inter-winding or stray capacitance of the transformer, but in the frequency range up to 2,5 kHz it can be assumed linear [Douglass]. In the frequency range up to 5 kHz, typical current transformers that are used for metering and relaying purposes have accuracies better than 3% [Watson], [Meynaud].

Under normal operating conditions, the primary current of these current transformers is lower than that necessary to saturate the core, therefore they operate at the linear section of magnetisation characteristic [Watson].

There are two types of cores of current transformers: for metering purposes and for protection equipment [IEC 44-1]. Metering cores are suppose to have high precision but for the nominal values of current. Protective cores should transform short-circuit currents more accurately and therefore the knee point of magnetization characteristic is higher but high precision is not so important. If the measured current is relatively small, both cores work in the linear part of characteristic. If the loading is high, metering core will saturate sooner and introduce errors in the harmonic measurement. In such a case using the protective core could give better results [Kojovic].

Analysis of current transformer saturation effects is not an aim of this work therefore it is not discussed here. Some measurements were nevertheless performed. The idea of these measurements was to compare results obtained using protective and metering cores, both with the burden and the burden shorted and to decide which of them should be used for the actual harmonic measurement. This measurement was performed at the TJE substation. One of the 400 kV CT's was used for that purpose. The parameters of the protective core were 2000/1A; 30VA; 5P; n=100; and of the metering core were 1000/1A; 30VA; 0,2; n=5. A low-inductive resistance connected in series with the secondary circuits was used and the voltage drop on it was measured, as shown in Figure 5.18 and Figure 5.19.

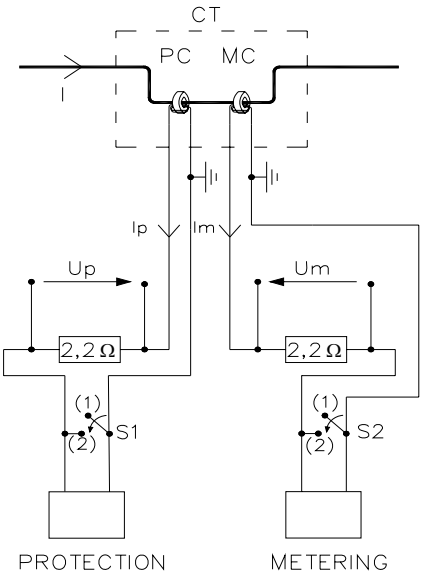

CT – current transformer
PC – protective core
MC – metering core
S1,S2 – switches
I – Primary current
Ip – current in protective circuit
Im – current in metering circuit
(1) – connected burden
(2) – burden shorted

Figure 5.18 Measuring arrangement for comparison of protective and metering cores.

Figure 5.19 The values were measured as a voltage drop on low-inductance resistors, using the Omicron CMC256 unit and B&K 24bit data acquisition unit.

Four measurements were performed, each time using both of the cores:

- Metering core loaded vs. Protective core loaded, see Figure 5.20
- Metering core loaded vs. Protective core shorted, see Figure 5.21
- Metering core shorted vs. Protective core shorted, see Figure 5.22
- Metering core shorted vs. Protective core loaded, see Figure 5.23

These plots show the amplitudes and phase angles of the harmonic current. The values are expressed in per unit of the fundamental frequency component. Harmonics Up to 39th were measured. The Y axis of the magnitude plots is in logarithmic scale. The harmonic levels are pretty low. The highest value is the 7th harmonic - 3,4% of the fundamental. then 11th - 2,1%; 13th - 1,6%; 5th - 1,1% and 3rd - 0,5%. The rms current value was approximately 225A. Metering core had the ratio 1000/1 A/A - so it was loaded in 22,5 % and protective core had the

ratio 2000/1 A/A - loaded in 11%. The measurements didn't show any particular difference between the magnitudes and phase angles measured in different way. The differences observable in the figures are for very low (uncharacteristic) harmonic values, visible only because of the logarithmic scale. The largest difference in magnitude which was observed was 0,01%, and the highest phase angle difference was 5 deg, except the phase angle of the 21st harmonics on Figure 5.21, where this difference is large. This is an error which has its origin in the fact that the magnitude of this harmonic at that moment was very low, below 0,001% of the fundamental.

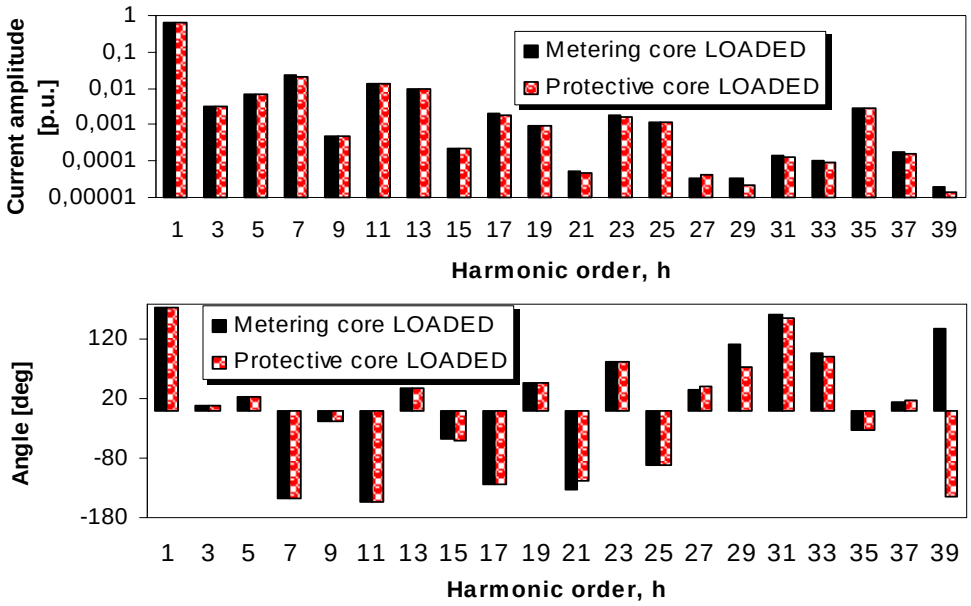

Figure 5.20 Amplitude and phase angle of harmonic currents measured on metering core loaded and protective core loaded.

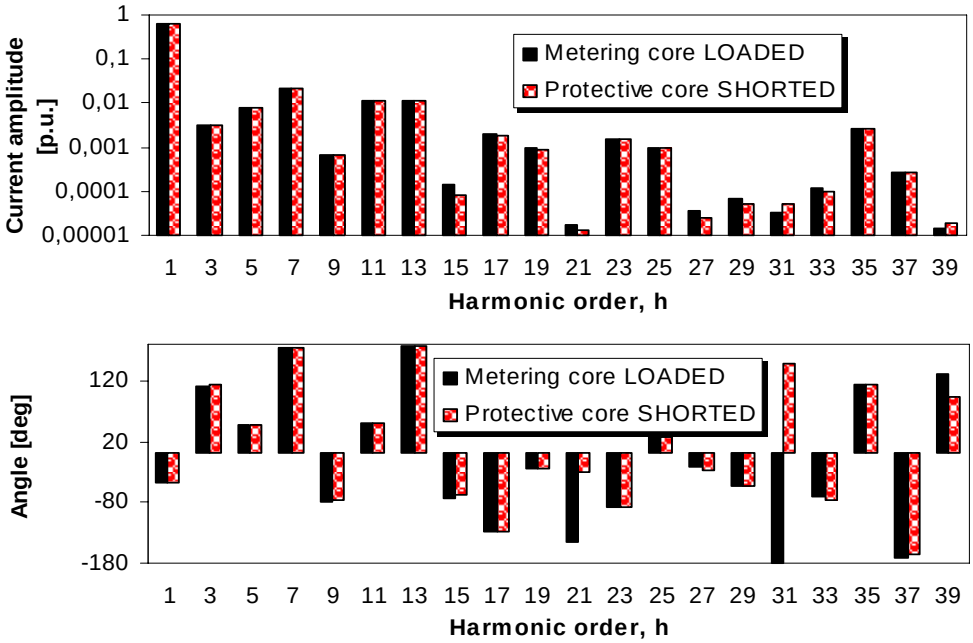

Figure 5.21 Amplitude and phase angle of harmonic currents measured on metering core loaded and protective core shorted.

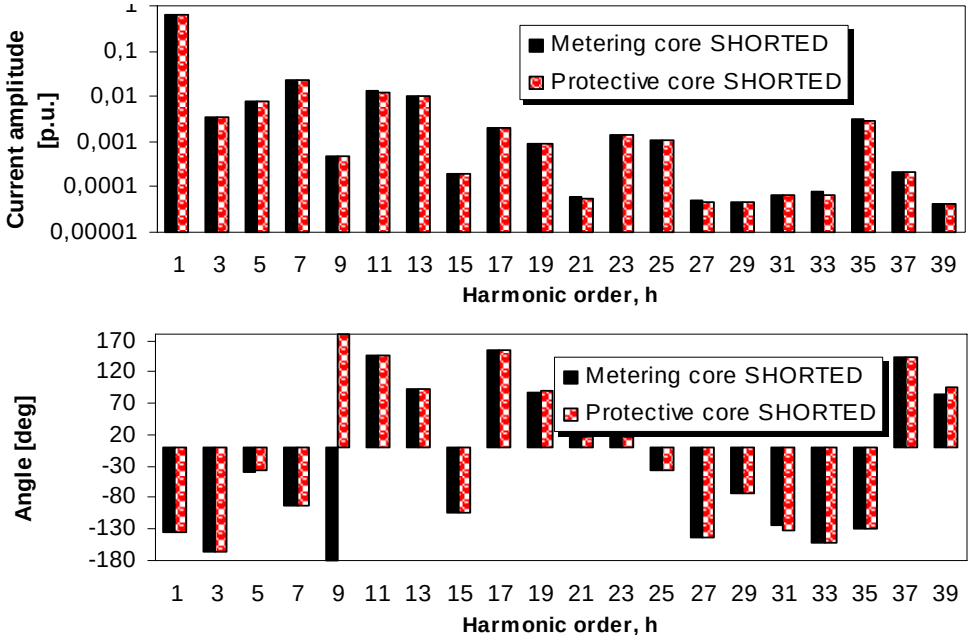

Figure 5.22 Amplitude and phase angle of harmonic currents measured on metering core shorted and protective core shorted.

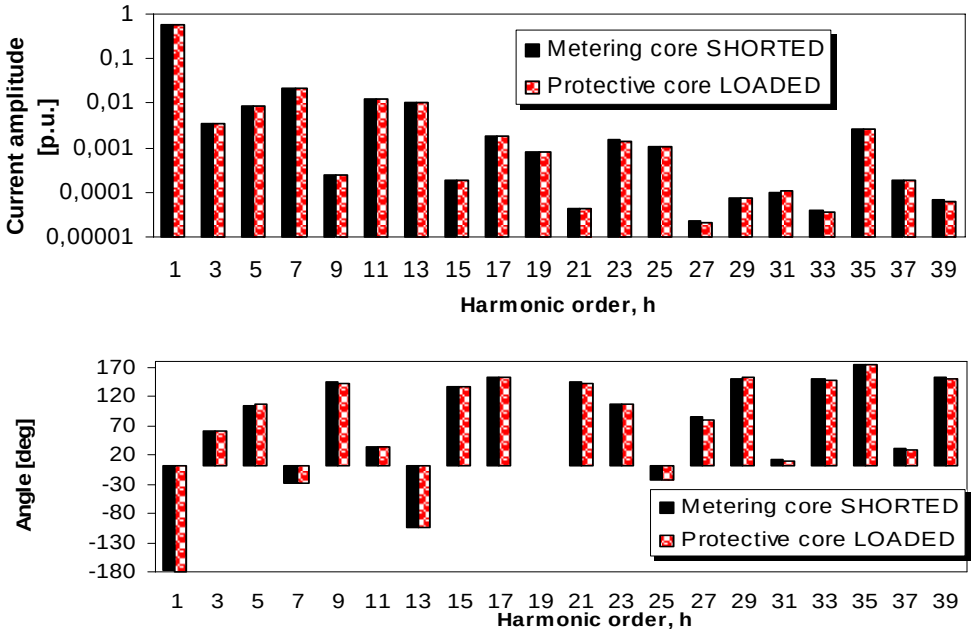

Figure 5.23 Amplitude and phase angle of harmonic currents measured on metering core shorted and protective core shorted.

There is practically no difference in the magnitudes and also only small differences in phase angles for all significant harmonic. Therefore, it may be stated that if the loading of a CT is low, then both protective and measuring cores may be used for harmonic measurements. Also the effect of burden was not really observable.

During the main measurement, harmonic distortion of currents was measured in a setup as shown in Figure 5.24, where the actual current that flows into the power line was measured with two current transformers located between the line and the busbars.

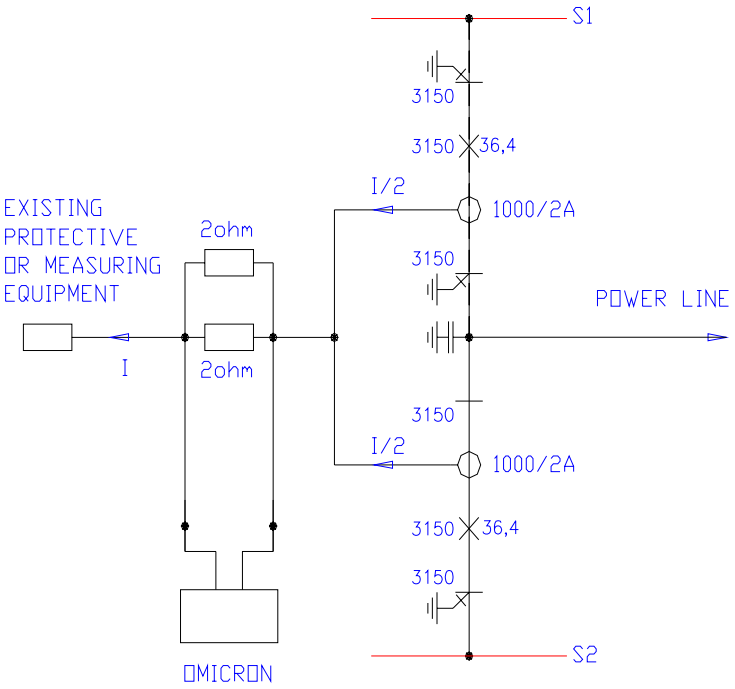

Figure 5.24 Measurement of current harmonics during the main measurement.

5.4.3 Wiring

In harmonic measurements, special attention must be given to the cables led from current and voltage transducers. These cables are the longest parts of such a harmonic measuring system, and so they act as antennas, picking up noise and lowering the signal-to-noise ratio SNR_{ph}.

These issues are described by [Ott], and the fundamental theory can be found in [Inan]. Harmonic measurements at high voltage levels are difficult with respect to induced noise because cable systems are led for distances of hundreds of meters and the picked up noise may reach high levels. Therefore some actions must be taken to lower this level of noise, for instance:

- Leading the cables in the way to maximize distance from the high voltage circuits
- Shielding the cables
- Proper grounding of the cables

The radiated noise is coupled to the cables by electromagnetic coupling. If the analysis is made for the near field (which means that the distance from the source of the fields is smaller then the wavelength of the noise divided by 2π) then electric and magnetic fields can be decoupled and analyzed separately [Ott]. Electromagnetic fields are described by Maxwell equations, but the analysis can be simplified using electric circuit theory and therefore capacitive coupling can be represented as an equivalent current source, and magnetic coupling can be represented as an equivalent voltage source, see Figure 5.25.

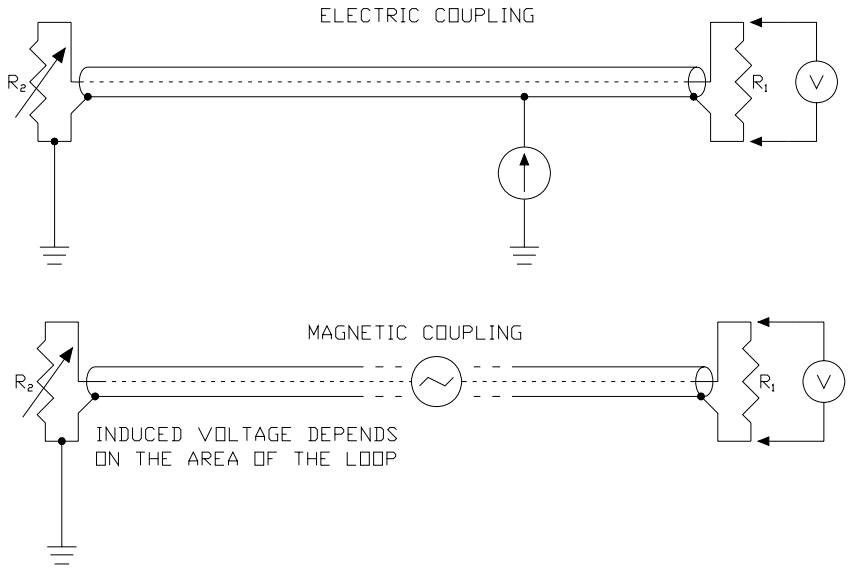

Figure 5.25 Electric and magnetic coupling represented as current and voltage sources.

It is known that the noise induced in a circuit through magnetic coupling is proportional to the area enclosed by this circuit. Therefore to minimize magnetic coupling, the distance between wires of this loop must be smallest possible. In practical terms, the existing cables used for that purpose can be coaxial cables, where shield of the cable is used as the return path for the signal, or twisted pair cables where twisting causes the induced noise to cancel out. Also grounding of the cables is important, because if a measuring circuit is grounded at more then one point, than part of the signal will return through the ground plane, and the effective area of such a circuit will be larger then if it was grounded at one point only.

Capacitive coupling can be reduced by shielding of the measuring circuit. The shield must be grounded, so the injected noise has a return path. If the shield is not grounded then its potential will rise and in turn the noise will be injected to the measuring circuit.

Based on such considerations proper wiring system was chosen for the harmonic measurements performed in this project. This decision was verified by measurements. For that purpose cables were laid in the high voltage switchyard of the substation Tjele, in various configurations. Several cable arrangements and grounding techniques were inspected and the results are shown in this section. However, it must be emphasized that issues related to coupling mechanisms and grounding techniques are complex and detailed analysis of such phenomena is not a subject of this work.

The cables used for the measurements were close to 200 meter long sections of coaxial cables RG-58. The cables were lead through the switchyard, in the same way as they were laid during main measurements. Different cable configurations are shown in Figure 5.26 - Figure 5.30. Figure 5.26 shows Configuration A where both shield and signal wire were not connected, and the shield was grounded at the measuring location. In this way in fact noise induced in the signal wire was measured. This noise was mainly an effect of magnetic coupling since the shield is grounded and shields against capacitive coupling. It can be seen that the amplitude of this noise reaches 0,4 V. The 50 Hz component is the dominant one, but strong influence of higher frequencies is also visible.

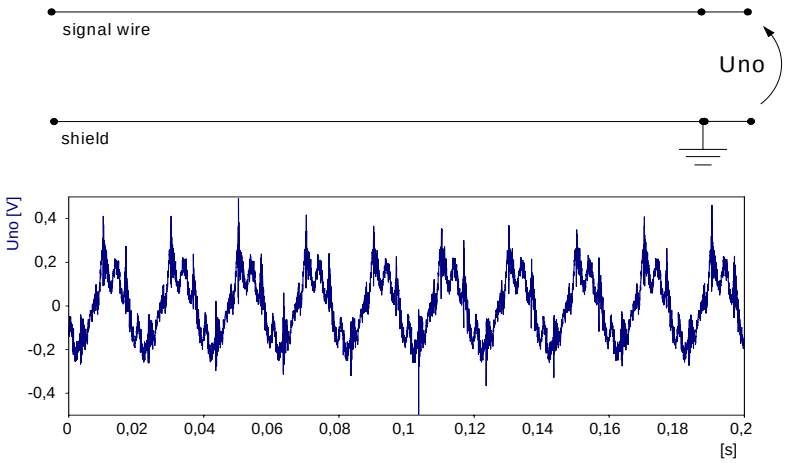

Figure 5.26 Noise Uno induced in a coaxial cable. Configuration A.

Figure 5.27 shows Configuration B, where the shield is grounded at the far end of the cable and the voltage drop on a 2 ohm resistor is measured. In this case magnetically induced noise will have the same polarity in both signal wire and the shield, and therefore it will to a large extent be cancelled out from the measured voltage Uno. It can be seen that the amplitude of this induced noise Uno is around $2 \cdot 10^{-3} V$, which is about 200 times smaller than in Configuration A. The 50 Hz component is relatively low; higher frequency components are dominating. Capacitivly coupled current in the shield will flow to ground, therefore it will not flow through the 2-ohm resistor and cause errors. The way it could affect the measurement is that while flowing to ground it will produce a small voltage drop on the shield resistance, therefore raising the potential at the end of the cable, where measurement is made.

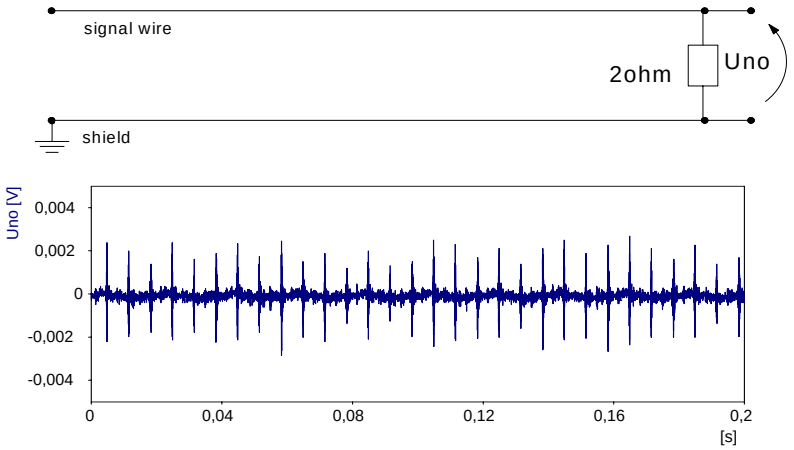

Figure 5.27 Noise Uno induced in a coaxial cable. Configuration B.

Figure 5.28 shows Configuration C, which is different than Configuration B, because the signal wire is connected to the shield at the far end of the cable. It can be seen that the magnitude of the induced voltage is 0,1 V. This is much higher than in Configuration B, though still lower than in Configuration A. This can be explained by the fact that the loop is closed and induced magnetically voltage (since there is still some area of the loop) will cause current to flow through the resistor. Comparing Configuration B and C it can be noticed that if the equivalent impedance of the circuit where the voltage is measured is high then the behaviour of induced noise will more resemble the noise in Configuration B.

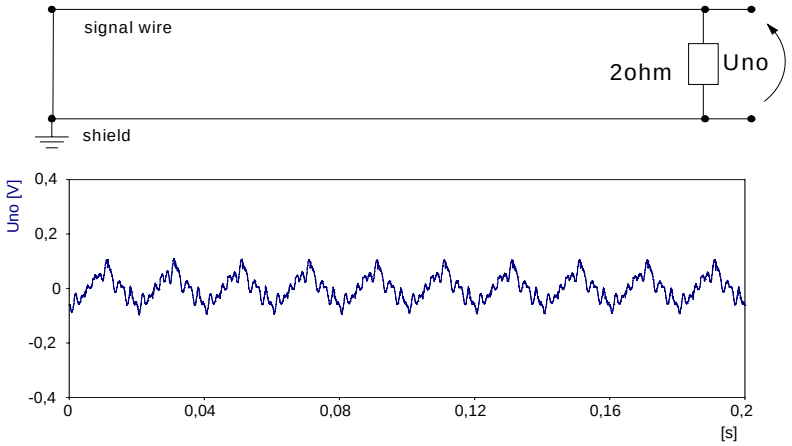

Figure 5.28 Noise Uno induced in a coaxial cable. Configuration C.

In Figure 5.29 and Figure 5.30 the shield and signal wire are shorted through a 2 and 4-ohm resistors. It can be seen that the noise level is the same like in Configuration C, about 0,1 V.

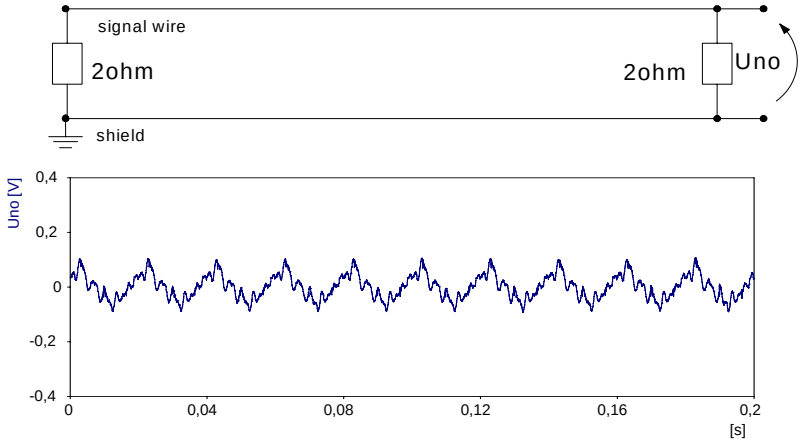

Figure 5.29 Noise Uno induced in a coaxial cable. Configuration D.

This suggests that if the equivalent impedance of the circuit where the measurement is made is low, then to learn how large will be the noise level, Configuration C must be used. In the case if this impedance is high, configuration B is the proper one. Generally it can be concluded that the best case with respect to the level of induced noise is Configuration B. To take the full advantage

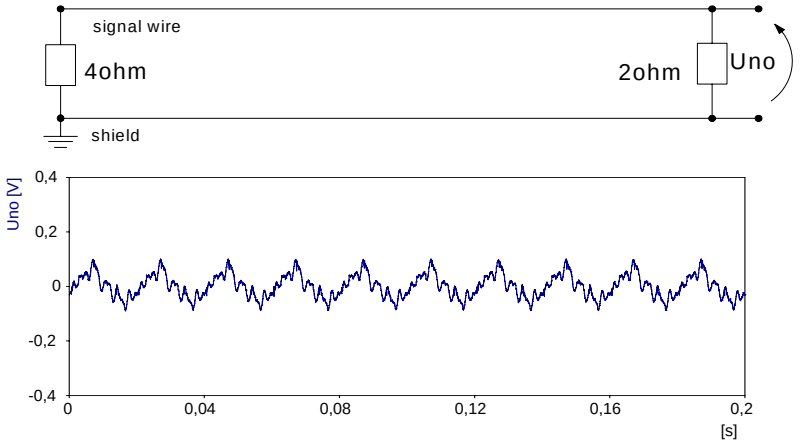

Figure 5.30 Noise Uno induced in a coaxial cable. Configuration E.

of it, we should have an idea about the equivalent impedance of the circuit where a measurement is done. In this project, capacitive taps in the bushings of transformers have the impedance of mega ohms, therefore Configuration B was chosen to be used in the measurement, and it also gives the best idea on the level of noise during the actual measurement. This level is very small, especially comparing to other topologies.

Transfer function of coaxial cables

Cables used for harmonic measurements can affect the accuracy of a measurement in two ways, first by the level of noise it is picking up, and second, by having a not flat transfer function. However, [Meliopoulos] has shown that the transfer function of coaxial cable sections of less than 200 meters is flat at frequencies of interest and therefore no error correction is necessary.

5.4.4 Equipment used for measurements [Omicron], [Brüel&Kjær].

During the main measurement, except that the instruments were installed at three substations, at the TJE substation a additional piece of equipment was installed, the Brüel & Kjær Pulse 3560B acquisition unit, which has higher sampling frequency, 65kHz and higher dynamic range of 24 bits. The reason of using it was just to confirm the values obtained from measurement performed using the Omicron CMC256 is a PC unit. The Brüel & Kjær Pulse 3560B acquisition unit was also triggered by the GPS unit.

Omicron CMC256 is a PC controlled unit designed for testing protective relays, which if used with the software test module *EnerLyzer,* can capture time domain voltages. In the Transient Analyzer mode, up to 10 channels can be synchronously recorded. The recording will start whenever triggered by external GPS unit. One measuring channel must be used as a binary input, dedicated for sensing the triggering signal. The maximum length of the recording depends on the number of channels and sampling rate used for measurements, and in this case was 3.52 s recording using all 10 channels, with the sampling rate 28.44 kHz.

The measuring equipment Omicron CMC256 can be external triggered by a signal from a GPS that permits triggering at exactly specified point in time. This feature allows performing synchronized measurements (recordings) using several CMC's 256.

In order to ensure the exact time stamp for each of three locations, these GPS receivers will be used. The GPS receiver itself is very accurate, i.e. the synchronization error can be as low as 1 μs, depending on the selected precision (number of satellites used). Available in the Omicron measuring option allows for triggering by external signal and one of the input channels of each of the measuring units is used for detecting the triggering impulse sent repeatedly from GPS units. Therefore, the overall accuracy is limited by the sampling rate of the Omicron unit of 28,44 kHz. For that reason, the overall maximal synchronization error can be approx. 35 μs.

Three Omicron CMC256 units, located at each substation were controlled remotely from the TJE station. Each unit was connected to a PC, with the Enerlyzer software installed. Each of the PC's was connected to the internet, and one computer, physically located at the TJE5 substation was used to control all of the units. The software used for controlling the remote control was the standard Microsoft Remote Desktop Connection.

For verifying the measurements performed with the Omicron units, an additional measuring instrument was used. The instrument used was the Brüel & Kjær Pulse 3560B acquisition unit, used for sound and vibration measurements. This instrument was installed at the TJE substation. Both instruments are shown in Figure 5.31.

Figure 5.31 Omicron CMC256 with CMGPS unit and Brüel & Kjær Pulse 3560B [Omicron], [Brüel&Kjær].

Both instruments were installed at the TJE substation, see Figure 5.32.

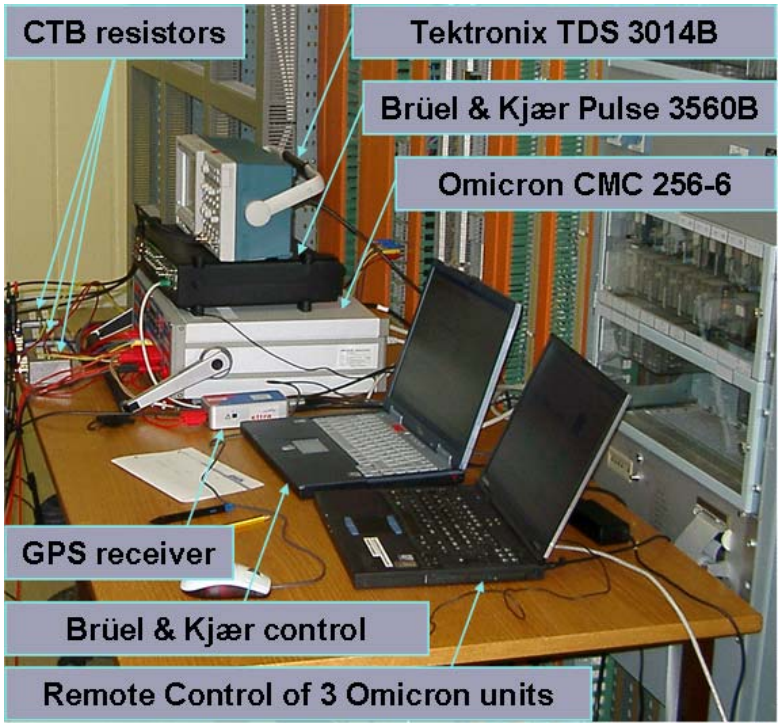

Figure 5.32 Measuring setup at TJE substation.

Technical specifications:

Omicron CMC 256-6 with the EnerLyzer option.

No of channels:	10 (9 + 1 for GPS triggering)
Theoretical dynamic range:	approx. 72 dB (12 bits)
Sampling freq:	28,44 kHz
Nominal input ranges:	100 mV, 1 V, 10 V, 100 V, 600 V (rms)
Bandwidth:	dc ... 10 kHz
Transient input buffer:	3.5s for all ten input channels at 28 kHz

GPS basic data.

Overall accuracy:	35 µs
Time till ready for operation:	typ. 5 min
Pulse polarity:	positive or negative
Pulse rate:	1 … 65535 s (in steps of 1 s)

Pulse width: 200 ms

Brüel & Kjær Pulse 3560B acquisition unit.

No of channels: 11 (10 + 1 for GPS triggering)

Theoretical dynamic range: approx. 144 dB (24 bits)

Sampling freq: 65 kHz

Nominal input ranges: 8 ranges, up to 12 V_{p-p}

Bandwidth: dc ... 26 kHz

Transient input buffer: No, direct streaming to the PC

5.5 Main measurement

The following values were measured during the measurement:

NVV substation
- 3-phase voltage
- 3 phase current in line FER-NVV
- 3 phase current in line NVV-VHA

FER substation
- 3-phase voltage
- 3 phase current in line FER-NVV
- 3 phase current in line FER-NVVX

TJE substation
- 3-phase voltage
- 3 phase current in line TJE-FER

These locations are shown in Figure 5.33. Power line FER5-NVV5-0 was disconnected and reconnected at one end, at the NVV5 substation, as shown in Table 5.9 and Figure 5.34. This operation was repeated 3 times in row, in order to verify if background harmonic distortion is stable, and to reduce possibility of errors. All the above mentioned quantities were measured during this time. 300 ms time domain snapshots were taken with the time gap of 30 seconds. The whole operation lasted for 45 minutes and during this period 90 snapshots of three-phase quantities, at three substations were captured synchronously. In total 24 quantities were captured. Then the results were processed in Matlab in order to obtain harmonic spectrum, and to extract the variation of each harmonic throughout the measurement. The signals were resampled with the frequency of 51.2 kHz, to obtain the 1024-point FTT.

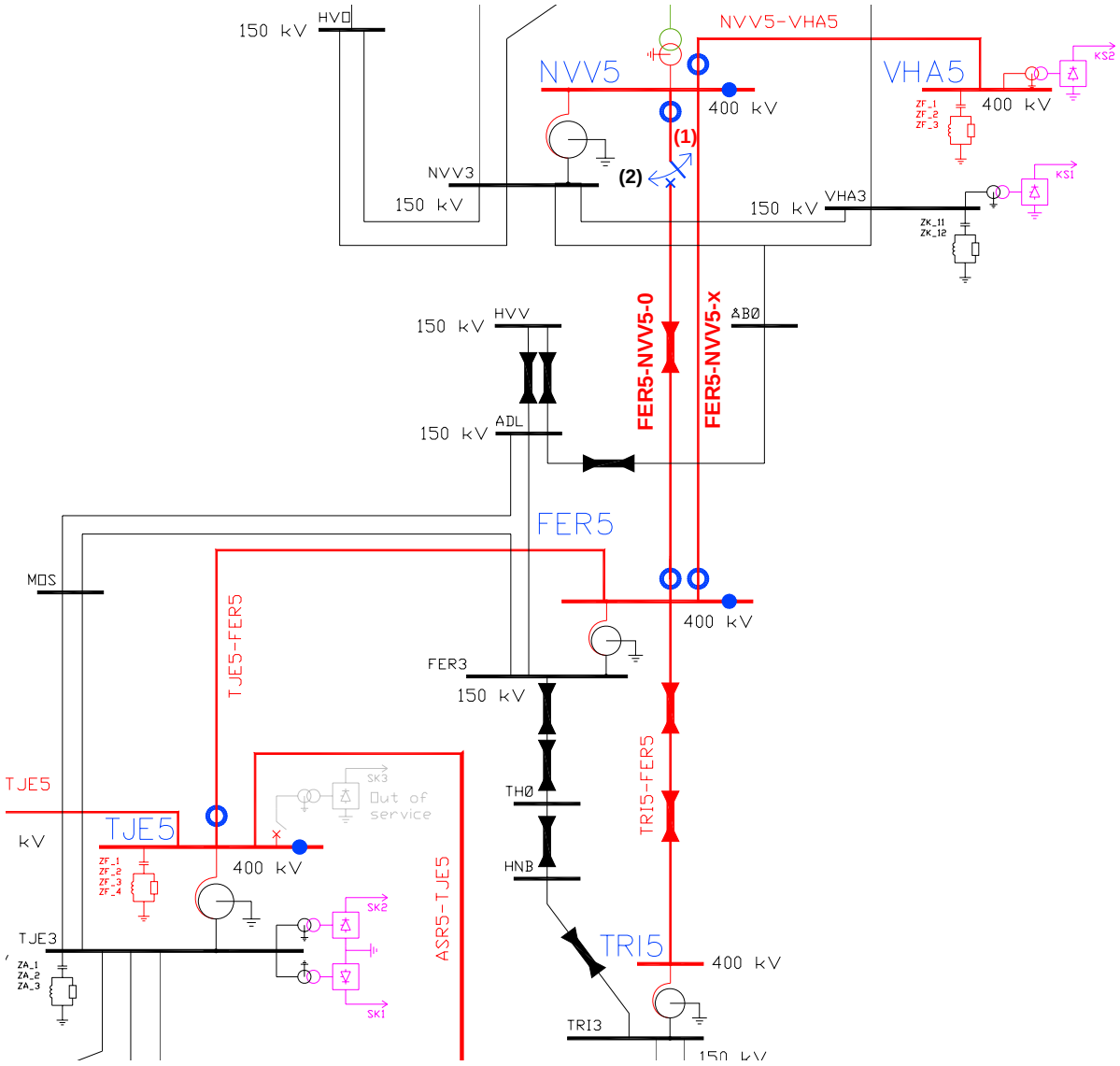

Figure 5.33 Location of the measuring points at substations NVV5, FER5 and TJE5. Power line FER5-NVV5-0 is disconnected at NVV5 substation.

The disconnection (1) / reconnection (2) times:		
2005-07-01_10:20:58.58	(1)	- first disconnection
2005-07-01_10:26:56.60	(2)	
2005-07-01_10:33:12.59	(1)	
2005-07-01_10:40:26.71	(2)	
2005-07-01_10:47:15.73	(1)	
2005-07-01_10:53:07.93	(2)	- final reconnection

Table 5.9 The disconnection / reconnection times of power line FER5-NVV5-0.

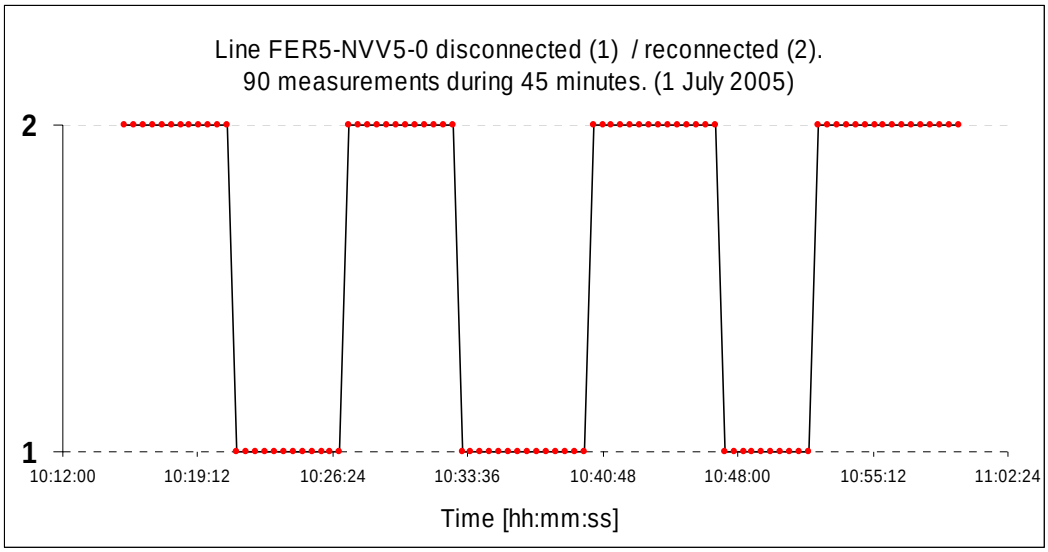

Figure 5.34 Disconnection sequence of the line FER5-NVV5-0.

During this measurement SCADA readings where performed. They are presented in Table 5.10. Readings at the times 10:25, 10:35, 10:40, 10:50 show values captured while the line FER5-NVV5-0 was disconnected. It can be seen that the line has been disconnected at the end connected to NVV substation. At FER substation the line was permanently connected, and this can be seen because still a current of 35A was flowing into the line, as a result of the shunt admittance of this line.

Time	Measured in FER						Measured in NVV					Measured in TJE	
	Current to NVV	Voltage measured at line NVV	Current to NVVX	Voltage measured at line NVVX	Current to TJE	Voltage measured at line TJE	Current to FER	Voltage measured at line FER	Current to FERX	Voltage measured at line FERX	Current to VHA	Current to FER	Voltage measured at line FER
	[A]	[kV]	[A]	[kV]	[A]	[kV]	[A]	[kV]	[A]	[kV]	[A]	[A]	[kV]
01-07-2005 09:50	**445**	413,2	**180**	412,5	326	413	**504**	413,7	**342**	413,8	**504**	**313**	413,2
01-07-2005 09:55	**445**	413,2	**180**	412,5	324	413	**504**	413,7	**341**	413,9	**500**	**315**	413,3
01-07-2005 10:00	**445**	413,3	**181**	412,7	324	413	**504**	413,7	**342**	413,9	**509**	**315**	413,4
01-07-2005 10:05	**440**	416,1	**178**	415,5	344	415,8	**506**	416,2	**340**	416,6	**497**	**326**	419
01-07-2005 10:10	**441**	413,3	**180**	412,7	324	413	**502**	413,9	**340**	414	**513**	**315**	413,3
01-07-2005 10:15	**444**	415,1	**181**	414,3	335	413,5	**509**	415,6	**343**	415,7	**448**	**320**	416,4
01-07-2005 10:20	**446**	415	**181**	414,3	335	415	**512**	415,5	**347**	415,6	**500**	**320**	416,4
01-07-2005 10:25	**35**	415	**439**	414,3	326	414,6	**2**	416,4	**826**	414,8	**460**	**310**	416,4
01-07-2005 10:30	**446**	415,1	**183**	414,5	336	414,6	**512**	415,3	**345**	415,5	**501**	**322**	416,4
01-07-2005 10:35	**35**	415,1	**438**	414,3	336	414,8	**2**	416,4	**828**	414,9	**466**	**315**	416,5
01-07-2005 10:40	**33**	415	**441**	414,3	329	414,8	**2**	416,4	**831**	414,9	**461**	**315**	416,4
01-07-2005 10:45	**454**	415	**184**	414,2	340	414,8	**519**	415,4	**349**	415,5	**509**	**328**	416,2
01-07-2005 10:50	**33**	415	**443**	414,3	340	414,8	**2**	416,3	**837**	414,8	**460**	**317**	416,1
01-07-2005 10:55	**456**	413,7	**185**	413	343	413,3	**518**	413,4	**351**	413,9	**503**	**326**	413,9
01-07-2005 11:00	**456**	413,8	**185**	413	336	413,8	**518**	414,4	**351**	414,2	**499**	**322**	414
01-07-2005 11:05	**456**	413,5	**185**	413	333	413,7	**516**	414	**350**	414,4	**504**	**324**	413,9
01-07-2005 11:10	**456**	413,7	**184**	413,2	335	413,7	**517**	414,3	**351**	414,4	**509**	**328**	413,9
01-07-2005 11:15	**456**	413,8	**184**	413	335	413,7	**517**	414,3	**350**	414,4	**502**	**328**	414
01-07-2005 11:20	**456**	413,8	**184**	413,2	335	413,7	**517**	414,3	**350**	414,2	**504**	**324**	413,9

Table 5.10 Results of SCADA measurements. Measurements with the line FER5-NVV5-0 disconnected were made at the times: 10:25, 10:35, 10:40 and 10:50.

Results of measurements

Signal analysis was made for harmonics up to 49th, for voltages and currents. Values of voltage harmonics are in percent of the fundamental frequency component and current harmonics are in amperes. The whole results of measurement are too extensive to be presented in this report but can be found on the compact disc attached to the report. Only the most interesting results are shown, namely the voltages at three substations NVV5, FER5, TJE5 and currents flowing in and out of the disconnected line FER5-NVV5-0, and only for harmonics which have shown the most interesting results: 5th, 13th, 23rd and 47th. All harmonic frequencies behaved differently during the whole measurement when the line was switched but these selected harmonics represent the extreme cases, good for illustration. The overall harmonic voltage distortion measured at each substation before and after the line disconnection is shown in Figure 5.37, Figure 5.36 and Figure 5.35. It can be seen that the harmonic distortion is relatively low at all substations. The lowest level of harmonic distortion is at substation TJE5, due to the fact that there are the harmonic filters installed. Since the filters are designed to filter out harmonic distortion of a converter in 12-pulse configuration, the level of 11th, 13th, 23rd and 25th harmonic is below 0.1%. The levels of 5th and 7th harmonic are higher, around 0.2%. 5th and 7th harmonic come from lower voltage levels and are not filtered. What should be also noticed is the relatively high content of 3rd harmonic, at the level of 0.3%. Content of 3rd harmonic is similar in phases A and C and is higher in phase B. The content of 3rd harmonic is almost the same at all three substations and does not change much when the line FER5-NVV5-0 is disconnected. Levels of 47th and 49th harmonic are in general low but the disconnection of line FER5-NVV5-0 affects their level relatively much. In substation FER content of 11th and 13th harmonics is higher, around 0.6%. Content of 23rd and 25th harmonics is also slightly higher, but it lowers when the line FER5-NVV5-0 is disconnected.

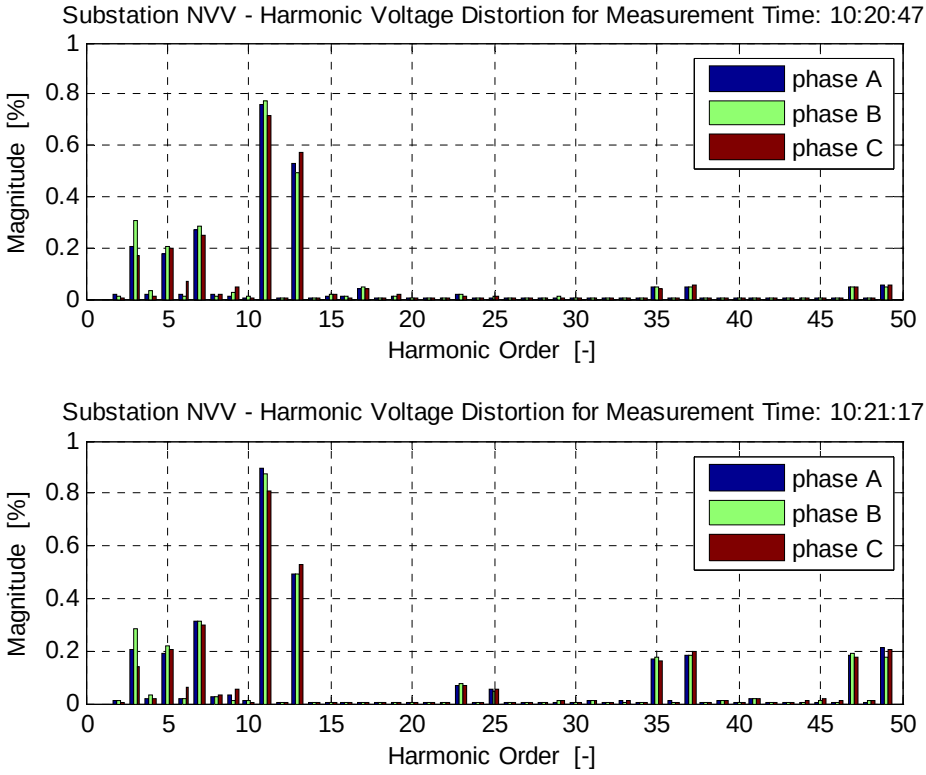

Figure 5.35 Harmonic distortion of the bus voltage at substation NVV5. Upper plot – with line FER5-NVV5-0, connected, lower plot – line FER5-NVV5-0 disconnected.

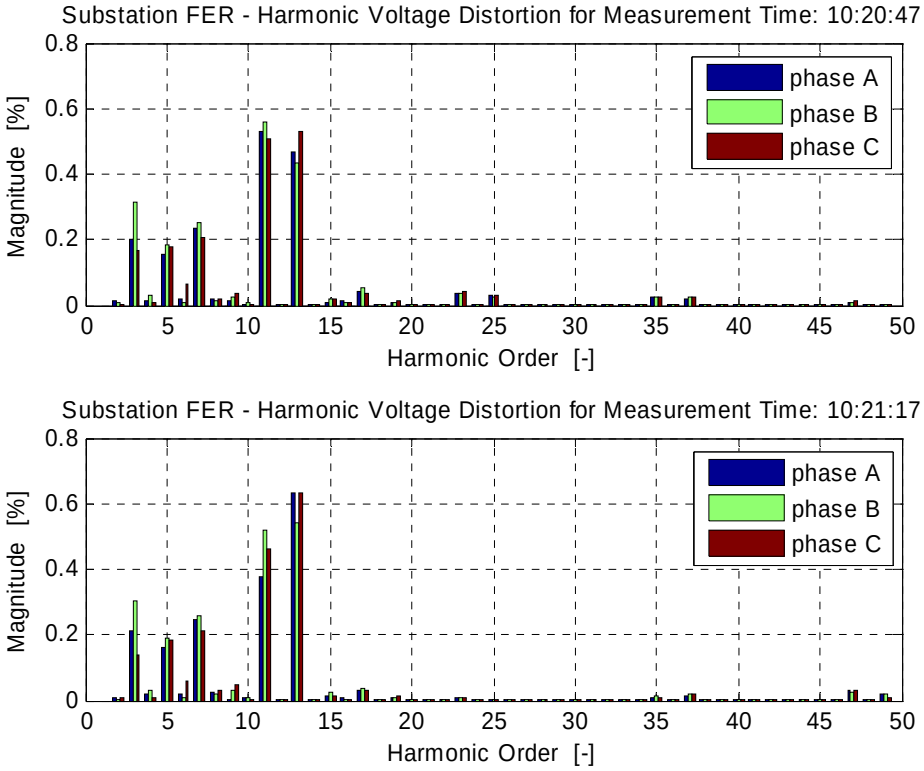

Figure 5.36 Harmonic distortion of the bus voltage at substation FER5. Upper plot – with line FER5-NVV5-0, connected, lower plot – line FER5-NVV5-0 disconnected.

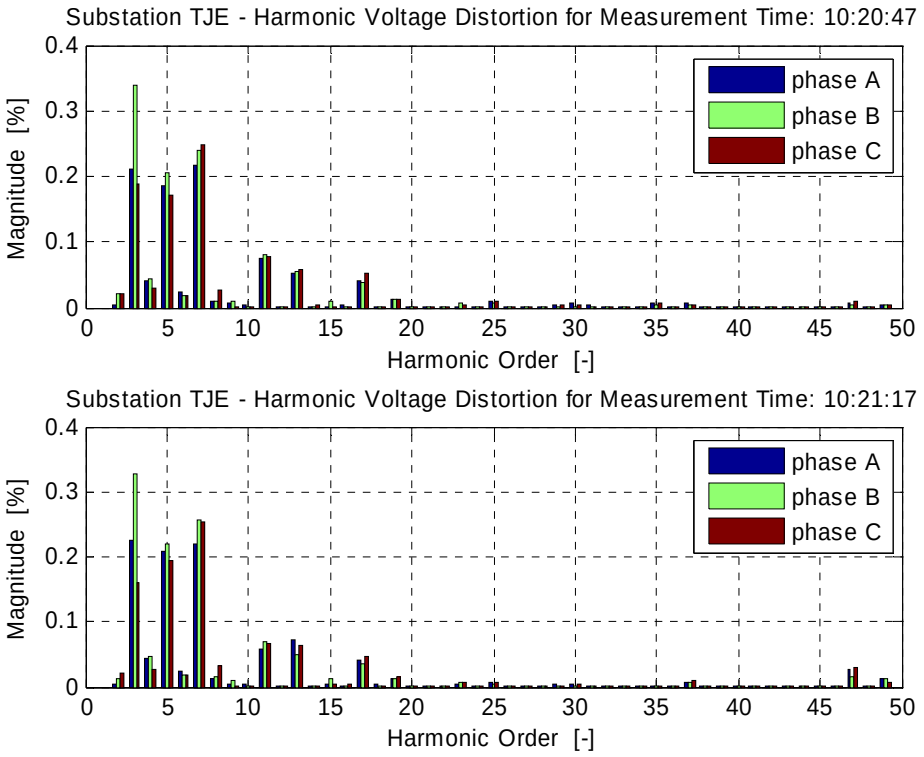

Figure 5.37 Harmonic distortion of the bus voltage at substation TJE5. Upper plot – with line FER5-NVV5-0, connected, lower plot – line FER5-NVV5-0 disconnected.

In substation NVV5, the content of 11^{th} and 13^{th} harmonics is even higher and reaches 0.8% and 0.6% respectively and also content of 47^{th} and 49^{th} is relatively high, and it rises when line FER5-NVV5-0 is disconnected, up to 0.2%. What is worth noticing is that the content of 23^{rd} and 25^{th} harmonic rises when the line FER5-NVV5-0 is disconnected, in contradiction to their content in the voltage at the other two substations. This will be commented later in this section when the behaviour of particular harmonics will be analyzed. In general it can be seen that the level of harmonic components below 500Hz is similar in all three substations and does not change much when the line FER5-NVV5-0 is disconnected. This suggests that the source of these frequencies can be found on both sides of the line FER5-NVV5-0 (comes from lower voltage levels) or that the impedance of the disconnected line is high at this frequency.

Figure 5.38 shows magnitude of 5^{th} harmonic component flowing in the disconnected line FER5-NVV5-0. The line was disconnected only at one end, at substation NVV5. The line remained connected at the FER5 substation and therefore current amplitude is not zero but is a result of shunt admittance of the line. It can be seen that the magnitude of this current is low, in the order of magnitude of 2 – 3.5A. The level of 5^{th} harmonic in bus voltages is shown in Figure 5.39. At all three substations it is around 0.2%. It can be seen that the variation of 5^{th} harmonic current injected from the line FER5-NVV5-0 does not have effect on the bus voltages. No correlation can be noticed. At the end of the measuring period, around 10:50:00, a change of the levels of harmonic distortion can be noticed in most of the plots. The reason of that may be due to switching in the network. It was requested to have no switching during the measuring period, until 10:50:00.

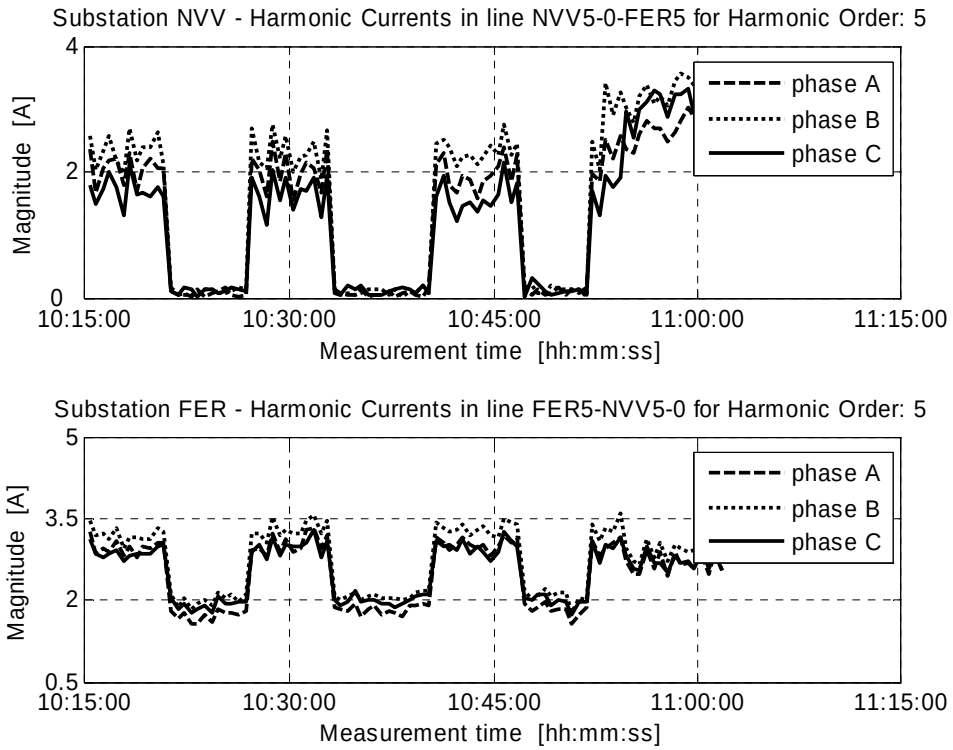

Figure 5.38 5th harmonic current flowing in the line FER5-NVV5-0. Upper plot shows the measurement at the NVV5 substation and lower plot shows the measurement at FER5 substation.

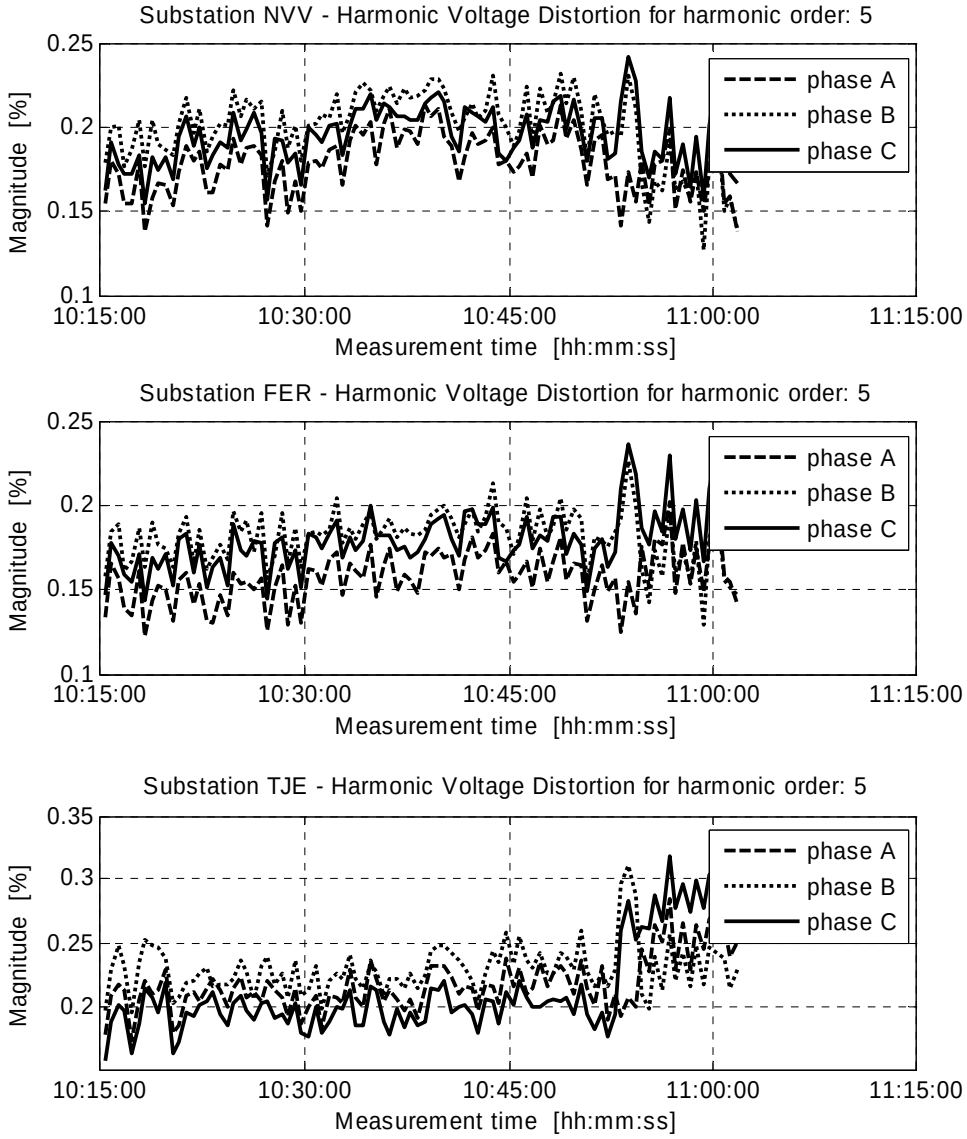

Figure 5.39 Variation of 5th harmonic in the bus voltage. Upper plot shows the measurement at the NVV5 substation, middle plot at FER5 substation and lower plot at TJE5 substation.

Figure 5.40 shows the 13th harmonic current in the disconnected line. It is interesting to see that the at FER5 substation harmonic current has an amplitude of 10 A when line is connected and 20 A amplitude when flows into the line open-ended. At the end connected to NVV5 substation, level of 13th harmonic current is 3-4 A when line is connected. The effect on voltages is shown in Figure 5.41. The effect on the voltage at TJE5 is low, due to the fact that harmonic filters are installed there. The amplitude of 13th harmonic is below 0.1%. The effect on voltages at substations FER5 and NVV5 is more pronounced. At substation FER5 13th harmonic voltage is not symmetrical in all three phases but it rises from 0.4-0.5% up to 0.5-0.6% after the line is disconnected, and at NVV5 substation the effect is opposite, magnitude lowers from 0.53-0.57% down to 0.5-0.53%.

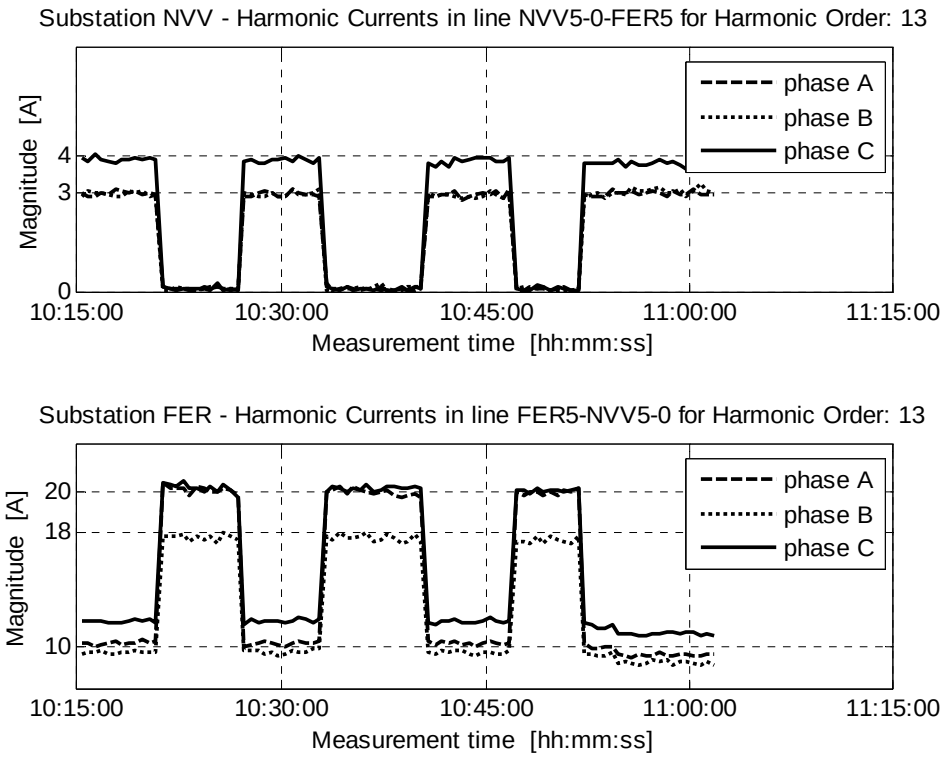

Figure 5.40 13th harmonic current flowing in the line FER5-NVV5-0. Upper plot shows the measurement at the NVV5 substation and lower plot shows the measurement at FER5 substation.

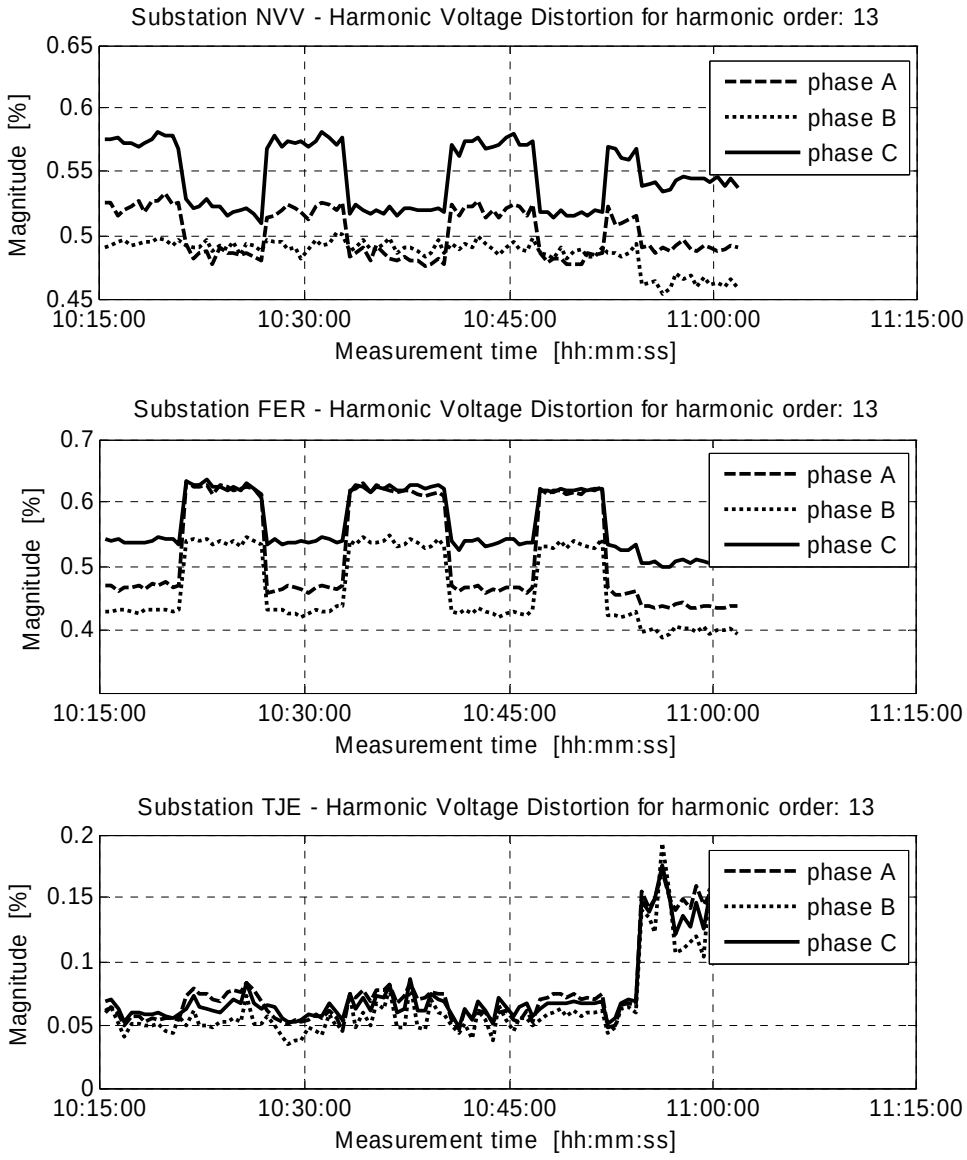

Figure 5.41 Variation of 13th harmonic in the bus voltage. Upper plot shows the measurement at the NVV5 substation, middle plot at FER5 substation and lower plot at TJE5 substation.

Figure 5.42 shows the variation of 23rd harmonic current in the disconnected line. Similarly like in the case of 13th harmonic, its magnitude rises, at the FER5 substation when the line is disconnected, but the level is much smaller. The change is approximately from 0.7A up to 1.3A. At substation NVV5 the effect is of course opposite and the magnitude lowers from 1.5A down to zero. The level of 23rd harmonic voltage at all three substations is shown in next Figure 5.43. Again at TJE5 substation due to harmonic filters the level of 23rd harmonic is very low, below 0.01% and does not depend on switching of the line FER5-NVV5-0. At FER5 substation 23rd harmonic lowers from 0.04% down to 0.01% after line disconnection, and at NVV5 substation the effect is opposite: level of 23rd harmonic rises after line disconnection from 0.02% up to 0.07%.

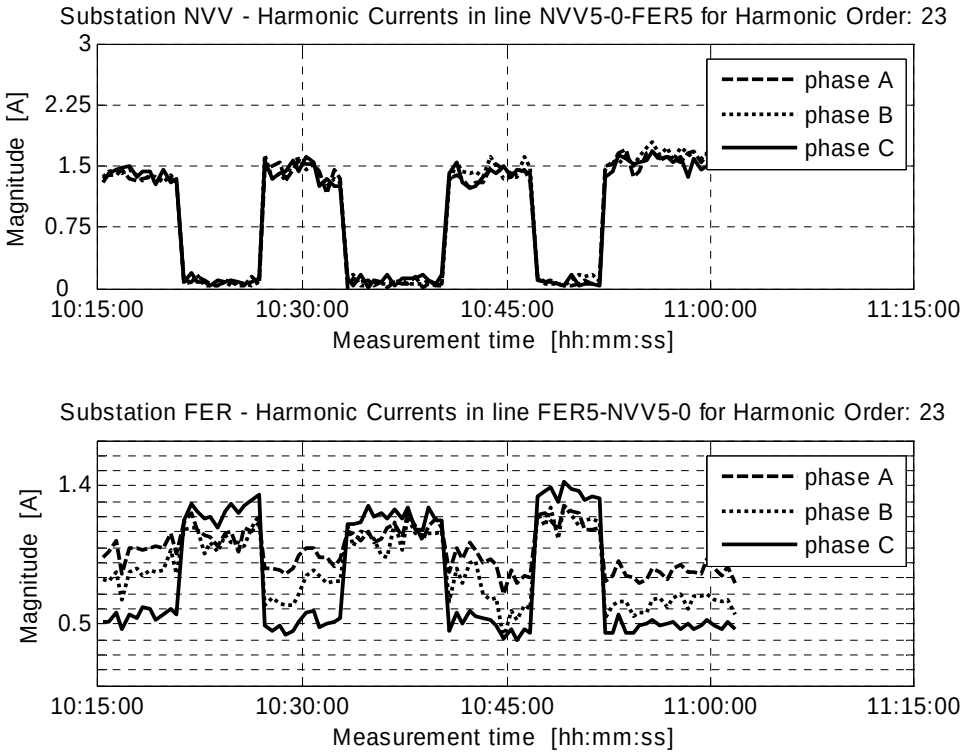

Figure 5.42 23rd harmonic current flowing in the line FER5-NVV5-0. Upper plot shows the measurement at the NVV5 substation and lower plot shows the measurement at FER5 substation.

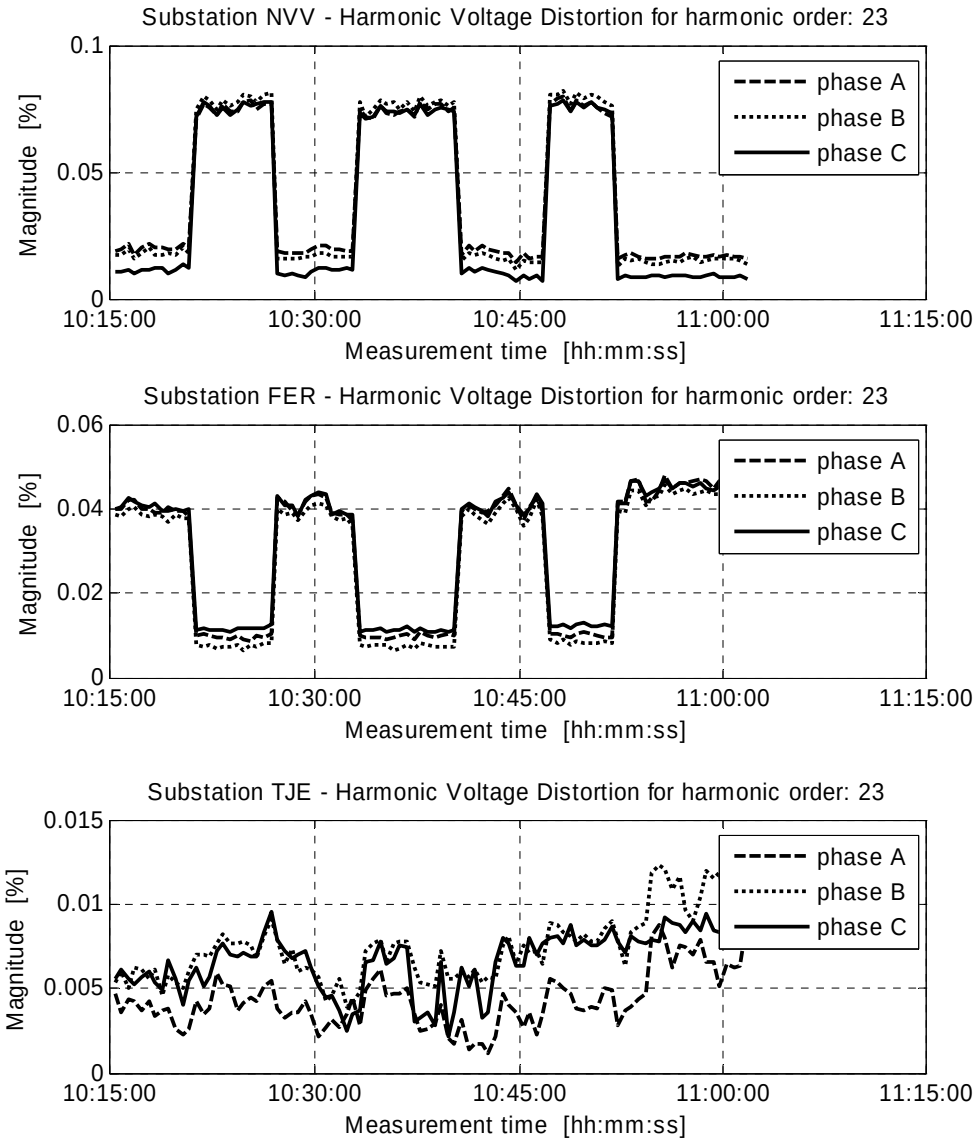

Figure 5.43 Variation of 23rd harmonic in the bus voltage. Upper plot shows the measurement at the NVV5 substation, middle plot at FER5 substation and lower plot at TJE5 substation.

Figure 5.44 shows the variation of 47rd harmonic current in the disconnected line. Its level rises from 0.5A up to 2A at FER5 substation after line disconnection, and at NVV5 substation it lowers from 1.5A to zero. The effect on voltage can be seen in Figure 5.45. It can be seen that this harmonic behaves differently from the others. It is not filtered so much at TJE5 substation, even that the harmonic filters installed there are double tuned + high pass filters. The effect of switching of the line can be clearly seen. When line is connected its magnitude is approx 0.01%, and after the line disconnection this magnitude rises to 0.03%. At FER5 substation the magnitude shows the same "shape" but it is just slightly higher and after line disconnection its magnitude rises to 0.04%. On the other side of the line FER5-NVV5-0 at substation NVV5 the magnitude is higher; before line disconnection it is 0.05% and after line disconnection it reaches 0.2%.

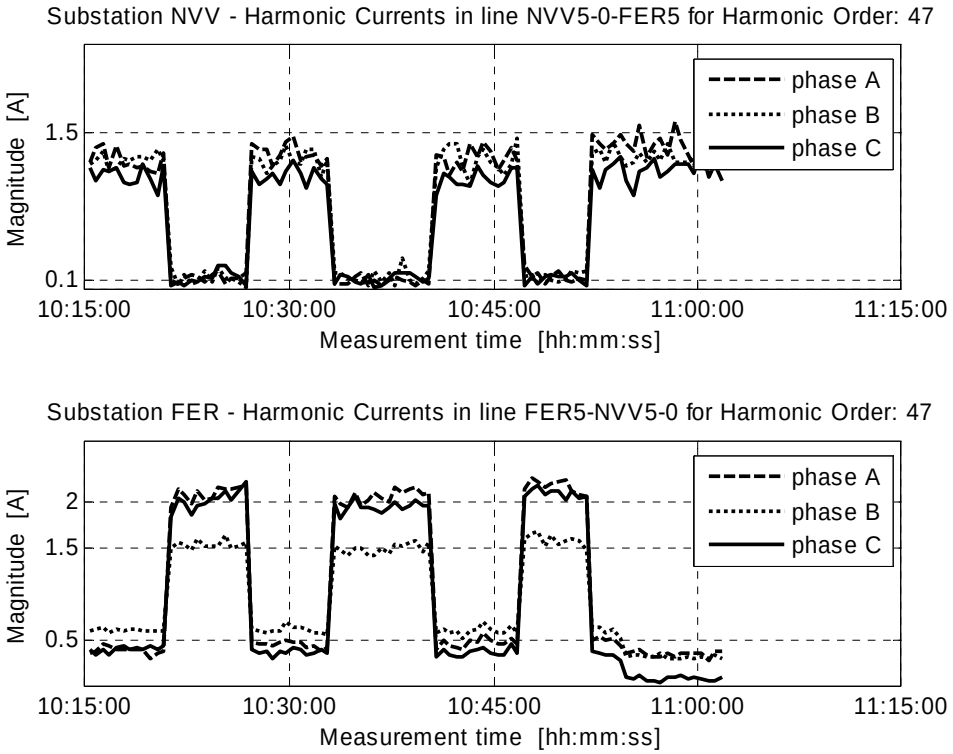

Figure 5.44 47th harmonic current flowing in the line FER5-NVV5-0. Upper plot shows the measurement at the NVV5 substation and lower plot shows the measurement at FER5 substation.

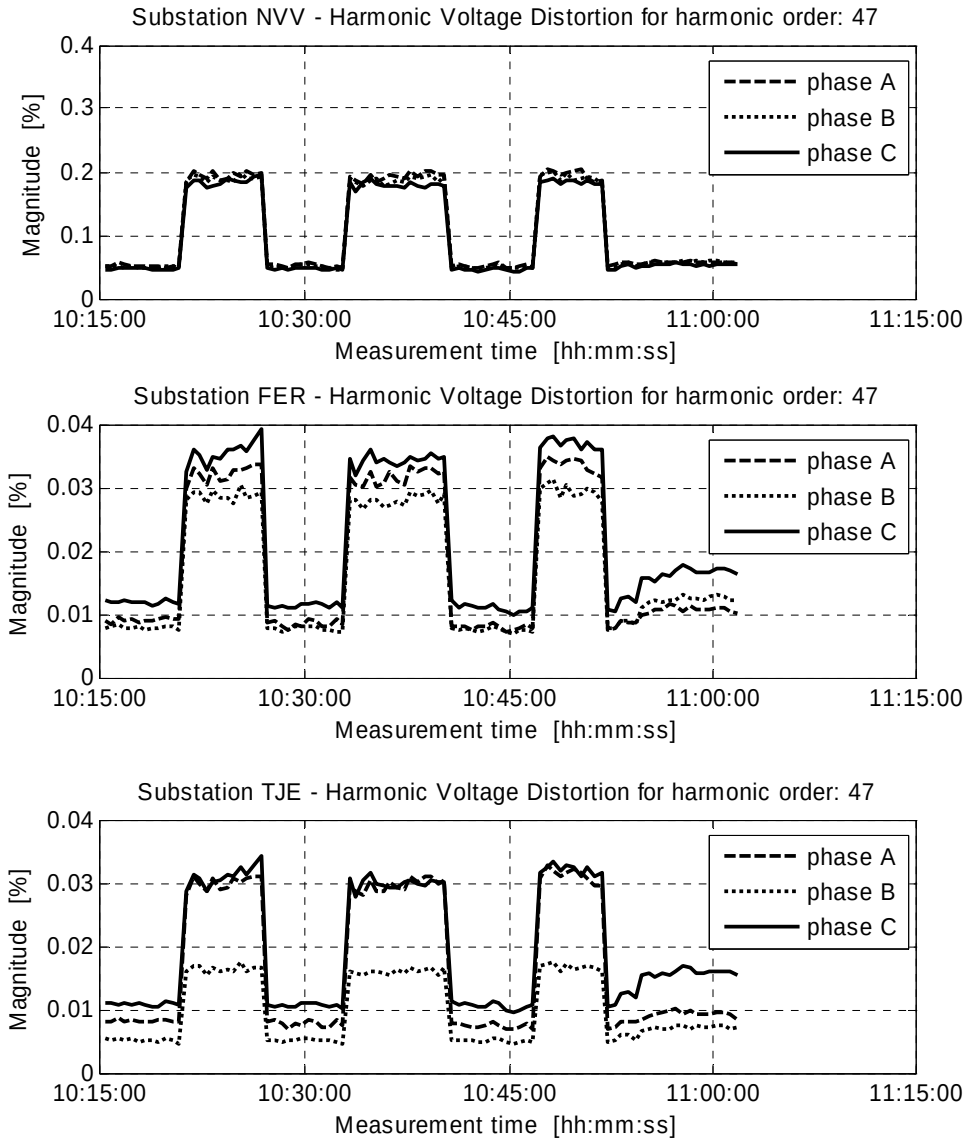

Figure 5.45 Variation of 47th harmonic in the bus voltage. Upper plot shows the measurement at the NVV5 substation, middle plot at FER5 substation and lower plot at TJE5 substation.

5.6 Comparison of the results of initial simulations with the results of the measurements

Results of the measurements were compared with the results of initial simulations from Table 5.4 and Table 5.5. Table 5.11shows all of these results of simulations and measurements for the base case 1 (line FER5-NVV5-0 connected) and case 4 (line FER5-NVV5-0 disconnected). Additionally the third part of the table shows the relative change in magnitudes of particular harmonics (in percent of the value in base case 1).

INITIAL SIMULATION				**MEASUREMENT RESULTS**			
BASE CASE							
VOLTAGE DISTORTION				VOLTAGE DISTORTION			
Station	TJE5	FER5	NVV5	Station	TJE5	FER5	NVV5
Harmonic	% fund	% fund	% fund	Harmonic	% fund	% fund	% fund
11	0,1566	0,2390	0,7577	11	0,5317	0,0773	0,7479
13	0,3224	0,8791	0,7439	13	0,4778	0,0561	0,5300
23	0,2900	0,6593	0,1393	23	0,0386	0,0047	0,0169
25	0,2836	0,7943	0,1333	25	0,0305	0,0086	0,0083
35	0,2449	1,7478	1,4691	35	0,0255	0,0059	0,0441
37	0,3220	0,2028	0,1649	37	0,0230	0,0059	0,0499
47	0,3288	0,1660	0,1718	47	0,0094	0,0079	0,0491
49	0,0269	0,1302	0,5289	49	0,0039	0,0042	0,0519
THD	0,8622	2,2441	1,9129	THD	0,7174	0,0968	0,9220
CASE 4 - line FER5-NVV5-0 switched off							
VOLTAGE DISTORTION				VOLTAGE DISTORTION			
Station	TJE5	FER5	NVV5	Station	TJE5	FER5	NVV5
Harmonic	% fund	% fund	% fund	Harmonic	% fund	% fund	% fund
11	0,1915	0,3629	0,7900	11	0,4531	0,0660	0,8597
13	0,3680	1,0939	0,5930	13	0,6028	0,0615	0,5045
23	0,5871	0,5365	1,0243	23	0,0096	0,0058	0,0723
25	0,6596	0,4424	1,1440	25	0,0030	0,0059	0,0513
35	0,2788	2,6867	2,8174	35	0,0119	0,0015	0,1689
37	0,4348	0,8813	1,3152	37	0,0182	0,0080	0,1888
47	0,7255	0,7593	0,6667	47	0,0301	0,0243	0,1825
49	0,0837	2,2640	1,0121	49	0,0146	0,0109	0,1973
THD	1,3236	3,9381	3,8039	THD	0,7552	0,0948	1,0667
RELATIVE DIFFERENCE BETWEEN CASE 1 AND CASE 4							
Station	TJE5	FER5	NVV5	Station	TJE5	FER5	NVV5
Harmonic	%	%	%	Harmonic	%	%	%
11	22,2447	51,7965	4,2699	11	14,7879	14,6470	14,9467
13	14,1574	24,4312	20,2853	13	26,1413	9,5793	4,8234
23	102,4716	18,6187	635,4301	23	75,2167	23,4593	327,9329
25	132,5573	44,3051	758,1340	25	90,0633	31,3941	521,3073
35	13,8505	53,7179	91,7732	35	53,3083	74,6980	282,9940
37	35,0344	334,6545	697,7733	37	20,9257	34,3613	278,2521
47	120,6739	357,3967	288,1603	47	220,7551	207,7331	272,0515
49	211,2915	1639,2921	91,3531	49	271,9119	162,3567	280,1365
THD	53,5247	75,4910	98,8545	THD	5,2566	2,1195	15,6872

Table 5.11 Results of simulations and results of measurements for the base case 1(line FER5-NVV5-0 connected) and case 4 (line FER5-NVV5-0 disconnected).

In general it can be seen that the magnitudes of particular harmonics obtained in initial simulations differ from the results of measurements. Such effect was somehow expected, since the harmonic distortion in initial simulation was originating only form the idealized models of HVDC converters. The model was not calibrated, loading of HVDC links was at the maximum, etc. Therefore, obtaining realistic results was not expected but rather the aim was to detect some correlation between the results of simulations and results of measurements (besides determining which component is to be used during the measurement and determining the best location of measuring points). Most likely the similarities should be visible when looking at the relative increments in magnitudes of particular harmonics, expressed in percents. These increments are given in the third section of Table 5.11. As can be seen some of the harmonics increased significantly. Higher increase can be noticed in the values obtained from simulations than in the measured values. It can be also seen that magnitude of higher order harmonics rise more than of lower order harmonics. This is in general true for results of initial simulations and for results of measurements. Therefore, in the attempt to extract more correspondence between simulations and measurements, all of the harmonics were put in a declining order, in terms of relative differences between case 1 and case 4. This is shown in Table 5.12. Now some correlation is visible, namely the order of decline is similar for results of measurements and results of simulations, especially for higher order harmonic frequencies. The similarities are more pronounced for harmonics at substation TJE5 and FER5. It is worse for the NVV5 substation, but when looking again at the result in Table 5.11, it can be seen that the differences between incremental values both for measurement and simulation are not large.

TJE5		**FER5**		**NVV5**	
Initial Simulation	**Measurement**	**Initial Simulation**	**Measurement**	**Initial Simulation**	**Measurement**
Harmonic order					
49	49	49	47	25	25
47	47	47	49	37	23
25	25	37	35	23	35
23	23	35	37	47	49
37	35	11	25	11	37
11	13	25	23	49	47
13	37	13	11	13	11
35	11	23	13	35	13

Table 5.12 Harmonics in order from the largest to smallest in terms of relative differences between cases 1 and 4.

5.7 Conclusion

The purpose of this chapter was to present the results of harmonic measurements performed on the 400 kV Western network of Energinet.dk.
Three, 400 kV substations were selected for locating the measuring equipment: TJE5, FER5 and NVV5. These substations are located near the HVDC links to Sweden and Norway. The substations are located in a distance of 100 km between the most distant ones, TJE5 and NVV5.
Before the main, GPS-synchronized measurement, initial simulations were performed. In these Initial simulations, as sources of harmonic distortion, the HVDC converters of the interconnections to Norway and Sweden were used. The idealized spectra of these converters were modelled using current source models. Various power components were switched out and switched in, in various configurations, and it was found that the highest increments of the harmonic voltages at the selected substations had the disconnection of one of the power lines - FER5-NVV5-0. The line is connected at the two substations where measuring equipment is installed, FER5 and NVV5.

Consequently, this power line was selected as the element that will be switched out and switched in. The harmonic currents were measured at both ends of the line, and harmonic voltages at both substations, to which the line was connected, FER5 and NVV5. Additionally, voltage at a third substation TJE5 was also measured. The measuring equipment at all three substations was synchronized by the GPS units. The GPS units were sending synchronizing pulses which were being detected by the Omicron CMC256 units. Each time an Omicron CMC256 unit was detecting the synchronizing pulse, it was taking a snap-shot measurement. 90 snapshot measurements were taken synchronously, by all three Omicron units. The synchronization error due to the delay in the detection of the synchronization pulse is discussed in the next chapter.

The measurement of harmonic currents and voltages in high voltage network is not done directly. Especially the measurement of the harmonic voltage is difficult, because the existing capacitive voltage transformers (CVT) experience resonances at higher frequencies. Therefore another procedure was employed, where the capacitive taps of the transformer bushings (CTB) were used. Current from these CTB's was lead for 100 – 200 meters through the high voltage switchyard and voltage drop on resistors was measured. It is shown that this technique amplifies higher order harmonic proportionally to their order, increasing the signal-to-noise ratio of the measurement.
A comparison was made between measuring harmonic voltage using the CTB's and the CVT's and it is shown that the result differs already at 5^{th} harmonic. Thanks to the amplification of high order harmonic frequencies, it was possible to measure them more precisely – they are not visible, when measured using a CVT. However, CVT are measuring precisely the 50 Hz component, therefore were used to determine the ratio of the CTB at this frequency.
Harmonic current was measured using the existing inductive voltage transformers (CT). Low inductance resistors were used for that purpose. These resistors were connected in series with the protective or metering equipment, and voltage drop on these resistors was measured. It was found that both protective and metering cores gave exactly the same results and both can be used for harmonic measurements.
Since the coaxial cables had to be led through the high voltage switchyard, where the levels of electric and magnetic fields are high, it had to be ensured that the level of noise induced in the coaxial cables will not introduce errors in the measurements. Therefore, various grounding arrangements were investigated. Measurements of the induced noise were also performed and an optimal grounding technique is found. It is shown that they key factor reducing the magnetically induced noise is to reduce the area of the loop, especially by not including the earth as a part of the return path. The way to reduce capacitive coupling is to provide shielding. By using the proper grounding technique, the level of both capacitive and inductive noise induced in the cables can be reduced to insignificant levels for harmonic measurements, despite that the coaxial cables

are laid for distances 100 – 200 meters through the high voltage switchyard. The level of noise was reduced by the factor of about 200 times.
The three pieces of Omicron CMC256 were synchronized using GPS clocks. All the units were controlled from one substation - there was nobody at the other two substations during the main measurement. The control was realised simply using an internet connection.
In total, there were 90 time domain "snap-shot" measurements performed during 45 minutes, each lasting of 300 ms. Three phase quantities were measured at three substations, voltages and currents, using 24 measuring channels. In total of 2160 measurements were processes later using Matlab. Harmonic amplitudes and phase angles were extracted up to the 50^{th} harmonic.
While the snap-shots were being taken, the power line FER5-NVV5-0 was disconnected and re-connected three times in row. The variation of harmonic currents and voltages was observed.
Additionally, SCADA measurements were also taken and were available later.
The line was disconnected at one end. A current of 35 A was flowing into this disconnected line, mainly due to the shunt admittance of the cable section.
The results of measurements show that the harmonic distortion in the voltage is quite low (summer, 10 – 11 am), and it reaches maximally, at NVV5 substation for 11^{th} harmonic - 0,9% at other frequencies is lower. At the FER5 substation, the magnitude of 11^{th} harmonic reaches 0,6% and at TJE5 the harmonic distortion is lower, maximally 0,3%, due to the installed harmonic filters.
The general observation is that the harmonic voltages below 500 Hz are not much affected by the switching of the line. At higher frequencies the differences are larger.
Switching off the line affected mainly the harmonic frequencies at substations NVV5 and FER5.

In general, the level of obtained harmonic distortion was lower than expected; however some correlation between the measurement results and the results of initial simulations can be observed.

The obtained in this chapter results of harmonic measurements will be used in the next chapter, where the verification of the entire harmonic model of the Western linear network will be shown.

Chapter 6

Verification of the linear transmission network model

In the previous chapters, the adaptation of the linear harmonic model of the Western transmission network was shown, and various verification techniques were analyzed. GPS-synchronized harmonic measurements were described. In this chapter, the created linear network model will be validated against performed harmonic measurements.

6.1 Introduction

Verification of the linear harmonic model was initially planned to be made using the developed method described in section 4.6, which was based on determination of transfer harmonic impedance by switching a series component composed of shunt and series elements. One of the assumptions of this method was that the injected harmonic currents are balanced. After performing the harmonic measurements described in chapter 5, it occurred that the harmonic currents are far more unbalanced than anticipated. Hence, the assumption of balanced currents was not acceptable and an alternative method had to be evolved. This alternative approach allows using the obtained results of measurements where harmonic currents are unbalanced.

Chapter outline

This chapter is organized as follows:

First, an explanation why harmonic currents should be balanced to measure harmonic admittance of an unbalanced component is given. An example of an unbalanced harmonic current measured at FER5 substation is shown. Next, an alternative approach to the model verification is evolved. Te general idea of the method is explained and the effect of synchronization error on the phase error of harmonic frequencies is discussed. Results of measurements are shown including the effects of synchronization error. The synchronization error effect on the modelling approach is presented and at the end, results of measurements are compared with the results of simulations using the created PowerFactory model. The overall conclusion is presented at the end.

6.2 Why harmonic currents should be balanced?

Power system components are characterized by some value of harmonic admittance. Because the system is three-phase, the admittance is written in a matrix form. If such a component can be assumed symmetrical, its admittance matrix contains self phase admittances, Y, equal for each phase and mutual admittances Y_m describing the coupling between phases, which are also the same between all the phases, as shown in Figure 6.1.

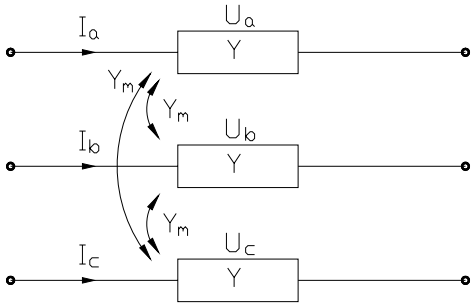

Figure 6.1 Balanced three-phase component.

For such a component the admittance matrix expressed in phase components has the form:

$$\begin{bmatrix} I_a \\ I_b \\ I_c \end{bmatrix} = \begin{bmatrix} Y & Y_m & Y_m \\ Y_m & Y & Y_m \\ Y_m & Y_m & Y \end{bmatrix} \begin{bmatrix} V_a \\ V_b \\ V_c \end{bmatrix}, \tag{6.1}$$

at each harmonic frequency.

The coupling between phases in practice means that harmonic current injected in phase *a* will cause voltage drop on the self phase impedance and induce some voltage in the other two phases *b* and *c* (the same value in both phases). Therefore, the phase voltage measured in each phase is a function of harmonic currents injected into all three phases and simple division of the injected phase current I_a by phase voltage U_a will not give a pure value of the phase admittance Y. After transforming Equation (6.1) to symmetrical components, it becomes:

$$\begin{bmatrix} I_0 \\ I_1 \\ I_2 \end{bmatrix} = \begin{bmatrix} Y+2Y_m & 0 & 0 \\ 0 & Y-Y_m & 0 \\ 0 & 0 & Y-Y_m \end{bmatrix} \begin{bmatrix} U_0 \\ U_1 \\ U_2 \end{bmatrix} = \begin{bmatrix} Y_{00} & 0 & 0 \\ 0 & Y_{11} & 0 \\ 0 & 0 & Y_{22} \end{bmatrix} \begin{bmatrix} U_0 \\ U_1 \\ U_2 \end{bmatrix}. \tag{6.2}$$

It can be seen that the sequential admittance matrix of a balanced element is diagonal; all mutual terms between sequences are zero. If the three-phase current at harmonic h is unbalanced and contains all sequences, the resultant voltage will also contain all sequences, but since there is no coupling between sequence admittances, zero-sequence current will produce only zero-sequence voltage, positive sequence current will produce only positive sequence voltage, etc. The ratio of the respective sequence values of currents and voltages will therefore allow to unequivocally determine the positive, negative and zero-sequence admittances, for example $Y_{00} = I_0/U_0$, etc.

In reality, the Y_{abc} admittance matrix is not symmetrical, due to the different distances between the phases, the phases and the ground wires, the ground itself, etc, as shown in Figure 6.2.

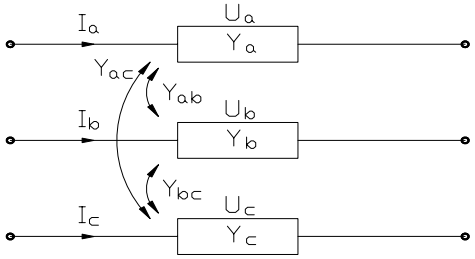

Figure 6.2 Unbalanced three-phase component.

Therefore, in general case the admittance matrix will have the form:

$$\begin{bmatrix} I_a \\ I_b \\ I_c \end{bmatrix} = \begin{bmatrix} Y_{aa} & Y_{ab} & Y_{ac} \\ Y_{ba} & Y_{bb} & Y_{bc} \\ Y_{ca} & Y_{cb} & Y_{cc} \end{bmatrix} \begin{bmatrix} V_a \\ V_b \\ V_c \end{bmatrix}, \tag{6.3}$$

and after transforming it into symmetrical components, it becomes:

$$\begin{bmatrix} I_0 \\ I_1 \\ I_2 \end{bmatrix} = \begin{bmatrix} Y_{00} & Y_{01} & Y_{02} \\ Y_{10} & Y_{11} & Y_{12} \\ Y_{20} & Y_{21} & Y_{22} \end{bmatrix} \begin{bmatrix} U_0 \\ U_1 \\ U_2 \end{bmatrix}, \tag{6.4}$$

where for example the term Y_{01} expressed in phase components is:

$$Y_{01} = \frac{1}{3} \cdot \left[\left(Y_{aa} + Y_{BA} + Y_{CA} \right) + \left(e^{j\frac{2\pi}{3}} \right) \cdot \left(Y_{ac} + Y_{bc} + Y_{cc} \right) + \left(e^{-j\frac{2\pi}{3}} \right) \cdot \left(Y_{ab} + Y_{bb} + Y_{cb} \right) \right].$$

Consequently, it can be seen that because of the coupling between the sequence components the problem is no longer simpler than in phase components. If the current injected at harmonic h will contain all sequences, then the resultant voltage drop will also contain all sequences, but additionally coupled, i.e. zero sequence voltage will be a result of injected zero, positive and negative sequence currents, etc, and simple division of respective sequential harmonic currents and voltages will not give correct admittance values.

From the above, the conclusion is that in order to measure these unbalanced harmonic admittances precisely, there are two ways of injecting the harmonic current. The first possibility is to determine the phase self and mutual admittances from Equation (6.9), by injecting current at harmonic h only into one phase at a time and measure the resultant voltage response in all phases. For example by injecting current into phase *a* and measuring resulting harmonic voltage responses U_a, U_b, U_c, the self and mutual terms from the first row of admittance matrix of Equation (6.9) can be determined: $Y_{aa} = I_a / U_a$, $Y_{ab} = I_a / U_b$ and $Y_{ac} = I_a / U_c$. To get the whole matrix, it has to be repeated for each phase.

Alternatively, the sequence admittances from (6.4) can be directly determined. The procedure is analogous to the previous one, i.e. only one row of the sequential admittance matrix can be determined at a time by injecting harmonic currents into three phases but *purely* positive, negative or zero sequence. For example injected purely positive-sequence harmonic current will give rise to voltage harmonics of all sequences and the following admittances can be calculated: $Y_{10} = I_1 / U_0$, $Y_{11} = I_1 / U_1$ and $Y_{12} = I_1 / U_2$.

Generalizing, injected harmonic current can be unbalanced but then the phase admittance matrix must be symmetrical or if phase admittance matrix is unbalanced, injected current must be single phase or balanced, purely sequential.

6.3 Example harmonic current measured at FER5 substation

In balanced systems, rotation of harmonic currents and consequently their phase sequence is described by Equation (6.5):

$$\begin{aligned} i_a(h,t) &= I_{hm} \cdot \sin(h(\omega t - \alpha)) \\ i_b(h,t) &= I_{hm} \cdot \sin\left(h\left(\omega t - \alpha - \frac{2\pi}{3}\right)\right), \\ i_a(h,t) &= I_{hm} \cdot \sin\left(h\left(\omega t - \alpha - \frac{4\pi}{3}\right)\right) \end{aligned} \tag{6.5}$$

where h is harmonic order, α is the initial phase shift. For example, the phase sequence of harmonics up to 13th is shown in Table 6.1.

Harmonic	dc	1	2	3	4	5	6	7	8	9	10	11	12	13	…
Sequence	0	1	2	0	1	2	0	1	2	0	1	2	0	1	…

Table 6.1 Sequence of harmonic frequencies in balanced systems.

One of the initial assumptions made when developing the method described in chapter 4.6 was that the injected harmonic currents are balanced. Therefore after performing harmonic measurements, the results were checked in this respect. This is illustrated by the example of 7th and 11th harmonic current injected at FER5 substation (the spectra of harmonic currents are shown in Figure 6.15 on page 168 and Figure 6.16 on page 169).

The phase values of the 7th and 11th harmonic current and the values transformed to symmetrical components are shown below:

The value of measured 7th harmonic three-phase current is

$$\begin{bmatrix} I_a^7 \\ I_b^7 \\ I_c^7 \end{bmatrix} = \begin{bmatrix} 4.8\angle 91.73^\circ A \\ 5.2\angle -33.48^\circ A \\ 5.0\angle -166.41^\circ A \end{bmatrix},$$

and after transforming to symmetrical components:

$$\begin{bmatrix} I_0^7 \\ I_1^7 \\ I_2^7 \end{bmatrix} = \frac{1}{3}\begin{bmatrix} 1 & 1 & 1 \\ 1 & e^{j\frac{2}{3}\pi} & e^{j\frac{4}{3}\pi} \\ 1 & e^{j\frac{4}{3}\pi} & e^{j\frac{2}{3}\pi} \end{bmatrix}\begin{bmatrix} 4.8\angle 91.73^\circ A \\ 5.2\angle -33.48^\circ A \\ 5.0\angle -166.41^\circ A \end{bmatrix} = \begin{bmatrix} 0.3358\angle 131.5^\circ A \\ \mathbf{4.9563}\angle 83.88^\circ A \\ 0.5902\angle 220.31^\circ A \end{bmatrix}.$$

Similarly the value of measured 11th harmonic three-phase current is

$$\begin{bmatrix} I_a^{11} \\ I_b^{11} \\ I_c^{11} \end{bmatrix} = \begin{bmatrix} 20.5\angle 138.79^\circ A \\ 20.7\angle -110.24^\circ A \\ 19.5\angle -15.63^\circ A \end{bmatrix},$$

and after transforming to symmetrical components:

$$\begin{bmatrix} I_0^{11} \\ I_1^{11} \\ I_2^{11} \end{bmatrix} = \frac{1}{3}\begin{bmatrix} 1 & 1 & 1 \\ 1 & e^{j\frac{2}{3}\pi} & e^{j\frac{4}{3}\pi} \\ 1 & e^{j\frac{4}{3}\pi} & e^{j\frac{2}{3}\pi} \end{bmatrix}\begin{bmatrix} 20.5\angle 138.79^\circ A \\ 20.7\angle -110.24^\circ A \\ 19.5\angle -15.63^\circ A \end{bmatrix} = \begin{bmatrix} 1.439\angle 172.98^\circ A \\ 0.830\angle -55.52^\circ A \\ \mathbf{20.139}\angle -135.91^\circ A \end{bmatrix}.$$

As can be seen, the 7th harmonic is predominantly positive sequence, and the 11th harmonic is predominantly negative sequence, but not entirely; both contain large amounts of other sequences, as much as 10%. Such large unbalance of the current would cause unacceptable errors when calculating the sequential harmonic admittances.

Difficulty of obtaining harmonic impedance in this way is also confirmed in the literature [Jonas].

For the reasons discussed above, the originally planned method was not used for verification purposes, but some another way of using the obtained results had to be found. Such approach is discussed in the following sections.

6.4 Original and modified approaches

6.4.1 The original approach

The original approach to the verification problem, derived in chapter 4, is best explained on the example of determining the driving-point harmonic admittance, as shown in Figure 6.3. Balanced harmonic current I_{012}^{M} is injected into a bus and it results in harmonic voltage distortion U_{012}^{M}. Using this current value and the measured harmonic voltage response, the self and mutual terms of the harmonic admittance matrix Y_{012}^{M} can be calculated. Admittance at other, not injected harmonic frequencies can later be interpolated. When this admittance is known, in second step, the analogous admittance of the created PowerFactory computer model $\mathbf{Y}_{012}^{C}$ is determined, using the frequency sweep method (1 p.u. sequential harmonic current is injected). The model is accurate if the measured admittance of the real system and the admittance of the computer model are equal in the frequency range of interest, for the positive, negative and zero-sequence values:

$$\mathbf{Y}_{012}^{M} = \mathbf{Y}_{012}^{C} . \tag{6.6}$$

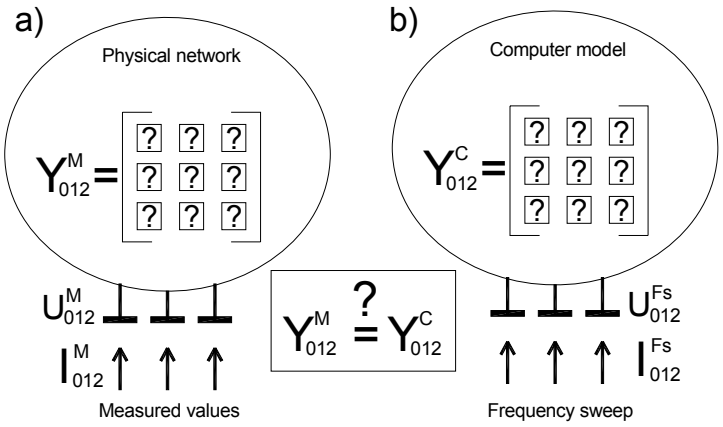

Figure 6.3 Determination of the harmonic admittance matrix (a) from the measurements, and (b) of the computer model.

Because the harmonic currents that are injected in reality are unbalanced, the calculated admittance matrix Y_{012}^{M} would contain errors and could not be used for verification of the admittance matrix of the computer model created in PowerFactory. Therefore, an alternative approach is developed in this project and is presented in the following section.

6.4.2 The alternative approach

Figure 6.4 shows both, the physical (a), and the modelled (b) transmission network represented by admittance matrices, $\mathbf{Y}_{012}^{M}$ and $\mathbf{Y}_{012}^{C}$ respectively.

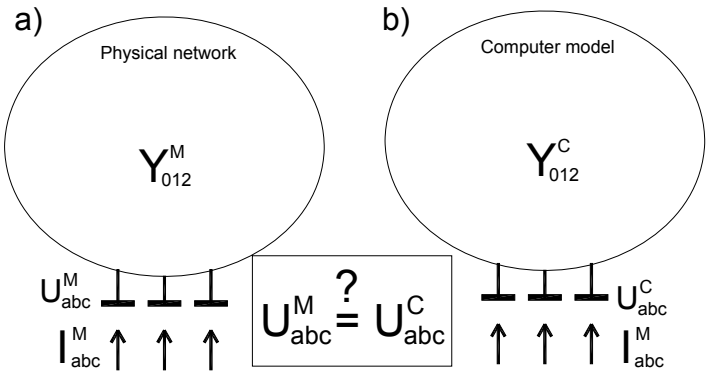

Figure 6.4 Verification of the computer model with the alternative method. (a) Physical measurements, and (b) injection of measured harmonic current into the computer model.

Harmonic currents I_{abc}^{M} are injected into the physical network. These currents are unbalanced. The resultant harmonic voltage is measured U_{abc}^{M}, but the admittance matrix cannot be calculated without errors. However, it can be realized that if the computer model is correct, both admittance matrices of the physical network and of the computer model must be the same: $\mathbf{Y}_{012}^{M} = \mathbf{Y}_{012}^{C}$. In such a case, if the injected harmonic current I_{abc}^{M} is measured, and in second step the same value of current is injected into the computer model using a current source, the resultant harmonic voltage response would be the same as in the case of the physical network:

$$U_{abc}^{M} = U_{abc}^{C} . \tag{6.7}$$

This would be true for any value of the admittance matrix, with any degree of coupling between sequences. This admittance matrix, calculated internally in PowerFactory software from the physical parameters of the models, would remain unknown, but it does not need to be known to state that the model reflects the behavior of the physical system. Moreover, if in this way the model is proven to be precise, it indicates that the admittance matrix of the model must be correctly modelled, and what follows is that it can be determined later, if needed, by the frequency sweep calculation.

Therefore, it can be stated that if the injected unbalanced harmonic currents are measured (together with the resultant harmonic voltage), and injected into the computer model, then the harmonic voltage response calculated by the computer model must be the same as the real voltage response of the physical system, regardless of the composition of the admittance matrix or of the level of unbalance of injected harmonic current.

This modified method will be extended to suit to the specific conditions of the harmonic measurements performed in the way depicted in chapter 5 and will be described in the following sections.

6.5 General idea of the verification method

During the measurements, measuring equipment has been setup at three high voltage substations, TJE5, FER5 and NVV5. The equipment was synchronized using GPS units. Power line FER5-NVV5-0, connected between substations FER5 and NVV5 has been disconnected and reconnected three times in row and harmonic voltages at all three substations have been measured, together with harmonic currents flowing into the disconnected line, at both ends. Since the power line was disconnected and reconnected only at one end at substation NVV5, harmonic current at this substation is zero when the line is disconnected and is not zero at FER5 substation, because of the shunt capacitance of the line. If it can be assumed that background harmonic distortion is stable during the measurement and that no switching was performed in the network during the measurement, then the only operation that affects the level of harmonic voltages at the three substations is switching of the power line FER5-NVV5-0. The general idea is shown in Figure 6.5 (a) below.

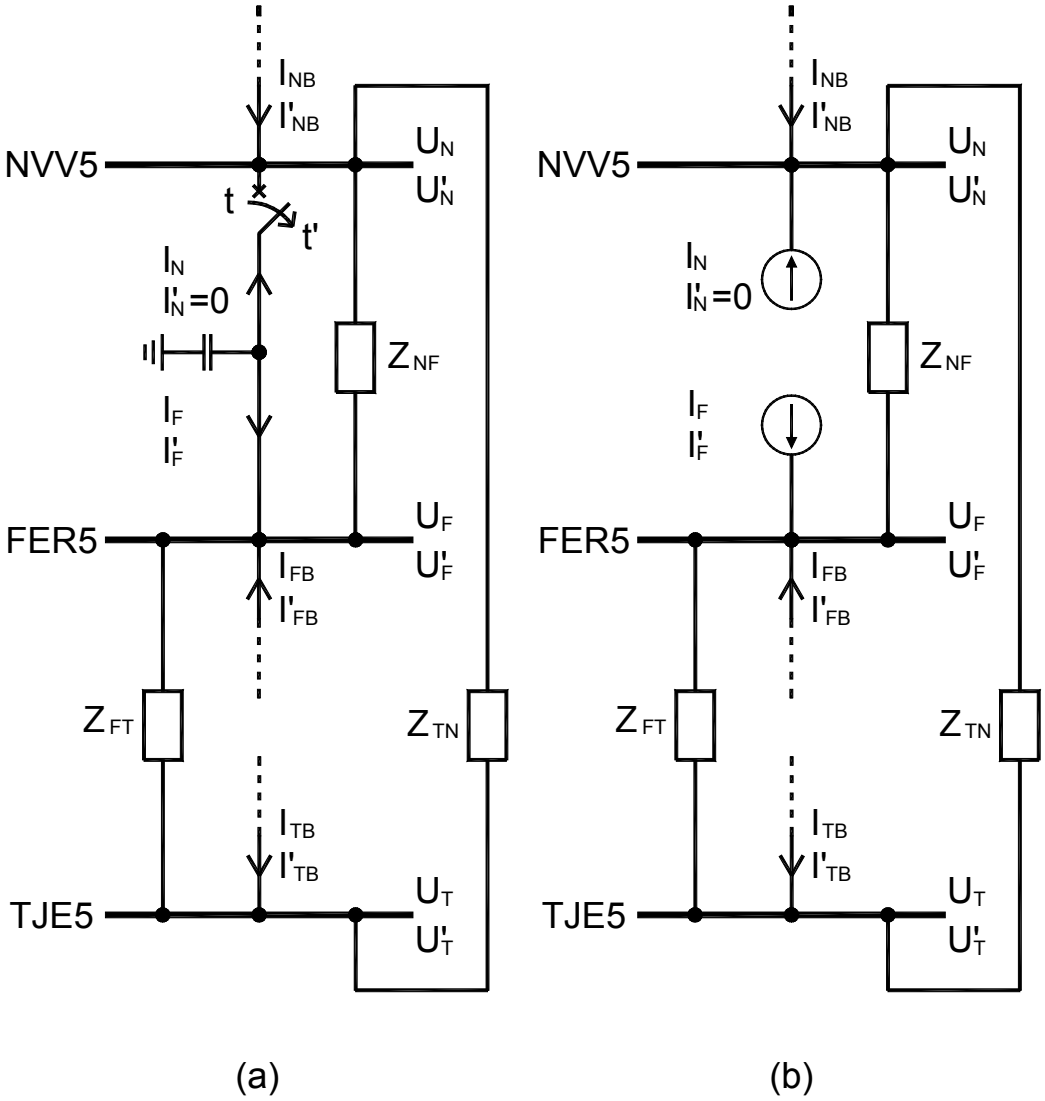

Figure 6.5 Conceptual diagram of the power network around substations NVV5, FER5 and TJE5. (a) – Switching of the power line FER5-NVV5-0 at NVV5 substation, (b) – Modelling approach with the power line represented as two current sources injecting harmonic currents into the network.

The three substations are interconnected through 400 kV and also 150 kV power lines. This interconnection can be represented by equivalent impedances Z_{NF} Z_{FT} and Z_{TN}. Initially at the time *t*, the switch in the power line FER5-NVV5-0 is closed and the line is in operation. There are no harmonic sources in the considered part of the network but background harmonic distortion is present due to harmonic currents I_{NB}, I_{FB} and I_{TB}. Harmonic voltages at the busbars of NVV5, FER5 and TJE5 have constant values U_N, U_F and U_T. Because of the harmonic voltage difference between busbars of NVV5 and FER5, harmonic current flows into the line FER5-NVV5-0. This current has in general different value at each end of the line $I_F \neq I_N$, due to the shunt admittance of the line. After the line is disconnected at the NVV5 substation, at instant *t'* current I_N becomes $I'_N = 0$, and on the FER5 side current I_F becomes I'_F. Despite of the assumption that the background harmonic distortion is constant, currents I_{NB}, I_{FB} and I_{TB} will change and become I'_{NB}, I'_{FB} and I'_{TB} due to the change of the network impedance. Harmonic voltages at substations NVV5, FER5 and TJE5 will become U'_N, U'_F and U'_T. It can be recognized that the only reason for the change in the values of bus voltages and line currents was the change in injected currents from the line FER5-NVV5-0. At NVV5 substation the current changed from I_N to $I'_N = 0$ and at FER5 substation the current changed from I_F to I'_F. It can be stated that if these currents were known, then the line could be actually represented by two ideal current sources. These current sources should inject the same values of harmonic currents at both substations NVV5 and FER5, as shown in Figure 6.5 (b). All the values of currents and voltages at other points of the network will not be changed by this replacement.

6.6 The modelling approach

Harmonic currents I_N, I'_N, I_F and I'_F should be measured together with the resultant changes in harmonic voltages U_N, U'_N, U_F , U'_F and U_T, U'_T. The increments $\Delta U_N = U_N - U'_N$, $\Delta U_F = U_F - U'_F$ and $\Delta U_T = U_T - U'_T$ are the combined result of current increments $\Delta I_N = I_N - I'_N$ and $\Delta I_F = I_F - I'_F$.

In the PowerFactory harmonic model the only source of harmonic distortion are the HVDC converters. It is however possible to define that these converters will behave as linear elements, injecting only fundamental frequency currents. All higher harmonics will be disregarded and there will be no harmonic distortion in the model in such case. Existing model of the power line FER5-NVV5-0 should be disconnected and two harmonic current sources shall be connected instead. Harmonic spectra that were measured at the instant *t*, I_N and I_F shall be assigned to these harmonic sources. After performing harmonic load flow calculation, some value of harmonic distortion will appear at substations NVV5, FER5 and TJE5: U_N, U_F and U_T, only as a consequence of the harmonic currents I_N and I_F. In the next step, harmonic spectra that were measured at instant *t'*, I'_N and I'_F (when the line was disconnected) should be assigned to the current sources and harmonic load flow calculation shall be repeated. New values of harmonic distortion U'_N, U'_F and U'_T will be obtained. It can be argued that if the harmonic model ideally reflects the behavior of the real network, then the calculated increments from the measured values must have exactly the same values as the increments calculated from the results of harmonic load flow simulations:

$$\left.\begin{aligned}\overbrace{\Delta U_N = U_N^M - U'^M_N}^{Measurement}\\ \Delta U_F = U_F^M - U'^M_F\\ \Delta U_T = U_T^M - U'^M_T\end{aligned}\right\} = \left\{\begin{aligned}\overbrace{\Delta U_N = U_N^S - U'^S_N}^{Simulation}\\ \Delta U_F = U_F^S - U'^S_F\\ \Delta U_T = U_T^S - U'^S_T\end{aligned}\right. \quad (6.8)$$

The above statement can be explained as shown in Figure 6.6 and Figure 6.7. Figure 6.6 (a) shows voltage U_T measured at TJE5 substation at a particular harmonic order *h*, at the instant *t*. it can be assumed that this measured value of voltage can be decomposed into the background harmonic voltage component U_B = const., voltage component $U(I_F)$, which is the effect of injected current from the power line FER5-NVV5-0 at substation FER5 and voltage component $U(I_N)$, which is the effect of injected current from the power line FER5-NVV5-0 at substation NVV5. Figure 6.6 (b) shows voltage U'_T measured at TJE5 substation at the instant *t'*. At this time line FER5-NVV5-0 is disconnected from the substation NVV5 completely, therefore the voltage component $U(I'_N) = 0$. Voltage component from current injected at FER5 has different value $U(I'_F)$ than before, and the background harmonic voltage component U_B is constant. If voltage measured at instant *t'* is subtracted from the value measured at instant *t* then the resultant incremental value $\Delta U_T = U_T - U'_T$ is like shown in Figure 6.6 (c). The same can be shown by subtracting particular components from each other, as shown in Figure 6.6 (d).

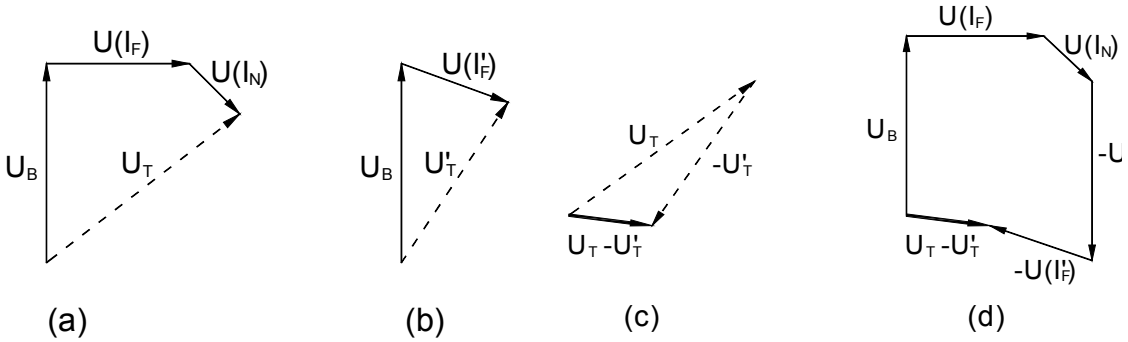

Figure 6.6 Voltage U_T measured at TJE5 substation at a particular harmonic order *h*. (a) – measured at the instant *t*, (b) – measured at the instant *t'*, (c) – resultant incremental value $U_T - U'_T$ and (d) – incremental value obtained from subtracting particular voltage components.

In The next step, the measured harmonic currents I_N, I'_N, I_F and I'_F shall be assigned to current sources in the PowerFactory harmonic model. Assuming that the model is ideally accurate, the voltage components $U(I_F)$ and $U(I_N)$ of the voltage U_T originating from the harmonic currents I_F and I_N will be exactly the same as in reality, as was shown in Figure 6.6 (a). Since there is no background harmonic distortion present in the harmonic model, $U_B = 0$ and the resultant voltage U_T calculated at substation TJE5 is a result of the injected currents I_N and I_F only, as shown in Figure 6.7 (a) on page 162. At instant *t'* voltage U'_T will be a result of the current injected at FER5 substation I'_F, as shown in Figure 6.7 (b). $U(I'_N)=0$ since $I'_N=0$. When calculating the voltage increment by subtracting U'_T from U_T it can be seen that the obtained vector from the simulation $\Delta U_T = U_T - U'_T$ is exactly the same as the vector obtained from measurements (compare Figure 6.6 (c) and (d) with Figure 6.7 (c) and (d)). This is only possible if the harmonic model of the network is exactly reflecting the behavior of the real network. In other words it has been shown that despite of the unknown value of background harmonic distortion, the incremental value obtained from measurements and from simulations are exactly the same, under the condition that the harmonic model is precise. This fact can be used for verification of the

harmonic model. The above reasoning was made here for the harmonic voltage at substation TJE5, but it is actually true for any measured value of voltage or current in the network.

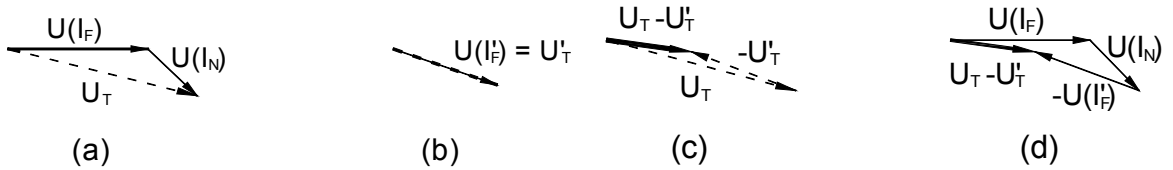

Figure 6.7 Voltage U_T that should be obtained as a result of harmonic load flow simulations at TJE5 substation, at a particular harmonic order *h*. (a) – calculated at instant *t*, (b) – calculated at instant *t'*, (c) – resultant incremental value $U_T - U'_T$ and (d) – incremental value obtained from subtracting particular voltage components.

6.7 Harmonic phase angles and synchronization error

All three Omicron units were synchronized by synchronizing pulses that were sent from the GPS units every 30 seconds (±0,5μs). The shape of the signal is shown in Figure 6.8.

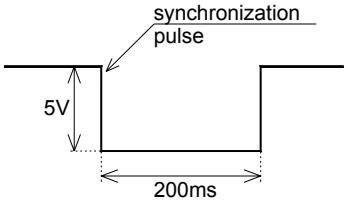

Figure 6.8 Synchronizing signal sent by the GPS unit. The falling edge of this signal represents the synchronization pulse [Omicron].

Since 30 second period contains integer number of fundamental frequency periods, in an ideal case, every 30 seconds the measuring window would begin exactly at the same distance from the zero-crossing of the fundamental frequency sinusoid. The information about phase angles of harmonic components measured at two different moments could be directly compared. In practice, the synchronizing pulses sent by GPS units had to be detected by one of the Omicron input channels, where the sampling rate was 28,44 kHz. This means that the time gap between two samples was approx. 35μs, as shown in Figure 6.9. If the falling edge of the synchronizing pulse appears at point A (see Figure 6.9), sample number 1 detects it and there is no synchronization error. If the falling edge appears just a little bit later at point B, sample number 1 will miss it and it will take 35μs until next sample number 2 will detect the synchronization pulse. In this case the synchronization error is 35μs. If the synchronizing pulse appears at point C, synchronization error is very small, and at point D it is zero again. The maximal synchronization error is a delay and therefore the corresponding error in the phase angles of particular harmonics δ will be positive.

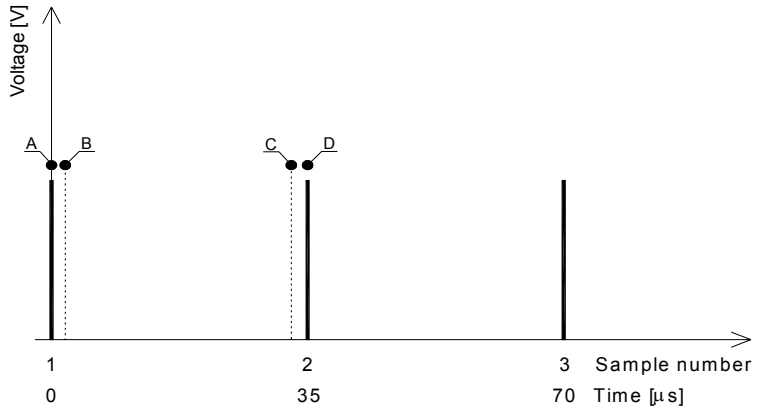

Figure 6.9 Sampling rate of 28,44 kHz results in maximal error of 35µs.

The corresponding phase angle errors of particular harmonics are given Table 6.2.

Harmonic order [-]	1	5	7	11	13	23	25	35	37	47
Max Error δ[º]	0,63	3,15	4,41	6,93	8,19	14,5	15,8	22,1	23,3	29,6

Table 6.2 Maximal errors in the phase angles of particular harmonics due to the sampling of the triggering input at the rate of 28,44 kHz.

Two kinds of synchronization errors could be distinguished:

- Synchronization error in time, between consecutive snapshots of the same Omicron unit
- Synchronization error between different measuring units for the same snapshot

The maximal error between consecutive snapshots (m1 and m2) of one unit is $\pm$ 35µs and the maximal synchronization error between different Omicron units (m1 and m2) for the same snapshot is $\pm$ 35µs. The maximal synchronization error δ between different Omicron units for consecutive snapshots (m1 and m2) is also $\pm$ 35µs, as shown in Table 6.3.

m1 [µs]	m2 [µs]	difference [µs]
0	0	t
35	0	t-35
35	35	t
0	35	t+35

Table 6.3 Maximum synchronization error for a single snapshot is always positive, but the difference between two snapshots may be positive or negative, t – time between snapshots.

This synchronization error δ resulted in magnitude error ε when calculating voltage increments $\Delta U = U - U'$, as shown in Figure 6.10 (a) and (b). The magnitude of the voltage increments depends on the synchronization error δ as well as on the phase shift α between both vectors U and U'. For values of α close to 0 º or 180 º, the magnitude error ε is small, and it is larger if α is close to 90 º or 270 º, as can be seen in Figure 6.10 (b).

When looking at Figure 6.10 (b) it can be noticed that it is possible to express the dependence of magnitude of voltage increments ΔU on angles δ and α by the following formula:

$$\Delta U = U - U' \cdot \cos(\alpha \pm \delta). \tag{6.9}$$

Where ΔU is the voltage increment, U is the voltage at harmonic h measured before line disconnection, U' is the voltage at harmonic h measured after line disconnection, α is phase shift between voltage vectors U and U' as a result of disconnection of the line and δ is the synchronization error.

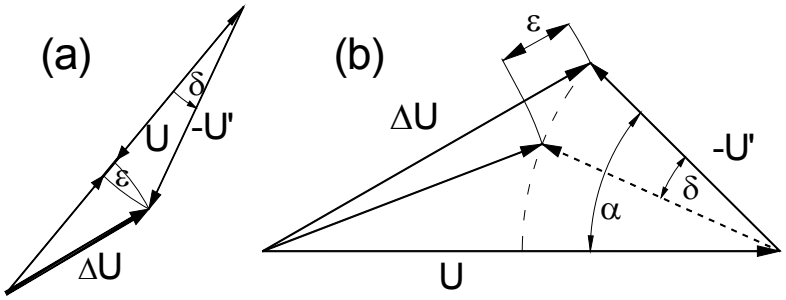

Figure 6.10 Synchronization error δ resulted in the magnitude error ε of the voltage increments (a) – for $\boldsymbol{\alpha = 0^o}$, (b) – for larger α magnitude error ε is higher.

6.8 Measured harmonic voltages and calculated voltage increments

Harmonic voltage amplitudes and phase angles before line disconnection (denoted U) and after line disconnection (denoted U') measured at substations NVV5, FER5 and TJE5 are shown in Figure 6.13, Figure 6.12 and Figure 6.11.

It can be seen that at all the substations, the levels of 5^{th} and 7^{th} harmonic are almost the same. The reason is that these harmonic frequencies are not filtered by the harmonic filters installed on the transmission level. Another explanation is that since these harmonics are injected from the lower voltage distribution networks, which are connected to the transmission network practically at every 150 kV node, the injection of these harmonics is quite uniformly distributed. It can be also seen that the switching of the line didn't affect much the amplitudes of 5^{th} and 7^{th} harmonic, but there is a little change in the phase angles.

At the NVV5 and FER5 substations, the harmonics of order 11^{th} and 13^{th} have the highest amplitudes, from 0,5% up to 0,9%. This is because these harmonic frequencies are generated both, at the lower voltage levels and by the 12-pulse converters of HVDC links. There are no harmonic filters installed at NVV5 and FER5 substations.

At the NVV5 substation, the effect of the disconnection of the line FER5-NVV5-0 causes relatively large increase in the amplitudes of the high order harmonics, namely 37^{th} and 47^{th}.

This is caused by the fact that 37^{th} and 47^{th} harmonics are injected from the HVDC station VHA5 directly to the NVV5 substation (through a single overhead line), and therefore, by disconnecting the line FER5-NVV5-0, the impedance "seen" by harmonic currents injected from the VHA5 substation is higher; hence harmonic voltages are also higher.

These higher order harmonics have rather low amplitudes at TJE5 and FER5 substations and are not affected to such an extent by the switching of the line. This confirms that the higher order harmonic frequencies tend not to propagate for large distances [Arrillaga].

It can be seen that at the TJE5 substation, the highest amplitudes have the low order harmonics, 5^{th} and 7^{th}, the source of which are typically the loads installed at the lower voltage levels. 11^{th} and 13^{th} harmonic, as well as 23^{rd}, 25^{th} and higher orders are filtered by the harmonic filters installed at this substation (characteristics of the filters are shown in chapter 3, section 3.4.2).

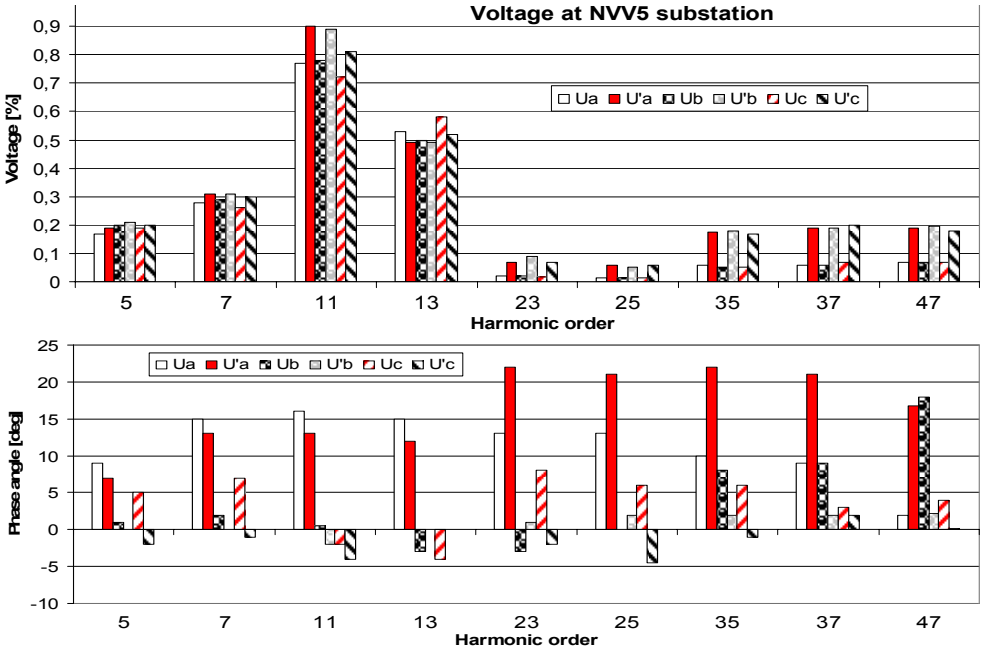

Figure 6.11 Harmonic voltages U and U' measured at substation NVV5.

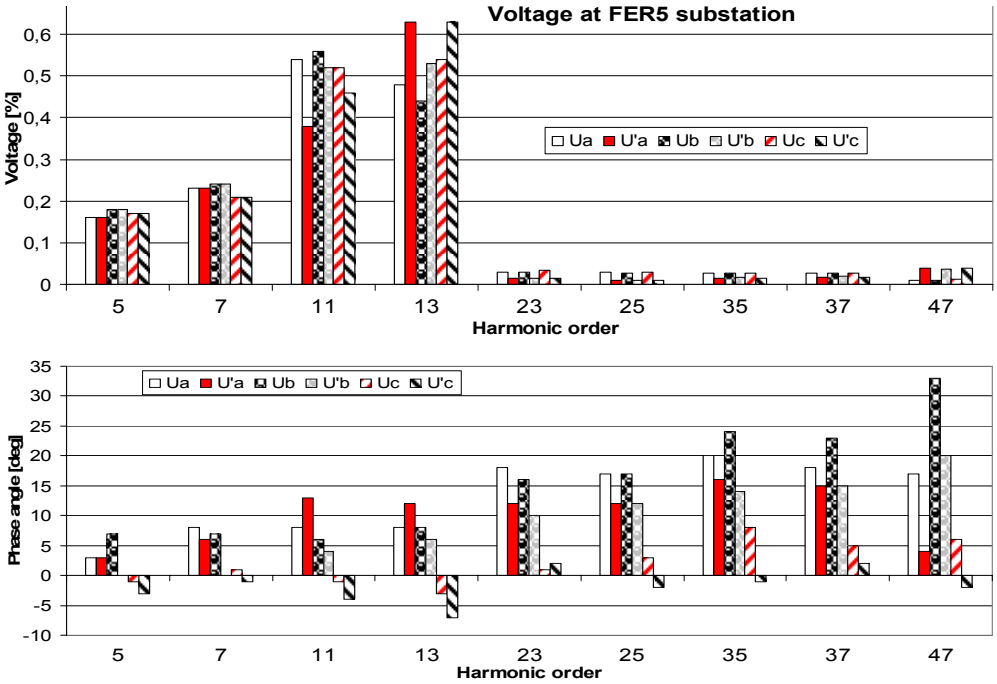

Figure 6.12 Harmonic voltages U and U' measured at substation FER5.

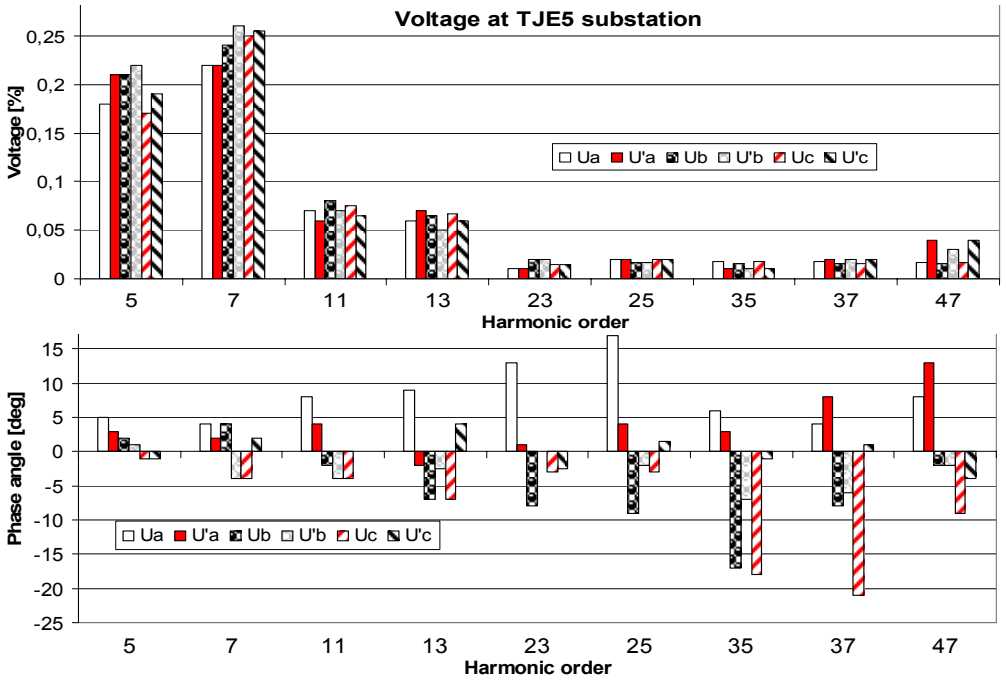

Figure 6.13 Harmonic voltages U and U' measured at substation TJE5.

These measurement results will be used for calculation of voltage increments that are to be used for model verification. To obtain the voltage increments ΔU, voltages U and U' are geometrically subtracted. Additionally, the effect of the synchronization error δ is calculated using equation (6.9). The resultant increments $\Delta U \pm \varepsilon$ are shown in Figure 6.14 on page 167. In this figure the effects of maximal synchronization error δ resulting in magnitude error ε are shown by the error bars. For the purpose of illustration, voltage increments for 25th harmonic are magnified on the upper plot. It can be seen that for phase C, both the maximal and minimal synchronization error δ resulted in positive magnitude error ε_c. Therefore the minimal value of voltage increment can be ΔU_c (without any error) and the maximal value of voltage increment can be $\Delta U_c + \varepsilon_c$. It is different for phase A, where the minimal synchronization error δ resulted in negative magnitude error ε_a, and therefore the minimal value of voltage increment can be $\Delta U_a - \varepsilon_a$, and maximal $\Delta U_a + \varepsilon_a$,.

It can be noticed that the voltage increments ΔU at TJE5 substation are the lowest - switching of the power line didn't affect the harmonic levels at this substation that much. It is firstly, because this substation is located in a distance from the disconnected line, and secondly, because of the harmonic filters installed directly at this substation. It can be seen that the incremental values are especially low at the 23rd and 25th harmonic; frequencies to which the filters are tuned.

The highest incremental values are for the 5th and 7th harmonic.

It can be also seen that in general, at all three substations, higher order harmonics have smaller amplitude errors ε than lower order harmonics. This is because the higher harmonics have generally lower amplitudes than the low order harmonics, so the errors ε that are shown in Figure 6.14 in absolute values are lower for these higher order harmonics, in accordance with equation (6.9).

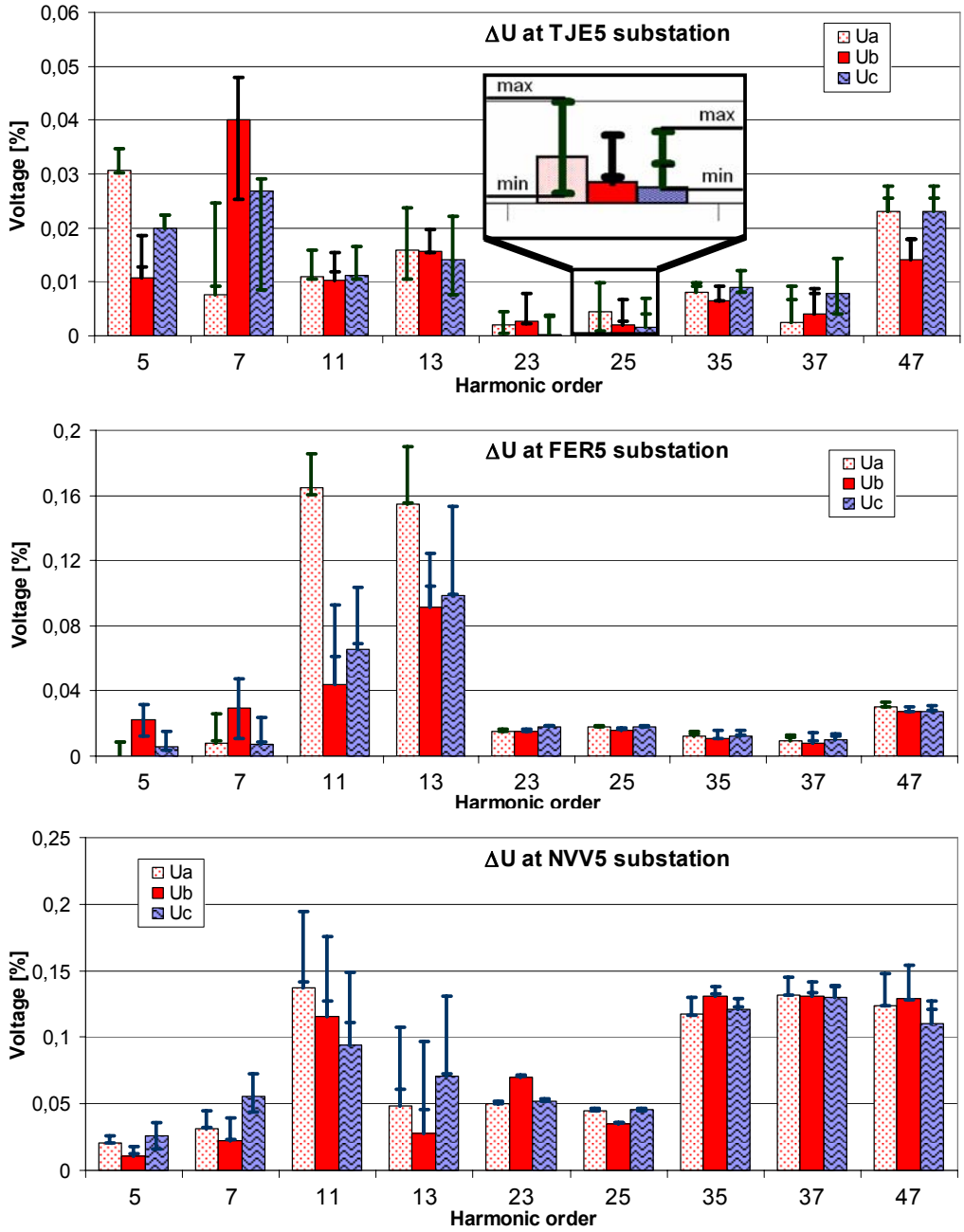

Figure 6.14 Harmonic voltage increments ΔU=U-U' calculated for all three substations, TJE5 (upper plot), FER5 (middle plot) and NVV5 (lower plot). The maximal and minimal magnitude error ε (result of synchronization error δ) is shown by the error bars.

These calculated voltage increments will be used for verification of the linear network model and this is described in the following sections of this chapter.

6.9 Effect of the synchronization error of the current measurement on the modelling approach

In order to use the determined in previous section voltage increments, according to the description presented in sections 6.5 and 6.6, the measured harmonic currents have to be injected in the computer network model, and the obtained in simulation voltage increments have to be compared with the voltage increments obtained from measurements, Figure 6.14. However, when the currents I_F, I'_F, I_N and I'_N were measured at both ends of the disconnected line FER5-NVV5-0, the same maximal synchronization error δ between consecutive snapshots or measurements made at different substations is present. The values of these harmonic currents are shown in Figure 6.15 and Figure 6.16. In order to account for the synchronization error δ, the phase angle error from Table 6.2 shall be added to the measured current phase angles.

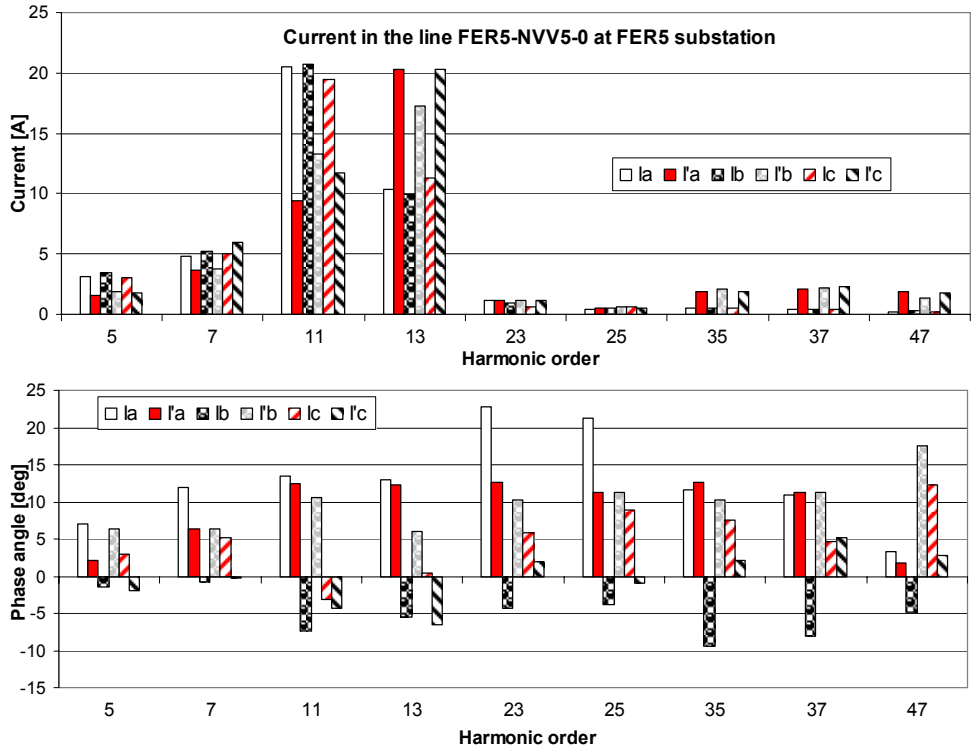

Figure 6.15 Magnitude (upper plot) and phase angle (lower plot) of harmonic currents measured at FER5 substation before line disconnection (I_F = Ia, Ib, Ic) and measured after line disconnection (I'_F = I'a, I'b, I'c).

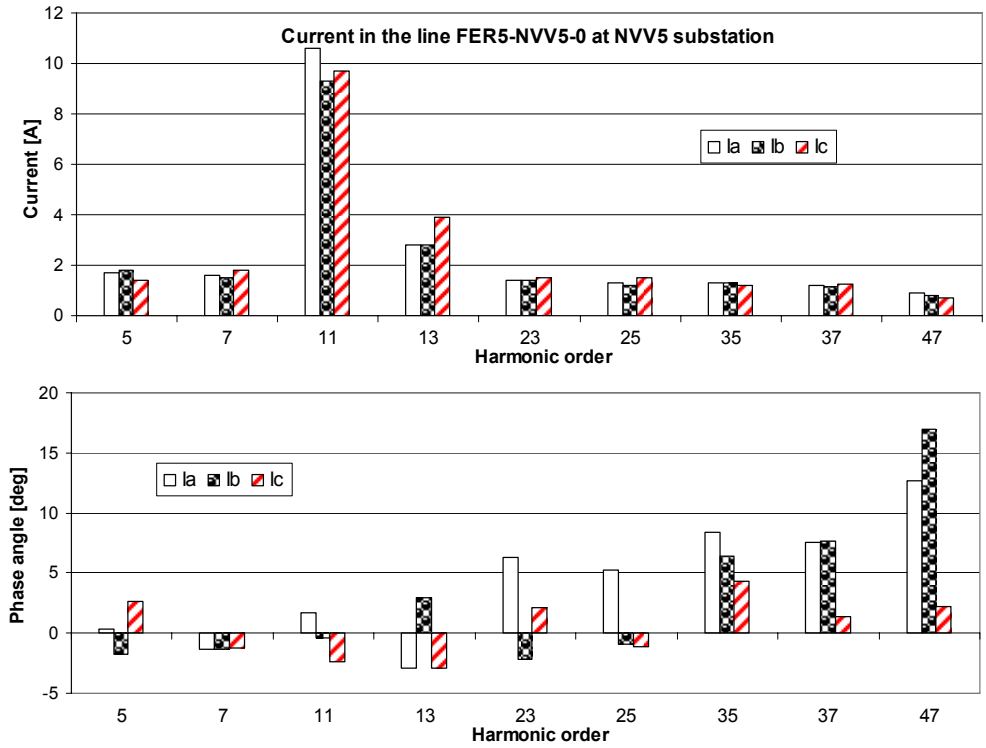

Figure 6.16 Magnitude (upper plot) and phase angle (lower plot) of harmonic currents measured at NVV5 substation before line disconnection (I_N = Ia, Ib, Ic). After line disconnection $I'_N = 0$.

There is no synchronization error between current and voltage harmonics measured at one substation during one snapshot, because all channels are sampled synchronously. In order to analyze the effects of this synchronization error on the results of verification, all possible combinations (extreme cases) have to be studied, as shown in Table 6.4.

IF	**IN**	**UF**	**UN**	**I'F**	**I'N**	**U'F**	**U'N**
Synchronization error [°]		Resultant voltage harmonics		Synchronization error [°]		Resultant voltage harmonics	
0	0	UF_{00}	UN_{00}	0	-	$U'F_0$	$U'N_0$
δ	0	$UF_{\delta 0}$	$UN_{\delta 0}$	δ	-	$U'F_\delta$	$U'N_\delta$
0	δ	$UF_{0\delta}$	$UN_{0\delta}$	-	-	-	-
δ	δ	$UF_{\delta\delta}$	$UN_{\delta\delta}$	-	-	-	-

Table 6.4 Synchronization error δ makes it necessary to analyze different variants of the injected harmonic currents I_F and I_N, with the initial phase shift 0 or δ. In total of 8 different results of voltage increments ΔU=U-U' can be obtained due to the synchronization error.

Due to the synchronization error, there can be 2 different values of the phase angle of current harmonics for currents at each end of the line (I_F and I_N) and 2 different values of the phase angle of current harmonics for current at NVV5 substation, after line disconnection. It results in 4 different values of harmonic voltages at both substations FER5 and NVV5 before line disconnection and 2 different values of harmonic voltages at both substations FER5 and NVV5 after line disconnection. At the end it makes in total 8 combinations of the voltage increments ΔU=U-U' that will be obtained from simulations. Therefore 8 cases had to be modelled, as listed by (6.10).

$$
\begin{aligned}
&\textit{CASE } 1\\
&\Delta U_F^{00-0} = U_{F00} - U'_{F0};\Delta U_N^{00-0} = U_{N00} - U'_{N0};\Delta U_T^{00-0} = U_{T00} - U'_{T0}\\
&\textit{CASE } 2\\
&\Delta U_F^{00-\delta} = U_{F00} - U'_{F\delta};\Delta U_N^{00-\delta} = U_{N00} - U'_{N\delta};\Delta U_T^{00-\delta} = U_{T00} - U'_{T\delta};\\
&\textit{CASE } 3\\
&\Delta U_F^{\delta 0-0} = U_{F\delta 0} - U'_{F0};\Delta U_N^{\delta 0-0} = U_{N\delta 0} - U'_{N0};\Delta U_T^{\delta 0-0} = U_{T\delta 0} - U'_{T0};\\
&\textit{CASE } 4\\
&\Delta U_F^{\delta 0-\delta} = U_{F\delta 0} - U'_{F\delta};\Delta U_N^{\delta 0-\delta} = U_{N\delta 0} - U'_{N\delta};\Delta U_T^{\delta 0-\delta} = U_{T\delta 0} - U'_{T\delta};\\
&\textit{CASE } 5\\
&\Delta U_F^{0\delta-0} = U_{F0\delta} - U'_{F0};\Delta U_N^{0\delta-0} = U_{N0\delta} - U'_{N0};\Delta U_T^{0\delta-0} = U_{T0\delta} - U'_{T0};\\
&\textit{CASE } 6\\
&\Delta U_F^{0\delta-\delta} = U_{F0\delta} - U'_{F\delta};\Delta U_N^{0\delta-\delta} = U_{N0\delta} - U'_{N\delta};\Delta U_T^{0\delta-\delta} = U_{T0\delta} - U'_{T\delta};\\
&\textit{CASE } 7\\
&\Delta U_F^{\delta\delta-0} = U_{F\delta\delta} - U'_{F0};\Delta U_N^{\delta\delta-0} = U_{N\delta\delta} - U'_{N0};\Delta U_T^{\delta\delta-0} = U_{T\delta\delta} - U'_{T0};\\
&\textit{CASE } 8\\
&\Delta U_F^{\delta\delta-\delta} = U_{F\delta\delta} - U'_{F\delta};\Delta U_N^{\delta\delta-\delta} = U_{N\delta\delta} - U'_{N\delta};\Delta U_T^{\delta\delta-\delta} = U_{T\delta\delta} - U'_{T\delta};
\end{aligned}
\tag{6.10}
$$

If all of these voltage increments ΔU obtained from simulations with the effects of the synchronization errors included, will have the magnitudes equal to the magnitudes of voltage increments ΔU obtained from measurement (shown in Figure 6.14, with the effects of synchronization error taken into account), then this can be considered as an indication that the harmonic model created and adjusted using the DIgSILENT PowerFactory software is reflecting the behavior of the real physical power network.

6.10 Modelling harmonic currents in PowerFactory.

The ideal ac current source model available in PowerFactory software can be used both in the frequency and time domain simulations. For the frequency domain simulations, the harmonic spectrum of the current source can be defined as a balanced or unbalanced spectrum. The defined harmonic spectrum is a separate type object (TypHmcCur) that the current source refers to [PowerFactory]. In case of balanced systems, only characteristic harmonics of orders 5, 7, 11, 13, 17, etc., can be defined. In the unbalanced case, magnitude and phase angle of each phase can be chosen individually for each harmonic frequency. The quantities of the spectrum type are rated to current at fundamental frequency. The actual harmonic current I_h at frequency f_h is calculated by [PowerFactory]:

$$I_h = k_h \cdot e^{\Delta\varphi_h} \cdot I_1 e^{\varphi_1}, \tag{6.11}$$

where

$$k_h = \begin{Bmatrix} I_h / I_1 \text{ if balanced} \\ I_{ah} / I_{a1} \text{ if unbalanced} \quad \text{phase a} \\ I_{bh} / I_{b1} \text{ if unbalanced} \quad \text{phase b} \\ I_{ch} / I_{c1} \text{ if unbalanced} \quad \text{phase c} \end{Bmatrix},$$

$$\Delta\varphi_h = \begin{Bmatrix} \varphi_h/\varphi_1 \quad if \text{ balanced} \\ \varphi_{ah}/\varphi_{a1} \text{ if unbalanced} \quad \text{phase a} \\ \varphi_{bh}/\varphi_{b1} \text{ if unbalanced} \quad \text{phase b} \\ \varphi_{ch}/\varphi_{c1} \text{ if unbalanced} \quad \text{phase c} \end{Bmatrix}.$$

The values at the fundamental frequency, I_1 and φ_1, are taken from a normal load-flow calculation, which is preceding a harmonic load-flow calculation.

6.10.1 Connecting ideal current sources. Displacement factor

To both substations FER5 and NVV5, three additional nodes were connected, two to substation FER5 and one to substation NVV5, as shown in Figure 6.17. To these three substations, harmonic current sources were connected, one for each phase. These current sources were injecting harmonic currents: I_F, I_N and I'_F. The fundamental frequency component of these currents was injected by an additional element, which was a linear unbalanced load. In the PowerFactory software, in order to define the phase shift between the fundamental frequency current and the fundamental frequency phase voltage, the displacement factor rather than the phase angle needs to be defined. The calculated displacement factor for the fundamental frequency components is shown in Table 6.5.

	Displacement factor before line disconnection					
	FER5			**NVV5**		
	Phase A	Phase B	Phase C	Phase A	Phase B	Phase C
Angle [º]	11,39	12,46	9,77	-167,79	-168,08	-169,76
Power factor	0,98031	0,97645	0,9855	-0,97738	-0,97844	-0,98407
	Displacement factor after line disconnection					
	FER5			**NVV5**		
	Phase A	Phase B	Phase C	Phase A	Phase B	Phase C
Angle [º]	88,36	88,31	85,83	-	-	-
Power factor	0,02862	0,02949	0,07272	-	-	-

Table 6.5 Calculated power factor for the fundamental frequency components of the current flowing into the line FER5-NVV5-0, before and after the disconnection at one end.

Phase angles of harmonic currents injected by the current sources were related to the fundamental frequency component injected by this linear unbalanced load. Harmonic amplitudes were related to the rated current of the current sources that was set to 100 ampers. Harmonic phase angles were related to the fundamental frequency current. The phase shift between fundamental frequency current and voltage components was entered by the help of the displacement factor from Table 6.5. For example, the dialog box of the load injecting the fundamental frequency component of the current at substation FER5 before line disconnection is shown in Figure 6.18, and the dialog box of the respective current source for phase A is shown in Figure 6.19.

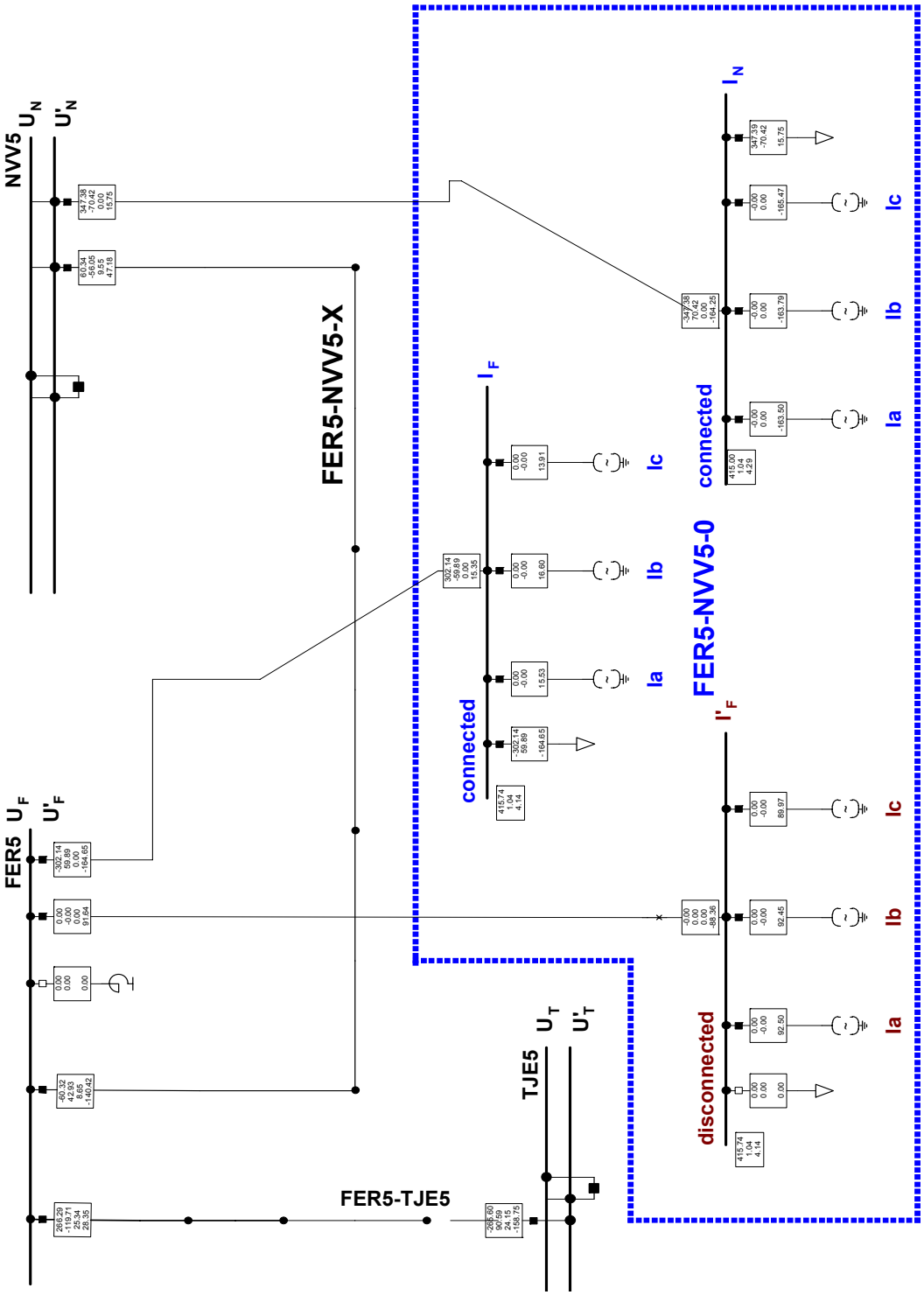

Figure 6.17 Example of PowerFactory simulations with part of the network with substations NVV5, FER5 and TJE5 shown. Line FER5-NVV5-0 is disconnected from both substations FER5 and NVV5 and current sources are connected instead to inject harmonic currents I_N, I_F and I'_F. Compensating reactor at FER5 substation is disconnected.

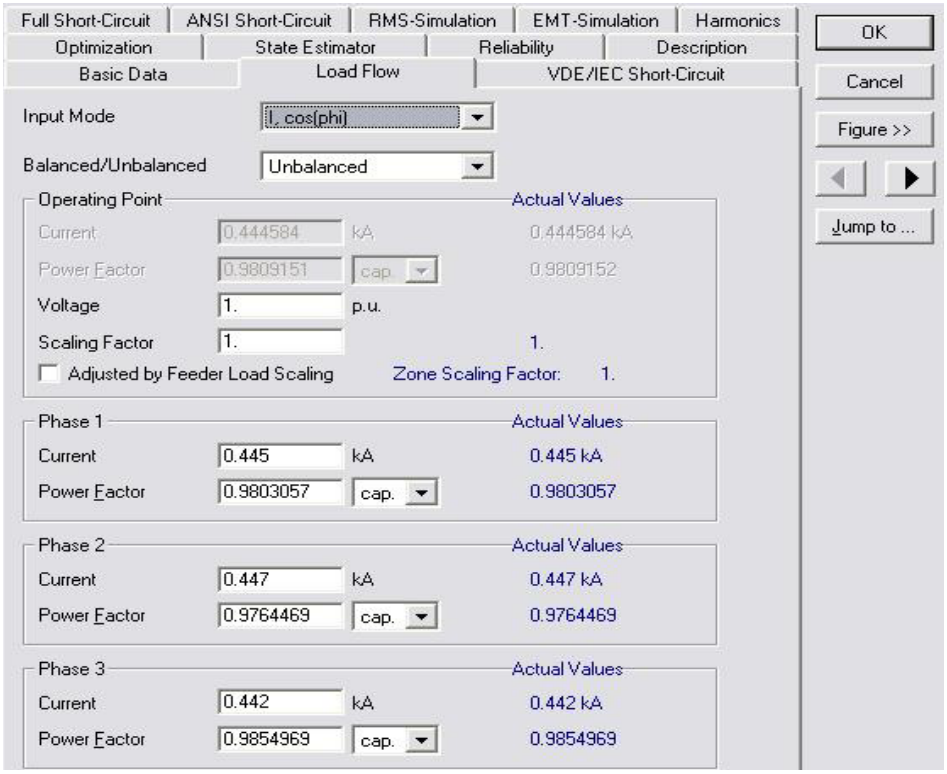

Figure 6.18 Dialog box of the additional linear unbalanced load, which was injecting fundamental frequency current component of the current I_F.

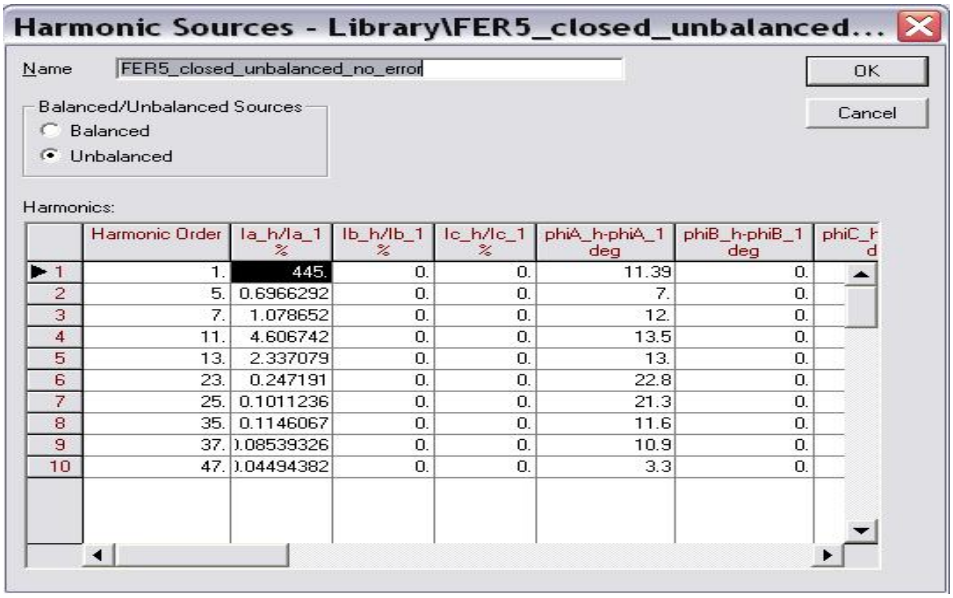

Figure 6.19 Example dialog box for phase A of current I_F. Amplitudes were related to the rated current and phase angles of the harmonic currents were related to the fundamental frequency component.

When I_F and I_N currents were injected, the harmonic voltage components of the bus voltages at substations TJE5 – U_T, FER5 – U_F, and NVV5 – U_N, were determined, before line disconnection. In the second step, the values after line disconnection are determined, by injecting only the currents I'_F. In order to determine the voltage increments $\Delta U=U-U'$, voltages obtained after line disconnection should be subtracted from the voltages obtained before line disconnection.

It can be however noticed that the easier, alternative way of calculating the voltage increments could be by taking advantage of the superposition principle, i.e. all currents at both ends of the line before and after the disconnection shall be injected into the harmonic model simultaneously, but current after line disconnection should be taken with the opposite sign: I_F, I_N and -I'_F. In this way, the result of harmonic load-flow calculation of the harmonic voltages at all three substations will be the voltage increments ΔU_T, ΔU_F and ΔU_N that can be directly compared with the increments obtained from the measurements, which were shown in Figure 6.14 on page 167.

6.10.2 Absolute phase angles.

PowerFactory software displays the phase angles of fundamental frequency and higher harmonic components as the absolute phase angle values against a global reference. These values differ from the phase angles of particular harmonics shifted with respect to the fundamental frequency components, as it was defined at the harmonic source dialog, shown in Figure 6.19 on page 173.

In order to be able to directly check and compare the absolute phase angles φ_{Ih}^{ABS} with the phase angles φ_{Ih} related to fundamental frequency component, the following general formula was derived:

$$\varphi_{Ih}^{ABS} = \left[\left(\frac{\left(\varphi_{I1}+\varphi_{U1}^{ABS}\right)\cdot h+\varphi_{Ih}}{360}\right)-\left(\mathbf{nint}\left(\frac{\left(\varphi_{I1}+\varphi_{U1}^{ABS}\right)\cdot h+\varphi_{Ih}}{360}\right)\right)\right]\cdot 360\,, \qquad (6.12)$$

where h is the harmonic order, φ_{Ih}^{ABS} is the absolute phase angle of harmonic of order h, φ_{I1} is the displacement angle of fundamental frequency current with respect to the fundamental frequency voltage, φ_{U1}^{ABS} is the absolute phase angle of the fundamental frequency voltage, φ_{Ih} is the phase angle of a harmonic current component with respect to the fundamental frequency component and nint is the nearest integer function and is defined such that the result is the integer number closest to the actual value.

Thanks to equation (6.12), by knowing harmonic phase angles with respect to fundamental frequency current, the displacement angle of fundamental frequency current with respect to the fundamental frequency voltage and the absolute value of phase angle of fundamental frequency voltage component, it is possible to calculate and verify the absolute phase angles, which are used in PowerFactory.

For the purpose of illustration, the absolute phase angles of the fundamental frequency component of the supplying bus voltage at FER5 substation were set to $U_A = U\angle 0°$, $U_B = U\angle -120°$ and $U_C = U\angle 120°$. Phase angles of the fundamental and higher harmonic components of current I_F are given in the left part of Table 6.6, and calculated absolute angles are shown on the right side of this table.

I_F					Absolute			
	Ia ph[º]	Ib ph[º]	Ic ph[º]			Ia ph[º]	Ib ph[º]	Ic ph[º]
					UF1	0,00	-120,00	120,00
1	11,39	12,46	9,77		IF1	11,39	-107,54	129,77
5	7	-1,5	3		5	63,95	-179,20	-68,15
7	12	-0,7	5,2		7	91,73	-33,48	-166,41
11	13,5	-7,3	-3,1		11	138,79	-110,24	-15,63
13	13	-5,5	0,5		13	161,07	36,48	-112,49
23	22,8	-4,4	5,8		23	-75,23	42,18	110,51
25	21,3	-3,8	8,9		25	-53,95	-172,30	13,15
35	11,6	-9,4	7,5		35	50,25	-173,30	-130,55
37	10,9	-8,1	4,6		37	72,33	-27,08	126,09
47	3,3	-4,9	12,3		47	178,63	-19,28	-8,51

Table 6.6 Harmonic phase angles of the current I_F defined with respect to the fundamental frequency component are given in the left part of the table, and on the right side, there are the absolute harmonic phase angles, calculated using equation (6.12).

6.10.3 Verification results

As it was described by Equations (6.12), all 8 cases have been modelled, and the results of simulations have been compared with the results from measurements, separately for each phase. These results are shown below, in Figure 6.20, Figure 6.21 and Figure 6.22. A discussion of all these results is present in section 6.11.

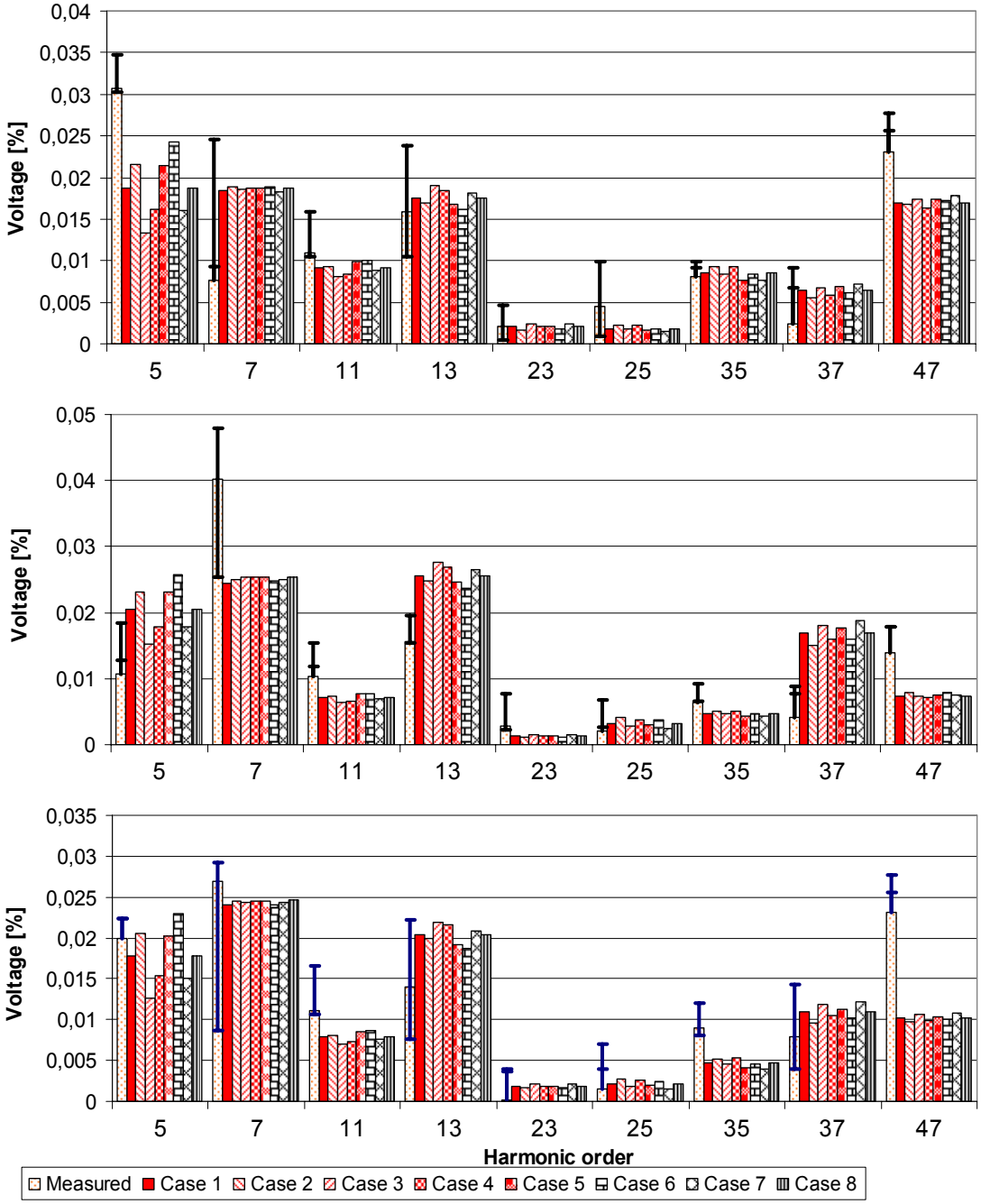

Figure 6.20 Voltage increments ΔU=U-U' at TJE5 substation. Results obtained from simulations compared to the voltage increments obtained from measurements. Upper plot – phase a, middle plot – phase b and lower plot – phase c. The bars from the left: ΔU obtained from the measurements, including the effect of synchronization error shown by the error bars ($\Delta U \pm \varepsilon$). Next are the bars showing voltage increments ΔU obtained from modelling cases 1 to 8.

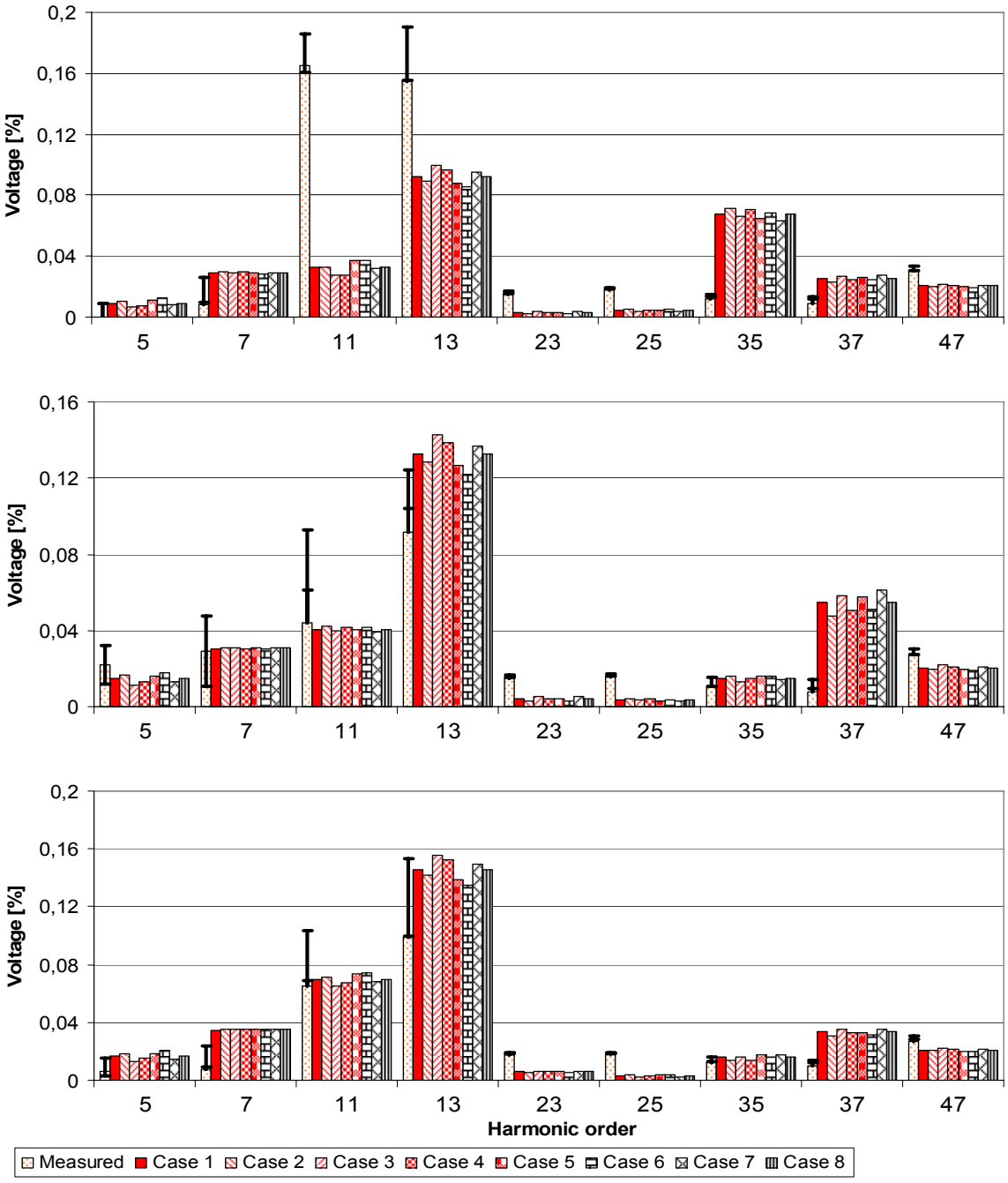

Figure 6.21 Voltage increments ΔU=U-U' at FER5 substation. Results obtained from simulations compared to the voltage increments obtained from measurements. Upper plot – phase a, middle plot – phase b and lower plot – phase c. The bars from the left: ΔU obtained from the measurements, including the effect of synchronization error shown by the error bars ($\Delta U \pm \varepsilon$). Next are the bars showing voltage increments ΔU obtained from modelling cases 1 to 8.

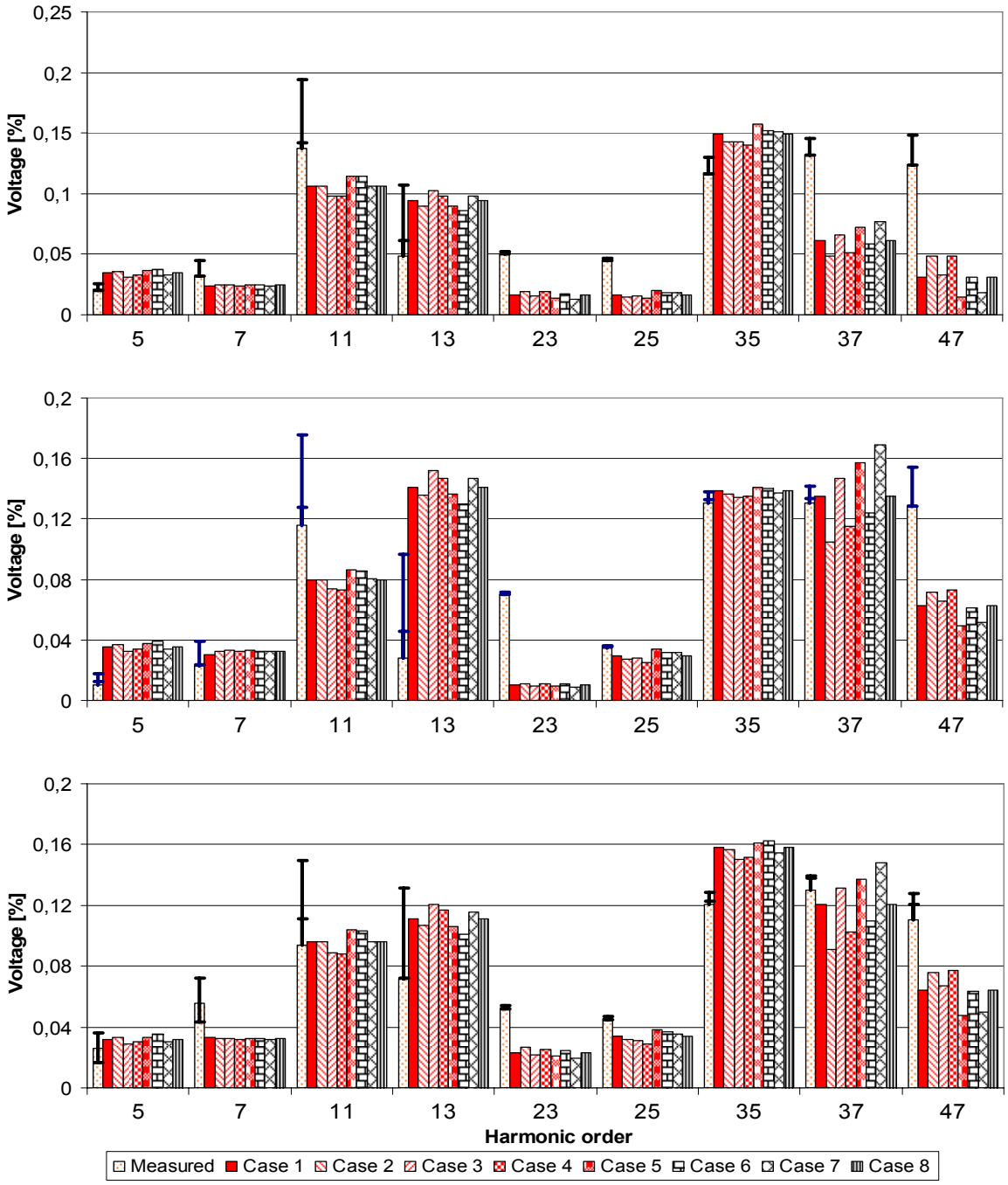

Figure 6.22 Voltage increments ΔU=U-U' at NVV5 substation. Results obtained from simulations compared to the voltage increments obtained from measurements. Upper plot – phase a, middle plot – phase b and lower plot – phase c. The bars from the left: ΔU obtained from the measurements, including the effect of synchronization error shown by the error bars ($\Delta U \pm \varepsilon$). Next are the bars showing voltage increments ΔU obtained from modelling cases 1 to 8.

6.11 Discussion of the results

Figure 6.20, Figure 6.21 and Figure 6.22 show the voltage increments $\Delta U \pm \varepsilon$ at substations TJE5, FER5 and NVV5. The first bar from the left, at each harmonic frequency is the voltage increment at this frequency, obtained (calculated) from the measured voltage values. The effect of synchronization error δ resulting in the magnitude error ε is shown by the error bars. The next 8 bars are the voltage increments obtained as the result of injection of the measured currents into the PowerFactory simulation model of the linear network. The voltage increments from simulations, in ideal case shall have values the same, or within the range determined by the magnitude errors ε, as the incremental values obtained from the measurements.

General observations

The general observation is that the voltage increments obtained from the simulations are not always the same as the voltage increments obtained from the measurements, but there is a reasonable correlation between them. For large values of voltage increments measured at a particular frequency, also the simulated voltage increments at this frequency are large. If the measured voltage increments have small values, then also the values obtained from simulations are small.

The exception is the 47th harmonic, where the differences are considerable, and reach 300%. It suggests that the model is not reflecting properly the behavior of the physical network at such high frequency. Also, there is a large difference for the 11th and 13th harmonic in phase A, at substation FER5. The origin of this difference has not been revealed.

The effect of synchronization error resulting in current phase angle errors didn't have much effect on the obtained in simulations incremental voltage values. These increments are similar for all 8 cases.

When taking into consideration the limits of the voltage increments due to the synchronization error $\Delta U \pm \varepsilon$, it can be said that most of the harmonic increments obtained in simulations are within these limits.

At all substations the voltage increments at 23rd and 25th harmonic are slow. At FER5 and NVV5 substations, the increments obtained from measurements are higher than these obtained from simulations. It suggests that the harmonic impedance of the model at this frequency is smaller than in reality. It is different at the TJE5 substation, where both the results of simulations and results of measurements show equally low increments. This is an indication that the harmonic filters installed at this substation are correctly represented in the model.

At all substations the voltage increments at 13th harmonic have relatively high amplitudes, both for measurements and simulations. This fact is also a sign of a correct behavior of the network model.

TJE5 substation

At TJE5 substation, the originally measured harmonic distortion was low, at the level 0,05% - 0,2%, as was shown in Figure 6.13.

As can be seen in the Figure 6.20, the lowest voltage increments have the 23rd and 25th harmonic. In general, all the incremental values are low, both in the measurements and in simulations. The average level is about 0,01%, which is very low. The reason of that is, besides the low level of harmonic distortion, also a large distance to the disconnected line, and consequently low influence on the voltage harmonics. However, such low values of both, the simulated and the measured voltage increments, indicate a good representation of the network by the computer model.

The highest incremental amplitudes, both in simulations and in measurements have the 5th and 7th harmonic, and the best agreement between measured and simulated values is for the harmonics 23rd, 25th, 35th and 37th. In general, the values of the voltage increments obtained from simulations are within the range shown by the synchronization error bars of the voltage increments obtained from the measurements.

FER5 substation

At FER5 substation, the originally measured harmonic distortion was higher than at TJE5 substation; the level was approx. 0,05% - 0,6%, as was shown in Figure 6.12.

Concerning the voltage increments, (see Figure 6.21), the lowest again are the 23rd and 25th harmonic. All the incremental voltage values at this substation have larger values than these at the TJE5 substation, but are lower than at the NVV5 substation. The highest increments are for the 13th harmonic, approx. 0,1% - 0,16%.

For most of the harmonics, the values of the voltage increments obtained from simulations are not exactly within the limits defined by the error bars, but can be said that are close to these values. The best agreement can be observed for the low order harmonics 5th and 7th.

NVV5 substation

At NVV5 substation, the originally measured harmonic distortion was the highest - the level was in the range 0,05% - 0,9%, as was shown in Figure 6.11.

As can be seen in the Figure 6.22, the lowest voltage increments have the following harmonic frequencies: 5th, 7th, 23rd and 25th, and the highest voltage increments have the following harmonic frequencies: 11th, 13th 35th and 37th.

In general, the values of the voltage increments obtained from simulations are within the range shown by the synchronization error bars of the voltage increments obtained from the measurements, except the 47th harmonic, and also 23rd and 25th, where the measured increments are higher.

6.12 Conclusion

In this chapter, first, an explanation to the question, why harmonic currents should be balanced to measure harmonic impedance of an unbalanced component, is given. It is concluded that in order to be able to determine all the terms of an impedance matrix; purely sequential harmonic current must be injected at a time; and the voltage response containing all sequences determined: from these values all the terms can be calculated. An alternative way is to inject harmonic current in one phase at a time and measure voltage responses in all the phases.

It is shown that the harmonic currents measured during the performed measurements at both ends of the disconnected line, were as much as 10% unbalanced; therefore the proposed in chapter 4 method of switching a series component would give erroneous results, because it assumes that the harmonic currents are purely sequential.

The developed alternative approach, in terms of verification of the model, allows reaching the aim, i.e. to verify a given model by measuring the voltage response to injected harmonic currents. Even if the injected harmonic currents are a “mixture” of all sequences, and the resultant voltage response is also a “mixture” of all sequences, it doesn’t matter – as long as the same value is obtained from simulations and measurements – the model is precise. The knowledge about the actual values of all the terms of the impedance matrix is not necessary.

The synchronization error between the GPS-synchronized units is given in μs. This error in time results in phase angle errors δ of measured particular harmonic components, and these phase

angle errors in turn result in magnitude errors ε of the calculated voltage increments at the substations NVV5, FER5 and TJE5.

The measured harmonic currents also contained the same synchronization error δ. Due to the fact that these currents were measured at two locations (both ends of the disconnected line), and at two instances, in total of eight combinations of currents, with different maximal values of the synchronization error δ were considered. These combined currents were injected into the linear, frequency dependent model of the Western transmission network of Energinet.dk, resulting in eight values of voltage increments at the busbars NVV5, FER5 and TJE5.

It is shown that these obtained in simulations incremental voltage values are not very much different with respect to each other.

A comparison is made between the eight values of voltage increments obtained from simulations and voltage increments calculated from direct voltage measurements at all three substations: NVV5, FER5 and TJE5.

The detailed discussion of the results of this verification is presented in previous section 6.11 on page 179. The main conclusions from this verification are:

The voltage increments obtained from the simulations are not exactly the same as the voltage increments obtained from the measurements; however the correlation between them is relatively good. For most of the harmonic frequencies the voltage increments obtained from simulations are within the limits $\Delta U \pm \varepsilon$.

At all substations, the agreement of voltage increments at the 47^{th} harmonic is poor; therefore the conclusion is that the model is not reflecting the behavior of the physical network correctly at such a high frequency.

As a final conclusion, it can be stated that the verification of the linear network model seemed to give quite acceptable results for the frequencies below the 23^{rd} harmonic, where the results of simulations are close to the results of measurements, taking the synchronization error into account. However, some of the apparent differences may be a result of change in the background harmonic distortion, which was assumed constant.

It has been shown that the verification approaches proposed in chapter 4 and in this chapter are theoretically a good way of verifying a linear model of power network at harmonic frequencies. However, in practice, the methods are quite difficult to apply, because they require very good synchronization between the measurements performed at different locations and at different instances.

Moreover, the background harmonic distortion, both the amplitude and the phase must not change during the measurement. To reach this condition, the time span between two consecutive measurements should be as short as possible, but of course the transients caused by switching of the component must decay. An alternative approach would be to perform continuously time domain measurement, so the signals are recorded before, during and after the switching of the component. Then, proper "slices" of the signals can be selected to be used for verification.

Switching a shunt capacitor and measuring continuously the time domain signals could be a good approach, provided that the harmonic currents flowing into this capacitor have such values that it would make a difference in harmonic voltages significant enough, to be measured and to calculate the voltage increments.

The third option that would be to use an external source of harmonics for instance an active filter. Such filter, if possible, could be controlled in a way, to inject harmonic currents for instance into

one phase at a time, and the resultant voltage harmonics in each phase should be measured, so all of the components of the impedance matrix could be determined. Such option was considered in this project for a while, but had o be abandoned, due to the costs of such operation.

Chapter 7

Hybrid time/frequency domain modelling of nonlinear components

In this chapter a method that has been developed during this PhD project work is described. Taking into consideration its principal features, the method should be named as: iterative, three-phase, hybrid – time/frequency load-flow method of modelling HVDC converters. The implementation of the method is described in detail. The results of verification are shown and convergence properties are analyzed. The full DPL source code of the method can be found in the attached compact disc.

7.1 Introduction

Modelling of nonlinear components in harmonic domain is time-consuming and difficult because a set of non-linear equations must be derived. Moreover, a different model must be created for each non-linear device [Bathurst], [Bathurst, 2000], [Bathurst, 2001], [Arrillaga], [Arrillaga, 1997], [Watson, 2005].

On the other hand, modelling of linear frequency dependent components in time domain also causes problems: for frequency-dependent untransposed transmission lines, the modal transformation matrices T_V and T_I are frequency-dependent [EMTDC] (see also chapter 3). If the calculation is to be performed in the frequency domain, it is easy to evaluate theses transformation matrices T at each frequency of interest. Therefore frequency domain modelling using the modal circuits gives exact solution [EMTDC], [Marti]. If the transmission line is to be modelled in the time domain, these transformation matrices T are assumed constant (like if they were balanced) or curve-fitted by rational functions [Marti], [EMTDC], [PowerFactory]. The fitting of transformation matrices T of some configurations of overhead lines may be problematic [Wedepohl], [Gustavsen], [Gustavsen, 1998], [Castellanos], [Abur]. An additional disadvantage of using time domain for modelling large frequency dependent networks is longer simulation time [EMTDC].

Therefore, to overcome such problems, hybrid methods can be developed, where linear frequency-dependent network is modelled in the frequency domain and nonlinear components are modelled in the time domain. According to the author's knowledge, not much work has been done in this area. The initially presented hybrid algorithm, developed by [Semlyen] is used for solution of single-phase systems. Hybrid time/frequency algorithms

"have potential (…) for the solution of larger single phase systems. It is an interesting alternative of solution in merit to its ability to represent the system components in their natural frame of reference, leading to efficient, robust periodic steady state solutions for the complete network. To date it has been successfully applied to the solution of single phase systems, being in progress its application to the periodic steady state solution of practical three phase systems.",

wrote [Medina] in 2004.

However already in May 2003 [Moreno] presented a three-phase load-flow in the frequency and time domains, where as the indication of the convergence he uses the differences in updated magnitudes of fundamental frequency bus voltages.

In this project, a three-phase HVDC model is developed in the hybrid time/frequency domain, where as the indication of convergence, the magnitudes and phase angles of the fundamental and low order characteristic harmonics will be used. In this way it is verified if the harmonic frequencies have reached the periodic steady state. As the nonlinear element, a three-phase, 12-pulse HVDC converter model is used. The model is implemented in the DIgSILENT PowerFactory software using the DLP language and verified with precise time domain simulations. The HVDC benchmark model will be used for that purpose. The model is presently limited to work for harmonic frequencies up to 2,5 kHz.

Chapter outline

This chapter is organized as follows:

First, a general idea of the developed hybrid time/frequency algorithm is presented. Next, flow-chart of the algorithm is shown, followed by a detailed description (33 points). The algorithm is verified against time domain simulation and the results of verification are shown. Next, the convergence process is discussed, and the process of reaching periodic steady state is shown, where the dynamically varying harmonic content of the converter currents is observed. At the end of the chapter, a limitation of the method is revealed and final conclusions are presented.

7.2 Basics of harmonic transfer through a six-pulse converter

HVDC converters generate harmonic voltages and currents on the DC and AC side, respectively. These harmonics can be separated into characteristic harmonics and noncharacteristic harmonics. A converter of p number of pulses in ideal case generates only characteristic voltage harmonics of order h=pk on the DC side and, current harmonics of orders h=pk$\pm$1 on the AC side (where k is an integer). HVDC converters generate idealized characteristic harmonics under the following assumptions [Arrillaga, 1998]:

1. The supply voltage is a purely positive sequence voltage and is purely sinusoidal, consisting only of the fundamental frequency.
2. The direct current is perfectly constant, which can be only achieved if the DC smoothing reactor has infinite inductance.
3. The valves begin conducting at equal time intervals.
4. The commutation impedances are the same in the three phases.

Moreover, in the absence of a commutation reactance, the commutation angle is zero and the converter will generate the idealized phase current waveforms, which after calculating their Fourier series, will contain characteristic harmonics of order pk$\pm$1 with a magnitude of $I_h=I_1/(pk\pm1)$, where I_1 is the magnitude of the fundamental frequency component.

Such ideal conditions are never met in practice [Arrillaga, 1998]. Apart from the other assumptions, the AC voltage will be always somewhat unbalanced and distorted. There are two reasons of that: the first reason are the unbalanced or nonlinear loads in the network and the second is the HVDC converter itself. The converter injects harmonic currents into the network impedance causing harmonic voltage drop and distortion of the bus voltage. This distorted bus voltage changes the spectrum of the harmonic currents generated by the converter. The changed current spectrum will in turn alter the bus voltage distortion, etc. A good way of portraying the harmonic transfer through a six-pulse converter is to use the transfer function concept [Arrillaga,

1997; pages 144-157]. Two transfer functions describe the interconnection between the dc and ac sides of the converter. The dc voltage is calculated by summing each phase voltage multiplied by its associated transfer function:

$$u_d = N\sum_{\psi} Y_{\psi dc} u_{\psi} \ , \tag{7.1}$$

where u_d is the dc side voltage, ψ = 0, 120 and 240 degrees for phases a, b and c, N is the converter transformer ratio, and u_ψ are the tree phase voltages. $Y_{\psi dc}$ has the values between -1 and 1, where 1 signifies a connection of the dc side positive bus to the phase in question, -1 signifies a connection of the dc side negative bus to the phase in question, 0 signifies no connection. Similarly the ac current is:

$$i_{\psi} = NY_{\psi ac} i_{dc}, \tag{7.2}$$

Where i_{dc} is the dc side current, and $Y_{\psi ac}$ is similar to $Y_{\psi dc}$, except that during the commutation period the ac current rises or falls in a continuous matter. Any frequencies present on the ac or dc side of the converter are subjected to exactly the same modulation process by the converter. Additionally the switching pattern of the HVDC converter bridges is affected by distortion in the ac voltage or dc current waveforms. As stated in [Arrillaga, 1998], the dc current directly affects the firing instants of the thyristors through the converter control, and the commutation period is directly affected by both ac voltage and dc current.

The modulation of the switching instances and the transfer function shapes involve approximations, which can be avoided by performing time domain simulations.

In the harmonic calculations of PowerFactory simulation software, power converters can be modelled as current sources injecting idealized harmonic spectra regardless of the voltage waveforms and the system impedance. The alternative is that it is possible to freely define the harmonic spectrum injected by a converter, but in such a case, this spectrum is also independent on the bus voltage and system impedance. To determine this actual harmonic spectrum of the converter, harmonic measurements could have been performed, or alternatively, a precise time domain simulation can be made from which these harmonic spectra can be computed.

7.3 General idea of the hybrid time/frequency algorithm

In simple words, the idea of the developed algorithm can be explained as follows. At the beginning, a 3-phase load-flow calculation is performed for the entire network containing both the linear and nonlinear part. All the loads and converters are linear in this calculation. From this calculation, the unbalanced positive, negative and zero-sequence voltages at the HVDC converter bus are obtained. In next step, these voltages are assigned to a voltage source that is used in the time domain simulation of the nonlinear network, see Figure 7.1.

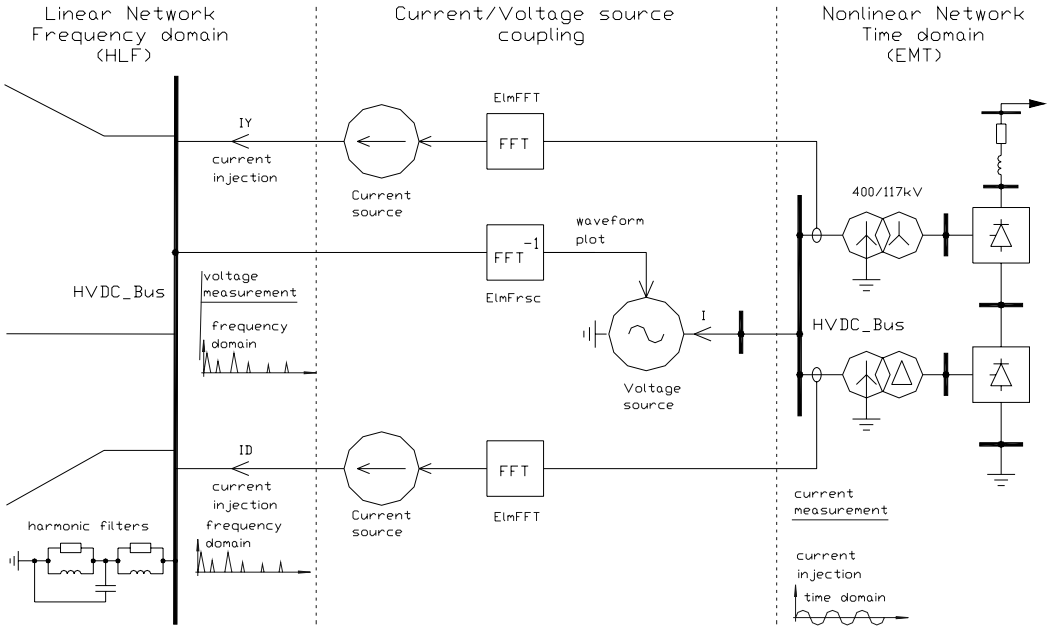

Figure 7.1 General idea of the developed hybrid time/frequency algorithm

Before the time domain simulation of the nonlinear network is performed, initial conditions are calculated, with the voltage source setpoint taken from the preceding load-flow. Next, the time domain simulation is run and the distorted three-phase currents of both converters are measured. After some initial oscillations, the periodic steady state is detected, and then the harmonic amplitudes and phase angles of the currents are calculated using FFT blocks. This is done for harmonics up to the 51st, and assigned to two, three-phase current sources. In the next step, these current sources are used in the direct harmonic analysis (in the software called harmonic load flow, HLF) of the linear part of the network. The harmonic flow is calculated and then the voltage at the bus HVDC_Bus is measured. The fundamental frequency unbalanced voltages are again measured and used to update the values used by the voltage source in the calculation of the initial conditions. The harmonic voltages up to 51st are measured, from which the inverse FFT is calculated and the distorted waveforms are assigned to the voltage source. Again time domain simulation is performed with the voltage source producing the distorted waveforms and new values of the harmonic currents are obtained. Again, after reaching the periodic steady state, the harmonic currents are calculated and assigned to the current sources, and a new direct harmonic analysis is performed. The convergence is reached when the differences in voltage harmonic amplitudes and harmonic phase angles calculated in consecutive iterations, for the following harmonics: 1st, 5th, 7th, 11th and 13th are less than predefined precision indexes.

Figure 7.2 on page 187 explains the basic principles of the hybrid method.

In Figure 7.2 (a) an example equivalent circuit is shown, with the voltage U_B at the interfacing bus linking the linear and the nonlinear networks. Z_S is the equivalent impedance of the linear network seen from the HVDC converter side, without the harmonic filters, Z_f is the impedance of harmonic filters, U_{th} is the Thévenin voltage of the network, I_{HVDC} is the HVDC converter current.

In practice, the HVDC converter harmonic current is not constant but depends on the value of distorted bus voltage U_B [Arrillaga], [Arrillaga, 1998]. This dependence may be represented by the converter Norton equivalent circuit with a constant current source and frequency dependent impedance Z_N, see Figure 7.2 (b). Converter harmonic current I_{HVDC} can be understood as a superposition of the constant current I_h and current I_N that flows as the result of bus voltage

distortion U_B. The linear part of the network can be represented as a voltage source of value U_B connected at the interfacing bus. For a network to be represented at any conditions, its equivalent Thévenin circuit is needed with the Thévenin voltage source behind an equivalent impedance. However, as shown in Figure 7.3 on page 188, if the impedance connected to the equivalent network is constant, the current *I* will have correct value even when the linear network is represented by a pure voltage source U_B. Therefore, in the time domain simulation of the hybrid method, the linear network can be replaced by a voltage source applying the initially sinusoidal bus voltage U_B to the HVDC converter. The converter will convert a part of the energy to harmonic frequencies and inject it back as harmonic currents superimposed on the fundamental frequency current.

This is illustrated in Figure 7.2 (c) - at fundamental frequency, and in Figure 7.2 (d) – at harmonic frequencies. As can be seen, at higher frequencies the only source of energy is the converter. Since the applied voltage is sinusoidal, harmonic currents see the voltage source as a short-circuit (assuming it has zero internal impedance). Therefore, the entire harmonic current I_h injected by the converter and not suppressed by the voltage source is short-circuited and flows freely, and its value is higher than when injected on the equivalent impedance of the linear network. In the next step, The FFT of this current I_{HVDC} is calculated and injected by a current source into the linear network, as shown in Figure 7.2 (e). This current injected into the full linear network impedance will cause harmonic voltage distortion that superimposed on the original bus voltage resulting in a new value U_B^1:

$$U_B^1 = \frac{Z_f}{Z_s + Z_f} U_{th} + \frac{Z_S \cdot Z_f}{Z_s + Z_f} I_{HVDC} \,. \tag{7.3}$$

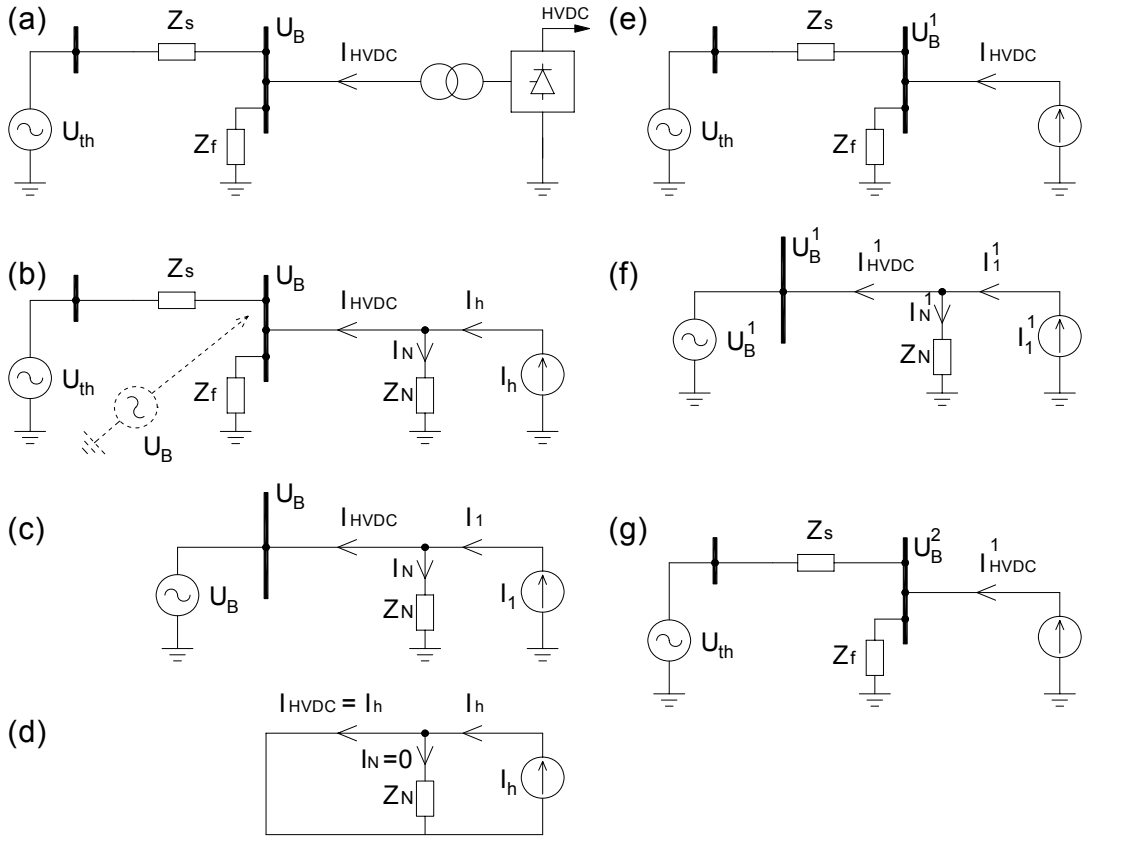

Figure 7.2 Hybrid calculation of the voltage U_B at the interfacing bus between the linear network and the nonlinear network. The symbols are described below.

In Figure 7.2 Z_S is the equivalent impedance of the network seen from the HVDC converter, without the harmonic filters, Z_f is the impedance of harmonic filters, U_{th} is the Thévenin voltage of the network (may be sinusoidal or distorted), I_{HVDC} is the HVDC converter current. (a) – Linear and nonlinear networks, (b) – HVDC converter replaced with its Norton equivalent circuit and linear network replaced with a voltage source of value U_B, (c) – equivalent circuit valid at fundamental frequency, illustrating the time domain simulation, (d) - equivalent circuit valid at harmonic frequencies, illustrating the time domain simulation, (e) - Equivalent circuit used for harmonic flows calculation in the linear part of the network, (f) – resultant interfacing bus voltage is updated to the value U_B^1, (g) - updated bus voltage value U_B^1 is used in the time domain simulation to update HVDC current value I_{HVDC}^1.

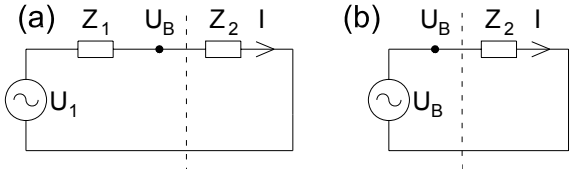

Figure 7.3 Voltage source U_1 and impedance Z_1 can be represented simply by a voltage source U_B if the impedance Z_2 is constant. Current I will be the same in cases (a) and (b).

However, this new voltage value U_B^1 is excessively distorted, because of the excessive harmonic current I_{HVDC}. Then the inverse FFT of the voltage U_B^1 is calculated and in the next step applied to the voltage source and the time domain simulation of the nonlinear network is run for the second time. A new value of converter current is obtained, I_{HVDC}^1. This time the value of the current is smaller than in reality because the harmonic components are suppressed by the excessive value of harmonic voltage U_B^1. Again, the FFT of this current I_{HVDC}^1 is calculated and injected with a current source back into the linear network, as shown in Figure 7.2 (g). This time the updated bus voltage U_B^2 is less distorted than in reality. In such a way, by performing simulations once in time domain, once in frequency domain, and injecting the updated harmonic currents I_{HVDC}^n and applying back the updated harmonic voltages U_B^n, an equilibrium is approached. The updated harmonic voltage U_B^n is alternating, one time is more distorted, one time less distorted than in reality. At the moment when the difference between two consecutive harmonic voltage values U_B^{n-1} and U_B^n is less than a predefined precision index ε, it is assumed that the convergence is reached and the converter harmonic current as well as the harmonic bus voltage are determined.

For the purpose of illustrating the effect of the distorted bus voltage applied to a six-pulse converter, a small time domain simulation has been made. In this simulation, the voltage applied to a converter had the value of 1 p.u. of the fundamental frequency. At the top of this voltage, an 11^{th} harmonic has been superimposed with amplitude of 0.3p.u. Three cases have been compared:

- pure sinusoidal voltage,
- sinusoidal voltage distorted with 11^{th} harmonic
- sinusoidal voltage distorted with 11^{th} harmonic, but shifted 180 degrees.

The result is shown in Figure 7.4. Figure 7.4 (a) shows the three applied voltages, Figure 7.4 (b) shows the resultant converter currents, and Figure 7.4 (c) shows the amplitude of the 11^{th} harmonic in the converter current for three cases. It can be seen that this harmonic amplitude had some level when supplied with pure sinusoidal voltage, but when the voltage was distorted, 11^{th} harmonic current had smaller or higher amplitude, depending on the phase of the applied harmonic voltage.

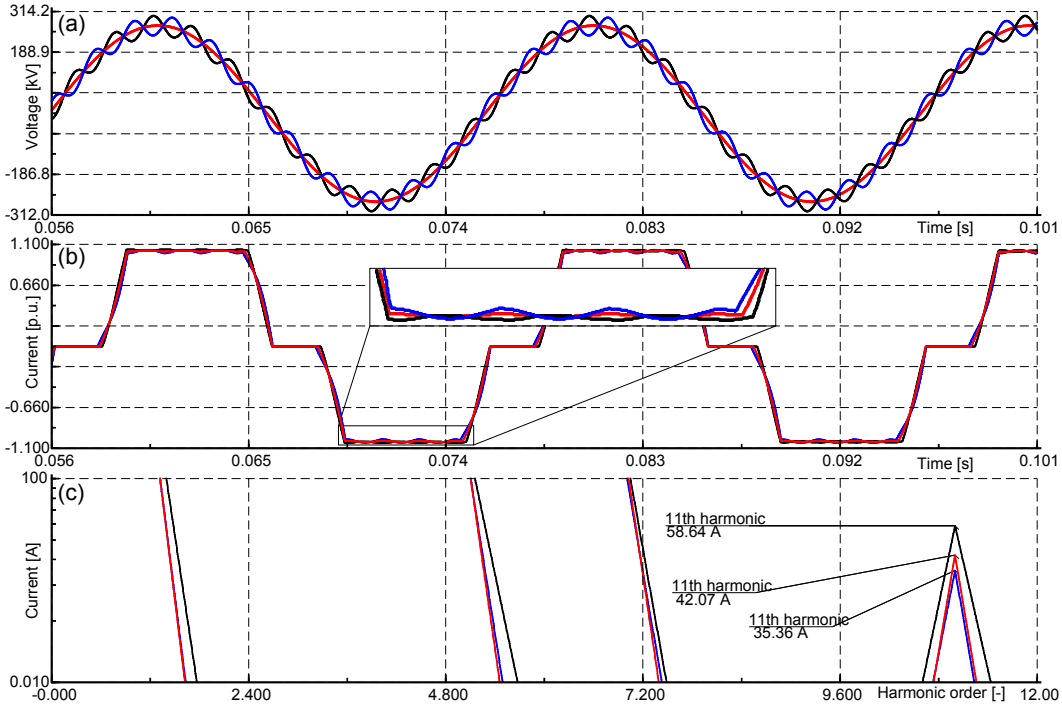

Figure 7.4 11^{th} harmonic flowing into the finite converter impedance. (a) – supplying voltage, (b) – resultant converter current, (c) – amplitude of 11^{th} harmonic current for three values of 11^{th} harmonic voltage, 0; $0{,}3\angle 0^{\circ}$ p.u. and $0{,}3\angle 180^{\circ}$ p.u.

7.4 Flow-chart of the Hybrid algorithm

The flow-chart of the developed and implemented in the DIgSILENT PowerFactory software hybrid algorithm is shown in Figure 7.5 on page 190, and its detailed description can be found in the following section 7.5 on page 191.

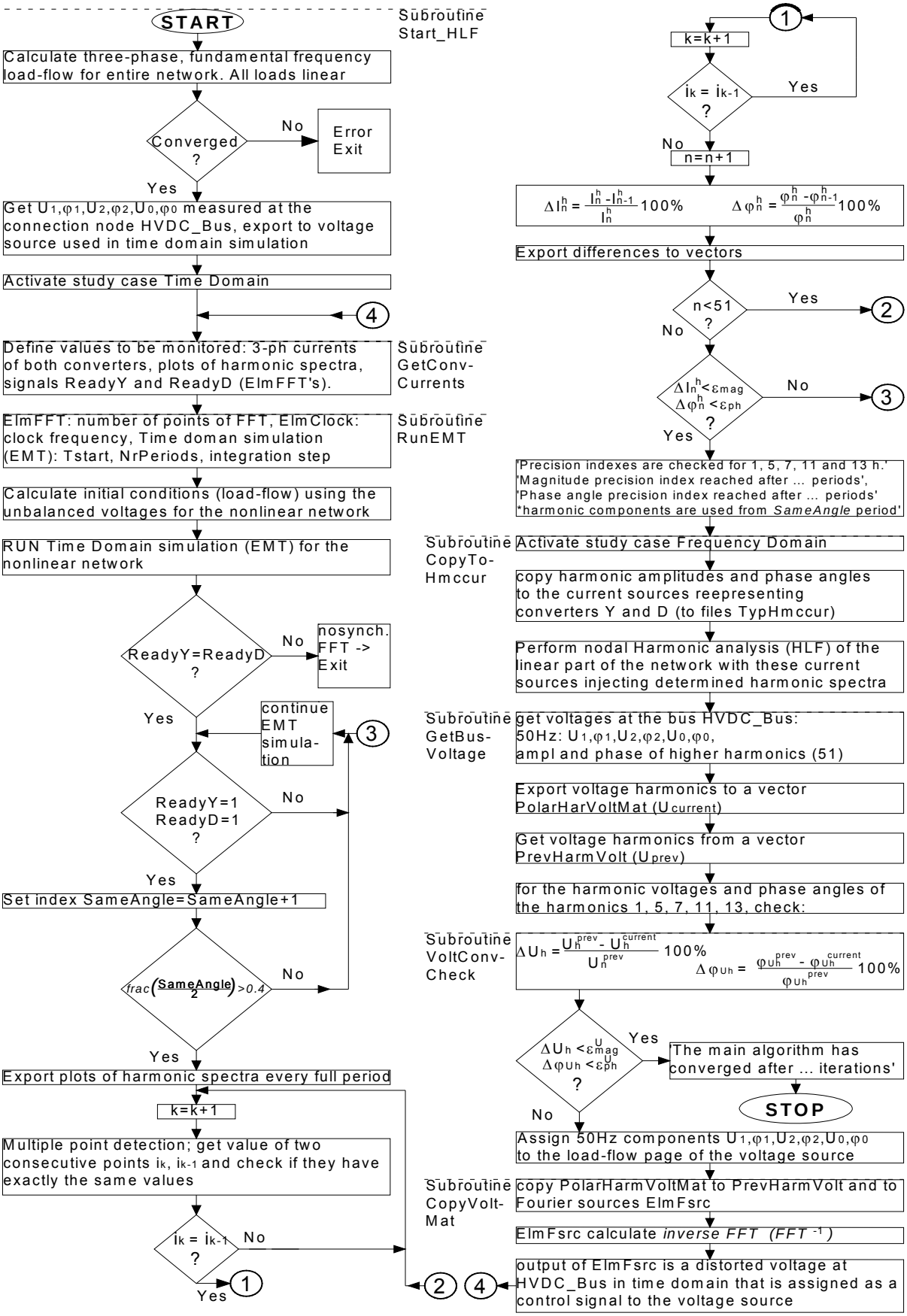

Figure 7.5 Flow-chart of the developed Hybrid Time/Frequency algorithm.

7.5 Detailed description of the algorithm

The algorithm has been implemented in the DIgSILENT PowerFactory software. Powerfactory has the capability of performing both time domain and frequency domain calculations. A modified HVDC benchmark model has been used for the implementation and testing of the algorithm, see Figure 7.6 [Szechtman]. The linear part contains additionally a small linear network. All the impedances in the linear network are lumped, and constant, not dependent on frequency. Therefore the entire model can be also precisely modelled purely in time domain, for verification purposes.

Two study cases have been setup, "Frequency domain" and "Time domain". Study case Frequency domain uses the entire network model shown in Figure 7.6. The harmonic voltage at the interfacing bus HVDC_Bus is calculated and monitored. The harmonic currents are assigned directly to both rectifiers Y and D. The time domain simulation is performed in the Time domain study case. A "system stage" of the network has been used in this study case, see Figure 7.8 on page 192. The system stage enables to create a new network based on the original one. This network in the system stage can be freely modified without any change to the original network. In this system stage the linear network has been removed and replaced with a voltage source.

The steps executed in the hybrid algorithm are described in the following 33 points:

1. For the transmission network shown in Figure 7.6, perform unbalanced, 3-phase, fundamental frequency load-flow. In this calculation the entire network is modelled, where all nonlinear loads are replaced with linear equivalents.

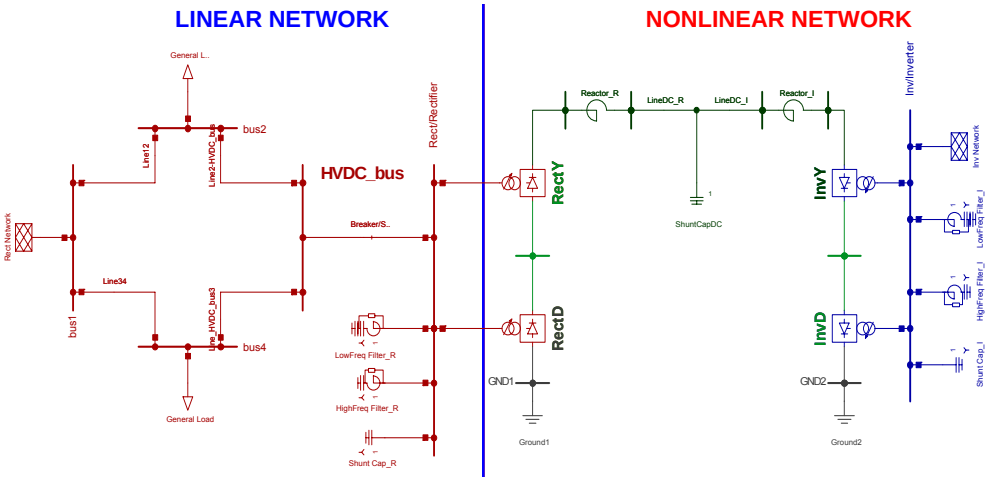

Figure 7.6 Model of the network used in the load flow and harmonic load flow calculation.

2. Get the unbalanced voltage values $u1, \varphi 1, u2, \varphi 2, u0, \varphi 0$ at the interfacing HVDC_bus and assign them automatically to the load-flow dialog of the AC Voltage source that will be used in the time domain simulation, see Figure 7.7.

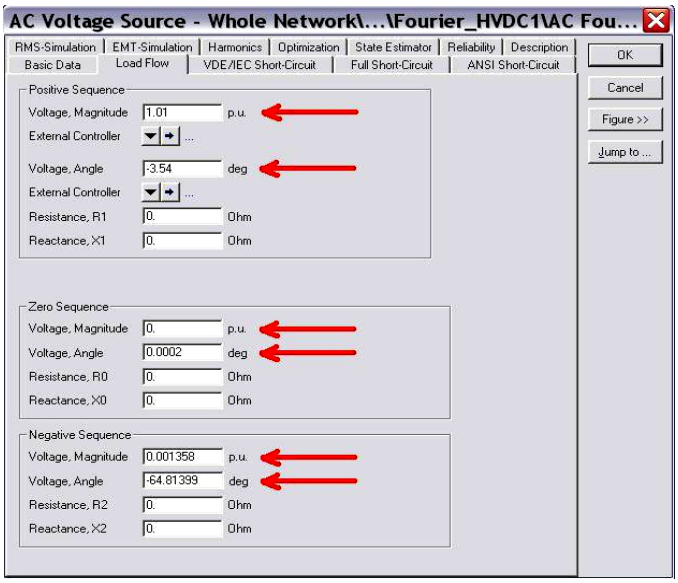

Figure 7.7 Load-flow dialog of AC Voltage source that will is used for initializing time domain simulation.

3. Activate study case Time domain. In this study case, only the nonlinear part of the network will be modelled – with the linear part replaced with a voltage source: AC Fourier Source, see Figure 7.8.

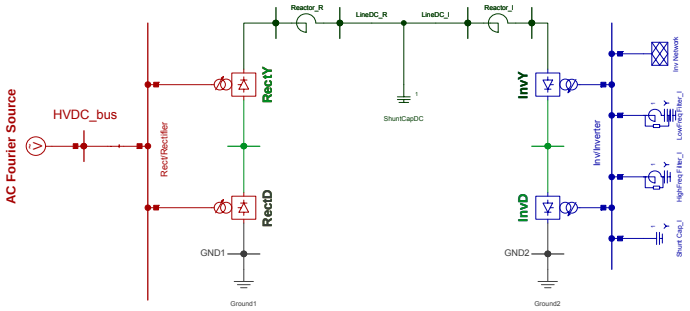

Figure 7.8 Nonlinear network – HVDC link modelled in time domain. The linear network is replaced with a voltage source, in the figure: AC Fourier Source.

4. Define the values to be monitored: six phase currents of both converters Y and D. Phase currents will be monitored between the HVDC AC bus and the converter transformers, before canceling of the $6k\pm1$ (k odd) harmonics.

5. Setup ElmFFT objects that will be performing the "on-line" FFT calculation of the phase currents. The result of the FFT calculation is available every half a period (10 ms overlap). The harmonic magnitudes and phase angles of the harmonics from 1st up to the 51st are monitored. A composite model [PowerFactory] is used for that purpose, see Figure 7.9. Clock provides the sampling rate to the ElmFFT elements. ElmRec elements are the rectifiers connected in Y and D. input_A_Y, etc, are the monitored phase currents (ElmRec elements have built in converter transformers, so the current is monitored at the points as defined in previous point. The FFT calculation of the dynamically varying signal may result in spectral leakage, which can be suppressed if needed by using the Hanning window function.

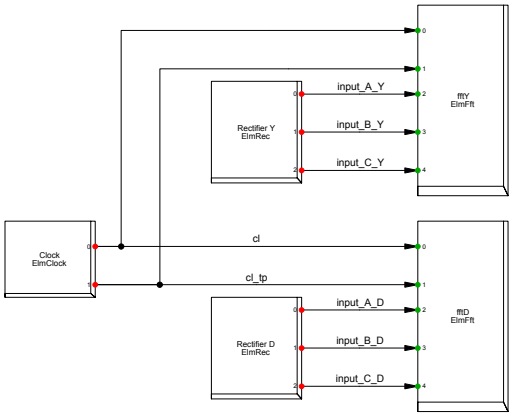

Figure 7.9 Diagram of the composite model FourierRec. The model is composed of both three-phase ElmFFT elements, to which information about the three-phase time domain current is provided from both rectifiers, and a clock element ElmClock.

6. Automatically assign the parameters, which can be freely defined before the simulation: clock frequency, (sampling rate of ElmFFT elements, 25,6 kHz default), number of points in the FFT calculation (512 default), maximum time of the time domain simulation (number of fundamental frequency periods, 30 – default), start time of simulation (20 ms default), integration step size (10 μs default). Output of ElmFFT blocks are magnitudes and phase angles for three phases, + signal "ready". Signal ready is set to 1 exactly at the time FFT calculation is finished.
7. Run time domain simulation with the defined parameters. To calculate initial conditions the unbalanced load-flow is performed with the voltage values exported as was described in point 2.
8. Results are stored in a result file ElmRes "All calculations". In the next step, load them to memory.
9. Get signals readyY and readyD sent by both ElmFFT elements and compare them point by point to detect and prevent potential not synchronous FFT processing
10. ElmFFT elements calculate FFT every half a period (10 ms overlap). Phase angles of odd harmonics are rotated every half a period by $\pi \cdot h$. Therefore each time signals ready are set to 1, an index SameAngle is set to SameAngle+1. The following criterion is checked:

$$frac\left(\frac{SameAngle}{2}\right) \rangle 0.4\,, \tag{7.4}$$

11. Each time it is fulfilled, the harmonics are exported (take result only every full period).
12. Multiple point detection algorithm

    Due to the small integration step, a single point of the plot of harmonic spectra, calculated by ElmFFT elements does not correspond to a single harmonic frequency. These plots of harmonic spectra are actually plotted versus time, the same like the regular waveforms, with the same integration step size. Moreover, each harmonic magnitude and phase angle may be comprised of a variable number of points and also the separation between them can also contain varying number of points. The reason for that is the modelling of the switching in power electronic devices, which occurs in between time steps. In case of such an interrupt, all time dependent variables are interpolated to the instant of interrupt and the simulation restarts at that point (This prevents numerical oscillations and allows a much lower integration step size [PowerFactory]). In the implemented model, the HVDC converters cause additional switching instances. Therefore, it must be ensured that the correct point of the plot of

harmonic spectrum is taken and exported to the proper position in a harmonic vector. The idea is illustrated in Figure 7.10 below. First is it checked if the magnitude is larger than 0. The result of FFT at each harmonic amplitude and phase angle is never zero, due to residual values caused by errors in FFT, round-off, etc. Also the points separating harmonics never have purely zero values. The values of the points vary from point to point and the only case when they have *exactly* the same values are when there is a harmonic amplitude plotted. This is used as the criterion for recognizing that it is a harmonic amplitude. The first point recognized as a harmonic value is stored as a variable in the script. If the points representing this magnitude still repeat, all indexes are pushed until the harmonic magnitude ends and until the next harmonic magnitude is detected. In this way a single value of a point corresponds to a single harmonic magnitude. This value is exported to the vectors of harmonic magnitudes and phase angles. Multiple points detection is made only for one amplitude (variable), since all of the others are synchronously calculated, so they are directly taken and stored in the vectors. It has been verified that this algorithm is robust and an error has never been experienced. Multiple points do not cause errors with the FFT calculations because the Elmfft element interpolates the signals and preserves fixed sampling rate.

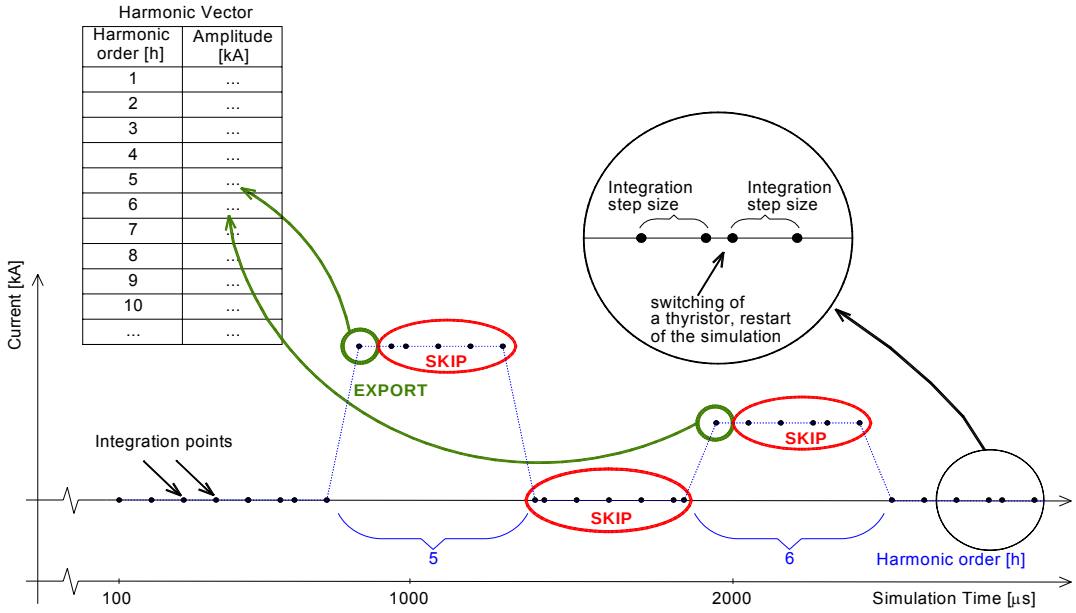

Figure 7.10 Main idea of the multiple point detection algorithm.

13. Harmonic amplitudes and phase angles of all six currents from 1st to 51st harmonic are constantly exported to vectors and to a result file DynCurrHarm. Therefore, plotting results stored in DynCurrHarm allows to see the variation of all harmonic amplitudes and phase angles for six currents, during dynamic oscillations (in total 612 variables, 6x2x51), see Figure 7.11.

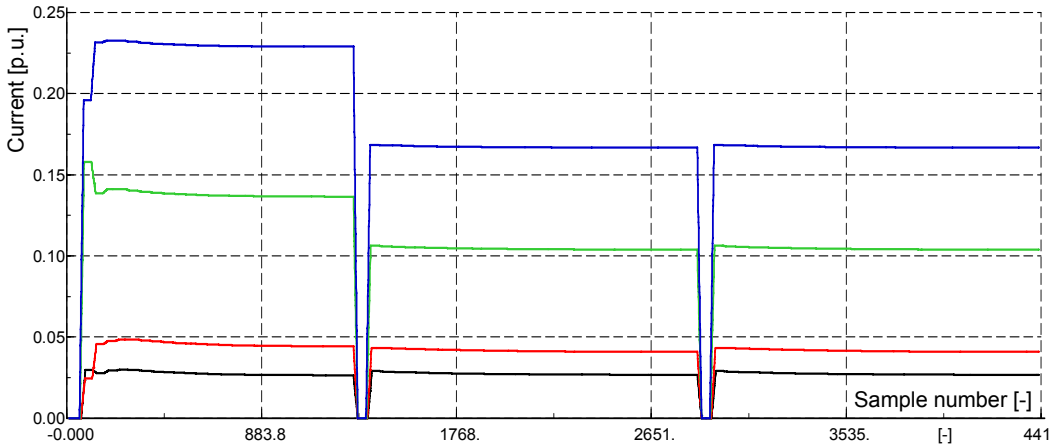

Figure 7.11 Example variation of harmonic amplitudes before the periodic steady state is reached. Blue line - 5th harmonic, green line - 7th harmonic, red line – 11th harmonic and black line – 13th harmonic. This plot shows time domain simulation repeated three times before the convergence is reached.

14. Detection of periodic steady state

For steady state harmonic analysis, harmonic currents injected by the HVDC converters need to be taken when the time domain simulation reaches the periodic steady state. Time domain simulations have some initial oscillations lasting for some periods, before the simulation settles down. For the purpose of this algorithm, in terms of harmonic distortion, it has been assumed that the periodic steady state is reached when magnitudes and phase angles of harmonics are not changing any more while simulation proceeds. An algorithm has been developed where it is constantly checked if the percentage variation of harmonic amplitudes and harmonic phase angles of significant harmonics:1st, 5th, 7th, 11th and 13th become less than specified precision indexes. Percentage variation of harmonic magnitudes is defined as the difference in amplitudes between the harmonic amplitude in the previous period and in current period, in percent:

$$\Delta I_h = \frac{I_h^{prev} - I_h^{current}}{I_h^{prev}} \cdot 100\%, \tag{7.5}$$

and the same for the phase angles:

$$\Delta \varphi_h = \frac{\varphi_h^{prev} - \varphi_h^{current}}{\varphi_h^{prev}} \cdot 100\%. \tag{7.6}$$

Periodic steady state is reached when:

$$\left.\begin{array}{l} I_{Y-A}, I_{Y-B}, I_{Y-C} : \Delta I_{1st}, \Delta I_{5th}, \Delta I_{7th}, \Delta I_{11th}, \Delta I_{13th} \\ I_{D-A}, I_{D-B}, I_{D-C} : \Delta I_{1st}, \Delta I_{5th}, \Delta I_{7th}, \Delta I_{11th}, \Delta I_{13th} \end{array}\right\} < \varepsilon_{mag}, \tag{7.7}$$

and simultaneously:

$$\left.\begin{array}{l} I_{Y-A}, I_{Y-B}, I_{Y-C} : \Delta \varphi_{1st}, \Delta \varphi_{5th}, \Delta \varphi_{7th}, \Delta \varphi_{11th}, \Delta \varphi_{13th} \\ I_{D-A}, I_{D-B}, I_{D-C} : \Delta \varphi_{1st}, \Delta \varphi_{5th}, \Delta \varphi_{7th}, \Delta \varphi_{11th}, \Delta \varphi_{13th} \end{array}\right\} < \varepsilon_{ph}, \tag{7.8}$$

where ε_{mag} and ε_{ph} are the predefined magnitude and phase angle precision indexes for all significant harmonics in all six currents of both converters. The idea is illustrated in Figure 7.12.

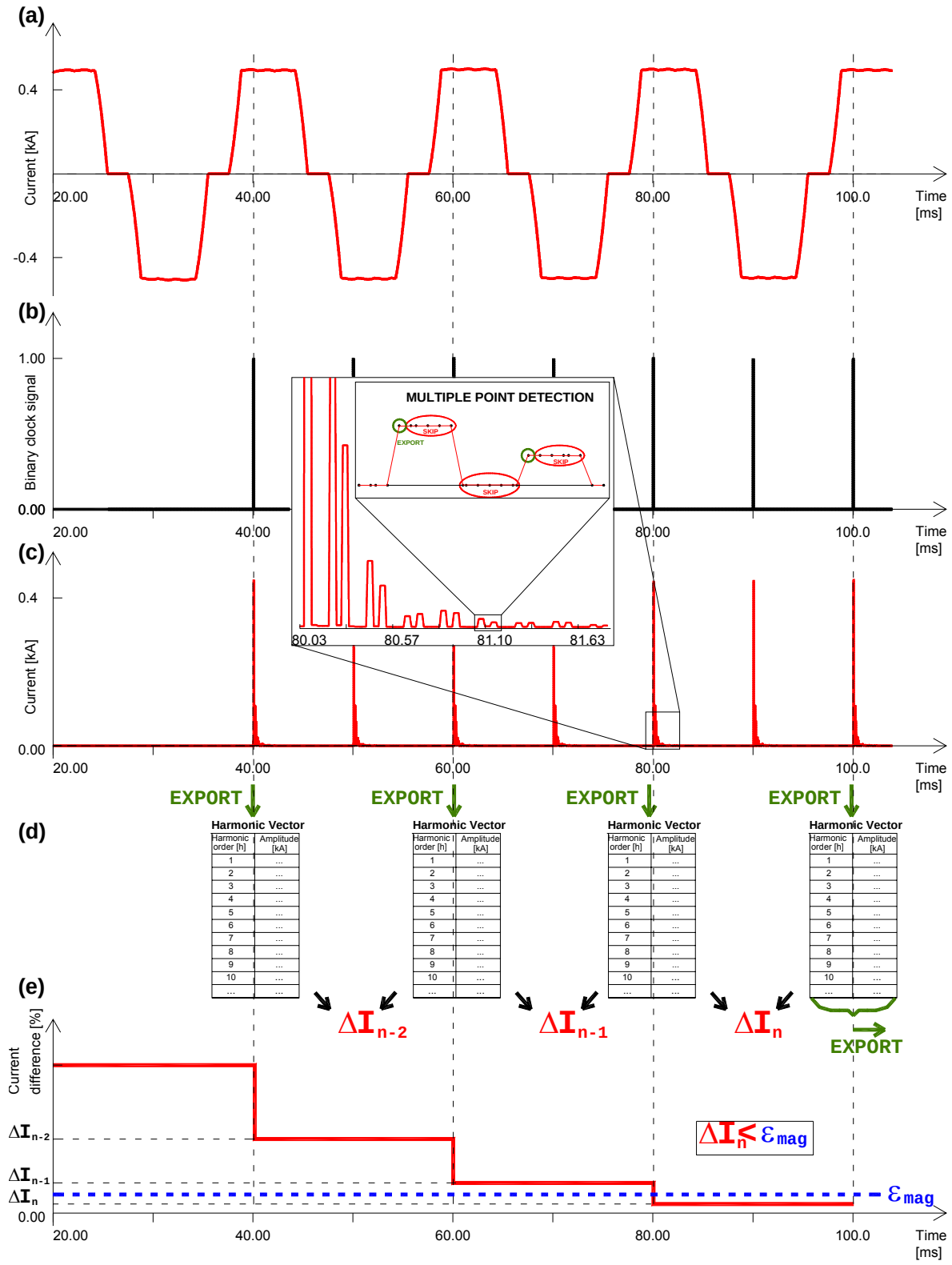

Figure 7.12 Detection of periodic steady state. (a) – time domain plot of current in rectifier Y, phase A, (b) – signal readyY=1 sent by the ElmFFT element each time FFT is calculated, (c) – output of the ElmFFT element that is a plot of harmonic spectrum, (d) properly selected harmonic amplitudes exported to vectors and calculation of harmonic differences ΔI, (e) –plot of harmonic differences ΔI and reaching the periodic steady state at period n.

15. These differences ΔI_h and $\Delta\varphi_h$ are also continuously exported to the result file DynCurrHarm and can be continuously observed and plotted (another 612 values). Example result of such plot is shown in Figure 7.13.

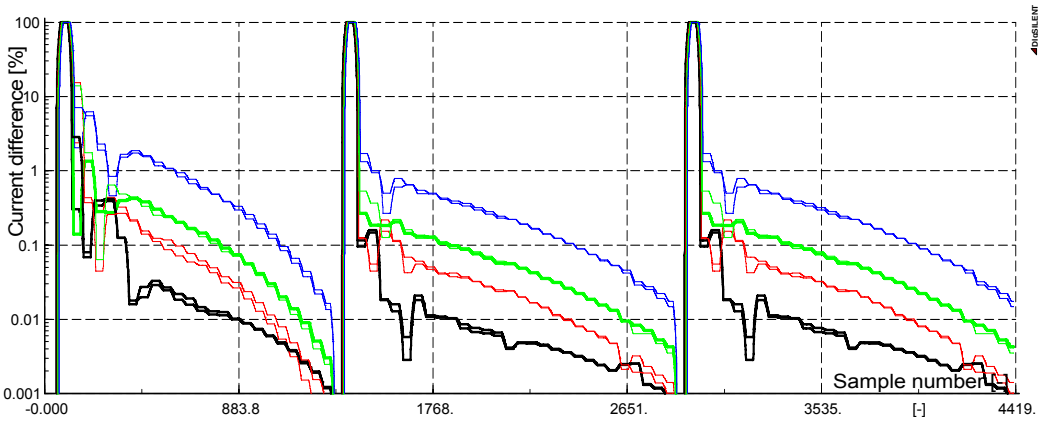

Figure 7.13 Difference in current harmonic magnitudes from period to period, phase A for both converters Y and D. Blue lines - 5th harmonic, green lines - 7th harmonic, red lines – 11th harmonic and black lines – 13th harmonic. This plot shows time domain simulation repeated three times before the convergence is reached. Precision index was set to 0.05%.

16. When periodic steady state is reached, the next period is used for performing the FFT calculation and exporting all the harmonic amplitudes and phase angles – 1st up to the 51st harmonic.

17. The following message is printed in the output window:

    'Precision indexes are checked for 1st, 5th, 7th, 11th and 13th harmonic'

    'Magnitude precision index of … has been reached after … periods',

    'Phase angle precision index of … has been reached after … periods'

    'For further calculations harmonic components are calculated at … period'

18. In the harmonic load–flow calculation of PowerFactory, HVDC rectifiers can be modelled as ideal rectifiers (ideal current spectra) or by defining 3-phase unbalanced harmonic spectra (files TypHmccur). This can be selected as shown in Figure 7.14.

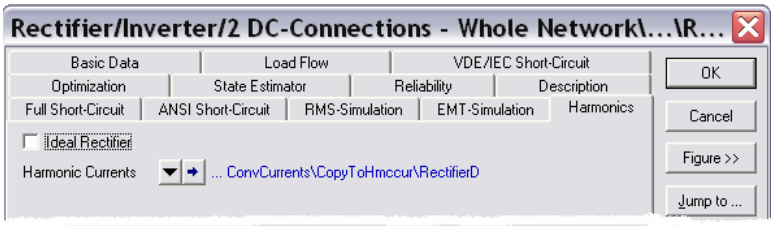

Figure 7.14 Dialog box "Harmonics" of the 6-pulse converters.

19. For each converter there are two files – matrices of harmonic currents (TypHmccur). Into these two matrices the results of FFT made in periodic steady state of time domain simulation are exported. Amplitudes are recalculated to the percentage values of the fundamental.

20. Deactivate study case Time domain and activate study case Frequency domain.

21. Get the command HLF (Harmonic Load-Flow), set it unbalanced and execute. This command in fact first runs the classical unbalanced load flow calculation, and in second step, performs unbalanced direct harmonic calculation, and the harmonic flows and harmonic bus voltages

in the linear part of the model are obtained. HVDC converters are modelled as current sources with harmonic spectra obtained in the last time domain simulation assigned.

22. After the HLF calculation, the calculated harmonic voltages at the HVDC bus are stored in the result file "Harmonics" together with the positive, negative and zero sequence values of the fundamental frequency voltage, as it was in point 2. The harmonic voltages are also exported at this step to a matrix PolarHarVoltMat.
23. The harmonic voltages are exported to the elements ElmFsrc. These elements perform the inverse FFT calculation, from the harmonic domain into the time domain. The outputs from these elements are controlling the three-phase AC voltage source which is used in time domain simulation. The composite model realizing this function is shown in Figure 7.15.

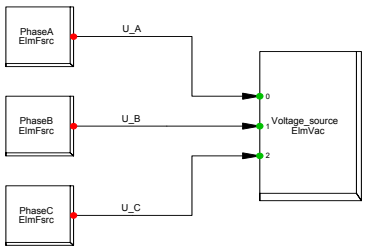

Figure 7.15 Structure of the composite model Fourier_Sources. Its function is to control the distorted voltage source used in time domain simulation

24. The algorithm imports harmonic vectors PolarHarVoltMat into the ElmFsrc's.
25. Define the following variables that will be used by the main algorithm: TotalConv =1 (total number of iterations), Iteration =0 (will be constant), Convergence =1; (will be constantly 1, until the full convergence is reached, then it is switched to 0).
26. **Start of main loop.** The main loop has the following form: for (Iteration = 0; Iteration < Convergence; Iteration = Iteration).
27. Copy the matrix of harmonic voltages PolarHarVoltMat into the matrix PrevHarmVolt and set TotalConv = TotalConv +1.
28. Activate the study case Time domain.
29. Run time domain simulation, as described in point 7. The time domain simulation is now run with the distorted voltage applied to the converters until the new periodic steady state is reached. The harmonic filters are not present in the network used for time domain simulation.
30. **Repeat all the points from 8 up to 22.**
31. Check the convergence of the entire algorithm. This is done analogously to the method used to detect the periodic steady state. The harmonic voltage magnitudes and phase angles stored in both matrices PolarHarVoltMat and PrevHarmVolt are compared. PrevHarmVolt contains values copied there in the previous iteration, PolarHarVoltMat contains the updated values. Calculate these differences in magnitudes and phase angles and store them in a previously initialized matrix ErrVolt:

$$\Delta U_h = \frac{U_h^{prev} - U_h^{current}}{U_h^{prev}} \cdot 100\%, \tag{7.9}$$

$$\Delta \varphi_{Uh} = \frac{\varphi_{Uh}^{prev} - \varphi_{Uh}^{current}}{\varphi_{Uh}^{prev}} \cdot 100\%. \tag{7.10}$$

Compare the values stored in ErrVolt for the significant harmonics: 1st, 5th, 7th, 11th, 13th with the precision indexes defined for differences in harmonic voltage magnitudes and phase angles (these are different precision indexes form the ones used for detecting the periodic steady state).

Convergence is reached when:

$$U_A, U_B, U_C, : \Delta U_{1st}, \Delta U_{5th}, \Delta U_{7th}, \Delta U_{11th}, \Delta U_{13th} \} < \varepsilon_{mag}^{U}, \tag{7.11}$$

and simultaneously:

$$U_A, U_B, U_C, : \Delta \varphi_{U1}, \Delta \varphi_{U5}, \Delta \varphi_{U7}, \Delta \varphi_{U11}, \Delta \varphi_{U13} \} < \varepsilon_{ph}^{U}, \tag{7.12}$$

where ε_{mag}^{U} and ε_{ph}^{U} are the predefined magnitude and phase angle precision indexes defined for all significant harmonics of the bus voltage at the HVDC_bus.

The convergence is checked in practice in the following manner:

Two indexes are set: StableMag=StablePhi=0.

If a magnitude difference of one harmonic magnitude in one phase gets smaller than the precision index ε_{mag}^{U}, the index StableMag is set StableMag + 1. If all the five significant harmonic magnitudes in all three phases are smaller than ε_{mag}^{U}, at the end the index StableMag should be equal to 15. If this condition is fulfilled, then it is assumed that the algorithm has converged in terms of harmonic magnitudes. Exactly the same procedure is repeated for phase angles. If all the phase angles of five significant harmonics in all three phases are smaller than ε_{ph}^{U}, then the corresponding index StablePhi is also 15. If both conditions are fulfilled in one iteration (StableMag=15.and.StablePhi=15), then the entire algorithm has converged.

32. Set variable Convergence=0. This variable is read by the main routine and the main loop is stopped (see points 25and 26).
33. The following message is printed in the output window:

    'The main algorithm has converged after TotalConv iterations'

The algorithm has been implemented using the DIgSILENT Programming Language (DPL). The tree structure of the DPL scripts is shown in Figure 7.16. Subroutine GetBusVoltage contains also vectors of harmonic voltages. Subroutine GetConvCurrents contains also vectors of harmonic currents and the current differences. All these harmonic currents can be plotted.

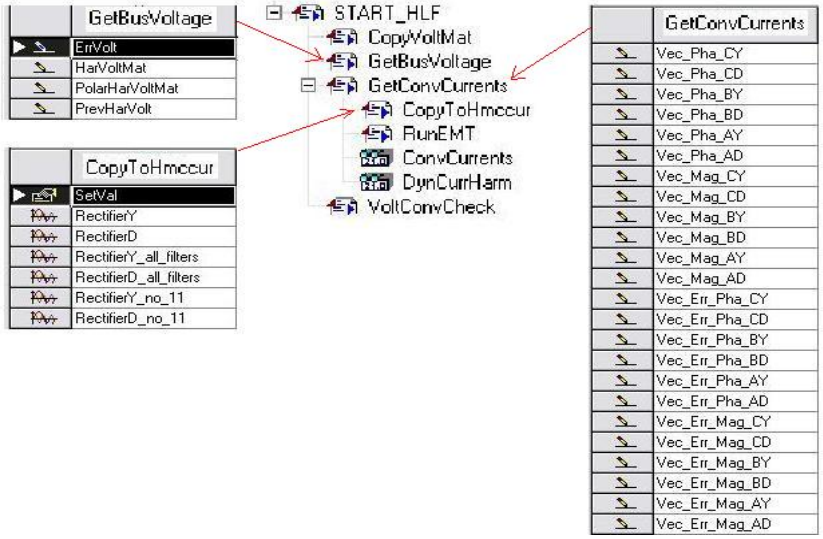

Figure 7.16 The tree structure of the implemented algorithm as DPL scripts.

Subroutine CopyToHmccur contains the harmonic spectra of converter currents used in harmonic domain calculation. More harmonic spectra can be prepared for different operating conditions and used afterwards without the need of performing the hybrid calculation each time.

The DPL codes of each subroutine can be found in appendix A.

The following parameters can be defined before run of the algorithm, in the main dialog box of the routine START_HLF:

type	Name	Initial value	Unit	Description
int	Fmin	50	Hz	Fundamental frequency
int	dF	50	Hz	Freq. step (50 Hz no inter-harmonics)
int	NPoints	512		nr of FFT points
int	SamplFreq	25600	Hz	sampling frequency
double	TStep	10	µs	integratin ste size
int	Window	0		0 - rectangular, 1 - Hanning
double	TStart	20000	µs	begining of the simulation
int	NrPeriods	30		Max lenght of EMT
double	MPrec	0.05	%	PSS - Mag index (1,5,7,11,13)
double	PhPrec	0.05	%	PSS - -Ph ind (1,5,7,11,13)
double	MagError	0.05	%	Main Iteration - Mag index (1,5,7,11,13)
double	PhiError	0.05	%	Main Iteration - Ph index (1,5,7,11,13)
string	Bus_Name	'HVDC_bus.ElmTerm'		bus name (string) (*.ElmTerm)
string	Net_Name	'Whole Network.ElmNet'		grid folder name (string) (*.ElmNet)
string	Res_Name	'Harmonics.ElmRes'		results object name (string) (*.ElmRes)
string	Comp_Name	'Fourier_HVDC1.ElmComp'		comp model name (string) (*.ElmComp)
string	RecYName	'RectY.ElmRec'		Full name of the rectifier Y
string	RecDName	'RectD.ElmRec'		Full name of the rectifier D

Table 7.1 Variables that can be defined in the HVDC hybrid model.PSS – periodic steady state.

It is possible to define different than 50 Hz fundamental frequency, and define Hanning window function. This shows the potential ability of the algorithm to be used for inter-harmonic studies, for instance in case of back-to-back interconnection of systems with different frequencies. Such possibilities will have to be further analyzed, but are not within the scope of this project.

7.6 Verification of the hybrid algorithm

The hybrid algorithm has been verified against precise time domain simulation. Two cases are studied. In first case, the unmodified network is used, and in the second case, the performance is investigated for higher level of harmonic distortion of the bus voltage, obtained by disconnection of the 11th high-pass harmonic filter, as shown in Figure 7.17. The impedance characteristic of the filter is shown in Figure 7.18.

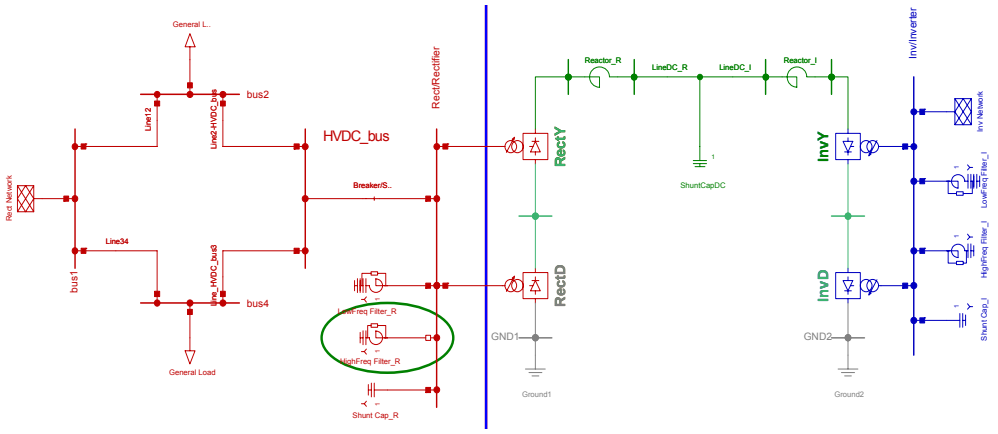

Figure 7.17 Entire network used for verification purposes. 11th high-pass harmonic filter is disconnected in the second case.

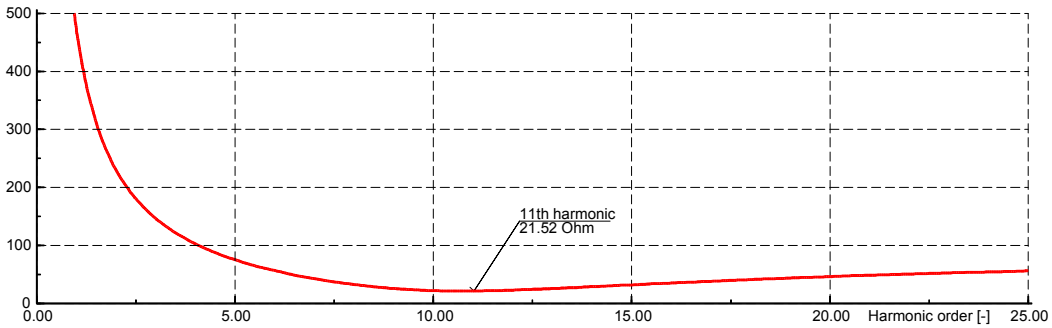

Figure 7.18 Impedance characteristic of thee disconnected in second case 11th and high-pass harmonic filter. Tuning frequency 527,8 Hz.

Harmonic currents of the converters are monitored, together with the harmonic voltage at the interfacing bus HVDC_Bus. In the linear part of the network lumped impedances of the components are defined. They are not frequency dependent. Therefore, the results of the time domain simulation can be used for precise verification of the algorithm. Results from the hybrid method are originally in frequency domain, and to compare them with time domain results, their inverse FFT is calculated. Calculated bus voltage HVDC_Bus is compared in time domain, and also in frequency domain with the time domain simulation results.

In this section only the final results of simulations and verification of the hybrid method versus time domain simulation is presented. A conclusion is drawn whether the algorithm gives correct results. Issues concerning the convergence process are discussed in the subsequent section 7.7.

For both cases 1 and 2, the following simulation parameters have been defined in the dialog box of the main script START_HLF, see Table 7.2.

Periodic steady state	
Magnitude precision index:	0.05%
Phase angle precision index:	0.05%
Main iteration	
Magnitude precision index:	0.05%
Phase angle precision index:	0.05%
FFT calculation	
Number of FFT Points	512
Sampling rate, kHz	25,6
Window function	rectangular
Time domain simulation	
Integration step size, μs	10
Start time, μs	20000
Max number of periods	80

Table 7.2 Simulation parameters of the Hybrid method used in cases 1 and 2.

7.6.1 Results of simulations for Case 1.

Converter currents calculated by the hybrid method is injected in the frequency domain into the linear network impedance. This current is also obtained in a full scale time domain simulation. Both currents are compared in Figure 7.19.

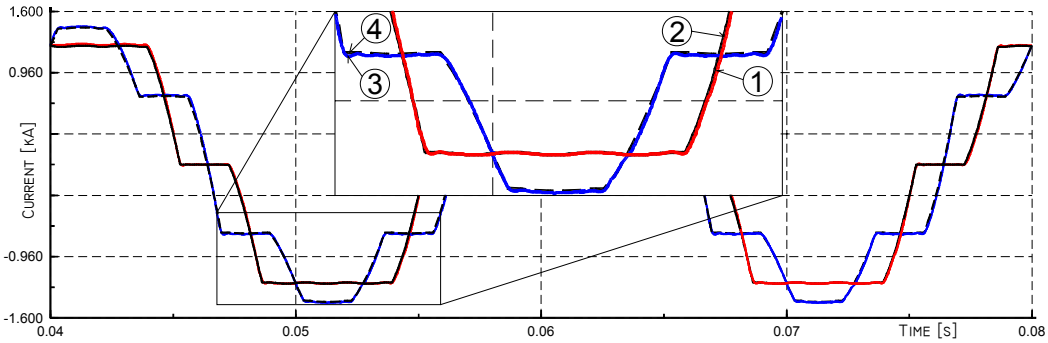

Figure 7.19 Verification of the algorithm - converter currents phase A. 1, 3 – Inverse FFT of the frequency domain currents (Hybrid method) of rectifiers connected in Y and D respectively, 2, 4 – Y and D rectifier currents obtained in a time domain simulation of the entire model.

It can be seen that both currents are practically the same. A very small difference may be noticed near the points that resemble discontinuities; this is caused by the Gibbs effect, the overshoot phenomenon exhibited by the truncated Fourier series.

As a result of this injected current into the linear impedance, the bus voltage at the HVDC_Bus becomes distorted. The comparison of the bus voltage obtained in the hybrid simulation with the one obtained in time domain simulation is shown in Figure 7.20 (a), (b) and (c).

As can be seen, the voltage at the bus HVDC_Bus is only slightly distorted (voltage THD is approx. 1%). The reason for that is that all the harmonic filters are in operation. In Figure 7.20 (a) comparison between the bus voltage in phase A, obtained using the hybrid method (Inverse FFT of voltage spectrum) is compared with the waveform obtained from a full time domain simulation. It can be seen that the agreement between these two results is very good. This I also confirmed when looking at their harmonic content, Figure 7.20 (b) – the time domain simulation result, and (c) – hybrid method result,. The values are also shown in Table 7.3 on page 203.

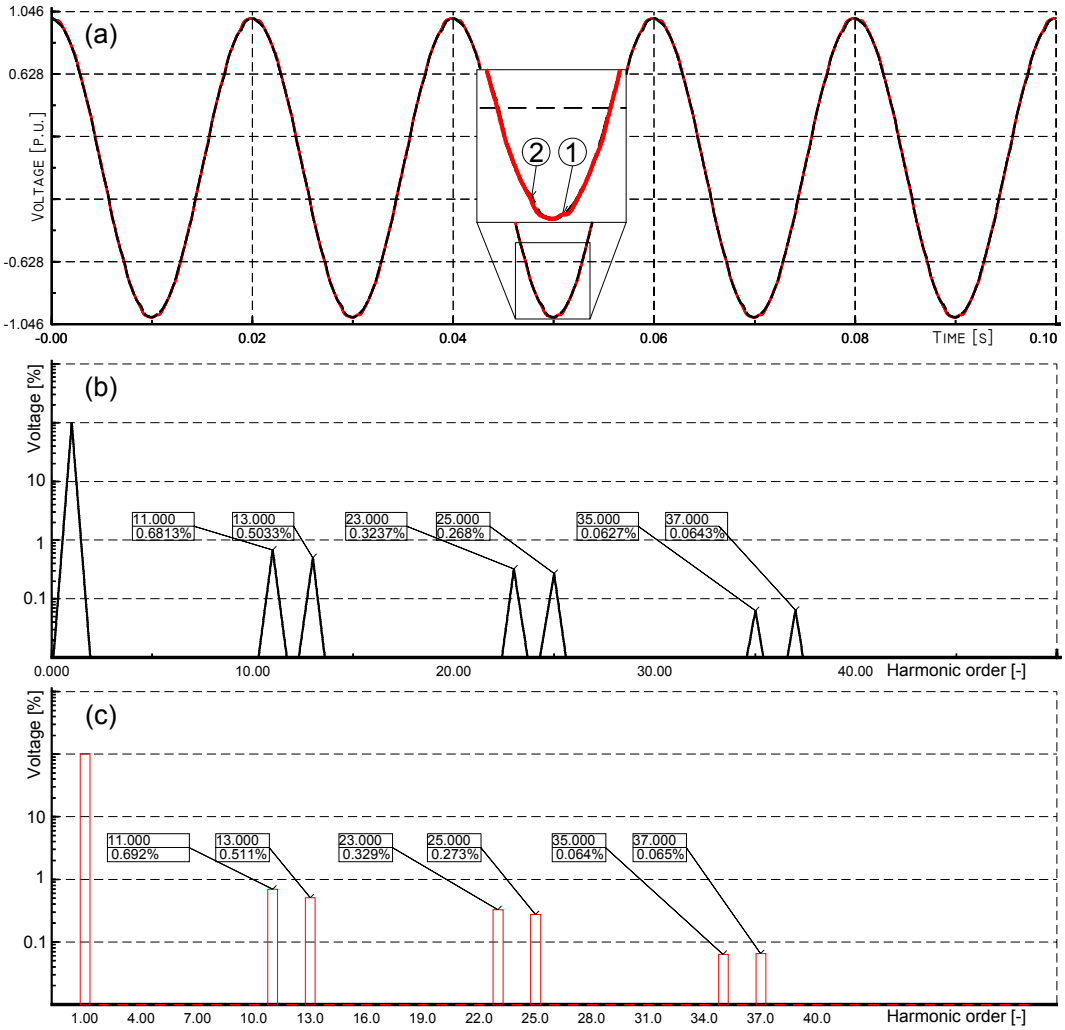

Figure 7.20 Distorted voltage at the HVDC_Bus. All harmonic filters connected. (a) Plot vs. time, where 1- Hybrid method (Inverse FFT) vs.2 - full time domain simulation; (b) – FFT of the time domain result; (c) – hybrid method

Harmonic order [-]	TD [%]	Hybrid [%]	difference [%]
11	0,6813	0,692	0,0107
13	0,5033	0,511	0,0077
23	0,3237	0,329	0,0053
25	0,2680	0,273	0,0050
35	0,0627	0,064	0,0013
37	0,0643	0,065	0,0007

Table 7.3 Difference in harmonic voltage magnitudes between time domain simulation results (TD) and the hybrid algorithm for case 1.

7.6.2 Results of simulations for Case 2

Because the bus voltage in case 1 was only slightly distorted, one more case was simulated in order to verify the hybrid method also for larger bus voltage distortion values. The simulations are performed with the 11th high-pass harmonic filter disconnected from the HVDC_bus, as was shown in Figure 7.17. Comparison of injected currents from the rectifiers, calculated using the hybrid method and time domain simulation is shown in Figure 7.21. It can be seen that the converter current is well represented in the hybrid simulation.

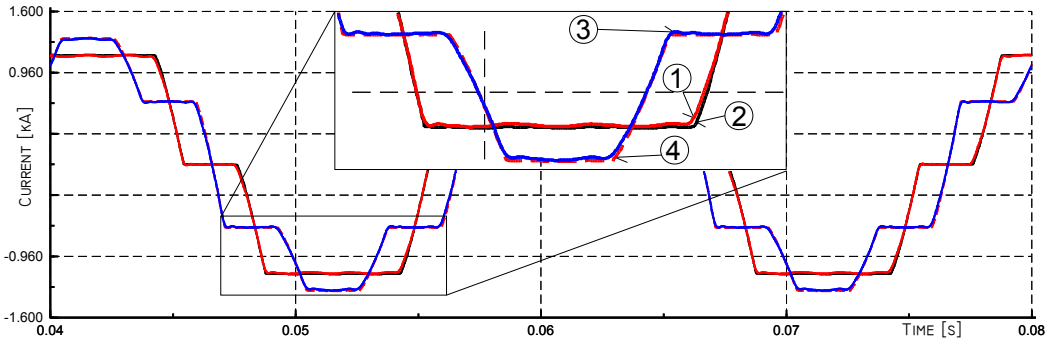

Figure 7.21 Verification of the algorithm - converter currents phase A. 1, 3 – Inverse FFT of the frequency domain currents (Hybrid method) of rectifiers connected in Y and D respectively, 2, 4 – Y and D rectifier currents obtained in a time domain simulation of the entire model.

The visible differences are small and caused mainly by the finite precision index (that could be set smaller, but then the simulation time may rise). The comparison of HVDC_Bus bus voltage obtained from the hybrid method with the time domain simulation is shown in Figure 7.22 (a), (b) and (c), on page 205.It can be seen that the bus voltage HVDC_Bus is more distorted now, with higher content of 11th and 13th harmonic, The THD of this signal is now 5,6%, but also in this case the agreement between hybrid method and time domain simulation is very good. As shown in Table 7.4, the differences are very small and practically ignorable. Therefore, it can be concluded that the hybrid time/frequency algorithm enables to precisely calculate in an iterative manner the solution of a network, where the power components are represented in their natural frames of reference, e.g., the linear in the frequency domain and the nonlinear and time-varying in the time domain.

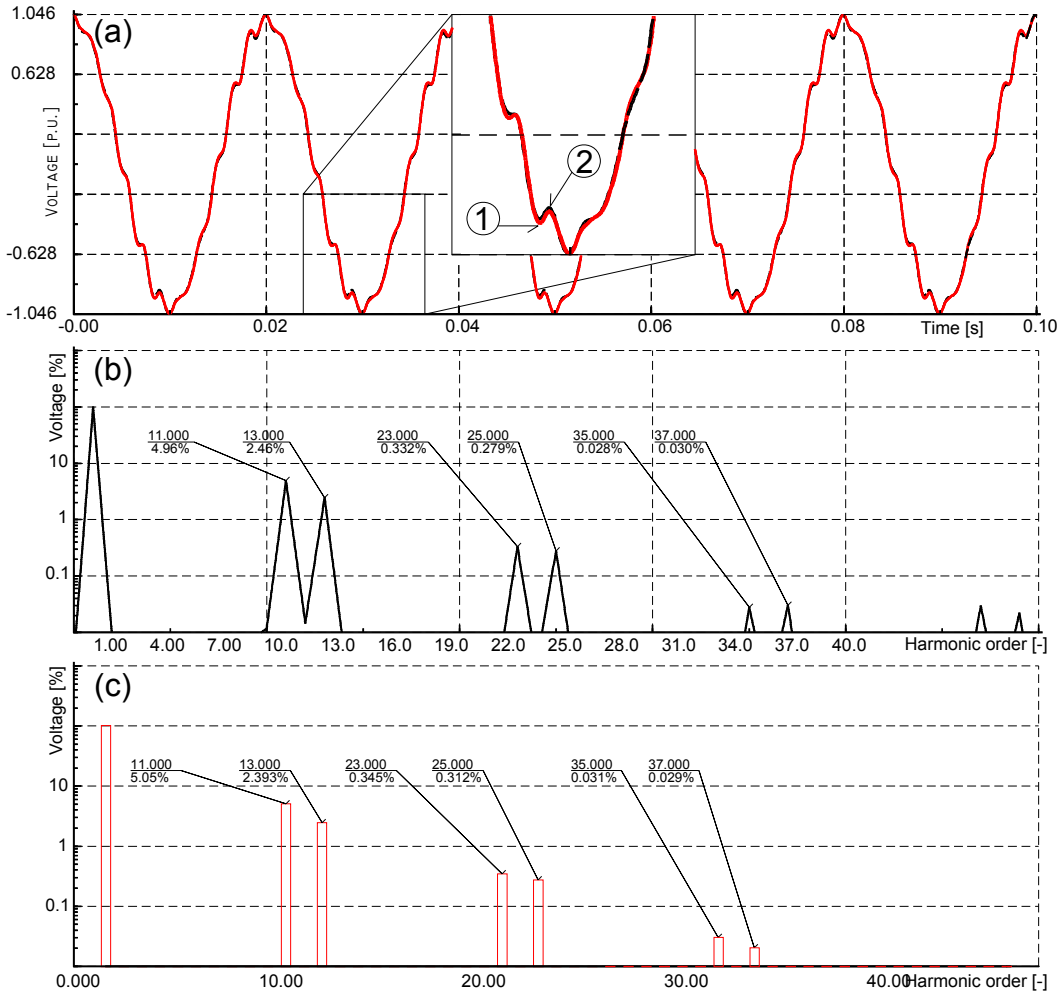

Figure 7.22 Distorted voltage at the HVDC_Bus. 11th harmonic filter disconnected. (a) Plot vs. time, where 1- Hybrid method (Inverse FFT) vs.2 - full time domain simulation; (b) – FFT of the time domain result; (c) – hybrid method.

Harmonic order [-]	TD [%]	Hybrid [%]	difference [%]
11	4,96	5,051	0,091
13	2,46	2,393	0,067
23	0,332	0,345	0,013
25	0,279	0,312	0,033
35	0,028	0,031	0,003
37	0,03	0,029	0,001

Table 7.5 Difference in harmonic voltage magnitudes between time domain simulation results (TD) and the hybrid algorithm for case 2.

7.7 Periodic steady state and convergence properties

In preceding section it was demonstrated that the algorithm works and provides precise solution of the voltage at a node where a nonlinear load is connected.

In this section the process of detecting the periodic steady state will be shown, the dynamic variation of the harmonic amplitudes and phase angles in the currents will be presented.

In the current implementation of the algorithm, the emphasis was put on reaching the maximum potential accuracy and precision of the developed methods, without concerns on the speed of simulations.

7.7.1 Convergence properties and reaching periodic steady state for Case 1.

For the case 1, all four precision indexes (indexes for reaching periodic steady state and for convergence of the entire algorithm) were set to 0,05%. As it was written, firstly the unbalanced load flow was performed in the linear network and the unbalanced voltages were assigned to the voltage source used in time domain simulation of the nonlinear network and the setpoint was calculated. The purpose of this operation was to limit the time domain initial oscillations. The time domain simulation is started and while it proceeds, the amplitudes and phase angles of the current harmonics are monitored. The difference (or mismatch) is monitored for all the harmonics and for the harmonics 1st, 5th, 7th, 11th and 13th it is checked when the differences get below the required precision indexes. Three figures show the dynamically varying content of the selected harmonic amplitudes and phase angles. Figure 7.23 shows the significant harmonics, for which the precision indexes were checked, 5th, 7th, 11th and 13th harmonic in phase A of converter Y. Figure 7.23 (a) shows their amplitudes. It can be seen that for case 1, the algorithm has converged after 5 iterations. Each time the periodic steady state (for the precision indexes of 0,05%) was reached after less than 30 periods. The values of the amplitudes are from 2,2% for 13th harmonic up to 22% for the 5th harmonic. Small initial oscillations are visible for the first 8 periods. However, when looking at Figure 7.23 (b) it can be seen that the difference between the amplitudes of consecutive periods varies and it takes more periods until the desired precision index is reached. At the beginning of each iteration error of 100% is obtained, which however fastly decreases, and after the first 8 periods is around 1-2%. To go further with the accuracy, from 1-2% down to 0,05% it roughly takes another 20 periods.
It can also be seen that the rate of settling down is very similar for every iteration, except the first one, which is somewhat different. The reason for that is that for the first iteration a sinusoidal voltage is applied, and in the subsequent iterations, the actual distorted voltage is used. The steady state is reached faster in the first iteration. In Figure 7.23 (c) the harmonic phase angles and in Figure 7.23 (d) the phase angle differences are shown. The phase angle difference of the 5^{th} harmonic settles down later than the others, the reason for that is the chosen way of calculating the phase angle difference. If a phase angle oscillates near zero degrees, a relative difference calculated using Equation (7.6) is larger, than in a case if it oscillates around, say, 100 degrees.
Figure 7.24 shows the 5^{th} and 11^{th} harmonic in phase A of both converters Y and D. It can be seen that the 11^{th} and also 5^{th} harmonic have the same amplitudes for both converters. The phase angles of 11th harmonic are also the same, and the 5th harmonics are shifted by 180 degrees. In general, the rate of settling down of harmonics is very alike for the same harmonic order in both converters Y and D.
Figure 7.25 shows what happens with some uncharacteristic harmonics during the initial oscillations. The selected for observation uncharacteristic harmonics are 2^{nd}, 3^{rd}, 12^{th} and 51^{st}.

When looking at Figure 7.25 (a) it can be seen that the uncharacteristic harmonics have very low magnitudes, and as the periodic steady state is reached, they decay practically to zero, since the converters didn't generate uncharacteristic harmonic distortion in this case. During the oscillations, the highest amplitudes had the lower order harmonics, in turn, 2nd, 3rd, 12th and 51st. As can be seen in Figure 7.25 (b), the differences were very large and were varying constantly, due to the very low magnitudes of these harmonics. It is not certain how much of these amplitudes actually were present in the currents during the initial oscillations because the contribution from the spectral leakage of calculating FFT of nonstationary signals could be large. Figure 7.25 (b) proves that the selection of only significant harmonics for the detection of periodic steady state and the convergence was justified.

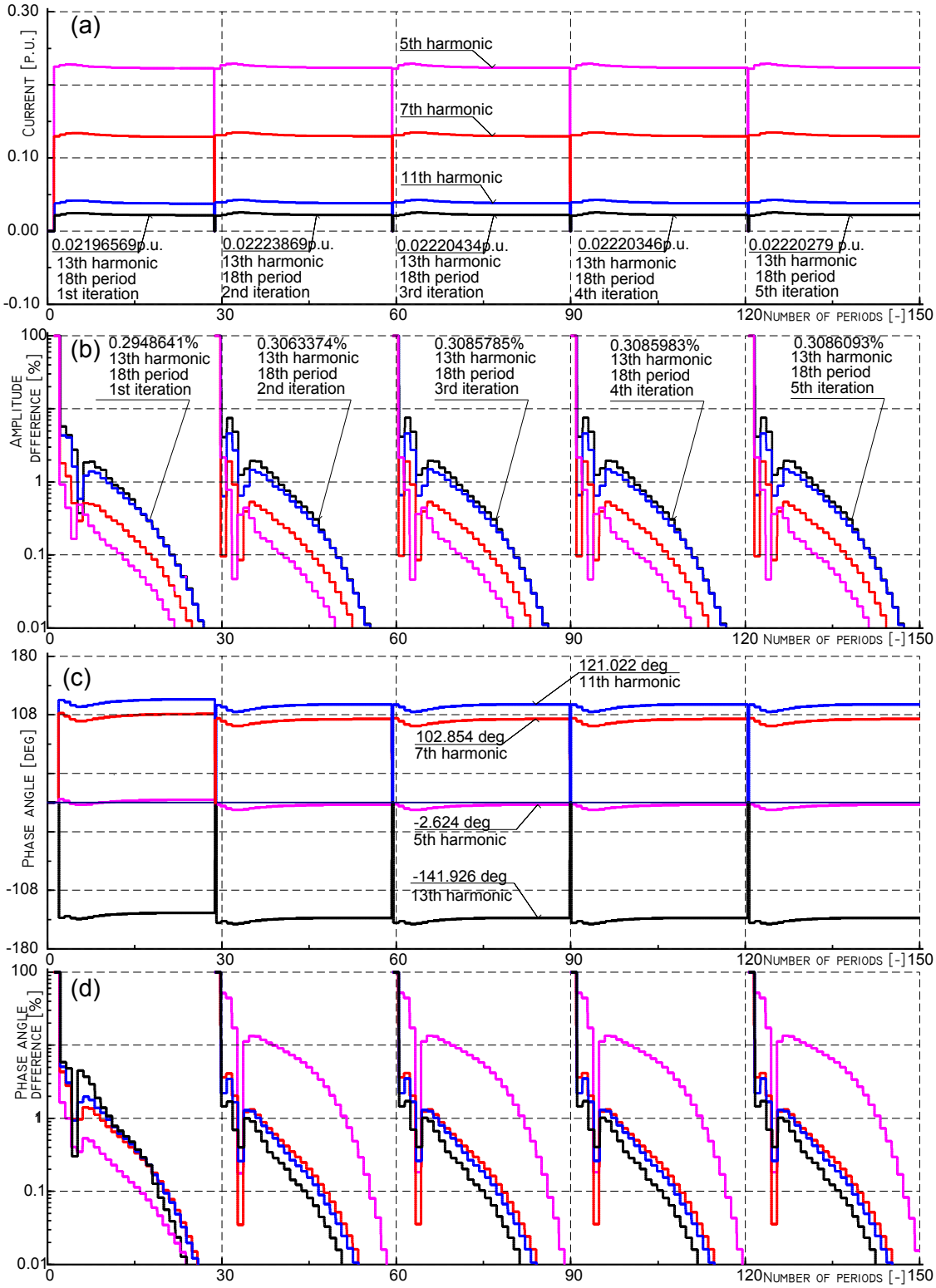

Figure 7.23 Variation of significant harmonic amplitudes and phase angles and their differences during initial oscillations, for converter Y, phase A, case 1. Magenta - 5th harmonic, red 7th harmonic, blue – 11th harmonic and black – 13th harmonic. (a) - Amplitudes, (b) – amplitude differences, (c) – phase angles, (d) – phase angle differences.

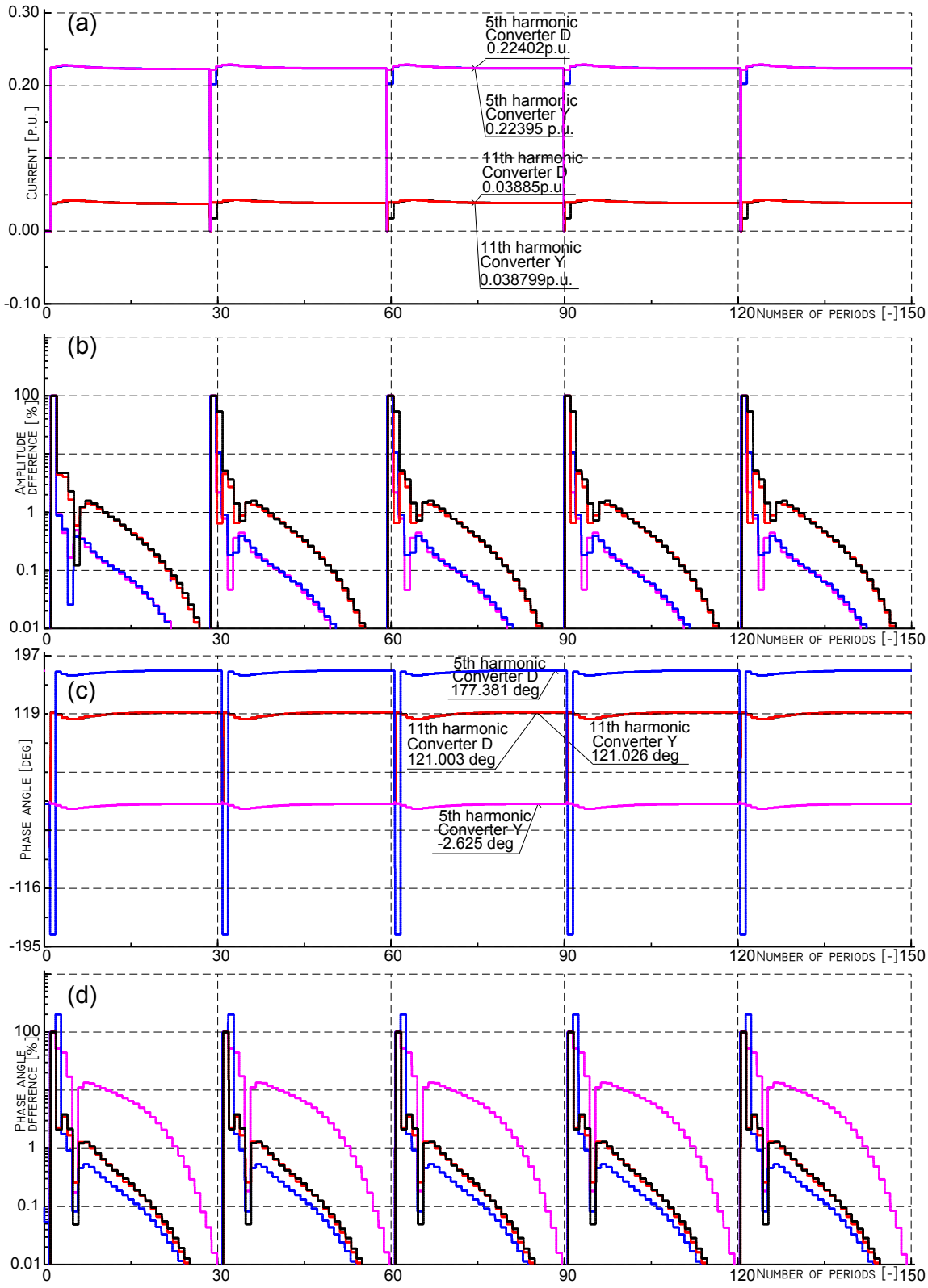

Figure 7.24 Variation of harmonic amplitudes and phase angles and their differences during initial oscillations for both converters Y and D, in phase A, case 1. Magenta - 5th harmonic (Y), red 11th harmonic (Y), black – 11th harmonic (D) and blue –5th harmonic (D). (a) - Amplitudes, (b) – amplitude differences, (c) – phase angles, (d) – phase angle differences.

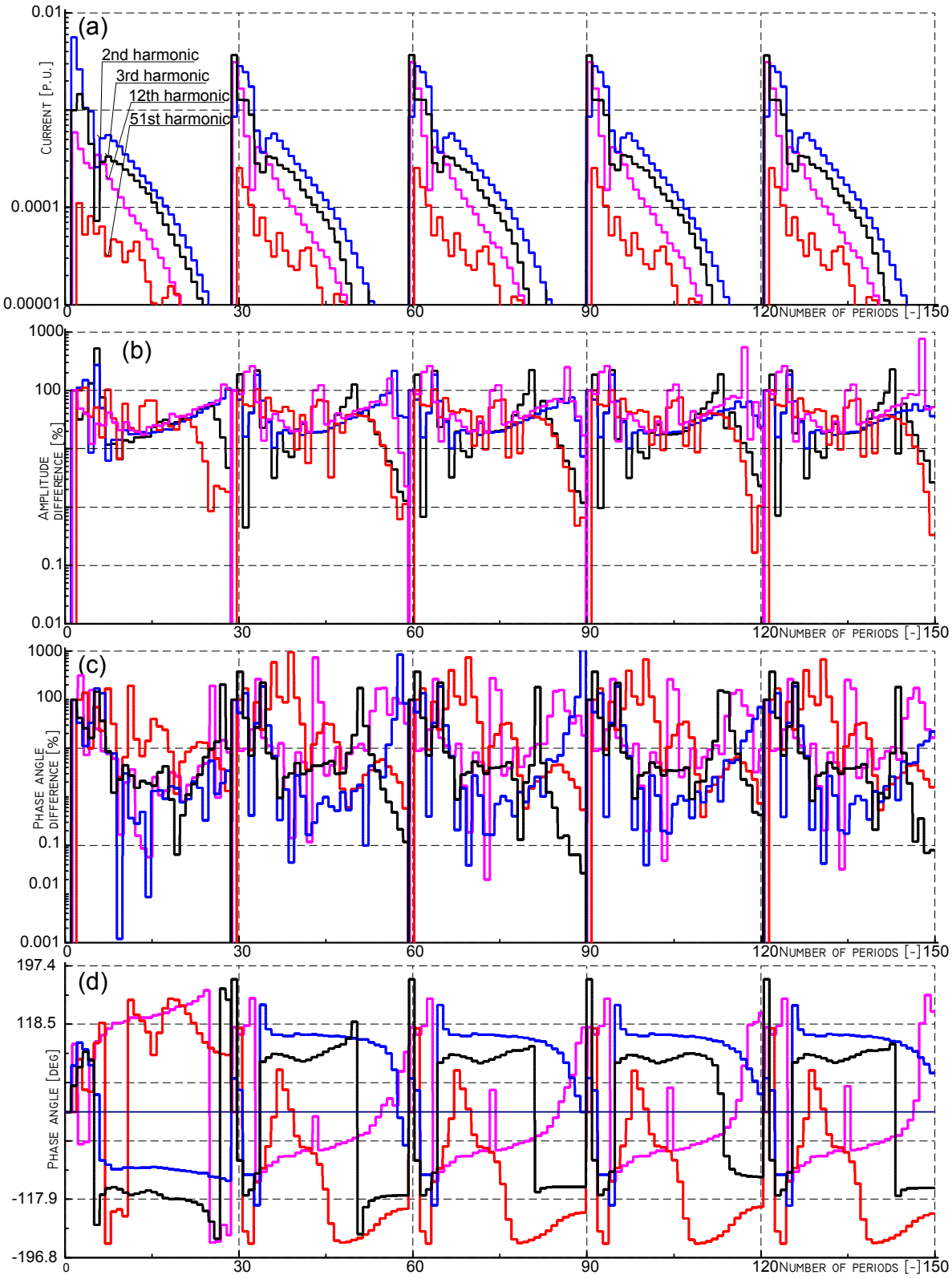

Figure 7.25 Variation of uncharacteristic harmonic amplitudes and phase angles and their differences during initial oscillations, for converter Y, phase A, case 1. Magenta - 12th harmonic, red – 51st harmonic, blue –2nd harmonic and black – 3rd harmonic. (a) - Amplitudes, (b) – amplitude differences, (c) – phase angles, (d) – phase angle differences.

7.7.2 Convergence properties and reaching periodic steady state for Case 2.

In Figure 7.26 levels of significant harmonics are shown for case 2 (case with disconnected harmonic filter). It can be seen that for this case with larger harmonic content in the bus voltage, one extra iteration was necessary to reach the precision indexes of 0,05%. The amplitudes of the harmonic currents were lower compared to case 1 (absolute values). When looking at the harmonic phase angles shown in Figure 7.26 (c) and comparing it with the phase angles in case 1 (Figure 7.23 (c)), it may be seen that they are altered. The explanation of this can be given by performing time domain simulation for both cases, see Figure 7.27. When studying this figure it may be seen that the current injected into linear network with the harmonic filter out of service has a smaller amplitude than if the filter is in operation, and the entire waveform is slightly shifted. In the lower plot of Figure 7.27 it is shown that the phase shift of the fundamental frequency $\varphi 1$ is approx. $3{,}5^{\circ}$. Because the phase angles presented in this plot are calculated against a global reference, if all other harmonics are not shifted with respect to the fundamental, their phase angles would change by factors $\varphi h = h * \varphi 1$. The phase angles obtained in both, cases 1 and 2, calculated using hybrid method and using time domain simulation are compared in Table 7.6.

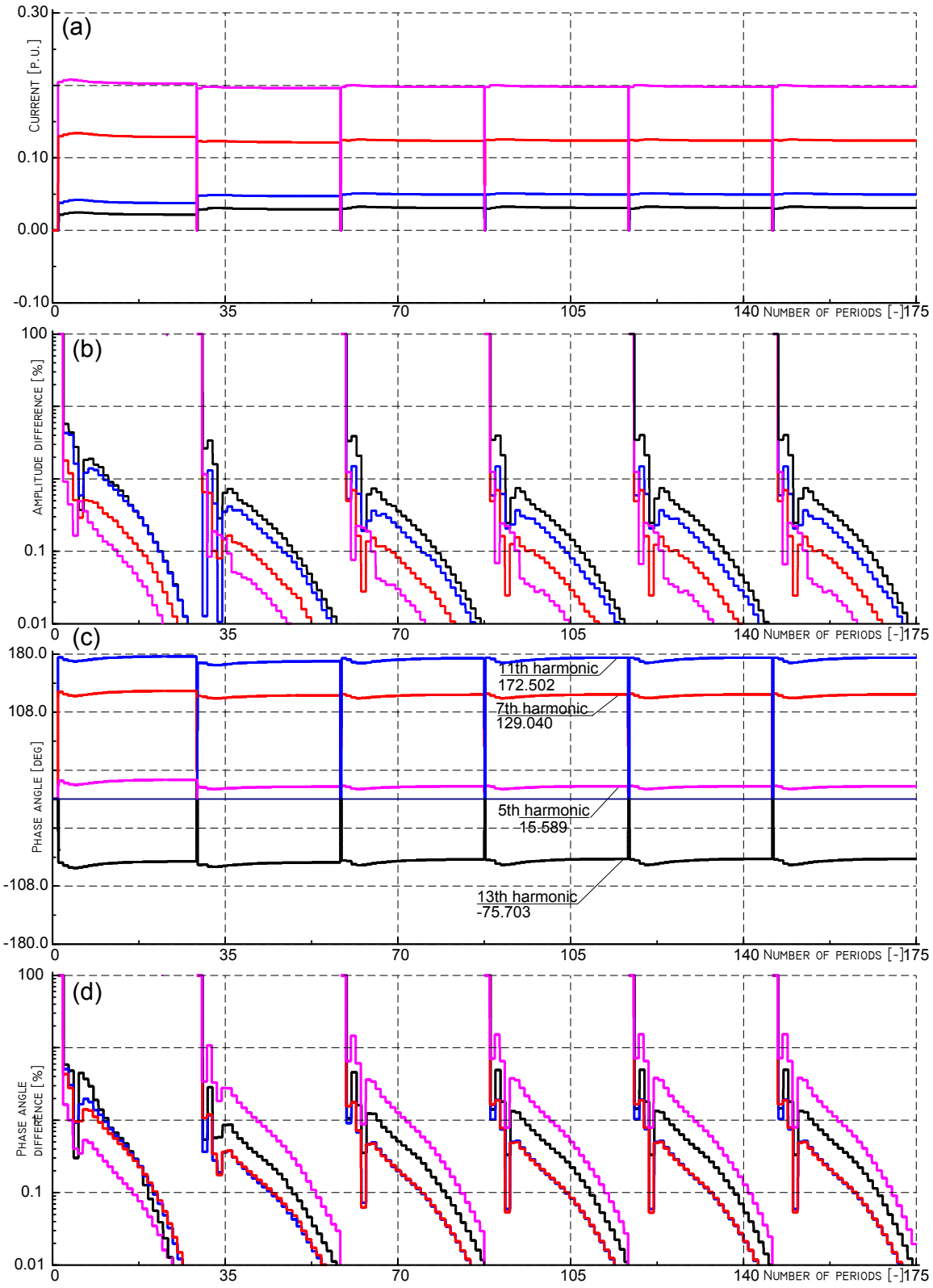

Figure 7.26 Variation of significant harmonic amplitudes and phase angles and their differences during initial oscillations, for converter Y, phase A, case 2. Magenta - 5th harmonic, red 7th harmonic, blue – 11th harmonic and black – 13th harmonic. (a) - Amplitudes, (b) – amplitude differences, (c) – phase angles, (d) – phase angle differences.

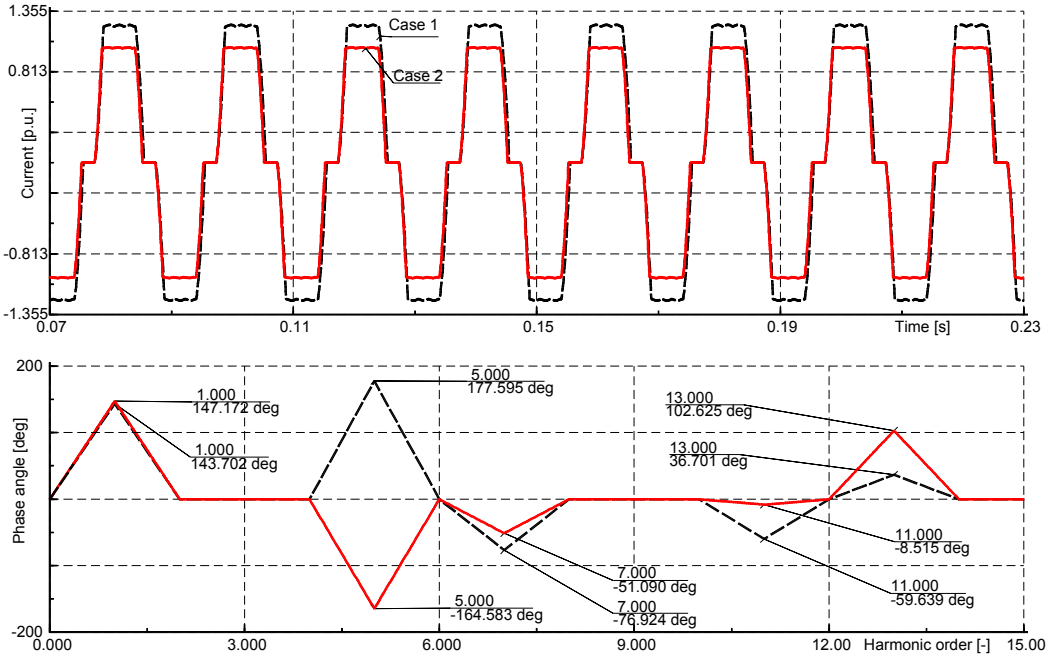

Figure 7.27 Result of time domain simulation. Current in phase A, converter Y injected into the linear network for two cases 1 and 2. Upper plot shows time domain waveforms, lower plot shows the harmonic phase angles calculated from the upper plot using FFT.

It may be seen that the phase angles obtained in time domain simulation and in the hybrid method have different values. This is caused just by performing the FFT on the time domain signal at a different moment. The relative differences between case 1 and 2, calculated using both methods are practically the same. It can be also seen that the phase angles of the harmonics of order 5th and 7th are not affected by the switching of the filter because they were shifted by the factors of $5*\varphi_1$ and $7*\varphi_1$ respectively. However, the phase angles of harmonics of order 11th and 13th were shifted also with respect to the fundamental by 12,6° and 20,4° respectively.

Time domain					**Hybrid method**				
h [-]	φh Case 1 [°]	φh Case 2 [°]	Δφh [°]	h*Δφ1 [°]	h [-]	φh Case 1 [°]	φh Case 2 [°]	Δφh [°]	h*Δφ1 [°]
1	143,70	147,20	**3,50**	3,50	1	-36,34	-32,83	**3,51**	3,51
5	177,60	-164,60	**17,80**	17,50	5	-2,60	15,59	**18,19**	17,55
7	-77,00	-51,00	**26,00**	24,50	7	102,85	129,00	**26,15**	24,57
11	-59,60	-8,50	**51,10**	38,50	11	121,0	172,50	**51,50**	38,61
13	36,70	102,60	**65,90**	45,50	13	-141,9	-75,70	**66,20**	45,63

Table 7.6 Comparison of phase angles of current harmonics for cases 1 and 2, calculated in time domain and using the hybrid method.

The reason of that was that the filter was tuned to the 11th and higher order harmonic frequencies and therefore had high effect on the harmonic voltage drops and in turn on the injected harmonic currents. The bus voltage HVDC_Bus, together with its harmonic content is shown in Figure 7.28.

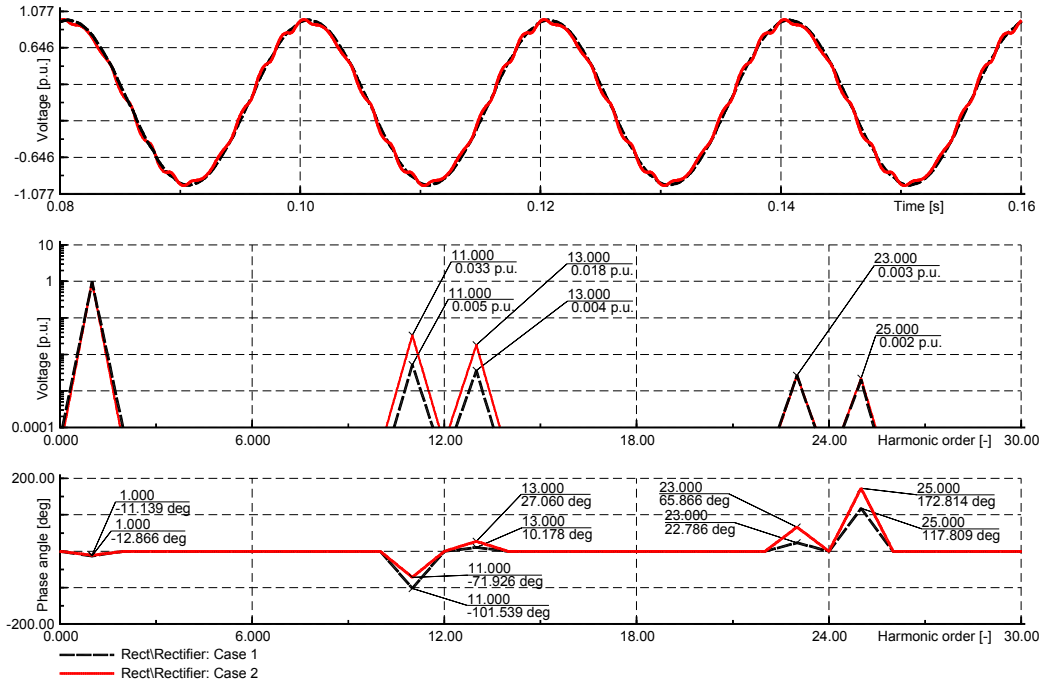

Figure 7.28 HVDC_Bus voltage for both cases 1 and 2.. Upper plot – time domain waveforms, middle plot – harmonic amplitudes and lower plot – harmonic phase angles.

It can be seen that there is no 5th and 7th harmonic content in the bus voltage, which is correct since these converter harmonic currents cancel out. Therefore the amplitude and phase angle of these harmonic currents do not depend on the disconnection of the harmonic filter. It can be also seen that the amplitudes of 23rd and 25th harmonic voltages are not changing noticeably. The only visible effect is on the amplitudes of the 11th and 13th harmonic voltages.

7.7.3 Nominal initial conditions in time domain simulation for Case 1 (Case 1a)

The hybrid time/frequency algorithm was implemented in the way where the time domain simulation at each iteration is preceded by a calculation of the initial conditions based on a three-phase load-flow calculation in the entire network. Therefore, the initial oscillations of the calculated converter currents are supposed to be minimized. In this section it is shown what would happen if the results of the three-phase load-flow were not used for calculation of the initial conditions but each time the simulation would be starting at a point corresponding to the nominal voltage value.

In Figure 7.29 three curves are shown, which are the time domain voltages applied to the converter. The red curve shows a fragment of the sinusoidal voltage, which is calculated from the initial conditions obtained in the preceding load-flow calculation. Point 1 corresponds to calculated load-flow voltage value U=0,9614 p.u., $\varphi 1=-8{,}929^{o}$. Based on this value, a sinusoidal voltage is created, therefore, there is no jump between points 1 and 2 of the red curve. The blue curve shows a segment of the distorted voltage obtained from the inverse FFT of the ElmFsrc elements. In this case, the calculation was also preceded by a calculation of initial conditions based on the load-flow results. Therefore this curve also starts at the same point 1, but then in next integration point jumps to the new value 2', and then continues as the calculated distorted waveform. The reason why there is this jump is the harmonic content in the voltage. The green curve is the case when no load-flow calculation is initially made, so the initial conditions are calculated for nominal values (point 1') U=1 p.u., $\varphi 1=0^{o}$, but the curve is a segment of the same distorted voltage curve. Therefore, there is this large jump between points 1' and point 2'. The consecutive voltage points (3, 4, etc) are independent on the calculated initial conditions because

they are a result of the given inverse FFT calculation. This large jump in values between point 1' and 2' has large effect on the current initial oscillations and the number of periods (time) before the current oscillations settle down. In order to verify and observe this effect, a simulation was setup, where no initial load-flow is calculated, so the applied voltage is the distorted voltage, updated at each iteration, but each time the initial conditions are calculated it is made for the 1 p.u. value. Therefore, each time a simulation starts, there is this large jump in the voltage present, see Figure 7.30.

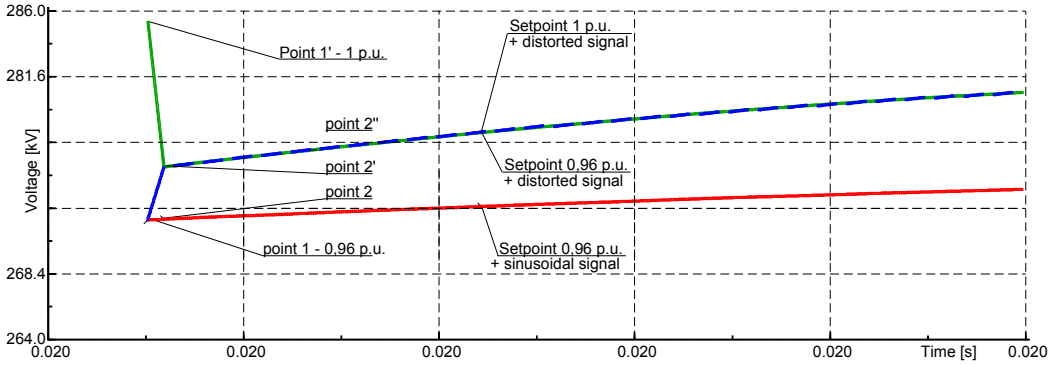

Figure 7.29 Effect of calculating initial conditions (setpoint) from preceding load-flow calculation.

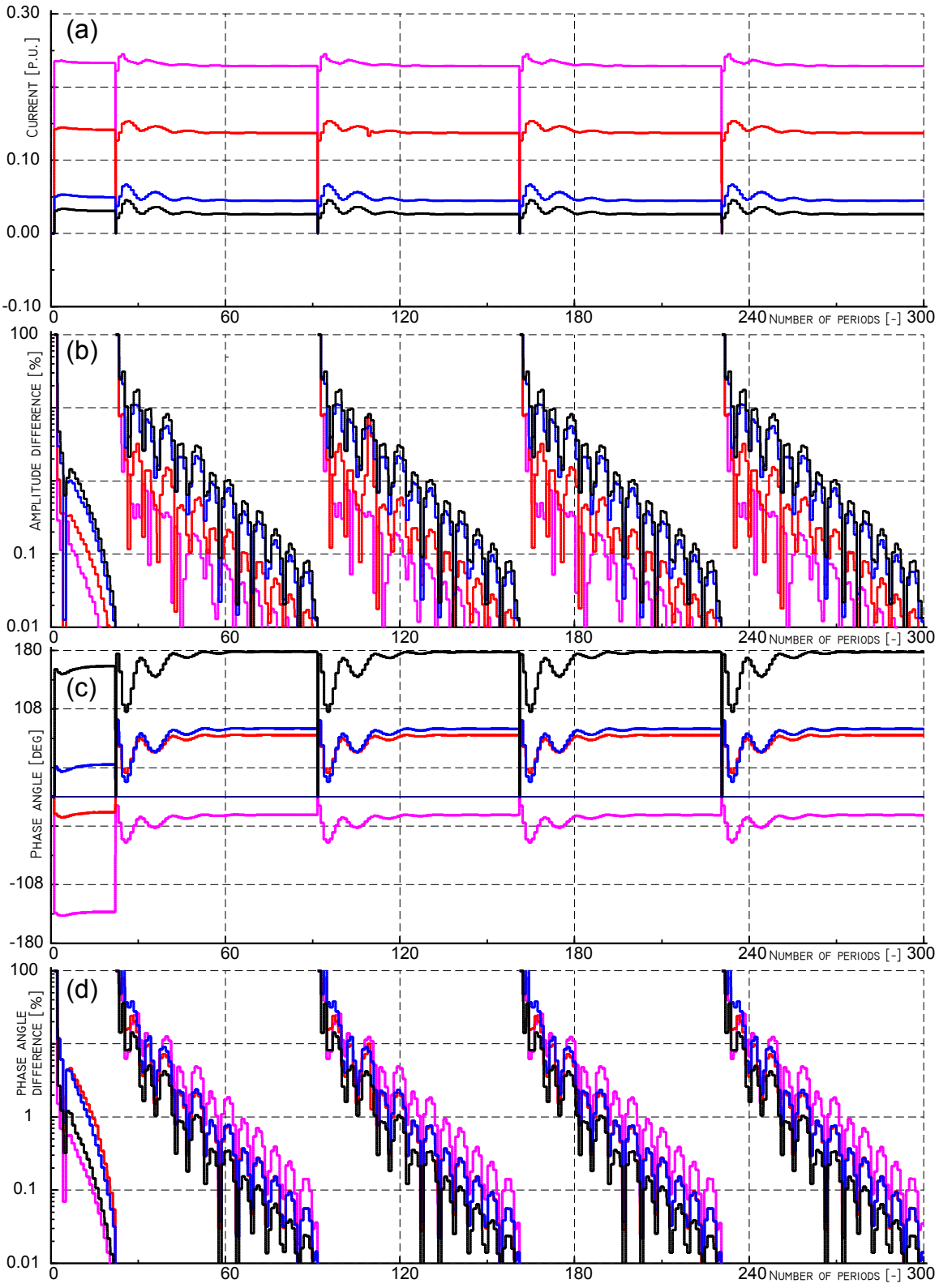

Figure 7.30 Variation of significant harmonic amplitudes and phase angles and their differences during initial oscillations, for converter Y, phase A, case 1a. Magenta - 5th harmonic, red 7th harmonic, blue – 11th harmonic and black – 13th harmonic. (a) - Amplitudes, (b) – amplitude differences, (c) – phase angles, (d) – phase angle differences.

Figure 7.30 well demonstrates the effect of lack of calculation of an initial 3-phase load-flow. In the first iteration, the initial conditions are calculated for the nominal voltage value of 1 p.u. The voltage applied in time domain simulation is sinusoidal, based on the initial conditions, therefore there is no initial "jump" (this corresponds to the red curve from Figure 7.29) and the resultant initial oscillations are minimal. Indeed, in this first time domain simulation, there are very small initial oscillations and they decay very fast, as can be seen in Figure 7.30 (a). In Figure 7.30 (b) the amplitude differences are shown; they get below the required precision index of 0,05% after 18 periods, and this process is smooth, comparing to the next iterations. The phase angles also don't oscillate much, and their differences get below 0,05% values after 18 periods.

In the next iterations, the distorted voltage is applied, but the initial conditions are again calculated using the nominal values, so the actual voltage curve corresponds to the green curve from Figure 7.29. The jump in voltage results in large current oscillations of all harmonics, as may be seen in Figure 7.30 (a). The period of these oscillations is approx. 10 periods of the fundamental frequency. It takes much more time to reach the periodic steady state, and in this case it was 69 periods before the precision indexes were reached. Values of harmonic phase angles also largely oscillate, and there is a phase shift comparing to the first period caused by the phase shift of applied voltage in first and next iterations. Both differences in the harmonic amplitudes and harmonic phase angles oscillate, and their values can vary by the factor of 10, i.e. the harmonic amplitudes may have similar values during two consecutive periods (the difference is small), but in the next period the amplitudes may change so the difference gets much higher.

Even though the initial conditions are calculated for the nominal values and there are large oscillations in the currents, the algorithm also provides precise results. Only the length of reaching a periodic steady state increases, and so the simulation time increases.

7.7.4 Limitation of the method

Because of the project limitation for harmonic analysis up to the 50^{th} harmonic, the developed hybrid time/frequency method was also made for harmonic frequencies up to the 50^{th}. As it was proven in the preceding sections, the algorithm works fine and provides precise results for realistic conditions inspected in cases 1 and 2. An attempt was therefore made in order to find the limitations of the method.

For that purpose a simulation was performed with all the harmonic filters and the capacitor bank disconnected from the HVDC_Bus, see Figure 7.17. In such a case, the bus voltage becomes largely distorted. The distorted bus voltage obtained in time domain simulation is shown in Figure 7.31 (a). The spectrum of this signal is shown in Figure 7.31 (b).

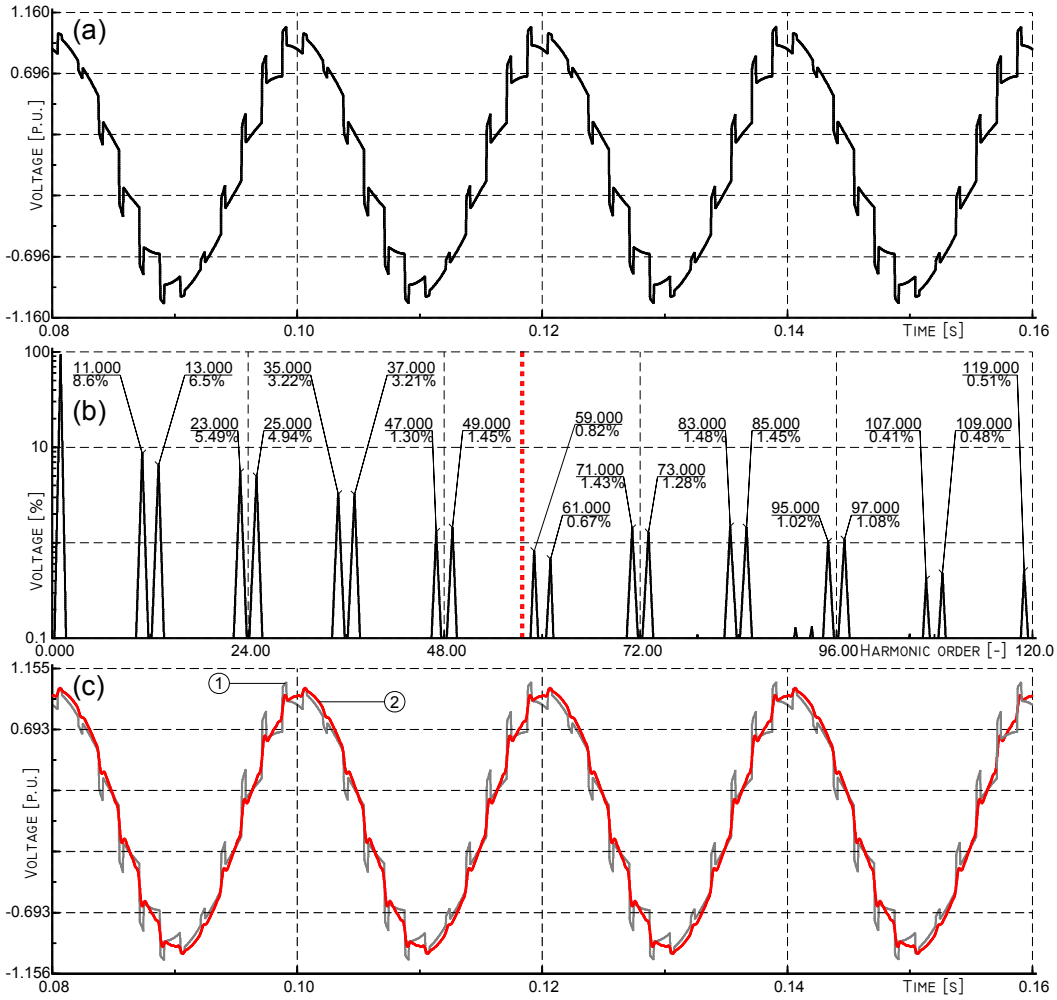

Figure 7.31 Bus voltage HVDC_Bus for a case where all harmonic filters are disconnected. (a) – time domain waveform plot, (b) – FFT of the time domain plot, (c) – original waveform plot – 1, and waveform created from a truncated Fourier series at 50th harmonic.

As may be seen there is a large content of higher harmonics. If this waveform is approximated with a Fourier series truncated at 50th harmonic, the resultant curve is shown in Figure 7.31 (c). It can be seen that the differences between the time domain result (curve 1) and its 50th harmonic approximation (curve 2) differ quite much. The hybrid method was nevertheless applied in an attempt to perform the simulation under such conditions. It has occurred that the hybrid method diverges on such a signal with higher frequency content. The course of harmonic amplitudes during the simulation is shown in Figure 7.32. it can be seen that during the first iteration the magnitudes were behaving like in the other cases, but later they started to vary, and finally at the 10th iteration the method diverges.

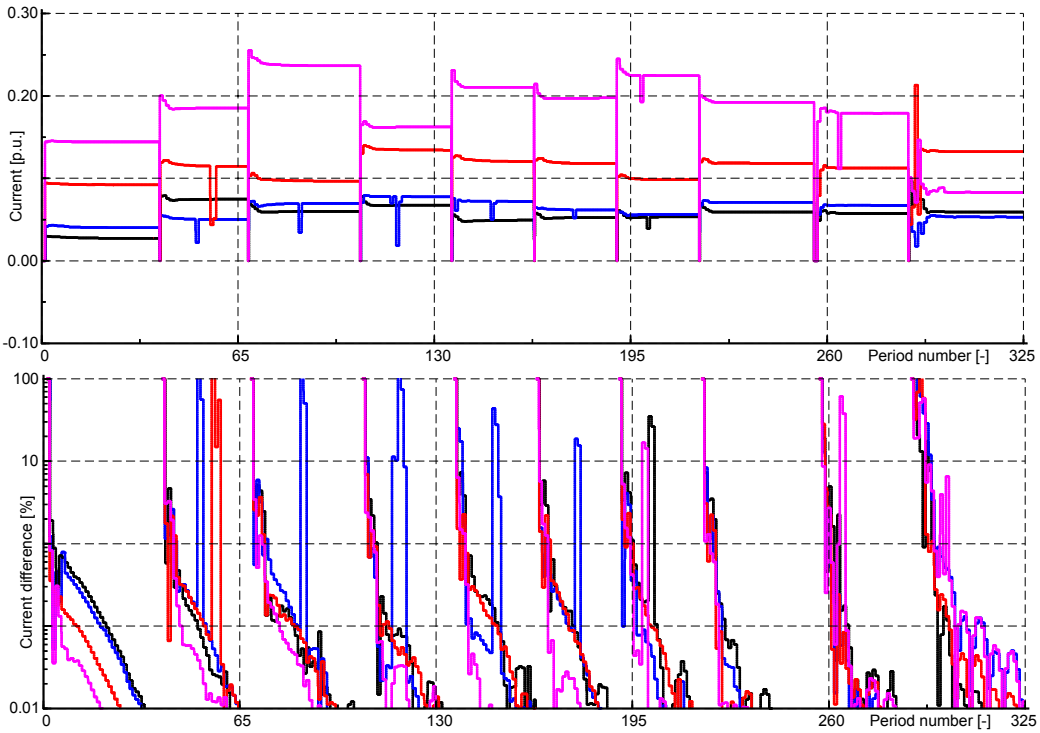

Figure 7.32 Variation of significant harmonic amplitudes and their differences during initial oscillations, for converter Y, phase A, case 1a. Magenta - 5th harmonic, red 7th harmonic, blue – 11th harmonic and black – 13th harmonic. Upper plot - Amplitudes, lower plot – amplitude differences.

Therefore, it can be concluded that even if the analysis is to be made for frequencies up to 50th harmonic, in some cases when the signal contains large amounts of higher than 50th harmonic frequencies, the method should include also higher order harmonics, perhaps as high as 6 kHz (120 harmonic).

However, it must be emphasized that for real-life cases, such distortion in the voltage at a transmission system is very unlikely to occur. For the typical (quite high anyway) harmonic distortion levels as analyzed in cases 1 and 2 the algorithm works, gives very good results and is reliable.

7.8 Conclusion

Frequency domain calculations of PowerFactory do not allow to precisely determine converter currents by simulation. The idealized spectra can be used, or alternatively results of real-life measurements may be used, or the third solution is to perform time domain simulation.

Performing time domain simulation EMT for large transmission networks is prohibitive for the reasons described in the introduction to this chapter. Therefore a hybrid time/frequency method was successfully developed in this project and was described in this chapter along with the verification results. The algorithm was implemented in the DIgSILENT PowerFactory software and is based on a modified HVDC benchmark model. The DPL simulation language was used.

Harmonic currents injected by the HVDC converters (current-source converters) are not constant but in general depend on the impedance into which they are injected and on the level of background distortion in the voltage.

Two procedures needed to be developed, the detection of periodic steady state procedure and the multiple point detection algorithm.

For both, the detection of periodic steady state and the convergence of the entire algorithm, the amplitudes and phase angles of the following significant harmonics were used: 1^{st}, 5^{th}, 7t, 11^{th} and 13^{th}.

For verification, two cases are performed. The cases differed in the level of distortion of the bus voltage obtained by disconnection of the harmonic filter. These levels of harmonic distortion were realistic. For both cases the hybrid algorithm has given results that were in a very good agreement with results of precise time domain simulation.

Various parameters of the hybrid simulation may be defined, including the precision indexes for reaching the periodic steady state and convergence of the entire algorithm. Selected precision indexes of 0,05% were demanding.

In general it took between 4 up to 6 iterations for the algorithm to converge.

The time-domain simulation was preceded with three-phase load–flow calculation and the resultant unbalanced bus voltages were used for calculating initial conditions for the voltage source. In this way the initial oscillations were largely limited. The major current oscillations disappeared after 8-10 periods, but to reach precision index of 0,05% another 20 periods needed to be simulated.

The first iteration of every simulation differs slightly from the other because sinusoidal voltage was used. In the next iterations distorted voltage was applied.

During initial oscillations uncharacteristic harmonic frequencies have low amplitudes, which decay fast to zero, for the considered cases. Their magnitudes were probably affected to a large extent by the spectral leakage originating in calculation of FFT of oscillating signals.

When simulating case 2 with more distorted bus voltage, one extra iteration was needed.

Disconnection of the harmonic filter in case 2 affected the converter currents, changing slightly the amplitude and shifting phase angles. The 5^{th} and 7^{th} harmonic currents were not affected because they circulate between both converters Y and D and do not see the system impedance. 11^{th} and 13^{th} harmonic were affected most, since at these frequencies there was the highest change in harmonic impedance.

If the initial conditions for the time domain simulations are calculated for 1 p.u. voltage value, not for the actual unbalanced voltage values, the jump between the integration points of the time domain voltage is large and results in large and long-lasting current oscillations - it takes up to 70 periods at each iteration to reach the periodic steady state (precision 0,05%). However it affects only the simulation time, not the accuracy of the final result.

The method is practically limited to signals that mainly contain harmonic orders up to 50^{th} harmonic. It was shown that if signals with large content of higher than 50^{th} harmonic frequencies are present, the algorithm may experience problems with convergence, and in the shown case it was diverging. To model high frequency components of converters that inject harmonic currents into high impedance, up to the 120 harmonic need to be included (6 kHz). However, it must be emphasized that this is a theoretical case, because for all practical applications in modelling transmission networks and HVDC converters such high levels of harmonic distortion are very unlikely. Therefore, it may be finally concluded that the developed hybrid time/frequency domain algorithm is reliable and provides precise results of calculations for realistic levels of harmonic distortion.

7.9 Future work

The hybrid method presented in this chapter was developed for the steady state harmonic analysis for harmonic frequencies up to 2,5 kHz.

In the present form, fundamental frequency of the calculated FFT is set to 50 Hz, which means that only harmonic frequencies are calculated. However, it is possible to define freely the fundamental frequency, for instance to a lover value: 5 Hz. In such a case, the result of FFT calculation would be given with a 5 Hz frequency step. This implies that in such a case also the inter-harmonic frequencies could be extracted from the time domain signals, as well.

Another feature of the method is the way of detecting the periodic steady state, namely by monitoring the amplitudes and phase angles of harmonic components. In the present realization of the method, the values are monitored until steady state is reached and then are exported and used in steady state calculations. However, the values of harmonic components are available every half a period, so it could be possible to export them every half a period, and each time perform harmonic penetration study. In this way the harmonic voltage distortion resulting from oscillating currents could be determined. The oscillations could be caused by any kind of transient event. This means that the method has potential with respect to modelling time-varying harmonics. Many cases can be studied, for instance dynamic interactions between several nonlinear loads installed in a large network, or disconnection of a harmonic filter installed in the "harmonic domain side". Even such studies like time-varying inter-harmonic or low-order harmonic analysis may be possible. According to Mark Halpin, the Chair of the Task Force responsible for the revision of IEEE standard 519-1992, the harmonic modelling and simulation requirements of the low-order and time-varying harmonics represent the greatest modelling and simulation challenge and are being addressed in the revised standard 519-1992 [Halpin].

Chapter 8

Modelling of transformer core nonlinearities

As there are two non-linear components directly installed on the transmission level, the HVDC converters and iron cores of transformers, this chapter describes implementation of the second nonlinear element - the iron transformer core. A method has been sought, that as input data requires some typical data present in the test reports. Such method has been found [Neves]. It occurred to be a modified procedure implemented earlier in the EMTP software [Dommel]. This chapter describes the implementation of this procedure in the PowerFactory software. As a contribution may be considered an evaluation of the recursive integrals presented originally in a compact form by [Neves] that are given here as ready to use in numerical programs. This algorithm is applicable to single-phase and three-phase (auto)transformers with vector group YNyn. The full DPL source code of this model is give at the attached compact disc.

8.1 Introduction

In harmonic analysis studies, power transformers can be either modelled as linear power system components, or by using more sophisticated models that take into account the iron core nonlinearity and its property of distorting currents which result in an "injection" of harmonic currents into the network. If the transformer core is to be modelled as a passive impedance, it is sufficient to model the iron core as a shunt linear inductance and a resistance, connected in parallel. In order to model the nonlinear behavior of the core, voltage dependence of an equivalent inductance and resistance shall also be included. In order to minimize the core size, power transformers are usually designed to operate just below the knee point. Therefore, when the voltage increases above a certain value, the transformer magnetising current becomes distorted; even at the nominal operating voltage the no-load current THD can be as high as 20 % [Dugan]. The harmonic contribution from power transformers can be most likely noticed in a grid with many transformers installed, during low load hours, when the load current is low and the voltage rises [Dugan]. DIgSILENT PowerFactory enables to precisely model the transformer core nonlinearity in the time domain (EMT) [PowerFactory]. In the frequency domain it is not possible to do it so far. Therefore, a new model is set up to model the transformer core nonlinearity in the harmonic domain calculations of DIgSILENT PowerFactory.

Several ways of modelling the iron core nonlinearities exist, described for instance in [Dugui], [Santesmases] or [Chua]. These methods require that the dynamic hysteresis loops of the material are known. This is not always possible, especially if the nonlinearities of older transformers are of interest. In this project the only data available for the autotransformers are typical test reports. Therefore, a different method has been found, where the core nonlinearities can be determined using a simpler set of input data [Dommel], [Neves]. For computation, the method requires only $V_{rms} - I_{rms}$ curves and the no-load losses. These data are present in the test reports. The method was implemented as an external script of DIgSILENT PowerFactory using the DIgSILENT Programming Language (DPL).

Chapter outline

In this chapter the results of implementation and verification of an already existing algorithm that allows for calculating saturation characteristics of single-phase power transformers are demonstrated. First, some background theory is refreshed, then, the algorithm and its implementation is described and a detailed structure of the implemented algorithm with all its subroutines is shown. All the recursive equations and integrals from [Neves] were evaluated and are presented in a ready-to-use fashion. Results of verifications are shown. Finally, a theoretical analysis of the core nonlinearities phenomena in single, and three-phase transformers and in autotransformers is presented.

8.2 Theoretical background

In an iron-core power transformer, the flux Φ and the flux density B within the core is proportional to the voltage u_1 applied across the primary winding, according to the Faraday's law. In the sinusoidal case it can be written [Arrillaga]:

$$u_1 = U_{1m}\sin\varpi t = \frac{d\phi}{dt},$$

$$\phi = \int U_{1m}\sin\varpi t\cdot dt = \frac{U_{1m}}{\varpi}\cos\varpi t = \Phi_m\cos\varpi t, \tag{8.1}$$

$$B = \frac{\phi}{S} = \frac{\int U_{1m}\sin\varpi t\cdot dt}{S}.$$

where S is the cross-section of the core.

The resultant magnetizing current I_m needed to produce this sinusoidal flux is related to the magnetic field strength H by a constant value, which is the ratio of number of turns N to the total length of the magnetic path l [Matsch]:

$$H = I\cdot\frac{N}{l}. \tag{8.2}$$

The magnetic flux density B is related to the magnetic field strength H by the magnetic permeability of the steel used in the transformer core μ [Matsch]:

$$B = \mu\cdot H. \tag{8.3}$$

Equation (8.3) shows that if the magnetic permeability μ is linear and B is sinusoidal, the magnetic field strength H (and what follows, the magnetizing current I_m) will be sinusoidal. If the transformer operates in saturation, μ is no longer linear and the magnetic field strength H is distorted, because the product of H with the magnetic permeability μ must still produce the sinusoidal flux density B, see Figure 8.1. If the magnetizing current I_m is allowed to flow freely (low impedance path Z for all harmonics), since it is symmetrical and since $i(\omega t+\pi) = -i(\omega t)$, after decomposing it to Fourier components, it will contain the fundamental frequency and all the odd harmonics: 3rd, 5th, 7th, 9th, etc.

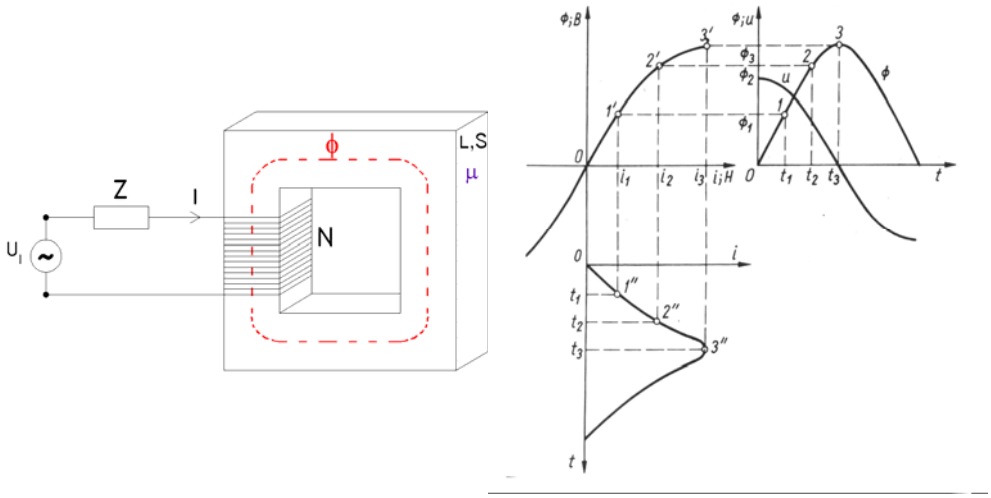

Figure 8.1 Typical relations between main flux Φ, supplying voltage U and no-load (magnetizing) current I (without hysteresis effects) [Bolkowski].

8.3 The algorithm and its implementation

In order to determine magnetizing current harmonics, a special algorithm has been implemented. Initially this technique was proposed by [Dommel] for estimating the magnetizing inductance L_m. [Neves] extended this algorithm with computation of the nonlinear resistance R_{Fe}, see Figure 8.2(a).

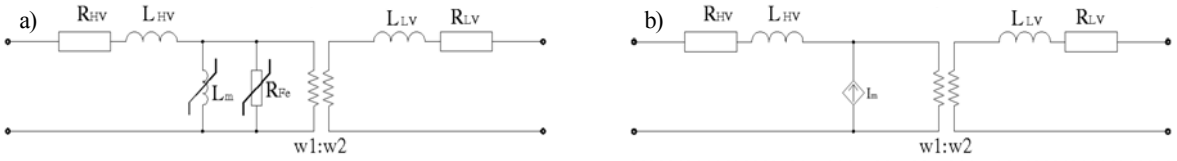

Figure 8.2 Equivalent diagram of a power transformer. R_{HV}, R_{LV} – winding resistances, L_{HV}, L_{LV} – Leakage inductances. (a) R_{Fe} – magnetizing resistance – hysteresis losses and eddy current losses in the core, L_m – magnetizing inductance. b) In the harmonic domain, nonlinearities are modelled as a current source: I_m – the magnetizing current.

The main advantage of this algorithm is that both the equivalent resistance R_{Fe} and inductance L_m are calculated directly from the conventional transformer no-load test data: V_{rms} – I_{rms} curve and the no-load losses at fundamental frequency. The equivalent resistance that accounts for the no-load losses varies with applied voltage magnitude, therefore, it should be modelled as voltage dependent, i.e. nonlinear. It accounts for two effects: linear eddy current loss and nonlinear hysteresis loss [Chen], [Neves], [Masoum]. In the implemented model it is included as a piecewise linear u-i_R characteristic. This resistance is found from the measured total no-load losses. Calculated in this way the resistive part of the total, measured no-load current can be subtracted geometrically. This allows for a calculation of the current flowing through the nonlinear inductance (piecewise linear λ-i_L characteristic). Next, the resulting, real and imaginary harmonic components are geometrically added and modelled as a current source. During harmonic load flow calculations, this current source will inject harmonic currents into the investigated network, Figure 8.2(b).

The algorithm requires that the following three assumptions are made: winding impedances are ignored and the supplying voltage and resulting flux are sinusoidal and the piecewise resistance and piecewise inductance are both symmetric with respect to the origin.

The algorithm has been implemented in the simulation software DIgSILENT PowerFactory (PF). In this software it is possible to create automatic simulation tasks and build miscellaneous models of power system components, as the program possesses its own programming language: DIgSILENT Programming Language (DPL). The syntax of this language is similar to C++. This language was used to implement the described algorithm. The basic idea was that the whole algorithm was programmed as several DLP subroutines and a main DPL controlling script. The structure of the algorithm implemented in PF is shown in Figure 8.3 on page 225, and the individual components of the algorithm are described in the following sections. Special emphasis is put on the implementation details, and the setup, ready-to-use equations.

8.3.1 Routine Main

The main script *Main* as shown in Figure 8.3 on page 225, when executed recalculates all input data stored in the Data matrix (U_m, I_m) from rms to the peak values and stores them in the matrix of results 'Results'. The Data matrix contains the results of measurements from the no-load tests, i.e. V_{rms} – I_{rms} curve and the no-load losses. Letter *m* denotes the number of available measurements stored in Data. Next, the script automatically connects a current source to the HV transformer bus. Then it initiates conventional load-flow calculations. As a result of the load-flow, the three-phase voltages at the transformer bus are obtained. Next, the script *Main* executes in turn all the subroutines, beginning with subroutine *volt_comp*.

8.3.2 Subroutine volt_comp

This subroutine compares the calculated terminal voltages with the voltages stored in Data matrix and returns the row number f of the closest voltage value. If the bus voltage is higher than the highest voltage in the input data, the subroutine returns the max number of rows f = m. This means that the distorted magnetizing current will be constant for higher voltage values. In most of the cases it shall be sufficient during normal operation, since the voltage in no-load tests must be varied up to levels, which are higher than at which the transformer is later operated continuously. When Subroutine *volt_comp* is accomplished, main script executes the next subroutine *iR*.

8.3.3 Subroutine iR

This subroutine calculates the first linear and next piecewise linear elements of the nonlinear resistance curve R. It is done in the following way. For the first segment, i.e. up to the first measured voltage, the peak current I_{r_1} and the first linear segment of the resistance curve is calculated directly from the rms input data [Neves]:

$$P_1 = V_{rms_1} \cdot I_{r-rms_1}; \quad I_{r_1} = \frac{2P_1}{V_1}; \quad R_1 = \frac{V_1}{I_{r_1}}. \tag{8.4}$$

The power measured at higher voltage values is a product of the sinusoidal voltage and nonsinusoidal current I_m, see Figure 8.4 on page 226. It can be seen that if linear resistance determined by (8.4) is used, the resultant current would be sinusoidal, regardless of the amplitude of the applied voltage. The peak value of this current would be much lower than the actual peak value of the distorted current. Therefore, in order to assess the real current and the next segments of the piecewise linear curve, the power definition must be used [Neves]:

$$P = \frac{2}{\pi} \int_0^{\frac{\pi}{2}} v(\alpha) \cdot i_r(\alpha) \cdot d\alpha. \tag{8.5}$$

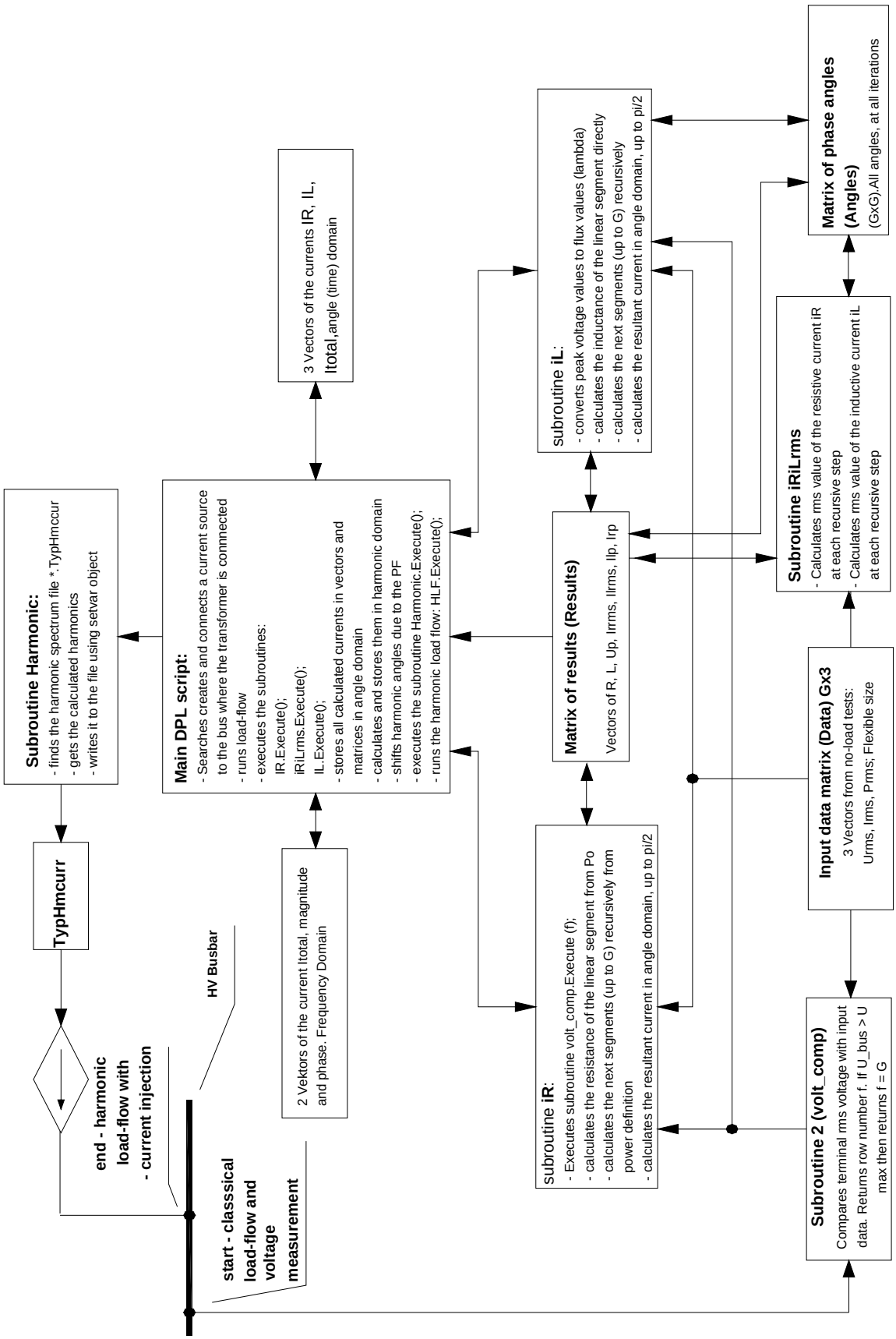

Figure 8.3 Flow-chart of the implemented algorithm.

It is sufficient to calculate the current shape for ¼ of a period because the voltage is assumed sinusoidal. Therefore, the resultant current will contain only odd harmonic components and therefore, will be symmetrical.

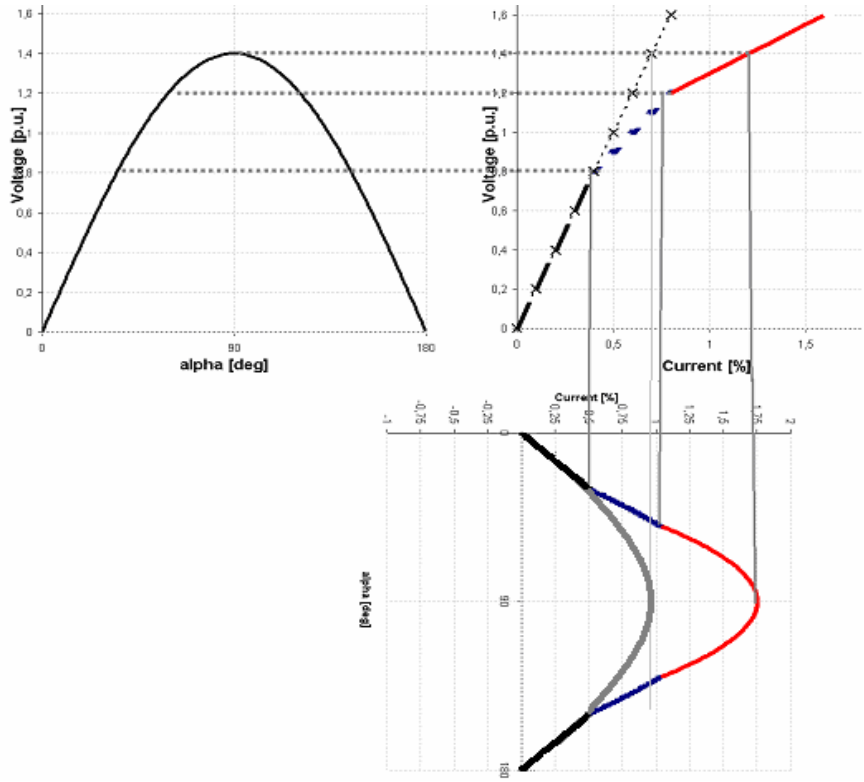

Figure 8.4 Sinusoidal voltage (left plot) applied to a linear V-I_R curve and the piecewise linear V-I_R curve (upper right plot) and the resultant, sinusoidal current (grey curve) and approximated distorted current (blue + red curve) (lower plot)

The applied voltage can be written as $v(\alpha) = V_k \sin(\alpha)$. The total no-load power loss is [Neves]:

$$P_k = \frac{2}{\pi}\left[\begin{array}{l} \underline{\int_0^{\alpha_1} (V_k \sin\alpha)\left(\frac{V_k \sin\alpha}{R_1}\right) d\alpha + } \\ \int_{\alpha_1}^{\alpha_2} (V_k \sin\alpha)\left(I_{r_1} + \frac{V_k \sin\alpha - V_1}{R_2}\right) d\alpha + \ldots + \\ \underline{\int_{\alpha_{k-1}}^{\frac{\pi}{2}} (V_k \sin\alpha)\left(I_{r_{k-1}} + \frac{V_k \sin\alpha - V_{k-1}}{R_k}\right) d\alpha} \end{array}\right]. \quad (8.6)$$

The angles $\alpha_1, \alpha_2, \ldots, \alpha_{k-1}$ are calculated from $\alpha_j = \arcsin(V_j / V_k), j = 1,2,\ldots,k-1$ and stored at each recursive step in the matrix of phase angles *Angles*. Term $V_k \sin\alpha$ is the sinusoid of the actual, entire voltage applied, $(V_k \sin\alpha)/R_1$ is the sinusoid of the corresponding current assuming no saturation (so linear resistance R_1 is used). Only the first part, up to the first knee point is taken, therefore the integration is from 0 to α_1. I_{rk-1} is the peak value of the current calculated at the k-1 recursive step and $V_k \sin\alpha - V_{k-1}$ is the "upper" part of the voltage sinusoid with the peak voltage V_{k-1} subtracted to get the corresponding current segment that can be added on the top of the already calculated current value. Computation using Equation (8.6) must be done recursively - segment by segment. The part of Equation (8.6) that is underlined with a single line shall be

recomputed at each recursive step, because the voltage V_k must be updated. Part of Equation (8.6) underlined with double line must be updated and computed recursively for each segment up to the last segment where α reaches π/2. For instance to calculate Equation (8.6) for k = 3, there would be 3 unknowns: R_2, I_{r2} and R_3, and only one equation. Therefore, first it is necessary to compute Equation (8.6) for k = 2. Then the only unknown is R_2 so it can be computed. Equation (8.6) can be rewritten in the form from which it is easy to determine the unknown value of resistance [Neves]:

$$P_k = a_{r_k} + \frac{b_{r_k}}{R_k} \quad \Rightarrow \quad R_k = \frac{b_{r_k}}{P_k - a_{r_k}}. \tag{8.7}$$

Components a_{r_k} and b_{r_k} were computed, and are given below in a ready-to-use fashion:

$$a_{r_k} = \frac{2}{\pi}\left[\frac{\frac{V_{(k)}^2}{R_1}\left(\frac{1}{2}\alpha_1 - \frac{\cos\alpha_1 \sin\alpha_1}{2}\right) +}{\underline{\underline{V_{(k)} I_{r(k-1)}\left(\cos\alpha_{(k-1)} - \cos\alpha_{(k)}\right)}}}\right], \tag{8.8}$$

$$b_{r_k} = \frac{2}{\pi}\left[\frac{\frac{V_{(k)}^2}{2}\left(\begin{matrix}\cos\alpha_{(k-1)}\sin\alpha_{(k-1)} - \cos\alpha_k \sin\alpha_k \\ +\alpha_k - \alpha_{(k-1)}\end{matrix}\right) -}{\underline{\underline{-V_{(k)} V_{(k-1)}\left(\cos\alpha_{(k-1)} - \cos\alpha_{(k)}\right)}}}\right], \tag{8.9}$$

Next, the subroutine iR must calculate the current I_{r2} from [Neves]:

$$I_{r_k} = I_{r_{k-1}} + \frac{V_k - V_{k-1}}{R_k}. \tag{8.10}$$

When R_2 and Ir_2 is known, the calculations can be started again, now for k = 3, to determine R_3. This procedure is repeated for each segment (each voltage in the Data matrix) except for the first one, i.e. for k ≥ 2. Resistance R and current peak Ir_k values are stored in the matrix *Results*.

8.3.4 Subroutine i_L.

The λ-i_L curve is calculated by the Subroutine i_L. Peak flux values λ_k are related to the peak voltage values V_k by the expression [Neves]:

$$\lambda_k = \frac{V_k}{\varpi}. \tag{8.11}$$

For sinusoidal voltages the harmonic components of the resistive and inductive currents are orthogonal [Neves] and therefore relation (8.12) applies:

$$I_{l-rmsk} = \sqrt{I_{t-rmsk}^2 - I_{r-rmsk}^2}. \tag{8.12}$$

where $I_{t\text{-}rmsk}$ is the total measured rms no-load current, $I_{r\text{-}rmsk}$ is the determined in previous section rms resistive current component and $I_{l\text{-}rmsk}$ is the inductive rms current component to be computed. For the first segment in the *λ-i_l* curve subroutine i_L calculates the linear inductance using the equations [Neves]:

$$I_{l_1} = I_{l-rms_1}\sqrt{2}; \qquad \lambda_1 = \frac{V_1}{\varpi}; \qquad L = \frac{\lambda_1}{I_{l_1}} = \frac{V_1}{\varpi I_{l_1}}; \tag{8.13}$$

For segments k ≥ 2, assuming $\lambda_k(\alpha) = \lambda_k \sin(\alpha)$, rms definition for the current will be [Neves]:

$$I_{l-rms_k}^2 = \frac{2}{\pi}\left[\begin{array}{l}\int_0^{\alpha_1}\left(\frac{\lambda_k \sin\alpha}{L_1}\right)d\alpha + \int_{\alpha_1}^{\alpha_2}\left(\frac{I_{l_1} + \lambda_k \sin\alpha - \lambda_1}{L_2}\right)d\alpha + \ldots + \\ \int_{\alpha_{k-1}}^{\frac{\pi}{2}}\left(I_{l_{k-1}} + \frac{\lambda_k \sin\alpha - \lambda_{k-1}}{L_k}\right)d\alpha\end{array}\right]. \tag{8.14}$$

This equation is analogous to equation (8.6), i.e. it must be computed segment by segment. This equation can be rewritten in the form [Neves]::

$$a_{lk}\left(\frac{1}{L_k}\right)^2 + b_{lk}\left(\frac{1}{L_k}\right) + \left(c_{lk} + x_0\right) = 0. \tag{8.15}$$

For this quadratic equation it is assumed [Neves] that $a_{lk} > 0$, $b_{lk} > 0$ and $(c_{lk} + x_0) < 0$. Therefore, the linear segments of the inductance L_k are calculated from [Neves]:

$$L_k = \frac{2a_{lk}}{-b_{lk} + \sqrt{b_{lk}^2 - 4a_{lk}\left(c_{lk} + x_0\right)}}. \tag{8.16}$$

Components $a_{L_k}, b_{L_k}, c_{L_k}, x_0$ were computed and are given below in a ready-to-use fashion:

$$x_0 = \frac{\lambda_k^2}{L_1^2}\left[\begin{array}{l}\frac{\cos\alpha_{(k-1)}\sin\alpha_{(k-1)}}{2} - \frac{\cos\alpha_{(k)}\sin\alpha_{(k)}}{2} + \\ \frac{\alpha_{(k)} - \alpha_{(k-1)}}{2}\end{array}\right]. \tag{8.17}$$

$$a_{lk} = \left[\begin{array}{l}-\lambda_{(k)}^2 \cdot x_1 + \lambda_{(n-1)}^2\left(\alpha_{(n)} - \alpha_{(n-1)}\right) - \\ 2\lambda_{(k)}\lambda_{(n-1)}\left(\cos\alpha_{(n-1)} - \cos\alpha_{(n)}\right)\end{array}\right], \tag{8.18}$$

where x_1 from Equation (8.18) above is:

$$x_1 = \left[\begin{array}{l}\frac{\cos\alpha_{(n-1)}\sin\alpha_{(n-1)}}{2} - \frac{\cos\alpha_{(n)}\sin\alpha_{(n)}}{2} + \\ \frac{\alpha_{(n)} - \alpha_{(n-1)}}{2}\end{array}\right], \tag{8.19}$$

And the other components of Equation (8.16) are:

$$b_{lk} = \left[\begin{array}{l}-2\lambda_{(k)}I_{L_{(n-1))}}\left(\cos\alpha_{(n-1)} - \cos\alpha_{(n)}\right) - \\ 2\lambda_{(n-1)}I_{L_{(n-1))}}\left(\alpha_{(n)} - \alpha_{(n-1)}\right)\end{array}\right], \tag{8.20}$$

$$c_{lk} = \left[-I_{L_{(n-1)}}^2\left(\alpha_{(n)} - \alpha_{(n-1)}\right)\right], \tag{8.21}$$

and the peak current I_{lk} must be also computed at each segment from [Neves]:

$$i_{l_k} = i_{l_{k-1}} + \frac{1}{L_k}\left(\lambda_k - \lambda_{k-1}\right). \tag{8.22}$$

8.3.5 Subroutine *iRiLrms*.

This subroutine calculates the rms value of the distorted resistive current component I_{rkrms} and later, the rms value of the distorted inductive component I_{Lkrms}, at each recursive step. The rms value of the resistive current I_{rkrms} is found from the rms definition [Neves]:

$$I_{rms}^2 = \frac{2}{\pi}\int_0^{\frac{\pi}{2}} i^2(\alpha)\cdot d\alpha \tag{8.23}$$

$$I_{r-rms_k}^2 = \frac{2}{\pi}\left[\begin{array}{l}\underline{\int_0^{\alpha_1}\left(\frac{V_k \sin\alpha}{R_1}\right)^2 d\alpha +} \\ \int_{\alpha_1}^{\alpha_2}\left(I_{r_1}+\frac{V_k \sin\alpha - V_1}{R_2}\right)^2 d\alpha + \ldots + \\ \underline{\int_{\alpha_{k-1}}^{\frac{\pi}{2}}\left(I_{r_{k-1}}+\frac{V_k \sin\alpha - V_{k-1}}{R_k}\right)^2 d\alpha}\end{array}\right] \tag{8.24}$$

Equation (8.24) is given below in a ready-to-use fashion:

$$I_{r-rms_k}^2 = \frac{2}{\pi}\left[\begin{array}{l}\underline{\frac{V_k^2}{R_1^2}\left(-\frac{\cos\alpha_{(1,k)}\sin\alpha_{(1,k)}}{2}+\frac{\alpha_{(1,k)}}{2}\right)+} \\ \underline{\frac{V_k^2}{R_n^2}\left(\begin{array}{l}\frac{\cos\alpha_{(n-1,k)}\sin\alpha_{(n-1,k)}}{2}- \\ \frac{\cos\alpha_{(n,k)}\sin\alpha_{(n,k)}}{2}+\frac{\alpha_{(n,k)}-\alpha_{(n-1,k)}}{2}\end{array}\right)+} \\ \underline{\left(2I_{r_{(n-1)}}\frac{V_{(k)}}{R_{(n)}}-2\frac{V_{(k)}V_{(n-1)}}{R_n^2}\right)\left(\begin{array}{l}-\cos\alpha_{(n-1,k)}- \\ \cos\alpha_{(n,k)}\end{array}\right)+} \\ \left(I^2_{r_{(n-1)}}-2I_{r_{(n-1)}}\frac{V_{(n-1)}}{R_{(n)}}+\frac{V^2_{(n-1)}}{R^2_{(n)}}\right)\left(-\alpha_{(n)}-\alpha_{(n-1)}\right)\end{array}\right] \tag{8.25}$$

If a sinusoidal voltage is applied to the parallel connection of linear inductance and resistance, the resistive current will be in phase with the applied voltage and the inductive current will be shifted by 90˚. In case of nonlinear resistance and inductance, the resistive and reactive currents will be distorted, i.e. they will contain harmonics but still the adequate harmonic components will be orthogonal with respect to each other [Neves]. Based on this assumption, the subroutine computes the inductive part of the current subtracting geometrically the computed above resistive rms component form the total measured rms no-load current.

Determined in the angle domain inductive and resistive current components are stored in separate vectors of the length 256 points each. Next, a DFT function available in DPL is applied to the vectors, and the resultant harmonic magnitudes and phase angles are geometrically added and assigned to a current source. This current source shall inject the calculated harmonic currents into the investigated network during harmonic load flow studies.

8.4 Verification of the algorithm

The implemented algorithm has been verified in two steps. In the first step, the data from [Neves] were used in order to verify if the algorithm was implemented correctly. In the second step, the no-load current of a single-phase 2kVA transformer was measured. V_{rms} – I_{rms}, no-load loss curves and the harmonic content was determined. The results of verification are presented in sections 8.4.1 and 8.4.2.

8.4.1 Algorithm verification using the data taken from [Neves]

Piecewise linear V_{rms} – I_{rms} and no-load loss curves were measured by [Neves] on a silicon iron core assembled in an Epstein frame. These input data are shown in Figure 8.5.

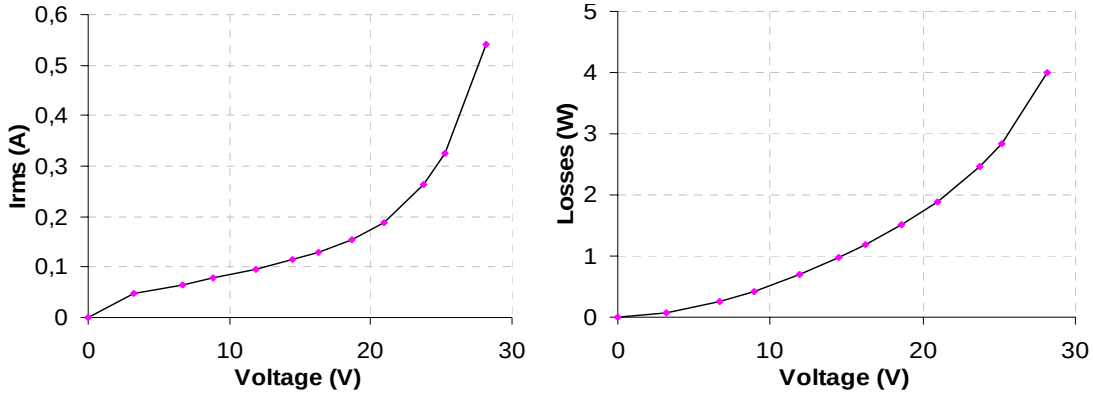

Figure 8.5 Input values: Left diagram shows V_{rms} – I_{rms} and the right one shows no-load losses (both piecewise linear curves) measured by [Neves].

The resultant piecewise linear characteristics λ-i_L and u-i_R are shown in Figure 8.6 below. It can be seen that both characteristics λ-i_L and u-i_R are in a perfect agreement as the characteristics obtained originally by [Neves]. This proves that the implemented in PowerFactory algorithm and the performed calculations are exactly the same as in the original algorithm.

As an example result, the obtained resistive, inductive and total magnetizing current waveshapes are shown in Figure 8.7 on page 231. These current values correspond to the iron core saturated to the maximal level, for which data were available. As can be seen these currents are highly distorted. The resistive and the inductive currents are shifted with respect to each other by 90 degrees, and after summing them up they give the total, magnetizing current.

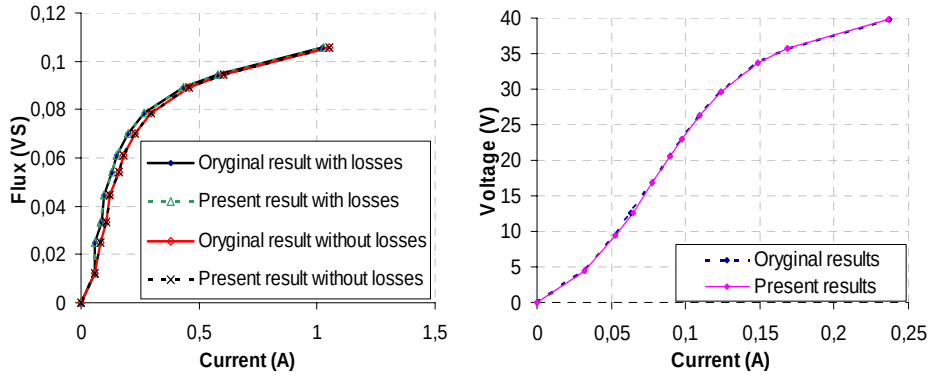

Figure 8.6 Results of verification – comparison of the presently obtained characteristics with the original characteristics obtained by [Neves]. Left diagram shows the piecewise linear λ-i_L characteristics (computed with and without subtracting the losses) and right diagram shows the piecewise linear u-i_R characteristics.

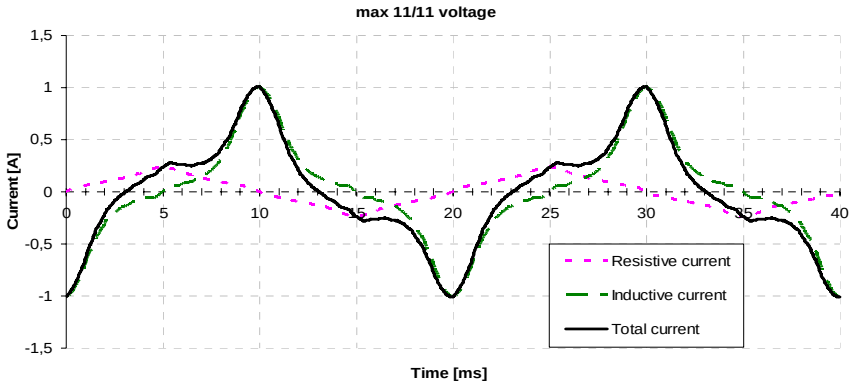

Figure 8.7 Resistive, inductive and total magnetizing current waveshapes determined using the implemented in PowerFactory algorithm, for the input values of $V_{rms} - I_{rms}$ curves and the no-load losses taken from [Neves].

In Figure 8.8 below the resistive current waveshape is shown for the operation point corresponding to different saturation levels, beginning from the lowest voltage level, (V 1/11) up to the most saturated, (V 11/11). It can be seen that the shape is initially sinusoidal when the voltage is increased, it becomes distorted.

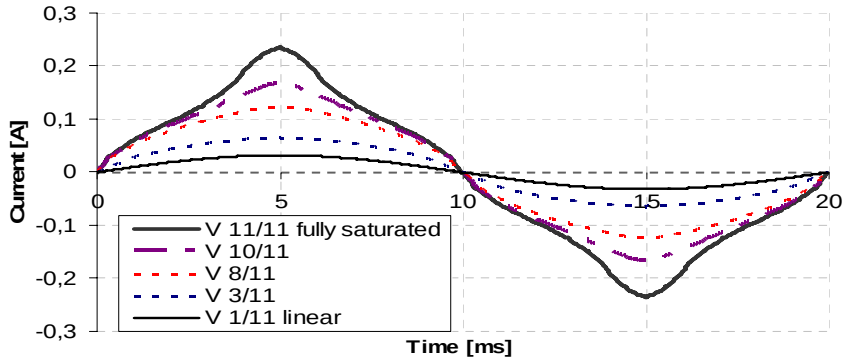

Figure 8.8 Resistive current waveshape determined using the implemented algorithm. The input values were taken from [Neves] for operating points corresponding to different saturation levels, from linear (lowest voltage, V 1/11) up to the most saturated, (V 11/11).

8.4.2 Verification with the $V_{rms} - I_{rms}$ and no-load losses obtained from laboratory measurements on a single-phase transformer

A no-load test was performed and the voltage has been changed in the range form 0.1 p.u. up to 1.3 p.u. and the following values have been measured: sinusoidal supplying voltage U_{rms}, no-load current I_{rms}, harmonic distortion of the no-load current, harmonics 3^{rd}, 5^{th}, 7^{th}, 9^{th}, 11^{th}, 13^{th}, no-load losses P_0. Next, the measured no-load current and no-load losses were used as input data for the implemented algorithm. The determined piecewise linear resistance R and inductance L are shown in Figure 8.9 on page 232. The resultant inductive and resistive current waveshapes for the saturated core (U = 1.3 p.u.) are shown in Figure 8.10 on page 232. Figure 8.11 on page 233 shows the content of no-load current harmonics versus exciting voltage. It can be seen that the variation of the no-load current harmonics versus exciting voltage measured and determined using the algorithm is comparable, especially for a heavily saturated core. However, higher order harmonics show better agreement with the measured values than lower order harmonics. Also a difference between the measured and calculated 3^{rd} harmonic component for low exiting voltage (0.8 – 0.9 p.u.) can be noticed. In general, the measured harmonic values were higher than the

calculated using the algorithm. The transformer was already saturating at the voltage value of 0,8 p.u. The reason for this discrepancy has not been revealed. The effects of omitting some of the parameters should be studied, for instance the winding impedances or perhaps the effects of the internal transformer capacitances.

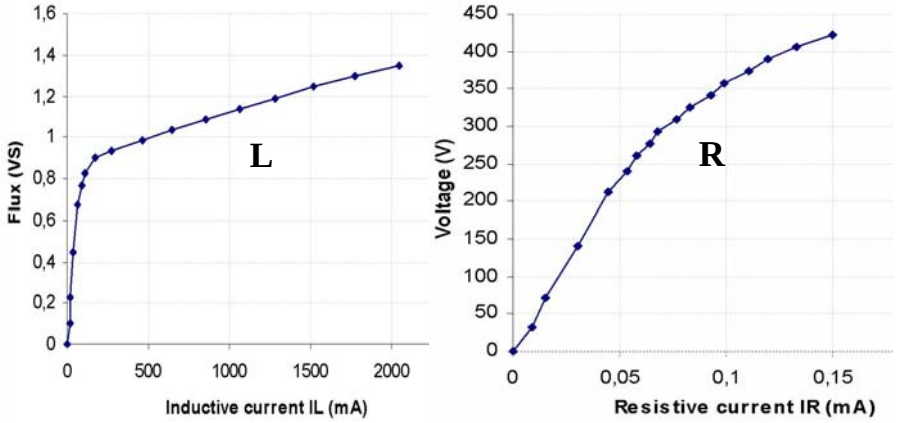

Figure 8.9 Determined piecewise linear inductance L and resistance R.

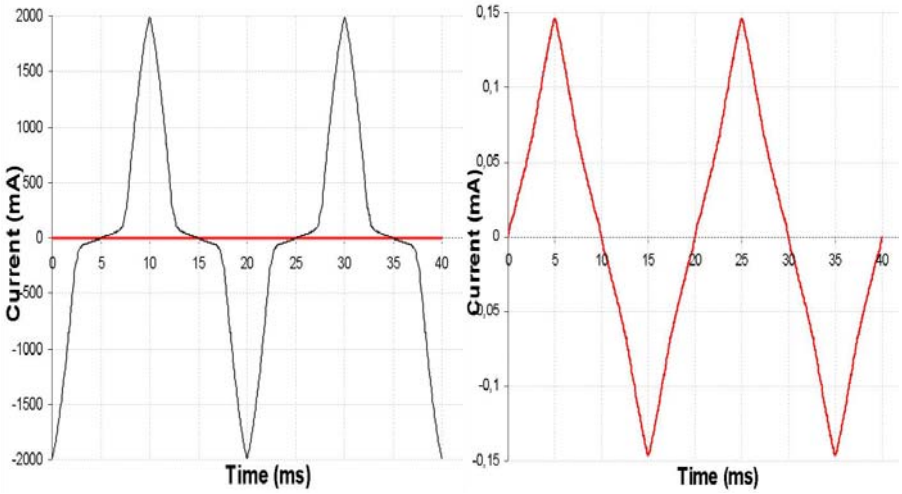

Figure 8.10 Left figure - Inductive (black) and resistive (red) current components determined by the algorithm. Right figure shows amplified resistive current component. Core saturated (U = 1.3 p.u.).

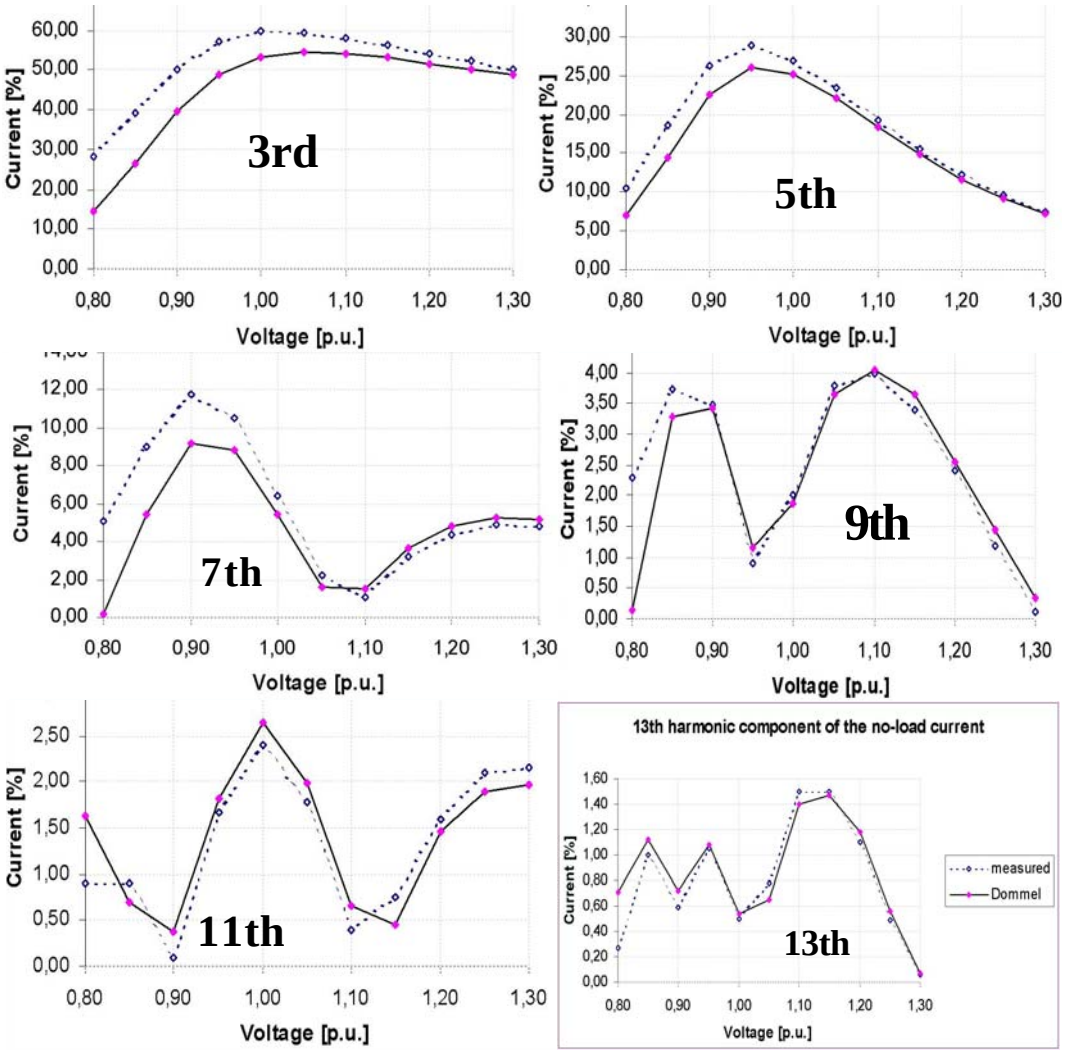

Figure 8.11 No-load current harmonics versus exciting voltage. Dotted line – measured values, continuous line – calculated using the algorithm.

8.5 Theoretical analysis on three-phase transformers

8.5.1 Three-limb three-phase transformer

Now, a case where three, single-phase transformers are combined, to create a three-limb transformer but with all three windings supplied with the same sinusoidal (zero-sequence) voltage U_1 is considered, see Figure 8.12 (a) on page 234. The resultant fluxes will have the same direction in all three legs, and therefore, they will be pushed-out of the ferromagnetic core and run in the air, oil, tank walls, etc. The magnetic permeability of the air or oil μ_{air} is much lower than the permeability of the ferromagnetic core μ, and therefore, the resultant zero-sequence flux Φ_{air} will be much lower than the positive/negative sequence flux Φ. This in turn means that the zero-sequence equivalent core inductance L'_m is much smaller than the positive/negative sequence inductance Lm, where the voltages and resultant fluxes, shifted with respect to each other by 120 deg run entirely in the magnetic core, see Figure 8.12 (b). Moreover the zero-sequence inductance L'_m may be assumed linear, because the flux practically depends on the linear air/oil permeability, and the flux will be reduced because of the higher equivalent reluctance, which will cause the core to be less saturated. For the same reason the zero-sequence core losses may be ignored.

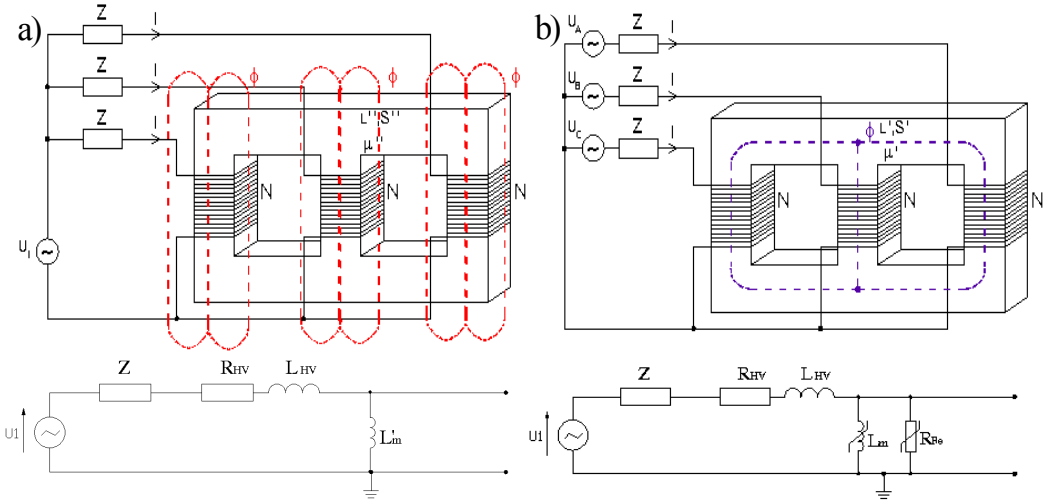

Figure 8.12 Three-phase transformer supplied with a) purely zero-sequence voltage U_1 and its equivalent circuit, b) three-phase positive sequence voltages U_A, U_B, U_C, and its equivalent circuit.

Therefore, justified would be the assumption that for three-leg transformers, the magnetizing current caused by the zero-sequence, sinusoidal voltage is also sinusoidal. Besides, it can be concluded that even if the magnitudes of supplying voltages are the same in both cases shown in Figure 8.12 (a) and (b), The magnetizing current in case (a) will be larger than in case (b). If the flux Φ_{air} would run entirely in the air, the resultant equivalent inductance would have similar value like the leakage inductance of the primary winding L_{HV}. In reality the fluxes still enter the core and therefore, the inductance L'_m is several times higher than the leakage inductance of the windings $L_{HV} < L'_m << L_m$ [Bolkowski]. In case (b), the three-phase sinusoidal voltage will create a three-phase sinusoidal flux that will run entirely in the core. The consequence is that the flux will pass only through the material that is characterized by a high and nonlinear value of permeability μ, and the magnetizing current will be nonlinear in the same way like in the case of a single-phase transformer (ignoring core asymmetries that introduce coupling between sequences).

8.5.2 Effect of winding connections

The analysis presented above was made with the assumption that the primary winding is connected in grounded star, so the impedance for all harmonics is Z. In that case the magnetizing current will contain all odd harmonics including that of the zero-sequence, which are the 3rd, the 9th, 15th, etc. If the grounding of the starpoint is removed, the impedance Z for all zero-sequence harmonics would become infinitely large, which means that the triplen current harmonics will be blocked, see Figure 8.13. Since Equation (8.3) must be always true, the blocked triplen current harmonics will cause the magnetic flux and the voltage at the winding terminals to be distorted. This is a very undesirable phenomenon. The zero-sequence flux components will be pushed out of the core (this will result in the lower magnitude of the flux, due to the higher reluctance) and this flux will in turn induce back zero-sequence voltage in the primary winding.

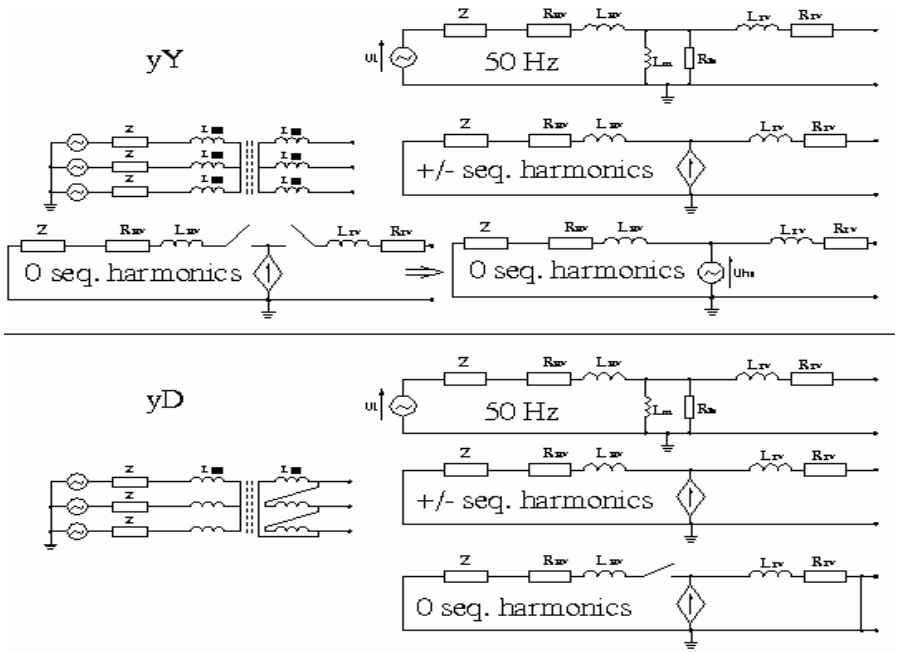

Figure 8.13 Equivalent diagrams of transformers connected in yY and yD.

Therefore, a power transformer connected in ungrounded Wye (with no delta connected winding) if exposed to saturation will produce zero-sequence harmonic voltages. This voltage distortion can be modelled as a voltage source connected across the transformer terminals as was shown in Figure 8.13. In this figure, the equivalent diagrams for the fundamental and higher frequencies of the positive, negative and zero-sequence harmonics are shown, for two transformer winding arrangements: Yy and Yd. When looking at the equivalent diagram, the advantage of including a winding connected in delta becomes apparent. If the starpoint of the primary winding is isolated, winding connected in delta will provide the only path for zero-sequence currents generated by the core. Therefore, the presence of a delta winding will prevent the transformer from distorting the supplying voltage with zero-sequence harmonics. A power system can usually cope with relatively high levels of current distortion. Bearing in mind that the measure of power quality in a power system is actually the voltage quality [Dugan], it can be emphasized that the distorted current does not have the direct influence on the power quality – it must be first coupled by the system impedance Z, and then, by the created harmonic voltage drops it will affect the power quality. All the harmonics for which the diagrams are valid are created within the transformer, due to the saturation. It shall be also stated that the 4 or 5-legged transformers will behave principally like single-phase transformers – the flux will always have a return path through the core. There can be small differences noticed for each phase due to the core asymmetries

8.5.3 Restrictions when using the algorithm for three-phase transformers.

The algorithm described in this paper works for single-phase transformers. However, under certain circumstances it can be used also for modelling the nonlinearities of three-phase power transformers. From the theoretical analysis arises that the following restrictions regarding the no-load tests shall apply:

- The three-phase transformer must be supplied through a star connected winding YN,
- The starpoint of this primary winding shall be grounded (YN) because otherwise all triplen harmonics will be blocked,
- The voltage source that is used for supplying the transformer must be connected in grounded star YN.

- Delta connected winding shall not be used as primary because the triplen harmonics will circulate in the winding and will not be present in the measured current,
- Also none of the secondary windings shall be connected in delta. This can be deducted from the equivalent diagram shown on Fig. 9. The zero-sequence harmonic currents originating in the core will split and flow into the supplying winding Yn, any other winding connected in grounded star yn terminated with a load impedance connected in YN, or any winding connected in delta.

It does not matter if the transformer core is 3, 4 or 5-legged, because the supplying voltage and the resulting flux in the core is sinusoidal and purely positive sequence. No zero-sequence flux will appear due to the core nonlinearity because the supplying winding is connected in grounded star.

8.5.4 Power autotransformer.

The main difference between a regular transformer and an autotransformer is that the autotransformer has the primary and secondary windings connected in the way that the voltage drop on the primary winding raises the potential of the secondary winding, see Figure 8.14.

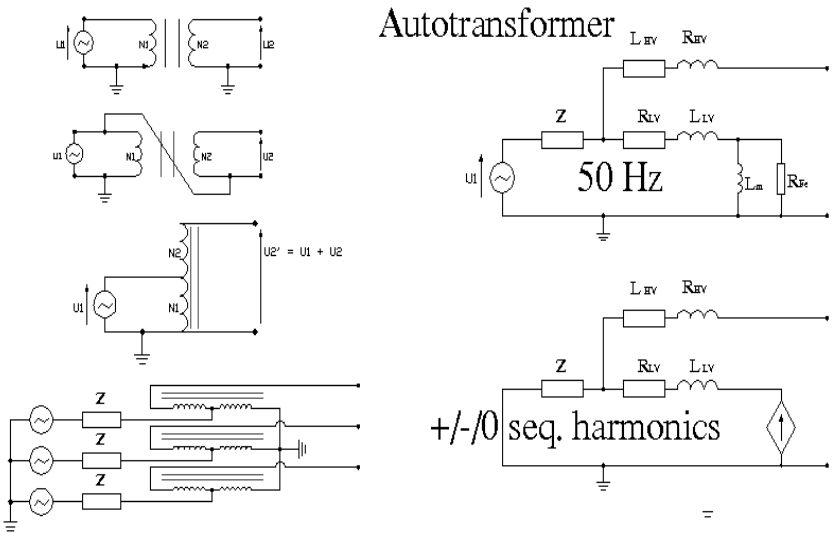

Figure 8.14 Process of creating the equivalent diagram of an autotransformer, which is useful for harmonic analysis.

Therefore, the secondary voltage to ground is the sum of the voltage drops on the primary and secondary coils. By raising the voltage, the power that can be transferred through the transformer is higher. However, this operation removes the galvanic insulation between the windings. There is also a difference for the dc component. The dc current is not transferred through a regular transformer while in an autotransformer it will split and the major part will run through the resistance of the primary winding and the remaining part can flow into the secondary side, depending on the dc (zero-sequence) resistance of the loads. The no-load testing procedure performed on an autotransformer does not differ from the procedure applied when testing a regular transformer. If the transformer is supplied with nominal voltage, the resultant flux density in the core has also its nominal value, whichever winding is used as the primary. The core nonlinearity of power autotransformers can be modelled using the described algorithm if they comply with the restrictions described for regular three-phase power transformers. The autotransformers installed in the Energinet.dk power system are YNyn connected and some of them have an additional tertiary winding. However, this winding is normally not used and therefore, it is connected in open delta. Consequently it will not affect the flow of harmonic currents because no current can circulate and they cannot produce opposing flux. Consequently it

can be concluded that if three-phase power autotransformers comply with the restrictions described in section 8.5.3, the algorithm can be used for modelling their core nonlinearities.

8.6 Conclusion

In this chapter the implementation and verification of an algorithm that allows for calculating saturation characteristics of single-phase power transformers were demonstrated. This algorithm for computation requires only $V_{rms} - I_{rms}$ curves and the no-load losses at fundamental frequency.

Some of the main conclusions have been:

- The algorithm has been correctly implemented in the PowerFactory simulation software
- For the practical cases in power systems, the only available data that can be used are the $V_{rms} - I_{rms}$ curves and the no-load losses obtained from the no-load transformer tests. In such cases the application of the presented algorithm is the only practical possibility for assessing the harmonic content in the magnetizing current of such transformer and its voltage dependence.
- Comparing with the measurements made on a single-phase transformer it can be stated that the higher order harmonics show better agreement with the measured values than lower order harmonics,
- A difference in the measured and calculated 3rd harmonic content in the no-load current, for low exiting voltage (0.8 – 0.9 p.u.) has been noticed but the reason for this has not been revealed. The possible causes were the simplifications made.
- Based on the performed theoretical analysis it can be stated that the algorithm initially valid for single-phase transformers can be used for modelling nonlinearities of three-phase autotransformers,
- For modelling power transformers that have windings connected in delta, the triplen harmonics will be missing in the no-load current and therefore, different approach shall be made, for instance as presented in [Neves, 1995]
- The algorithm allows assessing the levels of harmonic distortion produced by power transformers in a satisfactory way for the purpose of modelling entire transmission network and the aggregated effect of power autotransformers on the harmonic levels.
- For the future work, measurements on a full size three-phase power transformer and an autotransformer shall be made to verify the implemented algorithm.

Chapter 9

Conclusion

In this project, the process of modelling the entire Western transmission network of Energinet.dk using the simulation software DIgSILENT PowerFactory is shown. A fundamental frequency load-flow model is used as a basis that is to be extended. The model was extended to be valid for harmonic frequencies in the range from 50 Hz up to 2,5 kHz. The verification of the linear model was made by performed real-life harmonic measurements at three 400 kV substations, with measuring instruments synchronized by GPS receivers.

Additionally, the main nonlinearities present on the transmission level are modelled. Since the modelling of large frequency dependent networks can be best done in the frequency domain and the nonlinear elements such as power electronic converters are best modelled in the time domain, a hybrid time/frequency iterative method was developed, for modelling the HVDC converters. The developed method was verified against exact time domain simulations using the HVDC benchmark model, and can be universally implemented for incorporating time domain modelling of any nonlinear components into harmonic domain calculations of PowerFactory software.

The second nonlinear element directly present on the transmission level are the autotransformers and with their nonlinear cores. A method was found in the literature [Neves], where based just on the rms I-U curves and the no-load losses, the transformer core nonlinearity can be recursively computed.

Both nonlinear models were implemented in the DIgSILENT PowerFactory software using the DIgSILENT Programming Language (DPL). Both source codes are given in the appendices A and B.

The main aim of the project was reached, i.e. the linear network model was created and verified with extensive harmonic measurements. Additionally, some new verification techniques were proposed.

Also, the iterative HVDC hybrid model was developed and the model of a nonlinear transformer core was implemented in the DIgSILENT PowerFactory software.

9.1 Main conclusions

The main results and conclusions from this research project are summarized below. The conclusions are grouped into sections, each section concerning a part of the project.

State-of-the-art modelling of the linear transmission network

It has occurred that the existing model of Western transmission network model is quite detailed, i.e. all the components installed directly on the transmission level, 400 kV, 220 kV and 150 kV are present in the model, proper network configuration is maintained.

It is possible to model transmission lines in the PowerFactory software in detail. The frequency dependent effects, i.e. the skin effect and non-ideal earth return path are modelled as well. The frequency dependent effects were verified by hand calculations. Skin effect was verified by the Bessel series equations and ground return was verified using the Carson series equations. The skin effect is very well represented in the software, and the earth return also, but in this case there are some inaccuracies, for lines installed at large heights, and for high frequencies. Also the line unbalance can be modelled well in the software, if the tower geometry is provided.

Such simplifications that were present in the load-flow model like ideal transposition of conductors, ignored skin effect or lumped circuit model instead of a distributed one have been adjusted. It was also shown that the linear shunt conductance may cause excessive damping of harmonic distortion in the network and it is better to ignore the corona effect in harmonic studies than to include it in the form of a shunt linear conductance.

The skin effect plays an important role at resonant frequencies because it alleviates the effects of resonances. At other frequencies it's effect is not so pronounced, so for frequencies below the first resonant frequency, it may be ignored if the precision of calculations is not that crucial.

The most critical aspect of modelling transmission lines is to represent the long line effects using the equivalent Pi circuit model, because of the line parallel and series resonances that if not correctly represented, may affect the network impedance dramatically. The alternative to the equivalent Pi circuits is to use a cascade of nominal Pi circuits, but the number should be larger, the larger the frequency of interest and it will increase the computation burden.

In the existing load flow model, the harmonic filters were modelled as pure capacitors. All of them have been upgraded by including the inductive and resistive components.

Synchronous and asynchronous machines and shunt reactors are correctly represented in the software, according to the state-of-the-art techniques described in the literature, except that the frequency dependence of the resistive part is not modelled. This frequency dependence was easily implemented in the software using the frequency polynomial characteristic.

The principal assumption in modelling the rotating machines is that the harmonic fluxes produced by stator the windings are rotating faster than the rotor. The models shall not be created on the basis of fundamental frequency power consumption of rotating machines.

In the existing distribution network equivalents, the large synchronous and asynchronous machines are separated from the overall load value and modelled as aggregated. The loading at each 60 kV busbar is predominantly domestic. For loads with relatively small motor load participation, a parallel connection of a resistance and an inductance is used.

The PFC capacitors have a significant effect on the harmonic impedance of the distribution network in the frequency range of interest, but the location and size is important; the estimated overall value of capacitance, attached as an aggregated element directly at a single busbar may give worse results than to simply use a purely inductive/resistive load models.

Verification of linear network model using incremental values measured by GPS-synchronized harmonic measurements

For validation of a linear harmonic model of a network, it does not matter if the driving-point or transfer impedance is used for that purpose.

In cases if the level of background harmonic distortion cannot be ignored, the injected harmonic signal need to be varied and the varying response need to be measured. The ratio of the incremental voltage to incremental current will be the driving-point harmonic impedance of the node and the effect of the background harmonic distortion is eliminated

If sufficient level of background distortion is present in the voltage, a linear shunt or series element can be switched and the harmonic current that flows into it will affect the harmonic voltage distortion, so it can be used for calculation of driving-point or transfer harmonic impedance, as well.

A series element may be simply a connection between two sections of a busbar at a substation. In such case the impedance is changed from zero to infinity.

In practical terms, driving point impedance is usually more desired, because the nonlinear loads that are connected to a power network are mostly shunt loads that inject harmonic currents into the driving-point impedance. However, such transfer harmonic impedance is needed if a Thyristor Controlled Series Capacitor (TCSC) or a Thyristor Controlled Series Reactor (TCSR) are to be installed.

Three, located near HVDC interconnections, 400 kV substations were selected for locating the measuring equipment: TJE5, FER5 and NVV5. The distance between the most distant ones is of 100 km.

Initial simulations were performed using the created linear network model. Various components were switched out and switched in the simulation, in various configurations, and it was found that the highest increments of the harmonic voltages at substations TJE5, FER5 and NVV5 has the disconnection of one of the power lines - FER5-NVV5-0.

The harmonic currents were measured at both ends of the line, and harmonic voltages at both substations, to which the line was connected, FER5 and NVV5. Additionally, voltage at a third substation TJE5 was also measured.

The measuring equipment at all three substations was synchronized by the GPS units. The GPS units were sending synchronizing pulses which were being detected by the Omicron CMC256 units. 90 snapshot measurements were taken synchronously, by all three Omicron units.

Existing capacitive voltage transformers (CVT) are not suitable for harmonic measurements. Capacitive taps of the transformer bushings (CTB) were used, this is a precise method of performing harmonic measurements, and moreover if voltage drop on resistors is measured, the higher order harmonics are amplified. However, attention is required and proper overvoltage protection must be installed.

Both protective and metering cores of current transformers can be used for harmonic measurements if the cores are not saturated.

The three pieces of Omicron CMC256 were synchronized using GPS clocks. All the units were controlled from one substation

Harmonic amplitudes and phase angles were extracted up to the 50th harmonic. While the snap-shots were being taken, the power line FER5-NVV5-0 was disconnected and re-connected three times in row. The variation of harmonic currents and voltages was observed.
The results of measurements show that the harmonic distortion in the voltage is quite low and reach at NVV5 substation for 11th harmonic - 0,9%, at FER5 substation the magnitude of 11th harmonic reaches 0,6% and at TJE5 the harmonic distortion is lower, maximally 0,3%, due to the installed harmonic filters.
Generally, the harmonic voltages below 500 Hz are not much affected by the switching of the line. At higher frequencies the differences are larger. Switching off the line affected mainly the harmonic frequencies at substations NVV5 and FER5.
The level of obtained harmonic distortion was lower than expected; however some correlation between the measurement results and the results of initial simulations can be observed.

After the measurements it occurred that the harmonic currents measured during the performed measurements at both ends of the disconnected line, were unbalanced; therefore the proposed in chapter 4 method of switching a series component would give erroneous results. The resultant voltage response is a mixture of all sequences, therefore it is impossible to determine all components of the impedance matrix.

The developed alternative approach allows to verify the model by measuring the voltage response to injected harmonic currents. The measured harmonic currents are assigned to current sources and injected into the network model. The obtained incremental voltage responses shall be exactly the same as the voltage increments obtained from simulations.

The synchronization error between the GPS-synchronized units results in phase angle errors δ of measured particular voltage and current harmonic components. The phase angle errors in turn result in magnitude errors ε of the calculated voltage increments at the substations NVV5, FER5 and TJE5.

The voltage increments obtained from the simulations are not exactly the same as the voltage increments obtained from the measurements; however the correlation between them is relatively good. For most of the harmonic frequencies the voltage increments obtained from simulations are within the limits $\Delta U \pm \varepsilon$.

At all substations, the agreement of voltage increments at the 47th harmonic is poor; therefore the conclusion is that the model is not reflecting the behavior of the physical network correctly at such a high frequency.

The verification of the linear network model give acceptable results for the frequencies below the 23rd harmonic, where the results of simulations are close to the results of measurements, taking the synchronization error into account.

Verification methods that are based on harmonic measurements at different locations and/or different instances require very good synchronization between the measuring equipment.

If switching of a linear network component is performed in order to obtain harmonic increments, the time span between two consecutive measurements should be as short as possible, so it can be assumed that the background harmonic distortion is constant.

The hybrid time/frequency model

Since it is not possible to model precisely power converter in frequency domain simulation of PowerFactory software, and on the other hand, performing time domain simulation EMT for large transmission networks is a worse solution that harmonic simulations, because of applied approximations and longer simulation times, a hybrid time/frequency method was successfully developed in this project and verified with exact time domain simulations. The algorithm was

implemented in the DIgSILENT PowerFactory software and is based on a modified HVDC benchmark model. The DPL simulation language was used. For the detection of periodic steady state and the convergence of the entire algorithm, the amplitudes and phase angles of the following significant harmonics were used: 1^{st}, 5^{th}, 7t, 11^{th} and 13^{th}. In general it took between 4 up to 6 iterations for the algorithm to converge. The method is practically limited to signals that mainly contain harmonic orders up to 50^{th} harmonic. It was shown that if signals with large content of higher than 50^{th} harmonic frequencies are present, the algorithm may experience problems with convergence, and in the shown case it was diverging. To model high frequency components of converters that inject harmonic currents into high impedance, up to the 120 harmonic need to be included (6 kHz).

Transformer core nonlinearities

An algorithm on modelling transformer core nonlinearities was implemented [Neves]. This algorithm for computation requires only $V_{rms} - I_{rms}$ curves and the no-load losses at fundamental frequency. The algorithm has been verified by using the original data from [Neves] and in second step, laboratory measurements were performed on a single phase transformer.

For the practical cases in power systems, the only available data that can be used are the $V_{rms} - I_{rms}$ curves and the no-load losses obtained from the no-load transformer tests. In such cases the application of the presented algorithm is the only practical possibility for assessing the harmonic content in the magnetizing current of such transformer and its voltage dependence.

Based on the performed theoretical analysis it can be stated that the algorithm initially valid for single-phase transformers can be used for modelling nonlinearities of three-phase autotransformers,

For modelling power transformers that have windings connected in delta, the triplen harmonics will be missing in the no-load current and therefore, different approach shall be made, for instance as presented in [Neves, 1995]

9.2 Contributions

The main contributions of this research project are:

- state-of-the-art model of the linear part of the Western transmission network of Energinet.dk
- analysis of known validation techniques
- development of a verification technique based on switching a linear series element
- development of a verification technique based on switching a linear series/shunt element
- development of a verification technique based on direct injection of measured incremental values of harmonic currents into the linear network and comparison of the resultant voltage increments with he measurements
- development of the procedure of performing harmonic measurements at three 400 kV substations, with measuring units synchronized with GPS receivers
- development of an hybrid time/frequency model of the HVDC converter
- implementation of the transformer core nonlinearities model

9.3 Future work

Based of the result achieved in this research project, the following items can be considered as worth being proposed for future work:

- integration of the three models, linear transmission network model with the hybrid/time frequency models and the models of transformer core nonlinearities
- lot of interesting work can be done with respect to the hybrid time/frequency model, especially, the inter-harmonic simulations and modelling of dynamically varying harmonics and also modification of the algorithm so it can be used for higher frequencies as well,
- verification of the transformer core nonlinearities model by measurements on an three-phase autotransformer
- implementation of the transformer core nonlinearities algorithm that will give precise results for transformers with windings connected in delta
- measurement of the network harmonic impedance using an external source of harmonics, like for instance an active filter, and injection harmonic currents into one phase at a time, in order to determine all components of the impedance matrix

Bibliography

Abur, A.; Ozgun, O.; Magnago, F.H., *Accurate modeling and simulation of transmission line transients using frequency dependent modal transformations*, Power Engineering Society Winter Meeting, 2001. IEEE, Volume 3, 28 Jan.-1 Feb. 2001 Page(s):1443 - 1448 vol.3

Acha, E., Madrigal M., *Power Systems Harmonics: Computer Modeling and Analysis*, John Wiley & Sons; 1 edition, 2001, ISBN**:** 0471521752

Andersen, B., *Equipment failure report, Fejl på filter R3-ZK4*, 1998

Arrillaga, J., Watson N., *Power System Harmonics*, John Wiley and Sons, 2003, ISBN 0-470-85129-5.

Arrillaga, 1995, J.; Medina, A.; Lisboa, M.L.V.; Cavia, M.A.; Sanchez, P., *The Harmonic Domain. A frame of reference for power system harmonic analysis*, Power Systems, IEEE Transactions on, Volume 10, Issue 1, Feb. 1995 Page(s):433 - 440

Arrillaga, 1997, J., Bruce C. Smith, Neville R. Watson, Alan R. Wood, *Power System Harmonic Analysis*, John Wiley & Sons, 1997, ISBN: 0471975486

Arrillaga, 1998, J., *High Voltage Direct Current Transmission*, second ed., Inspec/Iee, ISBN: 0852969414

Bathurst, G.N.; Smith, B.C.; Watson, N.R.; Arrillaga, J., *Modeling of HVDC transmission systems in the harmonic domain*, Power Delivery, IEEE Transactions on, Volume: 14 Issue: 3 Jul 1999, Page(s): 1075-1080

Bathurst, 2000, G.N.; Watson, N.R.; Arrillaga, J., *Modeling of bipolar HVDC links in the harmonic domain*, Power Delivery, IEEE Transactions on, Volume: 15 Issue: 3 Jul 2000, Page(s): 1034-1038

Bathurst, 2001, G.N.; Watson, N.R.; Arrillaga, J., *A harmonic domain solution for systems with multiple high-power AC/DC converters*, Generation, Transmission and Distribution, IEE Proceedings-, Volume: 148 Issue: 4 Jul 2001, Page(s): 312-318

Bolkowski, S., *Electric Circuit Theory* (in Polish), WNT, Warsaw, 1995

Bollen, M.H. J., Gu, I., *Signal Processing of Power Quality Disturbances*, Wiley-IEEE Press, 2006, ISBN: 0471731684

Brewer, G.D., Chow, J.H., Gentile, T.J. et al. (1982) *HVDC-AC harmonic interaction. I. Development of a harmonic measurement system hardware and software*, IEEE Trans. Power Apparatus Systems, PAS-101, 701–8.

Bridgeman, M.J.; Morrison, R.E.; Tenakoon, S.B., *Measurement of harmonic impedance on an LV system utilizing power capacitor switching and consequent predictions of capacitor induced harmonic distortion*, Harmonics And Quality of Power, 1998. Proceedings. 8th International Conference on, Volume 2, 14-16 Oct. 1998 Page(s):1141 - 1145 vol.2

Brüel&Kjær, *Brüel &Kjær Hardware manual*, IDAe Hardware Configurations for PULSE X. Types 3560 B, 3560 C, 3560 D and 3560E

Burch, R.; Chang, G.; Hatziadoniu, C.; Grady, M.; Liu, Y.; Marz, M.; Ortmeyer, T.; Ranade, S.; Ribeiro, P.; Xu, W., *Impact of aggregate linear load modeling on harmonic analysis: a comparison of common practice and analytical models*, Power Delivery, IEEE Transactions on, Volume 18, Issue 2, April 2003 Page(s):625 - 630

Carson, R., J., *Wave propagation in Overhead wires with Ground return*, Bell System Technical Journal, pp. 539-554.

Castellanos, F.; Marti, J.R., *Full frequency-dependent phase-domain transmission line model*, Power Systems, IEEE Transactions on, Volume 12, Issue 3, Aug. 1997 Page(s):1331 – 1339

Chen, X.S.; Neudorfer, P., *Digital modelling of modern single-phase distribution transformers*, Advances in Power System Control, Operation and Management, 1991. APSCOM-91., 1991 International Conference on, 5-8 Nov 1991 Page(s):914 - 920 vol.2

Chua, L., O., Stromsmoe, K., A., *Lumped Circuit Models for Nonlinear Inductors Exhibiting Hysteresis Loops*, IEEE Trans. On Circuit Theory, vol. CT-17, No. 4, Nov.1970, pp. 564-574

CIGRE SC22/WG12, *Alternating Current (AC) resistance of helically stranded conductors*, Cigre Brochure, 2005.

Cividino, L., *Power factor, harmonic distortion; causes, effects and considerations*, Telecommunications Energy Conference, 1992. INTELEC '92., 14th International 4-8 Oct. 1992 Page(s):506 - 513

De Lorenzi, A.; Bettini, P.; Zanotto, L., *Harmonic impedance measurements and calculations in the EHV transmission network*, Harmonics and Quality of Power, 2002. 10th International Conference on, Volume 1, 2002 Page(s):162 - 168 vol.1

De Oliveira, A.; de Oliveira, J.C.; Resende, J.W.; Miskulin, M.S., *Practical approaches for AC system harmonic impedance measurements*, Power Delivery, IEEE Transactions on, Volume 6, Issue 4, Oct. 1991 Page(s):1721 - 1726

Dommel, H. W., *Electromagnetic Transients Program Reference Manual*, Bonneville Power Administration, Portland, Oregon, December 1999.

Dorf, R., C., Svoboda, J., A., *Introduction to Electric Circuits*, Wiley, 6 ed, 2003, ISBN: 0471447951

Douglass, D.A., *Current Transformer Accuracy with Asymmetric and High Frequency Fault Currents*, IEEE Transactions on Power Apparatus and Systems, Vol. PAS-100 No. 3, March 1981.

Du, Z.P.; Arrillaga, J.; Watson, N.R.; Chen, S., *Implementation of harmonic state estimation*, Harmonics And Quality of Power, 1998. Proceedings. 8th International Conference on, Volume 1, 14-16 Oct. 1998 Page(s):273 - 278 vol.1

Dugan, R.C., M.F. McGranaghan, S. Santoso and H.W. Beaty, *Electrical Power Systems Quality*, 2002, McGraw-Hill, New York, ISBN: 007138622X

Dugui, W., Zheng, X., *Harmonic model of power transformer*, 1998. In Proc. POWERCON '98, 1998, International Conference on Power System Technology, 18-21 Aug. 1998 pp. 1045 – 1049

Elmoudi, A., A., *Evaluation of power system harmonic effects on transformers*, doctoral dissertation, Helsinki University of Technology, 2006, ISBN 951-22-8077-9

EMTDC, *EMTDC User's Guide*, EMDC V3.0.7, Manitoba HVDC research centre, 1998.

Energinet.dk, ELTRA document ELT2003-138a, 160420 v1, *Modelling the Eltra Grid in PSS/E.*

Fardanesh, B.; Zelingher, S.; Sakis Meliopoulos, A.P.; Cokkinides, G.J., *Harmonic monitoring system via synchronized measurements*, Harmonics And Quality of Power, 1998. Proceedings. 8th International Conference on, Volume 1, 14-16 Oct. 1998 Page(s):482 - 488 vol.1

Germain, B., B. Mathias, K. Robert, M. Stefano, M. Xavier and S. John, on behalf of CIGRE WG 36.07 /CIRED, *Power Quality Indices and Objectives for MV, HV and EHV Systems CIGRE WG 36.07/CIRED Progress*, 17th International Conference on Electricity Distribution, Barcelona, 12-15 May 2003

Ghassemi, F., P. F. Gale, B. Clegg, T. Cumming, and C. Coutts, *Method to Measure CVT Transfer Function*, IEEE Trans. Power Delivery, Vol. 17, No. 4, pp. 915-920, Oct. 2002

Grainger, J., Jr., Stevenson, W., *Power System Analysis*, 1994, McGraw-Hill Science/Engineering/Math; 1 ed., ISBN: 0070612935

Gross, Ch., A., *Power System Analysis*, Wiley; 2 edition, 1986, ISBN: 0471862061

Gustavsen, B.; Semlyen, A., *Combined phase and modal domain calculation of transmission line transients based on vector fitting*, Power Delivery, IEEE Transactions on, Volume 13, Issue 2, April 1998 Page(s):596 – 604

Gustavsen, 1998, B.; Semlyen, A., Simulation of transmission line transients using vector fitting and modal decomposition, Power Delivery, IEEE Transactions on, Volume 13, Issue 2, April 1998 Page(s):605 - 614

Hai, Yan Lu; Jian Guo Zhu; Hui, S.Y.R., *Experimental determination of stray capacitances in high frequency transformers*, Power Electronics, IEEE Transactions on, Volume 18, Issue 5, Sept. 2003 Page(s):1105 - 1112

Halpin, S.M., Harmonic modeling and simulation requirements for the revised IEEE standard 519-1992, Power Engineering Society General Meeting, 2004. IEEE, 6-10 June 2004 Page(s):783 - 784 Vol.1

Herraiz, S.; Sainz, L.; Clua, J., *Review of harmonic load flow formulations*, Power Delivery, IEEE Transactions on, Volume 18, Issue 3, July 2003 Page(s):1079 - 1087

Hidaka, K., *Electric field and voltage measurement by using electro-optic sensor*, High Voltage Engineering, 1999, Eleventh International Symposium on, Volume 2, 23-27 Aug. 1999 Page(s):1 - 14 vol.2

Hingorani, N., G., Gyugyi, L., *Understanding FACTS: Concepts and Technology of Flexible AC Transmission Systems*, 1999, Wiley-IEEE Press, ISBN: 0780334558

IEC 44-1, International Standard, *Instrument transformers: Part 1: Current transformers*, Dec. 1996

IEC 61000-4-7, International Standard, *Electromagnetic Compatibility (EMC), Part 4: Limits, Section 7: General guide on harmonics and inter-harmonics measurements and instrumentation, for power supply systems and equipment connected thereto*, 1991

Inan, U., S., A., S., Inan, *Engineering Electromagnetics*, Prentice Hall; 1st edition, 1998, ISBN**:** 0805344233

Jonas, F., Juhlin, L., E., Numan, A., *Penetration of Harmonics from the Baltic Cable HVDC Station into the Feeding AC System*, CIGRÉ Session 1996, Paris, Paper 36-302

Kanao, N.; Yamashita, M.; Yanagida, H.; Mizukami, M.; Hayashi, Y.; Matsuki, J., *Power system harmonic analysis using state-estimation method for Japanese field data*, Power Delivery, IEEE Transactions on, Volume 20, Issue 2, Part 1, April 2005 Page(s):970 - 977

Kojovic, Lj.A., *Guidelines for current transformers selection for protection systems*, Power Engineering Society Summer Meeting, 2001. IEEE Volume 1, 15-19 July 2001 Page(s):593 - 598 vol.1

Kreyszig, E., *Advanced Engineering Mathematics, 7th Edition*, John Wiley & Sons Inc; 7th edition 1992, ISBN: 0471553808

Kujszczyk, S.**,** *Electric power transmission systems (in Polish)*, WNT, 1997, ISBN: 83-2041857-7

Kundur, P., *Power System Stability and Control*, 1994, McGraw-Hill Professional, 1 ed., ISBN: 007035958X

Liew, M.C.; Bodger, P.S¸ *Incorporating capacitance into partial-core transformer models to determine first natural resonant frequencies*, Generation, Transmission and Distribution, IEE Proceedings- Volume 149, Issue 6, Nov. 2002 Page(s):746 - 752

Machowski, J., Kacejko, P., *Faults in electrical power systems (in Polish)*, WNT, 2002, ISBN: 83-204-2750-9

Mack Grady, W.; Santoso, S., *Understanding power system harmonics*, Power Engineering Review, IEEE, Volume 21, Issue 11, Nov. 2001 Page(s):8 - 11

Marti, L., *Simulation of transients in underground cables with frequency-dependent modal transformation matrices*, Power Delivery, IEEE Transactions on, Volume 3, Issue 3, July 1988 Page(s):1099 – 1110

Masoum, M.A.S.; Fuchs, E.F.; Roesler, D.J., *Large signal nonlinear model of anisotropic transformers for nonsinusoidal operation. II. Magnetizing and core-loss currents*, Power Delivery, IEEE Transactions on, Volume 6, Issue 4, Oct. 1991 Page(s):1509 - 1516

Matsch, L., W., Morgan, D., J., Electromagnetic and electromechanical machines, John Wiley & Sons, 1987, ISBN**:**0-471-61305-3

Medina, A., *Harmonic simulation techniques (methods & algorithms)*, Power Engineering Society General Meeting, 2004. IEEE, 6-10 June 2004 Page(s):762 - 765 Vol.1

Meliopoulos, A. P. S., F. Zhang and S. Zelingher, *Hardware and Software Requirements for a Transmission System Harmonic Measurement System*, Harmonics in Power Systems, ICHPS V International Conference, pp. 330 –338, Sept. 1992.

Meliopoulos, 1993, A.P.S.; Zhang, F.; Zelingher, S.; Stillman, G.; Cokkinides, G.J.; Coffeen, L.; Burnett, R.; McBride, J., *Transmission level instrument transformers and transient event recorders characterization for harmonic measurements*, Power Delivery, IEEE Transactions on, Volume 8, Issue 3, July 1993 Page(s):1507 - 1517

Meliopoulos, 1994, A.P.S.; Fan Zhang; Zelingher, S., *Power system harmonic state estimation*, Power Delivery, IEEE Transactions on, Volume 9, Issue 3, July 1994 Page(s):1701 - 1709

Meliopoulos, 2000, A., P., S., Fardanesh, B., Zelingher, S., Cokkinides, G.J., *Harmonic measurement system via synchronized measurements*, Power Engineering Society Summer Meeting, 2000. IEEE, Volume 2, 16-20 July 2000 Page(s):1094 - 1100 vol. 2

Meynaud, P. *Transformers and instruments for measuring harmonics*, CIGRE Working Group 36.05 (Interference), ELECTRA, No 124, pp:92-97, 1989.

Miller, A., J., V., Dewe, M., B., *Multichannel continuous harmonic analysis in real-time*, Power Delivery, IEEE Transactions on, Volume 7, Issue 4, Oct. 1992 Page(s):1813 - 1819

Minkner, R., *A universal RC voltage transformer for High Voltage Networks*", ETZ vol 22/2002, pp 22 – 29, VDE Verlag

Mohan, N.; Robbins, W.P.; Undeland, T.M.; Nilssen, R.; Mo, O., *Simulation of power electronic and motion control systems-an overview*; Proceedings of the IEEE, Volume 82, Issue 8, Aug. 1994 Page(s):1287 - 1302

Moreau, G.; Le, H.H.; Croteau, G.; Beaulieu, G.; Portales, E., *Measurement system for harmonic impedance of the network and validation steps*, Quality and Security of Electric Power Delivery Systems, 2003. CIGRE/PES 2003. CIGRE/IEEE PES International Symposium, 8-10 Oct. 2003, Page(s):69 - 73

Moreno Lopez de Saa, M.A.; Usaola Garcia, J., *Three-phase harmonic load flow in frequency and time domains*, Electric Power Applications, IEE Proceedings-,Volume 150, Issue 3, May 2003 Page(s):295 - 300

Morgan, V.T.; Bo Zhang; Findlay, R.D., Effect of magnetic induction in a steel-cored conductor on current distribution, resistance and power loss, Power Delivery, IEEE Transactions on, Volume 12, Issue 3, July 1997 Page(s):1299 - 1308

Morrison, R.E.; Duggan, E., *Long term monitoring of power systems harmonics*, Three Phase LV Industrial Supplies: Harmonic Pollution and Recent Developments in Remedies, IEE Colloquium on, 14 Jun 1993 pp:2/1 - 2/3

Nagpal, M.; Xu, W.; Sawada, J., *Harmonic impedance measurement using three-phase transients*, Power Delivery, IEEE Transactions on, Volume 13, Issue 1, Jan. 1998 Page(s):272 - 277

Neves, L., A., Dommel, H., W., *On Modelling Iron Core Nonlinearities*, IEEE Transactions on Power Systems, Volume 8, Issue 2, May 1993, Page(s): 417 – 425.

Neves, 1995, W.L.A.; Dommel, H.W., *Saturation curves of delta-connected transformers from measurements*, Power Delivery, IEEE Transactions on, Volume 10, Issue 3, July 1995 Page(s):1432 - 1437

Omicron, *Omicron CMC-256-6 User Manual*, omicron Electronics, article number VESD2001, Version C256.AE.3

Ott, H.,W., *Noise reduction techniques in electronic systems*, second ed., AT&T Bell Lab., John Willey & Sons, 1988, ISBN 0-471-85068-3

Owen, E., L., *A history of harmonics in power systems***,** Industry Applications Magazine, IEEE Volume 4, Issue 1, Jan.-Feb. 1998 Page(s):6 – 12

Perkins, B.K.; Iravani, M.R., *Novel calculation of HVDC converter harmonics by linearization in the time-domain*, Power Delivery, IEEE Transactions on, Volume 12, Issue 2, April 1997 Page(s):867 - 873

PowerFactory, DIgSILENT PowerFactory Manual, version 13.1, DIgSILENT GmbH, 2005, Gomaringen, Germany

Pritpal S., *C2 Power Factor and Capacitance of ABB Type O plus C, AB, and Type T Condenser Bushings*, ABB Inc. publication, USA, 2005

Robert, A.; Deflandre, T.; Gunther, E.; Bergeron, R.; Emanuel, A.; Ferrante, A.; Finlay, G.S.; Gretsch, R.; Guarini, A.; Gutierrez Iglesias, J.L.; Hartmann, D.; Lahtinen, M.; Marshall, R.; Oonishi, K.; Pincella, C.; Poulsen, S.; Ribeiro, P.; Samotyj, M.; Sand, K.; Smid, J.; Wright, P.; Zhelesko, Y.S., *Guide for assessing the network harmonic impedance*, Electricity Distribution. Part 1. Contributions. 14th International Conference and Exhibition on (IEE Conf. Publ. No. 438) Volume 1, 2-5 June 1997 Page(s):3/1 - 310 vol. 2

Santesmases, J., G., Ayala, J., Cachero, S., H., *Analytical Approximation of Dynamic Hysteresis Loops and its Application to a Series Ferroresonant Circuit*, Proc. IEE 117, January 1970, pp. 234-240.

Santos, J.C., Taplamacioglu, M.C., Hidaka, K., *Pockels high-voltage measurement system*, Power Delivery, IEEE Transactions on, Volume 15, Issue 1, Jan. 2000 Page(s):8 - 13

Schlabbach, J., Blume, D., Stephanblome T., *Voltage Quality in Electrical Power Systems*, Iee Power & Energy Series, 36, 1st edition December, 2001, ISBN: 0852969759

Seljeseth, H., E. A. Sæthre, T. Ohnstand and I. Lien, *Voltage Transformer Frequency Response. Measuring Harmonics in Norwegian 300 kV and 132 kV Power Systems*, Harmonics And Quality of Power, 1998, Proceedings, 8th International Conference on, Vol. 2, Oct. 1998, pp. 820-824

Semlyen, A.; Medina, A., *Computation of the periodic steady state in systems with nonlinear components using a hybrid time and frequency domain methodology*, Power Systems, IEEE Transactions on, Volume 10, Issue 3, Aug. 1995 Page(s):1498 – 1504

Smith, C.W., Jr., *Power systems and harmonic factors*, Potentials, IEEE, Volume 20, Issue 5, Dec 2001-Jan 2002 Page(s):10 – 12

Soeder, E., *Active AC Filter - Operation manual - Eltra HVDC Converter Station – Tjele*. June 2002

Stationsdata, *Stationsdata 150, 220 og 400 kV*, 15 July, 2002, Energinet.dk catalogue

Stevenson, W., D., *Elements of Power System Analysis*, McGraw-Hill, New York, 1965, ISBN: 0070612781

STRI, *research report*, Swedish Transmission Research Institute, Ludvika, Sweden, S97-074, 1997

Sumner, M.; Palethorpe, B.; Thomas, D.; Zanchetta, P.; Di Piazza, M.C., *Estimation of power supply harmonic impedance using a controlled voltage disturbance*, Power Electronics Specialists Conference, 2001. PESC. 2001 IEEE 32nd Annual, Volume 2, 17-21 June 2001 Page(s):522 - 527 vol.2

Szechtman, M., Wess, T., and Thio, C., V., *First benchmark model for HVdc control studies*, ELECTRA, 1991, 135, pp. 55-75

Task Force on harmonics modeling and simulation, *Modeling and simulation of the propagation of harmonics in electric power networks. I. Concepts, models, and simulation techniques, II. Sample systems and examples*, Power Delivery, IEEE Transactions on, Volume 11, Issue 1, Jan. 1996 Page(s):452 – 465, Volume 11, Issue 1, Jan. 1996 Page(s):466 - 474

Thornton, K.P.; Makram, E.B., *Study of power system harmonics in an unbalanced system using the three-phase bus impedance matrix*, System Theory, 1988., Proceedings of the Twentieth Southeastern Symposium on, 20-22 March 1988 Page(s):30 - 34

Thunberg, E., *On the benefit of Harmonic Measurements in Power Systems*, PhD thesis, Royal Institute of Technology, Stockholm, 2001, ISBN: 1100-1607

Tsukamoto, M.; Ogawa, S.; Natsuda, Y.; Minowa, Y.; Nishimura, S., *Advanced technology to identify harmonics characteristics and results of measuring*, Harmonics and Quality of Power, 2000. Proceedings. Ninth International Conference on, Volume 1, 1-4 Oct. 2000 Page(s):341 - 346 vol.1

Ukai, H., Nakamura, K., Nishigaki, S., Ohta, Y., Matsui, N., *Advanced synchronized measurement system of harmonics using DSP and GPS*, Industrial Electronics Society, 2000. IECON 2000. 26th Annual Conference of the IEEE, Volume 2, 22-28 Oct. 2000 Page(s):748 - 753 vol.2

Wagner, V.E.; Balda, J.C.; Griffith, D.C.; McEachern, A.; Barnes, T.M.; Hartmann, D.P.; Phileggi, D.J.; Emannuel, A.E.; Horton, W.F.; Reid, W.E.; Ferraro, R.J.; Jewell, W.T., *Effects of harmonics on equipment*, Power Delivery, IEEE Transactions on, Volume 8, Issue 2, April 1993 Page(s):672 - 680

Wasilewski, J.; Wiechowski, W.; Bak, C.L., *Harmonic domain modeling of a distribution system using the DIgSILENT PowerFactory software*, Future Power Systems, 2005 International Conference on, 16-18 Nov. 2005 Page(s):7 pp.

Watson, N., Arrillaga, J., *Power Systems Electromagnetic Transients Simulation*, John Wiley and Sons, *2003*, ISBN: 0852961065

Watson, 2005, N.R., *Advanced harmonic assessment*, Power Engineering Society General Meeting, 2005. IEEE, 12-16 June 2005 Page(s):2230 - 2235 Vol. 3

Wedepohl, L.M.; Nguyen, H.V.; Irwin, G.D., *Frequency-dependent transformation matrices for untransposed transmission lines using Newton-Raphson method*, Power Systems, IEEE Transactions on, Volume 11, Issue 3, Aug. 1996 Page(s):1538 - 1546

Xia, D., Heydt, G.T. *Harmonic power flow studies, Part I—Formulation and solution, Part II—Implementation and practical application*, IEEE Trans. Power Apparatus Systems, 1982, PAS-101, 1257–70.

Xiao, Y., Fu, J., Hu, B., Li, X:; Deng, Ch., *Problems of voltage transducer in harmonic measurement*, Power Delivery, IEEE Transactions on, Volume 19, Issue 3, July 2004 Page(s):1483 - 1487

Xie, C.; Tennakoon, S.B.; Langella, R.; Gallo, D.; Testa, A.; Wixon, A., *Harmonic impedance measurement of 25 kV single phase AC supply systems*, Harmonics and Quality of Power, 2000. Proceedings. Ninth International Conference on, Volume 1, 1-4 Oct. 2000 Page(s):214 - 219 vol.1

Xu, W., Ahmed, E.E., Xiqin Zhang; Xian Liu, *Measurement of network harmonic impedances: practical implementation issues and their solutions*, Power Delivery, IEEE Transactions on, Volume 17, Issue 1, Jan. 2002 Page(s):210 – 216

Xu, 1991, W.; Marti, J.R.; Dommel, H.W., *A multiphase harmonic load flow solution technique*, Power Systems, IEEE Transactions on, Volume 6, Issue 1, Feb. 1991 Page(s):174 - 182

Xu, 2004, W., *Status and future directions of power system harmonic analysis*, 2004 IEEE Power Engineering Society general meeting Denver CO, 6-10 June 2004, SBN 0-7803-8465-2

Appendix A

Harmonic domain modelling of a distribution system using the DIgSILENT PowerFactory software

Harmonic domain modeling of a distribution system using the DIgSILENT PowerFactory software

Jacek Wasilewski, Wojciech Wiechowski and Claus Leth Bak

***Abstract*--The first part of this paper presents the comparison between two models of distribution system created in computer simulation software PowerFactory (PF). Model A is an existing simplified equivalent model of the distribution system used by Transmission System Operator (TSO) Eltra for balanced load-flow calculation and stability studies. Model B is accurate model of the distribution system created on the basis of the detailed data of the investigated network and is used as a reference. The harmonic impedance of the two models is compared. In the second part of the paper, the sensitivity of the harmonic impedance to basic system parameters (load active power, motor load fraction and reactive power of PFC capacitors) is analyzed.**

***Index Terms*--Harmonic analysis, frequency domain analysis, power system modeling, simulation software**

I. Introduction

SINCE some time Danish TSO Eltra has recognized that harmonic currents and voltages propagate in 400 kV transmission network. The appearance of harmonics may cause the malfunction of protective and measuring equipment. One of the reasons of the increase of harmonic level is the constantly growing number of non-linear loads connected at the lower voltage levels, as for instance computers, fluorescent lamps, arc furnaces, etc.

The whole Eltra's transmission system is modelled using a computer simulation program DIgSILENT PowerFactory (PF). This software is a computer aided engineering tool for analysis of electrical power systems. PF is equipped with ready-to-use models of different power system components. This computer model of Eltra's transmission system is presently used for load-flow and stability studies. Therefore all 400 kV and 150 kV transmission lines and cables, large generators and autotransformers are modelled in details. The lower voltage levels, i.e. 60 kV and below are represented as simplified equivalent models. It has been decided that the existing computer model shall be extended so it could be also used for harmonic analysis.

The distribution network is connected in many places with the transmission system and that is why it is expected that their impedance will have a significant effect on the propagation of harmonics on the transmission level. The harmonic impedance of a distribution system seen from the higher voltage side varies in the frequency. Therefore distribution feeders make a harmonic filter function for flow of harmonic currents in transmission system. For that purpose one, representative part of distribution network is closely investigated.

II. Description Of The Modelled Distribution Network

The analyzed distribution system belongs to the company Himmerlands Elforsyning (HEF) and is supplied from 150 kV busbar installed in Vilsted (VIL) substation. Such a distribution feeder is shown in Fig. 1.

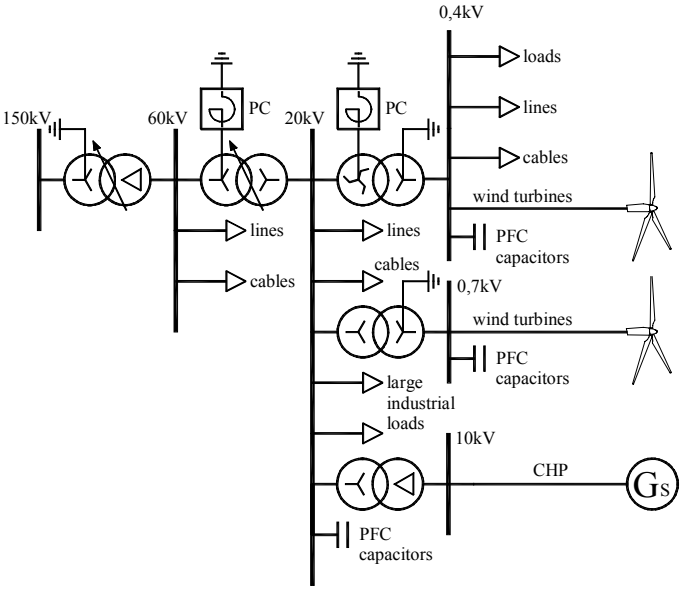

Fig. 1. Simplified diagram of investigated distribution feeder.

Analyzed distribution system contains the following 60/20 kV substations: Aggersund (AGG), Farsø (FSØ), Løgstør (LGS) and Nibe (NIB). Each 60/20 kV substation includes one or two distribution transformers (10, 16, 20 and 25

J. Wasilewski is with the Institute of Electrical Power Engineering, Warsaw University of Technology, 00661 Warsaw, Poland (e-mail: java81@o2.pl).

W. Wiechowski and C. L. Bak are with the Institute of Energy Technology, Aalborg University, 9220 Aalborg, Denmark (e-mail: wtw@iet.aau.dk, clb@iet.aau.dk).

MVA), single or double 60 kV and 20 kV busbar system, and PFC capacitors, all of them installed on the 20 kV voltage level. To all of the 60/20 kV substations some wind turbines are connected. All of them are connected to the 0,4 kV and 0,7 kV network. Next group of distributed power generation constitutes combined heat and power plants (CHP). It is about 30% of the dispersed power generation in HEF distribution system. The 20 kV network supplies small distribution substations 20/0,4 kV and large industrial loads. The majority of the electrical energy consumers are supplied from the 0,4 kV network. Basic description of investigated distribution feeder is presented in Table I.

TABLE I
BASIC INFORMATION ABOUT ANALYZED DISTRIBUTION SYSTEM

Rated apparent power of installed transformers in substations	150/60 kV – 80 MVA 60/20 kV – 10, 16, 20 and 25 MVA
Total length of the 60 kV overhead lines	54,5 km
Total length of the 60 kV underground cables	not appear
Installed active power of wind turbines	70 877 kW
Installed active power of CHP	19 228 kW

III. EQUIVALENT MODEL OF A DISTRIBUTION SYSTEM – MODEL A

Existing PF model of the transmission system is presently used for load–flow and stability studies. For that purpose, it is necessary to model in detail the whole 400 kV and 150 kV grids, but it is sufficient to model all the 60 kV level and below in simplified way – using the network equivalents. This representation of a distribution system is called Model A and it is shown in Fig. 2.

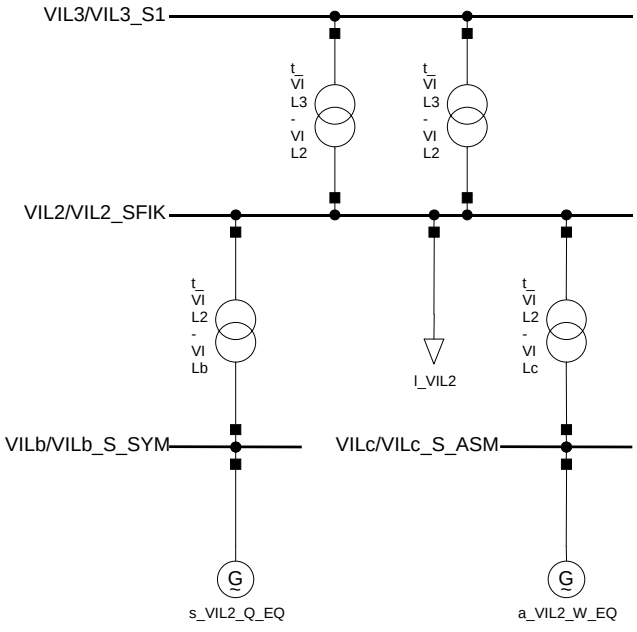

Fig. 2. Diagram of distribution system represented by Model A.

The generators and the loads are modelled as aggregated components. The equivalent synchronous generator represents total power generation in CHP. It is connected to 10 kV busbar and supplies 60 kV busbar through an equivalent transformer representing all unit transformers installed in CHP. The equivalent induction generator represents total power generated by wind turbines. It is connected to 0,7 kV busbar and supplies 60 kV busbar through an equivalent transformer representing all transformers connected wind turbines and medium voltage network. All other domestic and industrial loads are aggregated and modelled as one resistive and inductive load and connected directly to the 60 kV busbar. The equivalent model does not include underground cables, overhead lines and PFC capacitors. Transformer windings connections and neutral system of 60 kV network are not modelled, because Model A is used for balanced positive-sequence load-flow calculations and zero-sequence impedance are of no importance for this kind of analysis.

IV. EXACT HARMONIC DOMAIN MODEL OF THE DISTRIBUTION SYSTEM – MODEL B

In order to verify if the existing Model A sufficiently accurate represents the harmonic impedance of the distribution network seen from the transmission level, a very precise and detailed model of the distribution system has been created – Model B.

Very detailed data has been obtained from Eltra and HEF companies, and all the components have been modelled using commonly accepted theories recommended in the harmonic analysis literature [1], [6]-[8]. All of the harmonic domain models will be described in the following sections.

A. Overhead lines and underground cables

The overhead lines and underground cables are modelled by pi-circuit equivalent representation using distributed parameters [1]. Nominal line parameters can be expressed

$$\begin{aligned} Z' &= R' + jhX' \\ Y' &= jhB'/2 \end{aligned} \tag{1}$$

Corrected model of line (cable) for harmonic analysis is shown in Fig. 3.

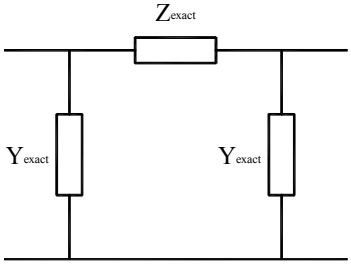

Fig. 3. Exact equivalent pi-circuit model for line and cable.

$$\begin{aligned} Z_{exact} &= Z_0 \sinh(\gamma l) \\ Y_{exact} &= \frac{1}{Z_0} \tanh \frac{(\gamma l)}{2} \end{aligned} \tag{2}$$

where $\gamma = \sqrt{Z'Y'}$ is a propagation constant and $Z_0 = \sqrt{Z'/Y'}$ is a characteristic impedance.

Due to the skin effect, the series conductor resistance is frequency dependent. PF allows to model the frequency dependence using Frequency Polynomial Characteristic [5].

$$y(f_h) = (1-a) + a\left(\frac{f_h}{f_1}\right)^b \quad (3)$$

where the parameters a = 1 and b = 0,5. The line frequency dependent resistance is expressed

$$R'(f_h) = R' \cdot y(f_h) \quad (4)$$

This line model is valid for positive-, negative- and zero-sequence. The long-line effect is more significant for underground cables, due to higher values of shunt capacitances in comparison with overhead lines [8].

B. Transformers

The transformers are modelled by a T equivalent circuit. The parameters of the equivalent circuit are determined from the vector group, transformer ratio and the quantities computed from short-circuit and open-circuit measurements. Due to the fact that the natural resonant frequencies of transformers appear usually above 5 kHz [4] and the winding capacitances are relatively small compared to line capacitances, the winding capacitances are not included in calculations.

For positive- and negative-sequence, the equivalent model of transformer is shown in Fig. 4.

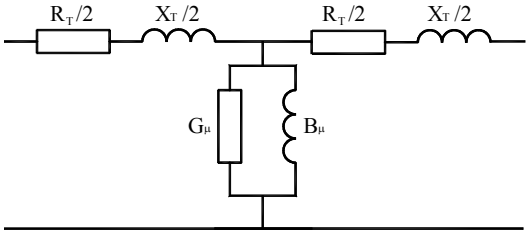

Fig. 4. The equivalent model of transformer for positive- and negative-sequence.

The equivalent transformer model for zero-sequence is dependent on the winding connections. Investigated distribution system consists of six transformers with Yy0 connection and two transformers with YNy0 connection. For Normal Operating Condition (NOC), one of the transformers operates with 60 kV neutral point compensated trough Petersen Coil (PC). Except the transformer grounded trough PC, the zero-sequence impedance for all other transformers approaches infinity (Yy0 winding connection blocks flow for zero-sequence currents [4]).

C. Synchronous machines

Because of the large number of small size CHP units, it would be difficult and very time-consuming to obtain all the necessary parameters for each particular CHP unit. Therefore, equivalent models for all CHP units connected to each 20 kV substation are created. The equivalent models are connected to 20 kV busbars trough 20/10 kV transformer adapted to equivalent generator rated apparent power. The unit parameters for synchronous generators are taken from Model A and referred to their rated power value. It is assumed, that all the generators are salient pole type. In Model B, the synchronous machine is represented for positive- and negative-sequence by the stator resistance R_{st} and average subtransient reactance value X''_{av} [7].

$$X''_{av} = \frac{X''_d + X''_q}{2} \quad (5)$$

$$Z_{sg} = y(f_h)R_{st} + jhX''_{av} \quad (6)$$

The frequency dependence of stator resistance is modelled using (3).

The synchronous machines block zero-sequence harmonic currents, because their stator windings are connected in delta or ungrounded. Therefore zero-sequence impedance is infinite.

D. Induction machines

In the investigated network, all the wind turbines are the fixed speed induction machines compensated with PFC capacitor banks [3]. In Model B, they are built as equivalent models installed to 0,7 kV busbar and connected trough 20/0,7 kV tranformers to 20 kV busbar in each distribution substation. The value of transformer rated apparent power and value of equivalent generator rated apparent power are equal. The reactive power consumed by induction generators is compensated by the PFC capacitor banks, which are connected to 0,7 kV busbar The unit rotor and stator parameters, synchronous and nominal speed values are taken from asynchronous generator equivalent in Model A. It is assumed that all the induction machines are built as squirell cage type. In Model B, the asynchronous machine is represented for positive and negative sequence by the stator resistance R_{st}, rotor resistance R_r dependent on the slip, rotor reactance X_{st} and stator reactance X_r [1]. The representation of induction machine is shown in Fig. 5.

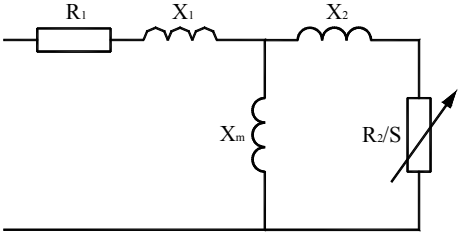

Fig. 5. The induction machine model.

The harmonic impedance is expressed as

$$Z_{ag} = R_1 + \frac{R_2}{S_h} + jh(X_1 + X_2) \quad (7)$$

S_h is apparent slip at the increased frequency

$$S_h = \frac{\pm h\omega_s - \omega_r}{\pm h\omega_s} \quad (8)$$

The plus sign is for positive-sequence and the minus sign is for negative-sequence.

Due to skin effect, the resistance is dependent on frequency by $y(f_h)$ formula, expressed in (3). The magnetizing branch is neglected, because all the parameters are taken with the rotor locked.

The induction machines do not provide a path for zero-sequence harmonic currents, because they are connected in delta or ungrounded wye [8].

E. Load models

The one single rule of determining load equivalents for harmonic analysis does not exist [6]. The derivation of harmonic resistance and reactance from given active P and reactive Q power flow will need additional information on the actual composition of the load. Power distribution companies should provide the information about participation for each type load in the system depending on the time of day. The domestic loads constitute not only the main element of the damping component, but may affect the resonance conditions at higher frequencies.

In Model B, a load model is represented as parallel impedance with passive (resistance R_2 and reactance X_2) and motive part (resistance R_1 and reactance X_1) [6]. Such representation is shown in Fig 6. These parameters are determined on the basis of load active power P and motor load fraction K.

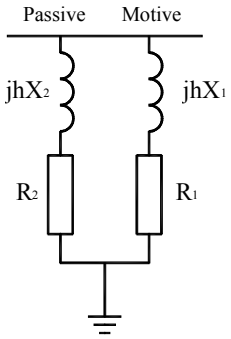

Fig. 6. Load model representation.

PF allows to model the loads by series resistance and reactance. Therefore, the load has been modelled by two separate impedances (passive and motive part).

$$R_2 = \frac{V^2}{(1-K)P} \tag{9}$$

$$X_1 = X_M \frac{V^2}{K_m K P} \tag{10}$$

$$R_1 = \frac{X_1}{K_3} \tag{11}$$

$$X_2 = 0{,}1R_2 \tag{12}$$

K_m is install factor (≈1,2), X_M is p.u. value of the motor locked rotor reactance expressed on the motor rating (≈0,2) and K_3 is effective quality factor of the motor circuit (≈8).

Modeling the power electronic loads is a more difficult problem, because besides being harmonic sources, these loads do not present a constant RLC configuration and their non-linear characteristics cannot fit within the linear harmonic equivalent model [1]. In the absence of detailed information the power electronic loads are neglected in the analysis.

V. The Comparison Of Model A And Model B

The magnitude and phase angle of the harmonic impedance for Model A and Model B is shown in Fig. 7. The harmonic calculation has been carried out for positive- and negative-sequence using *frequency sweep* option [5].

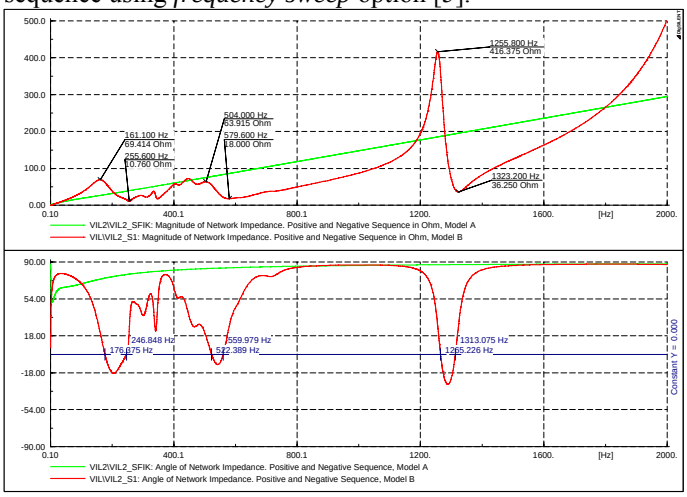

Fig. 7. Positive- and negative-sequence harmonic impedance for Model A and Model B.

The values of impedance magnitude for the most frequently appearing harmonic currents are presented in Table II. The discrepancy between values of impedance for Model A and B are significant. For instance, the discrepancy of impedance magnitude for 25th harmonic is above 100%.

TABLE II
IMPEDANCE MAGNITUDE FOR SELECTED HARMONIC ORDER

Harmonic order	Impedance magnitude	
	Model A	Model B
5	39,1Ω	13,3Ω
7	53,3Ω	18,5Ω
11	82,2Ω	28,4Ω
13	96,7Ω	26,4Ω
23	170,0Ω	142,3Ω
25	184,7Ω	397,7Ω

The curve of harmonic impedance magnitude for Model A is linear. The phase angle approaches 90°. In this case, resonance effects do not appear, because the model does not include any capacitances. All the system components are modelled by resistance and reactance, therefore the curve of harmonic impedance magnitude is linear.

Looking at the harmonic impedance for Model B, it can be seen, that in the frequency range from 80 Hz up to approx. 800 Hz significant variations of the harmonic amplitude and phase angle can be observed. It has been found out that these variations are related to the interaction between inductive system components and capacitance of PFC elements. Maximum and minimum values of harmonic impedance

magnitude and zero values for phase angle of harmonic impedance are not at the same frequency value. It means that for discussed frequency range, the main resonance for all system components does not appear. Fig. 8 shows the influence of installed PFC capacitor banks on harmonic impedance curve in mentioned frequency range. The reference curve is performed for all PFC capacitors connected to the system. In case of disconnection of PFC devices from wind turbines busbar or from 20 kV busbar, it can be observed the less number of resonances at lower frequency range compare to reference curve.

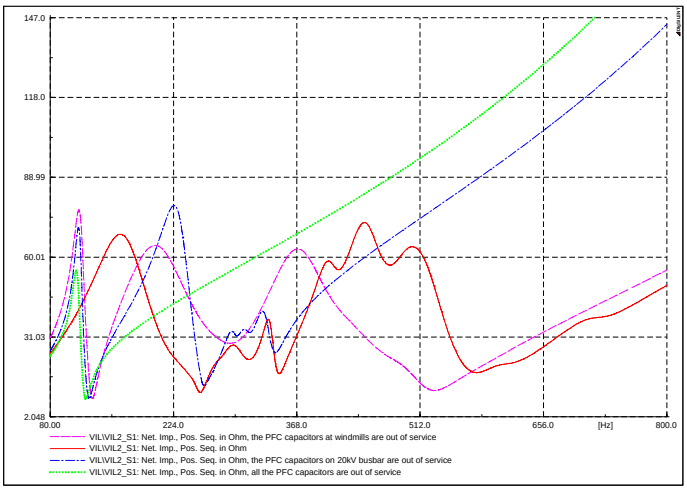

Fig. 8. The influence of installed PFC capacitors on harmonic impedance for Model B in low frequency range.

The second area consists of the resonance effects at frequencies: 1258,8 Hz (parallel resonance) and at 1323,2 Hz (series resonance). It has been revealed that it is determined by system components in one of the substations (AGG). In Fig. 9, the harmonic impedance curves for different values of reactive power of PFC capacitor connected and to 20 kV busbar are shown. If reactive power decreases, the considered resonance shifts towards the main resonance at higher frequency. The asynchronous machine equivalent includes low value of inductive reactance (in comparison with all of machine equivalent models). This inductance resonates with the PFC capacitor connected to the 20 kV busbar in the substation.

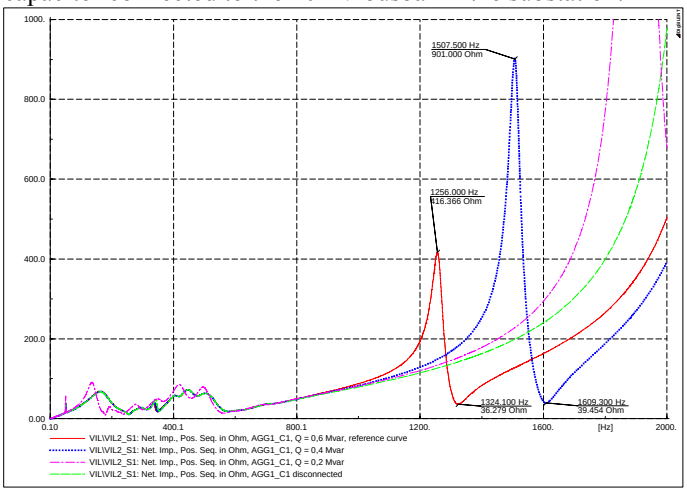

Fig. 9. The influence of PFC capacitor in AGG substation on harmonic impedance.

In the end of considered frequency range, close to 2 kHz, the trend to parallel resonance effect is observed. All the distribution system components (inductive and capacitive) resonate to each other. The resonance frequency is determined by the capacitance of 60kV lines, PFC devices and inductance of synchronous and asynchronous machines, transformers and loads.

The zero-sequence harmonic impedance for Model A and Model B is presented in the Fig. 10.

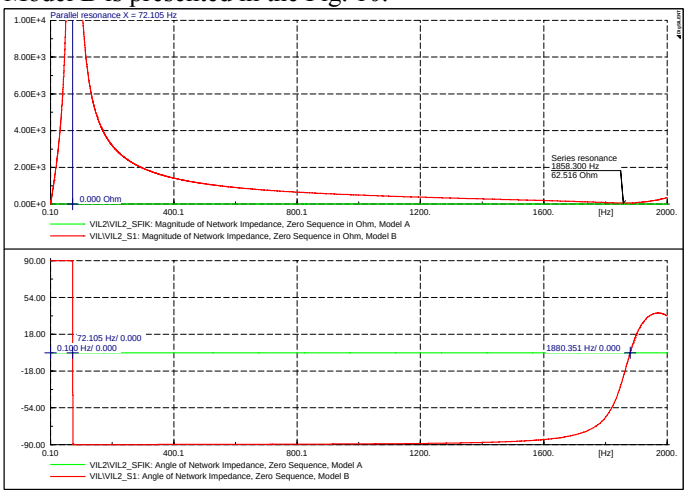

Fig. 10. Zero-sequence harmonic impedance for Model A and Model B.

Analyzing zero-sequence harmonic impedance for Model A, the impedance magnitude and angle equals zero, because the models of transformers do not include zero-sequence parameters and the both windings of transformers are wye connected with directly grounded neutral point. Therefore, the way for zero-sequence flow has zero value of impedance.

For Model B, two resonances are observed. The parallel resonance appears at 72,105 Hz frequency. It is effect of a resonance between the inductance of PC and capacitance of 60 kV lines. The inductance of PC is tuned to 50 Hz frequency.

$$L_{PC} = \frac{1}{3\omega^2 C_0} \tag{13}$$

The distribution network should not operate in overcompensated condition. Therefore the reactance value of PC is lower in comparison of total capacitive reactance of lines. This is the reason that parallel resonance appears above 50 Hz frequency. The amplitude of harmonic impedance approaches infinity, because the resistance of PC used in Model B equals zero. The series resonance at 1880,3 Hz frequency is observed. It is determined by zero sequence (inductive and capacitive) reactances of 60 kV lines.

VI. Modification Of Model A

The curve of positive- and negative-sequence harmonic impedance for Model A and Model B are not close. The Model A does not include the resonance effects, because it

does not consist capacitance components. The discrepancy of impedance magnitude for Model A and Model B is significant. Besides, Model A does not take the impedance for zero-sequence into consideration. To accomplish harmonic impedance curve close to Model B, the modification of Model A for all sequences has been made. After the corrections are applied to this model, Model A can be used for detailed harmonic analysis, for instance on transmission system level as more accurate distribution feeder equivalent. The substitute capacitance for distribution system is modelled by the 60 kV line representation connected to the main 60 kV busbar and operated in no-load state. The line model includes only shunt capacitance parameters. The values of series resistance and reactance should be close to zero. The line capacitance is modelled separately for positive-, negative- and for zero-sequence. It is possible to use shunt capacitors instead, but then it would be necessary to filter the zero sequence (for example, the shunt capacitor should be also connected to the wye neutral point of transformer). For this approach, the use of two components would be needed. First, for positive- and negative-sequence and second, for zero-sequence. The susceptance for the 60 kV substitute line model can be expressed

$$B_{SL(1,2)} = k_{L(1,2)} \cdot B_{L(1,2)} \tag{14}$$

$$B_{SL(0)} = \frac{B_{L(0)}}{k_{L(0)}} \tag{15}$$

$B_{L(1,2)}$ and $B_{L(0)}$ are positive-, negative- and zero-sequence total susceptance for all the 60 kV lines in investigated distribution system. Correction factors $k_{L(1,2)}$ and $k_{L(0)}$ for positive-, negative- and zero-sequence are dependent on the type and the network structure. Minimum value of average discrepancy for $k_{L(1,2)}$ = 0,26 and $k_{L(0)}$ = 0,7 was obtained. At this moment, it is difficult to state if the calculated factor is correct for each of distribution feeders. This problem should be analyzed for selected distribution networks.

Harmonic impedance curve for Model B and modified and unmodified Model A is presented in Fig. 11.

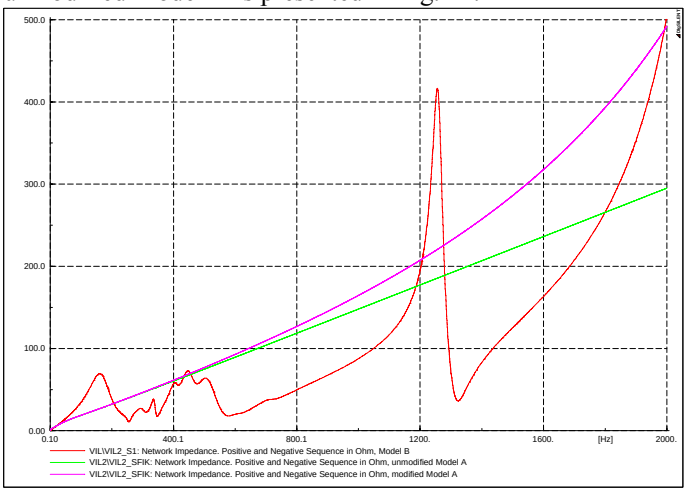

Fig. 11. The positive- and negative-sequence impedance magnitude for Model B, unmodified Model A and modified Model A.

Looking at Fig. 11, the main resonance effect (above 2 kHz) for modified Model A is observed. It is determined by total capacitance and inductance of all components in Model A. Modified harmonic impedance curve for Model A is close to harmonic impedance curve for Model B only at higher frequencies (2 kHz). For lower values of frequency, the modification of Model A gives worse results compared to unmodified Model A. The discrepancy between impedance magnitude for unmodified and modified Model A and impedance magnitude for Model B is shown in Fig. 12.

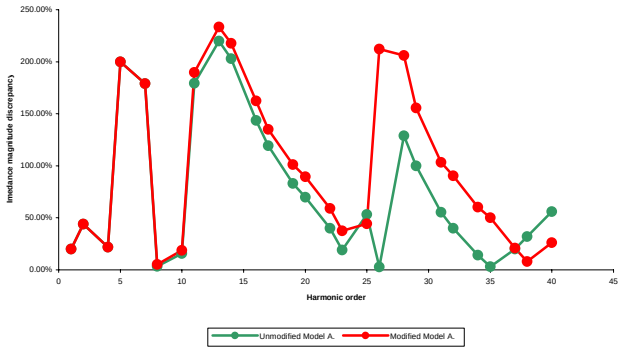

Fig. 12. The comparison of discrepancy between positive- and negative-sequence impedance magnitude for investigated cases.

Analyzing the modification test of Model A for positive- and negative-sequence, it can be concluded, that Model A should not be corrected in this way. The value of harmonic impedance discrepancy at significant frequency range for harmonic analysis (up to 25th harmonic) is higher in comparison of unmodified Model A.

In case of modification of Model A for zero-sequence, it is necessary to model the PC connected to the neutral point of wye winding in one of transformers. The value of PC inductance is the same, like in Model B. The resonance frequency is very close to the frequency for Model B (72,105 Hz). Except the lines capacitance and PC, the rest of system components should not include the flow for zero sequence. Therefore, the load model and the 60 kV side of second transformer should be ungrounded wye or delta connected. The comparison of harmonic impedance magnitude for Model B and modified on the basis of above-mentioned principles Model A is presented in Fig. 13.

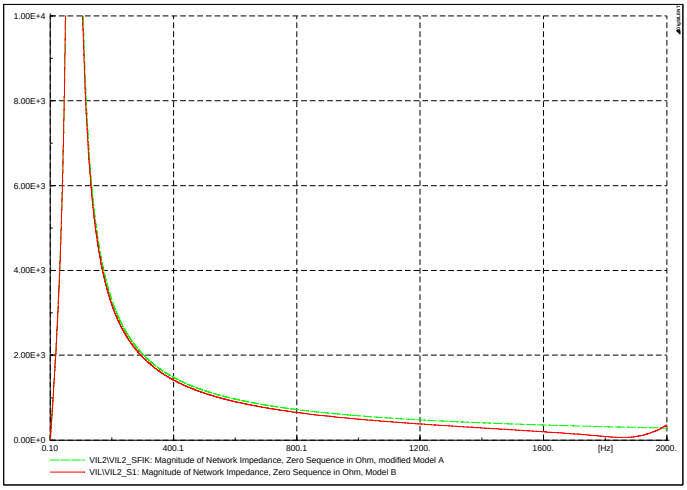

Fig. 13. Zero-sequence impedance magnitude for Model A and modified Model B.

Looking at Fig. 14, the discrepancy values for zero-sequence increase along with the frequency.

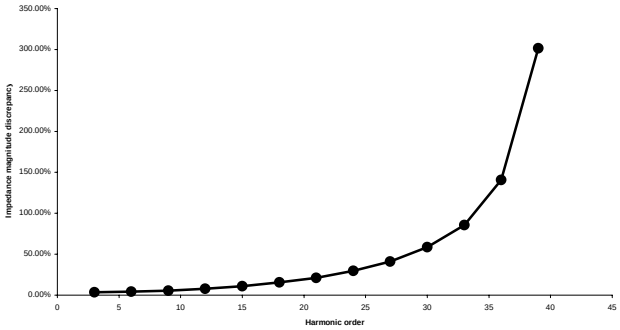

Fig. 14. The discrepancy of zero-sequence impedance magnitude between modified Model A and Model B.

For significant harmonic order (3, 9, 15, 21) the discrepancy between impedance magnitude for Model B and corrected Model A is relatively small. The most important thing for zero sequence analyzing is correct neutral system representation. For 60 kV network, the only flow for zero sequence currents is through the capacitance of 60 kV lines and PC. These system components cause the resonance effect a little bit above 50 Hz, due to the lower value of inductive reactance for PC than the value of capacitive reactance for 60kV overhead and cable lines.

VII. Conclusions

This paper discussed and analyzed problems related to harmonic calculations in PF software. In closing of the paper, the following conclusions can be drawn:

- The detailed distribution system model (Model B) was created for harmonic analysis. Each of the system elements was created basis of the state of the art calculations of the harmonic analysis literature. PF software makes possible to model system components in harmonic domain in simple way. Model B was used as reference representation for harmonic studies. The most accurate verification of Model A is to make a measurement. Besides, more accurate system model (Model B) represents real harmonic impedance to a larger extent than Model A
- Using *frequency sweep* function in PF, the harmonic impedance (magnitude and angle) was computed for Model A and B and compared. For all sequences, harmonic impedance curves for Model A and Model B are not close (the discrepancy is significant). System components are not modelled for zero-sequence in Model A Therefore, applying Model A for harmonic analysis, it is necessary to take into account big errors in calculation.
- The modification of Model A makes a sense for only zero-sequence. For significant harmonic frequency range, the results are satisfied. The modification test for positive- and negative-sequence has not been successful. The results have been worse compared to unmodified Model A. It is very difficult to model in simple way resonance effects determined by inductive and capacitive components installed in 60/20 kV substations and below. Therefore, the paper suggests the modification of Model A for zero-sequence only.

VIII. Acknowledgment

The authors wish to gratefully acknowledge the contributions of J. Bak-Jensen from Himmerlands Elforsying and H. Abildgaard from Eltra for help to get necessary data of investigated distribution power system.

IX. References

[1] J. Arrillaga, B. C. Smith, N. R. Watson, A.R. Wood, *Power System Harmonic Analysis*, Chicester: John Wiley & Sons, 1997, p. 46, 104.
[2] S. Bolkowski, *Teoria Obwodów Elektrycznych*, Warszawa: WNT, 1997, p. 146.
[3] N. Jenkins, R. Allan, P. Crossley, D. Kirschen, G. Srbac, *Embedded Generation*, London: The Institution of Electrical Engineers, 2000, p.37.
[4] S. Kujszczyk, Elektroenergetyczne Układy Przesyłowe, Warszawa: WNT, 1997, p. 131.
[5] PowerFactory Users Manual, ver. 13.1, 2005.
[6] Task Force on Harmonic Modeling and Simulation, IEEE Power Eng. Soc. T&D Committee, "Impact of Aggregate Linear Load Modeling on Harmonic Analysis: A Comparison of Common Practice and Analytical Models," in *IEEE Transactions on Power Delivery*, Vol. 18, No. 2, April 2003, pp. 625-630.
[7] A. C. Williamson: "The Effects of System Harmonics upon Machines," in *International Conference on Harmonics in Power Systems*, UMIST, 1981.
[8] W. Xu, "Component Modeling Issues for Power Quality Assessment," in *IEEE Power Engineering Review*, November 2001, pp. 12-15.

X. Biographies

Jacek Wasilewski was born in Elblag, Poland in 1981. He received the M.Sc. degree in electrical engineering from Warsaw University of Technology in 2005. He carried out the semester project as a M.Sc. student at the Institute of Energy Technology, Aalborg University. He manages currently the electrical systems design office.

Wojciech Wiechowski was born in Warsaw, Poland in 1976. He received the M.Sc. degree in electrical engineering from Warsaw University of Technology in 2001. From 2002 to 2003 he worked for HVDC SwePol Link as a technical specialist. Since 2003 he has been employed at the Institute of Energy Technology, Aalborg University, where he is currently a PhD candidate. His interests include EMC, modeling of power system components and harmonic measurements in high voltage systems.

Claus Leth Bak was born in Ugelbølle near Århus, Denmark, on April 13, 1965. He received the B.Sc (electrical power eng.) degree in 1992 from the engineering college in Århus and the M.Sc. (electrical power eng.) degree in

1994 from institute of energy technology, Aalborg University. From 1994 to 1999 he was working at Nordjyllandsværket power plant with planning, design operation and maintenance of 150 and 60 kV substations and relay protection. He was employed as an assistant professor at the dept. Of power systems and high voltage, institute of energy technology, Aalborg University in September 1999 and is currently holding a position as an Associate Professor. Main research areas are: High voltage engineering with focus on gaseous discharges and overhead line corona, relay protection with focus on power system simulation transient testing of relays.